Diversity of visual projections in vertebrates

Robin Vigouroux

▶ **To cite this version:**

Robin Vigouroux. Diversity of visual projections in vertebrates. Neurobiology. Sorbonne Université, 2020. English. NNT : 2020SORUS363 . tel-03376769

HAL Id: tel-03376769
https://theses.hal.science/tel-03376769

Submitted on 13 Oct 2021

HAL is a multi-disciplinary open access archive for the deposit and dissemination of scientific research documents, whether they are published or not. The documents may come from teaching and research institutions in France or abroad, or from public or private research centers.

L'archive ouverte pluridisciplinaire **HAL**, est destinée au dépôt et à la diffusion de documents scientifiques de niveau recherche, publiés ou non, émanant des établissements d'enseignement et de recherche français ou étrangers, des laboratoires publics ou privés.

Sorbonne Université

ED 158 – Ecole doctorale Cerveau, Cognition, Comportement

Institut de la Vision

SU UM80, Inserm U968, CNRS UMR7210

Diversity of visual projections in vertebrates

Doctoral Thesis in Neuroscience

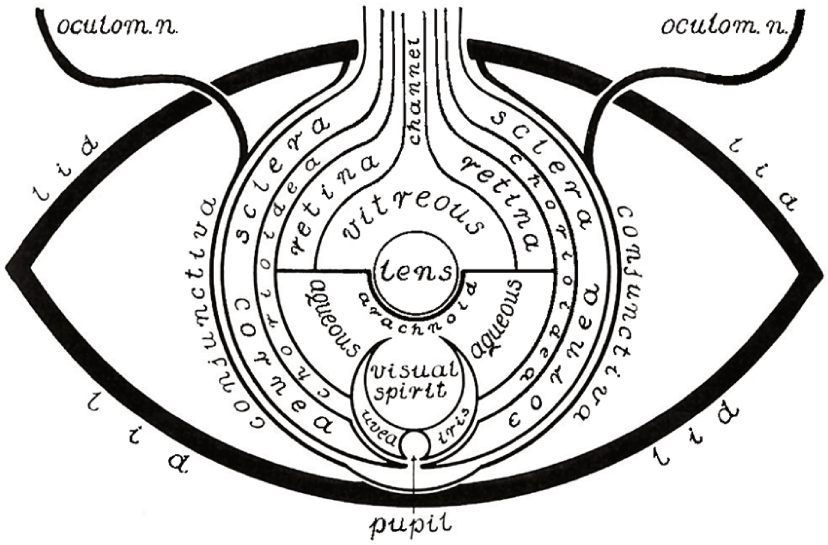

Presented by **Robin VIGOUROUX**

Publicly presented and defended on the 28th of September 2020

In front of a jury composed of :

Dr. Sylvie Rétaux	Reviewer
Dr. Robert Hindges	Reviewer
Dr. Eloisa Herrera	Examiner
Dr. Claire Wyart	Examiner
Dr. Kim Nguyen-Ba-Charvet	Advisor
Dr. Alain Chédotal	Examiner

Except where otherwise noted, this work is licensed under
http://creativecommons.org/licenses/by-nc-nd/3.0/

Remerciements

Une thèse est un long chemin construit, certes, de sciences (beaucoup de sciences) mais également d'expériences humaines inoubliables. Les remerciements sont toujours trop courts et certaines personnes ne seront pas citées, mais je tiens à dire Merci. Merci à toutes celles et ceux que j'ai croisés plus ou moins brièvement au cours de ce chemin. L'arrivée sain et sauf n'aurait certainement pas été possible sans vous.

First and foremost, I would like to thank my thesis committee composed of such well recognized experts in developmental neuroscience. I would like to thank Robert Hindges and Sylvie Rétaux who accepted to be reviewers for my thesis. I am extremely grateful for the precise, thorough, and positive feedback you have provided on this work. It has undoubtedly improved my manuscript. I would next like to thank Eloisa Herrera and Claire Wyart for accepting to be examiners for my defense. I believe that your expertise will add a tremendous depth to my thesis discussion.

Je tiens à remercier Patricia Gaspar et Muriel Perron. J'ai eu la chance que vous acceptiez de faire partie de mon comité de suivi de thèse au cours de ces quatre dernières années. Vos nombreux avis et conseils ont enrichi mes projets scientifiques et ont su me motiver d'année en année. Je vous en suis très reconnaissant.

Il est également important pour moi de remercier Professeur José-Alain Sahel. Vous m'avez accueilli au sein de l'Institut de la Vision : cet environnement unique à l'interface entre les sciences fondamentales et la clinique qui a grandement joué dans ma décision de devenir médecin-chercheur. Je tiens tout particulièrement à vous remercier de m'avoir accordé du temps pour discuter de ma reconversion en médecine. Je tâcherais de suivre vos conseils pour, je l'espère, suivre vos pas de médecin-chercheur.

Il est temps désormais de dire un immense merci à l'ensemble de l'équipe 1, à commencer par Alain. Il y a maintenant quatre ans, tu me donnais l'opportunité d'intégrer ton équipe. Ton enthousiasme et ton optimisme scientifique m'ont permis de mettre en place de nombreuses collaborations, d'assister à des colloques inoubliables et de m'épanouir dans le métier de chercheur. J'ai appris à tes côtés une rigueur scientifique inégalable que je mettrais à profit dans ma future carrière. Je souhaite aussi remercier ma directrice de thèse, Kim qui m'a encadré pendant ces quatre années. Tu as su me faire confiance et tu m'as accordé la liberté scientifique dont je rêvais. Tu as aussi su me mettre les limites nécessaires lorsque ma curiosité m'emmenait trop loin. Grâce à toi, je présente un travail riche et abouti. Manuela, ta franchise et ta sincérité font de toi une personne absolument géniale. J'apprécie ta vision de la science et ton plein investissement dans chaque projet que tu entreprends (dans ta recherche comme dans la vie). Pour tout ça, et pour ce dernier déjeuner au Marché d'Aligre, merci à toi. Un grand merci à Yvrick aussi. Nous avons partagé les bons mais comme les mauvais moments ces quatre années. Ton humour a toujours su me donner le sourire, tu as été un compagnon d'équipe en or ! Caro, bien que nous nous sommes que croisés, ce sont nos conversations sur l'enseignement qui m'ont poussé à enseigner pendant ma thèse. Quentin, nous sommes arrivés au même moment dans le laboratoire. J'ai adoré te voir évoluer au fil des années, je te souhaite de repousser tes limites et t'épanouir dans ce labo. Merci Elena, ton sourire et ta bonne

humeur (pour l'instant) m'ont fait beaucoup de bien pendant la rédaction de ma thèse. Merci à vous Anaïs, Ali, Chad et Edwin, même si nous ne nous connaissons que depuis peu, je vous souhaite que la force du « Blaze ».

Je tiens vraiment à remercier l'ensemble du personnel animalier. Merci à toi Alexis, c'est ton travail titanesque qui a permis à ma thèse d'avancer. Merci à vous Julie, Quénol, et Manu, pour votre aide avec les ERG, fonds d'œil, OKR, et j'en passe. Vous n'avez jamais hésité à me prêter main forte (même si cela demandait de transporter tout le matériel de fond d'œil depuis Jussieu sous la pluie). Vos accueils chaleureux à l'entrée de l'animalerie me manqueront.

Merci à toi Stéphane, j'ai apprécié nos nombreuses soirées de « bricolage » entre chambre d'imagerie maison et découverte de LED chez Thorlabs.

Mes travaux de thèse m'ont permis de collaborer avec plusieurs scientifiques à Paris. Je souhaite tout particulièrement remercier Fillipo Del Bene. Grâce à toi, ma thèse a pris un tournant tout à fait inattendu. Nous nous sommes plongés dans la littérature à la recherche de poissons à la vision 3D. Je garderais toujours un beau souvenir de nos multiples échanges scientifiques. Un jour, je te promets de goûter cette fameuse pizza Rossini ! Dans l'équipe de Fillipo, j'ai eu la chance de rencontrer Juliette qui a commencé cette collaboration avec moi. Les débuts étaient frustrants mais tu as gardé le cap et le projet a pu avancer. Grace à toi et à Karine, aujourd'hui c'est une partie essentielle de mon travail de thèse. Effectivement, Karine, je te remercie énormément pour notre collaboration qui a si rapidement porté ses fruits, nous formions une très belle équipe ! Merci à vous Shahad et Marion pour les voyages nocturnes où nous allions récupérer des zébras et pour vos précieux conseils « poisson ». Je remercie aussi Jérôme Roger pour une collaboration réussie et pour son aide précieuse. Enfin, je me dois de dire un grand merci à Isabelle Dusart. Tu n'as pas hésité un seul instant pour nous apporter ton aide lorsque nous voulions analyser les mutants Kanga. Mes travaux de thèse en ont été grandement enrichis.

Pendant ma thèse qui porte, pour ceux qui ne liront que les remerciements, sur l'évolution des projections visuelles, j'ai observé un lien entre l'Institut de la Vision et ma recherche. L'Institut est semblable à tout écosystème et peut donc se vanter de posséder de nombreux microenvironnements. Ces-derniers ont chacun leurs propres caractéristiques et leurs propres espèces.

Premier microenvironnement, et pas des moindres : le groupe cafétéria. J'ai partagé des déjeuners gargantuesques avec Quentin (le petit) et Quentin (le grand), Morgane, Antoine, Luisa, Solène, Elora, Céline, et Abdallah. Vous étiez mes yeux (quand je ne voyais pas l'entrée chaude du jour) et mes oreilles (quand je découvrais l'horreur de la pêche industrielle). Merci pour ces interludes toujours divertissants.

Il y a ensuite le « lunch group », probablement le microenvironnement le plus diverse, regroupant stagiaires, thésards, techniciens, et autres. Merci à vous de m'avoir supporté pendant mes anecdotes *Sodebo* interminable. Pendant ces déjeuners, Michael nous faisait part de ses « combines » incontournables et de ses découvertes culinaires. Je n'oublierais jamais les jets de dés de Marion qui nous ont sauvés plus d'une fois lors de nos longues parties confinées de donjons et dragons. Heureusement qu'il y avait Sarah aussi pour nous unir. Merci à toi pour ta coolitude éternelle. J'adore

la vision que tu as de l'amitié et je suis chanceux de te compter parmi mes proches amies. Merci à vous Gabriel, Alice, Oriol, et tous les autres !

Les rencontres fortuites dans les couloirs de l'institut constituent un microenvironnement en mouvement continu, imprévisible mais agréable. Merci notamment à toi Fiona. Il est difficile de pas être sensible à ton sourire et à ta bonne humeur quotidienne. J'ai beaucoup aimé nos petits cafés autour de Pastei de nata. Léa, j'ai beaucoup apprécié ton humour décalé et nos sorties culturelles. J'espère que nous aurons d'autres occasions de nous déprimer au Centre Pompidou.

Le week-end est un environnement tout particulier qui permettait de resserrer les liens entre les stressé(e)s, les acharné(e)s et les amateurs du travail le dimanche. Je pense tout particulièrement à Juan, un brillant post-doc du labo. Je n'oublierais jamais nos interminables conversations sur la Nétrine ! Ton excellence scientifique est un réel exemple pour moi. Nacim, il est tout naturel que je te cite dans cette fameuse équipe du week-end. Tu as cru en moi dès le premier jour et tu as vu un potentiel dont je n'étais moi-même pas au courant.

Bien évidemment, l'environnement dans lequel je me sentais le plus à l'aise et que j'ai le plus investi est le bureau. J'ai eu le bonheur de le partager avec des gens incroyables. Un grand merci à vous mes collègues de bureau : Eljo, Solène, Giuliana, Sergi, François et Franck. En arrivant j'ai pris la place de François, qui s'en allait. Quelle pression que de reprendre ton flambeau! Solène, tu m'as vite conquis, avec tes sublimes chaussons notamment. Pour ce qui est de Franck, je ne mesure peut-être pas encore entièrement la chance que j'ai eue de te rencontrer. Je ne te remercierais jamais assez pour ton écoute bienveillante et tes précieux conseils. Tu as été comme un grand frère dans cette aventure. Sergi, on a vécu nos thèses côte à côte. Tu adorais partager ta recherche avec tout le monde et tu rendais à la science un caractère chaleureux, presque intime. Tu étais là dans les moments de joie (comme danser *la macarena* avec Rüdiger Klein) comme dans les moments qu'on essaie encore d'oublier (ces fameuses 8h de train dans les alpes autrichiennes).

La vie à l'Institut ne cesse de se renouveler et de nouvelles espèces apparaissent régulièrement. Vers la fin de ma thèse, une vague de personnes géniales a déferlé sur la rue Moreau. Sandy, je t'ai d'abord cru timide et calme… mais que les apparences peuvent être trompeuses ! J'espère que nous pourrons entamer l'écriture de notre projet « le Rhinocéros blanc » très bientôt. Il est grand temps de parler de Johann (non, tu n'auras pas ton propre paragraphe) ! Je t'ai d'abord rencontré dans ce fameux « lunch group ». Tu enrichis quotidiennement ma culture, surtout féministe, il faut le dire. J'aurais beaucoup aimé mettre une citation de Kid Cudi pour t'exprimer mon éternelle reconnaissance, mais malheureusement je ne les connais pas par coeur. Ce sera à la place un simple merci. Merci pour ces soirées passées à refaire la science et le monde autour d'un verre de *Frappato*, et ces autres soirées passées à jouer au foot avec des voitures volantes. Allez, je sais bien que je te l'ai trop dit, mais je te le dis quand même, je t'aime.

Comme dans tout écosystème, l'ensemble de ces microenvironnements intéragit. A l'Institut, la symbiose se faisait autour d'un verre. *Le Gamin* était notre phare dans la nuit noire, notre repère. Nous y avons relâché la pression, ri, partagé nos frustrations d'expériences ratées, et même célébré des moments de vie. Merci à vous Imène et Mika pour votre accueil souriant et chaleureux.

Marion. Mesurer l'impact que tu as eu sur ma vie en si peu de temps est difficile. Tu es arrivée à une période charnière de ma vie, où les doutes étaient constants. Entre ma candidature en médecine, mes peurs professionnelles, et bien sûr ma thèse (confinés ensemble pendant 2 mois), tu as su m'aider à naviguer à travers chacun de ces tournants avec assurance et détermination. Ton impact se mesure jusque dans ce travail de thèse, où chaque recoin y reflète ton génie. Merci à toi pour tout. Nous formons une belle équipe tous les deux, et j'espère pouvoir un jour te rendre la pareille.

Je voudrais finir en remerciant ma famille. Il est difficile pour moi d'écrire ce paragraphe. J'aimerais vous dire tant de choses, j'aimerais que vous sachiez à quel point je vous suis reconnaissant. Merci surtout pour votre patience et votre compréhension. Vous m'avez toujours soutenu et même encouragé à aller plus loin. Ces dernières années, je n'ai pris que très peu de congés mais vous l'avez accepté et avez rendu chacun de ces moments inoubliables (je pense à Uzès, Venise ou encore à la Haye). Sachez que cette thèse n'aurait jamais vu le jour sans votre soutien sans failles et votre amour sans bornes. Ce travail c'est un peu le vôtre aussi. Cela fait maintenant très longtemps que vous êtes là, assis aux premières loges du spectacle de mes aventures académiques. Il me doit tout de même de vous dire que le rideau ne risque pas de se fermer tout de suite et que vous n'avez pas encore fini d'assister à mes « graduations ». Vous me suivez toujours, on repart pour un tour? Cette fois, direction médecine !

Merci à vous tous, je vous embrasse.

Table of contents

Table of Figures

Abbreviation list

ALCAM	Activated leukocyte adhesion molecule
AOT-IF	Inferior fasciculus of the accessory optic tract
AOT-SF	Superior fasciculus of the accessory optic tract
AOS	Accessory optic system
Ast	Astray
BDA	Biotin dextran amine
BMP	Bone morphogenic protein
Boc	Brother of Cdon
cAMP	Cyclic adenosine monophosphate
Cbln	Cerebellin
Cdh3	Cadherin 3
Cdh6	Cadherin 6
CF	Choroid fissure
CMZ	Ciliary margin zone
Cntn4	Contactin 4
CTB	Cholera toxin β subunit
CSPG	Chondroitin sulfate proteoglycan
Dcc	Deleted in colorectal cancer
dKO	Double knock out
dLGN	Dorsal lateral geniculate nucleus
dMTN	Dorsal terminal nucleus
DR	Dependence receptor
Draxin	Dorsal repulsive guidance molecule
DRD4	Dopamine receptor 4
DTN	Dorsal terminal nucleus
EC	Endothelial cell
ECM	Extracellular matrix
EdU	5-ethynyl-2'-deoxyuridine
Eph	Erythropoietin-producing hepatocellular carcinoma
ES	Embryonic stem cells
FoxD1	Forkhead box d1
FoxG1	Forkhead box g1
FN	Fibronectin type III
FP	Floor plate
GFAP	Glial fibrillary acidic protein
GFP	Green fluorescent protein
HEK	Human embryonic kidney

Hoxd10	Homeobox d10
HRP	Horseradish peroxidase
Ig	Immunoglobulin
IGL	Inner geniculate leaflet
ipRGC	Intrinsically photosensitive retinal ganglion cell
IRP	Ipsilateral retinal projections
ITN	Intertectal neuron
L-DOPA	L-3,4-dihydroxyphenylalanine
LGN	Lateral geniculate nucleus
LTN	Lateral terminal nucleus
MTN	Medial terminal nucleus
Mya	Million years ago
Nell2	Neural epidermal growth factor like-2
Nkx2	NK homeobox 2
NOT	Nucleus of the optic tract
NrCAM	Neural cell adhesion molecule
Nrp1	Neuropilin 1
Ntn1	Netrin-1
OC	Optic chiasm
OFL	Optic fiber layer
OKR	Optokinetic response
ON	Optic nerve
OPN	Olivary pretectal nucleus
OS	Optic stalk
OT	Optic tract
PIP2	Phosphatidylinositol 4,5-biphosphate
POM	Periocular mesenchyme
RC2	Radial-glia cell marker 2
RGC	Retinal ganglion cell
RITC	Rhodamine isothiocyanate
Robo	Roundabout
RPC	Retinal progenitor cell
RPE	Retinal pigment epithelium
SC	Superior colliculus
SCN	Suprachiasmatic nucleus
SDF	Stromal cell-derived factor
Sema	Semaphorin
Sfrp	Secreted frizzled related protein
Shh	Sonic hedgehog
SPIG1	SPARC-related protein containing immunoglobulin domains

SSEA	Stage specific embryonic antigen 1
Ten-m/Odz	Teneurin
tKO	Triple knock out
Vax	Ventral homeobox protein
Vegf	Vascular endothelial growth factor
vLGN	Ventral lateral geniculate nucleus
vMTN	Ventral medial terminal nucleus
VT	Ventro-temporal
WGA	Wheat germ agglutinin
Zic	Zinc finger protein
3D	Three dimensional
3DISCO	Three dimensional imaging of solvent-cleared organs
5HT	Serotonin

Introduction

1.1 An Introduction to the Organization Of The Visual System

Hippocrates (460-377$_{B.C.}$), the “father of medicine”, understood that the primary organ for vision was the eye, however he only had very brief accounts of the structure which he described as a series of layers called tunics. The first real description of the eye is attributed to the drawings of the Greek anatomist Heróphilos (344-320$_{B.C.}$) and their interpretation by the roman anatomist Galen of Pérgamos (Galen, 129-201$_{A.D.}$) (Polyak, 1957). Galen distinguished the retinal tunics in a series of anatomical structures, starting from the outermost layer: the cornea (horn-like tunic) a transparent avascular structure allowing light to enter the eye; the sclera (white tunic) an opaque tough protective layer; the vascular choroid (chorion-like tunic) a nutritive organ for the retina; the iris (grape-like tunic) permits light to enter the eye; the lens (crystalline-like tunic); and the retina (net-like tunic) a vascularized nervous tissue. Although anatomically identical to our current understanding of these structures, Heróphilos and Galen thought the lens was the photosensitive organ of the eye and that the highly vascularized structures such as the choroid and the retina served as nourishment to the lens. This notion remained relatively untouched until the swiss anatomist, Felix Platter (1536-1614) described the lens as a collector of light for the true photo-sensitive organ: the retina (Polyak, 1957). The development of compound microscopes allowed several anatomists, such as the Dutch Antoni van Leeuwenhoek (1632-1723) and the German Max Schultze (1825-1874), to further show that the photosensitive units within the retina were the photoreceptor cells rods and cones (Polyak, 1957).

At the turn of the twentieth century, the advances in histological methods gave great insights into the organization of the cellular networks within the retina. Using either methylene bleu *in vivo* (Ehrlich stain) or weak silver nitrate solution on specimens previously fixed with a combination of potassium dichromate and osmium tetroxide (Golgi stain), S. Ramón y Cajal, was able to observe isolated neuronal cells and all their ramifications in the retina of infra-primate vertebrates (Ramón y Cajal, 1892). S. Ramón y Cajal showed that the retina was composed of three distinct layers with the rod and cone photoreceptors located at the peripheral-most layer. The electric signal is transduced from the photoreceptors to the bipolar cells acting as a relay to the Retinal Ganglion Cells (RGCs) that transmit the signal along their axons into the optic nerve and towards the brain (Ramón y Cajal, 1892). In addition, S. Ramón y Cajal,

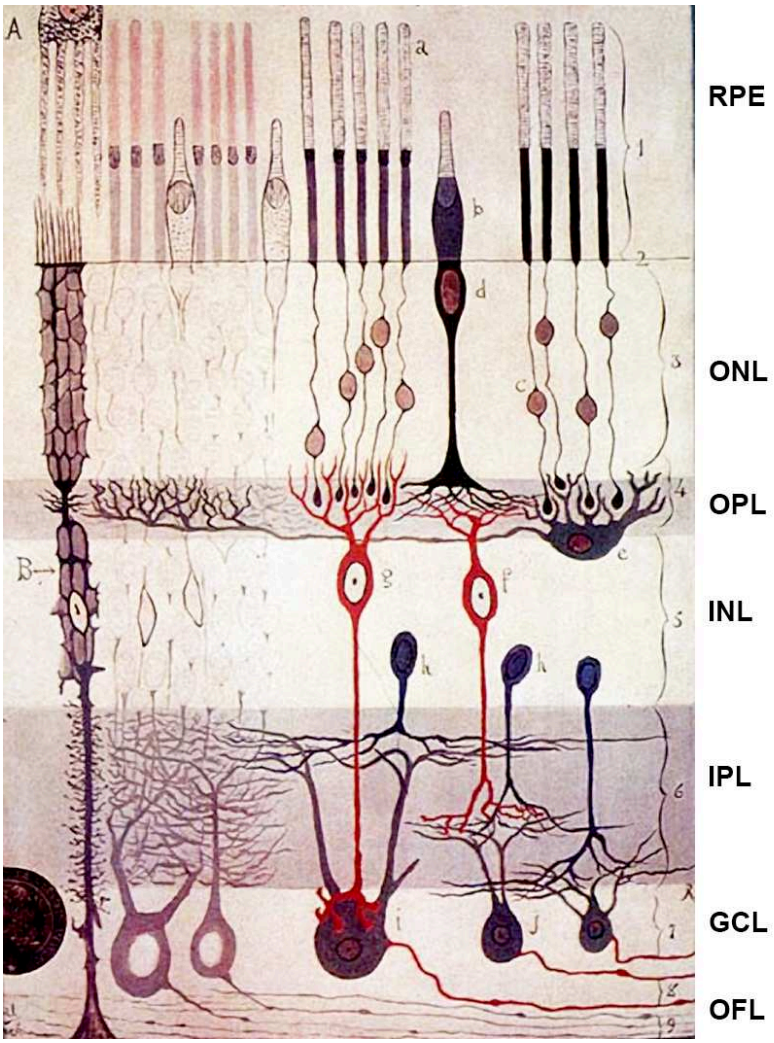

Figure 1 – The mammalian retina. Drawing made by Ramon y cajal showing the structure of the adult mammalian retina. All retinal cell types and layers are highlighted. At the most apical side, A, is the outer nuclear layer composed of the photoreceptors rods (low wavelength) and cones (high wavelength). The photoreceptors relay their signal to the bipolar cells (Red). Their signal is modulated by the horizontal cells (interneurons) in the outer plexiform layer. Bipolar cells in turn relay their signal to retinal ganglion cells in the ganglion cell layer in the inner plexiform layer. This signal is modulated by interneurons residing in the inner nuclear layer, the amacrine cells. RPE = retinal pigment epithelium; ONL = outer nuclear layer; OPL = outer plexiform layer; INL = inner nuclear layer; IPL = inner plexiform layer; GCL = ganglion cell layer; OFL = outer fiber layer.

described “associative” cells dispersed in the retina that he called horizontal and amacrine cells (Ramón y Cajal, 1892).

To this day, five classes of neurons and one type of glia have been identified in the vertebrate retina: The Müller glia that provide structure and homeostasis; the photoreceptors that detect light; horizontal, bipolar, and amacrine cells that process the signal from photoreceptors; and RGCs that relay the visual signal from the retina to the brain via the optic nerve (ON) (Figure 1; Cepko, 2014; Sanes and Masland, 2015; Seabrook et al., 2017). Each class of neuron can be further divided into certain types depending on a specific function, morphology and gene expressions. In mice, photoreceptors can be divided into three types. In mice, the most prominent type (90% or retinal cells) are the rods (Jeon et al., 1998) and there are two types of cone photoreceptors. Recent data shows that in mice there are two types of horizontal cells, fifteen types of bipolar cells (Shekhar et al., 2016), and sixty-three types of amacrine cells (Yan et al., 2020). The sole output of the retina, the RGCs, are divided into forty-six types in the mouse retina (Tran et al., 2019). To date with the use of single-cell RNA sequencing and electrophysiological recordings in mice, the vast diversity of retinal cell types has been estimated to harbor approximately 140 different subtypes of neurons (Yan et al., 2020).

As initially described by S. Ramón y Cajal (Ramón y Cajal, 1894), the retina is divided into three nuclear layers. The outer nuclear layer is composed of the somas of photoreceptor cells rods and cones. Both rods and cones project their inner and outer segments (photo-sensitive extension) apically towards the Retinal Pigment Epithelium (RPE) (Dhande and Huberman, 2014). Rods and cones differ in spectral sensitivities, rods are dark-adapted (scotopic) whereas cones are light-adapted (photopic, green or blue). They extend their projections towards the inner nuclear layer where they relay their signal. The inner nuclear layer is composed of what S. Ramón y Cajal called the “association cells”, namely, the horizontal, the amacrine, and the bipolar cells that together process and transmit the light signal from photoreceptors to the RGCs. This can allow for the extraction of many visual features such as contrast and movement. The nuclei of Muller glia and displaced RGGs also reside in this layer. The inner-most nuclear layer, the retinal ganglion cell layer is composed largely of RGC axons that together make up the ON. Two synaptic layers connect these layers. The outer

plexiform layer, between the outer and inner nuclear layer, is the zone of synaptic contact between photoreceptor cells, horizontal cells and bipolar cells. The inner plexiform layer contains synapses between bipolar, amacrine cells and RGCs (Cepko, 2014; Sanes and Masland, 2015; Seabrook et al., 2017). RGC axons exit the retina at the optic disc, into the optic stalk (OS) towards the ventral diencephalon. At this location, the ON from both eyes join at the optic chiasm (OC) and RGC axons project either to the same- (ipsi-lateral) or opposite-side (contra-lateral) of the brain to innervate the various visual nuclei. There are approximately 46 different target structures in the brain (Morin and Studholme, 2014). The visual input goes to three major pathways: 1) the primary visual system composed of the lateral geniculate nucleus and the superior colliculus, which encode complex visual features; 2) the accessory optic system, which encodes visually-driven reflexes; and 3) retinofugal projections regulating circadian rhythm.

1.2 Patterning of the eye

1.2.1 Eye morphogenesis

Although there is an immense diversity of eyes across the animal kingdom, the general structure of the eye emerged more than 500 million years ago (mya) during the Cambrian in early vertebrates (Schwab, 2018). Shortly after gastrulation, the first morphological changes occur when the neuroepithelium of the ventral forebrain evaginates to form two bilateral extensions known as the optic vesicle (OV) (Figure 2A; Adelmann, 1929). In mice and humans this event occurs as early as 8 days and 22 days of embryonic development respectively (Denis et al., 2017; Patel and Sowden, 2017). Upon contacting the surface ectoderm (lens placode), the distal-most portion of the OV induces the invagination of both the OV and the lens placode (Figure 2A; Heavner and Pevny, 2012). The invagination of the OV and the lens placode forms a two-layered tissue called the optic cup. The outer layer of the optic cup gives rise to the RPE whereas the inner layer gives rise to the neural retina (Figure 2A). The proper migration of the neuroepithelium towards the lens placode is critical for eye morphogenesis. The morphogen Sonic hedgehog (Shh) is critical in this migration since *Shh* deletion results in failure of the eye fields to split leading to cyclopia (Chiang et al., 1996). Moreover, the proper folding of the OV requires key transcription factors

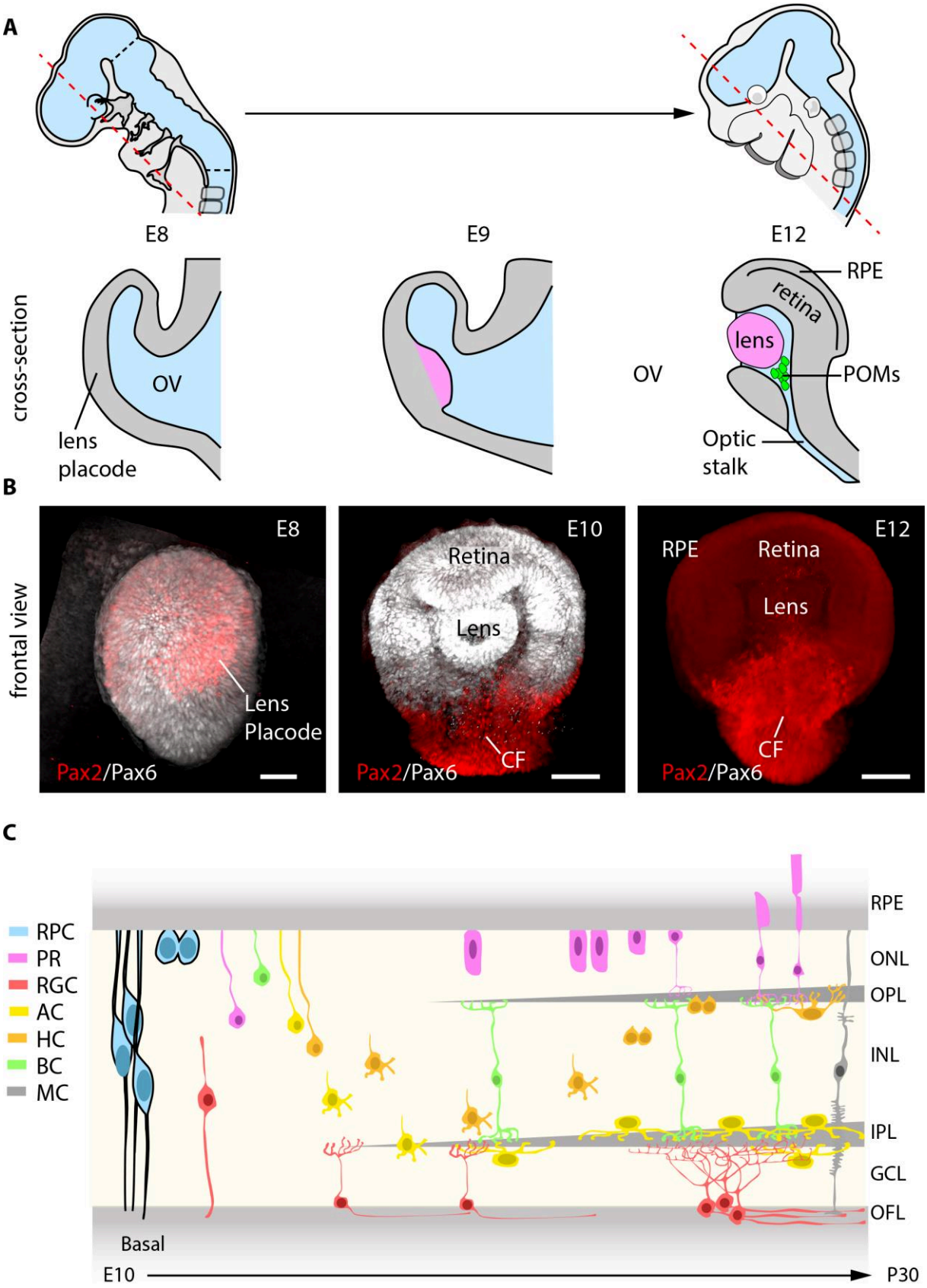

Figure 2 – A brief description of early eye development A. Upper panel Schematic representation of early eye development. The red dashed line represents the section plane. Lower panel shows schematic coronal cryosections. The optic vesicle extends

into the eye primordium (E8). The lens placode begins to invaginate (E9, pink). The lens has fully detached and is surrounded by the neural retina (E12, pink). Periocular mesenchymal cells invade the retina through the choroid fissure (12, green). **B**. Frontal view of whole eye following EyeDISCO clearing and labelled with the early retinal markers Pax6 (white) and Pax2 (red). At E8, the OV has extended into the eye primordium, Pax2 and Pax6-positive cells appear intermingled. At E10, the lens has fully detached. Pax6-positive cells (white) show a clear separation to the dorsal retina. Pax2-positive cells (red) reside in the ventral retina. The neural retina is highly proliferative and elongates circumferentially, a clear gap is present in the ventro-medial retina, which delineates the CF. **C**. A schematic representation of the developing mouse retina. The retinal development follows from left (E10) to the right (P30). In the early retina, RPCs (blue) undergo interkinetic migration and actively divide at the apical retina. The first retinal cell type to differentiate are the RGC (red), which detach from the apical retina and extend their axon in the OFL. PR (cones, pink), next differentiate, followed by BC (green), AC (yellow), and HC (orange). The last born retinal cell type are the Muller cells (grey). Interestingly, HCs detach from the apical retina and migrate to the basal retina before dividing and arborizing in the OPL. In contrast, ACs migrate to the basal retina and establish their arbors in the IPL. Adapted from (Amini et al., 2018). OV = Optic vesicle; POM = periocular mesenchymal cells; CF = Choroid fissure; RPC = Retinal progenitor cell; PR = Photoreceptor cell; RGC = Retinal ganglion cell; AC = Amacrine cell; HC = Horizontal cell; BC = Bipolar cell; MC = Muller cell; RPE = Retinal pigment epithelium; ONL = Outer nuclear layer; OPL = Outer plexiform layer; INL = Inner nuclear layer; IPL = Inner plexiform layer; GCL = Ganglion cell layer; OFL = Outer fibre layer

such as Pax6, Lhx2, Rax, and Six3; null mutations in these genes lead to small eye phenotypes (microphtalmia) (Furukawa et al., 1997; Glaser et al., 1994; Hill et al., 1991; M Hogan et al., 1988; Mathers et al., 1997; Porter et al., 1997; Tucker et al., 2001; Voronina et al., 2004; Yun et al., 2009; Zuber, 2003). Once folded, the two layers of the optic cup subdivide into the RPE, the neural retina, and the OS at the proximal end which acts as a path for RGC axons to reach the brain.

Several cell intrinsic signaling pathways are involved in patterning the optic cup (for reviews see Fuhrmann, 2010; Heavner and Pevny, 2012). Due to asymmetric cell proliferation, the optic cup expands circumferentially creating a slit in the ventral portion, known as the choroid fissure (CF; Figure 2B). The CF is a critical structure as it provides an exit for RGC axons forming the optic nerve and an entry for mesenchymal cells that pattern the retinal vasculature (Patel and Sowden, 2017). Both margins of the CF fuse except at the presumptive optic disc which leaves an opening for the ON and hyaloid artery. The process of CF fusion is complete by 13 and 37 days of development in the mouse and human respectively (Figure 2B; Denis et al., 2017;

Patel and Sowden, 2017). Current evidence shows that CF fusion begins at the midpoint of the fissure proceeding both proximally (towards the OS) and distally (towards the lens) (Hero, 1990). Moreover, electron microscopy studies showed that at the CF, there is a further invagination of the tissue where the RPE are juxtaposed (Hero, 1990). Hero (1990) also found evidence for cellular apoptosis of the RPE at the CF margin that was correlated with the disintegration of the basal lamina. As the basal lamina on each side of the CF margin gradually dissolves, epithelial cells intercalate with each other. This results in single sheet of neural retina with a single continuous basal lamina.

Failure of CF fusion leads to colobomas, a congenital defect present in 3-11% of pediatric blindness (Patel and Sowden, 2017). Persistence of the basal membrane is a major factor in preventing correct fusion of the CF (Hero, 1989; Hero et al., 1991). To date, thirty nine genes have been associated with colobomas (for an in depth review see Patel and Sowden, 2017). The paired domain-containing transcription factor Pax2 define the OS territory and shares a mutually antagonistic action on the neural retina by repressing Pax6 expression (Schwarz et al., 2000). Pax2 expression is transient and is repressed in the neural retina, and *Pax2* deletion results in failure of CF closure (Torres et al., 1996). Interestingly in *Pax2* null mice, the proximal but not distal CF is disrupted, suggesting that they may possess different mechanisms of action (Torres et al., 1996). The ventral anterior homeobox proteins (Vax1 and Vax2) are also critical transcription factors for CF morphogenesis (Barbieri et al., 2002; Bertuzzi et al., 1999; Hallonet et al., 1998). Both *Vax1* and *Vax2* deletion lead to colobomas. Of note, while *Vax1* deletion also leads to major defects in the forebrain, coloboma in *Vax2* null mice is not associated with other anomalies (Barbieri et al., 2002). Recently, the laminin-like protein Netrin-1 was found to be critical for CF closure (Hardy et al., 2019). Netrin-1 is highly expressed at the optic disc together with Pax2 and Vax2 (Deiner et al., 1997; Morcillo et al., 2006). Mice with a *Netrin-1* deletion results in highly penetrant colobomas (Hardy et al., 2019). The precise molecular signaling cascade responsible for the Netrin-1 mediated coloboma is not well understood apart from the observation that the basal lamina of the CF margin do not disintegrate. Future studies should elucidate whether Netrin-1 acts autonomously in CF closure.

1.2.2 Nourishing the neural retina

During early eye morphogenesis, the migration of neural crest-derived periocular mesenchymal (POM) cells through the CF establishes the consequent development of the retinal vasculature (Figure 2A; Gage et al., 2005; Le Lievre and Le Douarin, 1975). POM cells differentiate into endothelial cells (ECs) that proliferate to give rise to the embryonic vasculature of the eye called the hyaloid vasculature composed of the hyaloid artery, the vasa hyaloidea propria, and the tunica vasculosa lentis (Cairns, 1959). The hyaloid vessels are a transient vascular network in the mammalian retina that provides nourishment and oxygen for the developing lens and retina (Saint-Geniez and D'Amore, 2004). The regression of the hyaloid network is complete at P30 in mice and at birth in humans and is prompted by retinal angiogenesis (Selvam et al., 2018; Zhu et al., 2000). Of note, the direct vascularization of the retina is a specificity of the mammalian lineage since lower vertebrates only possess vitreal vessels (Chase, 1982). The retinal vascular plexus starts at the head of the optic nerve and progressively expands to cover the entire retinal surface by the first postnatal week (P7) in mice and just before birth in humans (40GW) (Rao et al., 2013; Selvam et al., 2018). Subsequent angiogenic sprouting forms a deeper vascular plexus, beginning at the optic nerve head and radiating outwards, invading the retina and establishing two laminar networks on either side of the inner nuclear layer (Gariano and Gardner, 2005).

Regression of hyaloid vessels is orchestrated by a series of cellular and molecular factors. Pericytes, that wrap around hyaloid ECs, dynamically regulate EC survival by secreting angiopoietin-2. The latter destabilizes ECs by binding to their Tie2 receptors and inducing apoptosis (Lobov et al., 2002). In addition to angiopoietin-2, pericytes express the ephrinB2 receptor, EphB4, which also contributes to EC apoptosis (Salvucci et al., 2015). Following cell death, ECs are phagocytosed by resident macrophages (Lang and Bishop, 1993). Retinal macrophages can also act on ECs by secreting Wnt7b and activating a Wnt-dependent apoptosis of ECs through their canonical Lrp5, Lrp6 receptors (Lang and Bishop, 1993; Lobov est al., 2005; Nayak et al., 2018; Rao et al., 2007). Interestingly, this highly coordinated molecular cascade is dependent on light detection. In early gestation, the maintenance of hyaloid vessels is dependent on the inhibition of dopamine by Neuropsin RGCs expressing ultra-violet sensitive opsins (opsin 5) (Nguyen et al., 2019). In late gestation, direct light stimulation of RGCs expressing melanopsin (opsin 4) inhibits the release of vascular endothelial growth factor (Vegf) and the subsequent destabilization of hyaloid vessels (Rao et al.,

2013). Of note, persistence of hyaloid vessels during fetal development causes severe congenital pathologies accounting for up to 4.8% of total blindness in the United States (Hegde and Srivastava, 2016).

The role of the laminin-like protein Netrin-1 is also studied in the context of vascular development. Initial reports hinted at an anti-angiogenic effect of Netrin1 since exogenous application of recombinant Netrin-1 leads to EC filopodia retraction (Larrivée et al., 2007; Lu et al., 2004). Moreover, deletion of one of the Netrin-1 receptors *UNC5b*, that is highly expressed in ECs, leads to aberrant angiogenesis (Lu et al., 2004). This model was challenged by the observation that morpholinos directed against Netrin1a during zebrafish development lead to a complete loss of parachordal vessels, highlighting a pro-angiogenic role of Netrin-1 (Wilson, 2006). In addition to its angiogenic role, Netrin-1 may act as a survival factor to ECs (Castets et al., 2009). The proposed model by Castets and colleagues (2009) indicates that Netrin-1 and UNC5b function antagonistically: the binding of Netrin-1 to UNC5b induces EC migration and survival (pro-angiogenic) whereas the absence of Netrin-1 leads to UNC5b-mediated apoptosis of ECs (anti-angiogenic). However, the report of a different *UNC5b* mutant showing reduced placental angiogenesis cannot be explained by the proposed model (Navankasattusas et al., 2008). Therefore, the precise role of Netrin-1 in angiogenesis remains to be fully understood.

1.2.3 Retinogenesis

Shortly after the neural retina is specified, the pseudo-stratified epithelium switches into a multipotent pool of retinal progenitor cells (RPCs) that gives rise to all retinal cell types (Figure 2C; Turner et al., 1990). Intra-viral infections showed that the multipotency of each RPC (clone) is highly heterogeneous generating as little as 1 to more than two hundred cells (Turner et al., 1990). These progenitors undergo inter-kinetic nuclear migration in an apico-basal manner, dividing at the apical retina (Amini et al., 2018). RPC division can either be symmetric, giving rise to two RPCs, or asymmetric, yielding a differentiated retinal class and a RPC (Figure 2C). Classical birth dating experiments showed that there is a temporal wave in the differentiation of retinal classes that is conserved in vertebrate species. The first retinal class to differentiate are the RGCs followed by the cone and horizontal cells (Figure 2C). In a third wave the amacrine, rod photoreceptors, and bipolar cells differentiate. The last

class to differentiate are the muller glia (Figure 2C; Cepko et al., 1996; Harris, 1997). RPC differentiation may be influenced by intrinsic factors, as evidenced by the observation that early RPCs transplanted into a “late” retinal environment still produced early fate retinal classes (Belliveau and Cepko, 1999). On the other hand, retinal classes could be generated due to stochastic differentiation of RPC during development. Live imaging experiments in zebrafish revealed that the birth order of cell classes within a clone do not always follow temporal differentiation waves (He et al., 2012). Overall, the precise molecular cascade controlling RPC differentiation remains elusive and may be influenced by a combination of intrinsic and stochastic factors (Amini et al., 2018; Cepko, 2014).

1.3 The origin of decussation in the vertebrate visual system

1.3.1 Phylogeny of visual projections

Early naturalists, philosophers, and anatomists had a brain-centric conception of vision, thinking that the eyes were merely an extension of the brain. For Galen, an image was perceived in the brain via two hollow extensions (optic nerves) that extended from the lateral ventricles to the eyes. The optic nerves joined the base of the diencephalon at the OC (due to its resemblance to the Greek letter x, chi), which he thought only served a mechanical function to avoid optic nerve damage (Polyak, 1957). René Descartes (1596-1650) appreciated that the lens of the eye exerted an inversion of the perceived image on the retina. He proposed that in order for images from both eyes to be re-aligned, the visual projections crossed (decussation) the hemispheres before being projected onto the visual organ of the brain that he believed to be the pineal gland (Figure 3; Polyak, 1957). It is worth noting that Descartes was the first to hypothesize that the retina created a topographical map of an object that was projected to the brain. The first report that the OC was the source of this decussation came from Isaac Newton (1642-1727) and was later refined by anatomical (Burdach 1819-26, and Van Gudden 1824-86) and clinical observations (A. Graefe 1856). The latter reported that the eye could anatomically be divided into meridians that section the eye vertically (naso-temporal) or horizontally (ventro-dorsal). Together, these meridians divide the retina into four quadrants. At the OC, the nasal half of each retinae completely decussates to the contra-lateral hemisphere whereas fibers originating from the temporal halves of the retina do not decussate at the OC and proceed to the ipsi-lateral hemisphere.

The latter observations were however questioned by anatomists of the classical era who reported that certain species possessed visual projections that completely decussate at the OC. S. Ramón y Cajal proposed a novel paradigm that took these observations into account. In species with laterally positioned eyes, an object is only seen by either the left or the right eye (panoramic vision). This image is inversed by the lens but corrected by the complete decussation of projections at the OC (Figure 3B). He further added that in order to accommodate for the complete visual crossing, sensory and motor pathways must also cross the midline. In the case of species with forward-facing eyes, he theorized that an object could be seen by either the left or right eye (monocular visual field) as well as by both eyes (binocular visual field). The

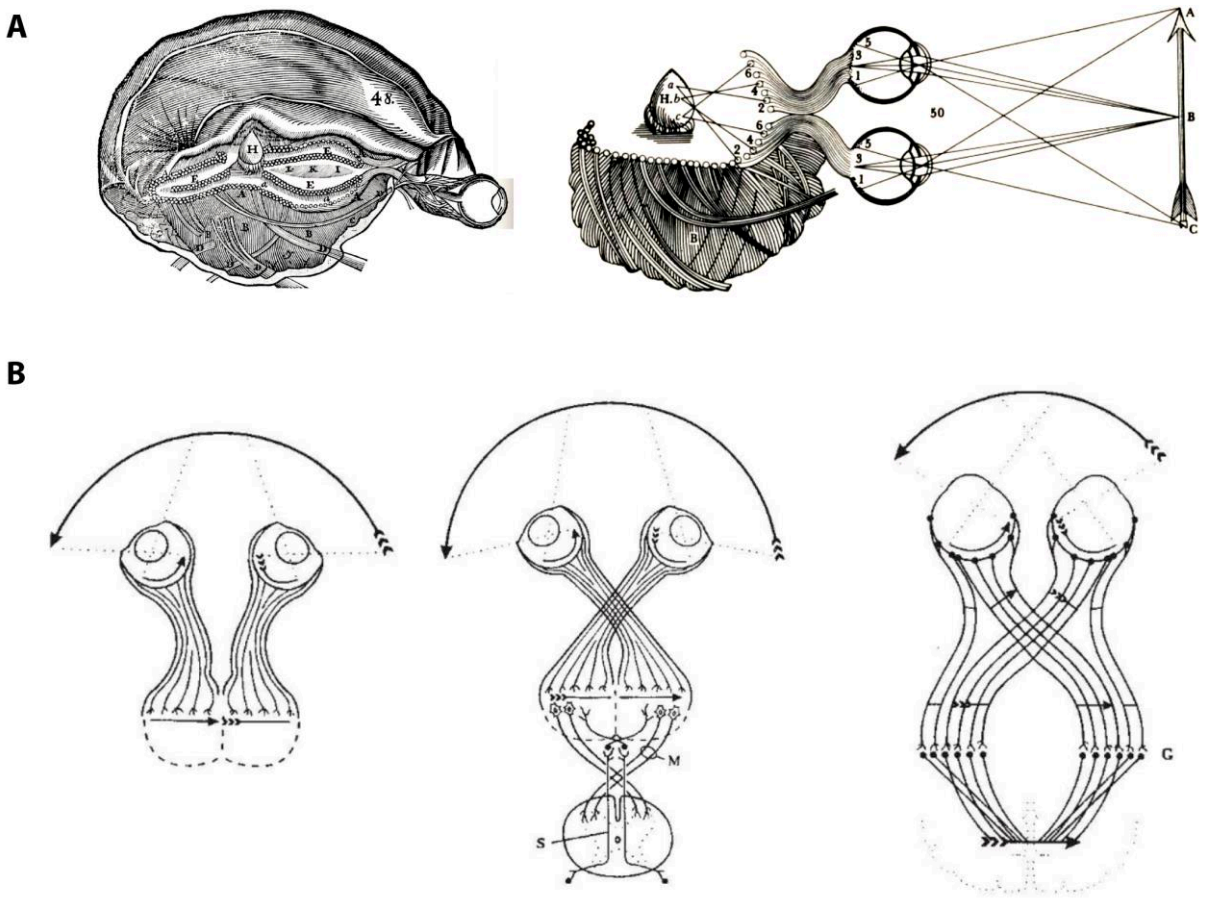

Figure 3 – Retinal projection representation in various species A. Left panel shows the drawing of the human visual system according to Descartes in his "*Tractatus de Homine*" published in 1686. The optic nerves project alongside each other without crossing. At the optic chiasm, optic nerves come in contact without crossing. In the center of the brain is the pineal gland (H) which Descartes described as the "seat of the soul". Right panel shows a drawing from Descartes of the human binocular visual system. Retinal images of the arrow are precisely matched onto the retina and projected onto the pineal gland, H. Here the precise point of the arrow, A is projected onto both retinas as 1 and 1. This signal is relayed to the ventricle as 2 and 2 and finally meets at a common point on the pineal gland, A. Despite the optic nerves not crossing (a misinformation Descartes took from Galen and Vesalius), the two monocular images are joined at the pineal gland. **B**. Diagrams made by Ramon y Cajal on his theory for the emergence of decussations. Left panel The problem is set by the lens which inverts the image onto the retina. In an organism devoid of optic chiasm, the visual scene (arrow) is reversed, creating a "broken arrow" in the optic tectum. middle panel represent the visual system of a lower vertebrate. The eyes are positioned laterally and lack a binocular field. The entire image is inverted by the lens and projected onto the retina. However, this image inversion is corrected by the total decussation of the optic nerves at the optic chiasm. Right panel shows the human visual system. Convergence of the eyes leads to a large proportion of the visual field to be binocular. Here, each eye partially decussates. The temporal side of each retina projects to the ipsilateral colliculus, whereas the nasal retina crosses to the opposite colliculus. Thalamocortical projections from each colliculi are parallel so that each neuron projects to its neighbor in the visual cortex.

monocular image of each eyes (nasal retina) completely crosses the OC, whereas the binocular image (temporal retina) does not cross the OC and projects ipsi-laterally (Figure 3B). This creates in each brain nucleus a superimposable image of both the left and the right eye. Therefore, in the panoramic system, each half of the viewed object is seen by a single eye; in a stereoscopic system, the object is viewed to a greater or lesser extent (depending on the degree of binocular overlap) with both eyes creating a slightly different image from the left and right eye. The functional relevance for this fusion of ipsi- and contra-lateral fibers is the basis of what we understand as stereopsis ('seeing solid'), also called depth of perception.

Cajal additionally reported that in vertebrates, the size of decussation varied in different species (Figure 4; Ramón y Cajal, 1909). This critical observation was further formulated by Walls, who coined the 'Newton-Müller-Gudden' law which states that the amount of partial decussation at the OC is correlated to the degree of frontal orientation of the eyes (Walls, 1942) . Simply put, animals with laterally positioned eyes have a complete decussation of visual projections whereas animals with frontally positioned eyes have an increasing degree of partial decussation correlated to the degree of their binocular field (Figure 4). Panoramic vision gives a great advantage to animals by providing them a wide array of available visual information. It is particularly advantageous to animals scouting for predators. What is the advantage of binocularity? According to Heesy, binocular vision gives at least three advantages: enhanced light sensitivity, expanded depth perception, and contrast discrimination (Heesy, 2009). This translates to the idea that there is an evolutionary trade-off between stereopsis and panoramic vision in the animal kingdom. The general organization of the visual system has largely been conserved since the emergence of vertebrates 530 mya (Lamb et al., 2007). The vertebrate lineage is a diverse phylum composed of fish, amphibians, reptiles, birds, and mammals, all of which possess different ecological niches with varying requirements for predation. It is therefore interesting to ask whether the 'Newton-Müller-Gudden' law is applicable to the wide array of species in the vertebrate phylum.

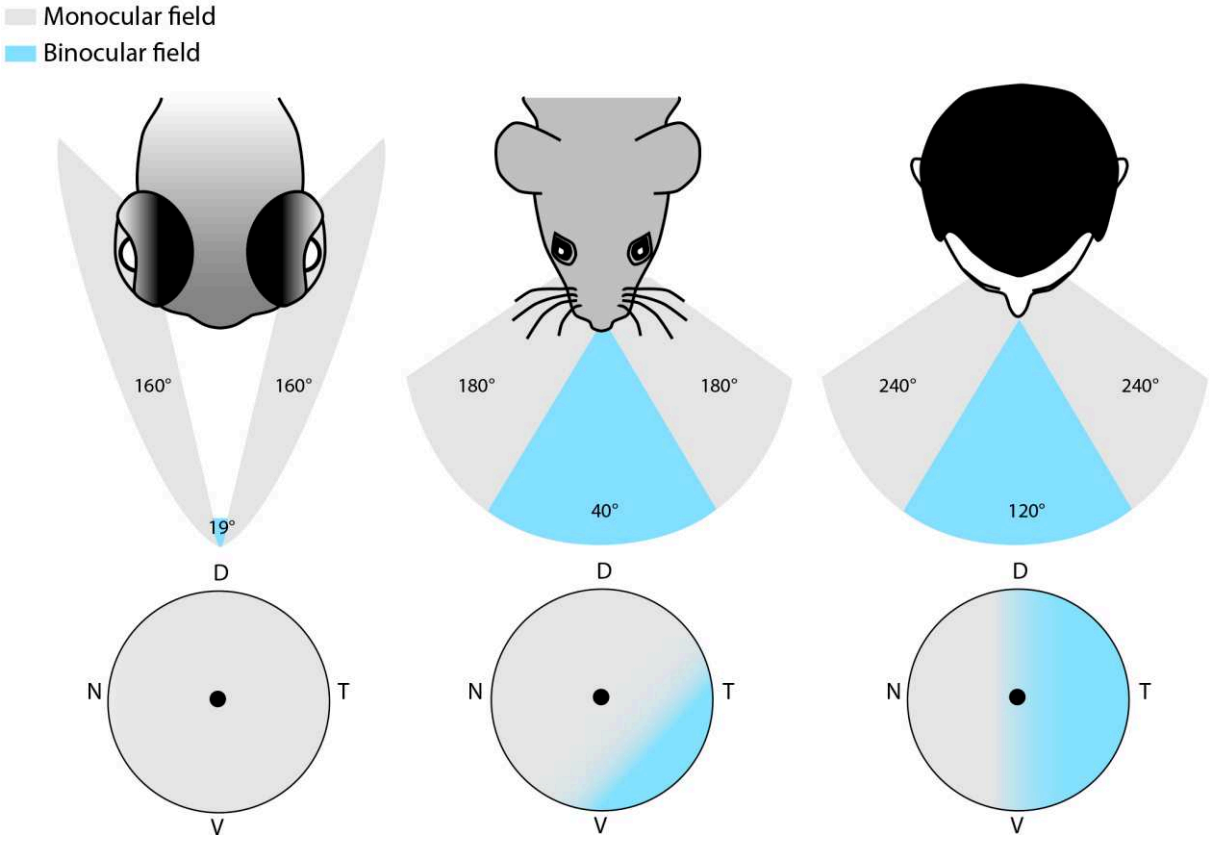

Figure 4 – The Newton-Muller-Gudden Law. Eye laterality is proportional to the amount of ipsilateral retinal projections. Zebrafish possess laterally-positioned eyes, with a small binocular field (19°, blue). No ipsilateral projections exist. Mice possess more convergent eyes than zebrafish, with a higher degree of binocularity (40°, blue). Mice possess a small contingent of ipsi-lateral projection in the ventro-temporal retina (5-6%). Humans possess frontally positioned eyes, with a high degree of binocularity (120°, blue). Approximately 50% of their retina are composed of ipsi-lateral retinal projections. This Law also postulates that there is an evolutionary trade-off for binocular vision. Preys must scout a higher degree of the visual field to escape predators (favor monocular vision). On the other hand, predators depend on depth perception to precisely strike at their prey (favor binocular vision).

The basal-most branch of vertebrates are the fish and can be subdivided into the cyclostomes (jawless fish), the chondrichthyes (cartilaginous fish), and the actinopterygii (ray-finned fish) (Figure 5; Long et al., 2019). The cyclostomes, are the earliest divergence in the vertebrate lineage (525mya) (Figure 5; Long et al., 2019). Both extant cyclostome representatives, lampreys (*Lampetra fluviatilis*) and hagfishes (*Myxinoidea*) lack paired appendages and possess laterally positioned eyes. Ipsi-lateral projections exist in both lamprey and hagfish, which puts them as a common ancestor for partial decussation (Vesselkin et al., 1980; Wicht and Northcutt, 1990). All gnathostomes possess paired appendages that form either fins (cartilaginous or bony fish) or limbs (tetrapods)(Figure5). The ray-finned fish are the most diverse group of vertebrates, with over 30,000 species (Figure 5; Long et al., 2019). They occupy all aquatic environments from deep ocean trenches to shallow pools. The most primitive clades of living ray-finned fish are the bichirs (*Polypterus senegalus*) and gars (*Lepisosteus osseus*). Both clades are predatory and possess laterally positioned eyes, and yet possess ipsi-lateral projections (Northcutt and Butler, 1976; Repérant et al., 1981). More modern clades of ray-finned fish with laterally positioned eyes also possess ipsi-lateral projections, such as the black piranha (*Serrasalmus niger*) and the Astyanax (*Astyanax mexicanus*) (Ebbesson et al., 1980; Voneida and Sligar, 1976). However, ipsi-lateral projections are not observed in all modern teleost fish since the zebrafish (*Danio rerio*) or medaka (*Oryzias latipes*) have complete visual projection decussation at the OC (Burrill and Easter, 1994; Yoda et al., 2004). Thus, in ray-finned fish, ipsi-lateral projections do not seem to be correlated with the positions of the eyes. Moreover, it is possible that ipsi-lateral projections were lost in the superclass of vertebrates.

The sarcopterygians (lobe-finned fish) evolutionarily diverged from the ray-finned fish 420mya (Figure 5; Long et al., 2019). Lobe-finned fish are a monophyletic group which includes tetrapods (amphibians, reptiles, birds, and mammals), comprising the dipnoan lungfish and the opterygian coelacanth (Figure 5; Long et al., 2019). While, there are no studies looking at the visual system of coelacanth it seems that the Australian lungfish (*Neoceratodus Forsteri*) possess ipsi-lateral projections (Glenn Northcutt, 1980). This finding is controversial since another species of lungfish were shown to lack ipsi-lateral projections (*Protopterus annectens*) (Northcutt, 1977). These findings raise the possibility of inter-species loss of ipsi-lateral projections.

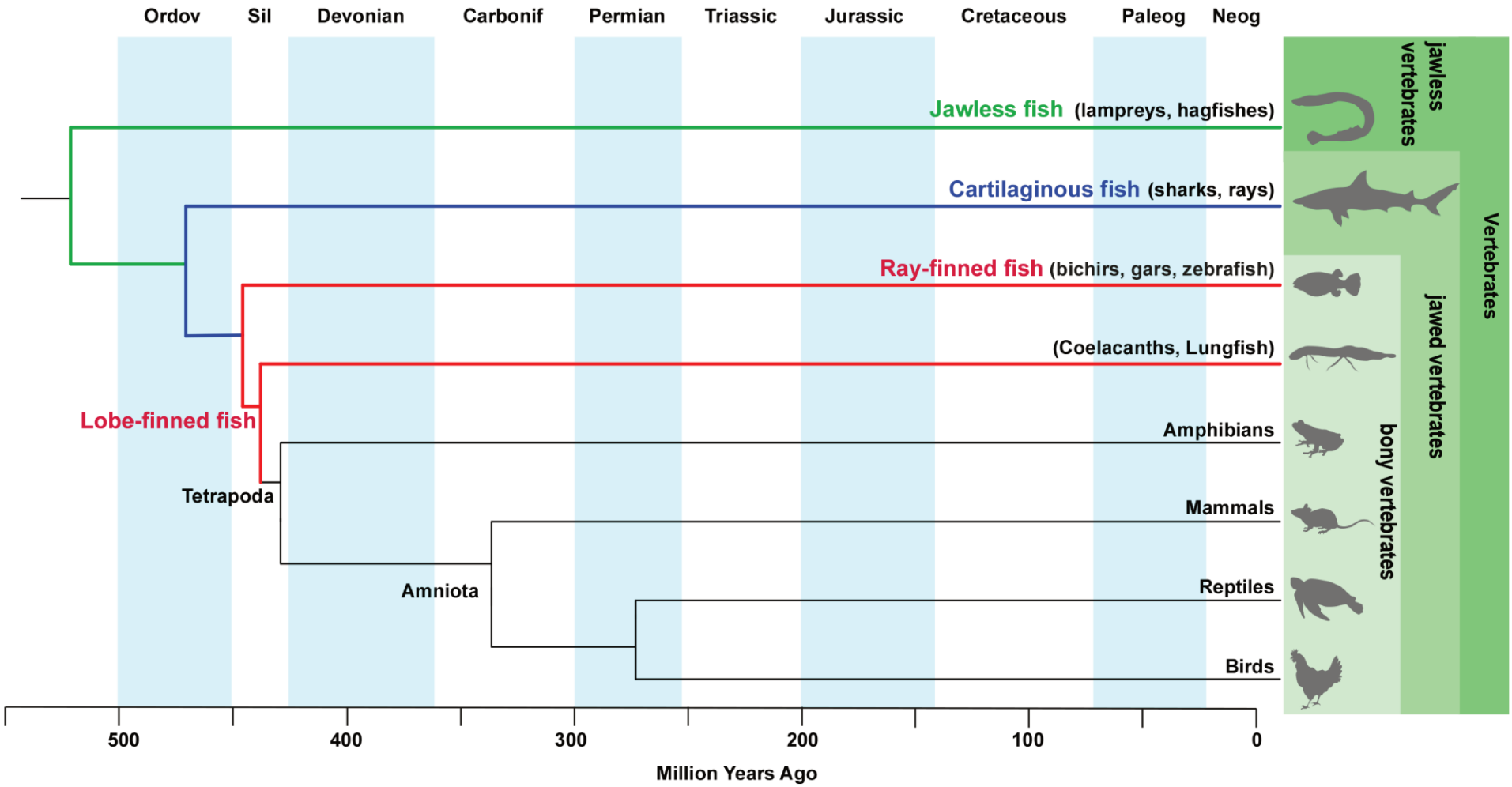

Figure 5 – The evolution of vertebrates. The first major divergence occurred more than 500 million years ago (mya) between jawless vertebrates (Cyclostomata, green) and jawed vertebrates (Gnathostomata, green). The next major divergence occurred more than 450mya between cartilaginous fish (Chondrichtyes, blue) and bony fish (Osteischtyes, blue). Approximately 450mya, bony fish separated into ray-finned fish (Actinopterygii, red) and lobe-finned fish (Sarcopterygii, red). Lobe-finned fish is a monophyletic group and is considered the closest relative to tetrapods. Tetrapods are composed of many phyla, the major represented are the amphibians, mammals, reptiles and birds.

Elucidating whether amphibians possess ipsi-lateral projections could give an evolutionary perspective on binocular disparities. The anurans (frogs) form the largest group of amphibians (Figure 5; Ward et al., 1995). Interestingly, in anuran tadpoles' visual projections completely decussate at the OC. However, during metamorphosis, their visual projections become partially crossed as their eyes migrate more frontally (Currie and Cowan, 1974). These ipsi-lateral projections are completely stable in several adult species such as the *Rana* and *Xenopus laevis* (Currie and Cowan, 1974; Levine, 1980; Singman and Scalia, 1991). This observation is in line with the 'Newton-Müller-Gudden' law: the developmental eye convergence is coupled to the appearance of partial decussation of visual projections. In contrast to these findings, the presence of ipsi-lateral projections in reptiles is less clear. The predatory leatherback turtle (*Tryonix cartilagineus*) possesses frontally positioned eyes but does not display ipsi-lateral projections (Hergueta et al., 1992). This observation is in clear opposition to the 'Newton-Müller-Gudden' law, since the pond turtle (*Chinemys reevesi*) that possesses laterally positioned eyes displays a strong ipsi-lateral projection (Hergueta et al., 1992). Similarly, chameleons possess a great ability for eye convergence and their predatory behavior highly depends on depth of perception due to their feeding behavior using tongue protraction (Bennis et al., 1994). However, the European chameleon doesn't possess ipsi-lateral projections (*Chamaeleo chameleon*) (Bennis et al., 1994). This is unlikely an isolated feature since other species lacking ipsi-lateral projections also possess the ability for eye convergence, such as zebrafish.

Birds are highly visual organisms with diverse ecological niches and are composed of over 9000 species (Figure 5; Pettigrew, 1986). In contrast to the anurans, birds do develop ipsi-lateral projections during development that completely regress prior to hatching (Singman and Scalia, 1991; Weidner et al., 1985). Therefore, birds are believed to possess completely crossed visual projections. Interestingly, some predatory birds with frontally positioned eyes such as the owls (*Tyto alba*) possess binocular disparity (Pettigrew and Konishi, 1976). While owls' visual projections completely cross at the OC they then re-cross the midline before projecting to an avian-specific visual organ, the visual Wulst (Karten et al., 1973; Pettigrew and Konishi, 1976). Despite the broad diversity in bird species, we currently have a poor understanding of their visual projections which is in part due to the large body of

literature in chick or pigeon. In mammals, the story is quite simple and follows the 'Newton-Müller-Gudden' law. The relative proportion of ipsi-lateral projection highly correlates to the extent of binocular overlap which ranges from 15% in horse, 22% in dogs, 30% in cats, to roughly 40% in primates and humans (Walls, 1942).

We have seen that binocularity in infra-mammalian species is somewhat mysterious and lacks a clear relationship to ecological niche and predatory lifestyle. Indeed, binocular overlap is not sufficient for ipsilateral projections to occur. Two strategies seem to have evolved to obtain binocular vision: partial decussation and the double crossing of visual projections. Evolutionarily, the occurrence of the visual Wulst in avian species is difficult to explain. In order for a topographic representation to be maintained, a common ancestor could not have possessed both a partial decussation at the OC and a double crossing at the visual Wulst. An argument could however be made that birds and mammals are an example of convergent evolution whereby each have achieved binocular vision by different means. Of particular interest, the diverse visual adaptations of the ray-finned fish make it likely that they evolved the capability for binocular vision. Whether they achieve binocularity by the same means as mammals or birds or by a third system remains to be studied.

1.3.2 A historical perspective on visualizing retinal projections

As discussed in the previous section, our ability to study RGC projections histologically can tremendously help our understanding of visual perception (binocularity) in various animal models. In the late 19th century, our understanding of neuronal morphology and neuronal circuitry was revolutionized by the observations of S. Ramón y Cajal using the Golgi stain (Golgi, 1873; Ramón y Cajal, 1892). Nonetheless, this method labels neurons in a non-specific manner limiting our understanding of specific tract circuitry. In the first half of the twentieth century, several groups improved the silver staining by exploiting the affinity of silver granules to myelinated fibers (Glees, 1946; Hoff, 1932; Nauta and Ryan, 1952). Following a physical, thermoelectric, or chemical lesion the axons undergo a sequence of microtubule disassembly and blebbing, a process known as Wallerian degeneration (Waller, 1850). The Nauta-Gygax stain takes advantage of this process: the lesioned portion of the axon becomes susceptible to the uptake of silver (Fink and Heimer, 1967; Nauta and Ryan, 1952). The first studies of RGC projections using the Nauta-Gygax stain reported that RGC projections of infra-

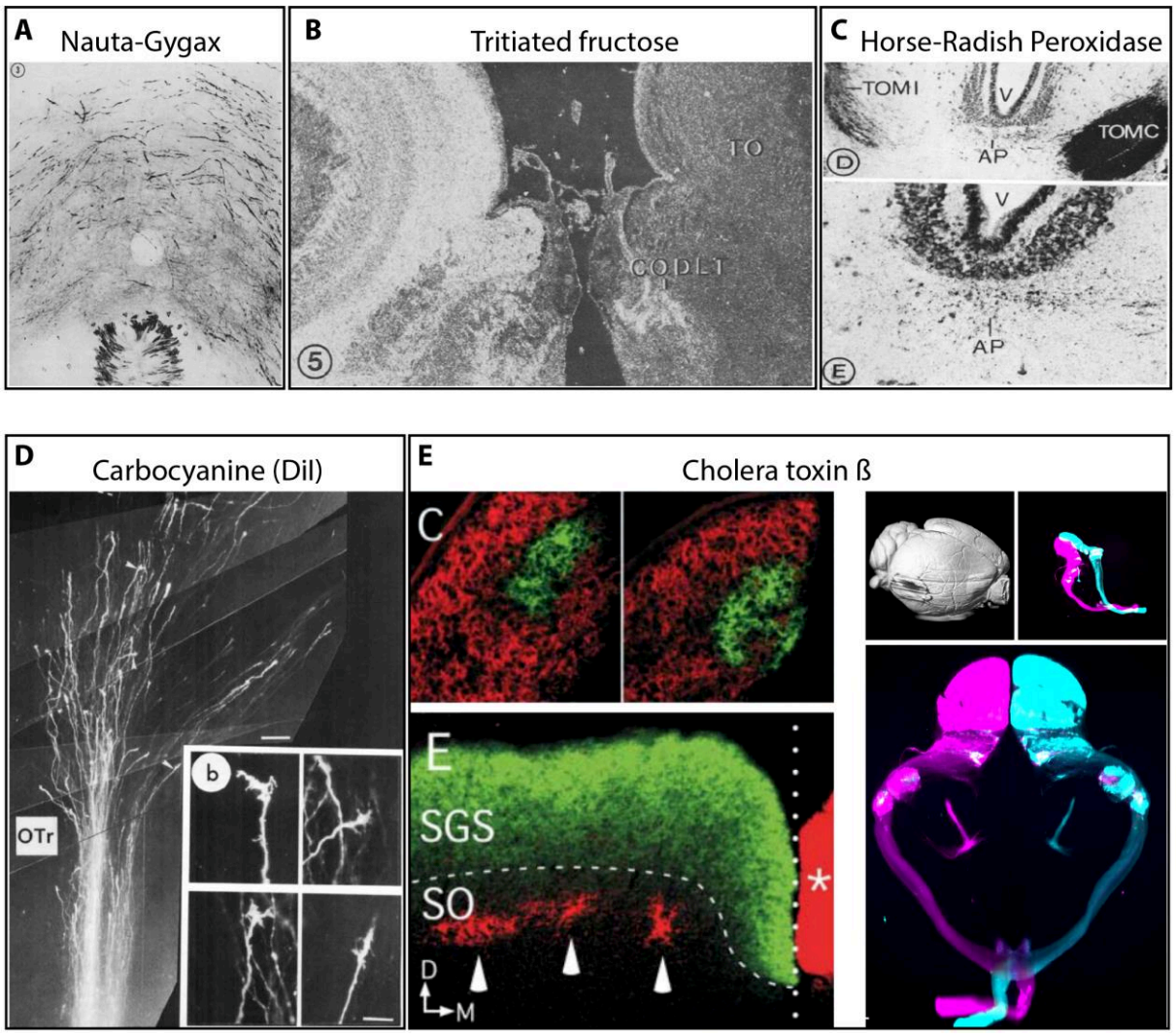

Figure 6 – The major historical tracing methods utilized for the study of retinal ganglion cell projections. **A**. A transverse section through the posterior commissure of the *Caiman Sklerops*. Black granules illustrate degenerating optic tract fibres crossing the midline using the Nauta-Gygax stain (Burns and Goodman, 1967). **B**. Dark-field autoradiograph of the teleost, *Sarcus erythrophthalmus*. A high concentration of Silver grains are observed in the contra-lateral optic tectu whereas a smaller concentration is seen in the ipsi-lateral optic tectum (Repérant et al., 1976). **C**. Brightfield radiograph of a transverse section in the lamprey (*Lampetra fluviatilis*). Upper panel shows labeling in the post-optic region.lower panel shows a higher magnification with labelling in the post-optic area (AP). V = ventricle; TOMI = ipsilateral optic tract; TOMC = contralateral optic tract (Vesselkin et al., 1980). **D**. Fluorescent photomicrograph of carbocyanine (DiI) labeled retinal ganglion cells in chick retina (E6). Panel B represent higher magnification images of fours isolated retinal ganglion cell projections. Scale bars: 50µm and 10µm (Thanos and Bonhoeffer, 1987). **E**. Left panel shows confocal images of coronal sections from the Lateral geniculate nucleus and the rostral Superior colliculus following an intraocular injection of fluorescent CTB conjugates (red = right eye, green = left eye) (Lyckman et al., 2005). Right panel shows an entire mouse brain following intraocular injection of two conjugated CTB dyes (cyan = right eye; magenta = left eye) followed by tissue clearing and 3D imaging with light-sheet fluorescence microscopy.

mammalian species were completely crossed (Figure 6A; Polyak, 1957; Walls, 1942; Ward et al., 1995).

The observation that the axonal transport machinery could be used for tracing methods propelled the field of axonal tracers for the next three decades (Weiss and Hiscoe, 1948). The axonal transport of injected materials can be separated into anterograde (from soma to periphery) or retrograde (from periphery to the soma) transport. Only the tracers that are most relevant to the visual system will be discussed here (for an in depth review on tracers, see Köbbert et al., 2000; Lanciego and Wouterlood, 2011; Saleeba et al., 2019). Anterograde tracers were first used to identify the anatomical targets of RGC projections within the brain (Cunningham and Freeman, 1977; Ekström, 1982; Repérant et al., 1976). The earliest of these tracers were radiolabeled amino acids, such as tritiated (^{3}H)-leucine or proline, that were incorporated as polypeptides and transported anterogradely to axon terminals. The radioactive isotope could then be visualized using autoradiography (Cowan et al., 1972; Droz and Leblond, 1962; Droz and Leblond, 1963). The major limitation of this method is that the morphology of axonal tracts is inferred from a pattern of silver grains (Figure 6B). The application of heavy metal atoms such as cobalt or nickel also became used for the study of visual projections (Fuller and Prior, 1975; Lázár, 1978). Here, cobalt chloride is applied to the cut end of the nerve trunk and iontophoresed along the nerve and then the tissue is bathed in ammonium sulfide to precipitate the cobalt (Pitman et al., 1972).

The emergence of retrograde tracers allowed the specific identification of neurons with respect to their axon terminals. While the Nauta-Gygax stain was one of the first retrograde tracing methods, it depends on the non-physiological degeneration of fibers. In the 1970's, the plant glycoprotein and enzyme horseradish peroxidase (HRP) was the first retrograde neuronal tracer used (Kristensson and Olsson, 1971a; Kristensson and Olsson, 1971b; Lavail and Lavail, 1972). Using hydrogen peroxide and a chromogenic substrate, such as tetramethylbenzidine, the oxidation of HRP can be visualized (Figure 6C; Lavail and Lavail, 1972). Comparison between the Nauta-Gygax stain and more recent labelling methods showed clear discrepancies in the pattern of RGC projections (Repérant et al., 1982; Vesselkin et al., 1980; Ward et al., 1995). Notably, species that were thought to possess completely crossing RGC projections were now reported to possess ipsi-lateral projections (Ward et al., 1995). For these reasons, the community largely discarded the visualization of degenerating fibers for

the study of visual projections and instead focused on more precise labeling methods such as the injection of HRP or radioisotopes. A major caveat of HRP staining however is that only the soma and the primary dendrites are revealed, creating an incomplete staining of the neuron. Another drawback to HRP staining pertains to the relatively weak staining that subsides overtime (Wan et al., 1982). Moreover, the presence of endogenous peroxidase in the peroxisomes and lysosomes of neurons generates a significant amount of background noise. To address these issues, the wheat germ agglutinin (WGA) lectin was coupled to HRP, which increased up to forty times the sensitivity of the signal (Gonatas et al., 1979).

In search for axonal tracers that were more sensitive than HRP, the development of fluorescent dyes, such as rhodamine-isothiocyanate (RITC), provided much simpler application and revelation of the dye than previous methods (Thanos and Bonhoeffer, 1983). Although RITC labeled RGC projections, the dye was less efficient than previously reported tracers as evidenced by a weaker signal intensity (Thanos and Bonhoeffer, 1983; Thanos and Bonhoeffer, 1987). In contrast, in 1986 Honig and Hume reported the first use of inorganic carbocyanine dyes (DiI and DiO) in preganglionic neurons, which relied exclusively on passive bi-directional transport along the plasma membrane (Honig and Hume, 1986). This staining method provides a complete staining of the soma and its entire dendritic tree, and can strongly label the lengthy RGC projections in chick (Figure 6D; Thanos and Bonhoeffer, 1987). In addition to the methodological ease in using carbocyanine dyes, they are highly photostable over prolonged periods and have a higher signal-to-noise ratio compared to other dyes (Honig and Hume, 1986; Thanos and Bonhoeffer, 1987). Carbocyanine tracing is also applicable to fixed tissues (Godement et al., 1987). However, the lipophilic nature of carbocyanine dyes makes them difficult to combine with immunohistochemistry protocols that use detergents for antibody penetration. Water-soluble dextran-based bi-directional tracers, such as the biotinylated dextran amine (BDA) are now tracers of choice due to their Golgi-like level of staining (Glover et al., 1986). BDA can be revealed in multiple ways, either conjugated to fluorochromes or by biotinylation. When compared with other tracers, BDA is less stable than the carbocyanine dyes (Lanciego and Wouterlood, 2011). The cholera toxin β subunit (CTB) was identified as a more sensitive bi-directional tracer than HRP (Stoeckel et al., 1977; Trojanowski et al., 1981). Unlike HRP which is passively endocytosed in the

axon, CTB uptake is receptor-mediated and leads to a superior sensitivity of staining (Stoeckel et al., 1977). Free CTB or directly coupled to a fluorochrome provides many advantages from rapid bi-directional transport and low toxicity to high photostability, making it the method of choice for pan-RGC projection visualization (Figure 6E; Conte et al., 2009a; Conte et al., 2009b; Luppi et al., 1990; Lyckman et al., 2005; Morin and Studholme, 2014; Saleeba et al., 2019).

The majority of axonal tracers rely on passive or active transport through endocytosis of homogenously expressed sugars on the surface of axons, which hinders the targeting of genetically specific RGC types. In parallel to axonal tracers, the development of viral vectors for the analysis of visual projections has accelerated over the past few years. Viral vectors provide a stable fluorescent expression and can be either targeted as pan-RGC or genetically specified RGC tracers (Martersteck et al., 2017). Furthermore, some replication-competent viruses were developed for trans-synaptic infection making it possible to visualize the entire RGC circuitry (Cruz-Martín et al., 2014; Nassi et al., 2015; Rompani et al., 2017). Viral tracers will not be discussed here (for an in depth review on viral-mediated axonal tracing, see Saleeba et al., 2019).

1.3.3 Modern strategies for visualizing retinal projections

The visualization of RGC projections was extensively improved by the optimization of neuronal tracers. However, understanding the vast RGC projection network is challenging as the projections span up to fifteen millimeters in rats and arborize in as many as forty-six different brain nuclei in mice (Morin and Studholme, 2014). RGC projections are largely observed in serial sections (cryosections or vibratomes sections) which provide a cellular and sub-cellular resolution when coupled to confocal or serial block-face electron microscopy respectively (Helmstaedter et al., 2013; Kim et al., 2019; Morin and Studholme, 2014). RGC projections are also studied *ex vivo* using hypothalamic preparations coupled with live imaging. This method was used together with DiI tracing to study the murine RGC growth cone dynamics at the OC (Godement et al., 1994; Sretavan and Reichardt, 1993). These methods helped gain insight into the cellular dynamics of RGCs, however, to fully appreciate the diversity of RGC projections in a non-biased manner it is critical to observe RGC projections in their three-dimensional (3D) nature.

More than a century ago, the German embryologist Werner Spalteholz understood the need to visualize biological tissues in 3D (Spalteholz, 1914). The main limitation for visualizing tissues in 3D is the opaqueness of the tissues due to their heterogeneous refractive indices (Vigouroux et al., 2017). When homogenizing the refractive index of a biological tissue (by removing lipids and water) and fully immersing it in an imaging medium that matches its refractive index, the tissue appears “transparent”. Spalteholz carried out this experiment on heart and fetal tissues using a combination of benzyl alcohol and methyl salicylate (Spalteholz, 1914). It was not until a century later that Dodt and colleagues optimized this protocol for the murine brain that expressed a green fluorescent protein (GFP) reporter driven by a pan-neuronal transcription factor Thy1 (Dodt et al., 2007). Adaptations of such clearing technologies for the analysis of RGC projections were first carried out by Kuwajima and colleagues (2013). Using a formamide-based clearing protocol (Clear^{T}), they showed that RGC projections labelled with DiI or CTB could be visualized in 3D in the embryonic (E14) and postnatal (P5) murine visual system (Kuwajima et al., 2013). Although this protocol was a great step forward, the 3D visualization of RGC projections was restricted to the developing murine visual system and only to 700µm-thick slices.

The subsequent development of organic clearing protocols, such as the three-dimensional imaging of solvent-cleared organs (3DISCO), allowed for total observation of CTB-labelled RGC projections in the adult murine visual system (Figure 6E; Ertürk et al., 2012; Renier et al., 2014). Of note, DiI labelling is incompatible with organic clearing solutions due to the removal of lipids during the clearing process. A focus on current tissue clearing protocols and their use in neurodevelopmental biology is highlighted in the “Annexe” section.

1.4 Intra-retinal pathfinding

1.4.1 Obtaining polarity

How did organisms develop different mechanisms to obtain binocularity? What are the sources for RGC laterality? In this following section we will attempt to better describe the cellular an molecular determinants of RGC development. The axonal projections from the retina to the brain are particularly interesting to study since they extend over a long distance and originate from regions that are spatially segregated but come to be arranged topographically. RGCs are the first-born retinal cells that follow a differentiation wave which proceeds in a center-to-periphery sequence (Hinds and Hinds, 1974). Injections of lucifer yellow in the retina of Xenopus embryos showed that RGCs differentiate from neuroepithelial cells at the apical side of the neural retina, in close proximity to the choroid fissure (central retina) (Holt, 1989). Interestingly, in frogs (Grant et al., 1980), mammals (Silver and Sidman, 1980), and birds (Halfter et al., 1985) RGCs initially originate from the dorsal retina whereas they initially originate from the ventral retina in fish (Laessing and Stuermer, 1996; Schmitt and Dowling, 1996). In all species, differentiating RGCs quickly polarize and extend a single axon towards the optic disc (Goldberg and Coulombre, 1972; Grant et al., 1980; Halfter et al., 1985). The axonal extension from the RGCs was proposed early on to arise from the basal process of the neuroepithelial cell (Hinds and Hinds, 1974). This was confirmed by live-imaging experiments which also showed that the extension from the basal process occurs concomitantly to the detachment of the apical process of the RGC (Zolessi et al., 2006). Worthy of note, such detachment is not required for axonal extension since morphants that lack apical retraction still manage to extend an axon towards the optic disc (Zolessi et al., 2006).

After acquiring their polarity and extending their axon, RGCs project onto the basal edge of neuroepithelial end-feet at the vitreal surface, a layer known as the Optic Fiber Layer (OFL) (Halfter et al., 1983; Holt, 1989; Prada et al., 1981). Once RGCs have invaded the OFL they extend a leading process towards the center of the retina through the choroid fissure, a site which will become the optic disc, and towards their targets in the brain. For many decades, researchers questioned why RGCs preferentially extend towards the optic disc. It was Ramon y Cajal who first proposed in his chemotactic hypothesis that “intelligent forces” could guide navigating axons by

secreting long-range attractive cues (Ramón y Cajal, 1892). Experimental embryology such as ablation, rotation, and grafting of various tissues allowed to test this hypothesis. Ablation experiments carried out in embryonic *Xenopus* revealed that complete removal of optic tectum (RGC final target) results in a normal trajectory by RGCs towards a "phantom target" (Harris, 1989). In addition, grafting experiments in chick retina showed that host RGCs enter the transplant and follow the orientation of the graft. Removal of the host optic disc or grafting additional optic discs in a host retina had no effect on the navigation of retinal axons (Halfter, 1996). Altogether, these experiments argue against the presence of long-range cues and suggest that local rather than long-range cues orchestrate the guidance of RGCs. Since long-range cues do not give directionality to growing RGCs and the optic disc does not guide the growth of RGCs, what are the intermediate sources of short-range cues guiding RGCs?

1.4.2 The inhibitory retina

Seminal experiments carried out in chick RGCs identified permissive and inhibitory zones within the eye. By carrying out co-cultures, Stier and Schlosshauer (1995) observed that chick RGCs grow preferentially on the basal-most layer of the retina (OFL), and that this effect is lost when neuroepithelial end-feet are ablated (Figure 7A). On the other hand, RGCs avoid outer retinal layers except when prior treatment with heat or protease is carried out. Thus, growth promoting factors secreted by neuroepithelial end-feet in the OFL are required for the growth of RGCs and a local inhibition from retinal outer layers mediated by inhibitory proteins forces RGC growth away from the retina (Figure 7A,B, Stier and Schlosshauer, 1995).

What mechanisms restrict RGC to the OFL? The molecular mechanism orchestrating this repulsion began to emerge with the identification of the inhibitory extracellular matrix (ECM) protein, *slit* (Rothberg et al., 1990). Three *slit* genes, *slit1*, *slit2* and *slit3*, exist in the vertebrate nervous system (Holmes et al., 1998; Itoh et al., 1998; Nakayama et al., 1998). They mediate their signal by binding to the transmembrane receptors Roundabout (Robo) (Kidd et al., 1999). In the developing mouse retina, *robo2* and *slit1* are expressed in the first born RGCs (dorso-central retina) (Erskine et al., 2000; Niclou et al., 2000; Ringstedt et al., 2000; Yuan et al., 1999). Interestingly, *slit1* is expressed in a ventral-high dorsal-low gradient in the developing retina, *robo1* and *slit2* then become expressed in the RGC layer and the future inner nuclear layer.

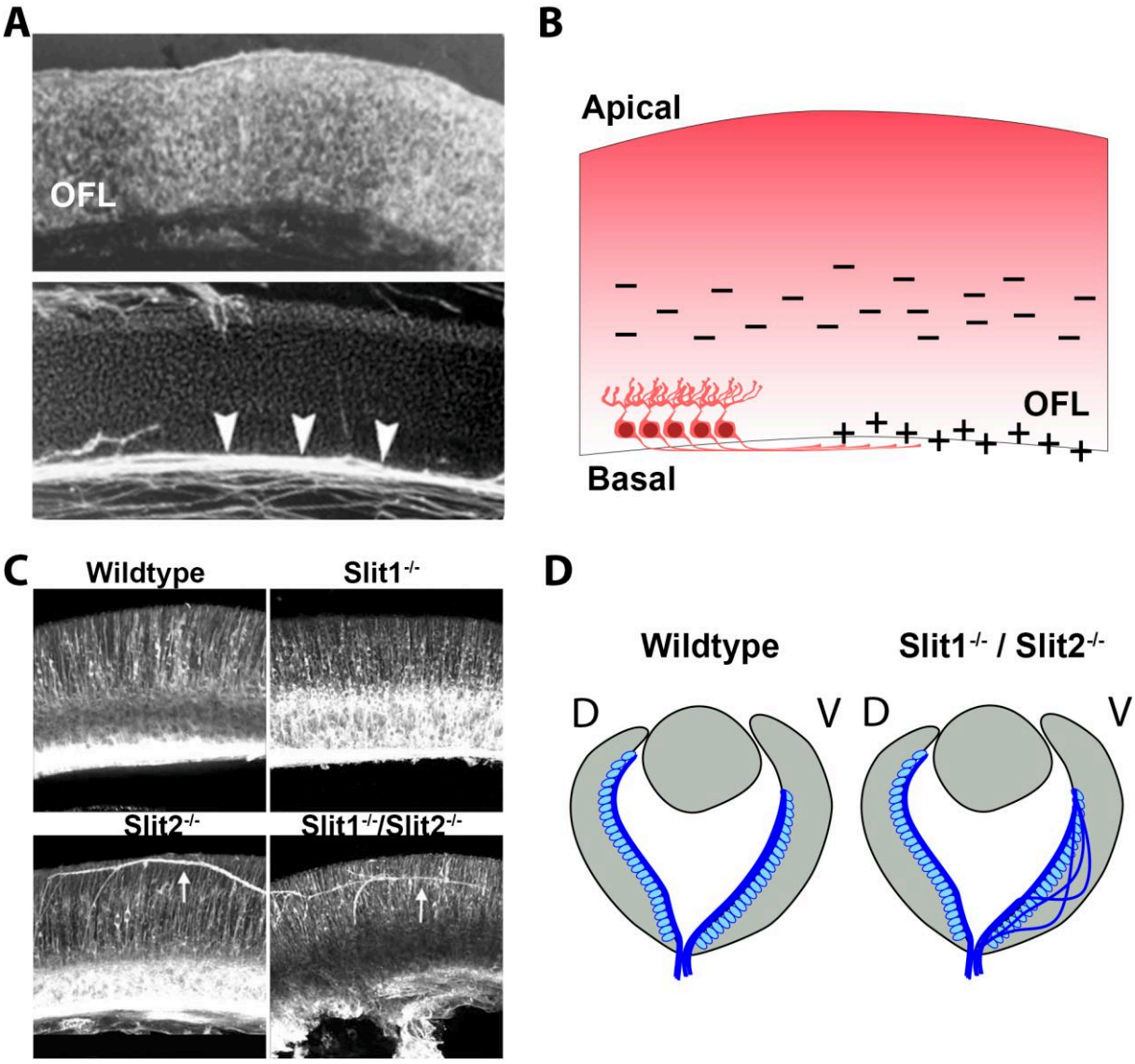

Figure 7 – The inhibitory retina. A. upper panel shows a phase contrast image of a chick retina. Lower panel shows the fluorescent image of the chick retina with exogenous laminin treatment. Despite the homogenous presence of laminin, retinal ganglion cell projections preferentially grow on the basal-most layer of the retina (arrowheads, OFL) (Stier and Schlosshauer, 1995). **B**. Schematic representation of the inhibitory regions of the neural retina and the permissive OFL of the retina. **C**. Confocal images of E16.5 mouse retinas in the dorsal OFL labeled with the pan-neuronal marker anti-tubulin (white) (Thompson et al., 2006). **D**. Schematic representation of intra-retinal pathfinding defects in Slit1-/-/Slit2-/- dKO mice. A significant portion of retinal ganglion cells in the dorsal retina stray away from the OFL and project into the apical retina. OFL = Outer fibre layer; D = dorsal; V = ventral.

Initial *in vitro* experiments showed that *slit2* is a potent inhibitor of RGC axonal outgrowth (Erskine et al., 2000; Niclou et al., 2000; Ringstedt et al., 2000). *slit2* and more significantly *slit1/slit2* double knockout (dKO) mice display several intraretinal pathfinding defects whereas *slit1* mutants do not display any phenotype (Figure 7C; Plump et al., 2002; Thompson et al., 2006). The phenotype observed in dKO mice varies along the dorso-ventral axis: in the dorsal retina, RGCs from dKO mice are correctly restricted in the OFL but project in a disorganized manner towards the optic disc; in the peripheral ventral retina, RGC from *slit2* mutants lose the restriction to the OFL and project aberrantly into the retina (Figure 7C,D; Thompson et al., 2006). Aberrant RGC projections in the ventral retina were successfully labelled by retrograde labelling from the optic tract, suggesting that although RGC axons diverge from their stereotypic projection pattern and invade retinal layers, they still are able to target the optic disc and enter the optic nerve (Thompson et al., 2006; Thompson et al., 2009).

Worthy of note, during early eye development all tissues are juxtaposed. It is therefore unsurprising that tissues outside of the retina mediate RGC directionality. Indeed, the lens epithelium secretes inhibitory cues which prevents RGCs from growing into the vitreous (Ohta et al., 1999). The secreted cue from the lens epithelium was subsequently identified as Slit2, since co-cultures of *Slit2* null lens, in contrast to wildtype lens, did not repel RGC axons (Thompson et al., 2006). The difference between *slit1* and *slit2* mutants could be due to their differential binding to Robo receptors. However the analysis that *robo2* but not *robo1* knockout mice phenocopy the *slit1/slit2* dKO mice discarded this possibility (Thompson et al., 2009). Robo2 has therefore been proposed as the predominant receptor mediating intra-retinal pathfinding of RGCs. The story appears more complicated in the case of *slit1*. While there is an absence of intra-retinal defects in *slit1* mouse mutants, loss-of-function of *slit1* in chick retina leads to RGC defasciculation (Jin et al., 2003). Mosaic overexpression of *slit1* using *in ovo* viral infection led RGC axons to preferentially grow on slit1 expressing cells, suggesting that slit1 may act as an attractive cue to RGC axons (Jin et al., 2003). In line with these results, *slit1* is known to possess different expression patterns across species. In the mouse, all RGCs express *slit1* whereas in the chick it is expressed in a mosaic pattern in the RGC layer. The differential expression pattern of *slit1* is also seen in zebrafish where the two homologues *slit1a* and *slit1b* are expressed by RGCs and amacrine cells in the inner nuclear layer

respectively, highlighting an evolutionary diversion in Slit1 function (Hutson et al., 2003).

The family of secreted frizzled-related proteins (Sfrp) also prevent RGCs from invading deeper retinal layers (Marcos et al., 2015). Retinal distribution shows that *Sfrp1* is expressed in the retinal pigment epithelium, ciliary margin zone, and the RGC layer whereas *Sfrp2* is expressed in the neuroblastic layer of the retina and the proximal OS (Marcos et al., 2015). In *Sfrp2* mutants and to a stronger degree *Sfrp1/Sfrp2* dKO mice, a subset of ventro-peripheral RGC axons invades deeper layers of the retina. *Sfrp1* single mutants, however, display no major defects (Marcos et al., 2015). This suggests a functional redundancy between Sfrps. The *Sfrp1/Sfrp2* dKO defects are reminiscent of *slit1/slit2* dKO and *robo2* KO phenotype and hint at a possible cross-talk between the signaling mechanisms. Sfrps therefore prevent RGCs from growing ectopically intro retinal layers and constrict RGC projections into the optic disc.

1.4.3 The basal lamina

Inhibitory cues from the surrounding retina and lens restrict growing RGC axons to the OFL. We now need to understand how RGCs obtain directionality towards the optic disc. The first clues emerged from studies showing that ECM in the vicinity of glial end-feet and more particularly axon-extracellular matrix interactions may be critical for axon guidance (Rogers et al., 1983). Interest was put on ECM proteins that would convey directionality to differentiating RGC axons and that possessed a graded expression in the retina. The ECM proteins Chondroitin Sulfate Proteoglycans (CSPG) are expressed homogeneously across the retinal basal lamina prior to RGC differentiation (Brittis et al., 1992; Snow et al., 1991). Proteoglycans are glycosylated proteins that covalently link to glycosaminoglycans such as chondroitin sulfate. Upon RGC differentiation, a developmental radial regression of CSPGs (from center-to-periphery) occurs in parallel to RGC growth (Figure 8A). Enzymatic disruption of CSPG localization, using chondroitinase ABC (cleaving glycosaminoglycan chains from CSPGs) leads to ectopically positioned and aberrantly projecting RGCs (Figure 8B; Brittis et al., 1992). In addition, exogenous injections of free chondroitin sulfate in the apical retina lead to a complete inversion of RGC polarity (Brittis and Silver, 1994). In chicks, injection of collagenase induces a retraction of the basal neuroepithelial endfeet leading to a disorganized optic fiber layer (Halfter et al., 2001). Thus, before

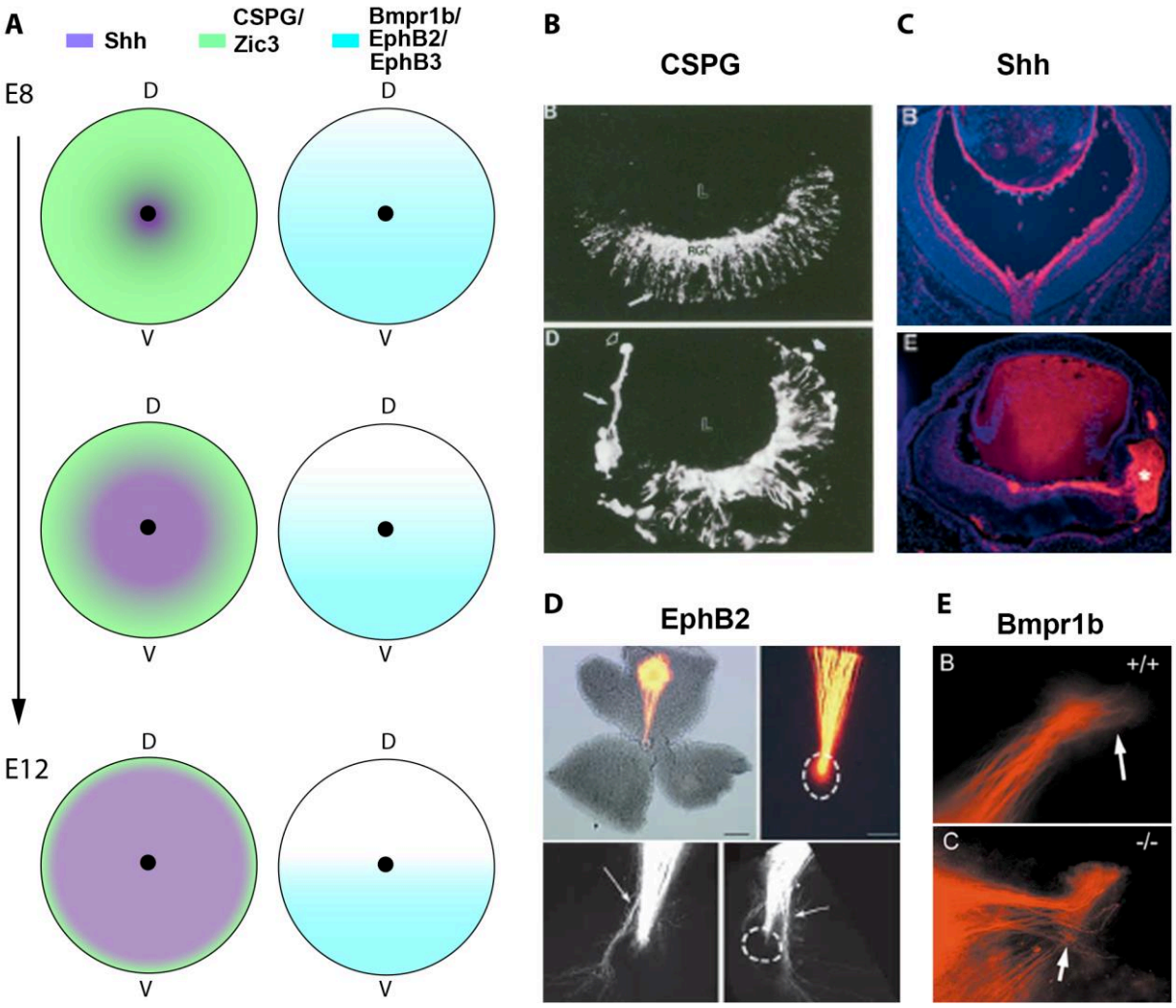

Figure 8 – Several gradients exist in the developing eye. A. A time course representation of the intra-retinal gradients in the developing eye. Shh (purple) is expressed in a high central-to-low peripheral gradient in the developing eye. CSPG and Zic3 (green) possess a high-peripheral-to-low central radial gradient. EphB2, EphB3, and Bmpr1b (blue) posses a high-ventral-to-low dorsal linear gradient in the developing retina. **B**. Shows the retinal defects following CSPG. Upper panel shows a control retina at E12.5 labeled with bIII-tubulin. Lower panel shows E12.5 retinas cultured for 48h in the presence of chondroitin sulfate ABC lyase. Many retinal ganglion cell project aberrantly (Brittis et al., 1992). **C**. E17 mouse retinal cryosections in Thy1-Cre;Shh cKO mice. Upper panel shows a control retina labelled with neurofilament. Lower panel shows a large portion of RGCs project aberrantly in the subretinal space (Dakubo et al., 2003). **D**. Flat-mounted retinas labelled with a DiI crystal. Upper panels show a Wildtype retina, with retinal projections targeting the optic disc (white dashed circle). Lower panel shows pathfinding defects in EphB2$^{-/-}$/EphB3$^{-/-}$ dKo mice (Birgbauer et al., 2000). **E**. Retinal ganglion cell projections labled with a DiI crystal. In control mice, retinal ganglion cells project to the optic disc (white arrow). In Bmpr1b-/- null mice, axons from the ventral retina make errors at the optic disc (white arrow) (Liu et al., 2003). D = dorsal; V = ventral.

the differentiation of the first RGCs, the retinal surface appears to be non-permissive for axonal growth. The developmental radial regression of CSPGs in the retina allows the differentiation of RGCs and their proper guidance towards the optic disc. It is important to note that no endogenous gradient of CSPG has been shown in neither chick nor fish (Halfter, 1998; Stuermer and Bastmeyer, 2000).

Other molecules bear a similar expression profile. The morphogen Sonic Hedgehog (Shh) is expressed in a high-central to low-periphery graded manner prior to RGC differentiation (Figure 8A; Kolpak et al., 2005). Gain-of-function or loss-of-function experiments in mouse and chick retina showed OFL disorganization and intra-retinal defects (Figure 8C; Dakubo et al., 2003; Kolpak et al., 2005). The Shh-mediated intra-retinal defect is attributed in part to the Shh receptor Patched1 since *in utero* electroporation of a dominant negative form of Patched1 led to many RGC axons projecting aberrantly and invading the peripheral retina (Sánchez-Camacho and Bovolenta, 2008). Hence, a tight balance of Shh seems necessary for proper RGC guidance to the optic disc. In line with this observation, low Shh concentrations (0.3-0.6 µg/ml) promote outgrowth whereas high concentrations (2.5-3.0 µg/ml) inhibit outgrowth of chick RGC explants (Kolpak et al., 2005).

In addition to morphogens, transcription factors also display a radial expression pattern in the developing retina. The Zinc finger (Zic) transcription factor Zic3 is expressed in a low-central and high-peripheral pattern prior to RGC differentiation in the chick retina (Figure 8A; Zhang et al., 2004). Similar to CSPGs and Shh, Zic3 expression recedes over the development of the retina, coinciding with RGC differentiation (Zhang et al., 2004). Disruption of the Zic3 gradient by viral *in ovo* overexpression leads to RGC projecting away from the OFL and into the subretinal space (Zhang et al., 2004). Of note, overexpression of Zic3 does not affect the differentiation pattern of retinal cell types nor does it impact other known guidance receptors such as CSPGs (Zhang et al., 2004). To date the transcriptional regulation induced by Zic3 remains unknown, but it is probable that it mediates the expression of repulsive guidance cues since RGC explants avoid Zic3 in a stripe assay (Zhang et al., 2004).

The radial expression pattern seen in previous molecules likely gives the proper orientation of RGCs to project towards the central retina. However, other molecules were identified to be expressed along the dorso-ventral axis. The erythropoietin-producing hepatocellular carcinoma (Eph) family of tyrosine kinase receptors,

EphB1/EphB2/EphB3 and their ligands ephrinB1/B2/B3 are all expressed uniformly in the developing retina (Birgbauer et al., 2000). At later stages, EphB2 expression shifts to a ventral-high dorsal-low expression pattern (Figure 8A; Birgbauer et al., 2000). In *EphB2/EphB3* dKO mice, RGC axons originating from the dorsal retina fail to exit the optic disc and extend into the peripheral retina (Figure 8D; Birgbauer et al., 2000). Eph receptors mediate their signaling through their intracellular kinase domain. Interestingly, kinase dead *EphB2* mutants rescue the intra-retinal defects. The latter observation along with the finding that the extracellular domain of EphB receptors is repulsive to RGC axons suggest that EphB2 mediates intra-retinal guidance independently of its kinase activity (Birgbauer et al., 2001). The model proposed was that high levels of EphB2 in the ventral retina ensure proper targeting of dorsal RGCs towards the optic disc and away from the ventral retina. The morphogen receptor for bone morphogenetic proteins (BMPs) also exhibits a dorso-ventral expression profile (Figure 8A). BMPs are critical in early eye development (Trousse et al., 2001). Mice lacking the BMP receptor 1b (*Bmpr1b*$^{-/-}$) display intra-retinal defects in the ventral retina (Figure 8E; Liu et al., 2003). In particular, ventral RGCs extend toward the optic disc but cannot exit the eye. In agreement with this phenotype, the BMP receptor 1b is expressed in a ventral-high and dorsal-low gradient in the developing mouse retina (Liu et al., 2003). Since BMP receptors are active regulators of transcriptional machinery (Tzavlaki and Moustakas, 2020), it is very likely that the phenotype observed in *Bmprlb*$^{-/-}$ is a consequence of a negative regulation of guidance receptors in ventrally located RGCs. It is nonetheless important to mention that the intra-retinal phenotype seen in *Bmprlb*$^{-/-}$ mice cannot be solely attributed to BMP signaling since several other guidance molecules are downregulated (Liu et al., 2003).

Finally, some molecules without any apparent graded expression within the retina play a critical role in intra-retinal pathfinding. For example, the planar cell polarity protein Vangl2 is uniformly expressed in the basal lamina of the developing murine eye (Leung et al., 2015). Vangl2 homozygous mutants display severe disruption of RGC projections, with RGCs projecting away from the OFL and intro the subretinal space. In addition to losing their polarity, RGC projections do not exit the eye properly, leading to a hypoplastic optic nerve (Leung et al., 2015).

1.4.4 From directionality to unison

Contact with previously formed axons is critical for projecting RGCs to maintain their correct polarity towards the optic disc (Drazba and Lemmon, 1994). This fasciculation is mediated by homo- and heterophilic interactions between adhesion molecules on adjacent axons. Both the neural cell adhesion molecule (NrCAM) and the cell adhesion molecule L1 promote RGC axon outgrowth (Bao, 2008). Brittis and colleagues (1995) studied the dynamics of the rat RGC intra-retinal axon extension following treatment with blocking antibodies targeting NrCAM and L1 (Brittis et al., 1995). Treatment of anti-NrCAM fab fragments cause RGC axons to halt, and fail to exit the optic disc without perturbing the overall orientation of projections, while treatment with L1-blocking antibodies severely disrupts the radial orientation of RGC axons (Brittis et al., 1995). Moreover, perturbations of NrCAM in chick retinal explants using blocking antibodies leads to failure of RGC axons to make the correct exit into the optic disc (Zelina et al., 2005). Genetic ablation of Activated leukocyte cell adhesion molecules (ALCAM) in mice shares a similar phenotype to L1 (Weiner et al., 2004). Therefore, whilst NrCAM may regulate axon fasciculation and correct exit out of the eye, L1 and ALCAM may mediate proper orientation towards the optic disc. Taken together, adhesion molecules provide a permissive substrate for growing RGCs to adhere to pioneer RGC axons towards the optic disc. This cannot however be the sole strategy since pioneer axons are devoid of prior tracts to adhere to. In addition, the possibility that pioneer RGCs pave the way for future RGCs has been partially discarded due to the observation that removal of dorsal pioneer RGCs in Xenopus embryos leads to correct pathfinding of ventrally projecting RGCs (Holt, 1984). Notably, inter-species variability exist in adhesion molecules : treatment of goldfish retina with L1-blocking antibodies disrupts RGC fasciculation but not their orientation towards the optic disc (Bastmeyer et al., 1995). Moreover, antibodies to the goldfish homologue of ALCAM, Neurolin, causes RGC defasciculation and aberrant projections in the dorsal retina (Ott et al., 1998). This evolutionary biased role of adhesion molecules may be explained by the observation that certain species possess asymmetric RGC fasciculation. In chick retina for example, ventral RGCs form larger axon fascicles (Mühleisen et al., 2006).

1.4.5 The optic disc as the highway out of the eye

Once the RGC axons have successfully projected towards the optic disc they must take the correct exit out of the retina and into the OS through the choroid fissure. In zebrafish, the stromal cell-derived factors (SDF-1) *sdf1-a* and *sdf1-b* are expressed in the proximal OS (Figure 9A; Li et al., 2005). Furthermore, the SDF-1 receptor Cxcr4b is expressed by RGC axons (Li et al., 2005). Antisense morpholino oligos targeted against *sdf1-a*, *sdf1-b*, and *cxcr4b* lead to RGC misrouting inside the retina (Figure 9B). These results were confirmed in *cxcr4b* mutant zebrafish (Odysseus) which display intra-retinal misrouting of RGCs (Li et al., 2005).

Interestingly, the laminin-like protein, Netrin-1 is strongly expressed by glial cells in the optic disc (Figure 9A; Deiner et al., 1997; Kennedy et al., 1994; Serafini et al., 1996). Moreover, the transmembrane receptor for Netrin-1, Deleted in Colorectal Cancer (Dcc) is expressed by RGCs (Deiner et al., 1997; Keino-Masu et al., 1996). *In vitro* Netrin-1 promotes neurite outgrowth and growth cone turning of RGC axons which are inhibited by Dcc-blocking antibodies (de la Torre et al., 1997; Deiner et al., 1997; Wang et al., 1996). Analysis of *Netrin-1* hypomorph mutants showed that RGCs project normally towards the optic disc but fail to exit the eye at the optic disc leading to a hypoplastic optic nerve (Figure 9C). In addition, RGCs project away from the OFL and can be seen in the subretinal space (Deiner et al., 1997). These defects are phenocopied in *Dcc* null mice that also possess a hypoplastic optic nerve with aberrantly projecting RGCs (Figure 9C; Deiner et al., 1997). In this context, Netrin-1 was first proposed as a permissive cue for RGC axons to exit the eye. However, Netrin-1 also mediates a repulsive signal that depends on cytosolic cyclic adenosine monophosphate (cAMP) levels (Ming et al., 1997). Experiments in Xenopus showed that a combination of Netrin-1 and laminin-1 can modulate RGC cytosolic cAMP levels (Höpker et al., 1999). Interestingly, laminin-1 is uniformly expressed across the basal lamina and at the optic disc whereas Netrin-1 is expressed at the optic disc and along the OS. In this new model, growing RGCs in contact with laminin-1 in the OFL are permissive to Netrin-1 at the optic disc. Upon reaching the optic disc , RGCs extending into the OS become repulsed by Netrin-1 and the increase in cAMP levels drives them away from the optic disc. Of note, ECM proteins such as laminin thus not only regulate substrate-mediated adhesion but also modulate RGC response to guidance cues.

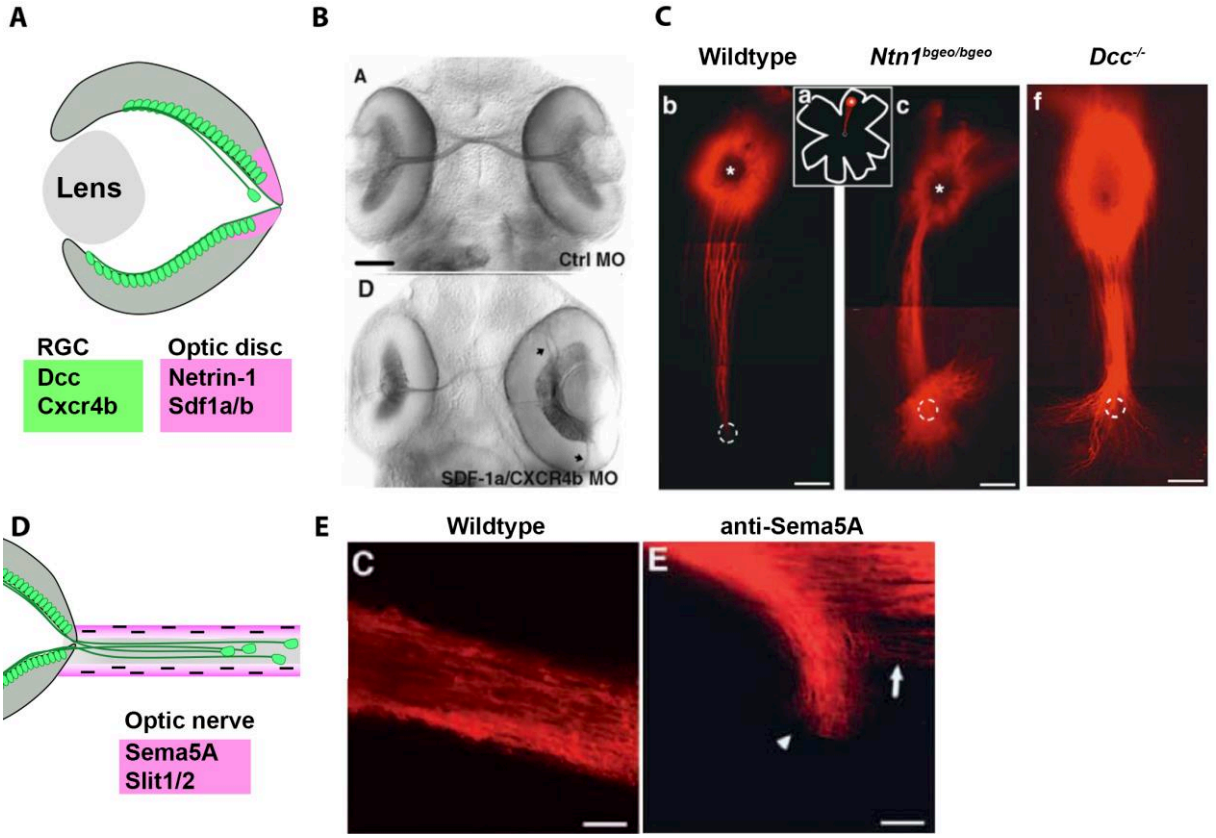

Figure 9 – The guidance molecules that help restrict retinal projections A. A schematic representation of an embryonic mouse retina. Retinal ganglion cell axons project towards the optic disc. Retinal ganglion cell express the membrane receptors Deleted in Colorectal carcinoma (Dcc) and the Cxcr4 receptors. At the optic disc, Netrin-1 and Sdf1 permissive ligands are expressed. **B**. Ventral view of 2 days post fertilization zebrafish larvae labelled with the retinal ganglion cell marker Zn5. Zebrafish larvae injected with Sdf1b and Cxcr4 morpholinos (Mo) display severe intra-retinal pathfinding defects (Li et al., 2005). **C**. DiI injections on E15 flat-mounted mouse retinas. Left panel shows Wildtype retinal ganglion cells project to the optic disc. Middle panel, Netrin-1 hypomorph mutants ($Ntn1^{\beta geo/\beta geo}$) display intra-retinal pathfinding defect. Right panel show DiI injections in $Dcc^{-/-}$ null mice, which phenocopy $Ntn1^{\beta geo/\beta geo}$ mutants (Deiner et al., 1997). **D**. A schematic representation of the developing mouse optic nerve. The expression of Slit1/Slit2 and Sema5A in the surrounding glial cells forms a collar which restrict the growth of retinal ganglion cells. **E**. E14 mouse optic nerves labeled with DiI. Wildtype mice show a well fasciculated optic nerve. Treatment of optic nerves with an anti-Sema5A antibody leads to defasciculation defects (Oster, 2003).

RGC axons projecting along the retina and exiting the optic disc must fray their way to their visual target in the brain. In opposition to what was reported in the retina, axons navigating in the OS possess no chronotropic organization. This suggests that both early- and late-born RGCs intermingle in the OS and carry out a “fascicle hopping” behavior (Silver, 1984). The previously mentioned inhibitory molecule Slit2 is also highly expressed at the optic disc and along the OS (Figure 9D, Niclou et al., 2000; Ringstedt et al., 2000). Indeed, *Slit1/Slit2* dKO mice display RGC fibers aberrantly projecting away from the presumptive optic nerve (Plump et al., 2002; Thompson et al., 2006). Therefore, Slit2 may function to restrict RGC axons in a tight fascicle forming the optic nerve.

The largest family of inhibitory guidance molecules are the Semaphorins (Sema) (Jongbloets and Pasterkamp, 2014). In the developing visual system, many Semaphorins are expressed. Sema5A shares a similar expression pattern to that of Netrin-1, it is localized as a collar around the optic disc and along the OS (Figure 9D; Oster, 2003). In addition, Sema5A induces an inhibitory response on RGCs: mouse retinas treated with Sema5A-blocking antibodies result in RGC fiber defasciculation at the optic disc and axon bundles straying away from the optic nerve (Figure 9E; Oster, 2003). Of note, the Sema5A-mediated RGC inhibition is maintained in combination to adhesive molecules such as laminin-1 and L1 as well as the permissive guidance molecule Netrin-1. Therefore, both Sema5A and Slit2 function simultaneously to restrict RGC growth in the presumptive optic nerve. The morphogen Shh also plays an important role in restricting RGCs within the optic nerve. Shh is expressed along the axons of RGCs in the optic nerve and mediates its signaling through Patched1 expressed in RGCs (Sánchez-Camacho and Bovolenta, 2008). Blocking Shh either by electroporating a dominant-negative Patched1 or by Shh-blocking antibodies results in RGCs detaching from the optic nerve and growing dorsally (Sánchez-Camacho and Bovolenta, 2008).

A few other molecules that promote the growth of RGCs along the OS are worth mentioning. The Ventral anterior homeobox 1 (Vax1) is a critical transcription factor controlling RGC development. Vax1 is expressed in the ventral anterior region of CNS with a high expression along the OS (Hallonet et al., 1998). *Vax1* null mutant mice display RGC axon stalling at the junction of the optic nerve and the ventral diencephalon and fail to form an OC (Bertuzzi et al., 1999; Hallonet et al., 1999). In

humans, successive nucleotide substitutions in the *VAX1* gene result in optic nerve hypoplasia and OC agenesis (Slavotinek et al., 2012). Complete stalling of RGCs in the OS of *Vax1* null mice was attributed to its transcriptional regulation of axon guidance cues since *Vax1* mutants display a major dysregulation of both EphB3 and Netrin-1 at the optic disc and OS (Bertuzzi et al., 1999). This explanation was recently challenged by the observation that mice lacking the nuclear translocation domain of Vax1 still induced RGC outgrowth (Kim et al., 2014). The authors further showed that Vax1 could be secreted both *in vitro* and *in vivo* and could be internalized by RGC axons, leading to *de novo* protein synthesis (Kim et al., 2014). As a result, the current model suggests projecting RGCs internalize Vax1 expressed along the OS which triggers protein synthesis and motivates the RGC growth towards the ventral hypothalamus.

1.5 Trafficking a versatile terrain

1.5.1 A unique tissue

In bilateria, sensory and motor events occurring on one side are largely processed by the opposite side of the brain. While the reason for this curious reversal of representation is still unclear, an important consequence is that many axonal pathways running to and from the brain must cross at the midline (decussation). Often, all axons projecting from and to the brain cross the midline forming a complete decussation, such as in the case for the cortico-spinal tract. However, in the mammalian visual system, RGCs projecting to the brain partially cross at the OC, in the midline of the ventral diencephalon (alar plate) (Figure 11A-C; Puelles and Rubenstein, 1993). This creates two main populations of RGCs, those projecting to the opposite side (contra-lateral RGCs) and those projecting to the same side of the brain (ipsi-lateral RGCs).

As RGC growth cones extend into the ventral diencephalon, their morphology dramatically changes from elongated to more complex filopodia patterns (Bovolenta and Mason, 1987; Godement et al., 1990; Sretavan, 1990). Live-imaging experiments described that upon reaching the midline, RGC growth cones pause and retract, often lasting several hours (Godement et al., 1994; Sretavan and Reichardt, 1993). Like the developing retina, the diencephalon midline is lined by radial glia processes (Silver,

1984). Throughout their development, RGCs share a complex interaction with radial glia that is critical for their navigation (Silver, 1984). We have seen that the close interaction of RGCs with the basal processes of radial glia in the retina is necessary for the invasion of the OFL. In the optic nerve, glia inter-fasciculate with RGC axons. At the base of the third ventricle, RGC projections invade the presumptive region of the hypothalamus. However, in this region radial glia lose their inter-fasciculation and organize in a radial manner by extending their processes into the midline and creating a palisade (Figure 10A-C; Bovolenta and Mason, 1987; Silver, 1984; Silver and Sidman, 1980). These radial glia express the Radial-Glia Cell marker-2 (RC2), Brain Lipid-Binding Protein, but not Glial Fibrillary Acidic Protein (GFAP) (Williams et al., 2003). Both contra- and ipsi-lateral RGCs invade the glial palisade, but ipsi-lateral RGCs never grow past a narrow strip along the ventral midline (100-200µm) (Figure 10C; Godement et al., 1990). Further analysis showed that radial glia are intersected by a narrow midline raphe of neurons expressing the stem cell marker Stage-Specific Embryonic Antigen-1 (SSEA-1) and the cluster of differentiation marker CD44 (Figure 10A-C; Marcus and Mason, 1995; Marcus et al., 1995; Sretavan et al., 1994).

Following midline crossing, RGCs extend dorsally along the lateral wall of the diencephalon lined by SSEA-1/CD44 neurons that cover the medio-lateral portion of the ventral hypothalamus (Figure 10B). Specific ablation of these neurons using CD44-blocking antibodies impedes OC formation, indicating that they are critical for the proper development of RGC projections (Sretavan et al., 1995). Much like the observations carried out by Stier and Schlosshauer (1995), *in vitro* studies showed that ipsi-lateral RGCs avoid islands of OC tissue or isolated membranes from chiasm cells whereas contra-lateral RGCs do not (Godement and Mason, 1993; Wang et al., 1995; Wizenmann et al., 1993). In addition, growing RGCs possess a stereotypic projection pattern: upon entering the diencephalon they avoid the ventral diencephalon and project first towards the midline and then dorsally into the thalamus. *In vitro* cultures of rat retinal explants showed that the hypothalamus and epithalamus release inhibitory soluble factors, whereas the dorsal thalamus promotes the growth of RGCs (Tuttle et al., 1998). Together, these observations hint at the idea that the radial glia palisade may function to sort RGC axons at the midline and that the surrounding tissues of the diencephalon may act as “guidepost” cells secreting spatially-restricted guidance cues.

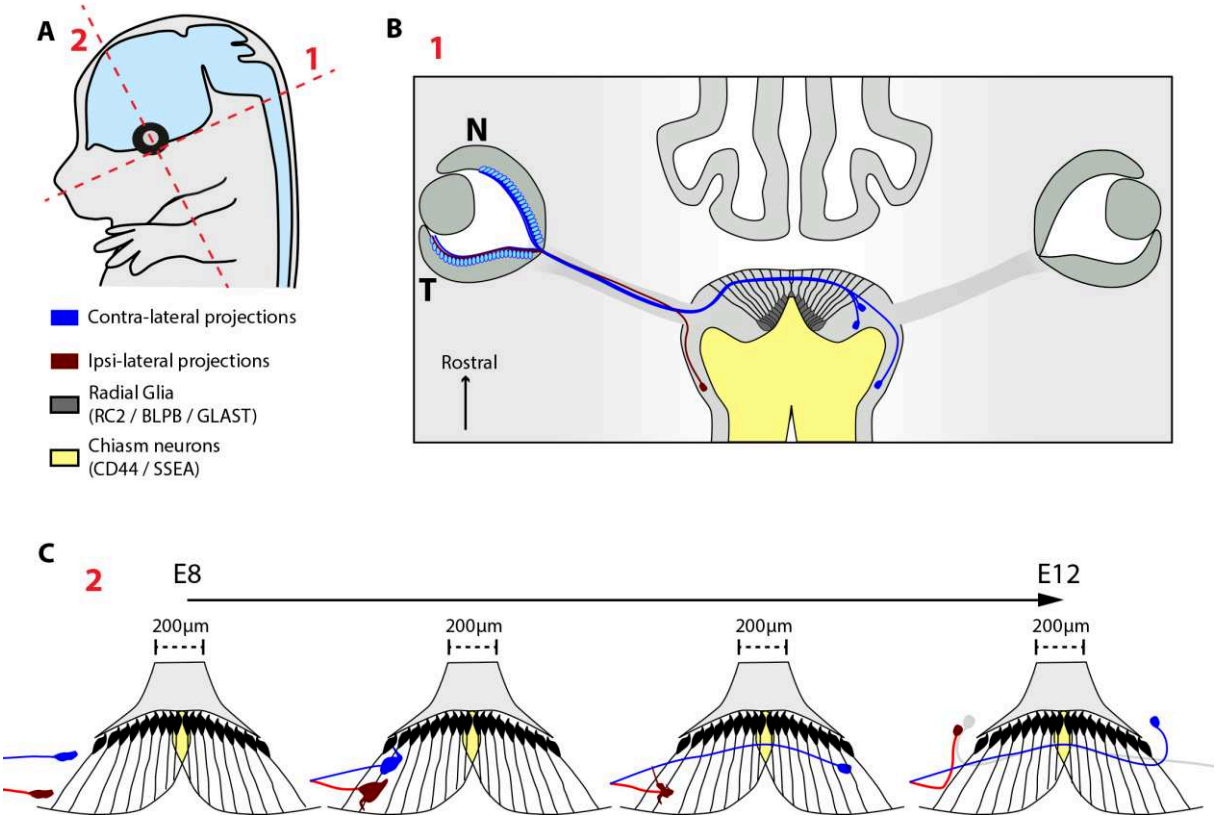

Figure 10 – Retinal projections enter the brain at the ventral diencephalon A. A schematic representation of an E12 mouse retina. Red dashed line outlines the section planes. **1**. Shows a schematic representation of a horizontal section of an E12 mouse diencephalon and eyes. Contra-lateral (blue) and ipsi-lateral (red) retinal projections are depicted. Retinal ganglion cells project along the optic nerve to the ventral diencephalon. They next interact with radial glia organized in a palisade, at the midline. Contra-lateral projections cross the midline and project caudally towards the dorsal diencephalon. Ipsi-lateral projections are repelled at the midline and project to the ipsi-lateral dorsal diencephalon. **2**. A time course representation (E8-E12) of ipsi- and contra-lateral retinal projections at the ventral diencephalon midline. Both ipsi- and contra-lateral projections enter the glial palisade at the midline. A thin raphe of CD44/SSEA neurons are present at the midline (yellow). Ipsi-lateral projections never reach closer to a 200µm radius from the CD44/SSEA neurons at the midline.

1.5.2 Positioning the optic chiasm

Early patterning of the ventral forebrain is critical to properly define the positioning of the presumptive OC. The role of morphogens in forebrain tissue patterning, and particularly that of the morphogen Shh, is largely documented (Chiang et al., 1996). In zebrafish, mutations affecting Shh signaling results in OC agenesis with RGCs projecting ipsi-laterally (Barresi et al., 2005; Karlstrom et al., 1996; Karlstrom et al., 1999; Karlstrom et al., 2003). In these mutants, RGC axons directly project ipsi-laterally without ever entering the OC territory. Shh mutants such as *you-too* (*yot*, *gli2*), *sonic-you* (*syu*), *detour* (*dtr*, *gli1*), reveal that the loss of Shh induces early patterning defects of the ventral diencephalon. Moreover, loss of Shh signaling leads to a loss of glial cell identity near the ventral midline resulting in an aberrant axon guidance profile along the OC (Barresi et al., 2005). It is essential to note that Shh also plays a critical role in the guidance of RGC axons which makes it difficult to tease apart its role in patterning and guidance of RGC growth cones at the midline (see section: *Defining the uncrossed visual projections*). The fine regulation of Shh domain within the ventral diencephalon is critical. During early development, the Paired box (Pax) transcription factors are expressed by specific organs (see section: *Patterning of the eye*). For instance, the *Pax2* gene has morphogenetic functions during early eye development (Torres et al., 1996). Like *Shh* mutants, *Pax2* mutant mice are achiasmatic, with RGCs projecting directly into the ipsi-lateral optic tract (Torres et al., 1996). *Pax2* is expressed along the optic stalk extending into the ventral midline, this creates a Shh-free region at the pre-optic region. Loss of *Pax2* leads to an expansion of the *Shh* territory, invading the ventral midline (Torres et al., 1996). Therefore, a fine balance exists between Pax2 and Shh to pre-pattern the presumptive OC.

In addition to *Shh*, the ventral diencephalon is lined by the expression of several regulatory genes. This is of particular interest since axon pathways project along regulatory gene boundaries. As a result, understanding the regulatory gene network that paves the ventral diencephalon may shed light on molecules responsible for RGC navigation. When RGC axons enter the ventral diencephalon, lateral to the midline, they navigate on overlapping domains of Forkhead box d1 (*Foxd1*), Distal-less Homeobox 2 (*Dlx2*), and NK2 Homeobox 2 (*Nkx2.2*) (Figure 11A-D; Marcus et al., 1999). Here, RGC axons follow a corridor lined by domains of Forkhead box g1 (*Foxg1*) (dorsally) and *Nkx2.2* (ventrally, Figure 11D). At the midline, RGC axons cross at a domain that is deprived of Dlx2 and Foxd1 expression but instead expresses both

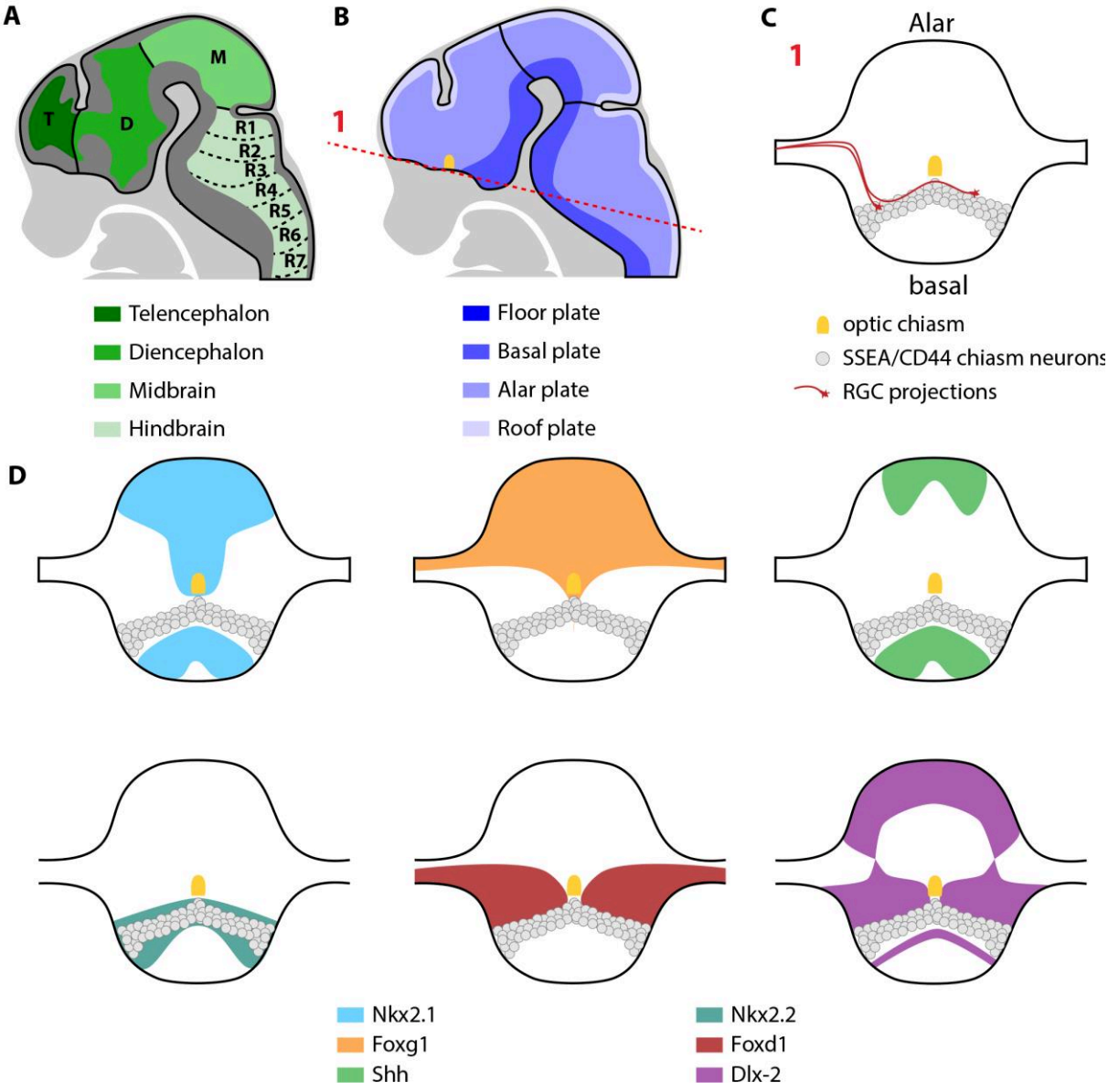

Figure 11 – Retinal projections cross and interact with multiple territories in the ventral diencephalon. A. A schematic representation of an E12 mouse brain. The brain is segmented along its rostro-caudal axis. The major delimitations are based on morphogen expression. The telencephalon is the rostral-most structure followed by the diencephalon, the midbrain, and the hindbrain at the caudal-most end. **B**. In addition to being segmented rostra-caudally, the central nervous system is further segmented dorso-ventrally. At the ventral-most region is the floor plate followed by the basal, the alar, and at the dorsal-most end reside the roof plate. The optic chiasm is located at the basal plate of the ventral diencephalon. The red dashed line outline the section plane of the schematics. **C**. A transverse section of an E12 mouse embryo. Retinal projections (red) follow a distinct trajectory across the ventral midline of the diencephalon and towards the contralateral dorsal diencephalon. **D**. Schematic representation of the various territories that delineate the projections of retinal ganglion cells adapted from (Marcus et al., 1999).

Nkx2.2 and *Foxg1* (Figure 11D). Throughout their route, RGC axons remain dorsal to the Shh domain of the hypothalamus, suggesting that the OC is formed in the alar plate. Previously, we saw that RGC axons follow the border of SSEA-1/CD44 neurons in the ventral diencephalon. Interestingly, the appearance of these neurons coincides with the *Nkx2.2* expression pattern (Figure 11D; Marcus et al., 1999). RGC axons therefore navigate through territories of overlapping regulatory genes that must be critical for their paths. These regulatory genes may induce the differentiation of specific cell types, such as SSEA-1/CDD44 neurons, that regulate RGCs trajectory by secreting guidance cues. The complementary expression patterns of both *Foxd1* and *Foxg1* at the chiasmatic plate indicate that a fine balance between the two is required at the midline. Indeed, both *Foxg1* and *Foxd1* mutant mice display an increase of ipsi-laterally projecting RGCs with abnormal OC shape (Herrera et al., 2004; Pratt et al., 2004).

Regulatory regions of the ventral diencephalon specify the cells that will secrete guidance cues to crossing RGCs. Examples of such molecules are the Slit which are essential for intra-retinal pathfinding as well as for the fasciculation of growing RGCs within the optic stalk. At the presumptive OC, Slit2 is expressed dorsal and caudal to the RGC axons and Slit1 is expressed around the optic stalk and caudal to the ventral diencephalon (Erskine et al., 2000; Niclou et al., 2000; Ringstedt et al., 2000). In the absence of both *Slit1* and *Slit2*, RGCs are no longer tightly bundled but instead project rostrally in the pre-optic area which creates a doubling of the chiasm (Plump et al., 2002). Both *Slit* single mutants show no chiasm defects, but an ectopic chiasm is seen in *Slit1*$^{+/-}$*/Slit2*$^{-/-}$ mutants suggesting that *Slit2* is particularly involved in restricting the proper formation of the OC (Plump et al., 2002). Considering that both *Slit1* and *Slit2* share complementary expression patterns at the ventral diencephalon, it is puzzling that single mutants do not induce specific phenotypes. This could be in part explained by the differential expression pattern of Slit1 and Slit2 proteins or by redundant guidance molecules expressed at the ventral diencephalon.

As observed in intra-retinal pathfinding, Slit proteins signal by binding to their Robo receptor. Analysis of *Robo2* null mutant mice showed OC expansion in its rostro-caudal axis like the *Slit1/Slit2* dKO mice (Plachez et al., 2008). Robo/Slit function appears to be evolutionarily conserved. As in rodent, zebrafish *slit2* is expressed in the optic stalk and ventral diencephalon rostral to RGC axon projections, whereas *Slit3* is expressed

caudal to RGC projections (Hutson and Chien, 2002). Shortly after differentiating, RGCs begin expressing *Robo2* transiently until the projections have fully crossed the midline (Fricke et al., 2001). Large-scale screens carried out in zebrafish (*Danio rerio*) identified a particular mutation, *astray* (*ast*), that displays a rostro-caudal expansion of the OC and aberrant RGC projections in the contralateral optic nerve as well as aberrant projections in the ipsi-lateral tectum (Fricke et al., 2001; Hutson and Chien, 2002; Karlstrom et al., 1996). The gene deletion exhibited by the *ast* mutants was mapped to the *Robo2* gene locus (Fricke et al., 2001). Grafting RGCs carrying the *ast* mutation into a wildtype host results in chiasm defects, conversely wildtype RGCs project normally in an *ast* mutant (Fricke et al., 2001). This result suggests that Slit-dependent pathfinding at the OC occurs cell autonomously through Robo2-expressing RGCs.

In mice, the observation that ectopic RGCs project rostral to and not caudal to the presumptive OC is particularly interesting. Aberrantly projecting RGCs in these mutants coincide with the pre-optic area, which may serve as a permissive route for RGC axons. Another possibility lies in the idea that additional inhibitory cues may be secreted from the caudal hypothalamus. Slit proteins thus act synergistically to create a “repulsion-free” corridor preventing Robo2-expressing RGC projections from straying away from their accurate trajectory. As a result, Slit are involved in defining the position of the presumptive OC. Notably, Slit/Robo signaling does not seem critical for retinal axon divergence since RGCs from all retinal quadrants express *robo2* and are responsive to Slit proteins (Erskine et al., 2000). At the OC, *Sfrp1/Sfrp2* dKO mice show an expansion of the RGC projections in the rostro-caudal axis (Marcos et al., 2015). Much like what was observed during intra-retinal pathfinding, Sfrps appear to share a similar function to the *Slit1/Slit2* and *Robo2* mutants. Sfrps are not expressed in the ventral diencephalon, which suggests that they may mediate their effect in a cell autonomous manner in RGC axons (Marcos et al., 2015).

1.5.3 Divergence of retinal projections

The combination of guidance molecules described so far helps RGCs navigate along the optic nerve into the ventral diencephalon and across the midline to their various visual nuclei. How do individual RGCs know to which side of the brain to project to and how are ipsi- and contra-lateral RGCs sorted at the OC? In order to begin answering these questions, one must understand the developmental waves at which both ipsi- and contra-lateral RGCs project into the brain. The first-born RGCs originate from the dorso-central retina. In the mouse, these RGCs reach the ventral diencephalon at E12-13.5 and project both ipsi- and contra-laterally irrespective of their location in the retina (Figure 12A-C; Colello and Guillery, 1990; Godement et al., 1987). Rather than projecting towards the midline, as was discussed earlier, these ipsi-RGC axons take a unique route and extend directly into the ipsi-lateral optic tract without contacting the glial palisade (Figure 12B; Godement et al., 1987; Marcus and Mason, 1995). However, retrograde labeling using HRP of thymidine-injected E11 mice showed ipsi-RGC axons only in the ventro-temporal retina (Drager, 1985). Closer analysis of these projections using GFP electroporation revealed that this population is largely pruned postnatally and that very few ipsilateral fibers ever reach their visual targets (Soares and Mason, 2015).

A second wave of RGCs is observed from E14.5-E17.5 in the mouse (Figure 12B). At this stage, ipsi-RGCs arise exclusively from the ventro-temporal (VT) retina whereas contra-lateral RGCs arise from all other regions of the retina as well as within the VT crescent (Figure 12B,C; Drager, 1985; Marcucci et al., 2019). Upon reaching the OC, irrespective of their divergence, RGCs project towards the midline of the ventral diencephalon and closely interact with RC2-positive radial glia (Marcus et al., 1995). At this point, contra-RGCs project across the midline whereas the growth cones of ipsi-RGCs take a complex pattern and extend a secondary filopodia. Over multiple pauses, extensions, and retractions, the primary growth cone prunes and the extending filopodia is stabilized and will turn ipsi-laterally (Godement et al., 1994). A third wave occurs at E15.5-P0 in which late-born RGCs arise from the VT retina and project contra-laterally (Figure 12B,C; Drager, 1985; Marcucci et al., 2019). Therefore, in the adult mouse, contra-lateral RGCs originate from the entire extent of the retina whereas ipsi-lateral RGCs are restricted to the ventro-temporal retina (Drager, 1985; Dräger and Olsen, 1980).

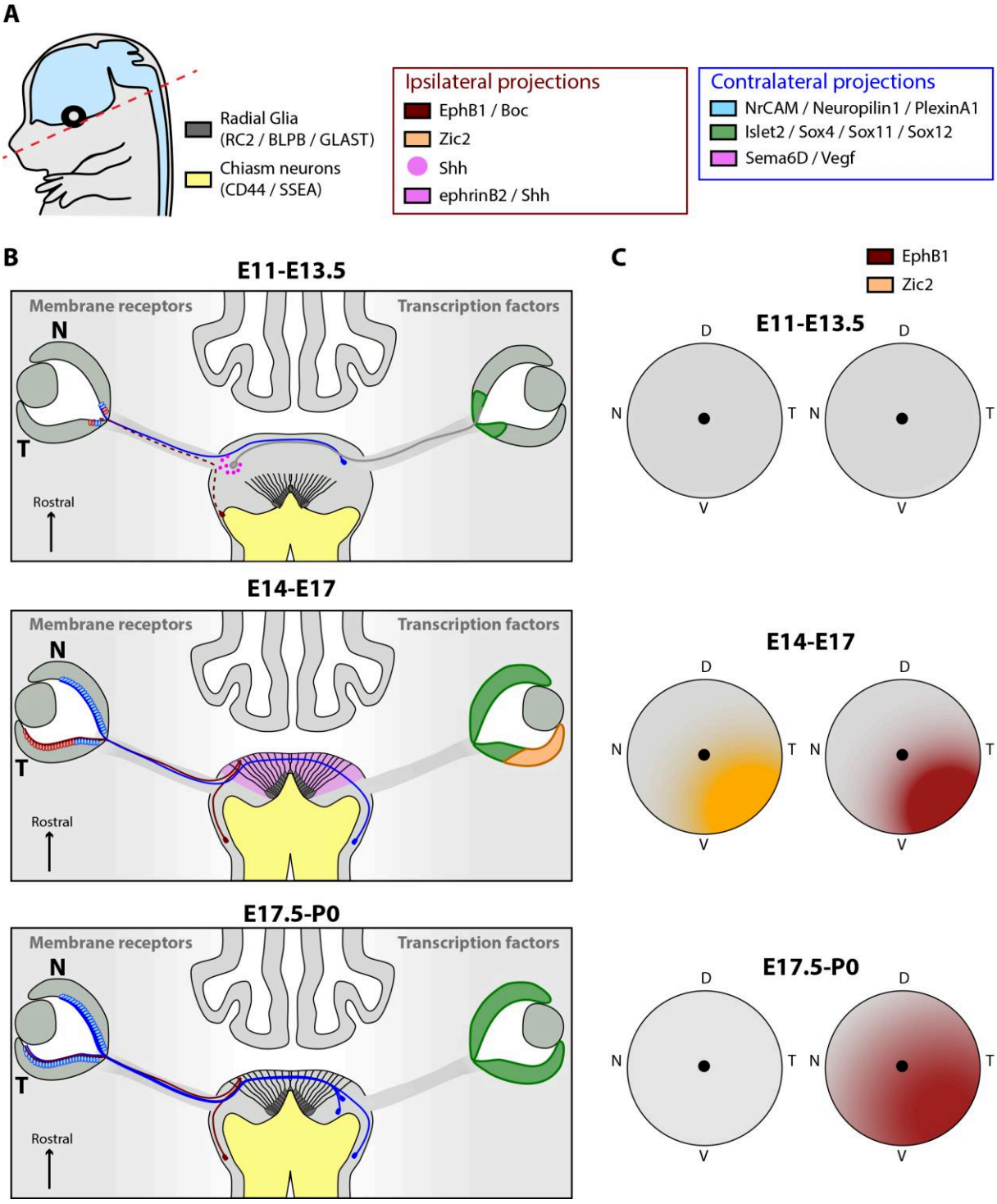

Figure 12 – The molecular interplay during the development of retinal projections **A**. Schematic of an E12 mouse. The red dashed line outlines the section plane. **B**. A representation of a transverse section of the mouse ventral diencephalon from E11 to E17. At E11, contra-lateral retinal ganglion cells (RGCs) express NrCAM/Neuropilin1 /PlexinA1 cross the midline (expressing Sema6D/Vegf) and project to the dorsal diencephalon. Upon crossing, they secrete Shh. Transient Ipsi-lateral RGCs project without reaching the midline. At E14, ipsi-lateral RGCs expressing Boc/EphB1 reach the midline and come in contact with Shh (secreted by contra-lateral RGCs, pink) and ephrinB2 (secreted by SSEA neurons at the midline, pink) and are repelled. **C**. A schematic of the developmental expression of Zic2 and EphB1 in the mouse retina.

1.5.4 Defining the uncrossed visual projections

The observation that RC2-positive glia has a differential effect between ipsi- and contra-RGCs shows that a specific guidance cue must be secreted at this site. The *Xenopus laevis* serves as a good model to study this dynamic process. Early during development, *Xenopus* tadpoles possess laterally positioned eyes and fully crossed RGC projections. However, during metamorphosis, *Xenopus's* eyes move dorso-medially and ipsi-RGCs are differentiated in the ventral retina (Currie and Cowan, 1974). Transplantation of ventral retina from post-metamorphic Xenopus into tadpoles results in all transplanted RGCs to project contra-laterally (Nakagawa et al., 2000). Therefore, the cues at the OC required to induce ipsi-RGCs are absent in the tadpoles.

The transmembrane ligand ephrinB2 is expressed at the OC of metamorphosing frogs and that ectopic expression of ephrinB2 leads to precocious ipsi-laterally projecting RGCs (Nakagawa et al., 2000). Moreover, the transmembrane EphB receptors are expressed in the retina (Nakagawa et al., 2000). Further analysis shows that while EphB1, EphB2, EphB3, and EphB6 are expressed in the retina only EphB1 is restricted to the VT retina (Williams et al., 2003). In addition, EphB1/B2/B3 triple KO (tKO) mice display a severe reduction in ipsi-lateral projecting RGCs that is comparable to that of EphB1 single mutants (Williams et al., 2003). These results suggest a model whereby VT EphB1-expressing ipsi-RGC axons contact ephrinB2-expressing RC2-positive radial glia at the OC and are repulsed into the ipsi-lateral optic tract (Figure 12A-C). This molecular signaling cascade appears to be evolutionarily conserved since EphB1 and ephrinB2 are expressed in the fetal human temporal retina and OC respectively (Lambot et al., 2005). On the other hand, ephrinB2 is absent at the OC of chick, that lack ipsi-lateral projections (Nakagawa et al., 2000). One remaining question subsides, in *Xenopus* as in most cold-blooded animals, RGCs are constantly replenished from the peripheral retina (Glucksmann, 1940) whereas ephrinB2 expression is known to be transient in the murine OC (Williams et al., 2003). Therefore, future studies should study whether ephrinB2 expression recedes in cold-blooded species.

An important aspect in the development of RGC divergence at the OC is the binocular interaction between RGCs from opposite eyes. Early experiments showed that monocular enucleations hindered the formation of ipsi-lateral projections (Chan and Guillery, 1993; Godement et al., 1987; Godement et al., 1990; Guillery, 1989). This reduction appears to depend on the stage at which the procedure was done. Early

enucleations, prior to any RGC crossing the midline, result in a complete loss of ipsi-RGC projections whereas late enucleations result in a milder ipsi-lateral projection defect. Of note, ipsi-RGC axons that project correctly in the ipsi-lateral optic tract target the visual nuclei normally (Guillery, 1989). These results shed light on the idea that contra-lateral RGC axons at the midline are critical for proper ipsi-RGC projection development. They further reveal that early born ipsi-RGCs (dorso-central) do not play a significant role in guiding later-born ipsi-RGC axons into the optic tract.

The morphogen Shh is specifically expressed and transported along contra-RGC axons (Peng et al., 2018; Sánchez-Camacho and Bovolenta, 2008; Traiffort et al., 2001). Interestingly, Shh protein appears at the ventral midline at E13.5, coinciding with the entry of the first RGCs at the OC (Peng et al., 2018). By electroporating Shh fused to a pH-sensitive GFP variant, Peng and colleagues confirmed that Shh was preferentially exocytosed at the OC (Peng et al., 2018). The Shh receptor, Brother of Cdon (Boc) is specifically expressed by ipsi-RGCs and exogenous treatment with Shh induces growth cone collapse of ipsi-RGCs in a Boc- and dependent manner. Mice lacking the Boc receptor ($Boc^{-/-}$) present a significant decrease in ipsi-lateral projections (~45%) (Fabre et al., 2010; Sanchez-Arrones et al., 2013). On the other hand, monocular electroporation of small interfering RNA to Shh leads to an increase in ipsi-lateral projections crossing the midline (Peng et al., 2018). Therefore, Shh secreted by early contra-RGCs at the ventral midline acts non-cell-autonomously on ipsi-RGCs and repels them to the ipsi-lateral optic tract (Figure 12A-C). It should nonetheless be noted that the temporal resolution of ipsi- and contra-lateral RGCs' arrival at the OC is based on the *Slc6a4-Cre* mouse line and that the early-born RGCs may not be targeted by this Cre line. The Teneurin (Tenm/Odz) family of adhesion molecules plays a role in RGC divergence. Tenm2 is uniformly expressed in the developing retina (Young et al., 2013). *Tenm2* null mice display a 40% reduction in ipsi-RGC projections, which correlates with a decreased ratio of ipsi to contra-lateral RGCs (Young et al., 2013). Therefore ipsi-RGCs may be sorted ipsilaterally by several distinct mechanisms, but what these populations give rise to and whether they project differentially within the brain visual nuclei remains to be studied.

A specific array of transcription factors is required by ipsi-lateral RGCs in order to regulate the expression of guidance receptors along their trajectory. The family of Zic transcription factors is pivotal to ipsi-RGC fate. The transcription factor Zic2 is

expressed in the VT retina, beginning at E14.5 and receding at E17.5 (Figure 12A-C; Herrera et al., 2003). *Zic2* hypomorphic mutants display a dramatic reduction in ipsi-lateral projections at the OC (Herrera et al., 2003). In addition, ectopic expression of Zic2 in the mouse central retina results in a higher proportion of ipsi-lateral projecting RGCs (García-Frigola et al., 2008). Interestingly, *EphB1* expression is absent in *Zic2* hypomorphic retinas, suggesting that Zic2 may act upstream to regulate EphB1 expression (García-Frigola et al., 2008). Indeed, electroporation of *Zic2* in contra-RGCs (central retina) drives an increased expression of *EphB1* and an ectopic expression of Zic2 in EphB1 null mice reduces the number of ipsi-lateral projecting RGCs (García-Frigola et al., 2008). As previously mentioned, the molecular cascade responsible for ipsi-lateral repulsion at the ventral midline appears to be evolutionarily conserved. Zic2 expression also appears to be evolutionarily conserved since Zic2 expressing cells in the VT retina of Xenopus appear during metamorphosis (Herrera et al., 2003). Moreover, the amount of Zic2-positive cells in the VT retina of various species, including humans, correlates with the degree of their binocular vision (Herrera et al., 2003; Lambot et al., 2005). In addition to regulating *EphB1*, *Zic2* regulates ipsi-RGCs' fate through *Boc* activity. *Boc* seems to act in the VT retina as a feedback loop with Zic2 to help ipsi-RGC growth cones sense Shh expressed from contra-RGCs. Disruption of this feedback loop, such as in *Boc* null mutant mice, leads to an increase in contra-RGCs at the expense of ipsi-RGCs (Sanchez-Arrones et al., 2013). Interestingly, Tenm2 regulates the fate of ipsi-RGCs.

In contrast to Zic2, Tenm2 is homogeneously expressed in the developing murine retina and follows the central-to-peripheral RGC differentiation wave (Young et al., 2013). In addition to its expression in RGC axons along the ON, Tenm2 is also expressed at the OC. Interestingly, Tenm2 expression was absent near radial glia cells of the OC, suggesting that RGC divergence at the OC is unlikely to involve Tenm2 (Young et al., 2013). Morevoer, while *Tenm2* null mice show a significant loss of EphB1 expression, Zic2 expression appears normal (Young et al., 2013). Therefore, further research is warranted to understand whether Tenm2 acts in parallel to- or downstream of Zic2.

The regulatory gene network specifying Zic2 expression in ipsi-RGCs has just begun to be studied. As previously mentioned, the complementary expression of Foxd1 and Foxg1 is important in patterning the ventral diencephalon. In the VT retina, *Foxd1* and

Foxg1 have complementary expression domains, with Foxd1 expression overlapping with that of Zic2 (Hatini et al., 1996; Herrera et al., 2004). Mice lacking *Foxd1* show a complete loss of both *Zic2* and *EphB1* expression, indicating *Foxd1* may act upstream to *Zic2* (Carreres et al., 2011; Herrera et al., 2004). Overexpressing *Foxd1* in contra-RGCs leads to an increase in ipsilateral projections (Carreres et al., 2011). The Wingless (Wnt) family of morphogens negatively regulates ipsilateral RGCs. Activating Wnt signaling using lithium chloride treatment decreases the number of ipsi-RGCs by 50% (Iwai-Takekoshi et al., 2018). To date, no direct link has been made between Wnt signaling and Zic2 in the retina.

1.5.5 Defining the crossed visual projections

Live-imaging, *in vivo* and *in vitro* experiments all show that the OC is inhibitory to RGC axons. Therefore, how do contra-RGC projections cross the midline? In contrast to ipsi-RGCs, contra-laterally projecting RGCs do not express EphB1 or Boc, suggesting that crossing the midline could be a default behavior that occurs in the absence of repulsion. Another possibility could be that contra-RGCs express a different set of molecules mediating their active growth across the midline. In search for other guidance molecules expressed at the OC, Sema6D was identified in RC2-positive cells at the medio-rostral midline. Indeed *Sema6D* mutant mice display an increase in ipsi-lateral projections originating from all quadrants of the retina (Kuwajima et al., 2012). While Sema6D is repulsive to RGC outgrowth, the application of Sema6D in combination with chiasm cell preparations promotes RGC axon outgrowth (Kuwajima et al., 2012). This suggests that the association of Sema6D with other partners present within the OC switches RGC response from repulsive to attractive. Interestingly, the Sema6D receptor PlexinA1 is also expressed at the midline in the adjacent SSEA-1/CD44 neurons. Using cell co-cultures, Kuwajima and colleagues showed that retinal explants grew better on human embryonic kidney (HEK) cells expressing both Sema6D and PlexinA1 compared to Sema6D-expressing HEK cells alone. Furthermore, RGC outgrowth was maintained in HEK expressing Sema6D and PlexinA1-ectodomain, showing that PlexinA1-mediated Sema6D attraction occurs in trans (cell-to-cell interaction) (Kuwajima et al., 2012). While *PlexinA1* mutants show a slight defasciculation of contra-lateral projections, they do not phenocopy the *Sema6D*

defects suggesting another receptor may mediate the Sema6D-mediated attraction at the midline.

In addition to PlexinA1, Sema6D binds to the cell adhesion molecule NrCAM (Lustig et al., 2001). Indeed, NrCAM expression co-localises with Sema6D and the radial glia marker RC2 (Kuwajima et al., 2012). Moreover, whilst *NrCAM* single mutants display no obvious defects in decussation, *PlexinA1/NrCAM* dKO show a major contra-lateral projection defasciculation and an 87% increase in ipsi-lateral projections, phenocopying the Sema6D observed defects. Further analysis showed that both NrCAM and PlexinA1 are expressed by contra-RGCs. Kuwajima and colleagues demonstrated that NrCAM/PlexinA1-expressing contra-RGCs could bind homotypically to NrCAM-expressing radial glia and Sema6D/PlexinA1-expressing SSEA-1/CD44 neurons (Figure 12B). This tripartite molecular signaling helps lure contra-RGC axons across the midline. Although an increase in ipsi-laterally projecting RGCs is observed in *NrCAM/PlexinA1* dKO mice and *Sema6D* mutants, still a large number of contra-laterally projecting RGCs manage to cross the midline.

Searching for other guidance molecules secreted by the midline, Erskine and colleagues showed that the vascular endothelial growth factor (Vegfa) possessed a spatiotemporal overlapping expression pattern with RGC axons. In addition to promoting angiogenesis, Vegfa also promotes axon outgrowth *in vitro* (Böcker-Meffert et al., 2002). Vegfa can undergo alternative splicing giving rise to several protein isoforms. The major isoforms are $Vegfa_{120}$, $Vegfa_{164}$, and $Vegfa_{188}$. The known guidance receptor to Semas, Neuropillin1 (Nrp1), can also bind to Vegfa (Soker et al., 1998). Interestingly, Vegfa isoforms have different binding affinities with $Vegfa_{164}$ and $Vegfa_{188}$ that bind Nrp1 whereas $Vegfa_{120}$ does not (Tillo et al., 2015). In addition to the strong expression of Vegfa at the ventral midline, Nrp1 is highly expressed in contra-lateral RGCs (Erskine et al., 2011; Tillo et al., 2015). $Nrp1^{-/-}$ null mice display a major increase in ipsi-lateral projections at the expense of contra-lateral projections (Erskine et al., 2011). Nrp1 is required in a cell autonomous manner since RGC-specific deletion of Nrp1 using the Brn3b promoter as a Cre driver completely phenocopies $Nrp1^{-/-}$decussation defects (Erskine et al., 2017). Vegfa/Nrp1 signaling is required at the midline since mice lacking both Nrp1-binding $Vegfa_{164+188}$ isoforms ($Vegf^{120/120}$) completely phenocopy the *Nrp1* RGC projection defects (Erskine et al., 2011). Interestingly, $Vegfa_{188}$ isoform seems sufficient to promote Nrp1/Vegfa-

mediated crossing of RGCs since mice only expressing Vegfa$_{188}$ (*Vegfa$^{188/188}$*) show no obvious decussation defect at the chiasm. In addition, rescuing a single allele of the Vegfa$_{188}$ isoform in *Vegf$^{120/120}$* mice restores contra-lateral RGC projections (Tillo et al., 2015).

The zebrafish model has been extensively used for the study of the vertebrate visual system development due to the facility of genetic manipulation and the transparency of larvae that render them optically accessible (Karlstrom et al., 1996). In addition, zebrafish RGC projections completely cross at the OC providing a perfect model to study contra-lateral RGC machinery (Burrill and Easter, 1994). Making use of the zebrafish, Panza *et al.* screened the entire leucine-rich repeat molecule repertoire expressed in RGCs at the time of axonal decussation (~30 hours post fertilization) (Panza et al., 2015). The islr2 receptor was identified to be expressed specifically in RGCs, with the onset of expression appearing at 36 hours post fertilization (Panza et al., 2015). Strikingly, *islr2* null larvae display partial decussation of RGC projections innervating the ipsi-lateral optic tectum with a complete penetrance. By carrying out a protein-protein interaction screening assay, two trophic ligands to islr2 were identified, namely Vasna and Vasnb. Intriguingly, *Vasna* and *Vasnb* as well as *Vasna/Vasnb* double mutants display normal decussation at the OC indicating that they are dispensable for RGC crossing at the midline (Panza et al., 2015). Molecules identified in zebrafish appear to be conserved in evolution since mouse mutants for *islr2* (*Lynx$^{-/-}$*) show increased ipsi-lateral projections (Panza et al., 2015). The role of Nrp1 in contra-lateral projections is also conserved since zebrafish embryos injected with morpholinos against Nrp1 induces aberrant ipsi-lateral projections (Dell et al., 2013). However, in this context, Nrp1 appears to bind to a class 3 Sema3D instead of Vegfa (Dell et al., 2013; Sakai and Halloran, 2006). Therefore, the Nrp1 ligand has not been conserved in evolution. Several studies argue in favor to this idea since the only expressed Sema in the murine midline, Sema6D is unable to bind to Nrp1 (Kuwajima et al., 2012). Moreover, mice carrying a point mutation in the a1 extracellular domain of Nrp1 (Sema binding site) possess a normal decussation pattern (Erskine et al., 2011).

Like ipsilateral RGCs, transcription factors specifying contra-lateral RGC fate have begun to emerge (Figure 12B). The Lim homeobox transcription factor Islet2 is expressed in ~50% of RGCs that project to multiple visual nuclei beginning at E13.5 in the mouse (Brown et al., 2000; Triplett et al., 2014). In the VT crescent of the retina,

Islet2 only appears at E15.5 in a complementary pattern to the ipsi-RGC-specific transcription factor Zic2 (Pak et al., 2004). Indeed, *Isl2*$^{-/-}$ null mice display a significant increase in ipsi-lateral projections. Retrograde labelling indicates that the increased ipsi-lateral projections originate specifically from the VT crescent of the retina, suggesting that Isl2 deletion does not lead to an expansion in the ipsi-lateral territory of the retina (Pak et al., 2004). In line with this observation, *Isl2*$^{-/-}$ retinas show a 50% increase in the number of Zic2- and EphB1-positive cells in the VT retina (Pak et al., 2004). These results suggest that Islet2 acts as a repressor to Zic2 to restrict the ipsi-RGC lineage in the VT retina. However, Islet2 does not seem to be required for contra-lateral RGC fate since contralateral RGCs still differentiate and project normally outside of the VT retina in *Isl2*$^{-/-}$ mutants (Pak et al., 2004). Together, the VT retina appears to be a distinct genetic domain where the specific balance between Zic2 and Islet2 regulates the proportion of RGC laterality.

The SoxC family of transcription factors are also critical regulators of contra-lateral RGC fate (Figure 12B; Chang et al., 2017; Kuwajima et al., 2017). More particularly Sox4, Sox11, and Sox12 are essential in regulating contra-lateral RGCs fate by inhibiting notch signaling (Kuwajima et al., 2017). These transcription factors possess direct binding sites to genes encoding for NrCAM and PlexinA1 which mediate contra-lateral attraction at the OC. A significant increase in ipsi-lateral projections is observed in *Sox4*$^{-/-}$*/Sox11*$^{-/-}$*/Sox12*$^{-/-}$ triple KO (Kuwajima et al., 2017). A large population of RGCs still however manage to project contra-laterally in these triple KO. This could in part be explained by the presence of other transcription factors in contra-lateral RGCs with redundant functions. Another non-mutually exclusive possibility is that deletion of *Sox4/Sox11/Sox12* does not result in a complete reversal of RGC identity from contra to ipsi. The latter is partially suggested by the observation that *SoxC*-deficient RGCs do not upregulate Zic2.

The Brn3 class of POU homeodomain factors are expressed in the developing retina (Quina et al., 2005). Indeed, Brn3a, Brn3b, and Brn3c are expressed by RGCs in complementary and overlapping patterns. Targeted deletion of *Brn3a* by introducing a bovine tau/β-galactosidase fusion gene revealed that Brn3a-postitive RGCs preferentially project into the contralateral optic tract (Quina et al., 2005). Furthermore, *Brn3a* null mice display an increase in ipsi-lateral projections without affecting either Zic2 or Islet2 expression. Therefore, Brn3a appears to define RGC laterality

independently from known transcription factors and requires further studies to decipher the precise molecular cascade. As previously described (see section: *Defining the uncrossed visual projections*), in the retina the regulatory genes *Foxd1* and *Foxg1* possess a complementary expression pattern. Foxg1 is specifically expressed in the nasal retina and *Foxg1*$^{-/-}$ mutants display a significant increase in ipsi-lateral projections (Pratt et al., 2004). These ipsi-lateral projections originate from several retinal quadrants (nasal and temporal) suggesting that ipsi-lateral projections are gained at the expense of contra-lateral projections in *Foxg1* mutants (Pratt et al., 2004). Worthy of note, *Foxg1* mutants show severe optic stalk defects which make the analysis of RGC projections difficult to tease apart (Pratt et al., 2004). It remains to be understood if Foxg1 regulates contra-lateral/ipsi-lateral genetic programs in RGCs.

In conclusion, several molecules orchestrating contra-lateral RGC fate and guidance co-exist. Despite significant increases in ipsilateral projections, a large amount of contra-lateral RGCs still manage to project normally. One possibility could be that this is due to a highly redundant mechanism which could explain these partial phenotypes. Alternatively, the molecules described thus far may impact the proper fasciculation of contra-RGCs and the latter may indeed project across the midline in a passive manner (Guillery et al., 1995).

1.5.6 What can we learn from pathologies of the optic chiasm?

In 1911, S. Ramón y Cajal hypothesized that the lens exerted an inversion of the image onto the retina which was corrected by a crossing at the OC. He argued that if visual projections did not cross but carried their signal ipsi-laterally, this would produce a partial map reversal. How could the brain account for this reversal? This intriguing question was partially answered by the reports of several achiasmatic human children (Apkarian and Bour, 2001; Apkarian et al., 1994). Intriguingly, the achiasma phenotype observed in these children is an isolated ontegenic anomaly without any defects on other commissural tracts of the CNS. Although these patients lack binocular vision, they display a normal visual field without any apparent reversal. The discovery of achiasmatic Belgian sheepdogs provided an animal model for this mutation (Williams et al., 1994). Through inbreeding, Williams et al. found that the achiasmatic phenotype was caused by an autosomal recessive mutation. Both human patients and the Belgian sheepdogs display a nystagmus (involuntary movement of the eyes), suggesting that

subcortical centers controlling eye movements do not compensate for the map reversal. Interestingly, the overall topography of retinal input in the subcortical visual targets is maintained in the achiasmatic mutants, highlighting the fact that topography of an object is independent of the OC. Descartes, Newton and Cajal had correctly hypothesized that the polarity of the projections was reversed. It nonetheless remains to be understood by which mechanism the brain can compensate for this subcortical reversal. It was suggested that homeobox genes may play a role in achiasmatic patients, the precise mechanism is still under active study (Biega et al., 2007). This surprisingly understudied phenotype deserves more attention as it may yield interesting insight into many aspects of visual system development.

At the turn of the century, several teams had independently isolated the “albino gene”, a recessive gene encoding for the enzyme tyrosinase (Raper, 1927; Witkop et al., 1970; Wright, 1925). It was not until the 1960’s that albino mutations were linked to visual deficits. Analysis of RGC projections in Albino rats and Siamese cats revealed an abnormal decussation pattern at the OC (Guillery, 1969; Lund, 1965). These striking observations made by Lund and Guillery were further confirmed in many other species that lack the retinal pigment melanin (albinism) and display a severe reduction in both ipsi-lateral projections and ipsi-lateral RGCs (Apkarian and Bour, 2001; Creel et al., 1982; Guillery, 1971; Guillery and Kaas, 1973; Guillery and Updyke, 1976; Guillery et al., 1974; Guillery et al., 1975; Lavail et al., 1978; Sanderson, 1975). The reduction in ipsi-lateral projections is reminiscent of the phenotype from monocular enucleations discussed previously (see section *Defining the uncrossed visual projections*). It was initially thought that monocular enucleations could share a common cellular mechanism with the albino mutation. While Chan and Guillery showed that albino rats and ferrets indeed possess a severe reduction of ipsi-lateral fibers, a shift of the naso-temporal border of the retina towards the temporal periphery is also apparent (Chan and Guillery, 1993; Stone et al., 1978). Early monocular enucleation of rats and ferrets revealed that the correct naso-temporal border of ipsi-lateral RGCs in the retina was maintained (Chan and Guillery, 1993). From these experiments we can conclude that both defects are fundamentally different; the authors proposed that: “the enucleation is likely to act at the chiasm whereas the albino gene probably acts in the eye” (Chan and Guillery, 1993). Indeed, early enucleation of albino ferret does not exacerbate the loss of ipsilateral projections (Guillery, 1989). Albino rat retinal explants have poorer

outgrowth on both wildtype and albino chiasm preparations compared to wildtype retinal explants, suggesting that the albino phenotype is likely to be cell autonomous (Marcus et al., 1996).

At which cellular level does the albino gene impact RGC laterality? Albino retinas display defects in the spatiotemporal genesis of RGCs (Rachel et al., 2002). In addition, albino mice show a severe reduction in the number of Zic2-positive cells in the VT crescent (Herrera et al., 2003). Interestingly, using 5-ethynyl-2'-deoxyuridine (EdU) incorporation as birth-dating indicator, Bhansali and colleagues showed that there was a decrease in RGC numbers in the albino retinas at E14 (Bhansali et al., 2014). This decrease is compensated by E17 at which time albino retinas show a higher amount of Islet2-positive RGCs than wildtype retinas (Bhansali et al., 2014). There is a delay in RGC genesis in the VT crescent of albino retinas compared to wildtype retinas, suggesting that this delayed VT neurogenesis favors contra-lateral RGC fate at the expense of the ipsi-lateral one. The notion that timing is critical for fate specification of cell class in the retina has been greatly studied (Cepko, 2014). In that respect, the neurogenic wave in the VT retina lags behind the dorsal retinal wave (Marcucci et al., 2019).

To begin probing at the differential neurogenic program of albino mice, retrogradely labelled ipsi-RGCs and contra-RGCs of wildtype mice were sorted using fluorescence-activated cell sorting followed with a DNA microarray analysis (Wang et al., 2016). The cell cycle related gene *CyclinD2* was identified to be highly expressed in the proliferative ciliary margin zone (CMZ) as well as in the VT retina (Wang et al., 2016). In agreement with the expression pattern of CyclinD2, no differences were observed in the dorsal retina of *CyclinD2*$^{-/-}$ mutant mice. In contrast, in the ventral CMZ fewer cells undergo mitosis in *CyclinD2*$^{-/-}$ mice which is concomitant to a 22% reduction in Zic2-positive ipsi-lateral RGCs and a 25% reduction in ipsi-lateral projections at the OC (Marcucci et al., 2016). Besides, in albino mice, the number of CyclinD2-positive cells in the ventral CMZ is significantly reduced (Marcucci et al., 2016). Together, CyclinD2 may function as a molecular clock regulating the wave of RGC differentiation in the VT retina. In albino mice, CyclinD2 expression at the ventral CMZ is altered which generates a shift in the neurogenic wave of the VT retina leading to both a decrease in Zic2-positive RGCs and an increase in Islet2-positive contra-lateral RGC fate. Since both ipsi- and contra-lateral cells are present in the VT retina, an open

question remains as to whether they arise from the same or from distinct progenitor pools. How is the neurogenic wave of the VT retina specified? The Wnt ligand, Wnt2b is increased in the embryonic albino RPE (Iwai-Takekoshi et al., 2018). Activating Wnt signaling by using lithium in pregnant mice induces a significant reduction in Zic2-positive ipsi-RGCs (Iwai-Takekoshi et al., 2018). As a result, it appears pertinent for future studies to focus on the interaction between the RPE and the neural retina.

A puzzling question pertains to how pigmentation relates to RGC laterality. In the retina, melanin forms as the eye cup invaginates and is localized in melanosomes in the RPE. Within the RPE, the enzyme tyrosinase is critical in the molecular cascade for the production of melanin (Raper, 1927). Indeed, early studies described that the degree of ipsi-lateral projections correlated significantly with the amount of pigmentation and the activity of tyrosinase (Lavail et al., 1978). Further support for this hypothesis came with the finding that mice lacking the expression of tyrosinase during the critical period of ipsi-RGC genesis (E13-E16) displayed reduced ipsi-lateral projections (Cronin et al., 2003). Of note, visual deficits occur in both tyrosinase-positive and -negative human albino patients, raising the possibility that the process to produce melanin is more essential that melanin itself (Preising et al., 2011). Another important precursor to melanin is L-3,4-dihydroxyphenylalanine (L-DOPA). Embryonic albino retinas are devoid of L-DOPA and treatment of pregnant albino mice with L-DOPA rescues the number of Zic2-positive ipsi-lateral RGCs (Mason and Guillery, 2019; Roffler-Tarlov et al., 2013).

1.6 Central projections of retinal ganglion cells

1.6.1 A description of retinorecipient targets

In mice, after the optic chiasm, RGC axons will project to as many as forty six different retinorecipient brain targets, which can be separated into image forming and non-image forming nuclei (Figure 13A; Morin and Studholme, 2014). Image forming pathways give rise to sight such as locating shapes, whereas non-image forming pathways support sight indirectly by coordinating the circadian clock or pain sensitivity (Figure 13A; Seabrook et al., 2017). In mice, the largest structure in the image forming pathway is the superior colliculus (SC) located in the dorsal midbrain (Figure 13A), that

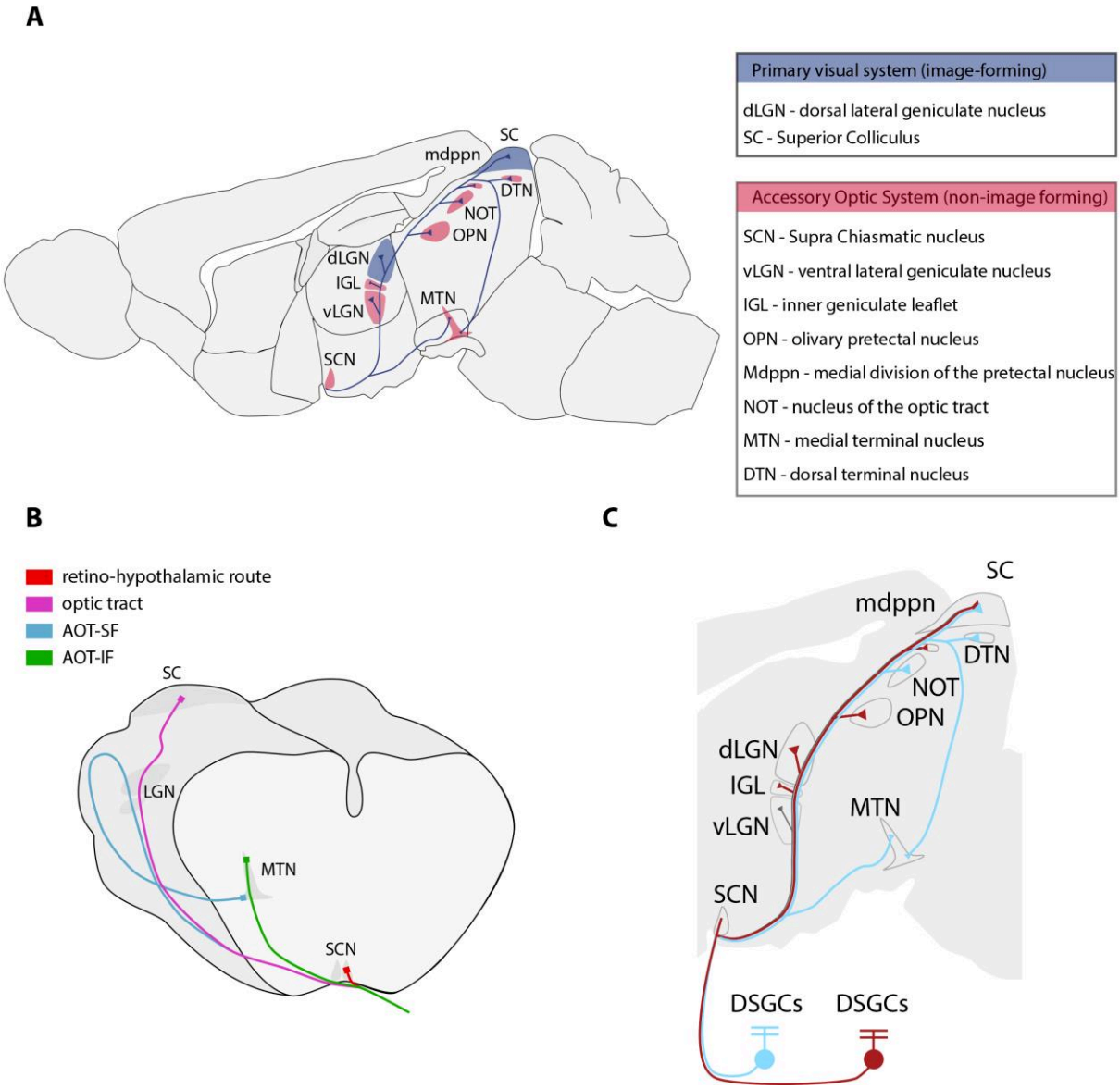

Figure 13 – The retinal ganglion cell projectome A. Schematic sagittal cryosection of an adult mouse brain highlighting the main retinorecipient brain nuclei. Image-forming nuclei (blue) and non-image forming nuclei (red) can be seen. **B**. A schematic coronal cryosection of an adult mouse brains showing the four routes taken by retinal ganglion cells, adapted from (Dhande and Huberman, 2014). **C**. A schematic representing the diversity of retinorecipient targeted by a single retinal ganglion cell type, adapted from (Dhande et al., 2015).

receives approximately 90% of RGC inputs in rodents (Ellis et al., 2016; Linden and Perry, 1983). In the murine visual system the SC, which is homologous to the optic tectum in lower vertebrate species, regulates complex behaviors such as looming-evoked escape or freezing responses (Wang et al., 2010). The SC is a multi-sensory structure that receives topographic visual inputs in its superficial layers, as well as somatosensory and auditory inputs in deeper layers (Drager and Hubel, 1975; Drager and Hubel, 1976). The other major structure in the image forming pathway is the lateral geniculate nucleus (LGN), located in the thalamus (Figure 13B). The visual thalamus harbors three retinorecipient nuclei: the ventral LGN (vLGN), the inner geniculate leaflet (IGL), and the dorsal LGN (dLGN) (Figure 13A). Only the dLGN relays visual information (~37% of RGC projections) to the primary visual cortex for higher order visual perception (Martin, 1986).

The visual circuits responsible for non-image forming behaviors belong to the accessory optic system (AOS, Figure 13B). The term “accessory”, coined by Bochenek in 1908, may not accurately represent the importance this system plays in our visual perception (Simpson, 1984). One of the best studied circuits of the AOS is related to light-dark cycles that co-ordinate circadian rhythm and pupillary light reflex. Twenty years ago, the master circadian clock was identified to be regulated by a population of neurons in the suprachiasmatic nucleus (SCN) in the dorsal hypothalamus (Figure 13A; Berson et al., 2002; Gooley et al., 2001; Hattar et al., 2002). The SCN is innervated by melanopsin-expressing RGCs that are sensitive to light called intrinsically photosensitive RGCs (ipRGCs) (Berson et al., 2002; Gooley et al., 2001; Hattar et al., 2002). In addition to projecting into the SCN, ipRGCs also target the vLGN and the IGL in the visual thalamus (Hattar et al., 2006). Interestingly, ipRGCs projecting to the vLGN and IGL create a geniculo-hypothalamic feedback loop with the SCN which is critical for maintaining the light-dark cycle (Delogu et al., 2012). The olivary pretectal nucleus (OPN, also called olivary pretectal tract) is another retinorecipient nucleus of ipRGCs in the midbrain that regulates the pupillary light reflex (Figure 13A; Ecker et al., 2010; Hattar et al., 2002; Hattar et al., 2006; Sweeney et al., 2014; Trejo and Cicerone, 1984; Young and Lund, 1994).

During movement and head turns, image representation “slips” on the retina, which can induce a blurry perception of the image. The AOS, and more precisely the vestibulo-ocular reflex (fast movement) and the optokinetic reflex (OKR) (slow

movement) can both accommodate for such distortions by correcting eye and head movements (Yonehara et al., 2009). The major RGC type involved in this behavior are direction-sensitive RGCs (DSGCs), which respond to either horizontally or vertically moving objects (Barlow and Hill, 1963; Marg, 2006). HRP-mediated retrograde labelling and electrophysiological recordings identified several AOS nuclei involved in image-stabilization, namely: the nucleus of the optic tract (NOT), the medial terminal nucleus (MTN), the dorsal terminal nucleus (DTN), and the lateral terminal nucleus (LTN) (Figure 13A; Simpson, 1984). RGCs encoding for forward motion target the NOT and the DTN which drives horizontal eye movement, whereas upward and downward motion is processed by the dorsal MTN and the ventral MTN respectively (Marg, 2006; Simpson, 1984; Yonehara et al., 2009). Of note, the AOS circuitry responsible for image stabilization is highly conserved across jawed vertebrates (Masseck and Hoffmann, 2009; Simpson, 1984).

1.6.2 The many lanes on the road to the brain

Navigating RGC projections must accurately match with their targets, arborize in the appropriate layer, and correctly segregate. Early observations by Von Gudden (1870) already described that RGC axons take multiple routes to reach their final targets (Simpson, 1984). To date, four major routes can be described in the murine visual system (Figure 13B; Simpson, 1984). The first route named the retino-hypothalamic route is composed entirely of ipRGCs and innervates the non-image forming SCN which is the first target RGCs will encounter in their journey towards the brain (Figure 13B; Dhande et al., 2015). The second route is composed of projections from all RGC types that have passed through the OC and fasciculate together forming the optic tract (Figure 13B). The optic tract projects dorso-caudally from the ventral diencephalon to the dorsal midbrain and innervates the majority of retinorecipient nuclei (90%) (Varadarajan and Huberman, 2018). The third and fourth route deviate from the optic tract at different locations. The inferior fasciculus of the optic tract (AOT-IF) is formed by a group of late crossing direction-sensitive RGCs that deviate from the optic tract at midway between the OC and the lateral edge of the cerebral peduncle, and proceeds caudally to terminate in the ventromedial midbrain innervating the dorsal MTN (Figure 13B). The superior fasciculus of the optic tract (AOT-SF), composed of DSGCs, is

formed by multiple deviations from the optic tract between the dLGN and the SC that project ventrally to innervate the ventral MTN (Figure 13B; Simpson, 1984).

The nature of specific routes taken by RGCs as well as the process by which an axon distinguishes among specific targets is poorly understood. An aspect that appears to mediate target matching is the relative birthdate of a RGC (Osterhout et al., 2014). One of the earliest born RGC types are the ipRGCs expressing the adhesion molecule cadherin-3 (cdh3) (Osterhout et al., 2014). Interestingly, Cdh3-RGC projections extend the entire length of the visual pathways before innervating specific visual nuclei. In contrast, later-born RGC types such as DSGCs expressing either the homeobox d10 (Hoxd10) or the dopamine receptor 4 (DRD4) specifically project to their target (Dhande et al., 2013; Huberman et al., 2009; Osterhout et al., 2014). These observations show that RGC types may exploit different strategies for axon-target matching which could be regulated by axon-axon competition or differential expression of guidance molecules. In addition, specific RGC types, such as ipRGCs, can target multiple retinorecipient nuclei. ipRGCs target the hypothalamic SCN, the IGL and the vLGN in the thalamus, but also the lateral habenula or the OPN in the pre-tectum (Figure 13C; Hattar et al., 2006). In addition, direction sensitive RGCs expressing SPARC (secreted protein acidic and rich in cysteine)-related protein containing immunoglobulin domains (SPIG1) project to the NOT, the SC, and both the vMTN and dMTN (Figure 13C; Dhande et al., 2015; Yonehara et al., 2008). How do RGC types know which nucleus to target? Chen and colleagues elegantly showed that ipRGCs projecting to the SCN were devoid of the transcription factor Brn3b, whereas Brn3b-expressing ipRGCs projected to other retinorecipient nuclei (Chen et al., 2011). Therefore, distinct RGC subtypes may exist within RGC types that possess a different transcription factor profile as well as different target-matching characteristics.

1.6.3 Making the first connection

Despite this specificity in axon-target matching, several molecules are known to play a role in overall RGC projections. The intracellular protein Gap43 was found to be critical for optic tract formation (Kruger et al., 1998; Strittmatter et al., 1995; Zhang et al., 2000). In *Gap43* null mice RGC axons enter the optic disc, navigate the optic nerve, and cross the OC without any defects. However, 450-500 µm lateral to the midline, RGC axons turn back towards the midline and fail to form an optic tract (Kruger et al., 1998; Zhang et al., 2000). Mix-and-match grafting experiments showed that retinal

explants from control mice grew well on diencephalic preparations regardless of their genotype. In contrast, retinal explants from *Gap43* null mice never grew past 500 µm lateral to the midline when grafted on control diencephalic preparations, suggesting Gap43 functions cell autonomously in RGCs (Kruger et al., 1998).

ECM proteins are also implicated in optic tract formation. Recall the repulsive ECM Slit proteins discussed in the section: “positioning the OC”, that are expressed in a corridor pattern to restrict RGC axons towards the OC. Plump and colleagues reported that RGC axons project aberrantly away from the optic tract and into the pre-optic area (Plump et al., 2002). However, *Slit1/Slit2* KO mice die at birth and studying the full array of axon-target matching defects in these mutants should therefore be further studied.

In addition to Slit, the ECM molecule reelin (reln) is critical for RGC targeting to the visual thalamus (Su et al., 2011). By comparing mRNA transcripts of several visual nuclei, Su and colleagues identified that both the vLGN and IGL expressed reln. Reln binds two canonical receptors: the very low density lipoprotein receptor (vldlr) and the low density lipoprotein receptor related protein 8 (lrp8) (Benhayon et al., 2003). This binding activates the downstream effector disabled 1 (Dab1) (Sheldon et al., 1997). Interestingly, ipRGCs, that project to the non-image forming nuclei vLGN and IGL, express both vldlr and lrp8 as well as the downstream target Dab1 (Su et al., 2011). Both *reln*$^{rl/rl}$ and *Dab1*$^{scm/scm}$ mutants display a severe reduction of ipRGC projections to the vLGN and the IGL (Su et al., 2011). However, *vldlr*$^{-/-}$ and *lrp8*$^{-/-}$ mutants have a reduced penetrance and strength of these phenotypes compared to reln mutants, suggesting that reelin may have vldlr- and lrp8-independent roles (Su et al., 2013). Evolutionarily, reln is critical for the proper targeting of RGC axons in the zebrafish optic tectum (Di Donato et al., 2018). Interestingly, Di Donato and colleagues extended previous studies and showed that reln is expressed as a gradient in the zebrafish optic tectum (superficial high – to – deep low). Disruption in this gradient by overexpressing reln in deeper periventricular neurons leads to major RGC targeting defects, suggesting RGCs have a dose-dependent response to reln (Di Donato et al., 2018). The resulting model suggests that RGC with high levels of vldlr project to the superficial-most layer whereas RGCs with low vldlr levels project to the deepest-most layer of the optic tectum.

Cell adhesion molecules play a determinant role in target matching in the visual system of invertebrates and may be an effective mechanism for guiding RGCs (Sanes and Zipursky, 2020). N-cadherin, a member of the cadherin family of cell adhesion molecules, is essential for the proper targeting of photoreceptor neurons to the lamina of the *Drosophila* brain (Lee et al., 2001; Prakash et al., 2005). In the murine visual system, at least fifteen classical cadherins are expressed (Sanes and Zipursky, 2020). The widely accepted view of cadherin-mediated adhesion occurs by homophilic interactions whereby cells expressing a specific cadherin family member preferentially bind to cells expressing the same cadherin (Sanes and Zipursky, 2020; Takeichi, 2007). Cadherin-6 (cdh6) appears to be specifically expressed in the OPN of the AOS (Osterhout et al., 2011). Interestingly, RGC axons of *Cdh6*$^{-/-}$ null mice course caudally to the SC without innervating the OPN. RGCs projecting to the OPN co-express a combination of cadherins -3 and -6, suggesting that target matching in the OPN may not be based on homophilic but rather heterophilic interactions between different cadherins (Osterhout et al., 2011). Cdh6 binding specificities require further study to elucidate the exact interaction at play in AOS-mediated target matching.

In addition to cadherins, the immunoglobulin (IgG) superfamily of adhesion molecules is implicated in target recognition of RGC axons. The Contactin-4 (Cntn4) IgG is specifically expressed in the image stabilization nucleus NOT. Indeed, *Cntn4*$^{-/-}$ null mice show a reduced innervation of the NOT (Osterhout et al., 2015). In addition to being required for NOT innervation, Cntn4 is sufficient for RGC targeting since overexpression of *Cntn4* in the retina leads to a 5-fold increase in innervation of the NOT (Osterhout et al., 2015). Cntn4 binds to amyloid precursor protein (App) (Osterfield et al., 2008). However, monocular enucleation showed that App is not expressed by the parvalbumin neurons of the NOT but rather by RGCs (Osterhout et al., 2015). Although the *in vivo* binding partner for Cntn4 and its co-receptor App remains to be identified, chick retinal explants uncovered the cell adhesion molecule NgCAM (L1 chick homologue) as a potential mediator for App/Cntn4-dependent axonal outgrowth and future research should focus on this molecular triad (Osterfield et al., 2008).

Outside of cell adhesion molecules, the fibroblast growth factor receptor (FGF) tyrosine kinase plays a key part in axon target recognition in amphibians (McFarlane et al., 1995). Ectopic treatment of FGF-2 or transfection of a dominant negative FGF receptor

in *Xenopus laevis* retina leads to a failure of RGCs to enter their main retinorecipient target, the optic tectum (McFarlane et al., 1995; McFarlane et al., 1996). In addition, guidance molecules have recently been described for DSGCs-targeting of the AOS. Indeed, DSGCs project to the horizontal and vertical reflex centers DTN and MTN, respectively. Sema6A expressed by DSGCs was shown to bind to PlexinA2 and PlexinA4 transmembrane receptors expressed in the DTN as well as the MTN (Sun et al., 2015). Indeed, *Sema6A*$^{-/-}$ or *PlexinA2*$^{-/-}$/*A4*$^{-/-}$ dKOs display a substantial loss of DSGC projections to the MTN and DTN (Sun et al., 2015). However, initial targeting of MTN and DTN appears independent to Sema6A or PlexinA2/A4.

1.6.4 The formation of retinal maps

The necessity for maintaining a dimensional relationship between the visual scene and its representation in the brain was experimentally evidenced by Munk (1881) and Schafer (1889) and coined the “cortical retina” by the Swedish neurologist S.E Henschen (1911) (Polyak, 1957). We now refer to this process as topography whereby neighboring RGCs project onto neighboring terminal zones in the visual targets. In this model, the naso-temporal axis of the retina projects along the rostro-caudal axis of SC, or its fish and bird homologue the optic tectum (Figure 14A; Polyak, 1957). Moreover, the dorso-ventral axis of the retina projects in a medio-lateral manner in the SC or optic tectum (Figure 14A). In fish and amphibians RGC projections initially target the appropriate terminal zone in the optic tectum with little refinement occurring in the axonal shaft (Figure 14B; Holt and Harris, 1983). In contrast, mammalian RGC axons initially overshoot their terminal zone and occupy the entire rostro-caudal axis of the SC (Figure 14B; Simon and O’Leary, 1992; Yates et al., 2001). Subsequently, RGC axons develop *de novo* interstitial branches in the medio-lateral axis, leading to a higher frequency of branches in the topographically accurate termination zone (Figure 14B; Hindges et al., 2002; Yates et al., 2001). Finally, axonal refinement occurs, leaving behind a single terminal zone for each RGC in the appropriate topographic location (Figure 14B; Hindges et al., 2002; Yates et al., 2001).

Of great interest is the question of how such topography can be generated? One possibility could be that RGC axons are already pre-ordered along the optic nerve and the optic tract, therefore maintaining retinotopy along the visual pathway. Such pre-ordering was reported in non-mammalian vertebrates including fish, amphibians,

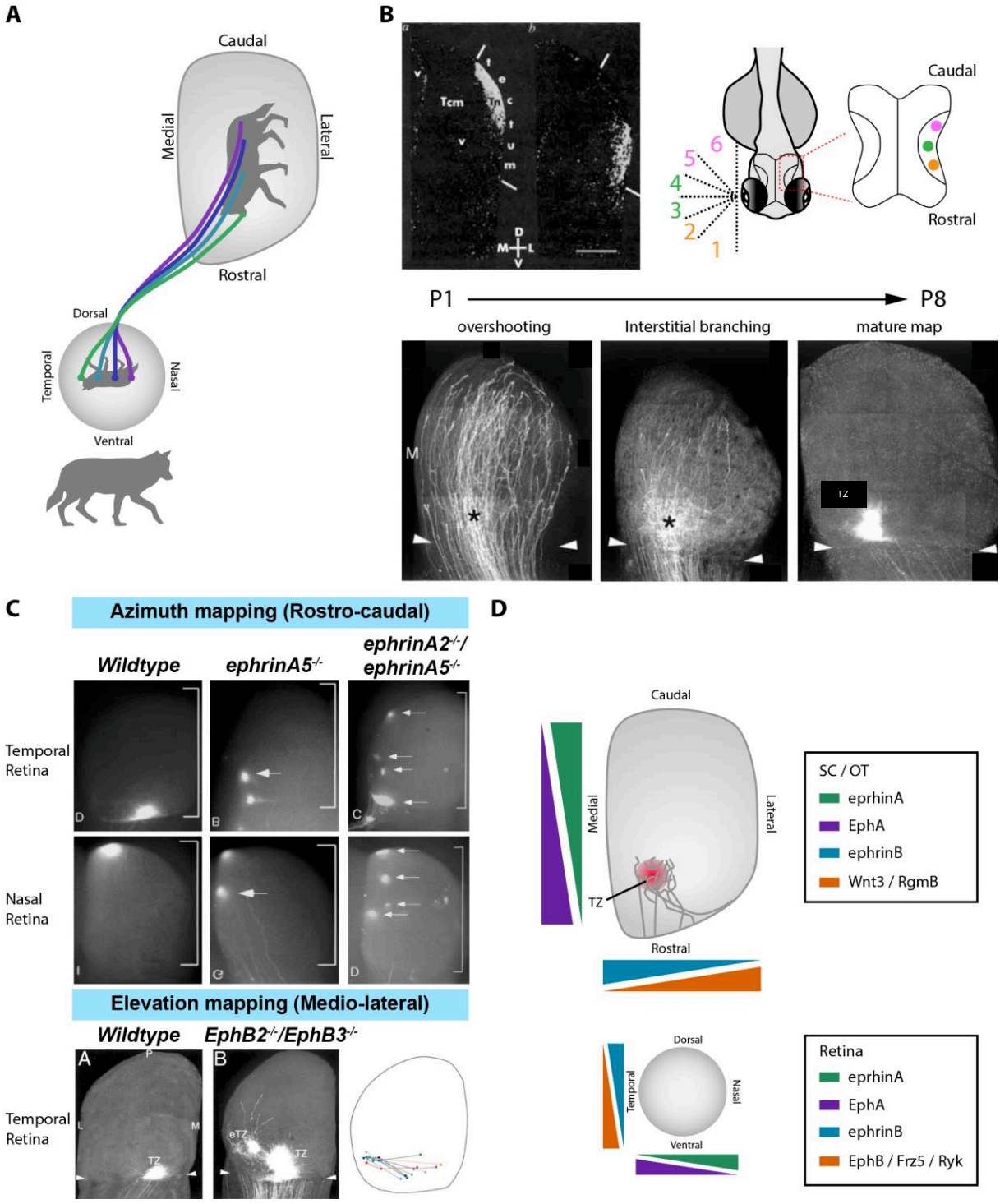

Figure 14 – Retinotopy is evolutionarily diverse A. A schematic representation of retinotopy. A wolf is mapped onto the retina, each point is relayed from the retina to neighboring neurons in the superior colliculus. Adapted from (Seabrook et al., 2017). **B**. Dark-field autoradiograph showing the topographic projections of Xenopus (St.39) retinal ganglion cells. Axons from the ventral retina project to the dorso-medial optic tectum whereas dorsal projections target the ventro-lateral tectum (Holt and Harris, 1983). DiI injections into the ventro-temporal retina of mice. At P1, retinal projections overshoot and span the entire superior colliculus. At P3, a nascent termination zone emerges. Retinal projections remain broadly distributed. At P8, retinal projections have fully refined to their terminal zone (TZ) (Hindges et al., 2002). **C**. Focal injections of DiI

in the temporal or nasal retina. In wildtype mice, temporal axons terminate in the rostral superior colliculus (SC) whereas nasal axons project to the caudal SC. *ephrinA5*$^{-/-}$ null mice and to a greater extent *ephrinA2*$^{-/-}$*/ephrinA5*$^{-/-}$ dKo mice show ectopic branches that have not fully refined in the rostro-caudal axis. Injections of DiI in the ventro-temporal retina of *EphB2*$^{-/-}$*/EphB3*$^{-/-}$ dKO mice reveals ectopic termination zones that lie lateral to their expected site (Hindges et al., 2002). **D**. A schematic representation of the dorso-ventral and naso-temporal gradients that match their rostro-caudal and medio-lateral gradients in the SC.

reptiles, and birds (Cima and Grant, 1982; Easter et al., 1981; Scholes, 1979; Thanos and Bonhoeffer, 1984). In these species, the initial targeting of RGC axons within the optic tectum is topographically accurate (Holt and Harris, 1983). Since mammalian RGC targeting is different, could mammalian RGC axons still adopt a similar strategy? Classical studies showed that mammalian RGC axons lose their retinotopy within the optic nerve (Chan and Guillery, 1994; Plas et al., 2005; Silver and Sapiro, 1981; Simon and O'Leary, 1990; Williams and Rakic, 1985). Interestingly, after the OC RGC axons re-acquired their topography within the optic tract (Chan and Guillery, 1994; Plas et al., 2005; Simon and O'Leary, 1991; Sitko et al., 2018). Tracing discrete populations of RGCs in mice using DiI/DiD injections, Sitko and colleagues showed that RGCs in the dorso-ventral and the naso-temporal axis of the retina mapped to the medio-lateral and rostro-caudal axis of the optic tract respectively (Sitko et al., 2018). Moreover, ipsi-lateral RGC axons segregated laterally to the contra-lateral RGC axons, suggesting that RGC axons may also be sorted by typography (RGC type) (Sitko et al., 2018). It is curious that in mammals retinotopy is lost in the optic nerve but regained in the optic tract. No mechanism has yet been proposed for this active sorting of RGC axons in the optic tract, it may be that interactions between RGC axons are responsible for this pre-ordering.

1.6.5 Azimuth mapping

Pre-sorting of RGC axons in the optic tract can help maintain topography, the remaining question is how do RGCs know which precise post-synaptic neuron to target in the SC or optic tectum? In the 1940's, Roger Sperry observed that by transecting optic nerves of salamanders (*Urodeles*) and rotating their eyes 180°, regenerating RGC axons grew back to their original destination in the optic tectum rather than re-orienting to the rotated position (Sperry, 1943). From these observations, Sperry

proposed the “chemoaffinity theory”. This theory posits that chemical tags distributed as gradients in the retina give neighboring RGCs a positional identity that would be matched to a similar gradient in the retinorecipient targets, creating a “lock and key” molecular mechanism (Sperry, 1963).

In the 1980’s Walter and colleagues developed the *in vitro* stripe assay, in which chick RGC axons can navigate along alternating stripes of membrane fragments from different sources (Walter et al., 1987a). In these assays, temporal RGC axons preferentially grew on stripes of rostral optic tectum rather than caudal, proving Sperry’s chemoaffinity theory (Walter et al., 1987a). Furthermore, the preference of temporal RGC axons to the rostral tectum was not mediated by an attractive mechanism but was rather due to a repulsive activity of the caudal tectum (Walter et al., 1987b). Of note, nasal axons did not show any preferred stripes and grew equally well on rostral or caudal tectal membranes (Walter et al., 1987a). Using a nonfunctional approach, Drescher and colleagues (1995) were able to clone a 25 kilodalton (KDa) protein from the caudal optic tectum of chick (Drescher et al., 1995). This protein, called repulsive axon guidance signal (RAGS) was expressed in a high caudal – to – low rostral graded manner in the chick tectum (Drescher et al., 1995). In parallel to this study, Cheng and Flanagan (1994) cloned a tyrosine kinase binding protein named Eph ligand family-1 (ELF-1) (Cheng and Flanagan, 1994). ELF-1 shared a similar expression pattern to RAGS with a high caudal – to – low rostral graded manner in the chick tectum and bound a tyrosine kinase receptor Mek4 that possesses a high temporal – to – low nasal expression pattern in the retina (Cheng et al., 1995). Mectopic expression of ELF-1 is sufficient to repel temporal RGC axons *in vivo* (Nakamoto et al., 1996). We now know ELF-1 and RAGS as ephrinA2 and eprhinA5, respectively. Ephrins are ligands to the Eph receptor family. Mek4 is now known as EphA3 and belongs to the Eph family of proteins.

The ephrin family of ligands is divided into A and B subclasses based on sequence homology and is composed of five ephrinAs (A1-A5) and three ephrinBs (B1-B3) (Gale et al., 1996; Hirai et al., 1987). EphrinAs are glycosylphosphatidylinositol (GPI)-anchored proteins whereas ephrinBs are transmembrane proteins; they bind to EphA and EphB receptors, respectively (Triplett and Feldheim, 2012). Currently, there are nine EphA (EphA1-A8 and EphA10) and six EphB (EphB1-B6) identified receptors. Targeted deletion of *ephrinA2* or *ephrinA5* in mice led to moderate targeting errors in

the SC, with temporal RGC axon termination zones displaying a slight caudal shift (Figure 14C; Feldheim et al., 2000; Frisén et al., 1998). This observation suggests that caudal SC of *ephrinA2*$^{-/-}$ or *ephrinA5*$^{-/-}$ mice lose their repulsive activity. *ephrinA2*$^{-/-}$*/A5*$^{-/-}$ dKOs display a more severe phenotype than single mutants, suggesting that ephrinAs possess redundant roles in azimuth map formation (Figure 14C; Feldheim et al., 2000). EphrinA3 is also expressed in the murine SC, but in a uniform manner (Pfeiffenberger et al., 2005). *EphrinA2*$^{-/-}$*/ A3*$^{-/-}$*/A5*$^{-/-}$ tKOs nonetheless display a significantly stronger phenotype than *ephrinA2*$^{-/-}$*/A5*$^{-/-}$ dKOs with >70% of RGC fibers shifted caudally and an increased number of termination zones (Pfeiffenberger et al., 2006).

EphA receptors largely phenocopy the ephrinA defects since ectopic expression of a dominant negative form of EphA3 in chick RGCs induces a caudal shift of temporal RGCs (Feldheim et al., 2004). Interestingly, mouse RGCs do not express EphA3 but instead express EphA5 and EphA6 in a high temporal manner (Feldheim et al., 2004). Indeed, *EphA5*$^{-/-}$ mutants also display a caudal shift of temporal RGC axons (Feldheim et al., 2004). Taking advantage of the fact that EphA3 is not expressed in the murine visual system, Brown and colleagues (2000) induced ectopic expression of EphA3 under the Islet2 promoter, expressed in half of RGCs (Brown et al., 2000). Interestingly, Islet2-postitive RGCs projected to the rostral-most SC compared to Islet2-negative RGCs. As a result, the proposed model states that RGC axons align in the SC or optic tectum depending on their relative expression of EphA receptors. Temporal RGCs expressing high levels of EphAs terminate in the rostral SC or optic tectum with low levels of ephrinAs. Nasal RGCs expressing low levels of EphAs project caudally in the SC or optic tectum expressing high levels of ephrinAs.

The finding that a number of RGC axons in *ephrinA2*$^{-/-}$*/A3*$^{-/-}$*/A5*$^{-/-}$ triple mutants still manage to arborize in the retinotopically accurate termination zone, hinted at the possibility that other molecules may be important in regulating retinotopy (Feldheim et al., 2000; Pfeiffenberger et al., 2006). Another GPI-anchored molecule initially identified from the chick visual system was proposed as a critical rostro-caudal topographic cue (Stahl et al., 1990). This GPI-anchored protein, later identified as the repulsive guidance molecule (RGM), is expressed in the chick as a rostro-caudal gradient similar to ephrinAs (Monnier et al., 2002; Müller et al., 1996). RGM binds to the transmembrane receptor Neogenin, which is expressed by chick RGCs in a graded

naso-temporal manner (Rajagopalan et al., 2004). By repelling Neogenin-expressing RGCs from the caudal chick optic tectum, RGM functions as a repulsive cue. Disruptions in RGM levels using short-interfering RNA lead to retinotectal projection defects in the chick (Matsunaga, 2006; Tassew et al., 2008). However in mice, targeted deletion of *RGMa*, one of the three RGM family members, does not result in altered topography of retinotectal projections (Niederkofler et al., 2004). This finding may be explained by a redundancy of other RGM family members, composed of RGMa, RGMb, and RGMc. In amphibians, the homeodomain transcription factor Engrailed 2 (En2) is expressed in a gradient and regulates the expression of guidance cues, such as ephrinAs (Retaux and Harris, 1996). Moreover, membrane-bound En2 is expressed as a rostral low to caudal high gradient in the *Xenopus* optic tectum and acts directly on RGC axons (Brunet et al., 2005). In both chick and *Xenopus* blocking antibodies targeted against En2 leads to aberrant temporal RGC axons in the caudal optic tectum (Wizenmann et al., 2009). Extracellular Engrailed is proposed to act by sensitizing RGC axons to ephrinA5 (Wizenmann et al., 2009).

1.6.6 Elevation mapping

Although the rostro-caudal mapping is severely perturbed when manipulating EphA/ephrinA signaling, the elevation mapping (medio-lateral axis) remains intact suggesting that other molecules may be critical in patterning the elevation axis. Interestingly, the class of EphB/ephrinB signaling molecules are critical in this process (Figure 14C; Hindges et al., 2002). Of note, both EphBs and ephrinBs are transmembrane molecules that can function bi-directionally to mediate cell-to-cell interactions (Holland et al., 1996). This implies that RGC axons expressing the EphB receptor undergo a forward signaling whereas the post-synaptic ephrinB-expressing cells undergo a reverse signaling. Within the retina, the EphB2/ B3/ B4 receptors are expressed in a low dorsal-to-high ventral manner (Birgbauer et al., 2000; Connor et al., 1998; Henkemeyer et al., 1996; Hindges et al., 2002; Holash and Pasquale, 1995). This graded expression of Eph receptor is complementary to the expression of the ephrinB1 ligand expressed in a high medial-to-low lateral manner in the optic tectum and SC (Braisted et al., 1997; Hindges et al., 2002). Therefore, highly expressing EphB RGCs in the ventral retina project to highly-expressing EphB post-synaptic neurons of the medial SC, suggesting that EphB/ephrinB signaling promotes branch attraction.

Indeed, using focal DiI injections in the ventro-temporal retina of *EphB2*$^{-/-}$/*B3*$^{-/-}$ dKOs mice, Hindges and colleagues observed that RGC axons possess a laterally-shifted duplication of their terminal zone (Figure 14C; Hindges et al., 2002). To question whether forward or reverse EphB/ephrinB signaling is at play in elevation mapping of the visual system, Hindges and colleagues carried focal DiI injections of a mutant lacking the intracellular domain of *EphB2* (*EphB2*^{ki}, lacking the forward signaling). *EphB2*^{ki}/*B3*$^{-/-}$ dKOs phenocopy the *EphB2*$^{-/-}$/*B3*$^{-/-}$ dKOs mice showing that forward EphB signaling plays a stronger contribution to elevation mapping in the murine visual system (Hindges et al., 2002).

The observation that RGC axons in *EphB2*$^{-/-}$/*B3*$^{-/-}$ dKOs are not randomly displaced along the medio-lateral axis shed light on the possibility that other molecules may be implicated in this directionality. Schmitt and colleagues (2006) identified Wnt3 to be expressed in a medial-high to lateral-low graded manner in the chick and mouse optic tectum and SC respectively. Wnt3 elicited an attractive response on Frizzled5-expressing RGCs *in vitro*, whereas it induced a repulsive response on RGCs expressing the tyrosine kinase receptor Ryk (Schmitt et al., 2006). Interestingly, while Frizzled5 is expressed uniformly in the chick and mouse retina, Ryk is expressed in a high-ventral to low-dorsal gradient (Schmitt et al., 2006). Using a dominant-negative approach, Schmitt and colleagues (2006) showed that ventral RGC projections shifted towards the medial optic tectum. Therefore, Wnt3 acts as a lateral driving force to dorso-ventral RGC axons depending on their relative expression of Ryk (Figure 14D). In addition, RGMb was recently shown to regulate medio-lateral RGC mapping. In contrast to classical guidance molecules, RGMb mediates medio-lateral mapping due to its phosphorylation by a graded expression of the extracellular tyrosine kinase VLK (Harada et al., 2019). Phosphorylated RGMb in turn modulates the activity of the Wnt receptor Lrp5 in a Wnt3a-dependent manner (Harada et al., 2019).

1.6.7 Activity for fine tuning

Early during visual system development, bursts of action potentials arise from the ventro-temporal retina (Ackman et al., 2012). Moreover, these waves of action potentials are critical for proper topographic map formation (Cline and Constantine-Paton, 1989; Galli and Maffei, 1988; Shatz and Stryker, 1988). We now refer to these waves of activity as “spontaneous activity” since they occur prior to eye opening in the

mouse and are therefore independent of visual experience (Wong, 1999). Three consecutive developmental stages of spontaneous waves have been characterized (Bansal et al., 2000; Blankenship and Feller, 2010; Syed et al., 2004). During embryonic development, gap junctions between adjacent RGCs induces fast retinal waves that are known as Stage I retinal waves (Bansal et al., 2000; Syed et al., 2004). During the first postnatal week in mice, these fast retinal waves dissipate and are replaced by a network of randomly firing cholinergic starburst amacrine cells (Zhou, 2001). This Stage II of retinal waves induces neighboring RGCs to fire synchronous bursts of action potentials that propagate along the entire visual pathway (Ackman et al., 2012; Jimmy Zhou, 1998; Wong et al., 1995). Prior to eye opening, starburst amacrine cells stop expressing nicotinic acetylcholine receptors and no longer drive retinal waves. The subsequent loss of cholinergic waves coincides with the maturation of ribbon synapses of bipolar cells onto RGCs within the IPL (Miller et al., 1999). This marks the onset of Stage III waves that are driven by glutamate release from bipolar cells (Blankenship and Feller, 2010).

Spontaneous waves are suggested to strengthen and to stabilize the synapses between co-active cells through voltage-dependent calcium influx, since interfering with spontaneous waves impacts retinotopy in the dLGN and SC (Chandrasekaran et al., 2005; McLaughlin et al., 2003; Stellwagen and Shatz, 2002). However, the mechanisms by which topographic mapping is achieved by guidance cues or activity-dependent processes appear to be distinct. Indeed, *β2*$^{-/-}$ mice that lack a subunit of the nicotinic acetylcholine receptor and exhibit disrupted retinal waves (Stage II), possess a roughly correct retinotopic projection. In contrast, RGC projections exhibit dramatically enlarged terminal arbors that fail to refine (Bansal et al., 2000; Cang et al., 2008; Chandrasekaran et al., 2005; Dhande et al., 2011; Stafford et al., 2009). Likewise, overexpression of the inwardly rectifying channel Kir2.1 that abrogates spontaneous waves results in correct retinal topography and diffuse axonal arborization (Benjumeda et al., 2013). Altogether, the combination of guidance cues and activity-dependent refinement is critical for mediating RGC topography in the SC since mice lacking ephrinAs and *β2*$^{-/-}$ have a near complete loss of retinal topography both anatomically and functionally (Cang et al., 2008; Pfeiffenberger et al., 2006). The current model proposes that topographic cues give a crude map for RGC axons to

arborize topographically, and later spontaneous retinal waves are required for the activity-dependent fine tuning of RGC arborization.

1.6.8 Eye segregation

In binocular species, retinotopic map formation is not sufficient to create an accurate map of the visual scene. In addition to maintaining topography, each image-forming nucleus must align with the projections of both eyes (eye segregation). During normal development, both ipsi- and contra-lateral RGCs project widely across the dLGN and SC (McLaughlin et al., 2003; Sretavan et al., 1988). During the first postnatal week in mice, ipsi-lateral projections significantly refine to occupy the dorso-medial core of the dLGN and the rostro-medial SC (Drager and Hubel, 1975; McLaughlin et al., 2003). Moreover, ipsi- and contra-lateral RGC projections arborize in separate layers of both the dLGN and SC. While contra-lateral RGCs occupy the outer shell of the dLGN and the superficial stratum griseum superficiale layer of the SC, the ipsi-lateral RGCs occupy the inner core of the dLGN and the deeper stratum opticum layer of the SC (Drager and Hubel, 1975; Drager and Hubel, 1976; Dräger and Olsen, 1980).

EphA/ephrinA mutants display eye segregation defects, but it is difficult to untangle the eye-specific effect of this perturbation since both ipsi- and contra-lateral RGCs are impacted in these mutants (Pfeiffenberger et al., 2006). A growing amount of evidence identifies a new potential candidate for the regulation of eye-specific segregation. The Ten-m are type II transmembrane proteins that are essential for cell adhesion and guidance in multiple systems via homophilic interactions (Feng et al., 2002; Leamey and Sawatari, 2019). In vertebrates, there are four identified Teneurin genes: Ten-m1-4 (Feng et al., 2002). Interestingly, Ten-m3 is expressed in a high ventral-to-low dorsal graded manner in the retina and is also expressed in a graded manner in the dLGN and SC (Dharmaratne et al., 2012; Leamey et al., 2007). Targeted deletion of *Ten-m3* leads to a medio-lateral expansion of ipsi-lateral projections in the SC, which is complementary to the graded expression of Ten-m3 in the retina and is in line with a homophilic mechanism (Dharmaratne et al., 2012). *Ten-m3* mice also display a rostro-caudal expansion of ipsi-lateral projections (Dharmaratne et al., 2012). The latter phenotype cannot be explained by a homophilic interaction of Ten-m3 suggesting an alternative mechanism of action for Ten-m3 mediated ipsi-lateral projection refinement. Indeed, the intracellular domain of Ten-m3 binds to the ipsi-lateral transcription factor

Zic2 (Glendining et al., 2017). This interaction is able to regulate EphB1 expression since both *Zic2* and *EphB1* are upregulated in *Ten-m3* mutants (Glendining et al., 2017).

In addition to Ten-m3, Ten-m2 is also expressed in the murine retina, the dLGN, and the SC in a uniform manner (Young et al., 2013). Unexpectedly, *Ten-m2* mutants display a broad reduction in the size of ipsi-lateral projections in the dLGN and SC. The relative number of ipsi-lateral RGCs in the ventro-temporal crescent of the retina is reduced in *Ten-m2* mutants, without affecting Zic2 expression (Young et al., 2013). The fact that both Ten-m2 and Ten-m3 are expressed beyond ipsi-lateral RGCs but modulate ipsi-lateral projections specifically remains poorly understood. Further studies should aim at better understanding the interaction between EphB1, Zic2, Ten-m2/3 and other RGC fate determining factors. In contrast to Ten-m, the neural epidermal growth factor-like 2 (Nell2) modulates contra-lateral RGCs. Nell2 is expressed in the dorso-medial dLGN and targeted deletion of *Nell2*$^{-/-}$ leads to a reduced ipsi-lateral terminal zone at the expense of invading contra-lateral RGCs (Nakamoto et al., 2019). *In vitro*, Nell2 induces growth cone collapse of contra-lateral but not ipsi-lateral RGCs, suggesting that Nell2 acts as an inhibitory molecule for contra-lateral RGCs. Nell2 seems to act as a positional cue marking the ipsi/contra-lateral territory in the dLGN. The role of Nell2 in other binocular nuclei, such as the SC, as well as the potential mechanism of action regulating Nell2-mediated contra-lateral RGC repulsion remain to be studied.

In addition to topographic cues, eye segregation is further refined by activity-based mechanisms (Rebsam et al., 2009). Blocking neural activity in the eye or in visual brain targets prevents accurate eye segregation (Fawcett et al., 1984; Shatz and Stryker, 1988). The neurotransmitter Serotonin (5HT) is a key player in mediating neural activity in RGCs, since mice lacking an enzyme that breaks down serotonin (monoamine oxidase A) exhibit defects in eye-specific segregation (Upton et al., 1999). Activation of the serotonin receptor $5HT_{1B}$ inhibits cAMP production in axon terminals (Salichon et al., 2001). In addition to $5HT_{1B}$, the 5HT transporter Sert internalizes extracellular 5HT which alleviates $5HT_{1B}$-mediated inhibition of cAMP (García-Frigola and Herrera, 2010). Interestingly, Sert is specifically expressed in ipsi-lateral RGCs and its transcription is directly regulated by Zic2 (García-Frigola and Herrera, 2010; Gaspar et al., 2003). Therefore, during RGC refinement, transient expression of 5HT in the LGN

and SC activates $5HT_{1B}$ in contra-lateral RGCs while Sert expression in ipsi-lateral RGCs induces a cAMP-dependent refinement.

Correlated bursts of activity within each eye lead to homogenous refinement in the visual targets. However, for eye segregation to occur, bursts of activity between each eye must be asynchronous. The precise mechanism orchestrating this process is poorly understood. One hypothesis could be that eyes must co-ordinate between each other to maintain this asynchrony. Anatomical observations tend towards this hypothesis as there is evidence for transient RGC axons projecting from one retina to the other via the OC, forming a so called retino-retinal projection (Avellaneda-Chevrier et al., 2015; Bunt and Lund, 1981; Mcloon and Lund, 1982; Murcia-Belmonte et al., 2019). These projections arise from the naso-ventral retina and project on starburst amacrine cells of the opposite eye, suggesting that they could modulate spontaneous activity (Murcia-Belmonte et al., 2019). Interestingly, retina-retinal RGCs express a Netrin-1 receptor Unc5c and in the presence of Netrin-1 at the OC, get repelled towards the opposite optic nerve (Murcia-Belmonte et al., 2019). The full mechanism regulating retino-retinal projections remains to be elucidated since mice lacking microRNA function (*Dicer*$^{fl/fl}$) as well as *Slit1/2* dKO mice also display an increase in retino-retinal projections (Pinter and Hindges, 2010; Plump et al., 2002). This raises the possibility that the opposite optic nerve may serve as a permissive tissue for RGCs in the absence of repulsive cues surrounding the OC.

1.7 The One Who Guides

1.7.1 Netrin-1: a multi-functional protein

In 1892 Santiago Ramón y Cajal proposed the chemotropic theory whereby intelligent forces at intermediate targets would guide growing axons (Ramón y Cajal, 1909). As previously discussed in the section “Azimuth mapping”, initial experimental evidence revealed that such forces were repulsive (Walter et al., 1987b). Tessier-Lavigne and colleagues showed the first evidence of attractive forces using the developing spinal cord as a model system (Figure 15A; Tessier-Lavigne et al., 1988). In the dorsal spinal cord, commissural neurons extend axons ventrally towards an intermediate structure, the floor plate (FP). FP preparations as well as grafting experiments showed that the

FP secretes outgrowth promoting molecules able to guide commissural neurons (Tessier-Lavigne et al., 1988; Yaginuma and Oppenheim, 1991). Based on axonal outgrowth assays, two proteins were subsequently purified from embryonic chick brain: Netrin-1 and Netrin-2 (Serafini et al., 1994). Indeed, Netrin-1 specifically expressed by FP cells and recombinant Netrin-1 was able to re-orient commissural axons *in vitro* (Kennedy et al., 1994). Gene-trapping studies generated a loss-of-function mutant of the murine Netrin-1 (*Ntn1*$^{\beta geo/\beta geo}$), which displays severe guidance defects of commissural neurons (Serafini et al., 1996; Skarnes et al., 1995). *Ntn1*$^{\beta geo/\beta geo}$ mice are hypomorph mutants since some wild-type transcripts are produced (Serafini et al., 1996). In addition to its expression in the spinal cord, Netrin-1 is also specifically expressed within the developing OS and optic disc

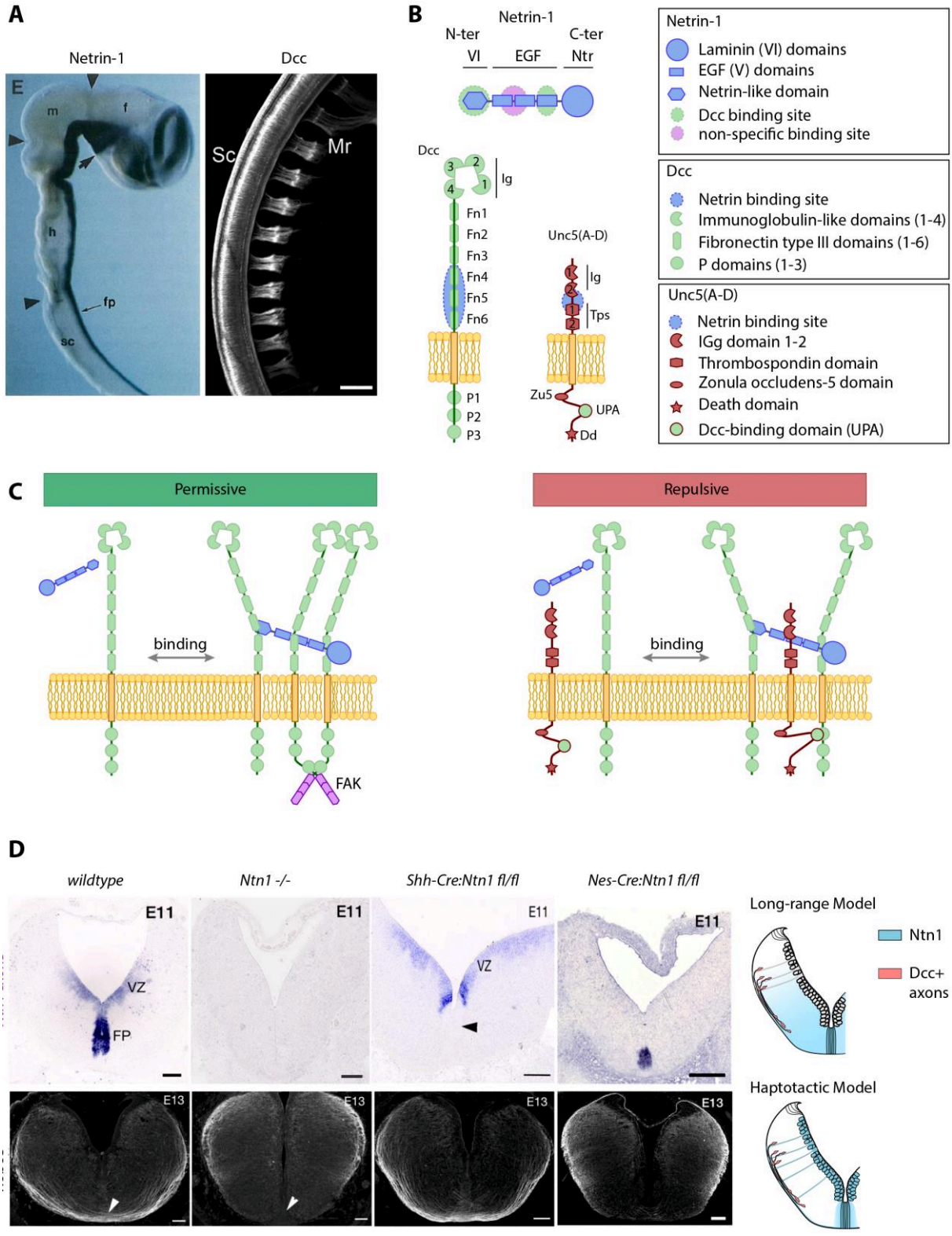

Figure 15 – The chemotactic or haptotactic Netrin-1. A. Lateral view of a Chick (St.15) labeled with a *Netrin-1* riboprobe. *Netrin-1* is expressed in the floor plate. arrowheads specify the boundaries between the spinal cord, hindbrain, midbrain, and forebrain (Kennedy et al., 1994). 3D rendering of a duck embryo spinal cord labeled for the transmembrane receptor Deleted in colorectal carcinoma (Dcc). Dcc is expressed in commissural neurons of the spinal cords (Sc) as well as in the motor nerve roots (Mr) (Friocourt et al., 2017). **B**. The structures of Netrin-1, Dcc, and Unc5

are shown. The specific binding sites are outlined. **C**. A structure-based schematic of Netrin-1 binding to Dcc and Unc5. Upon Netrin-1 binding, three Dcc molecules cluster at the membrane. While the outer segment of Dcc does not dimerise, the cytosolic P3 domain of Dcc dimerise to phosphorylate focal adhesion kinase (FAK). Replacement of Dcc by Unc5 on the binding site 2 switches the permissive response of Netirn-1 to a repulsive response. Instead, the UPA domain of Unc5 binds the P1 domain of Dcc. Adapted from (Meijers et al., 2019). **D**. Wildtype mice show strong mRNA expression of *Netrin-1* in the ventricular zone and the floor plate of the hindbrain. Robo3 expressing commissural neurons cross the floor plate normally. In $Ntn1^{-/-}$ mice, no *Netrin-1* expression is seen. No Robo3 axons are seen crossing the midline. Floor-plate deletion of *Netrin-1* (*Shh-Cre;*$Ntn1^{fl/fl}$) shows no mRNA transcript of Netirn-1 in the floor plate. A strong Robo3 expressing commissure is seen. Ventricular zone deletion of *Netrin-1* (*Nes-Cre:*$Ntn1^{fl/fl}$) shows the complete loss of netrin-1 transcript. A complete loss of Robo3 crossing commissural neurons is seen (Dominici et al., 2017).

(Deiner et al., 1997; Kennedy et al., 1994). $Ntn1^{\beta geo/\beta geo}$ mice display significant ON hypoplasia resulting from aberrantly projecting RGC axons (Deiner et al., 1997). Insights into the mechanism of action of netrins came from parallel studies on the nematode (*Caenorhabditis elegans*). Mutants displaying uncoordinated movements were named after the *unc* family of genes (Brenner, 1974). In the nematode, pioneer axons undergo circumferential migration and run dorsally or ventrally along the body wall (Hedgecock et al., 1990). Mutations in the *unc-40* gene only impact the ventral circumferential migration of neurons whereas mutations in the *unc-5* gene lead to dorsal migration defects (Hedgecock et al., 1990). Interestingly, mutations affecting the *unc-6* gene affect both the dorsal and ventral migration of these neurons, thereby impacting both the attraction of dorsal neurons and the repulsion of ventral neurons (Hedgecock et al., 1990). Therefore, the *unc-6* gene displays a bi-functional role on migrating neurons by being both permissive and repulsive. *Unc-6* is homologous to netrins, sharing 50% sequence homology to Netrin-1 and Netrin-2 (Ishii et al., 1992; Serafini et al., 1994). Furthermore, *NetrinA* and *NetrinB* in the fly are homologous to *unc-6*, showing that the function of netrins is phylogenetically conserved from nematodes to chordates (Harris et al., 1996; Mitchell et al., 1996). Analysis of the *unc-5* and *unc-40* genes shed light onto the bifunctional role of netrins. The *unc-5* gene encodes for a single homologue in the fly, UNC5, and four homologues in vertebrates, UNC5A-UNC5D (Colavita and Culotti, 1998; Hamelin et al., 1993; Leonardo et al., 1997). Upon binding to Netrin-1, UNC5 elicits a repulsive signal (Hamelin et al., 1993). On the other hand, *unc-40* binding to *unc-6* mediates a permissive response to ventral migrating neurons. Double deletion of $unc\text{-}40^{-/-}/unc\text{-}6^{-/-}$ does not result in additive

effects, suggesting they may exert similar functions (Hedgecock et al., 1990). *Unc-40* encodes for a transmembrane receptor homologous to the vertebrate receptor Deleted in colorectal cancer (Dcc) (Figure 15A; Chan et al., 1996; Keino-Masu et al., 1996). Addition of a function-blocking antibody against Dcc hinders commissural neuron outgrowth in response to Netrin-1 (Keino-Masu et al., 1996). Using homologous recombination, *Dcc* null mice were generated and displayed aberrant commissural neuron trajectories in the spinal cord (Fazeli et al., 1997). Dcc is also expressed in the RGCs of the developing eye and $Dcc^{-/-}$ mutant mice display ON hypoplasia reminiscent of the Netrin-1 hypomorph mutants (Deiner et al., 1997).

Recent reports on the crystal structures of Netrin-1 binding to either Dcc or UNC5 help our understanding of the precise signaling of these molecules (Finci et al., 2014; Xu et al., 2014). Netrin-1 is a small protein composed of three protein domains (Figure 15B). At the N-terminal side, Netrin-1 is composed of a laminin-like domain (VI domain), followed by three epidermal growth factor-like repeats (V domain) and a netrin-like domain (NTR) at its C-terminal (Figure 15B; Kennedy et al., 1994; Serafini et al., 1994). Interestingly, the VI and V domains are the most highly conserved and are sufficient for Netrin-1 signaling (Finci et al., 2014; Serafini et al., 1994). Dcc belongs to the superfamily of immunoglobulins (Ig) and is a type I transmembrane receptor (Figure 15B; Keino-Masu et al., 1996). Its ecto-fragment is composed of four Ig-like domains that fold into a horseshoe conformation and six fibronectin type III domains (FN) (Figure 15B; Chen et al., 2013). The cytosolic fragment of Dcc does not fold into a defined three-dimensional protein domain, however, three highly conserved motifs P1, P2, and P3 are critical for Dcc signaling (Kolodziej et al., 1996). UNC5 is also a type I transmembrane receptor with a short two Ig-like domain and two thrombospondin type I domains in its ecto-fragment. The intracellular fragment of UNC5 possesses a Dcc-binding domain (UPA) and a death domain (Figure 15B; Leung-Hagesteijn et al., 1992).

Remarkably, the crystal structure of Netrin-1 binding to Dcc shows three potential binding sites suggesting that one netrin molecule clusters three Dcc receptors (Figure 15B; Finci et al., 2014). This ternary complex sorts Dcc in parallel, suggesting that Netrin-1 binding at the FN4 and FN5 domains acts to assemble Dcc at the membrane (Finci et al., 2014; Geisbrecht et al., 2003; Kruger et al., 2004; Xu et al., 2014). In this conformation, Netrin-1 binding does not result in the ecto-fragments of Dcc to interact

with each other. However, it brings the cytosolic P3 motif of Dcc receptors in close proximity leading to their dimerization (Figure 15C; Stein et al., 2001). This dimerization leads to the recruitment of focal adhesion kinase and phosphatidylinositol 4,5-biphosphate (PIP2) at the membrane and the subsequent activation of Src kinase for cytoskeleton extension (Goñi et al., 2014; Li et al., 2008; Liu et al., 2004; Xu et al., 2018). The observation that co-expressing Dcc and UNC5 in *Xenopus* spinal neurons switched the response to Netrin-1 from permissive to repulsive hinted towards an interaction between the two receptors (Hong et al., 1999). Moreover, the yeast-two-hybrid system revealed an interaction between the intracellular domains of Dcc and UNC5 (Tong et al., 2001). Upon closer analysis, one of the three binding sites of Netrin-1 to Dcc is less specific and is interchangeable with UNC5 (Finci et al., 2014). The binding of UNC5 to Netrin-1 and the juxtaposed Dcc receptors leads to the heterodimerization of the P1 domain of Dcc and the cytoplasmic DCC-binding domain of UNC5 (Figure 15C; Hong et al., 1999; Tong et al., 2001; Wang et al., 2009). Therefore, the ternary structure adopted by Netrin-1 binding to Dcc and UNC5 provides a platform for receptor-mediated attraction or repulsion depending on the axonal environment.

In addition to guiding axons towards or away from its source, Netrin-1 also acts as a cell survival protein (Mehlen et al., 2011). The *DCC* gene was originally identified as a candidate tumor suppressor located on the human chromosome 18q (Fearon et al., 1990). Indeed, there is a loss of heterozygosity in the *DCC* locus in colorectal cancers (Fearon et al., 1990). The tumor suppressor activity of Dcc is attributed to its role as a dependence receptor (DR) (Mehlen et al., 1998). Unlike conventional receptors, DRs can both signal positively (cell survival) and negatively (cell death) in the absence of their ligand (Mehlen et al., 2011). Therefore, the survival of a cell expressing a DR requires the constant expression of the trophic ligand. There are currently twenty-two identified DR that are critical during embryonic development and tumorigenesis (Negulescu and Mehlen, 2018). The pro-apoptotic cascade triggered by Dcc is independent of intrinsic apoptotic pathways (cytochrome c or the formation of apoptosomes) (Forcet et al., 2001). In contrast, apoptosis triggered by Dcc is induced via proteolytic cleavage of the intracellular domain of Dcc by caspase 9, which generates a truncated protein (Forcet et al., 2001; Mehlen et al., 1998). The exposed intracellular domain of Dcc, also known as the “dependence domain”, is prone to

caspase amplification, in a caspase 3-dependent manner (Forcet et al., 2001; Mehlen et al., 1998). Mice bearing a mutated Dcc proteolytic cleavage site (*Dcc*$^{mut/mut}$) are unable to induce apoptosis *in vitro* and display an increased prevalence of colorectal cancers *in vivo* (Castets et al., 2011). Interestingly, the multimerization of Dcc appears to be critical for cell survival since sequestering Dcc as a monomer induces a pro-apoptotic signal (Castets et al., 2009). Of note, the caspase cleavage site of DRs is conserved among mammalian species but is lacking in invertebrates, this suggests that the pro-apoptotic nature of DRs occurred as a relatively late event during evolution (Mehlen and Thibert, 2004).

1.7.2 From a chemotactic to a haptotactic model

Early *in vitro* experiments showed that commissural neurons oriented towards a distant source of Netrin-1 (Kennedy et al., 1994; Tessier-Lavigne et al., 1988; Xu et al., 2018). Moreover, expression analysis showed that Netrin-1 protein was expressed in a high ventral-to-low dorsal graded manner in the chick spinal cord (Kennedy et al., 2006). Together, these experiments led to the widespread idea that Netrin-1 acts as a long-range axon guidance cue (Tessier-Lavigne and Goodman, 1996). Intriguingly, the biochemical properties of Netrin-1 mitigate the possibility of it being a diffusible cue as it anchors to the ECM and to the cell membrane (Kennedy et al., 1994; Tessier-Lavigne et al., 1988). Indeed, a few early *in vitro* reports showed that Netrin-1 acted as a substrate-bound guidance cue. When Netrin-1 covalently attached to freely floating silica beads were supplemented in the media of spinal commissural neurons, no apparent phenotype occurred (Moore et al., 2009). However, when these beads were immobilized, the growth cone of commissural neurons oriented towards the beads, suggesting that Netrin-1 acted as a substrate-bound guidance cue. More evidence against the diffusible action of Netrin-1 came from *in vivo* studies. Mutant flies carrying a trans-membrane Netrin-1 (unable to be secreted) show no commissural defects (Brankatschk and Dickson, 2006). These studies raised the interesting possibility that Netrin-1-mediated axonal guidance occurred by haptotaxis (bound to a surface) and not by chemotaxis (in a soluble fluid).

In order to fully address the chemotactic model, four independent laboratories generated Netrin-1 floxed mice, giving the possibility to remove Netrin-1 in a tissue-specific manner (Bin et al., 2015; Dominici et al., 2017; Varadarajan et al., 2017;

Yamauchi et al., 2017; Yung et al., 2015). Indeed, Netrin-1 null mice (*Ntn1*$^{-/-}$), generated by crossing Netrin-1 floxed mice to a germline Cre driver, resulted in a complete loss of ventral commissures in the spinal cord (Figure 15D; Bin et al., 2015; Yung et al., 2015). However, spinal commissural neurons successfully migrated ventrally and crossed the midline when Netrin-1 floxed mice were crossed to a FP-specific Cre driver (Figure 15D; Dominici et al., 2017; Varadarajan et al., 2017; Yamauchi et al., 2017). These observations showed that FP-derived Netrin-1 is not required for guiding commissural neurons ventrally. Interestingly, *Netrin-1* mRNA also localizes in progenitor cells at the ventricular zone of the spinal cord (Kennedy et al., 1994; Serafini et al., 1996). In contrast, Netrin-1 protein accumulates at the pial surface of the spinal cord, suggesting that Netrin-1 expressed by ventricular zone progenitors is transported along their processes and deposited at the pial surface in contact with the growing commissural axons (Dominici et al., 2017; Varadarajan et al., 2017). Indeed, conditional deletion of the ventricular zone-derived Netrin-1 resulted in a dramatic reduction of commissural crossing at the midline (Figure 15D; Dominici et al., 2017; Varadarajan et al., 2017; Yamauchi et al., 2017). These results therefore put forward a model whereby Netrin-1 guides growing commissural neurons by haptotaxis (Figure 15D).

Aim of the PhD project

As described throughout the introduction, our understanding of the developmental sequence of RGC differentiation and their subsequent targeting to the brain proper are well characterized. Despite this broad understanding, many specific aspects of RGC development remain poorly understood. One fundamental unanswered question is how this diverse neuronal pool decides to target a large number of brain nuclei using such a restricted set of axon guidance molecules. Moreover, there is very little knowledge about whether this narrow set of cues is evolutionarily conserved.

In the past several years, histological analysis has been revolutionized with the emergence of tissue clearing strategies. These techniques allowed for the re-evaluation of a vast majority of complex axon guidance defects. However, no techniques currently exist to target the visual system due to the physical hindrance of the retinal pigmented epithelium. This study is largely centered around the design and use of a novel tool to access the entire visual system in 3D, from the eyes to the brain proper. The development of this method allows us to begin probing at these questions with the following aims:

1. Is the program orchestrating decussation at the optic chiasm evolutionarily conserved in vertebrates?

One of the major decision points for an RGC axon is whether to project ipsi- or contra-laterally at the optic chiasm. This binary response of RGCs has been extensively characterized in the mammalian visual system. However, the variety of species displaying a partial decussation at the optic chiasm remains largely unstudied. We want to shed light on the potential conservation of this program throughout the vertebrates.

2. What is the precise function of the receptor/ligand pair Dcc/Netrin-1 in RGC axons?

Dcc and Netrin-1 are broadly expressed throughout the CNS. While their role in optic nerve development is well accepted, evidence is lacking regarding their role in later stages of visual system development. As a result, the second aim of this thesis was to analyze whether the highly conserved Dcc and Netrin-1 guidance molecules are required by all RGCs for optic nerve entry as well as proper targeting in the brain proper using conditional mutant mice.

Results

Chapter 1 : Bilateral visual inputs are evolutionary conserved in non-teleost bony fish, preceding aerial vision adaptation

Robin J. Vigouroux, Karine Duroure, Juliette Vougny, Peter Kozulin, Eloisa Herrera, Kim Nguyen-Ba-Charvet, Ingo Braasch, Rodrigo Suarez, Filippo Del Bene* and Alain Chédotal*

Contribution: R. J. Vigouroux, F. Del Bene, and A. Chédotal designed the experiments, the figures and wrote the manuscript. R. J. Vigouroux and F. Del Bene carried out the eye tracing experiments except for the Australian lungfish. R. J. Vigouroux carried out clearing, imaging and analysis of visual projections that make up Figure 1, Figure 2, and associated movies. R. J. Vigouroux carried out the immunostaining, eye clearing, and quantifications that make up Figure 3, and Figure 4A-G. K. Duroure designed and generated the riboprobes and carried out the FISH in Figure S2 E and F. R. J. Vigouroux carried out the *in situ hybridization* that make up Figure 4 J to L, Figure S1, and Figure S2. For Figure 4 M to P, J. Vougny, and K. Duroure carried out the molecular biology, and injections; eye enucleations and imaging was carried out by J. Vougny, K. Duroure, and R. J. Vigouroux.

Bilateral visual inputs are evolutionary conserved in non-teleost bony fish, preceding aerial vision adaptation

Robin Vigouroux[1], Karine Duroure[1], Juliette Vougny[2], Peter Kozulin[3], Eloisa Herrera[4], Kim Nguyen-Ba-Charvet[1], Ingo Braasch[5], Rodrigo Suarez[3], Filippo Del Bene[1]* and Alain Chédotal[1]*

[1]Sorbonne Université, INSERM, CNRS, Institut de la Vision, 17 Rue Moreau, 75012 Paris, France

[2]Institut Curie, PSL Research University, INSERM U934, CNRS UMR3215, Paris, France

[3]Queensland Brain Institute The University of Queensland, Building 79, St Lucia Campus, Brisbane, QLD 4072, Australia

[4]Instituto de Neurociencias Av. Ramón y Cajal s/n San Juan de Alicante 03550 Spain

[5]Department of Integrative Biology and Program in Ecology, Evolutionary Biology and Behavior, Michigan State University, 288 Farm Lane, East Lansing MI 48824, USA

One sentence summary (40 characters): Bilateral visual system preceded water-to land transition

*Corresponding authors

filippo.del-bene@inserm.fr and alain.chedotal@inserm.fr

In most vertebrates, two bilaterally symmetrical camera-style eyes with a multilayered neural retina containing photoreceptors, interneurons and retinal ganglion cells (RGCs) are present. RGC axons project, via the optic nerves, to visual brain centers in the diencephalon (e.g. thalamus) and mesencephalon (tectum/colliculus). Eye position on the head is highly variable between species, but frontal eyes have long been considered critical for depth perception (stereopsis) by increasing the overlap of the right and left eye visual fields (*1*). In all vertebrates, the two optic nerves cross over at the optic chiasm to enter the brain on the contralateral side. In mammals the two optic nerves intermingle at the chiasm but in some fish they simply overlap (*2*).

Classic neuroanatomical studies showed that in mammals, eye projections are bilateral with a variable fraction of RGC axons continuing in the ipsilateral optic tract after crossing the chiasm. The proportion of ipsilateral projections is low (2-3%) in rodents but reaches around 40% in primates (*3*, *4*). The comparative analysis of many vertebrate species conducted over several decades has led to conclude that ipsilateral visual axons exist in all mammals, anuran amphibians, some reptiles, and that they are essentially absent or were secondarily lost in birds (*4–7*). Accordingly, developmental transcriptional programs specifying ipsilateral RGCs described in mammals are conserved in Xenopus but not in chick and zebrafish (*4*, *8*). This textbook view implies that visual axon bilaterality evolved in early tetrapods and might have provided a visual advantage, in particular for nocturnal and predatory terrestrial species (*9*), while secondarily lost in others such as the avian lineage. However, a review of the extensive literature on fish visual systems gives a more complex image with reports, sometimes contradictory, of ipsilateral RGC projections in some fish species (*5*, *10*). Most of these pioneering studies relied on histological staining of degenerating axons following enucleation and optic nerve crush or via intra-ocular

injections of radiolabelled-amino acids followed by autoradiography or lipophilic tracers, all methods known to be imprecise and suboptimal (*11*). Here, we assessed the laterality of visual projections in bony fishes (**Fig. 1A**) using the B fragment of the cholera toxin (CTb) (*11*), an axonal tracer that has not been used in fish yet. CTb is a more accurate and compatible with whole-brain clearing and 3D light sheet fluorescence microscopy (LSFM) (*12*).

With more than 30,000 species, fishes account for at least half of the extant vertebrate species (*13*). We initially focused on ray-finned fishes (Actinopterygians; **Fig. 1A**) which separated from lobe-finned fish (Sarcopterygians including tetrapods) more than 450 Million years ago (Ma)(*14*). Within ray-finned fishes, we initially selected 6 species among clupeocephalans, the largest of the three subdivisions/lineages of teleost fishes which account for most (about 96%) of extant teleosts (*15*). Three represent ostariophysians (Mexican tetra *Astyanax mexicanus*, redeye piranha *Serrasalmus rhombeus*, and zebrafish *Danio rerio*) and three are percomorphs (green-spotted pufferfish *Tetraodon nigroviridis*, Atlantic mudskipper *Periophtalmus barbarous,* and four-eyed fish *Anableps anableps*), the two largest clades of teleosts, with 9,000 and 16,000 species respectively. They have diverse eye positions, feeding behaviors, and habitats and some were previously reported to have ipsilateral visual projections (*10*).

Teleost fishes have totally crossed visual projections

The visual system of the zebrafish has been extensively studied using lipophilic dye tracing or genetic methods and shown to be exclusively contralateral (*16*). Accordingly, we found that fluorescent CTb axons were only present on the contralateral side of adult zebrafish brains (**Fig. 1B** and **movie S1**; n=6). Importantly, all the previously identified retino-recipient visual nuclei (*17*) could be detected with CTb, thereby

validating the use of this tracing method in fish (**Fig. 1C**). Mexican tetra is a classic fish model, as some 'cavefish' populations, living in caves, lost their eyes (*18*). 3D LSFM imaging of CTb injected fish, showed that visual projections were only contralateral in Mexican tetra surface fish (**Fig. 1, B** and **E** and **movie S1;** n=7), contradicting a previous study (*19*). Likewise, eyes in the redeye piranha only projected contralaterally (**Fig. 1, F** and **G** and **movie S1**; n= 3), in disagreement with earlier work in other piranha species (*20*, *21*). This suggests that ostariophysians only have crossed visual projections.

In the fresh water green-spotted pufferfish (*22*) the optic nerves did not fuse at the chiasm and visual projections were exclusively contralateral (**Fig. 1, H** and **I** and **movie S1**; n= 4) as previously described in another pufferfish (*23*). We next studied the four-eyed fish, a surface dweller fish whose remarkable large protruding eyes with duplicated corneas and pupils allows seeing under and above the water (*24*). Again, CTb tracing showed that in this species, visual projections were also completely crossed (**Fig. 1, J** and **K**; n= 3). Similar results were obtained in the mudkskipper with amphibious lifestyle that uses aerial vision (**Fig. 1L** and **M** and **movie S1**; n= 3). Together, these results show that in percomorph eyes, RGCs only project to visual nuclei on the opposite side of the brain.

Osteoglossomorphs (bonytongues) and elopomorphs (e.g. eels and tarpons), are the two sister groups of clupeocephalans, although the exact phylogenetic relationships of the three teleost lineages are still debated (*13*, *25*). Osteoglossomorphs are considered a group of basal teleosts constituted of mostly extinct species and about 200 living ones. We chose to trace visual projections in the African butterflyfish (*Pantodon buchholzi*), a predator living close to the surface of freshwater system, and found a small contingent of retinal axons (**Fig. 2, A and B** and **movie S2,** 2.33±0.23

% ipsilateral projections in the OT; n=3) projected to the ipsilateral side, corroborating an earlier report (*26*). The main portion of ipsilateral axons targeted the optic tectum and some others targeted pretectal nuclei. Ipsilateral visual axons were also described in mormyrid electric fish (*Gnathonemus petersii*) (*27*), another osteoglossoform, suggesting that bilateral visual projections exist in osteoglossomorphs and that ipsilateral projections were lost in clupeocephalans. In mammals, binocular inputs to visual targets/areas are either segregated (thalamus, colliculus) or intermingled (suprachiasmatic nucleus). As both eyes were injected with 2 distinct Alexa-conjugated-CTbs, we also studied the relative distribution of ipsilateral and contralateral RGC axons in butterflyfish brain areas receiving inputs from both eyes. This showed that axons from both sides segregated in binocular visual centers of the African butterflyfish (**Fig. 2C**) as in the thalamus and colliculus of mammals.

Non-teleost ray-finned and sarcopterygian fishes have bilateral visual projections

These results on teleosts led us to study retinal projections in more basally branching, non-teleost ray-finned lineages (Holostei, Cladistia and Chrondrostei, **Fig. 1A**) which split from teleosts before the teleost gene duplication that occurred around 320 Ma in the ancestor of extant teleosts (reviewed in (*28*)). Holostei and Chrondrostei are considered to have only slowly evolved since they branched from other vertebrates 350 Ma (*29*). Bilateral visual projections (**movie S2, n=5/5**) were observed in the spotted gar (*Lepisosteus oculatus*), one of the seven extant species of garfish, a representative of the Holostei. The spotted gar is a unique animal model as its genome is thought to provide a “bridge” between tetrapods and teleosts (*30*). Bilateral CTb injections revealed an important ipsilateral projection in the rostral optic tectum of the

spotted gar, with RGC axons targeting several pretectal nuclei, such as the magnocellular superficial pretectal nucleus. There was no overlap of the contralateral and ipsilateral axons (**Fig. 2, D** to **F** and **movie S2**, n=5/5) which represented 4.78±0.46 % of visual inputs in the OT, a ratio comparable to rodents. Next, we traced visual projections in the chondrostean sterlet sturgeon (*Acipenser ruthenus*), Acipenseriforms; n=2/2). CTb tracing demonstrated the existence of a binocular domain in the tectum of the sterlet sturgeon as well as in several pretectal nuclei (**Fig. 2, G** to **J** and **movie S2**; 9.77±1.28 % ipsilateral projections in the OT, n=2). No re-crossing of visual inputs after entering the brain were detected contrary to previous observations in *Acipenser güldenstädti* (*31*). We then studied the armored bichir (*Polypterus delhezi,* Cladistia; n=2/2), a carnivorous nocturnal fish possessing a paired lung structure and representing the most basally branching Cladistia. Ipsilateral axons projected to numerous pretectal nuclei such as the nucleus opticus dorsolateralis anterior thalami and , the area optica ventrolateralis thalami, and the nucleus commissurae posterior par magnocellularis (**Fig. 2, K** to **N** and **movie S2**). This corroborates previous studies in *Polypterus senegalus* (*32*). These results, together with similar observations in longnose gar (*Lepisosteus osseus*) and the bowfin (*Amia calva*) (*33*, *34*) indicate that bilateral visual projections likely arose before the diversification of actinopterygians and that the ipsilateral component was subsequently lost in clupeocephalans. Last, and to further test this hypothesis, we analyzed visual projections in the Australian lungfish (*Neoceratodus fosteri;* Ceratodontiforms). Lobe-finned fish (Sarcopterygii) (the monophyletic group that includes tetrapods) and ray-finned fish diverged about 450 Ma and lungfish are now considered the closest relative of tetrapods (*14*). In all injected animals (n=6/6) a small ipsilateral projection was found innervating the optic tectum (**Fig. 2, O** to **S** and **movie S3,** n=6). In contrast to other

fish species analyzed here, ipsilateral projections intermingled with contralateral ones without segregating (**Fig. 2, R** and **S**; n=6). This was consistent with an earlier analysis of a single specimen of Australian lungfish (*35*) and supports the existence of bilateral visual projections in the bony vertebrate ancestor of actinopterygians and sarcopterygians. This indicates that the bilateral organization of the visual system did not appear in amniotes but is an ancestral vertebrate feature that emerged much earlier in evolution.

Spotted gars possess ipsilateral projections independently of Zic2

These results raised questions about the evolution of the genetic mechanisms underlying visual system binocularity. Are they conserved in ray-finned fish with bilateral visual projections? The zinc-finger transcription factor Zic2 has been shown to specify the ipsilateral identity of RGCs in developing Xenopus, mice and ferrets (*4*). To further evaluate the implication of Zic2 in the control of RGCs laterality in the mammals, we analyzed the expression of Zic2 in the human eye where half of the retina contains ipsilateral RGCs and compared it with in mice by performing immunohistochemistry in whole-mount retinas. Using the EyeDISCO clearing protocol (*36*) we observed that at E16, the peak of Zic2 expression in mice (*4*) the retinal domain positive for Zic2 represented about 5.34±0.36 % of the total retina surface (**Fig. 3, A** to **C and K** and **Table S1**; n=6 eyes). Flat-mounted human retinas from post-conception week 9 (pcw9) embryos, the equivalent embryonic stage of Zic2-expressing retinas in mice (*37*), showed ZIC2+ cells restricted to the temporal quadrant (representing about 18.95±0.98 % of the retina surface), the region known to contain ipsilaterally projecting RGCs in humans. However, cells immunoreactive for the pan-RGC marker, RNA-binding protein with multiple splicing (RBPMS)(*38*) were present throughout the retina

(**Fig. 3, D** to **J** and **movie S4**; n=3 eyes). Little overlap was observed between RBPMS+ cells and ZIC2+ cells, with the latter occupying a deeper position in the retina (**Fig. 3I** and **movie S4**). However, as previously shown in mice(*4*), most ZIC2+ cells coexpressed the early RGC marker ISLET1 (*39*) (**Fig. 3 G** and **H**). Double staining with SOX2, a marker of retinal progenitors, demonstrated that ZIC2 is present only in differentiated (ISLET1+ SOX2-) RGCs (**Fig. 3J**). These data suggest that, as in rodents (*4*), human ZIC2 is transiently expressed in recently differentiated ipsilateral RGCs as their axons approach the midline. This pivotal role for Zic2 in the specification of an ipsilateral axonal growth program was also well correlated with the absence of transcripts of the two *zic2* co-orthologs (*zic2a* and *zic2b*) in zebrafish RGCs (*40*) (**Fig. S2 A** to **D**). Double fluorescent *in situ* hybridization for *zic2b* and *atoh7* (a RGC marker) confirmed that *zic2b* is only expressed in the ciliary marginal zone (CMZ), which contains dividing progenitors producing all retinal cell types, even in adult teleosts (*41*) (**Fig. S2 E** and **F**; n=5).

The presence of a significant ipsilateral visual projection in the spotted gar, as large as that of mice, together with its well characterized genome and the accessibility of gar embryos (*30*, *42*), led us to evaluate the expression of *zic2* in the developing gar retina. We first analyzed the development of the gar visual system using whole-mount immunolabelling, iDISCO clearing and 3D LSFM (**Table S1**) (*36*). In the spotted gar, Islet1- immunoreactive RGCs were detected at 2-3 days post fertilization (dpf) (**Fig. 4, A** and **B** and **movie S5**; n=5) . At 6-7dpf, optic nerves could be observed and had reached the optic chiasm (**Fig. 4, C** and **D** and **movie S5**; n=5). By 17-18dpf the retina contained many RGCs and the optic tract was well developed (**Fig. 4, E** to **G** and **movie S5**; n=5). The highly proliferative CMZ could be identified by the presence of cells expressing the s-phase marker, proliferating cell nuclear antigen marker (PCNA),

which was absent from neighbouring post-mitotic Islet1+ RGCs (**Fig. 4, H** and **I**). As early as 2-3dpf, *zic2* mRNA was detected in proliferating cells of the developing neuroretina and progressively became restricted to the CMZ where it was still present in adult (**Fig. S1, A** to **D**). We did not detect *zic2* mRNA in Islet1+ RGCs (**Fig. 4, J** to **L**). Zic1 and zic5, also enriched in ipsilateral RGC in mice (*43*), were absent from the embryonic gar retina (**Fig. S1, E** to **L** and **Table S1**). These results show that Zic2 or its paralogs Zic1 and Zic5 do not specify ipsilateral RGCs in the spotted gar. Zic2 acts in part by activating the expression of the receptor tyrosine kinase EphB1 in ipsilateral axons (*7*, *44*), whose ligand ephrinB2, localized at the chiasm, prevents crossing (*6*). According to the lack of Zic2 in the gar RGCs, we did not detect *EphB1* mRNA either in the developing retina and *ephrinB2*, was absent from the chiasm (**Fig. S1, M** to **W**). In mice, *Zic2* overexpression in the retina, outside the ipsilateral domain, increases the proportion of ipsilaterally projecting RGC axons (*44*). Therefore, we tested the hypothesis that despite its absence in fish RGCs, the forced expression of Zic2 in zebrafish RGCs could affect their axonal targeting. We used a human *Zic2-T2A-GFP* overexpression construct to express Zic2 and GFP in the zebrafish eye under the control of the *atoh7* promoter. To visualize the projections coming from ZIC2 overexpressing RGCs derived from a single eye, we removed one eye at 2 dpf. As previously reported, under normal conditions retinal fibers from the remaining eye developed normally to the contralateral tectum (**Fig. 4, M** and **N**; n=11) (*45*, *46*). In contrast, ZIC2-expressing RGCs generated ipsilateral retinotectal afferent fibers (**Fig. 4, O** and **P**; n=10/13). This striking result was specific, and we did not observe other pathfinding mistakes. These results show that *zic2*, although not normally expressed in zebrafish RGCs, can still specify an ipsilateral program.

It has been proposed that the evolution of terrestrial vertebrates followed a dramatic increase of eye size in aquatic animals able to see through air, adopting a lifestyle similar to modern crocodiles or fish species similar to the four-eye fish and mudskippers (*47*). The existence of ipsilateral projections in the most basal groups of both actinopterygians and sarcopterygians indicates that ipsilateral connections were already present in ancient bony fishes. This example highlights the importance of assessing a variety of species in order to draw evolutionary significant conclusions that may remain obscured when focusing only on a handful of model species (*48*). Giving the reduced visual system development in lungfish and some basally branching actinopterygians (e.g. *Acipenser* and *Polypterus*), and the nocturnal predatory habit of some of those species, it is unlikely that ipsilateral retinal projections serve a function similar to what is commonly considered in mammals. On the contrary, visual system bilaterality might have been recently used as the neural substrate to compute stereopsis following the acquisition in diurnal mammals of visual-based predatory abilities following the Cretaceous–Paleogene (K–Pg) extinction event. Interestingly, and supporting this view, the amount of ipsilateral projections in reptiles (chelonians and squamates) correlates neither with eye position nor the degree of binocular field (*10*, *49*). To date the function of ipsilateral RGCs in non-mammalian vertebrates remains elusive and behavioral studies in non-canonical model species such as the gar will be required to answer these questions.

The conservation of the main families of axon guidance cues and receptors in bilateria suggested that the mechanisms underlying the development of neuronal connectivity are evolutionary conserved (*50*, *51*). However, the loss of the gene encoding Deleted in Colon Cancer (DCC) receptor in some bird species(*52*) and the uniqueness of the Roundabout3 receptor in mammals (*53*) challenged this view. The guidance program

specifying visual axon ipsilaterality does not appear to be conserved across vertebrates as we failed to detect expression of a *zic2* and other *zic* genes or *ephB1* in spotted gar RGCs. Hence, the classical Zic2/EphB1 bilaterality textbook model based on studies in mammals does not simply translate to fish and further experiments are needed to address the molecular mechanisms underlying visual bilaterality in ancient fish species. However, the ectopic expression of human ZIC2 in the developing zebrafish retina still induces the formation of ipsilateral RGC axons without causing other targeting defects. This unexpected finding supports a conservation of the genetic program downstream of Zic2 in the gar. As previously mentioned, the gar thus could serve as a critical model to better understand the molecular determinants of visual system evolution.

Acknowledgements

The authors wish to thank Anais Favre and Ali Abjaghou for assistance with light sheet microscopy, Fabio Cortesi for help with lungfish experiments and all members of Alain Chédotal and Del Bene teams for helpful discussions and input during the project. We thank Sylvie Rétaux (Paris Saclay University) for help with Astyanax work and helpful comments on the manuscript. We thank Allyse Ferrara and Solomon David (Nicholls State University) and members of the Braasch Lab for help with gar work, which is supported by NIH R01OD011116. This work was completed with the financial support of the Programme Investissements d'Avenir IHU FOReSIGHT (ANR-18-IAHU-01) and Inserm cross-cutting program HuDeCA 2018 to AC. RS received salary from a UQ Amplify Fellowship.

Authors contribution

AC, FB and RV designed the experiments. FB, KD, JV, RV, PK, RS conducted the experiments. AC and FB obtained funding for the project. IB provided *Lepisosteus* samples and EH the human *ZIC2* cDNA. AC, FB and RV designed the figures and wrote the manuscript. All authors discussed the results and commented on the manuscript.

List of supplementary materials

Materials and Methods

Figs. S1 to S2

Table S1

Movies S1 to S5

References (54–59)

References

1. S. Ramón y Cajal, *Histologie du système nerveux de l'homme & des vertébrés* (1909).
2. G. L. Walls, *The vertebrate eye and its daptative radiation* (Hafner Publishing company, Bloomfield Hills Michigan., 1942).
3. G. Jeffery, L. Erskine, Variations in the architecture and development of the vertebrate optic chiasm. *Prog. Retin. Eye Res.* **24**, 721–753 (2005).
4. E. Herrera *et al.*, Zic2 Patterns Binocular Vision by Specifying the Uncrossed Retinal Projection. *Cell*. **114**, 545–557 (2003).
5. M. L. Larsson, Binocular vision, the optic chiasm, and their associations with vertebrate motor behavior. *Front. Ecol. Evol.* **3**, 89 (2015).
6. S. Nakagawa *et al.*, Ephrin-B regulates the Ipsilateral routing of retinal axons at the optic chiasm. *Neuron*. **25**, 599–610 (2000).
7. S. E. Williams *et al.*, Ephrin-B2 and EphB1 Mediate Retinal Axon Divergence at the Optic Chiasm. *Neuron*. **39**, 919–935 (2003).
8. A. Seth *et al.*, Belladona/(lhx2) is required for neural patterning and midline axon guidance in the zebrafish forebrain. *Development*. **133**, 725–735 (2006).
9. C. P. Heesy, Seeing in stereo: The ecology and evolution of primate binocular vision and stereopsis. *Evol. Anthropol.* **18**, 21–35 (2009).
10. R. Ward, J. Repérant, S. Hergueta, D. Miceli, M. Lemire, Ipsilateral visual projections in non-eutherian species: random variation in the central nervous

system? *Brain Res. Rev.* **20**, 155–170 (1995).
11. C. Saleeba, B. Dempsey, S. Le, A. Goodchild, S. McMullan, A Student's Guide to Neural Circuit Tracing. *Front. Neurosci.* **13**, 897 (2019).
12. Z.-C. Luo *et al.*, Maternal and fetal leptin, adiponectin levels and associations with fetal insulin sensitivity. *Obesity*. **21**, 210–216 (2013).
13. L. C. Hughes *et al.*, Comprehensive phylogeny of ray-finned fishes (Actinopterygii) based on transcriptomic and genomic data. *Proc. Natl. Acad. Sci. U. S. A.* **115**, 6249–6254 (2018).
14. C. T. Amemiya *et al.*, The African coelacanth genome provides insights into tetrapod evolution. *Nature*. **496**, 311–316 (2013).
15. R. Betancur-R *et al.*, Phylogenetic classification of bony fishes. *BMC Evol. Biol.* **17**, 162 (2017).
16. R. O. Karlstrom *et al.*, Zebrafish mutations affecting retinotectal axon pathfinding. *Development*. **123**, 427–38 (1996).
17. E. Robles, E. Laurell, H. Baier, The Retinal Projectome Reveals Brain-Area-Specific Visual Representations Generated by Ganglion Cell Diversity. *Curr. Biol.* **24**, 2085–2096 (2014).
18. D. Casane, S. Rétaux, Evolutionary Genetics of the Cavefish Astyanax mexicanus. *Adv. Genet.* **95**, 117–59 (2016).
19. T. J. Voneida, C. M. Sligar, A comparative neuroanatomic study of retinal projections in two fishes: Astyanax hubbsi (the blind cave fish), and Astyanax mexicanus. *J. Comp. Neurol.* **165**, 89–105 (1976).
20. E. Fiebig, S. O. E. Ebbesson, D. L. Meyer, Afferent connections of the optic tectum in the piranha (Serrasalmus natteren). *Cell Tissue Res.* **231**, 55–72 (1983).
21. S. E. Ebbesson, H. Ito, B. R. Projections, Bilateral Retinal Projections in the Black Piranah (Serrasalmus niger). *Cell Tissue Res.* **213**, 483–495 (1980).
22. O. Jaillon *et al.*, Genome duplication in the teleost fish Tetraodon nigroviridis reveals the early vertebrate proto-karyotype. *Nature*. **431**, 946–957 (2004).
23. D. L. Meyer, E. Fiebig, S. O. E. Ebbesson, A note on the reciprocal connections between the retina and the brain in the puffer fish Tetraodon fluviatilis. *Neurosci. Lett.* **23**, 111–115 (1981).
24. L. N. Perez *et al.*, Eye development in the four-eyed fish Anableps anableps: Cranial and retinal adaptations to simultaneous aerial and aquatic vision. *Proc. R. Soc. B Biol. Sci.* **284** (2017), doi:10.1098/rspb.2017.0157.
25. C. Bian *et al.*, The Asian arowana (Scleropages formosus) genome provides new insights into the evolution of an early lineage of teleosts. *Sci. Rep.* **6**, 1–17 (2016).
26. A. B. Butler, W. M. Saidel, Retinal Projections in the Freshwater Butterfly Fish, Pantodon buchholzi (Osteoglossoidei). *Brain. Behav. Evol.* **38**, 127–140 (1991).
27. G. Lázár, S. Libouban, T. Szabo, The mormyrid mesencephalon. III. Retinal projections in a weakly electric fish, Gnathonemus petersii. *J. Comp. Neurol.* **230**, 1–12 (1984).
28. I. Braasch, J. H. Postlethwait, in *Polyploidy and Genome Evolution*, P. Soltis, D. Soltis, Eds. (Springer Berlin Heidelberg, 2012), pp. 341–383.
29. K. Du *et al.*, The sterlet sturgeon genome sequence and the mechanisms of segmental rediploidization. *Nat. Ecol. Evol.* **4**, 841–852 (2020).
30. I. Braasch *et al.*, The spotted gar genome illuminates vertebrate evolution and facilitates human-teleost comparisons. *Nat. Genet.* **48**, 427–437 (2016).

31. J. Repérant *et al.*, The Retinofugal Pathways in a primitive actinopterygian, the chondrostean Acipenser güldenstädti. An experimental study using degeneration, radioautographic and HRP methods. *Brain Res.* **251**, 1–23 (1982).
32. J. Repérant, J. P. Rio, D. Miceli, M. Amouzou, J. Peyrichoux, The retinofugal pathways in the primitive African bony fish Polypterus senegalus (Cuvier, 1829). *Brain Res.* **217**, 225–43 (1981).
33. R. G. Northcutt, A. B. Butler, Retinofugal pathways in the longnose gar Lepisosteus osseus (linnaeus). *J. Comp. Neurol.* **166**, 1–15 (1976).
34. A. B. Butler, R. G. Northcutt, Retinal Projections in the Bowfin, Amia calva: Cytoarchitectonic and Experimental Analysis. *Brain. Behav. Evol.* **39**, 169–194 (1992).
35. R. Glenn Northcutt, Retinal projections in the australian lungfish. *Brain Res.* **185**, 85–90 (1980).
36. R. J. Vigouroux, Q. Cesar, A. Chédotal, K. T. Nguyen-Ba-Charvet, Revisiting the role of Dcc in visual system development with a novel eye clearing method. *Elife*. **9**, e51275 (2020).
37. R. O'Rahilly, The prenatal development of the human eye. *Exp. Eye Res.* **21**, 93–112 (1975).
38. J. M. K. Kwong, J. Caprioli, N. Piri, RNA Binding Protein with Multiple Splicing: A New Marker for Retinal Ganglion Cells. *Investig. Opthalmology Vis. Sci.* **51**, 1052 (2010).
39. A. Hoshino *et al.*, Molecular Anatomy of the Developing Human Retina. *Dev. Cell*. **43**, 763-779.e4 (2017).
40. R. Toyama, D. M. Gomez, M. D. Mana, I. B. Dawid, Sequence relationships and expression patterns of zebrafish zic2 and zic5 genes. *Gene Expr. Patterns*. **4**, 345–350 (2004).
41. D. C. Otteson, A. R. D'Costa, P. F. Hitchcock, Putative stem cells and the lineage of rod photoreceptors in the mature retina of the goldfish. *Dev. Biol.* **232**, 62–76 (2001).
42. I. Braasch *et al.*, A new model army: Emerging fish models to study the genomics of vertebrate Evo-Devo. *J. Exp. Zool. B. Mol. Dev. Evol.* **324**, 316–41 (2015).
43. Q. Lo Giudice *et al.*, Single-cell transcriptional logic of cell-fate specification and axon guidance in early-born retinal neurons. *Development*. **146**, dev178103 (2019).
44. C. García-Frigola, M. I. Carreres, C. Vegar, C. A. Mason, E. Herrera, Zic2 promotes axonal divergence at the optic chiasm midline by EphB1-dependent and -independent mechanisms. *Development*. **135**, 1833–1841 (2008).
45. A. L. Dell, E. Fried-Cassorla, H. Xu, J. A. Raper, cAMP-Induced Expression of Neuropilin1 Promotes Retinal Axon Crossing in the Zebrafish Optic Chiasm. *J. Neurosci.* **33**, 11076–11088 (2013).
46. C. Gebhardt *et al.*, An interhemispheric neural circuit allowing binocular integration in the optic tectum. *Nat. Commun.* **10**, 5471 (2019).
47. M. A. MacIver, L. Schmitz, U. Mugan, T. D. Murphey, C. D. Mobley, Massive increase in visual range preceded the origin of terrestrial vertebrates. *Proc. Natl. Acad. Sci.* **114**, E2375–E2384 (2017).
48. G. Laurent, On the value of model diversity in neuroscience. *Nat. Rev. Neurosci.* **21**, 395–396 (2020).
49. S. Hergueta *et al.*, Overlapping visual fields and ipsilateral retinal projections in

turtles. *Brain Res. Bull.* **29**, 427–433 (1992).
50. C. S. Goodman, The likeness of being: Phylogenetically conserved molecular mechanisms of growth cone guidance. *Cell*. **78**, 353–356 (1994).
51. P. Heger, W. Zheng, A. Rottmann, K. A. Panfilio, T. Wiehe, The genetic factors of bilaterian evolution. *Elife*. **9** (2020), doi:10.7554/eLife.45530.
52. F. Friocourt *et al.*, Recurrent DCC gene losses during bird evolution. *Sci. Rep.* **7**, 37569 (2017).
53. P. Zelina *et al.*, Signaling Switch of the Axon Guidance Receptor Robo3 during Vertebrate Evolution. *Neuron*. **84**, 1258–1272 (2014).

Figure legends

Fig.1. Visual projections are only contralateral in teleosts.

(**A**) Schematic representation of the major groups of vertebrates. Divergence of each major group is displayed in million years. Asterisks indicate whole genome duplications. (**B**) Whole brain visualization of a juvenile Zebrafish (*Danio rerio)* injected with CTb, highlighting a completely contralateral projection. (**C**) High magnification showing anterior (a), medial (m), and posterior (p) pre-tectal (pT) nuclei and the optic tectum (OT). (**D** to **M**) 3D rendering of visual projections labelled by injecting AlexaFluor-555-conjugated CTb (left eye) and AlexaFluor-647-conjugated CTb (right eye) followed by iDISCO whole-brain clearing and 3D imaging using light sheet fluorescence microscopy. (**D** and **E**) Mexican tetra *Astyanax mexicanus*, surface form. (**F** and **G**) Redeye piranha *Serrasalmus rhombeus*. (**H** and **I**) Pufferfish *Tetraodon nigroviridis*. (**J** and **K**) Four-eyed fish *Anableps anableps.* (**L** and **M**) Mudskipper *Periophtalmus barbarus*. In all species, visual axons only project to the brain on the contralateral side. Abbreviations: Cb, Cerebellum; OB, Olfactory bulb; ON, Optic nerve. Scale bars are 500 μm in (B) and (D) to (M) and 200 μm in (C).

Fig. 2. **Bilateral visual projections in basal ray-finned fishes and lobe-finned fishes**

(**A** to **S**) 3D light-sheet fluorescence microscopy images of iDISCO cleared brains from fish injected into the eyes with 2 CTbs. The left panels show only one channel. (**C, G, K, N** and **S**) are optical sections through the brain region receiving bilateral visual inputs. (**I** and **M** and **R**) high magnification from whole-mount brains. (**A** to **C**) butterfly fish *Pantodon buchholzi***.** (**D** to **F**) spotted gar *Lepisosteus oculatus*. (**G** to **J**) sterlet sturgeon *Acipenser ruthenus*. (**K** to **N**) armored bichir *Polypterus delhezi*. (**O** to **S**) Australian lungfish *Neoceratodus forsteri*. (**C, G, K** and **N**) contralateral and ipsilateral projections segregate in 2 different OT layers. (**S**) They are intermingled in the OT. Red arrowheads indicate ipsilateral projections. Abbreviations: Cb, Cerebellum; OB, Olfactory bulb; OE, Olfactory epithelium; ON, Optic nerve; OC, Optic chiasm; pT, pretectal nuclei, OT, Optic tectum; T, Optic tract. Scale bars are 500 μm in (A, B, D, E, G, H, K, L, P and Q) and 80 μm in (C, G, K, N and S) and 100 μm in (M, O) and 150 μm in (I, R)

Fig. 3. Expression profile of Zic2 in the mammalian retina.

(**A** to **C**) Whole-mount immunohistochemistry of an E16 mouse eye labeled with the pan RGC marker Rbpms and the ipsilateral RGC marker Zic2. (A) frontal view and (B) top view. (C) Optical section. (**D** to **F**)**,** 3D light-sheet fluorescence microscopy images of iDISCO cleared pcw9 human embryonic eye labeled for Rbpms and Zic2. (D) frontal view and (E) top view. (F) Optical section. (**G** to **I**) retinal cryosection of a pcw9 human embryo eye labeled with Zic2 and Islet1. (**J**) flat-mount pcw9 human retina labeled for Rbpms and Zic2. (**K**) Flat-mount retinas labeled for Sox2 and Zic2. (**L**) Box and whiskers representation of the Zic2-positive surface in E16 mouse and pcw9 human

retinas. Abbreviations: D, dorsal ; V, ventral ; N, nasal ; T, temporal ; ON, optic nerve. Scale bars are 70 μm in (A and B) and 20 μm in (C) and 300 μm in (D and E) and 50 μm in (F and G to J).

Fig. 4. Zic2 is not expressed by RGCs in spotted gar and zebrafish

(**A** to **F**) Development of the visual system in *Lepisosteus oculatus*. All images are 3D light-sheet fluorescence microscopy images of iDISCO-cleared *Lepisosteus oculatus* embryos labeled with Islet1 and acetylated tubulin. (A and C and E) Top (dorsal) view of *Lepisosteus oculatus* at 2-3dpf (A), 6-7dpf (C), and 17-18dpf (E). (**B** and **D** and **F**) frontal views of whole *Lepisosteus oculatus* eyes at 2-3dpf (B), 6-7dpf (D), and 17-18dpf (F). The optic nerve (ON and asterisk) starts to form at 6-7dpf and is well developed at 17-18dpf. The optic chiasm (OC) is seen from 6-7dpf. (**G**) Coronal cryosection of *Lepisosteus oculatus* embryos at 17-18dpf labeled for ßIII-tubulin and Islet1. (**H)** Cryosection from 17-18dpf *Lepisosteus oculatus* eyes labeled for proliferating cell nuclear antigen (PCNA) and Islet1. (**I**) Higher magnification of the CMZ. (**J** to **L)** *In situ* hybridization of a 17-18dpf *Lepisosteus oculatus* eye with *zic2* riboprobe. (K) higher magnification image. (L) *In situ* hybridization for *zic2* coupled with an immunohistochemistry Islet1. (**M** to **P**) 3D rendering of whole-brain viewed from the top of zebrafish injected with Tg(Atoh7:Gal4,14UASubc:T2A-eGFP-pA (M and N) or Tg(Atoh7:Gal4,14UASubc:Zic2-T2A-eGFP-pA (O and P). N and P show segmented RGC projections. (P) A large ipsilateral projection is seen in the Tg(Atoh7:Gal4,14UASubc:Zic2-T2A-eGFP-pA (arrowhead). Abbreviations: ON, Optic nerve; OC, Optic chiasm; CMZ, Ciliary margin zone; GCL, Ganglion cell layer; INL, Inner nuclear layer; ONL, Outer nuclear layer. Scale bars are 50 μm in (A, D, F, K, L,

M to P) and 15 μm in (B) and 100 μm in (C, H and J) and 150 μm in (E) and 200μm in (G).

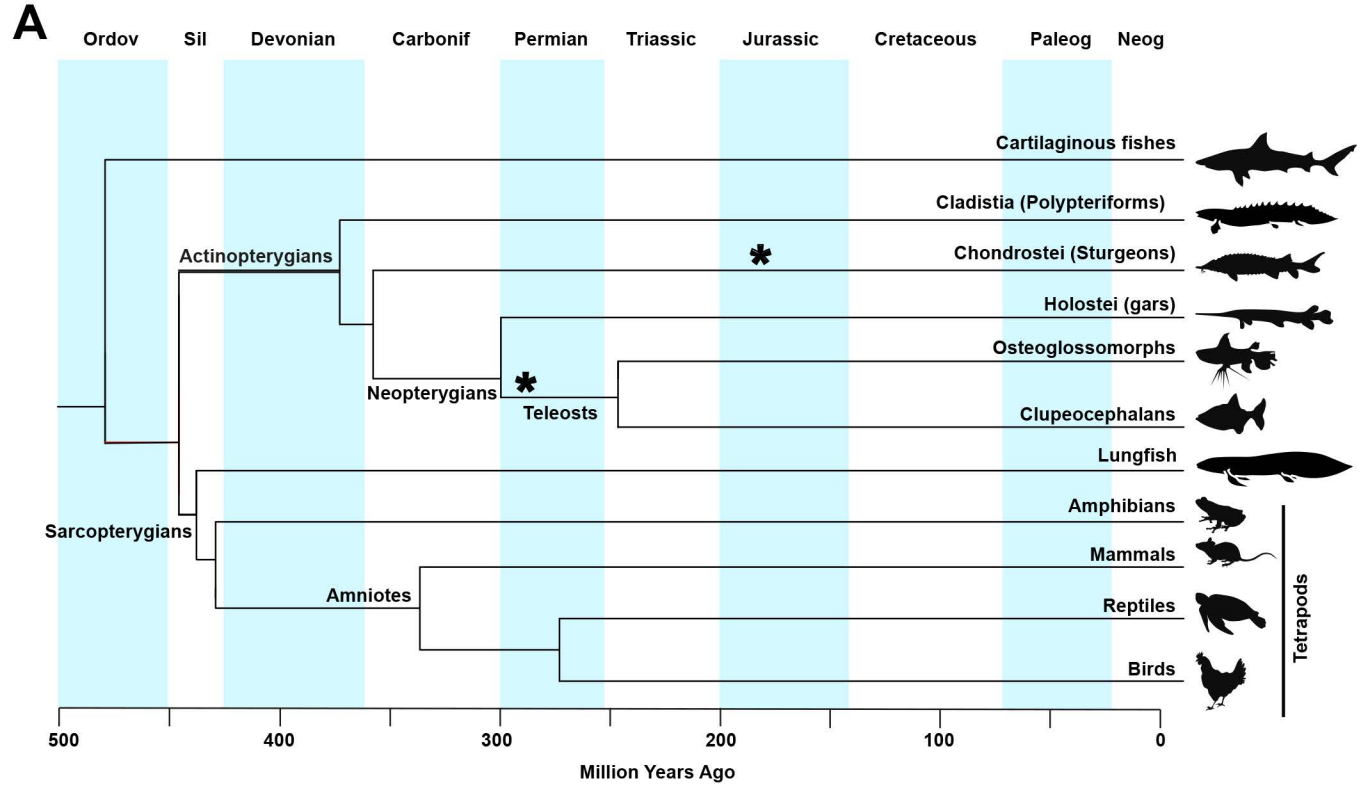
A
Ordov
Sil
Devonian
Carbonif
Permian
Triassic
Jurassic
Cretaceous
Paleog
Neog
Cartilaginous fishes
Cladistia (Polypteriforms)
Chondrostei (Sturgeons)
Holostei (gars)
Osteoglossomorphs
Clupeocephalans
Lungfish
Amphibians
Mammals
Reptiles
Birds
Tetrapods
Actinopterygians
Neopterygians
Teleosts
Sarcopterygians
Amniotes
500
400
300
200
100
0
Million Years Ago

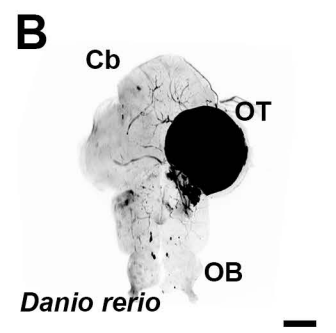
B
Cb
OT
OB
Danio rerio

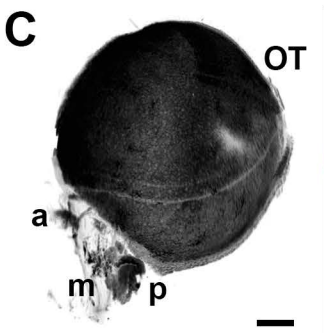
C
OT
a
m
p

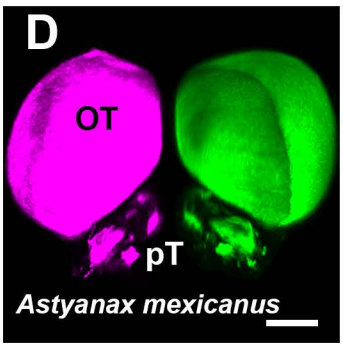
D
OT
pT
Astyanax mexicanus

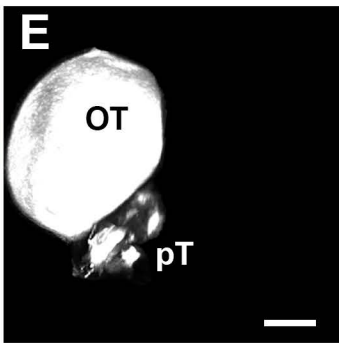
E
OT
pT

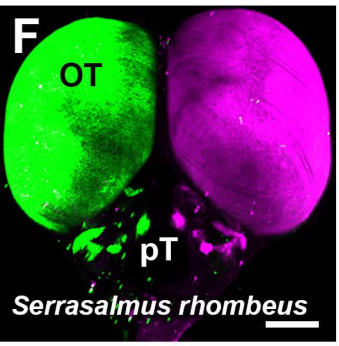
F
OT
pT
Serrasalmus rhombeus

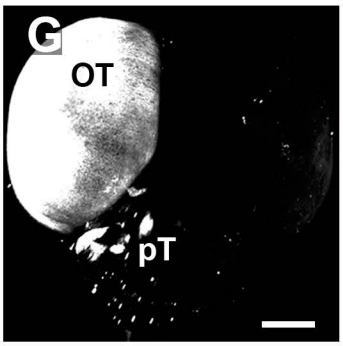
G
OT
pT

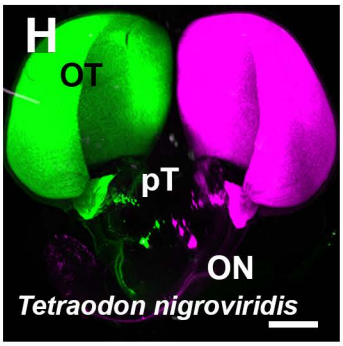
H
OT
pT
ON
Tetraodon nigroviridis

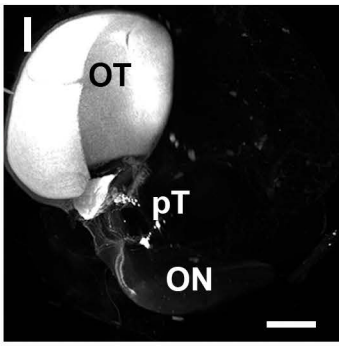
I
OT
pT
ON

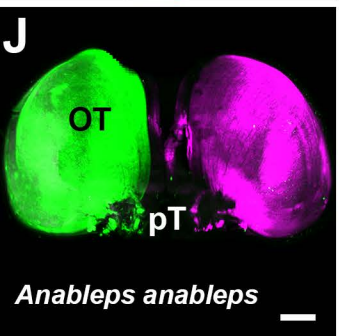
J
OT
pT
Anableps anableps

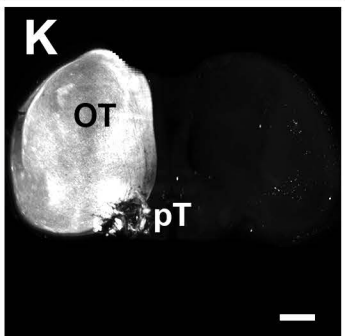
K
OT
pT

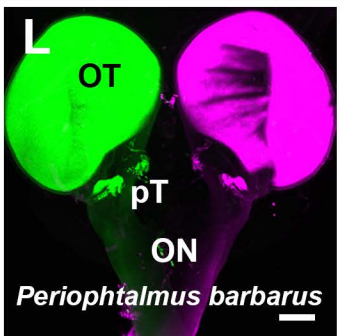
L
OT
pT
ON
Periophtalmus barbarus

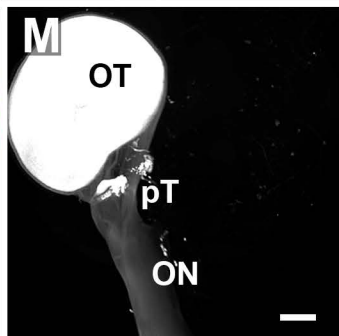
M
OT
pT
ON

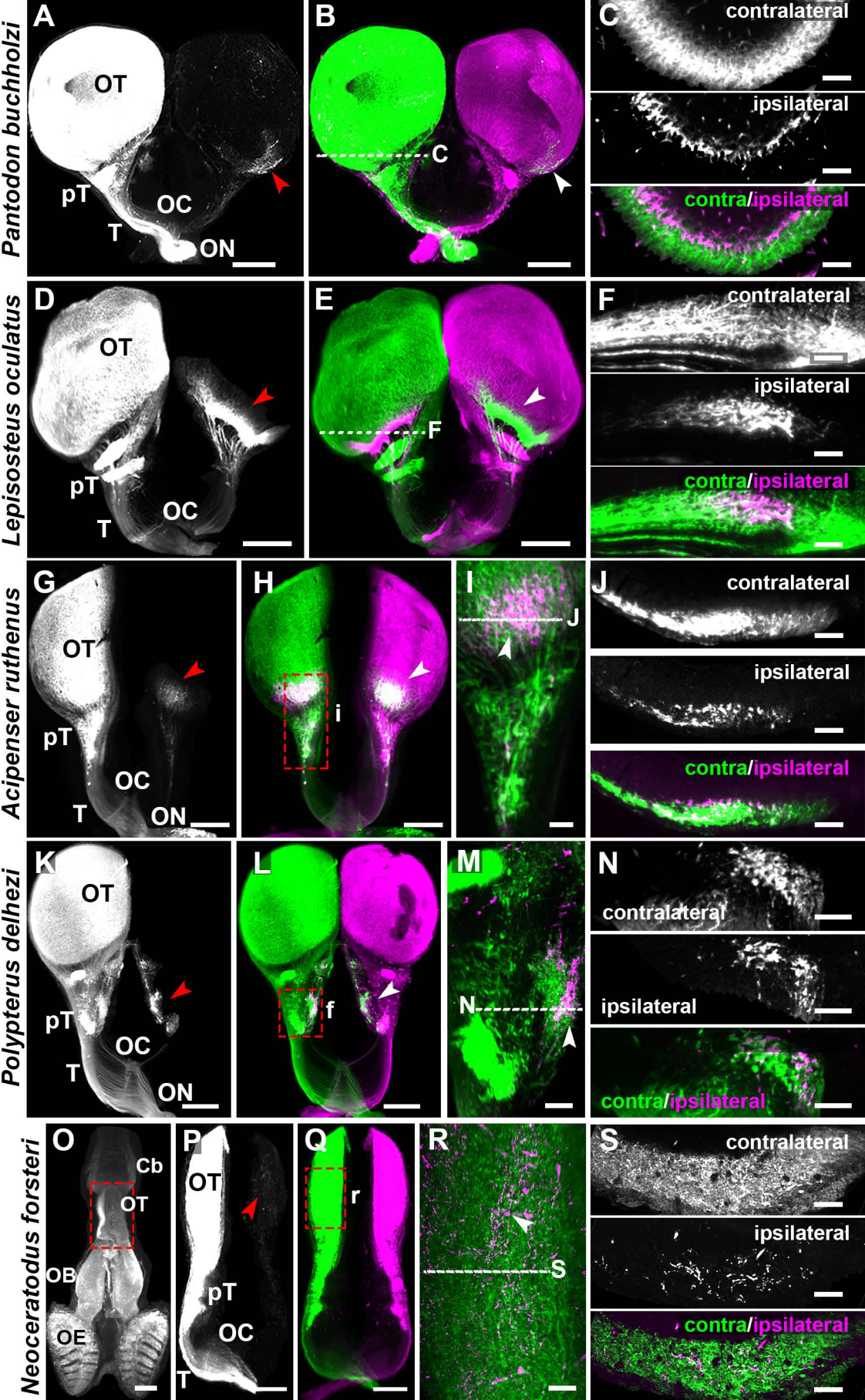
Pantodon buchholzi
Lepisosteus oculatus
Acipenser ruthenus
Polypterus delhezi
Neoceratodus forsteri
A
B
C
D
E
F
G
H
I
J
K
L
M
N
O
P
Q
R
S
OT
pT
OC
T
ON
Cb
OB
OE
i
f
r
contralateral
ipsilateral
contra/ipsilateral

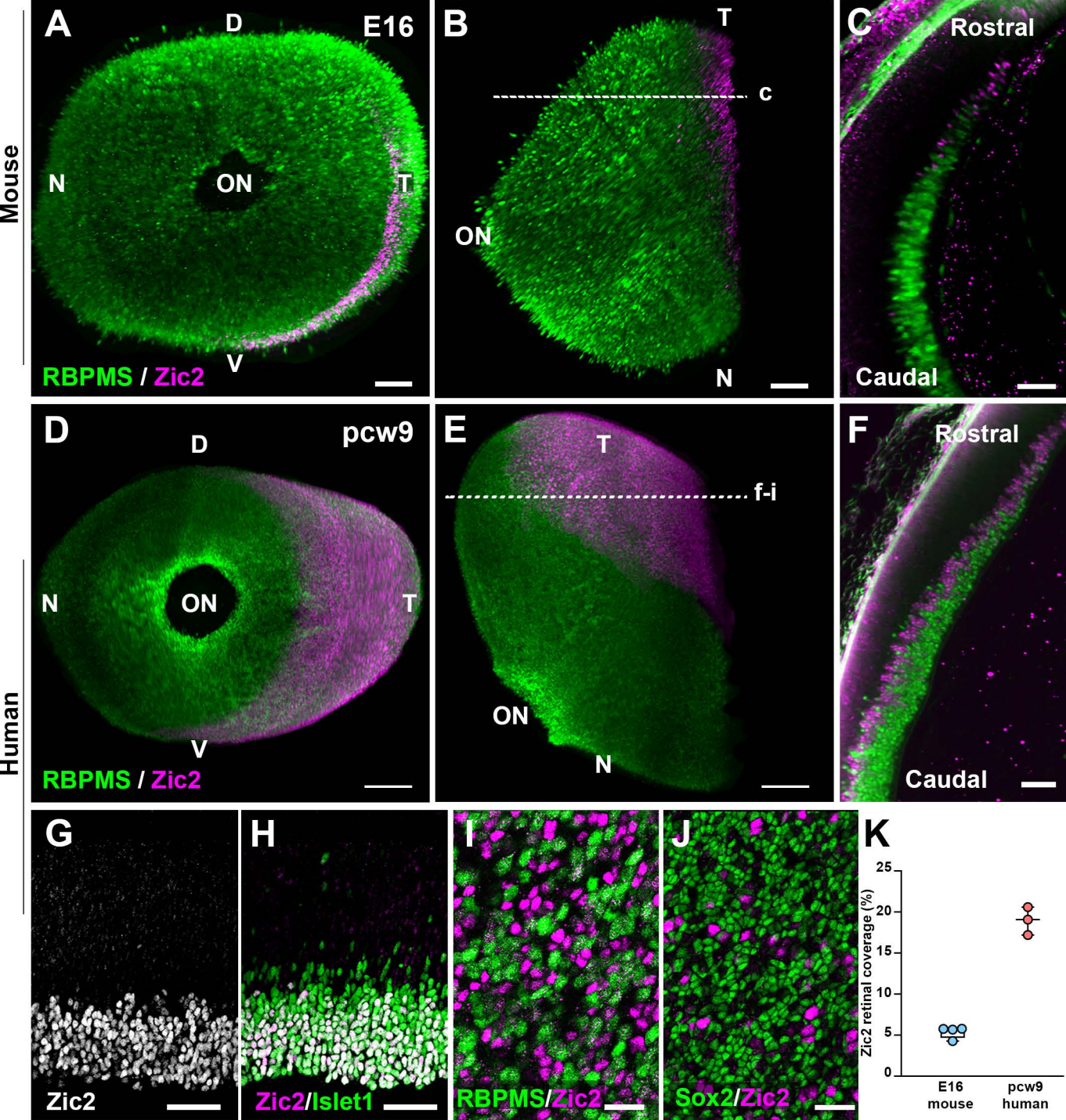
Mouse
Human
A
D
E16
N
ON
T
V
RBPMS / Zic2
B
T
c
ON
N
C
Rostral
Caudal
D
D
pcw9
N
ON
T
V
RBPMS / Zic2
E
T
f-i
ON
N
F
Rostral
Caudal
G
Zic2
H
Zic2/Islet1
I
RBPMS/Zic2
J
Sox2/Zic2
K
Zic2 retinal coverage (%)
25
20
15
10
5
0
E16
mouse
pcw9
human

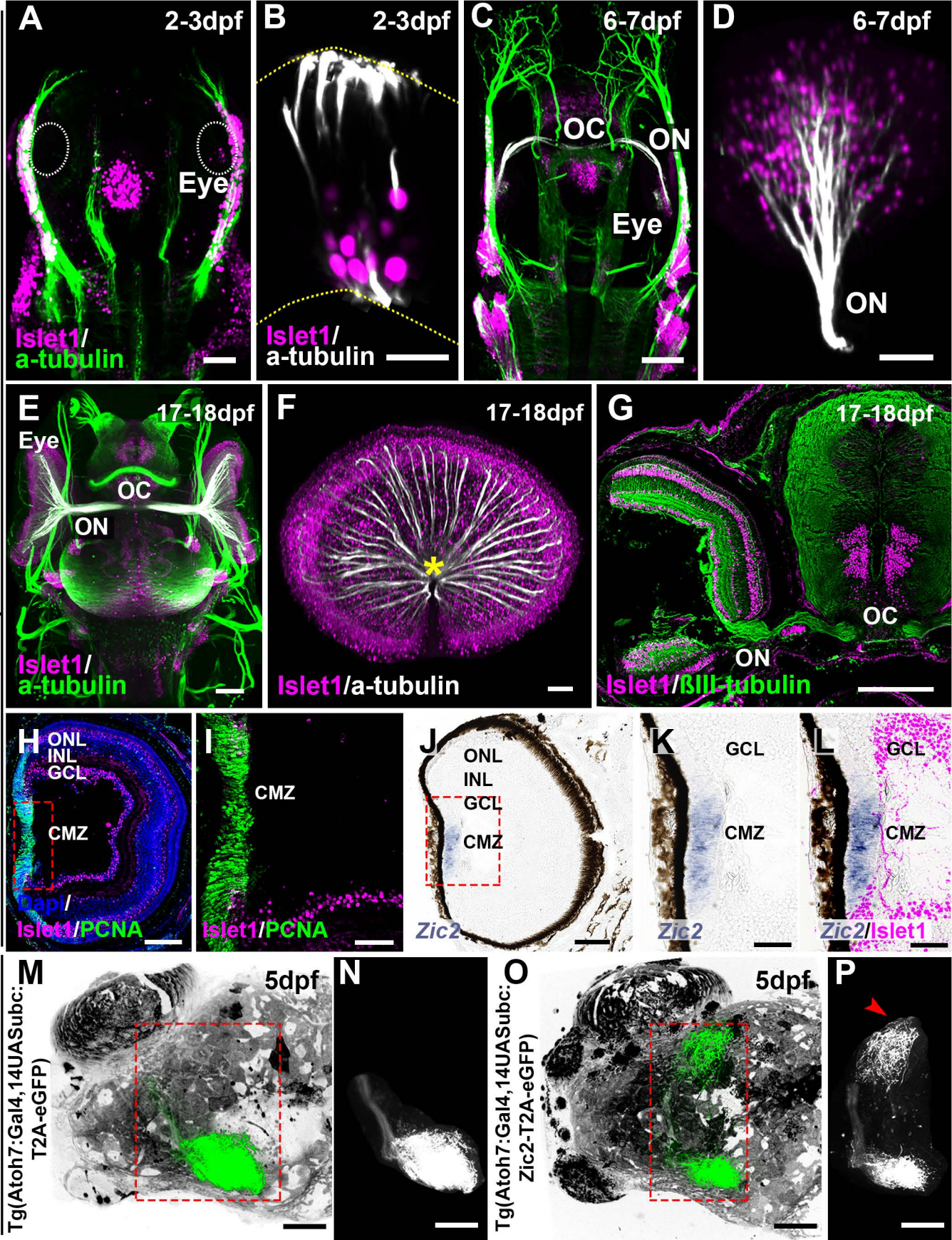
A
2-3dpf
Eye
Islet1/
a-tubulin
B
2-3dpf
Islet1/
a-tubulin
C
6-7dpf
OC
ON
Eye
D
6-7dpf
ON
Lepisosteus oculatus
E
17-18dpf
Eye
OC
ON
Islet1/
a-tubulin
F
17-18dpf
Islet1/a-tubulin
G
17-18dpf
OC
ON
Islet1/ßIII-tubulin
H
ONL
INL
GCL
CMZ
Dapi/
Islet1/PCNA
I
CMZ
Islet1/PCNA
J
ONL
INL
GCL
CMZ
Zic2
K
GCL
CMZ
Zic2
L
GCL
CMZ
Zic2/Islet1
Danio rerio
M
5dpf
Tg(Atoh7:Gal4,14UASubc:
T2A-eGFP)
N
O
5dpf
Tg(Atoh7:Gal4,14UASubc:
Zic2-T2A-eGFP)
P

Supplementary Materials for

Bilateral visual inputs are evolutionary conserved in non-teleost bony fish, preceding aerial vision adaptation

Robin Vigouroux, Karine Duroure, Juliette Vougny, Peter Kozulin, Eloisa Herrera, Kim Nguyen-Ba-Charvet, Ingo Braasch, Rodrigo Suarez, Filippo Del Bene* and Alain Chédotal*

Corresponding authors: filippo.del-bene@inserm.fr and alain.chedotal@inserm.fr

This PDF file includes:

Material & Methods

Animals

Juvenile *Astyanax mexicanus* (San Solomon Spring, Balmorhea State Park, Texas, USA) were maintained at 26°C (surface fish) on a 12:12 h light:dark cycle. Juvenile Zebrafish (*Danio rerio*) and embryos were maintained at 28.5°C on a 14h light/10h dark cycle. Juvenile *Neoceratodus forsteri* (10.2-13.5 cm body length; Jardini Pty Ltd, Brisbane, Australia) were on freshwater at 26°C on a 12:12 h light:dark cycle. Juvenile *Polypterus Delhezi, Acipenser ruthenus, Lepisosteus oculatus, Pantodon buchholzi, Tetraodon nigroviridis, Periophtalmus barbarus, Anableps anableps, Serrasalmus rhombeus* were acquired from commercial vendors. *Lepisosteus oculatus* embryos were spawned at Nicholls State University in Louisiana and then raised and maintained at Michigan State University as previously described (*1*). All animal procedures were performed in accordance with the French, Australian, and United States animal welfare guidelines. Gar work was performed according to the Michigan State University IACUC-approved protocol #10/16-179-00. Sizes of each specimen were recorded for future analysis. Juvenile specimens of either sex were used.

In Situ Hybridization

Lepisosteus oculatus sections were hybridized with digoxigenin-labeled riboprobes as described in (*2*). Briefly, tissue sections were postfixed for 10 minutes in 4% paraformaldehyde (PFA) before being treated with Proteinase K (10 µg/ml; Invitrogen, #03115852001) for 2 mins and subsequently postfixed for 5 mins in 4% PFA. Sections were then acetylated and permeabilized in PBS 1% Triton X-100. Sections were first homogenized with hybridization buffer (50% formamide (VWR #24311.291), 5× SSC (Euromedex, #EU0300-A), 1× Denhardt's, 250 µg/ml yeast tRNA, and 500 µg/ml

herring sperm DNA, pH 7.4) for 2 h at RT and then hybridized overnight at 72°C with riboprobes (1/200), see Table S1 for probe sequences. The next day, sections were rinsed for 2 h in 2× SSC at 72°C, and blocked in 0.1 M Tris, pH 7.5, 0.15 M NaCl (B1) containing 10% normal goat serum (NGS) for 1 h at RT. After blocking, slides were incubated o/n at 4°C with anti-DIG antibody conjugated with the alkaline phosphatase (1/5000, Roche Diagnostics) in B1 containing 1% NGS. After washing in B1 buffer, the alkaline phosphatase activity was detected by using nitroblue tetrazolium chloride (337.5 µg/ml) and 5-bromo-4-chloro-3-indolyl phosphate (175 µg/ml) (Roche Diagnostics). Sections were mounted in Mowiol (Calbiochem/Merck, Carlstadt, Germany).

Whole-mount in situ hybridization were carried out on *Danio* rerio as previously described (*3*). Embryos were then embedded in gelatin/albumin with 4% of Glutaraldehyde and sectioned (20 µm) on a VT1000 S vibrating blade microtome (Leica). Slides were scanned with either a Nanozoomer (Hamamatsu) or laser scanning confocal microscope (Olympus, FV1000).

Fluorescent In Situ Hybridization

To generate anti-sense probes, DNA fragments were obtained by PCR using Phusion™ High-Fidelity DNA polymerase (Thermo Scientific, #F530L) using the primers listed in Table S1. Total cDNA for 2dpf Zebrafish were used as a template. PCR fragments were cloned into the pCRII-TOPO vector (Invitrogen, #K280040) according to manufacturer's instructions. All plasmids used were sequenced for confirmation. Anti-sense DIG or fluorescein-labeled probes were in vitro transcribed using the RNA labeling kit (Roche, #11685619910 or #11277073910) according to manufacturer's instructions. De-chorionated embryos at the appropriate

developmental stages were fixed in fresh 4% PFA in 1X PBS (pH7.4) and 0.1% Tween20 (PBSTw) for 4h at RT. Embryos were immersed in alternating baths of 50% methanol/PBSTw (Sigma, #34860) and then 2 baths of PBSTw, followed by a 10min incubation in a 3% H_2O_2/0.5%KOH (Sigma, #P5958) solution, then rinsed in 50% methanol and finally 100% methanol at -20°C. Embryos were re-hydrated in PBSTw followed by treatment in 10µg/ml proteinase K at RT (1dpf=8min, 2dpf=20min, 3dpf=70min), and post-fixed for 20min in 4% PFA in PBSTw. Embryos were pre-hybridized at 68°C, and hybridized with either a fluorescein-labelled probe or DIG-labelled probe o/n at 68°C with gentle shaking. Embryos were then rinsed at 68°C in 50% formamide/2XSSC/0.1%Tween-20 twice, 2XSSC/0.1%Tween-20, 0.2XSSC/0.1% Tween-20 twice and finally in TNT buffer (0.1M Tris pH7.5, 0.15M NaCl, 0.1% Tween-20). Blocking was done in TNB buffer (2% DIG block (Roche, #11096176001) in TNT) for 2h at RT and incubated o/n with anti-Fluo-Fab-POD (Roche, #11426346910) diluted at 1:50 in TNB buffer at 4°C. All steps were performed in the dark. Embryos were then washed in TNT and revealed using 100µl Tyramide Signal Amplification (TSA) (PerkinElmer, #NEL741001KT) and incubated with Fluorescein fluorophore Tyramide diluted at 1:50 in TSA. The reaction was stopped by 5 washes in TNT. DIG revelation was carried out by incubating embryos for 20 min in 1%H_2O_2/TNT (Sigma, #18312-1L), and washed several times in TNT. A second blocking step was carried out for 1h in TNB buffer prior to incubating embryos in anti-DIG-POD (Roche, #11207733910) diluted at 1:100 in TNB buffer o/n at 4°C. revelation was done with Cy3 Fluorophore Tyramide solution (PerkinElmer, NEL#744001KT), washed and processed for imaging.

Molecular cloning

14xUAS:ubc-hZic2-T2A-GFP-pA or *14xUAS:ubc-GFP-pA* were obtained via Gibson assembly using the *pT1UciMP Tol1* (Addgene, #62215) destination vector described by (*4*). mRNA Tol1 was obtained from the plasmid (Addgene, #61388) digested by Not1 (NEB, #R3189S) and retro-transcribed with SP6 RNA polymerase (Roche, #10810274001). Human Zic2 (*hZic2*), *GFP*, and *T2A* were amplified via PCR from pCAG-hZic2 (gift from Dr. Eloisa Herrera), pUAS:Cas9T2AGFP;U6:sgRNA1;U6sgRNA2 (Addgene, #74009) respectively using the NEBuilder HiFi DNA Assembly Cloning kit (NEB, #E5520). Appropriate sequences were inserted after the ubc intron of the *pT1UciMP Tol1* destination vector opened by restriction digest with NcoI-HF (NEB).

Eye enucleation

Prior to eye enucleation, fish were selected for the atoh4 expression in green. At 2 dpf, eye enucleation was performed. The embryos were anesthetized in 0.004% tricaine MS222 in a 2% agarose gel solution (life technologies, #16520050). One eye was surgically removed using a pulled capillary and mouth pipetting. Embryos were then transferred into fish medium (egg medium with penicillin/streptomycin (Life technologies, #15140122) and 0.003% 1-phenyl-2-thiouera (Sigma, #189235) until 5dpf, for while-mount immune-histochemistry.

Immunohistochemistry

cryosections

Lepisosteus oculatus embryos were fixed by immersion in 4% PFA in 0.12 M phosphate buffer (VWR, 28028.298 and 28015.294), pH 7.4 (PFA) o/n at 4°C.

Following three washes in 1XPBS, the samples were incubated in 10% sucrose (VWR, 27478.296) in 0.12 M phosphate buffer o/n at 4°C. The next day, samples were transferred to a 30% sucrose solution in 0.12 M phosphate buffer o/n at 4°C. Samples were then embedded in 0.12 M phosphate containing 7.5% gelatin (Sigma, 62500) and 10% sucrose, frozen in isopentane at -40°C and then cut at 16 µm with a cryostat (Leica, CM3050S). Sections were blocked in PBS containing 0.2% gelatin (VWR) and 0.25% Triton-X100 (PBS-GT) for 1 h at RT. Following the blocking, sections were incubated with primary antibodies (see Table S1) diluted in a PBS-GT solution o/n at RT. Following three washes in PBST (0.05% Trinton-X100) secondary antibodies coupled to the appropriate fluorophore (see Table S1) were diluted in PBS-GT and incubated for 2 h at RT. Sections were counterstained with Hoechst (Sigma, B2883, 1:1000). For PCNA staining, an antigen retrieval step was performed by boiling sections in a 1X Sodium Citrate solution pH 6.0 for 5 mins using a microwave. Slides were scanned with either a Nanozoomer (Hamamatsu) or laser scanning confocal microscope (Olympus, FV1000).

Whole-Mount Immunostaining

Zebrafish whole-mount immunohistochemistry was adapted from (*5*). Briefly, embryos were fixed in 4% PFA diluted in PBS containing 0.1% tween-20 (VWR, #0777-1L)(PBSTw) for 4h at RT and stored o/n in 100% methanol. After re-hydration, embryos were incubated for 20min in pre-chilled acetone (Sigma, #650501). The embryos were rinsed several times with PBSTw and blocked for 2h in blocking solution (10% bovine serum albumin (BSA)(Euromedex, #04-100-812-C) in PBSTw). The primary antibodies were incubated o/n at 4° in 1% BSA in PBSTw according to the dilutions in Table S1. After several washes in PBSTw, the secondary antibodies were incubated o/n at 4°. The next day, embryos were rinsed in PBSTw and processed for imaging.

Whole-mount immunostaining on *Lepisosteus oculatus* embryos was carried out as previously described (*6*). Briefly, embryos were de-pigmented in a solution of 11% H_2O_2 (VWR, 216763) at 70 rpm exposed to an 11W warm white Light-Emitting Diode (LED) (3000° Kelvin) for 1-3 days. Samples were then blocked and permeabilized before being incubated with the primary antibodies for 7 days at RT (see Table S1) in a solution containing: 0.5% Tirton-X100, 5% donkey normal serum, 20% Dimethyl Sulfoxide, 1XPBS, 0.1 g/L thimerosal. The samples were further labeled with secondary antibodies (see Table S1) for 2 days at RT under agitation.

Retinal flat-mounts

For retinal flat mounts, human eyes were harvested and fixed in 4%PFA, followed by three washes in 1XPBS. Eyes were then de-pigmented using the EyeDISCO protocol as previously described (*6*). For immunohistochemistry, retinas were permeabilized and blocked in a solution containing 0.5% Triton-X100, 5% donkey normal serum, 1XPBS, 0.1 g/L thimerosal for 1 day at RT under agitation. Primary antibodies (see Table S1) were diluted in a solution containing 0.5% Triton-X100, 5% donkey normal serum, 20% Dimethyl Sulfoxide, 1XPBS, 0.1 g/L thimerosal for 3 days at RT under agitation. The retinas were then washed for 1 day in PBST (1XPBS, 0.5% Triton-X100). The secondary antibodies (see Table S1) were diluted in the same solution as primary antibodies and left for 2 days. After washing retinas for 1 day, they were mounted on slides and imaged using a scanning confocal microscope (Olympus, FV1000).

Tracing of visual projections

All fish were anesthetized with 0,04% MS222, tricaine-methanesulfonate (Sigma, #E10521) diluted in fish water. Australian lungfish were anesthetized with 0.05% clove oil in fresh water. Injection of cholera toxin β subunit was carried out as described in

(*6*). Briefly, using a capillary approximately 1µl of 2 µg/µl of AlexaFluor-conjugated cholera toxin β subunit (Thermo Fischer, AlexaFluor555-CTb C22843 and AlexaFluor647-CTb C34778) was injected intravitreally. 72-96 h following CTb injection, specimens were transcardially perfused with 4%PFA and the heads and/or brains were dissected for tissue clearing.

Tissue clearing and imaging

Clearing

Prior to clearing, *Lepisosteus oculatus embryos* were embedded in 1.5% agarose (Roth) in 1X TAE (Life Technologies). Clearing was carried out as previously described (*6*). Briefly, samples were gently de-hydrated in ascending baths of methanol (1h30). Samples were further treated with a solution containing 2/3 Dichloromethane (DCM, Sigma) 1/3 methanol o/n. The next day, samples were placed in DCM for 30 min prior to being immersed in Di-benzyl Ether (DBE, Sigma).

Imaging

Acquisitions were performed by using an UltraMicroscope I (Miltenyi Biotec, Germany) or UltraMicroscope Blaze (Miltenyi Biotec, Germany) with the ImspectorPro software (Miltenyi Biotec, Germany, 5.1.328 version). The light sheet was generated by a laser (wavelength 488, 561, 647 Coherent Sapphire Laser, LaVision BioTec, Miltenyi Biotec, Germany) or a second generation laser beam combiner (wavelengths 488, 561, 647 Coherent Sapphire Laser, LaVision BioTec, Miltenyi Biotec, Germany. All light sheets were matched within their Rayleigh lengths for optimal illumination at the sample site. Either a binocular stereomicroscope (Olympus, MXV10) with a 2x objective (Olympus, MVPLAPO) was used Or a MI Plan 1.1x (NA=0.1), a MI Plan 4X (NA=0.35), and a MI Plan 12X (NA=0.53) objectives were used (Miltenyi Biotec, Germany). Samples were

placed in an imaging reservoir made of 100% quartz (LaVision BioTec, Miltenyi Biotec compagny) filled with DBE and illuminated from the side by the laser light. A Zyla sCMOS camera (Andor, Oxford Instrument, 2,048 × 2,048, 6.5 x 6.5 μm^2, peak QE 82%) was used to acquire images. The step size between each image was fixed at 1 or 2 µm (NA = 0.5, 150 ms time exposure). All tiff images are generated in 16-bit.

Confocal microscopy

Whole-mount 5dpf zebrafish were mounted in a labtex plates (LabTex) in 2.5% agarose. For imaging, a scanning inverted confocal microscope (Olympus, FV1200) was used with a 30X objective (Olympus, UPLSAPO30XS, NA = 1.05, WD = 0,8 mm)

Image Processing

3D rendering of light sheet and confocal stacks were converted to an Imaris file (.ims) using ImarisFileConverter (Bitplane, 9.5.1 version) and then visualized using the Imaris x64 software (Bitplane, 9.5.1). To quantifiy ipsi-lateral territories, entire tectum volume and ipsilateral projections were automatically segmented with a surface detail of 5.00 µm, automatic threshold. Volumes were extracted from the surface. Movies were generated using the animation tool on Imaris x64 software (Bitplane, version 9.1.2) and movie reconstruction with .tiff series were done using ImageJ (1.50e, Java 1.8.0_60, 64-bit). All movie editing (text and transitions) was done using iMovie (Apple Inc., version 10.1.1).

Statistical analyses

An observer blinded to the experimental conditions realized all the quantifications. All data are represented as mean values ± SEM. Statistical significance was estimated using two-tailed unpaired tests for non-parametric tendencies (Kruskall-Wallis or

Mann-Whitney), two-way ANOVA and Bonferroni's multiple comparison test. * = $p < 0.05$; ** = $p < 0.01$; *** = $p < 0.001$, *** = $p < 0.0001$. All statistical measurements were carried out using GraphPad Prism 7.

Supplementary Figures

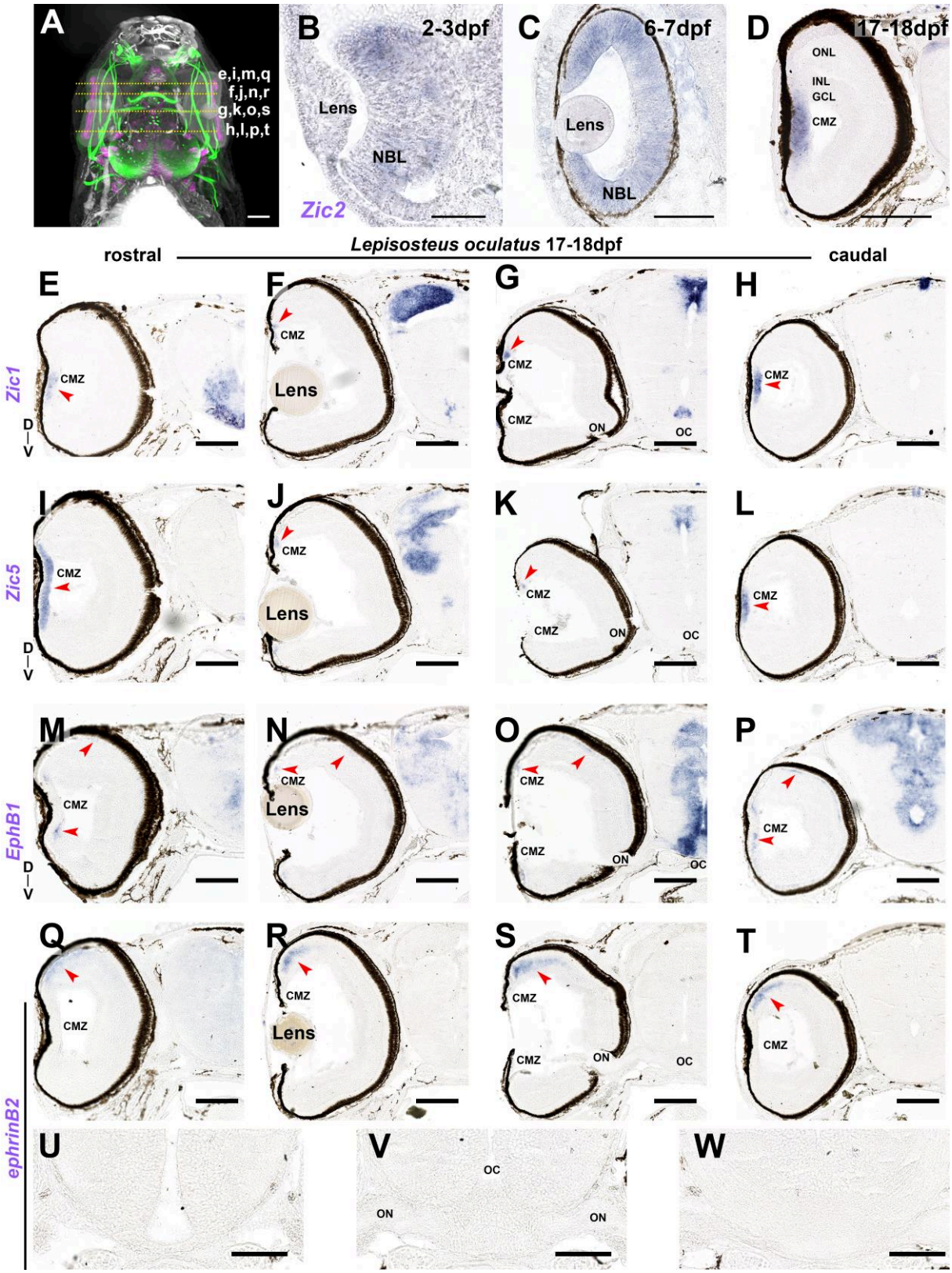

Fig. S1. Mammalian ipsilateral markers are not expressed in the spotted gar visual system.

A, 3D light-sheet fluorescence microscopy images of iDISCO-cleared 17-18dpf *Lepisosteus oculatus* highlighting anatomical regions corresponding to the identified cryosections. **B-D,** *In situ* hybridization for *zic2* on retinal cryosections of the developing *Lepisosteus oculatus* at 2-3dpf (**B**), 6-7dpf (**C**), 17-18dpf (**D**). Only proliferating cells express *zic2*. **E-T,** Rostral-to-caudal coronal cryosections from 17-18dpf *Lepisosteus oculatus*. **E-H, I-L,** *zic1* and *zic5* are only expressed in the ciliary marginal zone (CMZ; arrow). **M-P,** *EphB1* is absent from the retina and weakly expressed in the CMZ. **Q-T.** *ephrinB2* is expressed in the dorsal retina (arrow). **U-W**, are cryosections of the diencephalon of a 17-18dpf *Lepisosteus oculatus* hybridized for *ephrinB2. ephrinB2* is absent from the optic chiasm (asterisk). Immuno-reactive regions are highlighted (arrowhead). Abbreviations: NBL, Neuroblastic layer; ON, Optic nerve, OC, Optic chiasm; GCL, Ganglion cell layer; INL, Inner nuclear layer; ONL, Outer nuclear layer. Scale bars: **A**, 200 μm; **B**, 50 μm; **C,U-W**, 100 μm; **D-T,** 250 μm.

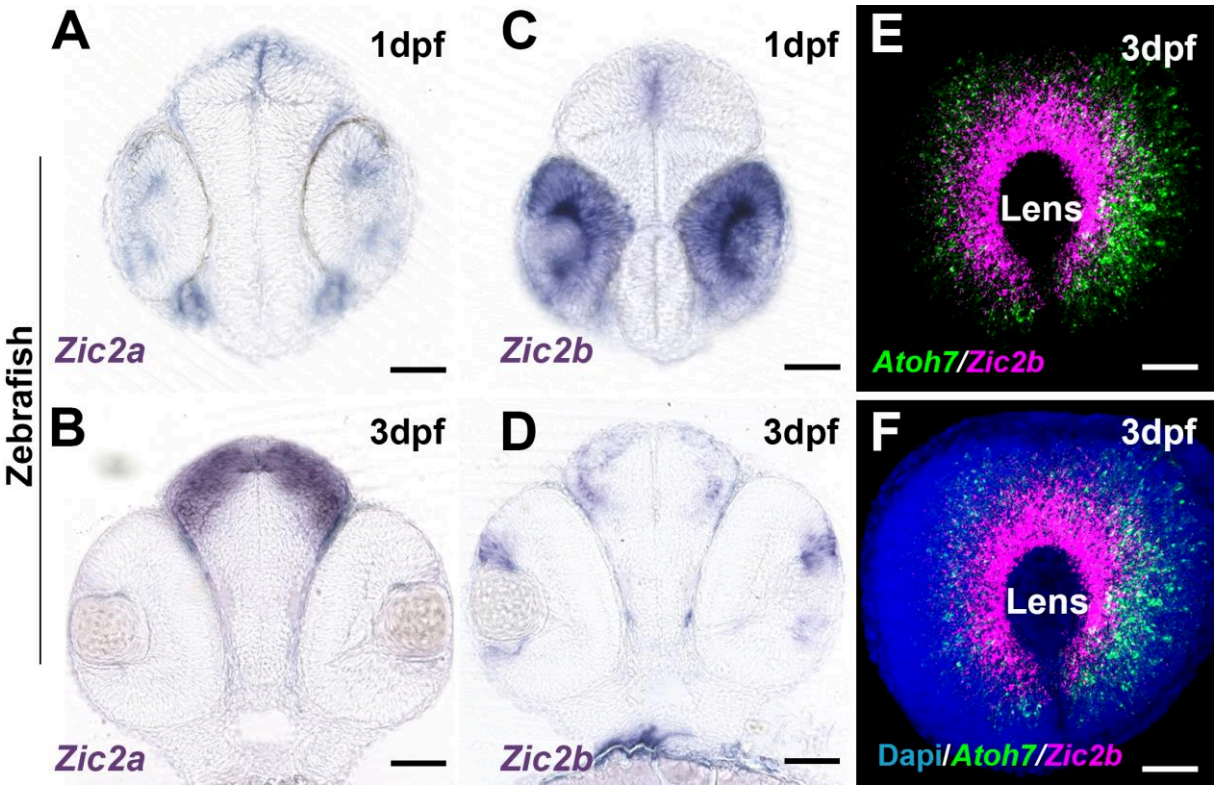

Fig. S2. Zic2 co-orthologs are restricted to the ciliary margin zone in *Danio rerio*. **A-D,** Whole-mount *in situ* hybridization of Zebrafish embryos for *zic2a* at 1dpf (**A**) and 3dpf (**B**) as well as *zic2b* at 1dpf (**C**) and 3dpf (**D**). **E,F,** Whole-mount Fluorescence *in situ* hybridization for *zic2b* and *atoh7* on 3dpf Zebrafish embryos. **F.** Delineates the retina using DAPI counterstaining. Abbreviations: D, dorsal ; V, ventral ; N, nasal ; T, temporal ; ON, optic nerve. Scale bars: **A-F,** 50 μm.

Table S1. Comprehensive table summarizing the antibodies and probes sequences.

In situ probes					
Name	**Sequence**			**Dilution**	**Immunohistochemistry**
L-Zic1 fwd	ACCTCCAGACATCACTCAAC			1:200	Cryosections
L-Zic1 rev	GGAACACTCTTCCCAGAAAC			1:200	Cryosections
L-Zic2 fwd	AAACTTAACCACGACCTCTCTC			1:200	Cryosections
L-Zic2 rev	CTCGTGCATTGTGCTGAAAG			1:200	Cryosections
L-Zic5 fwd	CTTTGAGCAAGAGGAATCCGGC			1:200	Cryosections
L-Zic5 rev	CCTGCCGCGATGTTCACATTTA			1:200	Cryosections
L-efnb2 fwd	TCCCCATTATGAGAAGGTGAGCGG			1:200	Cryosections
L-efnb2 rev	ACAGGCTACCACTTCAGAAGGCAG			1:200	Cryosections
L-EphB1 fwd	AGAACCTGAACACAATCCGCAC			1:200	Cryosections
L-EphB1 rev	ACAGTTTAATGGGCACGTCCAC			1:200	Cryosections
Zf-Zic2a fwd	ACAACAATCTGTCGCCTTCCTC			1:200	Cryosections
Zf-Zic2a rev	ACAAATGCCCCTGTTTAGCCC			1:200	Cryosections
Zf-Zic2b fwd	TCTTCCGCTACATGCGACAAC			1:200	Cryosections
Zf-Zic2b rev	GCAACACCGACATGCTGAGAAC			1:200	Cryosections
Primary antibodies					
Antigen	**Species**	**Catalog #**	**Company**	**Dilution**	**Immunohistochemistry**
Islet1	Rabbit	GTX128201	GeneTex	1:300	Cryosections/whole-mount
Acetylated-tubulin	Mouse	T6793	Sigma	1:300	Cryosections/whole-mount
PCNA	Mouse	P8825	Sigma	1:500	Cryosections
Islet1+2	Mouse	39D	DSHB	1:50	Cryosections
GFP	Chicken	GTX13970	GeneTex	1:5000	whole-mount
Rbpms	Guinea Pig	ABN1376	Millipore	1:400	Cryosections/flat-mount/ whole-mount
Zic2	Rabbit	Ab150404	Abcam	1:300	Cryosections/flat-mount/ whole-mount
Sox2	Goat	Sc17320	Santa-Cruz	1:300	flat-mount
Secondary antibodies					
Anti Rabbit cy3 mcr	Donkey	711-165-152	Jackson Immunoresearch	1:500	cryosections/whole-mount
Anti Rabbit Alexa 647 mcr	Donkey	711-605-152	Jackson Immunoresearch	1:500	cryosections/Flat-mount/whole-mount
Anti Goat Alexa 488	Donkey	A11055	Life Technologies	1:500	cryosections/Flat-mount/whole-mount
Anti Goat Alexa 555	Donkey	A21432	Life Technologies	1:500	cryosections/Flat-mount/whole-mount
Anti Goat cy3 mcr	Donkey	705-165-147	Jackson Immunoresearch	1:500	cryosections/Flat-mount/whole-mount
Anti mouse Alexa 488	Donkey	A21202	Life Technologies	1:500	cryosections/Flat-mount/whole-mount
Anti Guinea Pig Alexa cy3	Donkey	706-165-148	Jackson Immunoresearch	1:500	cryosections/Flat-mount/whole-mount
Anti mouse Alexa 647 mcr	Donkey	715-605-150	Jackson Immunoresearch	1:500	cryosections/Flat-mount/whole-mount
Tracers					

CTb-AlexaFluor555	n/a	C22843	Life technologies	2µg/µl	Whole-mount
CTb-AlexaFluor647	n/a	C34778	Life technologies	2µg/µl	Whole-mount

Captions for Supplementary Movies

Movie S1. Teleost fish only possess contra-lateral retinal projections.

Whole brain rendering of adult ostariophysans (zebrafish and Mexican tetra) and percomorphs (pufferfish and mudskipper) with bilateral injections of CTb coupled to either an Alexa-555 or and Alexa-647. Each species shows a complete decussation of retinal projections.

Movie S2. Bilateral projections exist in basal Actinopterygians.

Whole brain rendering of adult Butterflyfish (*Pantodon buchholzi*), spotted gar (*Lepisosteus oculatus*), sterlet sturgeon (*Acipenser ruthenus*), and armored bichir (*Polypetrus barbarous*), with bilateral injections of CTb coupled to either an Alexa-555 or and Alexa-647. A strong contingent of ipsilateral projections is seen in all species observed.

Movie S3. The Australian lungfish (Sarcopterygian) possesses non-segregated ipsilateral projections.

Whole brain rendering of visual projections in the Australian lungfish injected with either an Alexa-555 or an Alexa-647. Many ipsilateral projections are observed, with a major component in the optic tectum. Ipsialteral projections are inter,ingled with contralateral projections in the optic tectum.

Movie S4. ZIC2 expression is evolutionarily conserved in Humans.

Whole-mount immunohistochemistry of pcw9 human eyes using EyeDISCO clearing and labeled for the ipsilateral transcription factor Zic2 (magenta) and the pan-retinal ganglion cell marker RBPMS (green). A large Zic2-positive region can be seen in the temporal retina.

Movie S5. Development of the *Lepisosteus oculatus* visual system.

3D rendering of 2-3dpf, 6-7dpf, and 17-18dpf *Lepisosteus oculatus* embryos using EyeDISCO clearing and light-sheet fluorescence microscopy. *Lepisosteus oculatus* embryos were labeled with the pan-neuronal marker acetylated tubulin (a-tubulin, green) and the LIM/homeodomain family of transcription factor Islet1, which is critical for the proper specification of retinal ganglion cells and motor neurons (magenta).

References and Notes

1. I. Braasch *et al.*, Connectivity of vertebrate genomes: Paired-related homeobox (Prrx) genes in spotted gar, basal teleosts, and tetrapods. *Comp. Biochem. Physiol. Part C Toxicol. Pharmacol.* **163**, 24–36 (2014).
2. V. Marillat *et al.*, Spatiotemporal expression patterns of slit and robo genes in the rat brain. *J. Comp. Neurol.* **442**, 130–155 (2002).
3. C. Thisse, B. Thisse, High-resolution in situ hybridization to whole-mount zebrafish embryos. *Nat. Protoc.* **3**, 59–69 (2008).
4. V. Bercier *et al.*, Dynactin1 depletion leads to neuromuscular synapse instability and functional abnormalities. *Mol. Neurodegener.* **14**, 27 (2019).
5. D. Santos, S. M. Monteiro, A. Luzio, in *Methods in Molecular Biology* (Humana Press Inc., 2018; https://link-springer-com.proxy.insermbiblio.inist.fr/protocol/10.1007/978-1-4939-7883-0_19), vol. 1797, pp. 365–371.
6. R. J. Vigouroux, Q. Cesar, A. Chédotal, K. T. Nguyen-Ba-Charvet, Revisiting the role of Dcc in visual system development with a novel eye clearing method. *Elife*. **9**, e51275 (2020).

Chapter 2 : Revisiting the role of Dcc in visual system development with a novel eye clearing method

Robin J. Vigouroux, Quénol César, Alain Chédotal and Kim Nguyen-Ba-Charvet

Contribution: R. J. Vigouroux, K. Nguyen-Ba-charvet, and A. Chédotal designed the experiments, the figures and wrote the manuscript. R. J. Vigouroux carried out the experiments that make up Figures: 1 to 8 and Supplementary Figures: 1 to 11. Eye fundoscopy experiments as well as electroretinograms that make up Figure 8 C and D, Figure 8 Figure Supplementary 3, Figure 8 Figure Supplementary 4 A and C were carried out by Q. César.

eLIFE elifesciences.org

RESEARCH ARTICLE

Revisiting the role of Dcc in visual system development with a novel eye clearing method

Robin J Vigouroux, Quénol Cesar, Alain Chédotal*, Kim Tuyen Nguyen-Ba-Charvet*

Institut de la Vision, Sorbonne Université, INSERM, CNRS, Paris, France

Abstract The Deleted in Colorectal Carcinoma (Dcc) receptor plays a critical role in optic nerve development. Whilst Dcc is expressed postnatally in the eye, its function remains unknown as *Dcc* knockouts die at birth. To circumvent this drawback, we generated an eye-specific *Dcc* mutant. To study the organization of the retina and visual projections in these mice, we also established EyeDISCO, a novel tissue clearing protocol that removes melanin allowing 3D imaging of whole eyes and visual pathways. We show that in the absence of *Dcc*, some ganglion cell axons stalled at the optic disc, whereas others perforated the retina, separating photoreceptors from the retinal pigment epithelium. A subset of visual axons entered the CNS, but these projections are perturbed. Moreover, *Dcc*-deficient retinas displayed a massive postnatal loss of retinal ganglion cells and a large fraction of photoreceptors. Thus, Dcc is essential for the development and maintenance of the retina.

***For correspondence:**
alain.chedotal@inserm.fr (AC);
kim.charvet@inserm.fr (KTN-B-C)

Competing interests: The authors declare that no competing interests exist.

Funding: See page 24

Received: 22 August 2019
Accepted: 24 February 2020
Published: 25 February 2020

Reviewing editor: Carol A Mason, Columbia University, United States

© Copyright Vigouroux et al. This article is distributed under the terms of the Creative Commons Attribution License, which permits unrestricted use and redistribution provided that the original author and source are credited.

Introduction

Deleted in Colorectal Carcinoma (Dcc) is a transmembrane receptor discovered as a potential tumor suppressor (***Pierceall et al., 1994***). Dcc binds the extracellular matrix protein Netrin-1 (***Keino-Masu et al., 1996***; ***Serafini et al., 1994***). When bound to Netrin-1, Dcc activates downstream signaling partners such as MAP kinase, focal adhesion kinase (FAK) or Src kinases which ultimately influence cytoskeleton dynamics and cell motility (***Mehlen et al., 2011***; ***Ren et al., 2004***). However, Dcc is also a dependence receptor (***Mehlen et al., 2011***; ***Mehlen et al., 1998***) which triggers cell death in absence of Netrin-1 (***Llambi et al., 2005***; ***Mehlen et al., 2011***). Although direct evidence linking Dcc to tumorigenesis was obtained in mice (***Castets et al., 2012***; ***Krimpenfort et al., 2012***), mutations in *DCC* were also identified in patients suffering from rare neurodevelopmental disorders including congenital mirror movements (***Depienne et al., 2011***; ***Srour et al., 2010***) and corpus callosum dysgenesis (***Jamuar et al., 2017***; ***Marsh et al., 2017***).

Dcc is present in the developing central nervous system (CNS) and controls axon guidance and cell migration in the spinal cord, as well as in multiple brain areas (***Belle et al., 2014***; ***Fazeli et al., 1997***; ***Fothergill et al., 2014***; ***Laumonnerie et al., 2014***; ***Schmidt et al., 2014***; ***Srivatsa et al., 2014***; ***Yee et al., 1999***). Dcc expression persists in the postnatal and adult CNS where it is involved in synaptogenesis (***Horn et al., 2013***; ***Manitt et al., 2013***) and myelination (***Jarjour et al., 2008***). In vivo evidence supporting Dcc function in CNS development was primarily obtained using *Dcc* knockout (KO) mice (a null allele) which lack Dcc in all cells (***Fazeli et al., 1997***). One of the most striking phenotype, a hypoplasia of the optic nerve, was reported in the visual system (***Deiner et al., 1997***; ***Shi et al., 2010***). In *Dcc* KO embryos, a large fraction of the retinal ganglion cell (RGC) axons which connects the eye to the brain via the optic nerve is unable to exit the retina (***Deiner et al., 1997***). The presence of its ligand Netrin-1 at the optic disc, the exit point of the retina, together with the presence of hypoplasic optic nerves in *Ntn1* hypomorph mutant embryos suggested that Netrin-1

acts as a long range cue attracting Dcc-expressing RGC axons towards the optic nerve head (**Deiner et al., 1997**; **Shi et al., 2010**).

Dcc expression persists in RGC axons after they exit the retina and even postnatally (**Shi et al., 2010**) but as *Dcc* null mice die at birth (**Fazeli et al., 1997**), its function at later stages of visual system development is unknown. In *Xenopus laevis* tadpoles, Netrin-1 attracts RGC axons toward the optic disc (**Shewan et al., 2002**) and promotes RGC axon arborization and synapse formation within the tectum (**Manitt et al., 2009**). Importantly, recent studies using conditional knockout strategies have revisited the role of Netrin-1 in axon guidance at the CNS midline and suggested that Netrin-1 does not act as a long-range attractive cue for axons (**Dominici et al., 2017**; **Moreno-Bravo et al., 2019**; **Varadarajan et al., 2017**; **Wu et al., 2019**). Although the conditional ablation of *Dcc* in specific neuronal classes recapitulates the axon guidance defects found in *Dcc* KO embryos in some systems (**da Silva et al., 2018**; **Peng et al., 2018**; **Zelina et al., 2014**), there is also evidence for a non-cell autonomous role in cortical projection neurons (**Welniarz et al., 2017**). Here, we have generated eye-specific *Dcc* mutants which are fully viable. We found that these mutant mice display severe optic nerve hypoplasia as well as axon pathfinding defects in visual centers that persist postnatally. These defects are accompanied by a massive elimination of RGCs and the death of a large subset of photoreceptors. We also describe EyeDISCO, a novel tissue-clearing method allowing whole-eye immunostaining that could open novel perspectives in vision research.

Results

Dcc is broadly expressed in the developing retina

The presence of Dcc in RGCs had been previously shown (**Deiner et al., 1997**; **Shi et al., 2010**). Here, we first studied the temporal and spatial expression pattern of Dcc in the developing mouse retina using an antibody recognizing the C-terminal region of Dcc (**Mazelin et al., 2004**). The first Dcc-immunoreactive cells were detected at embryonic day 11 (E11) in the dorsal half of the retina and co-localized with the early RGC marker, Islet1 (**Figure 1A–B**; n = 3)(**Austin et al., 1995**). The specificity of the antibody was supported by the absence of staining in retinas from *Dcc* KO embryos (**Figure 1—figure supplement 1A–D**; n = 3). To get a better understanding of the spatial distribution of Dcc-expressing cells, we carried out whole-mount immunohistochemistry of Dcc and Islet1 at E11 followed by iDISCO+ clearing (**Renier et al., 2016**) and confocal microscopy for three-dimensional (3D) rendering. This confirmed that the early expression of Dcc at E11 is restricted to the medio-dorsal retina (**Figure 1C–D**; n = 4). By E12, Dcc expression expanded and still co-localized with Islet1-positive cells (**Figure 1E–H**; n = 3) but not with the transcription factor Sox2 (**Figure 1—figure supplement 1E–G**; n = 3), a retinal progenitor cell (RPC) marker (**Kamachi et al., 1998**). Thus, Dcc is only present in post-mitotic cells in the early retina. By E15, Dcc expression was broader and spanned both the apical and basal retina. Dcc-positive cells were either immunoreactive for Islet1 (**Figure 1I–L**; n = 3), or for Cone-rod homeobox protein Crx (Crx; **Figure 1—figure supplement 1H–J**; n = 3), which is expressed by post-mitotic photoreceptor cells.

A novel eye-specific Dcc mutant

Eyelid opening and retinal maturation in the mouse occur around the second postnatal week. As *Dcc* full knockout mice ($Dcc^{-/-}$) die a few hours following birth, whether Dcc could be involved in later stages of visual system development is unknown. To address this issue, we used mice driving the Cre-recombinase under the promoter of *Dickkopf-3* (*Dkk3*), a gene specifically expressed by RPCs (**Sato et al., 2007**). Crossing these *Cre* driver mice with mice carrying a *tdTomato* reporter, we found that the *Cre* was successfully driven in the retina (and not in other parts of the CNS) as early as E9 (n = 3) and with a complete retinal recombination by E10 (a time which precedes the onset of Dcc expression) (**Figure 2A–C**; n = 3). To ensure that Dcc protein was completely removed in the *Dkk3:cre;*$Dcc^{fl/fl}$ mice prior to optic nerve exit, we carried out a Dcc immunolabeling on E11 retinas. Dcc^{+} cells were found in $Dcc^{fl/fl}$ retinas, but not in *Dkk3:cre;*$Dcc^{fl/fl}$ retina (**Figure 2—figure supplement 1A–D**; n = 3 for each genotype).

We next questioned whether the retinal progenitor pool (expressing Ceh-10 homeodomain-containing homolog, Chx10, also known as visual system homeobox2, Vsx2) (**Liu et al., 1994**) as well as the generation of RGCs (Islet1) were maintained in *Dcc* mutants. At E12, no obvious defects were

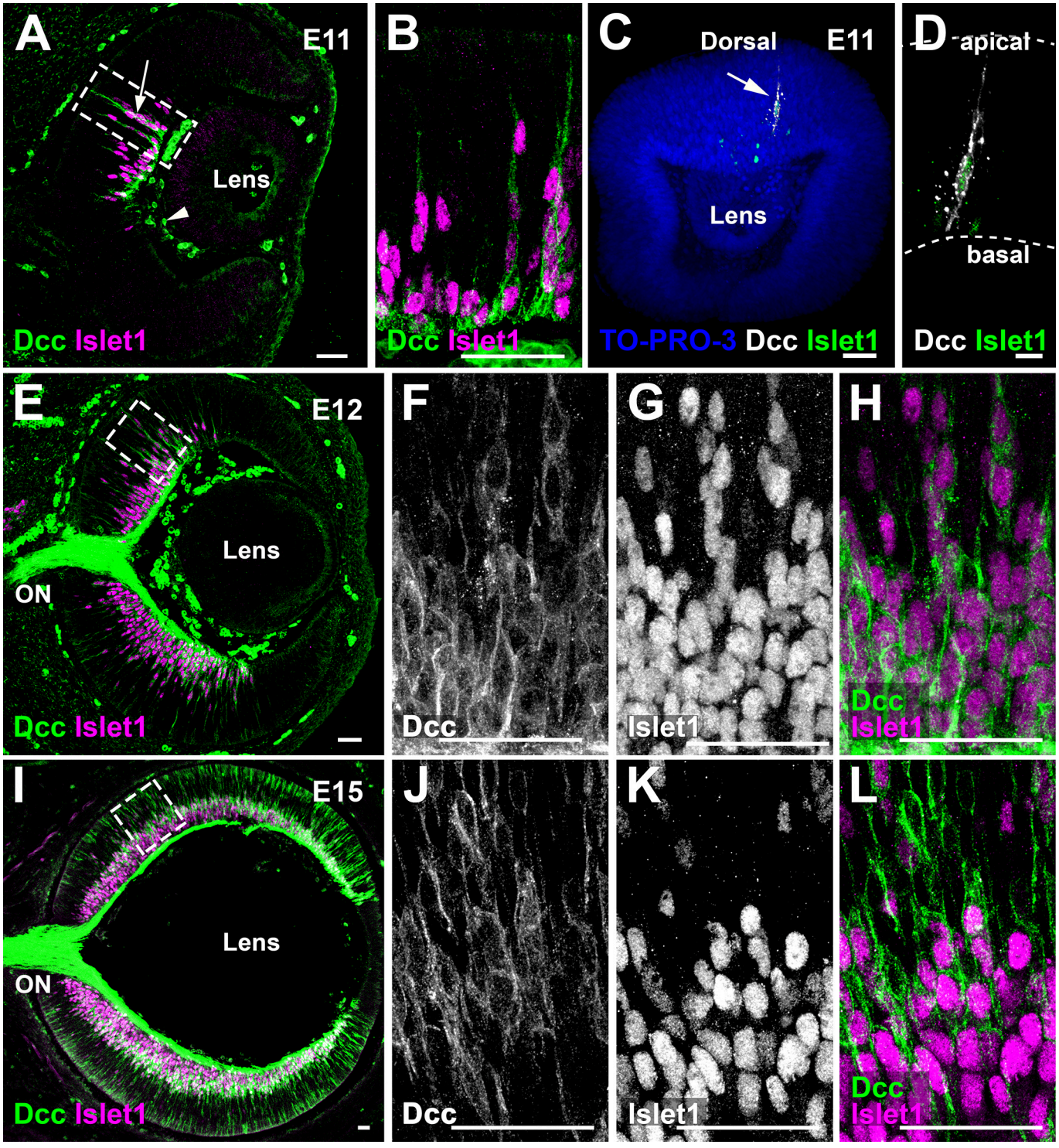

Figure 1. Dcc is broadly expressed in the mouse retina. (**A**) Immunohistochemistry (IHC) of Dcc (arrow, green) and the retinal ganglion cell marker Islet1 (magenta), at E11. Non-specific Dcc signal is seen in mesenchymal cells (arrowhead) (**B**) is a high magnification image. (**C,D**) Whole-mount IHC of an E11 eye for Dcc (white, arrow) and Islet1 (green) counterstained with the nuclear marker TO-PRO-3 (blue). (**E**) Dcc (green) and Islet1 (magenta) IHC at E12. (**F–H**) are high magnification images. (**I–L**) Dcc (green) and Islet1 (magenta) IHC at E15. Scale bars: (**A–H**) 50 µm, (**I,K**) 30 µm, (**J,L**) 10 µm. ON, Optic Nerve.

The online version of this article includes the following figure supplement(s) for figure 1:

Figure 1 continued on next page

Figure 1 continued

Figure supplement 1. Early Dcc expression is restricted to post-mitotic cells of the retina.

seen in mutants (n = 3) compared to $Dcc^{fl/fl}$ littermates (***Figure 2D–O***; n = 3). Furthermore, EdU incorporation showed no proliferation rate defects in progenitor cells (***Figure 2—figure supplement 1E–L***, ***Figure 2—source data 1***; n = 3).

Complexity of RGC guidance defects in Dcc KO revealed by a novel eye clearing method

Abnormal RGC projections towards the optic nerve head were previously reported in $Dcc^{-/-}$ embryos (***Deiner et al., 1997***) however, the long-term consequence of these defects on the retina are unknown and the exact spectrum of RGC projection defects have not been precisely studied. This is primarily due to the difficulty of inferring complex axon trajectories from simple retinal sections or retinal flat-mounts. In recent years, several tissue clearing protocols have been implemented to study the 3D cellular organization of complex organs such as the brain (***Klingberg et al., 2017***; ***Renier et al., 2016***; ***Richardson and Lichtman, 2015***; ***Tainaka et al., 2018***; ***Tomer et al., 2014***; ***Vigouroux et al., 2017***). However, these methods do not remove melanin from the layer of retinal pigment epithelium (RPE) cells which cover the retina (as early as E12), thereby blocking light. Therefore, successful eye clearing remains a burning issue in the field (***Susaki and Ueda, 2016***). The current solution to this problem is to dissect out the RPE but this does not maintain eye integrity. To solve this problem, we devised a novel tissue clearing protocol (see methods), EyeDISCO, that completely clears embryonic and adult mouse eyes (***Figure 3A–B'***).

Pioneer RGC axons, born at E11, extend their projections ventrally along the choroid fissure and into the presumptive optic disc (***Goldberg, 1977***; ***Silver, 1984***). To investigate whether *Dcc* deletion induced a defect in pioneer axon pathfinding, we carried out whole-mount immunostaining of Tag1 (Transient axonal glycoprotein 1, also known as Contactin 2) on E12 embryos followed by EyeDISCO clearing (***Figure 3A–B***). Tag1 is expressed by all sensory axons including RGC axons (***Chatzopoulou et al., 2008***). In $Dcc^{fl/fl}$ mice, $Tag1^{+}$ RGC projections extended ventrally towards the optic disc and into the optic nerve where they fasciculated (***Figure 3C–E***; n = 3). However, in *Dcc* cKO mice some RGC projections extended ventrally to the optic disc and stalled, forming thick RGC axon bundles (***Figure 3F–H***; n = 4). In addition, several RGCs misprojected and extended dorsally through the retina and into the sub-retinal space. Therefore, eye-specific deletion of *Dcc* leads to pioneer RGC projection defects.

To further assess RGC projections in *Dkk3:cre;*$Dcc^{fl/fl}$ mutant embryos, we carried out Tag1 immunostaining on whole E16 embryonic heads followed by EyeDISCO clearing (***Figure 4A–C***). Using manual segmentation (see methods) of the visual pathways (retina, optic nerve, optic chiasm, and optic tracts), we specifically isolated these structures from the rest of the head (***Figure 4D***). We next questioned whether RGC axon guidance defects in $Dcc^{-/-}$ embryos were phenocopied in *Dkk3:cre;*$Dcc^{fl/fl}$ embryos. In both $Dcc^{-/-}$ (n = 8 nerves) and *Dkk3:cre;*$Dcc^{fl/fl}$ mice (n = 6 nerves) there was a significant reduction in optic nerve volume compared to Wildtype mice (***Figure 4E–H***, ***Figure 4—source data 1***; n = 8 nerves). Heterozygous deletion of *Dcc* (*Dkk3:cre;*$Dcc^{lox/+}$) had no effect on optic nerve volume (n = 4 nerves).

We then investigated whether the optic nerve (ON) hypoplasia observed in *Dcc* mutant mice was a result of fewer RGCs projecting into the optic nerve head. Analysis of E16 *Dkk3:cre;*$Dcc^{fl/fl}$ mutant retinas immunolabeled for Tag1 showed that RGC projections exhibited multiple patterns. A subset of RGCs projected basally along the retinal lamina and into the optic nerve (***Figure 4G***; ***Figure 4—video 1***). Another subset extended apically into the sub-retinal space at many sites all along the eye (***Figure 4G***; ***Figure 4—video 1***). Interestingly, these projections separated the future photoreceptor cell outer segments from contacting with the RPE which is critical for their survival (***Figure 4I–L***; ***Strauss, 2005***). Analysis of retinal cryosections at P7 showed that aberrant RGC axons, expressing ßIII-tubulin, separated the photoreceptor outer segments from the RPE (***Figure 4—figure supplement 1A–D***). Of note, these abnormal projections either stalled in the sub-retinal space or joined the optic nerve. Importantly, manual segmentation showed that although these projections exited at

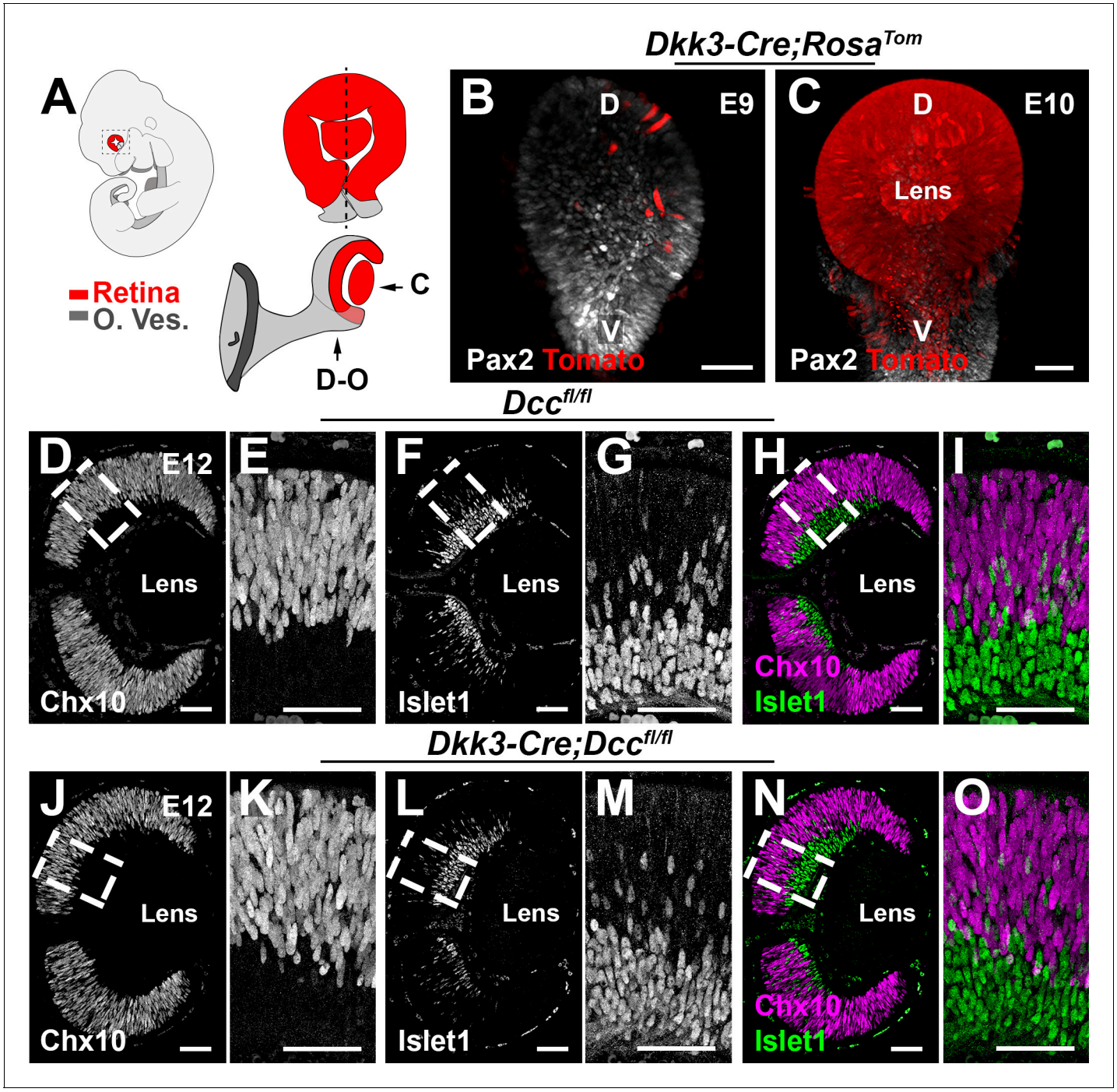

Figure 2. Retina-specific inactivation of Dcc. (**A**) Schematic representation of an E10 embryo (upper left) showing the neural retina (red) and the optic vesicle (gray). (**B,C**) Lateral views of the eye from *Dkk3:cre;Rosa*^{Tom} E9 and E10 embryos after whole-mount labeling for dsRed (Rosa tomato) and Pax2 (optic vesicle). (**C**) Represents the whole-mount lateral visualization, whereas (**D–O**) shows the orientation of the sagittal cryosections. (**D–O**) Cryosections of E12 *Dcc*$^{fl/fl}$ and *Dkk3:cre;Dcc*$^{fl/fl}$ embryos labeled for Chx10 (magenta) and Islet1 (green). Scale bars: (**B,C**) 30 µm, (**D–O**) 50 µm. D, dorsal; V, ventral; O. Ves, optic vesicle.

The online version of this article includes the following source data and figure supplement(s) for figure 2:

Source data 1. Eye-specific loss of Dcc does not impact the proliferation of retinal progenitor cells.

Figure supplement 1. *Dcc* deletion does not impact early retinal proliferation.

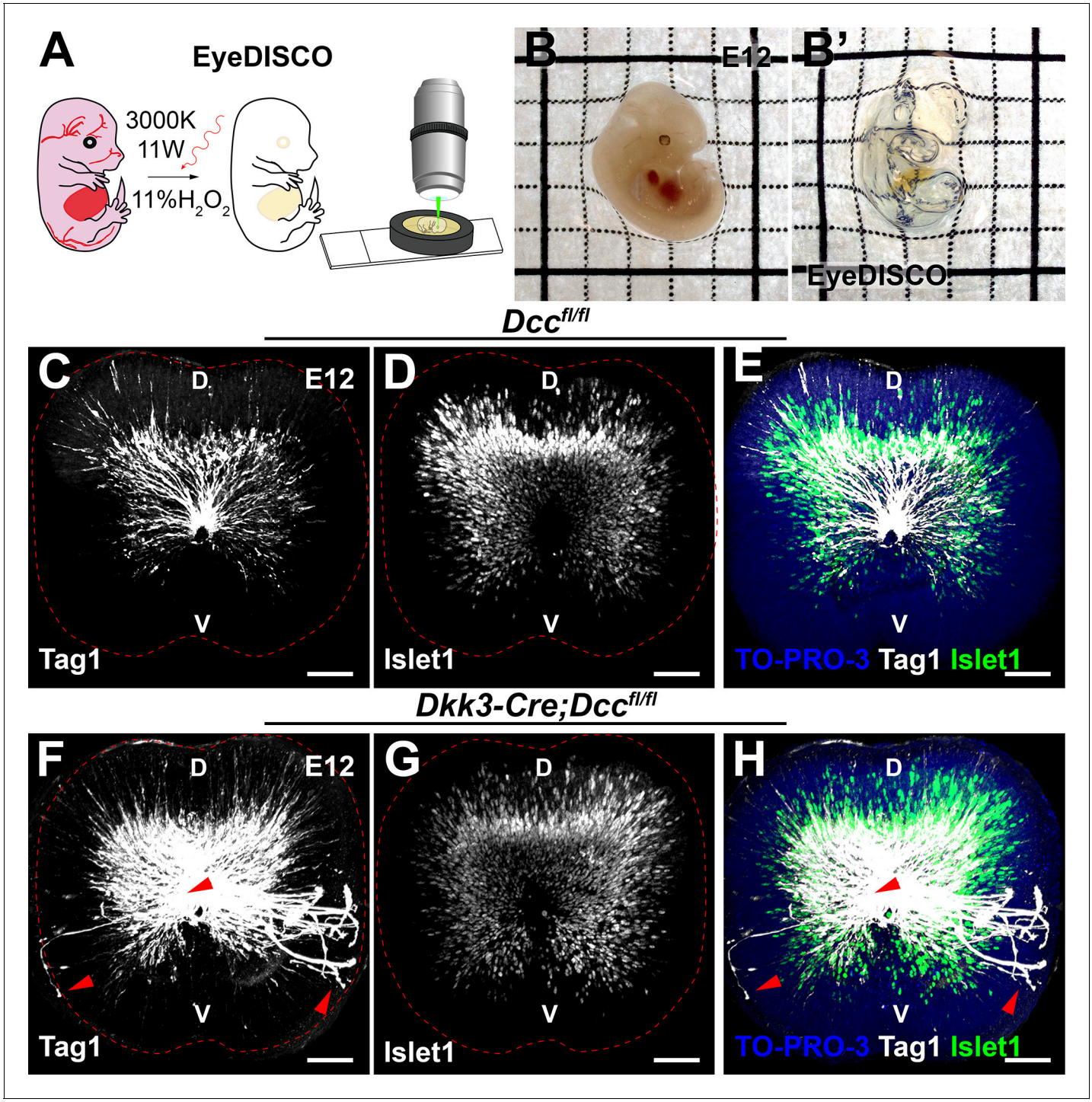

Figure 3. EyeDISCO, a novel tissue clearing protocol for embryonic eye visualization. (**A**) Schematic representation of the EyeDISCO protocol. The embryo is dehydrated in methanol and incubated in an 11% H_2O_2 solution irradiated with a 3000 ˚K warm white light. The sample is then included in a homemade chamber for confocal microscopy and 3D rendering. (**B,B'**) Images of an E12 embryo before and after EyeDISCO clearing. (**C–H**) Lateral view of whole-mount E12 eyes immunolabeled for the RGC axon marker, Tag1 (white) and the RGC nuclear marker (Islet1) counterstained with the nuclear marker TO-PRO-3 (blue). Several axons misproject in the *Dkk3:cre;Dcc*$^{fl/fl}$ mutants (red arrowheads) or are stalled at the optic disc. Scale bars: (**C–H**) 50 µm. D, dorsal ; V, ventral.

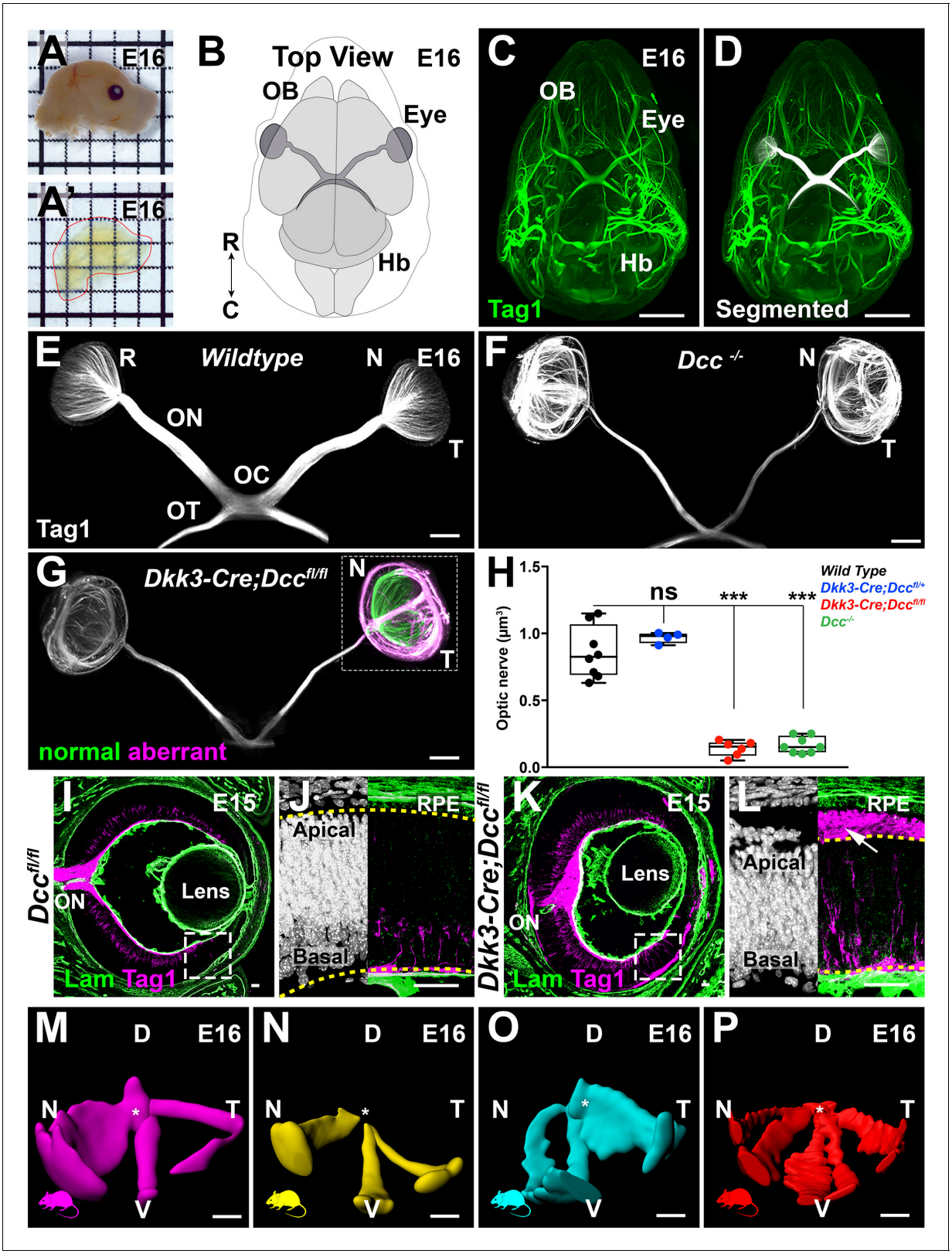

Figure 4. Early Dcc deletion leads to major intra-retinal axonal misprojections. (**A–A'**) Illustrates the clearing efficiency of the EyeDISCO protocol of an E16 mouse head. (**B**) Schematic representation of a top view of an E16 head, OB: olfactory bulb, Hb: hindbrain, R: rostral, C: caudal. (**C–G**) IHC whole-mount of E16 heads labeled for Tag1 (green). (**D**) E16 embryo head labeled with Tag1 in (**C**) with the visual projections manually segmented (white). (**E–G**) Segmented visual projections in E16 Wildtype, *Dcc*$^{-/-}$, and *Dkk3:cre;Dcc*$^{fl/fl}$ embryos. R: retina, ON: optic nerve, OC: optic chiasm, OT: optic tract, N:

Figure 4 continued on next page

Figure 4 continued

nasal, T: temporal. (**H**) Quantification of optic nerve volumes (μm^3) represented as a box plot, whiskers represent min to max values. *Dcc*$^{-/-}$ (0.165 ± 0.022 μm^3; n = 8 nerves) and *Dkk3:cre;Dcc*$^{fl/fl}$ embryos (0.140 ± 0.23 μm^3; n = 6 nerves) displayed a significant reduction in optic nerve volume compared to Wildtype embryos (0.858 ± 0.07 μm^3; n = 8 nerves) (p=0.0002 and p=0.0007 respectively, Mann-Whitney test). Heterozygous deletion of *Dcc* (*Dkk3:cre;Dcc*$^{lox/+}$) had no effect on optic nerve volume (0.97 ± 0.02 μm^3; p=0.2828; n = 4 nerves, Mann-Whitney test). Results were considered non-significant (ns) when p>0.05. ***=p < 0.001. (**I,J,K,L**) Cryosections of E15 *Dcc*$^{fl/fl}$ and *Dkk3:cre;Dcc*$^{fl/fl}$ eyes immunolabeled for Laminin (green) and Tag1 (magenta). (**I**) In controls, RGC projections (magenta) grow circumferentially and enter the optic nerve. (**K**) In *Dkk3:cre;Dcc*$^{fl/fl}$ embryos, RGC projections perforate the retina and stall at the optic disc, some projections manage to exit into the ON. (**J,L**) High magnification images. (**L**) In *Dkk3:cre;Dcc*$^{fl/fl}$ embryos, RGC projections extend apically and invade the sub-retinal space (arrow), separating the RPE and the apical retina (future photoreceptor outer segments). (**M–P**) Individual masks of aberrantly projecting RGCs across different mutants. Asterisks show the optic nerve. D, Dorsal; V, Ventral; N, Nasal; T, Temporal. Scale bars: (**C,D**) 1000 µm, (**E–G**) 300 µm, (**I–P**) 150 µm.

The online version of this article includes the following video, source data, and figure supplement(s) for figure 4:

Source data 1. Retina-specific deletion of Dcc leads to a significant reduction in optic nerve volume.
Source data 2. Early Netrin-1 deletion in the retina leads to a significant reduction in optic nerve volume.
Figure supplement 1. Eye-specific deletion of Dcc and Netrin-1 leads to major retinal defects.
Figure 4—video 1. Embryonic RGC projections are perturbed in *Dcc cKO* mice.
https://elifesciences.org/articles/51275#fig4video1

multiple sites, they fasciculated and formed major bundles that spanned the medial and ventral retina (***Figure 4M–P***; n = 4).

To determine whether the RGC axon phenotype observed in *Dcc* cKO mice was dependent on Netrin-1 signaling, we generated an eye-specific conditional deletion of *Netrin-1* (*Dkk3;cre;Ntn1*$^{fl/fl}$). At E16, we observed a significant reduction in optic nerve volume in *Ntn1* null mice (*Ntn1*$^{-/-}$) (***Moreno-Bravo et al., 2018***) (n = 9; ***Figure 4—figure supplement 1F,H***; ***Figure 4—source data 2***). Likewise, E16, *Dkk3;cre;Ntn1*^{flfl} embryos displayed a major reduction in optic nerve volume (n = 5) (***Figure 4—figure supplement 1G,H***; ***Figure 4—source data 2***).

Altogether, eye-specific deletion of *Dcc* prompted early RGCs to misproject apically through the retina. Furthermore, eye-specific deletion of Netrin-1 phenocopied the defect observed in *Dcc* cKO mice.

Retinal projections in the brain are altered in eye-specific Dcc mutants

The observation that a significant proportion of RGCs were still able to project their axons into the optic nerve in the absence of Dcc prompted us to study their projections within the brain. Mouse RGCs connect to at least 40 different brain nuclei (***Morin and Studholme, 2014***). To get the most comprehensive and faithful image of visual projections we used axonal tracers and iDISCO+ whole-brain clearing (***Renier et al., 2016***). Mice were injected intravitreally with AlexaFluor-555 or Alexa-Fluor-647-conjugated cholera toxin β-subunit (CTB) (see methods) allowing to distinguish ipsi- and contra-laterally projecting RGCs. iDISCO+ cleared brains were imaged using light sheet fluorescence microscopy (LSFM) (***Figure 5A,B***, ***Figure 5—video 1***).

We first focused on the primary visual system which consists of the optic nerve, optic chiasm, optic tract, lateral geniculate nuclei, and the superior colliculus. In order to quantify differences, we carried out automatic segmentation of CTB-stained nuclei using Imaris software (see materials and methods). From this segmentation we generated surfaces with Imaris that retraced RGC projections in each visual system nuclei (***Figure 5C***). Volume of each surfaces were extracted in μm^3 and quantified to analyze main differences. Analysis of *Dkk3:cre;Dcc*$^{fl/fl}$ mutant brains showed that despite some heterogeneity between the amount of reduction between eyes, optic nerve volumes were dramatically reduced by about half at P15 and 1 month (***Figure 5D,E,F***; ***Figure 5—source data 1***; n = 4 for *Dcc* cKO; n = 5 for *Dcc*$^{fl/fl}$). In addition, optic tract volumes were significantly reduced at P15 (n = 5) and 1 month (***Figure 5G***; ***Figure 5—source data 1***; n = 5 for *Dcc* cKO; n = 7 for *Dcc*$^{fl/fl}$). Thus, early RGC projection defects and RGC death translate to a major reduction in fiber volume projecting into the visual nuclei postnatally.

During RGC projections refinement, which occurs between P5 and P15 in mice, ipsilaterally projecting RGCs segregate to form a robustly stereotypic L-shaped rostral patch in the superior colliculus (***Godement et al., 1984***). We found that at 1 month, the ipsilateral patch represented ~5% (n = 5) of each superior colliculus in *Dcc*$^{fl/fl}$ mice. Interestingly, there was a significant expansion of

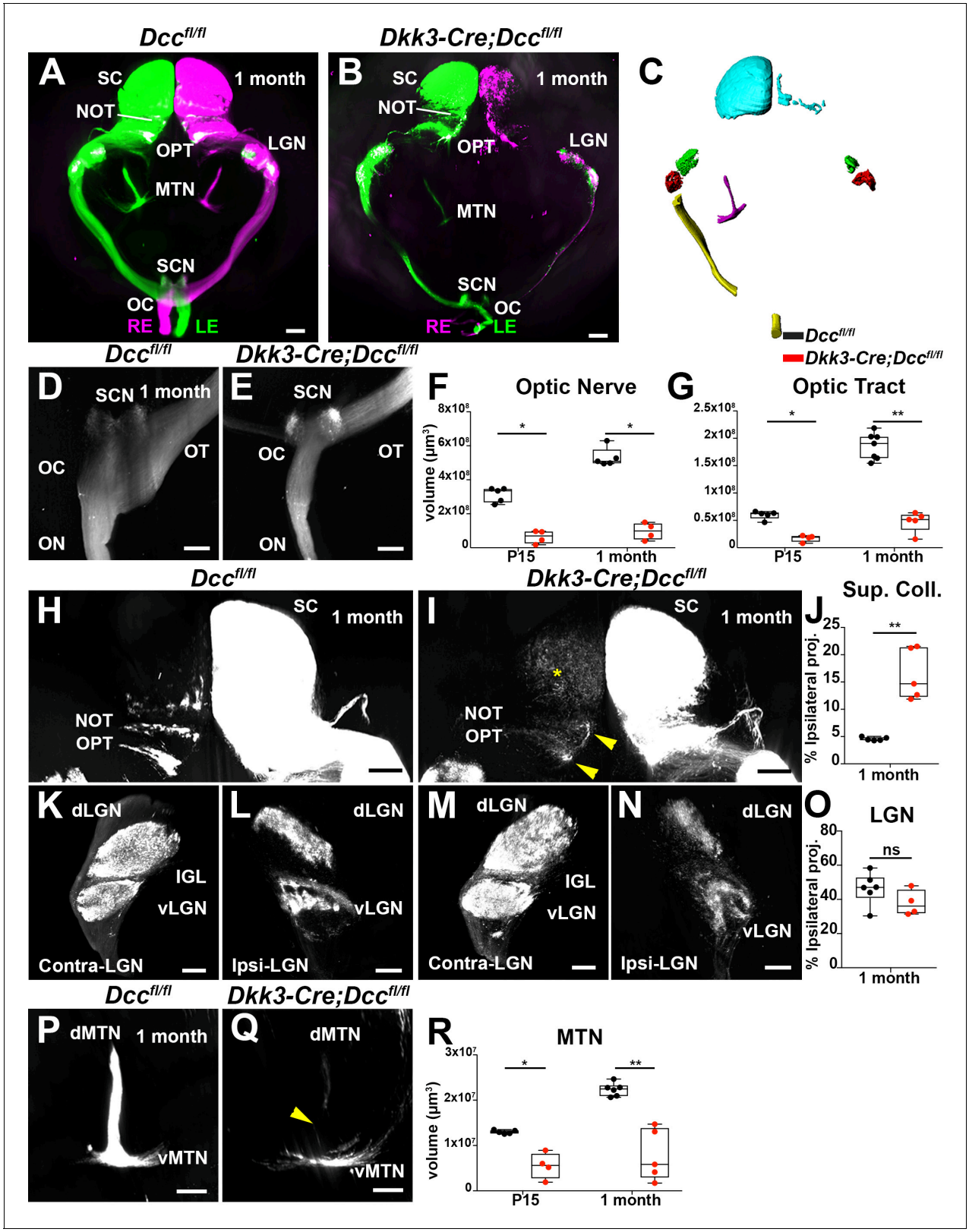

Figure 5. Retinal projections in the brain are altered in eye-specific *Dcc* mutants. (**A**,**B**) Frontal view of 3D-rendered brains using after anterograde axon tracing of visual projections with AlexaFluor-555 and/or AlexaFluor-647-conjugated cholera toxin β subunit (CTB). RE: right eye, LE: left eye, OC: optic chiasm, SCN: supra chiasmatic nucleus, MTN: medial terminal nucleus, LGN: lateral geniculate nucleus, NOT: nucleus of the optic tract, OPT: olivary pretectal nucleus, SC: superior colliculus. (**A**) Control brain, and (**B**) a *Dkk3:cre;Dcc*$^{fl/fl}$ brain. (**C**) Surfaces of manual and automatic segmentation of visual

Figure 5 continued on next page

Figure 5 continued

projections using Imaris software in a control brain. Superior colliculus (cyan), dorsal lateral geniculate nucleus (green), ventral lateral geniculate nucleus (red), medial terminal nucleus (magenta), optic nerve and optic tract (yellow). (**D,E**) Top view of the optic nerve, optic chiasm, and optic tract. (**F**) Quantification of optic nerve volumes at P15 ($6.36 \times 10^6 \pm 1.92 \times 10^6$ µm^3; n = 4; compared to $3.12 \times 10^7 \pm 1.92 \times 10^6$ µm^3; n = 5; p=0.0159) and 1 month ($9.67 \times 10^6 \pm 2.48 \times 10^6$ µm^3; n = 4; compared to $5.32 \times 10^7 \pm 2.51 \times 10^6$ µm^3; n = 5; p=0.0159). A Mann-Whitney test was used to measure the significance. (**G**) Quantification of optic tract volumes (µm^3) at P15 ($1.73 \times 10^7 \pm 3.13 \times 10^6$ µm^3; n = 4; compared to $5.97 \times 10^7 \pm 3.42 \times 10^6$ µm^3; n = 5; p=0,0159) and 1 month ($4.76 \times 10^7 \pm 8.37 \times 10^6$ µm^3; n = 5; compared to $1.86 \times 10^8 \pm 9.11 \times 10^6$ µm^3; n = 7; p=0.0025). A Mann-Whitney test was used to measure the significance. (**H,I**) Top view of the superior colliculus. *Dcc* cKO mice display a defasciculated NOT and OPT (yellow arrowhead), as well as an aberrant segregation of ipsilateral RGC projections (yellow asterisk). (**J**) Percentage of ipsilateral projections normalized to the contralateral projections (volume, µm^3) of the superior colliculus. At 1 month, ipsilateral superior colliculus volume represented 4.565 ± 0.1424% (n = 5) in *Dcc*$^{fl/fl}$ mice compared to 16.39 ± 2.091% in *Dkk3:cre;Dcc*$^{fl/fl}$ mice (p=0.0079, n = 5). A Mann-Whitney test was used to measure the significance. (**K–N**) Frontal view of the contra- and ipsi-lateral geniculate nucleus. dLGN: dorsal lateral geniculate nucleus, vLGN: ventral lateral geniculate nucleus, IGL: inner geniculate leaflet. (**F,K**) Ipsilateral lateral geniculate nucleus. (**O**) Percentage of ipsilateral projections normalized to the contralateral projections (volume, µm^3) of the lateral geniculate nucleus were not altered in *Dcc cKO* mice (37.89 ± 3.751%; n = 4) compared to control littermates (46.36 ± 3.795%; n = 6; p=0.352) A Mann-Whitney test was used to measure the significance. (**P,Q**) Frontal view of the medial terminal nucleus, dMTN: dorsal medial terminal nucleus, vMTN: ventral medial terminal nucleus. *Dcc* cKO mice show disturbed projections between the dMTN and the vMTN (yellow arrowhead). (**R**) Quantification of medial terminal nucleus volumes (ventral and dorsal, µm^3). At P15, *Dcc* cKO mice display a reduction ($5.51 \times 10^6 \pm 1.44 \times 10^6$ µm^3; n = 4) compared to control ($1.23 \times 10^7 \pm 1.79 \times 10^5$ µm^3; n = 5; p=0.0159). At 1 month, this loss was maintained ($7.89 \times 10^6 \pm 2.55 \times 10^6$ µm^3; n = 5; compared to $2.24 \times 10^7 \pm 5.95 \times 10^5$ µm^3; n = 6; p=0.0043). A Mann-Whitney test was used to measure the significance. Whiskers represent min to max values. *=p < 0.05, **=p < 0.01. Scale bars: (**A,B**) 1000 µm, (**H,I**) 500 µm, (**D,E,K,L,M,N, P,Q**) 300 µm.

The online version of this article includes the following video and source data for figure 5:

Source data 1. *Dcc* cKO mice show a significant reduction of RGC projection volumes in multiple brain visual nuclei.
Figure 5—video 1. Adult RGC projections display major defects in eye-specific *Dcc* deletion.
https://elifesciences.org/articles/51275#fig5video1

this ipsilateral territory to ~16% in *Dkk3:cre;Dcc*$^{fl/fl}$ mice (***Figure 5H,I,J***; ***Figure 5—source data 1***; n = 5). On the other hand, analysis of projections within the lateral geniculate nucleus (ventral and dorsal) did not show an expansion in ipsilateral territory (***Figure 5K–O***; ***Figure 5—source data 1***).

To date, very little is known about the development of the Accessory Optic System (AOS) (***Osterhout et al., 2015***; ***Sun et al., 2015***). We therefore wondered whether deletion of *Dcc* in RGCs could also lead to AOS defects. The most striking effect in *Dcc* cKO mice was observed in the medial terminal nucleus (MTN), which can be subdivided into a ventral (vMTN) and dorsal (dMTN) nucleus (***Lilley et al., 2019***). In *Dcc* mutant mice, RGCs targeted appropriately the vMTN and some RGCs also projected to the dMTN. Projections connecting the vMTN to dMTN were completely absent (***Figure 5P,Q***). In P15 *Dcc* cKO mice, MTN volume was significantly reduced (n = 4) compared to *Dcc*$^{fl/fl}$ mice (***Figure 5R***; ***Figure 5—source data 1***; n = 5). This effect was maintained at 1 month in *Dcc* cKO mice (n = 5) compared to control littermates (***Figure 5R***; ***Figure 5—source data 1***; n = 6). *Dkk3:cre;Dcc*$^{fl/fl}$ mice also displayed defects in other AOS nuclei such as the nucleus of the optic tract (NOT) and the olivary pretectal tract (OPT). Their projections appeared defasciculated (***Figure 5H,I***). Taken together, eye-specific *Dcc* deletion perturbs RGC axon targeting in the main and accessory visual systems.

Dcc intracellular signaling is required for retinal projection targeting in the brain

Dcc has been shown to act as a co-receptor to other guidance receptors (***Corset et al., 2000***; ***Hong et al., 1999***; ***Ly et al., 2008***) suggesting that the observed defect might not directly, or solely, involve Netrin-1/Dcc signaling. To address this question, we studied the visual system of *Dcc*^{Kanga} mice, which bear a mutation in the exon encoding for the intracellular P3 domain of Dcc (***Finger et al., 2002***). This domain is critical for Dcc signaling downstream of Netrin-1 (***Zhang et al., 2018***). As previously described, we were unable to obtain viable *Dcc*$^{kanga/kanga}$ mice (***Welniarz et al., 2017***). Thus, heterozygous Dcc kanga mutants (*Dcc*$^{kanga/+}$) were crossed with *Dcc* knockout animals (*Dcc*$^{+/-}$) to generate *Dcc*$^{kanga/-}$ mutants that possess one *Dcc* allele with the Kanga mutation and one null allele.

Dcc^{kanga} mice were injected with the CTB tracer and adult brains were cleared and imaged using LSFM for 3D rendering (***Figure 6***; ***Figure 6—video 1***). In *Dcckanga*$^{kanga/-}$ mice (n = 9), the optic nerve volume was significantly reduced compared to *Dcc*$^{kanga/+}$ mice (***Figure 6A–C***; ***Figure 6—***

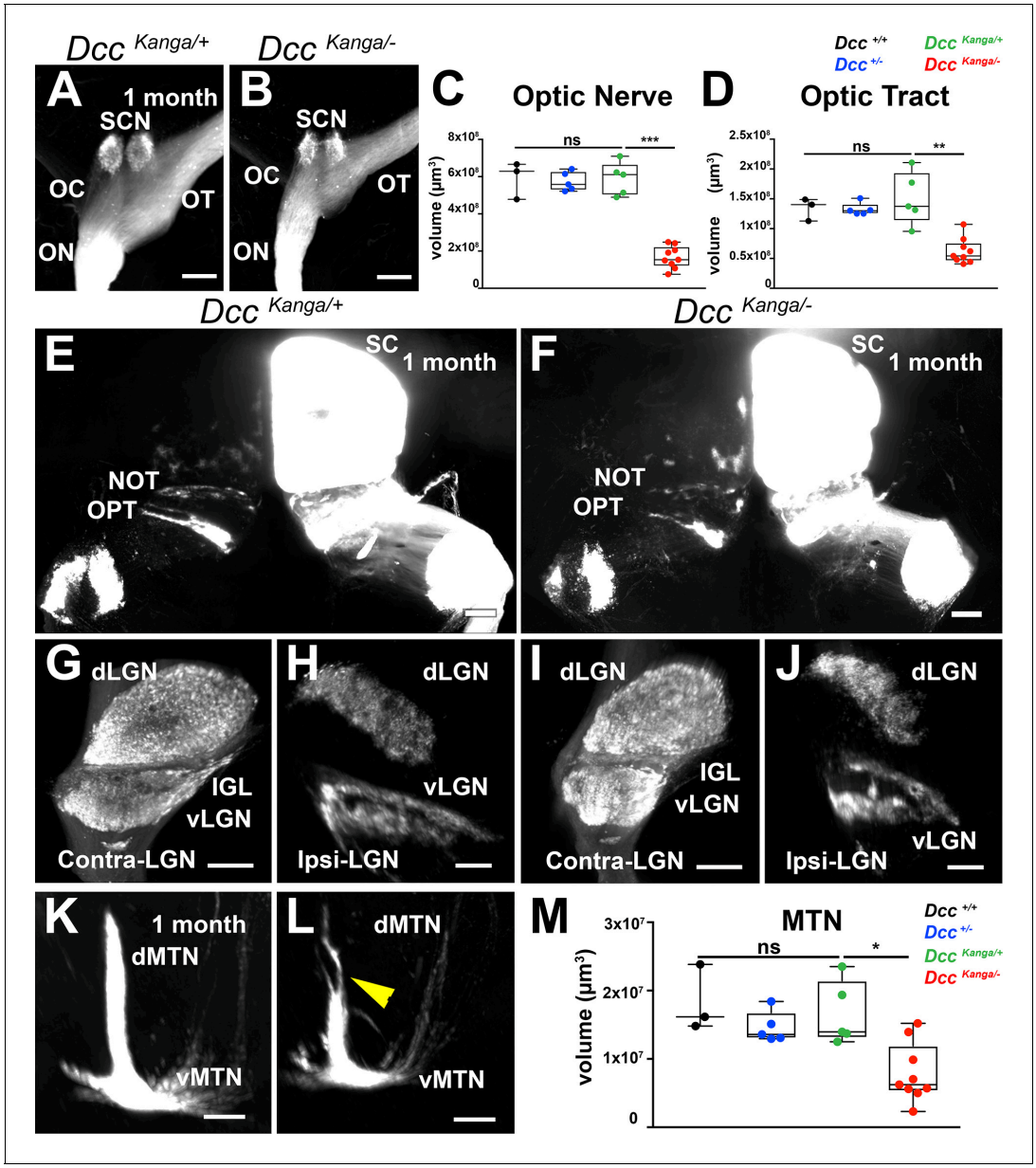

Figure 6. *Dcc* signaling is required for RGC projection targeting. (**A–M**) Whole-brain 3D rendering of RGC projections traced using AlexaFluor555-CTB or AlexaFluor647-CTB. (**A,B**) Top view of the optic nerve, optic chiasm, and optic tract of 1 month-old $Dcc^{kanga/+}$ and $Dcc^{kanga/-}$ mice. OC, optic chiasm; SCN, suprachiasmatic nucleus; OT, optic tract. (**C**) Quantification of optic nerve volume (µm^3) in $Dcckanga^{kanga/-}$ mice ($1.67 \times 10^7 \pm 1.97 \times 10^6$ µm^3; n = 9) were significantly reduced compared to $Dcc^{kanga/+}$ mice ($5.89 \times 10^7 \pm 3.98 \times 10^6$ µm^3; n = 5; p=0.0010, Mann-Whitney test). (**D**) Optic tract volume (µm^3) of $Dcckanga^{kanga/-}$ mice were also significantly reduced ($0.624 \times 10^8 \pm 7.09 \times 10^6$ µm^3; n = 9) compared to $Dcc^{kanga/+}$ mice ($1.50 \times 10^8 \pm 1.99 \times 10^6$ µm^3; n = 5; p=0.0020, Mann-Whitney test). (**E, F**) Top view of the superior colliculus. NOT, nucleus of the optic tract; OPT, olivary pretectal nucleus; SC, superior colliculus. (**G,H,I,J**) Frontal view of the contra-lateral LGN. dLGN, dorsal lateral geniculate nucleus; vLGN, ventral lateral geniculate nucleus; IGL, inner geniculate leaflet. (**K,L**) Frontal view of the MTN. dMTN, dorsal medial terminal nucleus; vMTN, ventral medial terminal nucleus. (**M**) Quantification of MTN volume (µm^3) of $Dcckanga^{kanga/-}$ mice ($0.788 \times 10^7 \pm 1.43 \times 10^6$ µm^3; n = 9) compared to $Dcc^{kanga/+}$ littermate controls ($1.66 \times 10^7 \pm 2.09 \times 10^6$ µm^3; n = 5; p=0.0190, Mann-Whitney test). Results were considered non-significant (ns) if p>0.05. *=p < 0.05; **=p < 0.01; ***=p < 0.001. Scale bars: (**A,B**) 150 µm (**E,F**) 300 µm, (**G,H,I,J, K, L**) 200 µm.

The online version of this article includes the following video, source data, and figure supplement(s) for figure 6:

Source data 1. Dcc Kanga mice display a major reduction of RGC projections in multiple brain visual nuclei.
Source data 2. Dcc kanga mice show a similar reduction in visual nuclei volumes compared to *Dcc* cKO mice.
Figure supplement 1. The reduction in retinal projections observed in *Dcc* cKO mice is phenocopied in Dcc^{kanga} mutant mice.
Figure 6—video 1. Dcc signaling is required for RGC projections to the MTN.
https://elifesciences.org/articles/51275#fig6video1

source data 1; n = 5). The optic tract volume was also significantly reduced (n = 9) in *Dcckanga*$^{kanga/-}$ mice compared to *Dcc*$^{kanga/+}$ mice (*Figure 6D*; *Figure 6—source data 1*; n = 5). Of note, no significant differences in optic nerve or optic tract volumes were observed between *Dcc*$^{+/+}$, *Dcc*$^{+/-}$, and *Dcc*$^{kanga/+}$ (*Figure 6C,D*; *Figure 6—source data 1*). Interestingly, comparisons between Dcc^{Kanga} mice and *Dcc* cKO mice showed no significant differences in optic nerve and optic tract volume (*Figure 6—figure supplement 1A,B*; *Figure 6—source data 2*). We next assessed whether projections within the superior colliculus were disturbed in *Dcckanga*$^{kanga/-}$ mice. Unlike in *Dkk3:cre;Dcc*$^{fl/fl}$ mice, no major defect was observed in the segregation of ipsilateral projections in *Dcckanga*$^{kanga/-}$ mutants compared to *Dcc*$^{kanga/+}$ control mice (*Figure 6E,F*). Furthermore, no major defects were observed in both thalamic nuclei of the ventral and dorsal lateral geniculate nucleus (*Figure 6G–J*).

The AOS was also affected in *Dcckanga*$^{kanga/-}$ mice, as shown by a significant reduction of the volume of the MTN (n = 9) compared to *Dcc*$^{kanga/+}$ littermate controls (*Figure 6K–M*; *Figure 6—source data 1*; n = 5). This reduction in MTN volume was comparable to that observed in *Dcc* cKO mice (*Figure 6—figure supplement 1C*; *Figure 6—source data 2*). RGC projections to the MTN in *Dcckanga*$^{kanga/-}$ mutants displayed multiple projection defects (*Figure 6—figure supplement 1D,E*). No defects were observed in other AOS nuclei.

Eye-specific deletion of Dcc alters retinal layer thickness

To determine whether Dcc could play a role beyond optic nerve formation, we first immunostained postnatal retinas to observe whether Dcc protein was still present. At P0 (n = 3) and P7 (n = 3), Dcc protein was absent from the cell bodies but was still heavily expressed in the postnatal retina (*Figure 7A–F*). It was localized to the neuropil layers of the retina, the inner and outer plexiform layers (*Figure 7A–F*).

Since early RGCs misproject in *Dcc* cKO mice we questioned whether RGCs were affected in postnatal and adult mice. P0, P15, and 1 month-old retinas were flat-mounted and labeled for a pan-RGC marker (*Kwong et al., 2010*), RNA-binding protein with multiple splicing (Rbpms; *Figure 7—figure supplement 1A–F*). Whole-eye immunostaining with Rbpms confirmed the gradual loss of RGCs from P15 to 1 month (*Figure 7—figure supplement 1G–J*; *Figure 7—source data 1*). Of note, RGC loss was homogeneously distributed in mutant retinas. Strikingly, the number of RGCs was dramatically reduced by ~60% in *Dkk3:cre;Dcc*$^{fl/fl}$ mice at P0 (n = 4 retinas) when compared to *Dcc*$^{fl/fl}$ mice (*Figure 7—figure supplement 1K*; *Figure 7—source data 1*; n = 6 retinas). The number of Rbpms-positive cells decreased to ~82% in P15, *Dkk3:cre;Dcc*$^{fl/fl}$ mice (n = 4 retinas) and even further to ~91% at 1 month (*Figure 7—figure supplement 1K*; *Figure 7—source data 1*; n = 6 retinas). Displaced RGCs were not included in our analysis. Thus, eye-specific loss of *Dcc* leads to a dramatic degeneration of RGCs.

Unlike *Dcc*$^{-/-}$ mice, *Dkk3:cre;Dcc*$^{fl/fl}$ conditional mutants are viable allowing us to investigate the role of Dcc in retinal lamination, which is established postnatally. The inner plexiform layer (IPL) is subdivided into 5 specific lamina named stratum 1 to 5 (S1-S5, S5 being closest to the RGC layer) (*Wässle, 2004*). Since *Dcc* deletion led to early retinal defects, we wondered whether the earliest born amacrine cells, starburst amacrine cells (SACs) (*Voinescu et al., 2009*) displayed defects. In control mice, both ON- and OFF- SACs express choline O-acetyltransferase (Chat) and their dendrites stratify in S2 and S4 of the IPL (*Figure 7I,K,L*). Whole-mount immunostaining of flat-mounted retinas with Chat revealed the mosaic distribution of SACs (*Figure 7—figure supplement 2A–F*). The number of SACs in the GCL was unchanged at P15 (n = 4) and 1 month (n = 6) in *Dcc* cKO mice compared to *Dcc*$^{fl/fl}$ mice (*Figure 7—figure supplement 2G*; *Figure 7—source data 2*). Furthermore, no significant difference was observed in the number of SACs soma in the inner nuclear layer in *Dcc* cKO mice at P15 (n = 4) and 1 month compared to *Dcc*$^{fl/fl}$ controls (*Figure 7—figure supplement 2H*, *Figure 7—source data 2*; n = 6). However, sagittal cryosections of 1 month-old *Dcc* cKO retinas labeled for Chat showed that the relative thickness of the S2-S4 was significantly reduced in *Dcc* cKO mice (*Figure 7O,P,R*; n = 3) compared to *Dcc*$^{fl/fl}$ mice (*Figure 7I,K,L*; *Figure 7—figure supplement 2I,J*; *Figure 7—source data 2*; n = 3). There were no aberrant dendrite projections of Chat^{+} SACs in *Dkk3:cre;Dcc*$^{fl/fl}$ mice compared to *Dcc*$^{fl/fl}$ littermates (n = 3 for each genotype).

This observation led us to question whether the overall thickness of the IPL was also affected. Horizontal cells as well as displaced amacrine cells were visualized using the calcium-binding protein Calbindin (CaBP) (*Wässle, 2004*). At 1 month, *Dcc*$^{fl/fl}$ retinas showed that displaced amacrine cell dendrites stratified at the border of S1-2, S2-3, and S3-4 (*Figure 7G,H,K,L*; *Wässle, 2004*). *Dkk3:*

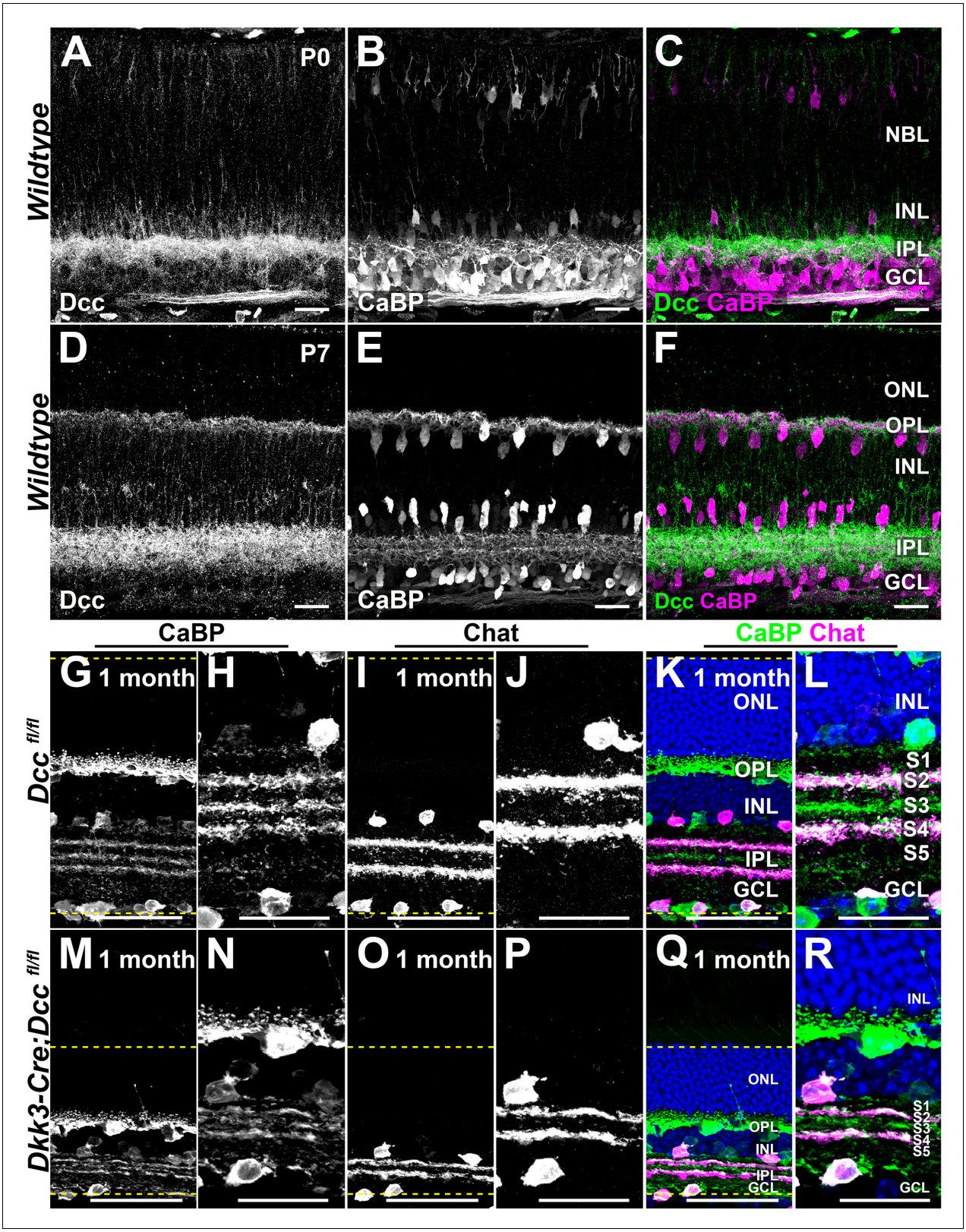

Figure 7. Eye-specific deletion of Dcc leads to reductions in retinal layers thickness. (**A–F**) IHC of postnatal retinas labeled for Dcc (green) and the horizontal and amacrine cell marker, Calbindin (CaBP, magenta). (**A–C**) P0 retinas. (**D–F**) P7 retinas. (**G–R**) Cryosections of 1 month-old retinas of *Dcc*$^{fl/fl}$ and *Dkk3:cre;Dcc*$^{fl/fl}$ mice. (**G,H,M,N**) CaBP IHC (green) that labels amacrine cells that stratify in the IPL strata S2, S3, and S4. (**I,J,O,P**) IHC for choline O-acetyltransferase (Chat) that labels starburst amacrine cells which arborize in the IPL strata S2 and S4. (**K,L,Q,R**) show merge images. Yellow dashed

Figure 7 continued on next page

Figure 7 continued

lines delineate the retinal contours. Scale bars: (**A–F,H,J,L,N, P,R**) 25 µm; (**G,I,K,M,O,Q**) 50 µm. NBL, Neuroblastic Layer; ONL, Outer Nuclear Layer; OPL, Outer Plexiform Layer; INL, Inner Nuclear Layer; IPL, Inner Plexiform Layer; GCL, Ganglion Cell Layer.

The online version of this article includes the following source data and figure supplement(s) for figure 7:

Source data 1. Early loss of Dcc leads to a significant and progressive degeneration of RGCs.
Source data 2. Eye-specific loss of Dcc does not induce a loss of SACs but impacts retinal thickness.
Source data 3. RGC loss is dependent on Dcc signaling.
Figure supplement 1. Eye-specific *Dcc* deletion leads to a dramatic reduction of RGC number.
Figure supplement 2. *Dcc* deletion does not affect Chat^{+} cell number.
Figure supplement 3. Dcc signaling is critical for RGC survival.

cre;Dcc$^{fl/fl}$ displayed a significant reduction in the IPL (n = 3) compared to *Dcc$^{fl/fl}$* mice (***Figure 7—figure supplement 2J***; ***Figure 7—source data 2***; n = 3). We nonetheless found that CaBP^{+} amacrine cells exhibited normal lamina-specific neurite stratification in the IPL (***Figure 7M,N,Q,R***). We analyzed the overall thickness of the retina from the outer segments of photoreceptors to the soma of RGCs. At 1 month, mutant retinas displayed a dramatic reduction in thickness compared to *Dcc$^{fl/fl}$* retinas (***Figure 7—figure supplement 2J***; ***Figure 7—source data 2***; n = 3). Of note, this reduction was homogeneous across the entire retina.

To determine whether loss of RGCs was dependent on Dcc signaling, we carried out a Rbpms whole-mount immunostaining of *Dcc^{Kanga}* eyes (***Figure 7—figure supplement 3A,B***). At 1 month, RGC numbers were dramatically reduced by ~72% in *Dcckanga$^{kanga/-}$* mutants (n = 4) compared to the *Dcc$^{kanga/+}$* control littermates (***Figure 7—figure supplement 3C***; ***Figure 7—source data 3***; n = 4). We next investigated whether the number of SACs were affected in *Dcc^{kanga}* mutants. In the RGC layer, SACs was not affected in *Dcckanga$^{kanga/-}$* mice (n = 4) compared to *Dcc$^{Kanga/+}$* mice (***Figure 7—figure supplement 3D,E***; n = 4). The total number of SACs in the inner nuclear layer was also unchanged in *Dcckanga$^{kanga/-}$* retinas (n = 4) compared to *Dcc$^{kanga/+}$* littermates (***Figure 7—figure supplement 3F***; ***Figure 7—source data 3***; n = 4).

Dcc deletion leads to major retinal dysplasia and visual deficits

In order to assess the overall eye phenotype in *Dkk3:cre;Dcc$^{fl/fl}$* conditional knockout mice, we adapted the EyeDISCO protocol for adult mouse eyes (see Materials and methods; ***Figure 8A–B'***). This led to a modest and isotropic (rostro-caudal/medio-lateral/dorso-ventral) shrinkage of the tissue of ~11% (***Figure 8—figure supplement 1A–D***, ***Figure 8—source data 2***, n = 8 eyes). By eye fundoscopy, large lesions were observed in *Dcc* cKO mutant retinas (***Figure 8C,D***). To analyze the precise localization and density of these lesions, we carried out whole-mount nuclear staining (TO-PRO-3) followed by EyeDISCO clearing and LSFM. 3D rendering showed that eye-specific *Dcc* mutants displayed abnormal conformation of photoreceptors that resembled rosette-like structures, reminiscent of photoreceptor degeneration (***Figure 8E,F***, ***Figure 8—video 1***; ***Chang et al., 2002***; ***Flynn et al., 2014***). Rosette-like structures were specifically located in the outer nuclear layer of the retina (photoreceptor layer) and the area they covered was manually segmented (***Figure 8G,H***, ***Figure 8—video 2***). This showed that unlike RGC loss, which was homogeneous in the retina, rosette structures were specifically localized as a band that spanned naso-temporally with a ventral bias (***Figure 8I–N***; n = 8). To confirm that rosettes were composed of photoreceptors, we carried out whole-mount immunolabeling for short-wavelength opsin (Opn1sw), which is known to be present in the ventral half of the retina (***Applebury et al., 2000***; ***Ortín-Martínez et al., 2014***). At 1 month, Opn1sw was expressed in high-ventral and low-dorsal gradient in the *Dcc$^{fl/fl}$* eyes (***Figure 8O***; ***Figure 8—video 2***; n = 6 eyes). In *Dcc* mutants, Opn1sw gradient was conserved, but rosette-like structures were observed in Opn1sw^{+} photoreceptor cells (***Figure 8P***; ***Figure 8—video 2***; n = 6 eyes). We next questioned whether specific types of photoreceptors would cluster in rosettes. To do so, we labeled retinas with short- and mid-wavelength opsins as well as Rod-specific opsin (Rhodopsin). All types of photoreceptors were present within rosettes (***Figure 8—figure supplement 2A–P***).

To determine whether loss of Dcc in early retinal development led to progressive photoreceptor degeneration, *Dkk3:cre;Dcc$^{fl/fl}$* mutant eyes were cleared at P15, 1 month, and 6 months (n = 5). The eyes were then manually segmented for rosette-like structures and the percentage of rosette territory covered in each retina was quantified (***Figure 8Q***). No significant differences were observed in

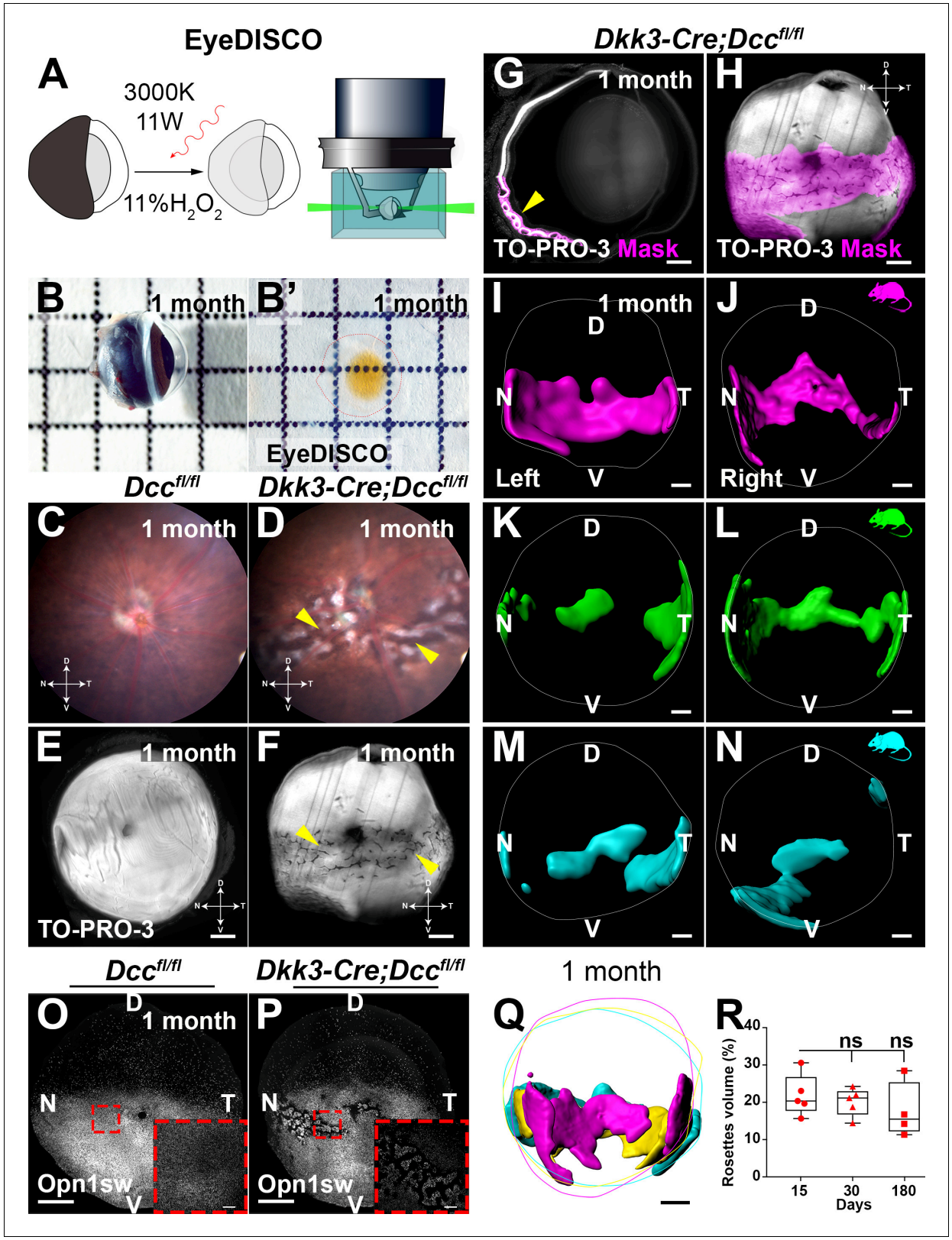

Figure 8. EyeDISCO, a novel tissue clearing protocol for whole eye visualization. (**A**) Is a representation of the EyeDISCO clearing pipeline. Adult eyes are dehydrated in methanol and immersed in an 11% H2O2 solution irradiated with a 3000˚K warm white light (red arrow). After immuno-labeling the eyes are cleared and imaged using light sheet microscopy. (**B, B'**) Side view image of an adult eye (1 month) before and after EyeDISCO clearing. (**C,D**) Eye fundoscopy of a 1 month-old *Dcc*$^{fl/fl}$ and a *Dkk3:cre;Dcc*$^{fl/fl}$ eye. *Dkk3:cre;Dcc*$^{fl/fl}$ fundoscopy shows a severe dysplasia (yellow arrows). Eye

Figure 8 continued on next page

Figure 8 continued

coordinates are highlighted, D, dorsal, V, ventral,N, nasal, T, temporal. (**E,F**) Whole eye of *Dcc*$^{fl/fl}$ and *Dkk3:cre;Dcc*$^{fl/fl}$ mice after EyeDISCO treatment labeled with a nuclear marker (TO-PRO-3, white). Major dysplasia can still be observed in *Dkk3:cre;Dcc*$^{fl/fl}$ eyes (yellow arrows). (**G**) Represents a slice of the 3D stack from a *Dkk3:cre;Dcc*$^{fl/fl}$ eye. The dysplasia can be isolated by manual segmentation with Imaris (magenta, yellow arrow). (**H**) The affected area visualized in 3D (magenta) following manual segmentation. (**I–N**) 3D surfaces of rosette masks in 3 separate *Dkk3:cre;Dcc*$^{fl/fl}$ mice showing both the left and right eye. (**O, P**) Whole-mount IHC of eyes of *Dcc*$^{fl/fl}$ and *Dkk3:cre;Dcc*$^{fl/fl}$ 1 month-old eyes labeled for short-wavelength Opsin (Opn1sw, white). (**Q**) A merge of 3 separate masks using Imaris from *Dkk3:cre;Dcc*$^{fl/fl}$ mice showing rosette area coverage and retina circumference. (**R**) Quantification of rosette area coverage in retinas. No differences in rosette coverage were seen between *Dcc* cKO and control littermates at P15 (21.85 ± 2.48%; n = 5 eyes), 1 month (20.11 ± 1.67%; n = 5 eyes; p>0.999) and 6 months (17.68 ± 3.76%; n = 5 eyes; p=0.6176). A Kruskal-Wallis test was used to measure significance. Data are represented as a box plot; whiskers represent min to max values. Results were considered non-significant (ns) if p>0.05. Scale bars: (**E–H, I–N**) 300 µm, (**O, P**) 500 µm, (**O, P**) high magnification) 150 µm, (**Q**) 400 µm.

The online version of this article includes the following video, source data, and figure supplement(s) for figure 8:

Source data 1. Rosette volume in *Dcc* cKO mice does not progress overtime.
Source data 2. EyeDISCO leads to a mild and isotropic shrinkage of the adult mouse eye.
Source data 3. Outer nuclear layer thickness is reduced in Dcc cKo mice.
Source data 4. Retinal-specific deletion of Dcc leads to a significant reduction in retinal physiology.
Figure supplement 1. EyeDISCO leads to a mild and isotropic shrinkage of the adult eye.
Figure supplement 2. Photoreceptors are ubiquitously present within rosettes.
Figure supplement 3. Eye-specific deletion of *Dcc* leads to functional visual deficits.
Figure supplement 4. Dcc Kanga mutants display retinal dysplasia.
Figure 8—video 1. Eye-specific *Dcc* deletion leads to major retinal dysplasia.
https://elifesciences.org/articles/51275#fig8video1
Figure 8—video 2. Rosette formation in *Dcc cKO* mice is specific to photoreceptor cells.
https://elifesciences.org/articles/51275#fig8video2

retinas between P15, 1 month, and 6 months (***Figure 8R***; ***Figure 8—source data 1***; n = 5 eyes). Thus, rosette structures in mutant mice do not progress over time. We then investigated whether photoreceptors outside of rosettes were also affected. To address this, we carried out an immunolabeling on 1-month-old retinas with the pan-photoreceptor marker, Recoverin. We observed that in *Dcc* cKO retinas (n = 3) photoreceptors were dramatically reduced compared to *Dcc*$^{fl/fl}$ controls (n = 3) (***Figure 8—figure supplement 2Q–U***; ***Figure 8—source data 3***).

Finally, we also observed that rosettes induce a significant loss in physiological visual response. Electroretinogram (ERG) at 1 month showed that the scotopic response of *Dcc* cKO mice was significantly reduced in a-wave but not b-wave complexes (***Figure 8—figure supplement 3A***; ***Figure 8—source data 4***). This reduction persisted at 6 months in a-wave but not b-wave complexes (***Figure 8—figure supplement 3A***). To assess cone function, we also analyzed the photopic response in *Dcc* cKO mice and found a dramatic loss of photopic response at 1 and 6 months (***Figure 8—figure supplement 3B***; ***Figure 8—source data 4***). Altogether, eye-specific deletion of *Dcc* leads to rosette formation in the photoreceptor layer of the retina. These rosettes are localized to the naso-temporal retina and do not progress overtime.

Strikingly, as was observed in our *Dcc* cKO mice, rosettes were present in *Dcc Kanga* mutants as early as P15 suggesting a developmental defect (***Figure 8—figure supplement 4E–F***; n = 4 eyes). These rosettes were still present at 1 month (***Figure 8—figure supplement 4F–G***; n = 9 *Dcc*$^{kanga/-}$ and n = 10 *Dcc*$^{kanga/+}$). Both short- and mid-wavelength cones were present within the rosettes (***Figure 8—figure supplement 4E–G***). Therefore, altered Dcc signaling leads to the formation of rosettes in the outer nuclear layer of the retina.

Discussion

Dcc is essential for RGC intraretinal axon guidance

Early eye development begins from the invagination of the optic vesicle to form the optic cup (***Bernstein et al., 2018***). This morphogenetic event gives rise to the neural retina and forms an opening along the ventral midline that will become the future optic disc, also known as the choroid fissure (***Bernstein et al., 2018***). Early RGCs are polarized and extend within the basal retina, constituting the optic fiber layer (OFL). RGC axons further extend circumferentially towards the presumptive

optic disc where they exit the retina (**Bao, 2008**). Therefore, two mechanisms are at play during the intraretinal navigation of RGC axons.

The first process involves the basal lamina at the vitreal side which provides a growth-promoting substrate for RGC axons. Several guidance cues such as Slits and Semaphorin3E restrict RGC axons to the OFL (**Jin et al., 2003**; **Steinbach et al., 2002**; **Thompson et al., 2006**). However, the basal lamina does not provide directionality (**Halfter et al., 1987**; **Halfter and Fua, 1987**) and other guidance cues such Sfrp1, Sfrp2, EphB2, EphB3, Netrin-1 present in the retina (**Birgbauer et al., 2000**; **Deiner et al., 1997**; **Marcos et al., 2015**), and Slit2 present in the lens (**Thompson et al., 2006**) orient RGC axons towards the optic disc.

Interestingly, pioneer RGC axons extend into the optic vesicle during choroid fissure closure (**Deiner et al., 1997**; **Kuwabara and Weidman, 1974**). Perturbations of this event have been associated with optic nerve defects (**Cai et al., 2013**; **Dakubo et al., 2003**; **Morcillo et al., 2006**; **Otteson et al., 1998**; **Silver and Robb, 1979**). It was recently shown that Netrin-1 is required for choroid fissure closure, and that *Ntn1*$^{-/-}$ mice display highly penetrant colobomas (**Hardy et al., 2019**). We observe that our Ntn1 cKO also exhibit colobomas (80% penetrance, n = 5), suggesting that Netrin-1 at the optic disc is required for proper choroid fissure closure. We could not detect any choroid fissure defects in either *Dcc* cKO or *Dcc* null mutant mice suggesting that Netrin-1 may mediate choroid fissure fusion in a Dcc-independent manner.

The first born RGCs arise in the dorso-central retina in close proximity to the pax2-positive optic disc cells (**Drager, 1985**) expressing Netrin-1 (**Deiner et al., 1997**). Interestingly, we observe no significant differences between the optic nerve hypoplasia displayed in Netrin-1 null mice and Ntn1 cKO mice. Thus, as it was described in the hindbrain and the spinal cord (**Dominici et al., 2017**; **Moreno-Bravo et al., 2019**; **Varadarajan et al., 2017**; **Wu et al., 2019**), it is likely that Netrin-1 acts intraretinally in a short-range manner.

Dcc is necessary for retinal ganglion cell projections in the primary and accessory optic systems

RGC projections initially reach the thalamus and the superior colliculus during embryonic development (**Godement et al., 1984**). Different axon guidance molecules are critical for the proper targeting of RGC projections to the thalamus and to the superior colliculus. In the absence of reelin, RGC axons fail to target the vLGN and the IGL correctly (**Su et al., 2011**). Once RGC axons have reached their target they then refine between ipsi- and contra-lateral territories. During this process, EphB or ephrinBs are required for RGCs to dictate their final position in the superior colliculus (**Hindges et al., 2002**; **Thakar et al., 2011**). In the *Dcc* cKO, RGCs target the LGN and superior colliculus normally but we observe an expansion of the ipsilateral territory, thus hinting at a possible refinement defect. Netrin-1 and Dcc have been shown to play a role in RGC axon arborization and synapse formation within the optic tectum of *Xenopus* tadpoles (**Manitt et al., 2009**). Here, we show for the first time that intra-retinal loss of Dcc leads to an expansion in ipsilateral territory in the murine SC. Nevertheless, we cannot rule out that the expansion in ipsilateral projections within the SC may be a result of the significant death of RGCs observed in *Dcc* cKO retinas.

The organization of the accessory optic system (AOS) projections to the MTN, the NOT, and the OPT is altered in *Dcc* mutants. These defects were constant and reproducible. Moreover, Alexa-Fluor-CTB is fluorescent enough to label isolated axons (**Li et al., 2015**) and therefore it is unlikely that a significant fraction of visual axons could not be traced. Although the major input to the AOS is constituted of ON Direction Selective Ganglion Cells (DSGC) (**Dhande et al., 2013**), ON-OFF DSGCs also project to AOS nuclei (**Kay et al., 2011**). The MTN is innervated by ON-OFF DSGCs which control eye movement and give information for upward motion (dMTN) or downward motion (vMTN) (**Borst and Euler, 2011**; **Yonehara et al., 2009**). However, RGCs projecting to the MTN are homogeneously spread across the retina (**Sun et al., 2015**). Little is known about the cues guiding DSGC axons to the MTN besides the transmembrane semaphorin Sema6A and its receptors PlexinA2/A4 (**Sun et al., 2015**). Contactin-4 and the amyloid precursor protein are necessary for DSGC's axons to project in the NOT, but not the MTN (**Osterhout et al., 2015**). As Dcc protein is homogeneously expressed in embryonic RGCs, one could wonder why we observe a specific guidance defect in the MTN. One hypothesis could be that co-receptors of Dcc, such as Unc5d could potentiate the MTN defect observed in our *Dcc* mutants (**Murcia-Belmonte et al., 2019**). Furthermore, the differential distribution of Netrin-1 protein within the visual nuclei could be another area of study to

explain the heterogeneous defects observed in our Dcc mutants. Still, we cannot rule out that the loss of RGCs in our Dcc mutants could impact axonal arborization due to a reduced competition between neighboring RGC axons. Further investigations should be performed to test whether DSGCs may be specifically impacted by Dcc perturbation using MTN-specific mouse lines such as the SPIG1:GFP (**Yonehara et al., 2008**) and Hoxd10:GFP (**Dhande et al., 2013**) knock-in mouse lines. Overall, we uncover a new role for Dcc in the innervation of the MTN, the NOT and the OPT.

Why do RGCs die in eye-specific *Dcc* mutants?

Although the overall death of RGCs is homogeneous, only a portion aberrantly invade the subretinal space. This suggests that the death of RGCs is not merely correlated to the misprojection phenotype. To survive, RGCs require trophic factors such as brain-derived neurotrophic factor (BDNF), ciliary neurotrophic factor (CNTF), neurotrophin 4 (NT4), and fibroblast growth factor (FGF) secreted by the superior colliculus (**Meyer-Franke et al., 1995**; **Raff et al., 1993**). A possibility is that too few RGC axons make it to the superior colliculus to provide sufficient trophic support. This massive RGC death could also result from the elimination of the misrouted RGCs axons as previously demonstrated in the zebrafish (**Poulain and Chien, 2013**). Netrin-1 through Dcc has been shown to promote synaptogenesis of cortical neurons (**Goldman et al., 2013**). Therefore, an abnormal synaptogenesis of *Dcc*-deficient RGC axons with their target neurons could also induce their degeneration.

Photoreceptor cell degeneration

In addition to RGCs death *Dcc* cKO mutants display major retinal dysplasia, limited to the retinal outer nuclear layer. These undulations in the ONL often referred as rosettes in the literature (**Mears et al., 2001**), are among the most prominent features of retinal degeneration along with photoreceptor cell death and underdeveloped outer segments (**Genové et al., 2014**). In *Dkk3:cre; Dcc$^{lox/lox}$* mice, the rosettes are only present in the inferior half of the retina but span from the nasal to the temporal sides. To our knowledge, localized rosettes have only been described in *Crb1* mutant mice. *Crb1^{rd8}/Crb1^{rd8}* mice display rosettes in the inferior nasal quadrant of the retina (**Mehalow et al., 2003**) whereas in *Crb1$^{-/-}$* mice retinal degeneration occurs in the inferior temporal quadrant (**van de Pavert et al., 2004**). Importantly, *Dcc* cKO mice have been backcrossed into a C57BL/6J background and are negative for the *rd10* mutations (**Supplementary file 3**). What could explain the degeneration of a subset of photoreceptors? Based on our results, it is more likely that this phenotype is related to the intra-retinal pathfinding defects. First, rosettes were observed as early as E15, concomitantly with the first misrouted axons in the retina. Therefore, misguided RGC axons invading the subretinal space could separate photoreceptors from RPE. Indeed, interactions between the RPE and presumptive photoreceptor outer segments are crucial for their proper development (**Marmorstein, 2001**). Early ablation (E10–11) of RPE in mouse retina also results in a disorganization of retinal layers (**Raymond and Jackson, 1995**). Moreover, rats with dysfunctioning RPE cells show photoreceptor death (**D'Cruz et al., 2000**). Second, several studies have linked rosette formation with outer limiting membrane defects (**Mehalow et al., 2003**; **Rich et al., 1995**; **Stuck et al., 2012**). It is thus likely that misguided RGC axons in our *Dcc* cKO mice alter the outer limiting membrane leading to photoreceptor degeneration. Third, we show that Dcc is expressed homogeneously in Crx^{+} cells at E15. Using the *Dkk3* promoter leads to a complete removal of *Dcc* in all retinal progenitors. If Dcc played a role in proper photoreceptor development we would expect that all photoreceptor cells would degenerate. Finally, we observe that M- and S-cones as well as rods are all present within rosettes. These results support the idea that in *Dcc* cKO mice, photoreceptor cell death is not limited to a specific cell type but rather triggered by RGC axons. Nonetheless, retinal physiology in our Dcc mutants is globally perturbed, indicating either that rosettes (which account for ~20% of the retina) are sufficient to impact the ERG or that photoreceptor defects may not only be restricted to rosette territories. Quantification of the ONL outside of rosettes in Dcc cKO mice shows a dramatic thinning compared to control littermates. It would be of interest to investigate whether Dcc plays a cell autonomous role in photoreceptors.

Dcc's mechanism of action

Here, we show that Dcc acts cell autonomously in RGCs to confine their axons to the retina but that the phenotype is heterogeneous. In *Dkk3:cre;Dcc*$^{fl/fl}$ mice, some RGC axons exit the retina and even project to the CNS, suggesting that they are still properly guided in the absence of Dcc. On the other hand, other RGC axons aberrantly project apically into the subretinal space. These results suggest that the long-range guidance of RGC axons to the optic disc is not mediated by Dcc. It rather acts as a short range guidance receptor preventing RGC axons from escaping the neural retina and staying in the OFL, as shown for hindbrain commissural axons (**Moreno-Bravo et al., 2018**; **Yung et al., 2018**). Another in vivo example of the short-range guidance role of Dcc/Netrin-1 signaling was shown in R8 photoreceptor growth cones in *Drosophila melanogaster*, which could successfully project but not attach properly in their terminal zone (**Akin and Zipursky, 2016**). Why the phenotype is heterogeneous is unclear as the expression levels of Dcc (based on immunocytochemistry) in embryonic RGCs appear similar across the retina. This could be explained by a differential expression of co-receptors or downstream partners in different subclasses of RGCs. Evidence for this phenotypic heterogeneity is also found at a later stage and further suggests that specific populations of RGCs are differentially affected by the loss of Dcc.

Most of Dcc's known functions such as growth cone attraction are mediated by its P3 intracellular domain (**Finger et al., 2002**). The *Dcc*^{Kanga} mice lacking the exon encoding the P3 intracellular domain present the same phenotype as the *Dcc* KO mice, with a missing corpus callosum and an aberrantly projecting corticospinal tract (**Finger et al., 2002**). The observation that *Dcc*^{Kanga} mice share many of the phenotypes observed in *Dcc* cKO mice suggests that they are indeed directly dependent on Dcc signaling and not the signaling of a Dcc co-receptor. Moreover, we show that deletion of Netrin-1 phenocopies the defects observed in the embryonic retina. Thus, we demonstrate that Dcc/Netrin-1 signaling is critical for the proper targeting of RGCs.

EyeDISCO is a powerful technique to study the eye

In the past decade, there have been significant developments in tissue clearing protocols. However, none have addressed the challenge of clearing densely pigmented tissues (**Susaki and Ueda, 2016**). Recent protocols allowing for whole-mouse visualization are still hindered by densely pigmented tissues such as the eyes or the skin (**Cai et al., 2019**; **Pan et al., 2016**; **Tainaka et al., 2018**). Efforts to remove densely pigmented tissues such as the melanophores of the RPE of the eye have almost entirely been carried out on tissue sections (**Alexander et al., 1996**; **Orchard, 2007**). For instance, using potassium permanganate and oxalic acid in aqueous conditions Iwai-Takekoshi and colleagues were able to remove RPE pigments in embryonic sections (**Iwai-Takekoshi et al., 2016**). This depigmentation protocol has however been shown to reduce the compatibility/efficacy of immunolabelling (**Alexander et al., 1996**). Recently, a de-pigmentation protocol of postnatal eyes amenable to tissue clearing has been published (**Henning et al., 2019**). This protocol carries out an H_2O_2 treatment in aqueous conditions which favors the generation of microbubbles that damage the retina and result in retinal detachment (**Henning et al., 2019**). In addition, the H_2O_2 treatment is done at 55˚C, further deteriorating as well as reducing antigenicity of the tissue. Only 2 antibodies were validated using this protocol. Here, we report an amenable tissue clearing protocol for whole-embryo and whole adult eye clearing compatible with immunolabeling. The immunolabeling protocol is carried out at RT and requires passive diffusion of low titer antibodies. Thus far, 17 antibodies have been validated, encompassing transcription factors, transmembrane and cytoplasmic proteins (**Supplementary file 2**).

A current limitation of our method is the cellular resolution at which we are able to carry out whole-eye imaging using LSFM, as our setup is composed of a macroscope with a 2X objective coupled to a 6.3X numerical zoom (12.6X) giving a maximum x/y resolution of 5.16 µm/pixel. However, the recent development of higher magnification objectives compatible with DBE will allow for more resolved images, equivalent to confocal microscopes, that enable whole-eye cell-counting approaches (**Pan et al., 2019**).

Altogether, EyeDISCO provides a novel opportunity to image the visual system like never achieved before. This protocol allows the study of visual projections from the eye to the brain, thereby constituting a powerful tool for the screening of mutants. This protocol could also prove extremely useful to study the eye as a whole for better understanding eye disorders.

Materials and methods

Ethics statement

All experiments were designed using the 3R rule: to reduce, refine, and replace the use of animals. All animal procedures were carried out according to approved institutional guidelines (#B-75-12-02) of the Institut de la Vision. The protocol was approved by the Sorbonne Université ethic committee (Charles Darwin) (Permit Number: 9571). In cases of animal handling, experiments were performed to minimize animal stress and suffering.

Animals

Dcc knockout mice (***Fazeli et al., 1997***), Dcc^{kanga} mice (Dcc^{kanga}; Jackson Laboratories) (***Finger et al., 2002***), *Dcc* floxed mice (***Krimpenfort et al., 2012***), *Ntn1* floxed mice (***Moreno-Bravo et al., 2018***), and *Dickkopf3:cre* (*Dkk3:cre*) mice (***Sato et al., 2007***) were previously described. All mice are kept in C57BL/6J background. Cre expression was monitored by crossing *Dkk3:cre* mice with the Ai9 $Rosa^{tdTomato}$ reporter line ($Rosa^{Tom}$; Jackson Laboratories). The day of the vaginal plug was counted as embryonic day 0.5 (E0.5). Mice were anesthetized with ketamine (80 mg/kg) (Axience) and xylazine (8 mg/kg) (Axience). Embryos and adult mice of either sex were used.

RD gene sequencing

$PDE6b^{rd1}$ mutations were investigated by direct Sanger sequencing. Genomic DNA was extracted using 50 mM NaOH for 30 min at 95˚C. The following primers were used Forward: 5'ctgcacacaga-catccagtc3' Reverse: 5'ccatgcctggctgaagttgt3'. PCR was done using a Gotaq DNA Polymerase (Promega). Next, PRC products were sequenced using Sanger sequencing (BigDyeTermv1.1 Cycle-Seq kit, Applied Biosystems) and analyzed on an automated 48-capillary sequencer (ABI3730 Genetic analyzer, Applied Biosystems), and the results interpreted by applying a software (Seqscape, Applied Biosystems).

Immunohistochemistry

Embryos were fixed by immersion in 4% paraformaldehyde in 0.12 M phosphate buffer (VWR, 28028.298 and 28015.294), pH 7.4 (PFA) o/n at 4˚C. Eyes were harvested and using a $30^{1/2}$G needle, a small hole was made in the cornea. The eyes were then fixed in 4%PFA for 1 hr at RT. Following three washes in 1XPBS, the samples were incubated in 10% sucrose (VWR, 27478.296) in 0.12 M phosphate buffer o/n at 4˚C. The next day, samples were transferred to a 30% sucrose solution in 0.12 M phosphate buffer o/n at 4˚C. Samples were then embedded in 0.12 M phosphate containing 7.5% gelatin (Sigma, 62500) and 10% sucrose, frozen in isopentane at −50˚C and then cut at 20 µm with a cryostat (Leica, CM3050S). Sections were blocked in PBS containing 0.2% gelatin (VWR) and 0.25% Triton-X100 (PBS-GT) for 1 hr at RT. Sections were then incubated with primary antibodies (see ***Supplementary file 1***) diluted in a PBS-GT solution o/n at RT. Following three washes in PBST (0.05% Triton-X100) secondary antibodies coupled to the appropriate fluorophore (see ***Supplementary file 1***) were diluted in PBS-GT and incubated for 2 hr at RT. Sections were counter-stained with Hoechst (Sigma, B2883, 1:1000). Slides were scanned with either a Nanozoomer (Hamamatsu) or laser scanning confocal microscope (Olympus, FV1000). Brightness and contrast were adjusted using ImageJ.

Retinal thickness

To measure the thickness of retinal layers, 1 month-old control and $Dkk3{:}cre;Dcc^{fl/fl}$ retinas were harvested and fixed in 4% PFA o/n at 4˚C. Retinas were processed as previously described. Calbindin (Swant, see ***Supplementary file 1***) and Chat (Millipore, see ***Supplementary file 1***) immunostaining were used to visualize the IPL layers and Hoechst (Sigma) to visualize all retinal layers. Using NDP viewer (version 2.2.6), 5 retinal sections from the optic nerve were analyzed (n = 3 mice per group). Using the measure tool, the thickness (µm) of each layer was measured.

EdU proliferation

Pregnant females were injected intraperitoneally with 5-ethynyl-2′-deoxyuridine (EdU;1 mg/10 g) and sacrificed 3 hr following injection. Proliferating cells were visualized using the Click-iT EdU Imaging kit (Invitrogen) and were co-labeled with antibodies against Chx10 (Exalpha, see ***Supplementary file 1***), a retinal progenitor cell marker. For co-localization of EdU/Chx10, the Imaris X 64 software (Bitplane, version 9.1.2) co-localization tool was used and the percentage of ROI co-localization was measured (threshold Chx10 = 320, threshold EdU = 147).

Tracing of visual projections

Mice were anesthetized with an intra-peritoneal injection of ketamine (100 mg/kg) and xylazine (10 mg/kg) and kept warm with a thermostatically controlled platform at 37˚C. Corneal analgesia was done by applying chlorhydrate oxybuprocaine (1.6 mg/0.4 ml). The eye was proposed using bulldog forceps (FST, 18039–45). A $30^{1/2}$-gauge needle was used to make a pre-hole at the dorsal side of the eye. Using a Nanofil syringe (World Precision Instruments, Nanofil) with a $33^{1/2}$–gauge beveled needle (World Precision Instruments, NF33-BV2), 1.2 µl 2 µg/µl of AlexaFluor-conjugated cholera toxin β subunit (Thermo Fischer, AlexaFluor555-CTB C22843 and AlexaFluor647-CTB C34778) was injected intravitreally. To avoid leakage, the needle was slowly withdrawn over the span of 3 s. 72 hr following CTB injection, mice were transcardially perfused with 4%PFA and the brains were dissected for tissue clearing.

Flat mount

For retinal flat mounts, eyes were harvested and the retina were dissected and fixed by gentle shaking at 50 rpm in 4%PFA for 45 min at RT. The retinas were then washed three times in 1XPBS. For immunohistochemistry, retinas were permeabilized and blocked in a solution containing 0.5% Triton-X100, 5% donkey normal serum, 1XPBS, 0.1 g/L thimerosal for 1 day at RT under agitation. Primary antibodies (see ***Supplementary file 1***) were diluted in a solution containing 0.5% Triton-X100, 5% donkey normal serum, 10% Dimethyl Sulfoxide, 1XPBS, 0.1 g/L thimerosal for 3 days at RT under agitation. The retinas were then washed for 1 day in PBST (1XPBS, 0.5% Triton-X100). The secondary antibodies (see ***Supplementary file 1***) were diluted in the same solution as primary antibodies and left for 2 days. After washing retinas for 1 day, they were mounted on slides and imaged using a scanning confocal microscope (Olympus, FV1000).

For quantifications of $Rbpms^+$ (Phosphosolutions, see ***Supplementary file 1***) and $Chat^+$ (Millipore, see ***Supplementary file 1***) cells, the Imaris X 64 'Spots' tool was used (Bitplane, version 9.1.2). For $Rbpms^+$ staining, automatic segmentation was done. For Chat staining, a manual segmentation was carried out to separate the inner nuclear layer from the retinal ganglion cell layer. Automatic cell counting was then carried out on each segmentation.

Electroretinogram

All experiments were carried out in double-blind. Following o/n adaptation, animals were prepared under red light and were anesthetized with an intraperitoneal injection of ketamine (80 mg/kg) (Axience) and xylazine (8 mg/kg) (Axience). Pupils were dilated with 0.5% tropicamide (CSP) and 5% neosynephrine (CSP, France). Corneal analgesia was performed by applying chlorhydrate oxybuprocaine (CSP). Eyes were proposed using bulldog forceps (FST, 18039–45). Recording small gold loop electrode contacting the cornea through a layer of Lubrithal (Centravet) was used to record the retinal response, with needle electrode placed in the head and back used as the reference and ground electrodes, respectively. Body temperature was maintained at 37˚C with a heating pad. Electroretinograms (ERGs) were obtained simultaneously from both eyes, the light stimulus was provided by Led in a Ganzfeld stimulator (Espion, Diagnosys LLC). Scotopic responses were measured in darkness, during flash stimulation (0.003 to 10 cd.s/m^2), a flash duration of 4 ms. Scotopic ERG response is the mean of five responses. Photopic cone ERGs were performed on a rod-suppressing background after 5 min of light adaptation (2 cd.s/m^2); recordings were obtained at light intensities of 10 cd.s/m^2. Photopic ERG response is the mean of ten responses. Responses were amplified and filtered (1 Hz-low and 300 Hz-high cutoff filters) with a one-channel DC-/AC- amplifier.

Eye fundoscopy

Eye fundoscopy was carried out using (MicronIV, Phoenix Research Labs, USA). Pupils were dilated with 0.5% tropicamide (CSP) and 5% neosynephrine (CSP). Next, mice were anesthetized with 5% isoflurane inhalation (Axience) and maintained at 2% Lubrithal (Centravet) was used to protect the cornea during acquisition. To visualize blood vessels in vivo, an 0.1% sodium fluorescein tracer (Serb) was injected intraperitoneal and eye fundoscopy was carried out.

Whole-mount labeling and tissue clearing

EyeDISCO

De-pigmentation

For samples E12-E16, samples were fixed o/n at 4˚C in 4% PFA. The embryos were then de-hydrated in succeeding baths of methanol for 2 hr each at RT (40% 1XPBS, 80% distilled water (dH_2O), 100% methanol). Samples were then placed o/n in a de-pigmentation solution of methanol containing 11% H_2O_2 (VWR, 216763) at 70 rpm exposed to an 11W warm white Light-Emitting Diode (LED) (3000˚ Kelvin).

For samples E16-P7, samples were processed as described above. However, the de-pigmentation solution was refreshed twice per day to ensure full activity. For complete de-pigmentation approximately 2 days were required.

For samples P7-Adult, samples were processed as described above. For complete de-pigmentation approximately 5 days were required.

Once completely de-pigmented, samples were gently re-hydrated in 2 hr baths at RT (100% methanol, 80% dH_2O, 40% 1XPBS, 1XPBS). Samples were kept at 4˚C for further processing.

Whole-mount immunostaining

For eyes after P15, an incision was done in the cornea (1/4 of the perimeter). Samples were then permeabilized in the blocking solution (0.5% Triton-X100, 5% donkey normal serum, 1XPBS, 0.1 g/L thimerosal) for 1 day at RT on agitation. For immunostaining, samples were incubated with the primary antibodies (see ***Supplementary file 1***) in a solution containing: 0.5% Triton-X100, 5% donkey normal serum, 20% Dimethyl Sulfoxide, 1XPBS, 0.1 g/L thimerosal. The primary antibody solution (see ***Supplementary file 1***) was incubated for 7 days at RT. The samples were then washed for 1 day (6 changes) in PBST (0.5% Triton-X-100, 1XPBS, 0.1 g/L thimerosal). The secondary antibody (see ***Supplementary file 1***) was diluted in the same solution as for the primary and passed through a 0.22 µm filter and incubated for 2 days in solution at RT under agitation. In some cases, samples were counterstained with the nuclear marker TO-PRO-3 (Life Technologies, T3605, 1:300). The samples were then washed for 6 times during 1 day in PBST, and 2 washes of 1XPBS prior to storing the samples in the dark at 4˚C until clearing.

Agarose embedding

Embryos (E12) and eyes were embedded in 1.5% agarose (Roth) in 1X TAE (Life Technologies) prior to tissue clearing.

Tissue clearing

The iDISCO+ protocol was adapted. All steps were carried out in the dark in a fume hood by agitation at 10 rpm (SB3 tube rotator, Stuart) at RT using 15 ml centrifuge tubes (TPP). Following embedding, eyes were placed in 20% methanol diluted in 1XPBS o/n. The next day, eyes were de-hydrated in succeeding baths of methanol for 2 hr (40% 1XPBS, 60% 1XPBS, 80% dH_2O, 100% methanol). The eyes were then placed in a solution containing 2/3 Dichloromethane (DCM, Sigma) 1/3 methanol o/n. The next day, eyes were placed in DCM for 30 min prior to being immersed in the imaging medium, Di-benzyl Ether (DBE, Sigma). The next day, samples were stored in individual light-absorbing glass vials (Roth) at RT.

3D imaging

Light sheet microscopy

All imaging was carried out as previously described ***Belle et al. (2017)***; ***Belle et al. (2014)***. Acquisitions were performed by using an ultramicroscope I (LaVision BioTec, Miltenyi Biotec) with the

ImspectorPro software (LaVision BioTec, Miltenyi Biotec, 5.1.328 version). The light sheet was generated by a laser (wavelength 488, 561, 64, or 780 nm, Coherent Sapphire Laser, LaVision BioTec, Miltenyi Biotec) and a cylindrical lens for large working distance. A binocular stereomicroscope (Olympus, MXV10) with a 2x objective (Olympus, MVPLAPO) was used at different magnifications (0.63x, 1x, 1.25x, 1.6x, 2x, 2.5x, 3.2x, 4x, and 5x). Samples were placed in an imaging reservoir made of 100% quartz (LaVision BioTec, Miltenyi Biotec) filled with DBE and illuminated from the side by the laser light. A Zyla SCMOS camera (Andor, Oxford Instrument, 2,048 × 2048 pixels size) was used to acquire images. The step size between each image was fixed at 1 or 2 µm (NA = 0.5, 150 ms time exposure). All tiff images are generated in 16-bit.

Confocal microscopy

For 3D imaging using the confocal microscope (Olympus, FV1000), homemade chambers were created. Two ¼" stainless steel washers were stacked and glued (Best Klebstoffe) on a SuperFrost slide (ThermoScientific) and left to dry o/n at RT. The next day, the washers were sealed using dental cement (Dentalon Plus, R010024) and were left to dry for 2 hr at RT. The samples were then placed in the chambers and covered with DBE, a coverslip was then placed to secure the samples and was sealed using dental cement and left to dry for 2 hr at RT prior to imaging. For imaging, a scanning upright confocal microscope (Olympus, FV1000) was used with a 25X objective (Olympus, XLPLN25XSVMP2, NA = 1.0, WD = 4 mm).

Image processing

3D rendering of light sheet and confocal stacks were converted to an Imaris file (.ims) using ImarisFileConverter (Bitplane, 9.1.2 version or 9.2.1 version) and then visualized using the Imaris x64 software (Bitplane, 9.1.2 version or 9.2.1 version).

To isolate the visual projections of E16 embryos labeled for Tag1 (R and D systems, see ***Supplementary file 1***), a manual segmentation of the retina, optic nerve, optic chiasm, and optic tracts was carried out. Optic nerve volumes were calculated by creating an automatic segmentation (x = 545, y = 300, z = 200, surface detail = 3.02 µm, automatic threshold) and volumes were extracted from the surface. For analyzing aberrant RGC projections, a manual segmentation was carried out to isolate RGC projections. This mask was then extracted by adjusting the outside pixels to 0 (black). To further isolate aberrant RGC projections, normal projections (inside the retina) were manually segmented and outside pixels were set to 0. Aberrant RGC projections were isolated by excluding normal RGC projections and a mask was generated and pseudo-colored.

For P15 and 1 month CTB-traced mouse brains, visual nuclei were segmented as follows. For optic nerves the surface was extracted by creating an automatic surface in a region of x = 545, y = 300, z = 200, surface detail = 8.13 µm and automatic threshold. For optic tracts, x = 526, y = 437, z = 797, surface detail = 8.13 µm and automatic threshold. For contra-lateral superior colliculi, x = 640, y = 640, z = 640, surface detail = 8.13 µm and automatic threshold. For segmentation of the optic nerve, optic tracts and contra-lateral superior colliculi, the semi-automatic surface was used with a surface details fixed at 8.13 µm and an automatic thresholding. For the contralateral and ipsilateral lateral geniculate nuclei, an automatic segmentation was applied using a set voxel box (x = 337, y = 265, z = 761), surface detail = 2.00 µm. The medial terminal nuclei were segmented using automatic segmentation using a set voxel box (x = 262, y = 232, z = 540) with a surface detail = 2.00 µm. Ipsilateral superior colliculi were manually segmented using the 'isoline' tool, with a reduced density at 10%. Once the structure was segmented, a surface was generated and the volume was extracted for further analysis.

For adult retinas, rosette-like structures were manually segmented and surfaces were generated. Surfaces were then pseudo-colored and aligned to each to the appropriate dorsal/ventral/nasal/temporal coordinates. To analyze rosette evolution, rosettes and retinas were separately segmented at P15, 1 month and 6 months. A surface was generated and the volume extracted. A ratio of rosette per retinal volume was then calculated.

Movies were generated using the animation tool on Imaris x64 software (Bitplane, version 9.1.2) and movie reconstruction with. tiff series were done using ImageJ (1.50e, Java 1.8.0_60, 64-bit). All movie editing (text and transitions) was done using iMovie (Apple Inc, version 10.1.1).

Statistical analyses

An observer blinded to the experimental conditions performed all the quantifications. All data are represented as mean values ± SEM. Statistical significance was estimated using two-tailed unpaired tests for non-parametric tendencies (Kruskall-Wallis or Mann-Whitney), two-way ANOVA and Bonferroni's multiple comparison test. *=p < 0.05; **=p < 0.01; ***=p < 0.001, ****=p < 0.0001. All statistical measurements were carried out using GraphPad Prism 7.

Acknowledgements

We thank Dr Alexandra Rebsam for helpful discussions. We thank the phenotyping facility, in particular Julie Dégardin and Manuel Simonutti for assistance with the eye fundoscopy and electroretinograms. We are also thankful to all the dedicated staff of the Vision Institute animal house facility and to Alexis Guerin in particular. We thank Dr Stephane Fouquet (Vision Institute Imaging Facility) for technical assistance. We thank Dr Anton Berns for providing the *Dcc* conditional knockout line. The *Dkk3:cre* line was provided by the RIKEN BRC through the National Bio-Resource Project of the MEXT, Japan. This work was supported by a grant from the LABEX LIFESENSES (reference ANR-10-LABX-65) supported by French state funds managed by the Agence Nationale de la Recherche (ANR) within the Investissements d'Avenir programme under reference ANR-11-IDEX-0004–02 (AC). The funders had no role in study design, data collection and analysis, decision to publish, or preparation of the manuscript.

Additional information

Funding

Funder	Grant reference number	Author
Fondation ARC pour la Recherche sur le Cancer	DOC20190508735	Robin J Vigouroux
Agence Nationale de la Recherche	ANR-11-IDEX-0004-02	Alain Chédotal
Agence Nationale de la Recherche	ANR-10-LABX-65	Alain Chédotal

The funders had no role in study design, data collection and interpretation, or the decision to submit the work for publication.

Author contributions

Robin J Vigouroux, Data curation, Formal analysis, Investigation, Visualization, Methodology; Quénol Cesar, Data curation; Alain Chédotal, Conceptualization, Formal analysis, Supervision, Funding acquisition, Validation, Investigation, Methodology, Project administration; Kim Tuyen Nguyen-Ba-Charvet, Conceptualization, Data curation, Formal analysis, Supervision, Validation, Investigation, Methodology, Project administration

Author ORCIDs

Robin J Vigouroux https://orcid.org/0000-0002-3217-895X
Alain Chédotal https://orcid.org/0000-0001-7577-3794
Kim Tuyen Nguyen-Ba-Charvet https://orcid.org/0000-0001-5398-0872

Ethics

Animal experimentation: All experiments were designed using the 3R rule: to reduce, refine, and replace the use of animals. All animal procedures were carried out according to approved institutional guidelines (#B-75-12-02) of the Institut de la Vision. The protocol was approved by the Sorbonne University ethic committee (Charles Darwin)(Permit Number: 9571). In cases of animal handling, experiments were performed to minimize animal stress and suffering.

Decision letter and Author response
Decision letter https://doi.org/10.7554/eLife.51275.sa1
Author response https://doi.org/10.7554/eLife.51275.sa2

Additional files

Supplementary files

- Supplementary file 1. List of primary and secondary antibodies used for the study.
- Supplementary file 2. List of primary antibodies validated with the EyeDISCO clearing protocol.
- Supplementary file 3. Sequencing of Phosphodiesterase 6b, cGMP, rod receptor, beta polypeptide (Pde6b) mutations in the *Dcc* cKO and *Dcc kanga* mice.
- Supplementary file 4. Key resources table.
- Transparent reporting form

Data availability

All data generated or analysed during this study are included in the manuscript and supporting files. All source files are provided.

References

Akin O, Zipursky SL. 2016. Frazzled promotes growth cone attachment at the source of a netrin gradient in the *Drosophila* visual system. *eLife* **5**:e20762. DOI: https://doi.org/10.7554/eLife.20762, PMID: 27743477

Alexander RA, Cree IA, Foss AJ. 1996. The immunoalkaline phosphatase technique in immunohistochemistry: the effect of permanganate-oxalate melanin bleaching upon four final reaction products. *British Journal of Biomedical Science* **53**:170–171. PMID: 8757696

Applebury ML, Antoch MP, Baxter LC, Chun LLY, Falk JD, Farhangfar F, Kage K, Krzystolik MG, Lyass LA, Robbins JT. 2000. The murine cone photoreceptor. *Neuron* **27**:513–523. DOI: https://doi.org/10.1016/S0896-6273(00)00062-3

Austin CP, Feldman DE, Ida JA, Cepko CL. 1995. Vertebrate retinal ganglion cells are selected from competent progenitors by the action of notch. *Development* **121**:3637–3650. PMID: 8582277

Bao ZZ. 2008. Intraretinal projection of retinal ganglion cell axons as a model system for studying axon navigation. *Brain Research* **1192**:165–177. DOI: https://doi.org/10.1016/j.brainres.2007.01.116, PMID: 17320832

Belle M, Godefroy D, Dominici C, Heitz-Marchaland C, Zelina P, Hellal F, Bradke F, Chédotal A. 2014. A simple method for 3D analysis of immunolabeled axonal tracts in a transparent nervous system. *Cell Reports* **9**:1191–1201. DOI: https://doi.org/10.1016/j.celrep.2014.10.037, PMID: 25456121

Belle M, Godefroy D, Couly G, Malone SA, Collier F, Giacobini P, Chédotal A. 2017. Tridimensional visualization and analysis of early human development. *Cell* **169**:161–173. DOI: https://doi.org/10.1016/j.cell.2017.03.008, PMID: 28340341

Bernstein CS, Anderson MT, Gohel C, Slater K, Gross JM, Agarwala S. 2018. The cellular bases of choroid fissure formation and closure. *Developmental Biology* **440**:137–151. DOI: https://doi.org/10.1016/j.ydbio.2018.05.010, PMID: 29803644

Birgbauer E, Cowan CA, Sretavan DW, Henkemeyer M. 2000. Kinase independent function of EphB receptors in retinal axon pathfinding to the optic disc from dorsal but not ventral retina. *Development* **127**:1231–1241. PMID: 10683176

Borst A, Euler T. 2011. Seeing things in motion: models, circuits, and mechanisms. *Neuron* **71**:974–994. DOI: https://doi.org/10.1016/j.neuron.2011.08.031, PMID: 21943597

Cai Z, Tao C, Li H, Ladher R, Gotoh N, Feng GS, Wang F, Zhang X. 2013. Deficient FGF signaling causes optic nerve dysgenesis and ocular coloboma. *Development* **140**:2711–2723. DOI: https://doi.org/10.1242/dev.089987, PMID: 23720040

Cai R, Pan C, Ghasemigharagoz A, Todorov MI, Förstera B, Zhao S, Bhatia HS, Parra-Damas A, Mrowka L, Theodorou D, Rempfler M, Xavier ALR, Kress BT, Benakis C, Steinke H, Liebscher S, Bechmann I, Liesz A, Menze B, Kerschensteiner M, et al. 2019. Panoptic imaging of transparent mice reveals whole-body neuronal projections and skull-meninges connections. *Nature Neuroscience* **22**:317–327. DOI: https://doi.org/10.1038/s41593-018-0301-3, PMID: 30598527

Castets M, Broutier L, Molin Y, Brevet M, Chazot G, Gadot N, Paquet A, Mazelin L, Jarrosson-Wuilleme L, Scoazec J-Y, Bernet A, Mehlen P. 2012. DCC constrains tumour progression via its dependence receptor activity. *Nature* **482**:534–537. DOI: https://doi.org/10.1038/nature10708

Chang B, Hawes NL, Hurd RE, Davisson MT, Nusinowitz S, Heckenlively JR. 2002. Retinal degeneration mutants in the mouse. *Vision Research* **42**:517–525. DOI: https://doi.org/10.1016/S0042-6989(01)00146-8

Chatzopoulou E, Miguez A, Savvaki M, Levasseur G, Muzerelle A, Muriel MP, Goureau O, Watanabe K, Goutebroze L, Gaspar P, Zalc B, Karagogeos D, Thomas JL. 2008. Structural requirement of TAG-1 for retinal ganglion cell axons and myelin in the mouse optic nerve. *Journal of Neuroscience* **28**:7624–7636. DOI: https://doi.org/10.1523/JNEUROSCI.1103-08.2008, PMID: 18650339

Corset V, Nguyen-Ba-Charvet KT, Forcet C, Moyse E, Chédotal A, Mehlen P. 2000. Netrin-1-mediated axon outgrowth and cAMP production requires interaction with Adenosine A2b receptor. *Nature* **407**:747–750. DOI: https://doi.org/10.1038/35037600, PMID: 11048721

D'Cruz PM, Yasumura D, Weir J, Matthes MT, Abderrahim H, LaVail MM, Vollrath D. 2000. Mutation of the receptor tyrosine kinase gene mertk in the retinal dystrophic RCS rat. *Human Molecular Genetics* **9**:645–651. DOI: https://doi.org/10.1093/hmg/9.4.645, PMID: 10699188

da Silva RV, Johannssen HC, Wyss MT, Roome RB, Bourojeni FB, Stifani N, Marsh APL, Ryan MM, Lockhart PJ, Leventer RJ, Richards LJ, Rosenblatt B, Srour M, Weber B, Zeilhofer HU, Kania A. 2018. DCC is required for the development of nociceptive topognosis in mice and humans. *Cell Reports* **22**:1105–1114. DOI: https://doi.org/10.1016/j.celrep.2018.01.004, PMID: 29386099

Dakubo GD, Wang YP, Mazerolle C, Campsall K, McMahon AP, Wallace VA. 2003. Retinal ganglion cell-derived sonic hedgehog signaling is required for optic disc and stalk neuroepithelial cell development. *Development* **130**:2967–2980. DOI: https://doi.org/10.1242/dev.00515, PMID: 12756179

Deiner MS, Kennedy TE, Fazeli A, Serafini T, Tessier-Lavigne M, Sretavan DW. 1997. Netrin-1 and DCC mediate axon guidance locally at the optic disc: loss of function leads to optic nerve hypoplasia. *Neuron* **19**:575–589. DOI: https://doi.org/10.1016/S0896-6273(00)80373-6, PMID: 9331350

Depienne C, Cincotta M, Billot S, Bouteiller D, Groppa S, Brochard V, Flamand C, Hubsch C, Meunier S, Giovannelli F, Klebe S, Corvol JC, Vidailhet M, Brice A, Roze E. 2011. A novel DCC mutation and genetic heterogeneity in congenital mirror movements. *Neurology* **76**:260–264. DOI: https://doi.org/10.1212/WNL.0b013e318207b1e0, PMID: 21242494

Dhande OS, Estevez ME, Quattrochi LE, El-Danaf RN, Nguyen PL, Berson DM, Huberman AD. 2013. Genetic dissection of retinal inputs to brainstem nuclei controlling image stabilization. *Journal of Neuroscience* **33**:17797–17813. DOI: https://doi.org/10.1523/JNEUROSCI.2778-13.2013, PMID: 24198370

Dominici C, Moreno-Bravo JA, Puiggros SR, Rappeneau Q, Rama N, Vieugue P, Bernet A, Mehlen P, Chédotal A. 2017. Floor-plate-derived netrin-1 is dispensable for commissural axon guidance. *Nature* **545**:350–354. DOI: https://doi.org/10.1038/nature22331, PMID: 28445456

Drager UC. 1985. Birth dates of retinal ganglion cells giving rise to the crossed and uncrossed optic projections in the mouse. *Proc R Soc B Biol Sci* **224**:57–77. DOI: https://doi.org/10.1098/rspb.1985.0021

Fazeli A, Dickinson SL, Hermiston ML, Tighe RV, Steen RG, Small CG, Stoeckli ET, Keino-Masu K, Masu M, Rayburn H, Simons J, Bronson RT, Gordon JI, Tessier-Lavigne M, Weinberg RA. 1997. Phenotype of mice lacking functional deleted in colorectal Cancer (Dcc) gene. *Nature* **386**:796–804. DOI: https://doi.org/10.1038/386796a0, PMID: 9126737

Finger JH, Bronson RT, Harris B, Johnson K, Przyborski SA, Ackerman SL. 2002. The netrin 1 receptors *Unc5h3* and dcc are necessary at multiple choice points for the guidance of corticospinal tract axons. *The Journal of Neuroscience* **22**:10346–10356. DOI: https://doi.org/10.1523/JNEUROSCI.22-23-10346.2002, PMID: 12451134

Flynn E, Ueda K, Auran E, Sullivan JM, Sparrow JR. 2014. Fundus autofluorescence and photoreceptor cell rosettes in mouse models. *Investigative Opthalmology & Visual Science* **55**:5643. DOI: https://doi.org/10.1167/iovs.14-14136

Fothergill T, Donahoo AL, Douglass A, Zalucki O, Yuan J, Shu T, Goodhill GJ, Richards LJ. 2014. Netrin-DCC signaling regulates corpus callosum formation through attraction of pioneering axons and by modulating Slit2-mediated repulsion. *Cerebral Cortex* **24**:1138–1151. DOI: https://doi.org/10.1093/cercor/bhs395, PMID: 23302812

Genové G, Mollick T, Johansson K. 2014. Photoreceptor degeneration, structural remodeling and glial activation: a morphological study on a genetic mouse model for pericyte deficiency. *Neuroscience* **279**:269–284. DOI: https://doi.org/10.1016/j.neuroscience.2014.09.013, PMID: 25224828

Godement P, Salaün J, Imbert M. 1984. Prenatal and postnatal development of retinogeniculate and retinocollicular projections in the mouse. *Journal of Comparative Neurology* **230**:552–575. DOI: https://doi.org/10.1002/cne.902300406, PMID: 6520251

Goldberg S. 1977. Unidirectional, bidirectional and random growth of embryonic optic axons. *Experimental Eye Research* **25**:399–404. DOI: https://doi.org/10.1016/0014-4835(77)90107-5, PMID: 590380

Goldman JS, Ashour MA, Magdesian MH, Tritsch NX, Harris SN, Christofi N, Chemali R, Stern YE, Thompson-Steckel G, Gris P, Glasgow SD, Grutter P, Bouchard JF, Ruthazer ES, Stellwagen D, Kennedy TE. 2013. Netrin-1 promotes excitatory synaptogenesis between cortical neurons by initiating synapse assembly. *Journal of Neuroscience* **33**:17278–17289. DOI: https://doi.org/10.1523/JNEUROSCI.1085-13.2013, PMID: 24174661

Halfter W, Reckhaus W, Kroger S. 1987. Nondirected axonal growth on basal lamina from avian embryonic neural retina. *The Journal of Neuroscience* **7**:3712–3722. DOI: https://doi.org/10.1523/JNEUROSCI.07-11-03712.1987

Halfter W, Fua CS. 1987. Immunohistochemical localization of Laminin, neural cell adhesion molecule, collagen type IV and T-61 antigen in the embryonic retina of the japanese quail by in vivo injection of antibodies. *Cell and Tissue Research* **249**:487–496. DOI: https://doi.org/10.1007/BF00217320, PMID: 3664600

Hardy H, Prendergast JGD, Patel A, Dutta S, Trejo-Reveles V, Kroeger H, Yung AR, Goodrich LV, Brooks B, Sowden JC, Rainger J. 2019. Detailed analysis of chick optic fissure closure reveals Netrin-1 as an essential mediator of epithelial fusion. *eLife* **8**:e43877. DOI: https://doi.org/10.7554/eLife.43877

Henning Y, Osadnik C, Malkemper EP. 2019. EyeCi: optical clearing and imaging of immunolabeled mouse eyes using light-sheet fluorescence microscopy. *Experimental Eye Research* **180**:137–145. DOI: https://doi.org/10.1016/j.exer.2018.12.001, PMID: 30578790

Hindges R, McLaughlin T, Genoud N, Henkemeyer M, O'Leary D. 2002. EphB forward signaling controls directional branch extension and arborization required for dorsal-ventral retinotopic mapping. *Neuron* **35**:475–487. DOI: https://doi.org/10.1016/S0896-6273(02)00799-7, PMID: 12165470

Hong K, Hinck L, Nishiyama M, Poo MM, Tessier-Lavigne M, Stein E. 1999. A ligand-gated association between cytoplasmic domains of UNC5 and DCC family receptors converts netrin-induced growth cone attraction to repulsion. *Cell* **97**:927–941. DOI: https://doi.org/10.1016/S0092-8674(00)80804-1, PMID: 10399920

Horn KE, Glasgow SD, Gobert D, Bull SJ, Luk T, Girgis J, Tremblay ME, McEachern D, Bouchard JF, Haber M, Hamel E, Krimpenfort P, Murai KK, Berns A, Doucet G, Chapman CA, Ruthazer ES, Kennedy TE. 2013. DCC expression by neurons regulates synaptic plasticity in the adult brain. *Cell Reports* **3**:173–185. DOI: https://doi.org/10.1016/j.celrep.2012.12.005, PMID: 23291093

Iwai-Takekoshi L, Ramos A, Schaler A, Weinreb S, Blazeski R, Mason C. 2016. Retinal pigment epithelial integrity is compromised in the developing albino mouse retina. *Journal of Comparative Neurology* **524**:3696–3716. DOI: https://doi.org/10.1002/cne.24025, PMID: 27097562

Jamuar SS, Schmitz-Abe K, D'Gama AM, Drottar M, Chan WM, Peeva M, Servattalab S, Lam AN, Delgado MR, Clegg NJ, Zayed ZA, Dogar MA, Alorainy IA, Jamea AA, Abu-Amero K, Griebel M, Ward W, Lein ES, Markianos K, Barkovich AJ, et al. 2017. Biallelic mutations in human DCC cause developmental split-brain syndrome. *Nature Genetics* **49**:606–612. DOI: https://doi.org/10.1038/ng.3804, PMID: 28250456

Jarjour AA, Bull SJ, Almasieh M, Rajasekharan S, Baker KA, Mui J, Antel JP, Di Polo A, Kennedy TE. 2008. Maintenance of axo-oligodendroglial paranodal junctions requires DCC and netrin-1. *Journal of Neuroscience* **28**:11003–11014. DOI: https://doi.org/10.1523/JNEUROSCI.3285-08.2008, PMID: 18945908

Jin Z, Zhang J, Klar A, Chédotal A, Rao Y, Cepko CL, Bao ZZ. 2003. Irx4-mediated regulation of Slit1 expression contributes to the definition of early axonal paths inside the retina. *Development* **130**:1037–1048. DOI: https://doi.org/10.1242/dev.00326, PMID: 12571096

Kamachi Y, Uchikawa M, Collignon J, Lovell-Badge R, Kondoh H. 1998. Involvement of Sox1, 2 and 3 in the early and subsequent molecular events of Lens induction. *Development* **125**:2521–2532. PMID: 9609835

Kay JN, De la Huerta I, Kim I-J, Zhang Y, Yamagata M, Chu MW, Meister M, Sanes JR. 2011. Retinal ganglion cells with distinct directional preferences differ in molecular identity, structure, and central projections. *Journal of Neuroscience* **31**:7753–7762. DOI: https://doi.org/10.1523/JNEUROSCI.0907-11.2011

Keino-Masu K, Masu M, Hinck L, Leonardo ED, Chan SS, Culotti JG, Tessier-Lavigne M. 1996. Deleted in colorectal Cancer (DCC) encodes a netrin receptor. *Cell* **87**:175–185. DOI: https://doi.org/10.1016/S0092-8674(00)81336-7, PMID: 8861902

Klingberg A, Hasenberg A, Ludwig-Portugall I, Medyukhina A, Männ L, Brenzel A, Engel DR, Figge MT, Kurts C, Gunzer M. 2017. Fully automated evaluation of total glomerular number and capillary tuft size in Nephritic kidneys using lightsheet microscopy. *Journal of the American Society of Nephrology* **28**:452–459. DOI: https://doi.org/10.1681/ASN.2016020232, PMID: 27487796

Krimpenfort P, Song J-Y, Proost N, Zevenhoven J, Jonkers J, Berns A. 2012. Deleted in colorectal carcinoma suppresses metastasis in p53-deficient mammary tumours. *Nature* **482**:538–541. DOI: https://doi.org/10.1038/nature10790

Kuwabara T, Weidman TA. 1974. Development of the prenatal rat retina. *Investigative Ophthalmology* **13**:725–739. PMID: 4412789

Kwong JMK, Caprioli J, Piri N. 2010. RNA binding protein with multiple splicing: a new marker for retinal ganglion cells. *Investigative Opthalmology & Visual Science* **51**:1052. DOI: https://doi.org/10.1167/iovs.09-4098

Laumonnerie C, Da Silva RV Kania A, Wilson SI. 2014. Netrin 1 and dcc signalling are required for confinement of central axons within the central nervous system. *Development* **141**:594–603. DOI: https://doi.org/10.1242/dev.099606, PMID: 24449837

Li S, He Q, Wang H, Tang X, Ho KW, Gao X, Zhang Q, Shen Y, Cheung A, Wong F, Wong YH, Ip NY, Jiang L, Yung WH, Liu K. 2015. Injured adult retinal axons with pten and Socs3 co-deletion reform active synapses with suprachiasmatic neurons. *Neurobiology of Disease* **73**:366–376. DOI: https://doi.org/10.1016/j.nbd.2014.09.019, PMID: 25448764

Lilley BN, Sabbah S, Hunyara JL, Gribble KD, Al-Khindi T, Xiong J, Wu Z, Berson DM, Kolodkin AL. 2019. Genetic access to neurons in the accessory optic system reveals a role for Sema6A in midbrain circuitry mediating motion perception. *Journal of Comparative Neurology* **527**:282–296. DOI: https://doi.org/10.1002/cne.24507, PMID: 30076594

Liu IS, Chen JD, Ploder L, Vidgen D, van der Kooy D, Kalnins VI, McInnes RR. 1994. Developmental expression of a novel murine homeobox gene (Chx10): Evidence for roles in determination of the neuroretina and inner nuclear layer. *Neuron* **13**:377–393. DOI: https://doi.org/10.1016/0896-6273(94)90354-9, PMID: 7914735

Llambi F, Lourenço FC, Gozuacik D, Guix C, Pays L, Del Rio G, Kimchi A, Mehlen P. 2005. The dependence receptor UNC5H2 mediates apoptosis through DAP-kinase. *The EMBO Journal* **24**:1192–1201. DOI: https://doi.org/10.1038/sj.emboj.7600584, PMID: 15729359

Ly A, Nikolaev A, Suresh G, Zheng Y, Tessier-Lavigne M, Stein E. 2008. DSCAM is a netrin receptor that collaborates with DCC in mediating turning responses to netrin-1. *Cell* **133**:1241–1254. DOI: https://doi.org/10.1016/j.cell.2008.05.030, PMID: 18585357

Manitt C, Nikolakopoulou AM, Almario DR, Nguyen SA, Cohen-Cory S. 2009. Netrin participates in the development of retinotectal synaptic connectivity by modulating axon arborization and synapse formation in the developing brain. *Journal of Neuroscience* **29**:11065–11077. DOI: https://doi.org/10.1523/JNEUROSCI.0947-09.2009, PMID: 19741113

Manitt C, Eng C, Pokinko M, Ryan RT, Torres-Berrío A, Lopez JP, Yogendran SV Daubaras MJ, Grant A, Schmidt ER, Tronche F, Krimpenfort P, Cooper HM, Pasterkamp RJ, Kolb B, Turecki G, Wong TP, Nestler EJ, Giros B, Flores C. 2013. Dcc orchestrates the development of the prefrontal cortex during adolescence and is altered in psychiatric patients. *Translational Psychiatry* **3**:e338. DOI: https://doi.org/10.1038/tp.2013.105, PMID: 24346136

Marcos S, Nieto-Lopez F, Sandonìs A, Cardozo MJ, Di Marco F, Esteve P, Bovolenta P. 2015. Secreted frizzled related proteins modulate pathfinding and fasciculation of mouse retina ganglion cell axons by direct and indirect mechanisms. *Journal of Neuroscience* **35**:4729–4740. DOI: https://doi.org/10.1523/JNEUROSCI.3304-13.2015, PMID: 25788689

Marmorstein AD. 2001. The polarity of the retinal pigment epithelium. *Traffic* **2**:867–872. DOI: https://doi.org/10.1034/j.1600-0854.2001.21202.x, PMID: 11737824

Marsh AP, Heron D, Edwards TJ, Quartier A, Galea C, Nava C, Rastetter A, Moutard ML, Anderson V, Bitoun P, Bunt J, Faudet A, Garel C, Gillies G, Gobius I, Guegan J, Heide S, Keren B, Lesne F, Lukic V, et al. 2017. Mutations in DCC cause isolated agenesis of the corpus callosum with incomplete penetrance. *Nature Genetics* **49**:511–514. DOI: https://doi.org/10.1038/ng.3794, PMID: 28250454

Mazelin L, Bernet A, Bonod-Bidaud C, Pays L, Arnaud S, Gespach C, Bredesen DE, Scoazec JY, Mehlen P. 2004. Netrin-1 controls colorectal tumorigenesis by regulating apoptosis. *Nature* **431**:80–84. DOI: https://doi.org/10.1038/nature02788, PMID: 15343335

Mears AJ, Kondo M, Swain PK, Takada Y, Bush RA, Saunders TL, Sieving PA, Swaroop A. 2001. Nrl is required for rod photoreceptor development. *Nature Genetics* **29**:447–452. DOI: https://doi.org/10.1038/ng774, PMID: 11694879

Mehalow AK, Kameya S, Smith RS, Hawes NL, Denegre JM, Young JA, Bechtold L, Haider NB, Tepass U, Heckenlively JR, Chang B, Naggert JK, Nishina PM. 2003. CRB1 is essential for external limiting membrane integrity and photoreceptor morphogenesis in the mammalian retina. *Human Molecular Genetics* **12**:2179–2189. DOI: https://doi.org/10.1093/hmg/ddg232, PMID: 12915475

Mehlen P, Rabizadeh S, Snipas SJ, Assa-Munt N, Salvesen GS, Bredesen DE. 1998. The DCC gene product induces apoptosis by a mechanism requiring receptor proteolysis. *Nature* **395**:801–804. DOI: https://doi.org/10.1038/27441, PMID: 9796814

Mehlen P, Delloye-Bourgeois C, Chédotal A. 2011. Novel roles for slits and netrins: axon guidance cues as anticancer targets? *Nature Reviews Cancer* **11**:188–197. DOI: https://doi.org/10.1038/nrc3005, PMID: 21326323

Meyer-Franke A, Kaplan MR, Pfrieger FW, Barres BA. 1995. Characterization of the signaling interactions that promote the survival and growth of developing retinal ganglion cells in culture. *Neuron* **15**:805–819. DOI: https://doi.org/10.1016/0896-6273(95)90172-8, PMID: 7576630

Morcillo J, Martínez-Morales JR, Trousse F, Fermin Y, Sowden JC, Bovolenta P. 2006. Proper patterning of the optic fissure requires the sequential activity of BMP7 and SHH. *Development* **133**:3179–3190. DOI: https://doi.org/10.1242/dev.02493, PMID: 16854970

Moreno-Bravo JA, Puiggros SR, Blockus H, Dominici C, Zelina P, Mehlen P, Chédotal A. 2018. Commissural neurons transgress the CNS/PNS boundary in absence of ventricular zone-derived netrin-1. *Development* **145**: dev159400 . DOI: https://doi.org/10.1242/dev.159400

Moreno-Bravo JA, Roig Puiggros S, Mehlen P, Chédotal A. 2019. Synergistic activity of Floor-Plate- and Ventricular-Zone-Derived Netrin-1 in spinal cord commissural axon guidance. *Neuron* **101**:625–634. DOI: https://doi.org/10.1016/j.neuron.2018.12.024, PMID: 30661739

Morin LP, Studholme KM. 2014. Retinofugal projections in the mouse. *Journal of Comparative Neurology* **522**: 3733–3753. DOI: https://doi.org/10.1002/cne.23635, PMID: 24889098

Murcia-Belmonte V, Coca Y, Vegar C, Negueruela S, de Juan Romero C, Valiño AJ, Sala S, DaSilva R, Kania A, Borrell V, Martinez LM, Erskine L, Herrera E. 2019. A Retino-retinal projection guided by Unc5c emerged in species with retinal waves. *Current Biology* **29**:1149–1160. DOI: https://doi.org/10.1016/j.cub.2019.02.052, PMID: 30905607

Orchard GE. 2007. Use of heat provides a fast and efficient way to undertake melanin bleaching with dilute hydrogen peroxide. *British Journal of Biomedical Science* **64**:89–91. DOI: https://doi.org/10.1080/09674845.2007.11978097, PMID: 17633145

Ortín-Martínez A, Nadal-Nicolás FM, Jiménez-López M, Alburquerque-Béjar JJ, Nieto-López L, García-Ayuso D, Villegas-Pérez MP, Vidal-Sanz M, Agudo-Barriuso M. 2014. Number and distribution of mouse retinal cone photoreceptors: differences between an albino (Swiss) and a pigmented (C57/BL6) strain. *PLOS ONE* **9**: e102392. DOI: https://doi.org/10.1371/journal.pone.0102392, PMID: 25029531

Osterhout JA, Stafford BK, Nguyen PL, Yoshihara Y, Huberman AD. 2015. Contactin-4 mediates axon-target specificity and functional development of the accessory optic system. *Neuron* **86**:985–999. DOI: https://doi.org/10.1016/j.neuron.2015.04.005, PMID: 25959733

Otteson DC, Shelden E, Jones JM, Kameoka J, Hitchcock PF. 1998. Pax2 expression and retinal morphogenesis in the normal and krd mouse. *Developmental Biology* **193**:209–224. DOI: https://doi.org/10.1006/dbio.1997.8794, PMID: 9473325

Pan C, Cai R, Quacquarelli FP, Ghasemigharagoz A, Lourbopoulos A, Matryba P, Plesnila N, Dichgans M, Hellal F, Ertürk A. 2016. Shrinkage-mediated imaging of entire organs and organisms using uDISCO. *Nature Methods* **13**:859–867. DOI: https://doi.org/10.1038/nmeth.3964, PMID: 27548807

Pan C, Schoppe O, Parra-Damas A, Cai R, Todorov MI, Gondi G, von Neubeck B, Böğürcü-Seidel N, Seidel S, Sleiman K, Veltkamp C, Förstera B, Mai H, Rong Z, Trompak O, Ghasemigharagoz A, Reimer MA, Cuesta AM, Coronel J, Jeremias I, et al. 2019. Deep learning reveals Cancer metastasis and therapeutic antibody targeting in the entire body. *Cell* **179**:1661–1676. DOI: https://doi.org/10.1016/j.cell.2019.11.013, PMID: 31835038

Peng J, Ferent J, Li Q, Liu M, Da Silva RV, Zeilhofer HU, Kania A, Zhang Y, Charron F. 2018. Loss of dcc in the spinal cord is sufficient to cause a deficit in lateralized motor control and the switch to a hopping gait. *Developmental Dynamics* **247**:620–629. DOI: https://doi.org/10.1002/dvdy.24549, PMID: 28691197

Pierceall WE, Reale MA, Candia AF, Wright CV, Cho KR, Fearon ER. 1994. Expression of a homologue of the deleted in colorectal Cancer (DCC) gene in the nervous system of developing *Xenopus* embryos. *Developmental Biology* **166**:654–665. DOI: https://doi.org/10.1006/dbio.1994.1345, PMID: 7813784

Poulain FE, Chien CB. 2013. Proteoglycan-mediated axon degeneration corrects pretarget topographic sorting errors. *Neuron* **78**:49–56. DOI: https://doi.org/10.1016/j.neuron.2013.02.005, PMID: 23583107

Raff MC, Barres BA, Burne JF, Coles HS, Ishizaki Y, Jacobson MD. 1993. Programmed cell death and the control of cell survival: lessons from the nervous system. *Science* **262**:695–700. DOI: https://doi.org/10.1126/science.8235590, PMID: 8235590

Raymond SM, Jackson IJ. 1995. The retinal pigmented epithelium is required for development and maintenance of the mouse neural retina. *Current Biology* **5**:1286–1295. DOI: https://doi.org/10.1016/S0960-9822(95)00255-7, PMID: 8574586

Ren XR, Ming GL, Xie Y, Hong Y, Sun DM, Zhao ZQ, Feng Z, Wang Q, Shim S, Chen ZF, Song HJ, Mei L, Xiong WC. 2004. Focal adhesion kinase in netrin-1 signaling. *Nature Neuroscience* **7**:1204–1212. DOI: https://doi.org/10.1038/nn1330, PMID: 15494733

Renier N, Adams EL, Kirst C, Wu Z, Azevedo R, Kohl J, Autry AE, Kadiri L, Umadevi Venkataraju K, Zhou Y, Wang VX, Tang CY, Olsen O, Dulac C, Osten P, Tessier-Lavigne M. 2016. Mapping of Brain Activity by Automated Volume Analysis of Immediate Early Genes. *Cell* **165**:1789–1802. DOI: https://doi.org/10.1016/j.cell.2016.05.007

Rich KA, Figueroa SL, Zhan Y, Blanks JC. 1995. Effects of müller cell disruption on mouse photoreceptor cell development. *Experimental Eye Research* **61**:235–248. DOI: https://doi.org/10.1016/S0014-4835(05)80043-0, PMID: 7556487

Richardson DS, Lichtman JW. 2015. Clarifying tissue clearing. *Cell* **162**:246–257. DOI: https://doi.org/10.1016/j.cell.2015.06.067, PMID: 26186186

Sato S, Inoue T, Terada K, Matsuo I, Aizawa S, Tano Y, Fujikado T, Furukawa T. 2007. Dkk3-Cre BAC transgenic mouse line: a tool for highly efficient gene deletion in retinal progenitor cells. *Genesis* **45**:502–507. DOI: https://doi.org/10.1002/dvg.20318, PMID: 17661397

Schmidt ERE, Brignani S, Adolfs Y, Lemstra S, Demmers J, Vidaki M, Donahoo AS, Lilleväli K, Vasar E, Richards LJ, Karagogeos D, Kolk SM, Pasterkamp RJ. 2014. Subdomain-mediated axon-axon signaling and chemoattraction cooperate to regulate afferent innervation of the lateral habenula. *Neuron* **83**:372–387. DOI: https://doi.org/10.1016/j.neuron.2014.05.036, PMID: 25033181

Serafini T, Kennedy TE, Gaiko MJ, Mirzayan C, Jessell TM, Tessier-Lavigne M. 1994. The netrins define a family of axon outgrowth-promoting proteins homologous to *C. elegans* UNC-6. *Cell* **78**:409–424. DOI: https://doi.org/10.1016/0092-8674(94)90420-0

Shewan D, Dwivedy A, Anderson R, Holt CE. 2002. Age-related changes underlie switch in netrin-1 responsiveness as growth cones advance along visual pathway. *Nature Neuroscience* **5**:955–962. DOI: https://doi.org/10.1038/nn919, PMID: 12352982

Shi M, Zheng MH, Liu ZR, Hu ZL, Huang Y, Chen JY, Zhao G, Han H, Ding YQ. 2010. DCC is specifically required for the survival of retinal ganglion and displaced amacrine cells in the developing mouse retina. *Developmental Biology* **348**:87–96. DOI: https://doi.org/10.1016/j.ydbio.2010.09.013, PMID: 20875817

Silver J. 1984. Studies on the factors that govern directionality of axonal growth in the embryonic optic nerve and at the chiasm of mice. *The Journal of Comparative Neurology* **223**:238–251. DOI: https://doi.org/10.1002/cne.902230207, PMID: 6707250

Silver J, Robb RM. 1979. Studies on the development of the eye cup and optic nerve in normal mice and in mutants with congenital optic nerve aplasia. *Developmental Biology* **68**:175–190. DOI: https://doi.org/10.1016/0012-1606(79)90252-5, PMID: 437315

Srivatsa S, Parthasarathy S, Britanova O, Bormuth I, Donahoo AL, Ackerman SL, Richards LJ, Tarabykin V. 2014. Unc5C and DCC act downstream of Ctip2 and Satb2 and contribute to corpus callosum formation. *Nature Communications* **5**:3708. DOI: https://doi.org/10.1038/ncomms4708, PMID: 24739528

Srour M, Riviere JB, Pham JMT, Dube MP, Girard S, Morin S, Dion PA, Asselin G, Rochefort D, Hince P, Diab S, Sharafaddinzadeh N, Chouinard S, Theoret H, Charron F, Rouleau GA. 2010. Mutations in DCC cause congenital mirror movements. *Science* **328**:592. DOI: https://doi.org/10.1126/science.1186463

Steinbach K, Volkmer H, Schlosshauer B. 2002. Semaphorin 3E/collapsin-5 inhibits growing retinal axons. *Experimental Cell Research* **279**:52–61. DOI: https://doi.org/10.1006/excr.2002.5595, PMID: 12213213

Strauss O. 2005. The retinal pigment epithelium in visual function. *Physiological Reviews* **85**:845–881. DOI: https://doi.org/10.1152/physrev.00021.2004

Stuck MW, Conley SM, Naash MI. 2012. Defects in the Outer Limiting Membrane Are Associated with Rosette Development in the Nrl−/− Retina. *PLOS ONE* **7**:e32484. DOI: https://doi.org/10.1371/journal.pone.0032484

Su J, Haner CV, Imbery TE, Brooks JM, Morhardt DR, Gorse K, Guido W, Fox MA. 2011. Reelin is required for class-specific retinogeniculate targeting. *Journal of Neuroscience* **31**:575–586. DOI: https://doi.org/10.1523/JNEUROSCI.4227-10.2011, PMID: 21228166

Sun LO, Brady CM, Cahill H, Al-Khindi T, Sakuta H, Dhande OS, Noda M, Huberman AD, Nathans J, Kolodkin AL. 2015. Functional Assembly of Accessory Optic System Circuitry Critical for Compensatory Eye Movements. *Neuron* **86**:971–984. DOI: https://doi.org/10.1016/j.neuron.2015.03.064

Susaki EA, Ueda HR. 2016. Whole-body and Whole-Organ clearing and imaging techniques with Single-Cell resolution: toward Organism-Level systems biology in mammals. *Cell Chemical Biology* **23**:137–157. DOI: https://doi.org/10.1016/j.chembiol.2015.11.009, PMID: 26933741

Tainaka K, Murakami TC, Susaki EA, Shimizu C, Saito R, Takahashi K, Hayashi-Takagi A, Sekiya H, Arima Y, Nojima S, Ikemura M, Ushiku T, Shimizu Y, Murakami M, Tanaka KF, Iino M, Kasai H, Sasaoka T, Kobayashi K, Miyazono K, et al. 2018. Chemical landscape for tissue clearing based on hydrophilic reagents. *Cell Reports* **24**:2196–2210. DOI: https://doi.org/10.1016/j.celrep.2018.07.056, PMID: 30134179

Thakar S, Chenaux G, Henkemeyer M. 2011. Critical roles for EphB and ephrin-B bidirectional signalling in retinocollicular mapping. *Nature Communications* **2**:431. DOI: https://doi.org/10.1038/ncomms1445, PMID: 21847105

Thompson H, Camand O, Barker D, Erskine L. 2006. Slit proteins regulate distinct aspects of retinal ganglion cell axon guidance within dorsal and ventral retina. *Journal of Neuroscience* **26**:8082–8091. DOI: https://doi.org/10.1523/JNEUROSCI.1342-06.2006, PMID: 16885222

Tomer R, Ye L, Hsueh B, Deisseroth K. 2014. Advanced CLARITY for rapid and high-resolution imaging of intact tissues. *Nature Protocols* **9**:1682–1697. DOI: https://doi.org/10.1038/nprot.2014.123

van de Pavert SA, Kantardzhieva A, Malysheva A, Meuleman J, Versteeg I, Levelt C, Klooster J, Geiger S, Seeliger MW, Rashbass P, Le Bivic A, Wijnholds J. 2004. Crumbs homologue 1 is required for maintenance of photoreceptor cell polarization and adhesion during light exposure. *Journal of Cell Science* **117**:4169–4177. DOI: https://doi.org/10.1242/jcs.01301, PMID: 15316081

Varadarajan SG, Kong JH, Phan KD, Kao T-J, Panaitof SC, Cardin J, Eltzschig H, Kania A, Novitch BG, Butler SJ. 2017. Netrin1 produced by neural progenitors, not floor plate cells, is required for axon guidance in the spinal cord. *Neuron* **94**:790–799. DOI: https://doi.org/10.1016/j.neuron.2017.03.007

Vigouroux RJ, Belle M, Chédotal A. 2017. Neuroscience in the third dimension: shedding new light on the brain with tissue clearing. *Molecular Brain* **10**:33. DOI: https://doi.org/10.1186/s13041-017-0314-y, PMID: 28728585

Voinescu PE, Kay JN, Sanes JR, Emanuela P, Kay JN, Sanes JR. 2009. Birthdays of retinal amacrine cell subtypes are systematically related to their molecular identity and soma position. *The Journal of Comparative Neurology* **517**:737–750. DOI: https://doi.org/10.1002/cne.22200

Wässle H. 2004. Parallel processing in the mammalian retina. *Nature Reviews Neuroscience* **5**:747–757. DOI: https://doi.org/10.1038/nrn1497, PMID: 15378035

Welniarz Q, Morel MP, Pourchet O, Gallea C, Lamy JC, Cincotta M, Doulazmi M, Belle M, Méneret A, Trouillard O, Ruiz M, Brochard V, Meunier S, Trembleau A, Vidailhet M, Chédotal A, Dusart I, Roze E. 2017. Non cell-autonomous role of DCC in the guidance of the corticospinal tract at the midline. *Scientific Reports* **7**:410. DOI: https://doi.org/10.1038/s41598-017-00514-z, PMID: 28341853

Wu Z, Makihara S, Yam PT, Teo S, Renier N, Balekoglu N, Moreno-Bravo JA, Olsen O, Chédotal A, Charron F, Tessier-Lavigne M. 2019. Long-Range Guidance of Spinal Commissural Axons by Netrin1 and Sonic Hedgehog from Midline Floor Plate Cells. *Neuron* **101**:635–647. DOI: https://doi.org/10.1016/j.neuron.2018.12.025

Yee KT, Simon HH, Tessier-Lavigne M, O'Leary DDM. 1999. Extension of Long Leading Processes and Neuronal Migration in the Mammalian Brain Directed by the Chemoattractant Netrin-1. *Neuron* **24**:607–622. DOI: https://doi.org/10.1016/S0896-6273(00)81116-2

Yonehara K, Shintani T, Suzuki R, Sakuta H, Takeuchi Y, Nakamura-Yonehara K, Noda M. 2008. Expression of SPIG1 Reveals Development of a Retinal Ganglion Cell Subtype Projecting to the Medial Terminal Nucleus in the Mouse. *PLOS ONE* **3**:e1533. DOI: https://doi.org/10.1371/journal.pone.0001533

Yonehara K, Ishikane H, Sakuta H, Shintani T, Nakamura-Yonehara K, Kamiji NL, Usui S, Noda M. 2009. Identification of retinal ganglion cells and their projections involved in central transmission of information about upward and downward image motion. *PLOS ONE* **4**:e4320. DOI: https://doi.org/10.1371/journal.pone.0004320, PMID: 19177171

Yung AR, Druckenbrod NR, Cloutier JF, Wu Z, Tessier-Lavigne M, Goodrich LV. 2018. Netrin-1 confines rhombic Lip-Derived neurons to the CNS. *Cell Reports* **22**:1666–1680. DOI: https://doi.org/10.1016/j.celrep.2018.01.068, PMID: 29444422

Zelina P, Blockus H, Zagar Y, Péres A, Friocourt F, Wu Z, Rama N, Fouquet C, Hohenester E, Tessier-Lavigne M, Schweitzer J, Roest Crollius H, Chédotal A. 2014. Signaling switch of the axon guidance receptor Robo3 during vertebrate evolution. *Neuron* **84**:1258–1272. DOI: https://doi.org/10.1016/j.neuron.2014.11.004, PMID: 25433640

Zhang JH, Zhao YF, He XX, Zhao Y, He ZX, Zhang L, Huang Y, Wang YB, Hu L, Liu L, Yu HL, Xu JH, Lai MM, Zhao DD, Cui L, Guo WX, Xiong WC, Ding YQ, Zhu XJ. 2018. DCC-Mediated Dab1 phosphorylation participates in the Multipolar-to-Bipolar transition of migrating neurons. *Cell Reports* **22**:3598–3611. DOI: https://doi.org/10.1016/j.celrep.2018.03.005, PMID: 29590626

eLIFE elifesciences.org

RESEARCH ARTICLE

Figures and figure supplements

Revisiting the role of Dcc in visual system development with a novel eye clearing method

Robin J Vigouroux *et al*

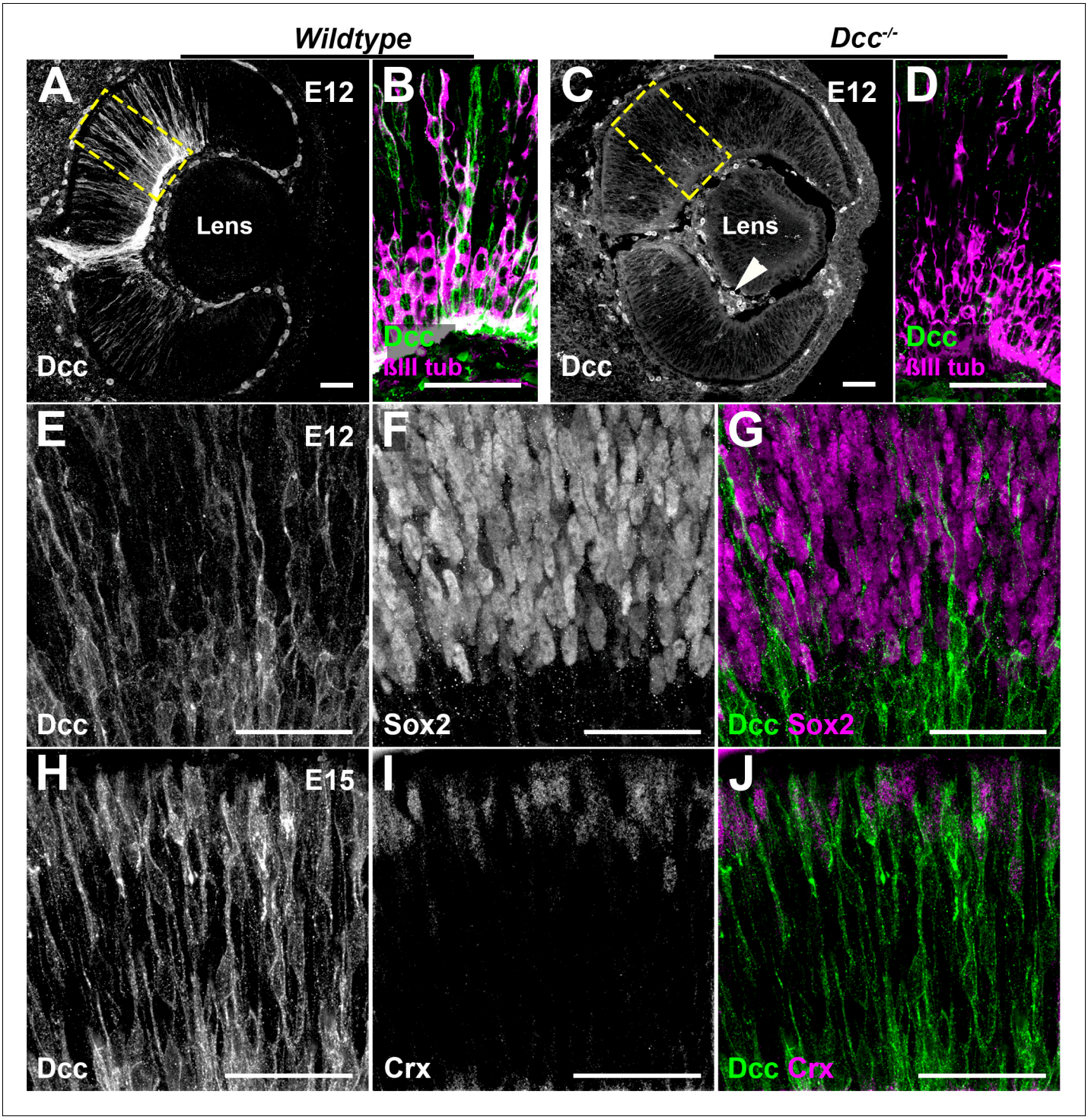

Figure 1—figure supplement 1. Early Dcc expression is restricted to post-mitotic cells of the retina. (**A–D**) Cryosection of E12 Wildtype and *Dcc*$^{-/-}$ mouse eyes immunolabeled for Dcc (white or green) and βIII-tubulin (magenta). Non-specific Dcc staining is seen in mesenchymal cells (arrowhead). (**B, D**) higher magnification images. (**E–G**) IHC of E12 Wildtype retina immunolabeled for Dcc (green) and the retinal progenitor cell marker, Sox2 (magenta). (**H–J**) IHC of E15 mouse retinas labeled for Dcc (green) and the post-mitotic photoreceptor cell marker, Cone-rod homeobox protein (Crx, magenta). (**B,D**) show high magnification images. Scale bars: **A–J** 50 μm.

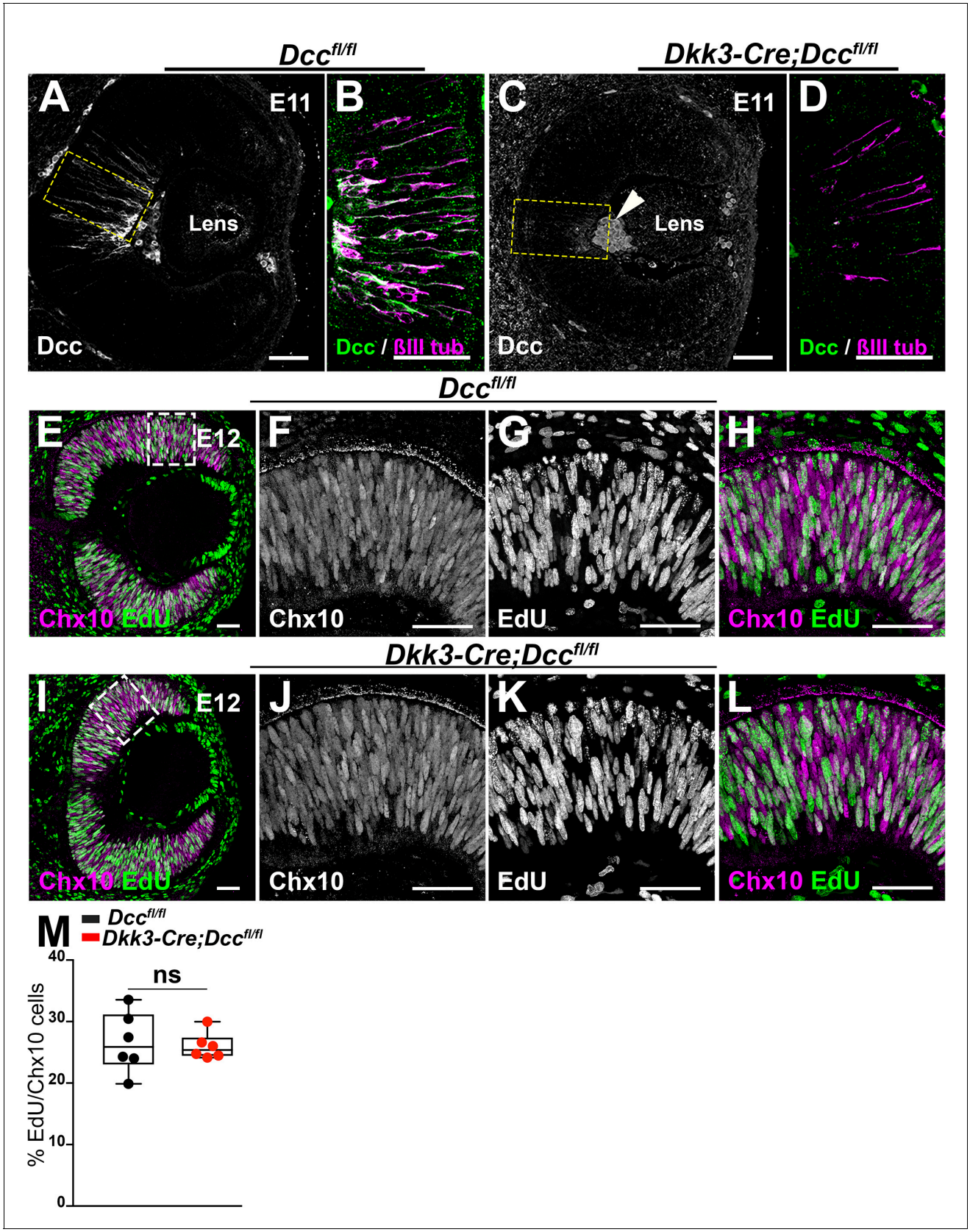

Figure 2—figure supplement 1. *Dcc* deletion does not impact early retinal proliferation. (**A–D**) sagittal cryosections of *Dcc*$^{fl/fl}$ and *Dkk3:cre;Dcc*$^{fl/fl}$ E11 mouse embryo eyes immunolabeled for Dcc (white or green) and β-III tubulin (magenta). Non-specific binding of Dcc in mesenchymal cells is shown

Figure 2—figure supplement 1 continued on next page

Figure 2—figure supplement 1 continued

(arrowhead). (**E–L**) Sagittal cryosections of EdU-treated *Dcc*$^{fl/fl}$ and *Dkk3:cre;Dcc*$^{fl/fl}$ E12 retinas labeled for the progenitor cell marker Chx10 (magenta) and EdU (green). (**M**) Quantification of EdU and Chx10-positive cells represented as a box plot; whiskers show min to max values. A Mann-Whitney test was used. Results were considered as non-significant (ns) when p>0.05. Scale bars: (**A–L**) 50 μm.

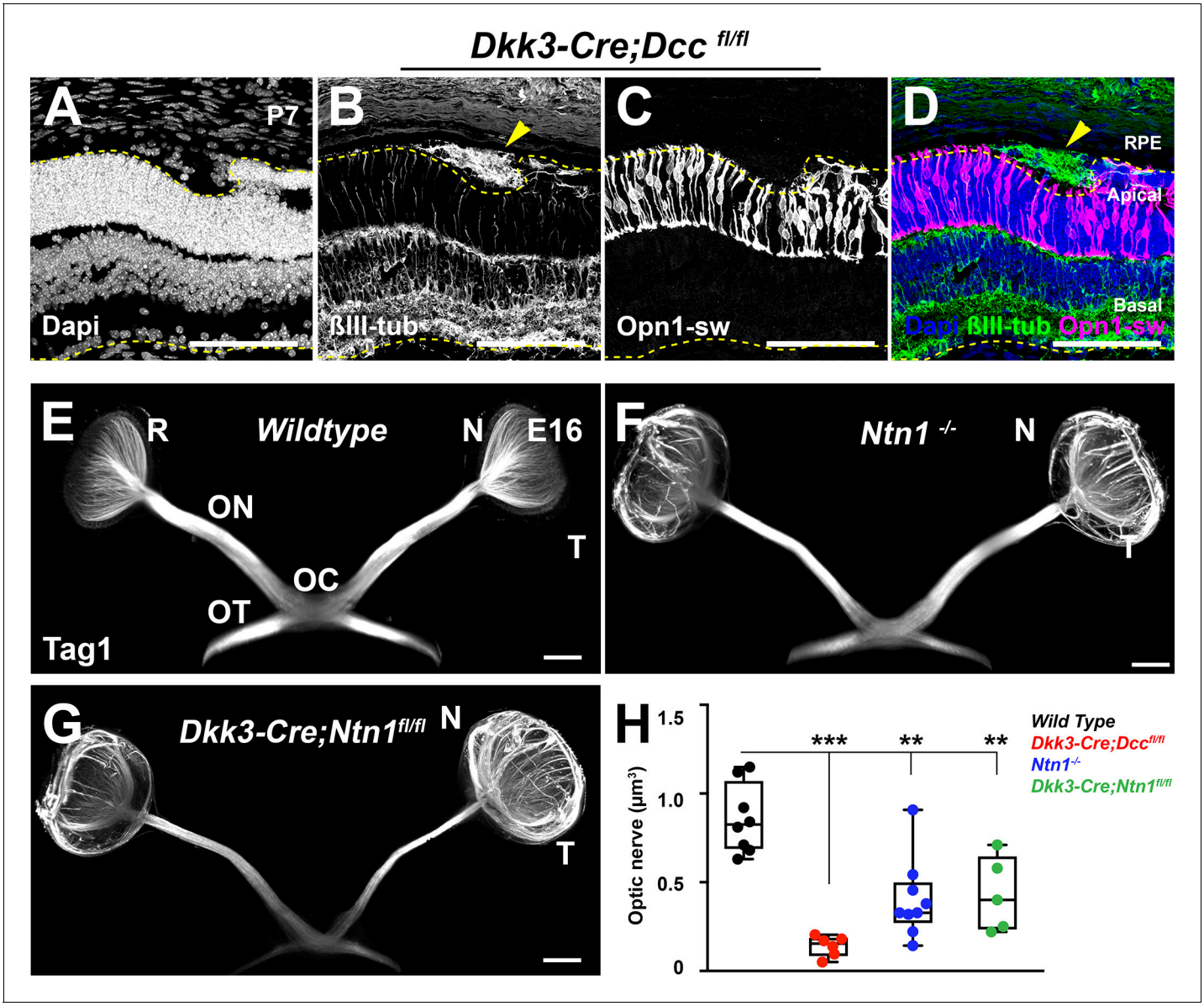

Figure 4—figure supplement 1. Eye-specific deletion of Dcc and Netrin-1 leads to major retinal defects. (**A–D**) Cryosections of P7 *Dkk3;cre;Dcc*$^{fl/fl}$ mice stained for ßIII tubulin (ßIII-tub, green) and short-wavelength Opsin (Opn1sw, magenta). Aberrant RGC projections appear in the subretinal space (yellow arrow). (**E–G**) Whole-mount labeling of E16 Wildtype, *Ntn1*$^{-/-}$, and *Dkk3:cre;Ntn1*$^{fl/fl}$ embryonic heads. R: retina, ON: optic nerve, OC: optic chiasm, OT: optic tract, N: nasal, T: temporal. (**H**) Quantification of optic nerve volumes (µm^3) represented as a box plot, whiskers represent min to max values. *Ntn1*$^{-/-}$ (0.403 ± 0.074 µm^3; n = 9 nerves) and *Dkk3:cre;Ntn1*$^{fl/fl}$ embryos (0.432 ± 0.094 µm^3; n = 5 nerves) displayed a significant reduction in optic nerve volume compared to Wildtype embryos (0.858 ± 0.07 µm^3; n = 8 nerves) (p=0.0016 and p=0.0078 respectively, Mann-Whitney test). Results were considered non-significant (ns) when p>0.05. **=p < 0.01. Scale bars: (**A–D**) 50 µm.

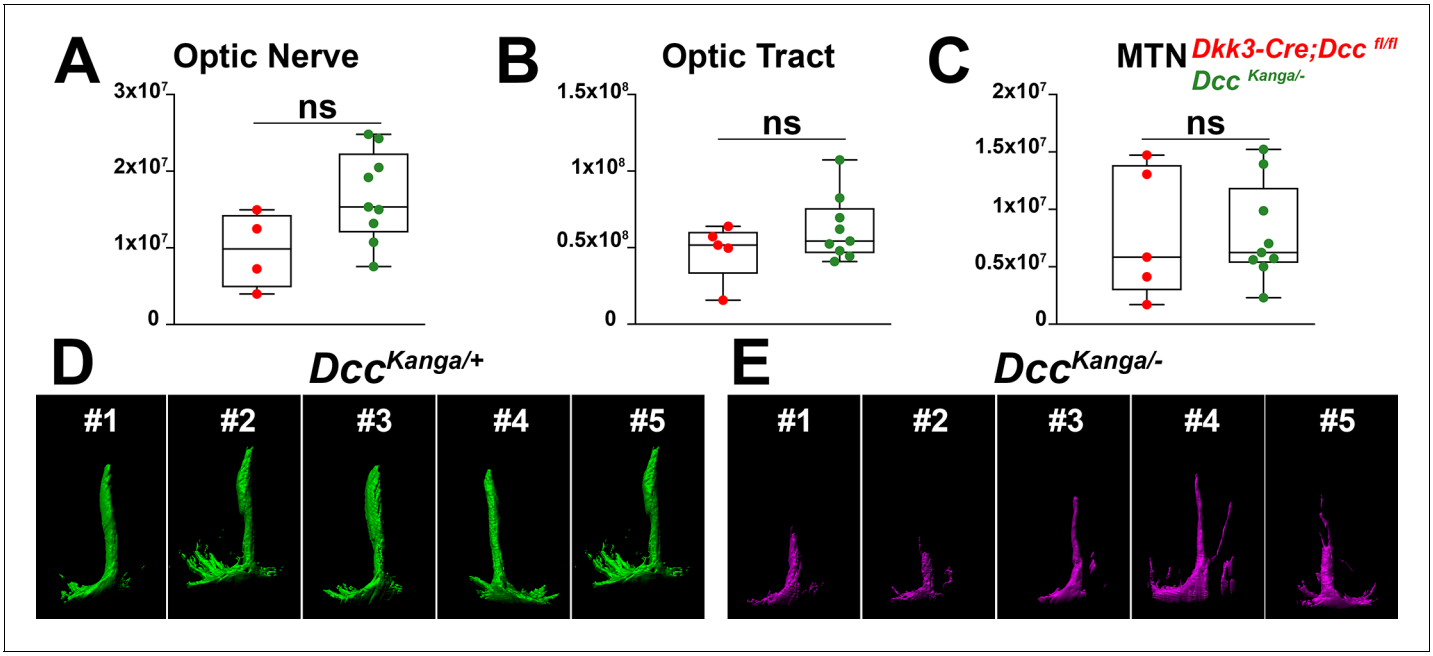

Figure 6—figure supplement 1. The reduction in retinal projections observed in *Dcc* cKO mice is phenocopied in *Dcc*^{kanga} mutant mice. (**A–C**) Comparison between *Dkk3:cre;Dcc*$^{fl/fl}$ and *DccKanga*$^{Kanga/-}$ mice. (**A**) Optic nerve volume (µm^3). (**B**) Optic tract volume (µm^3). (**C**) MTN volume (µm^3). A Mann-Whitney test was used. Results were considered non-significant (ns) if p>0.05. (**D,E**) Automatic segmentation of MTN from *Dcc*$^{fl/fl}$ (n = 5) and *DccKanga*$^{Kanga/-}$ mice using Imaris software (n = 5).

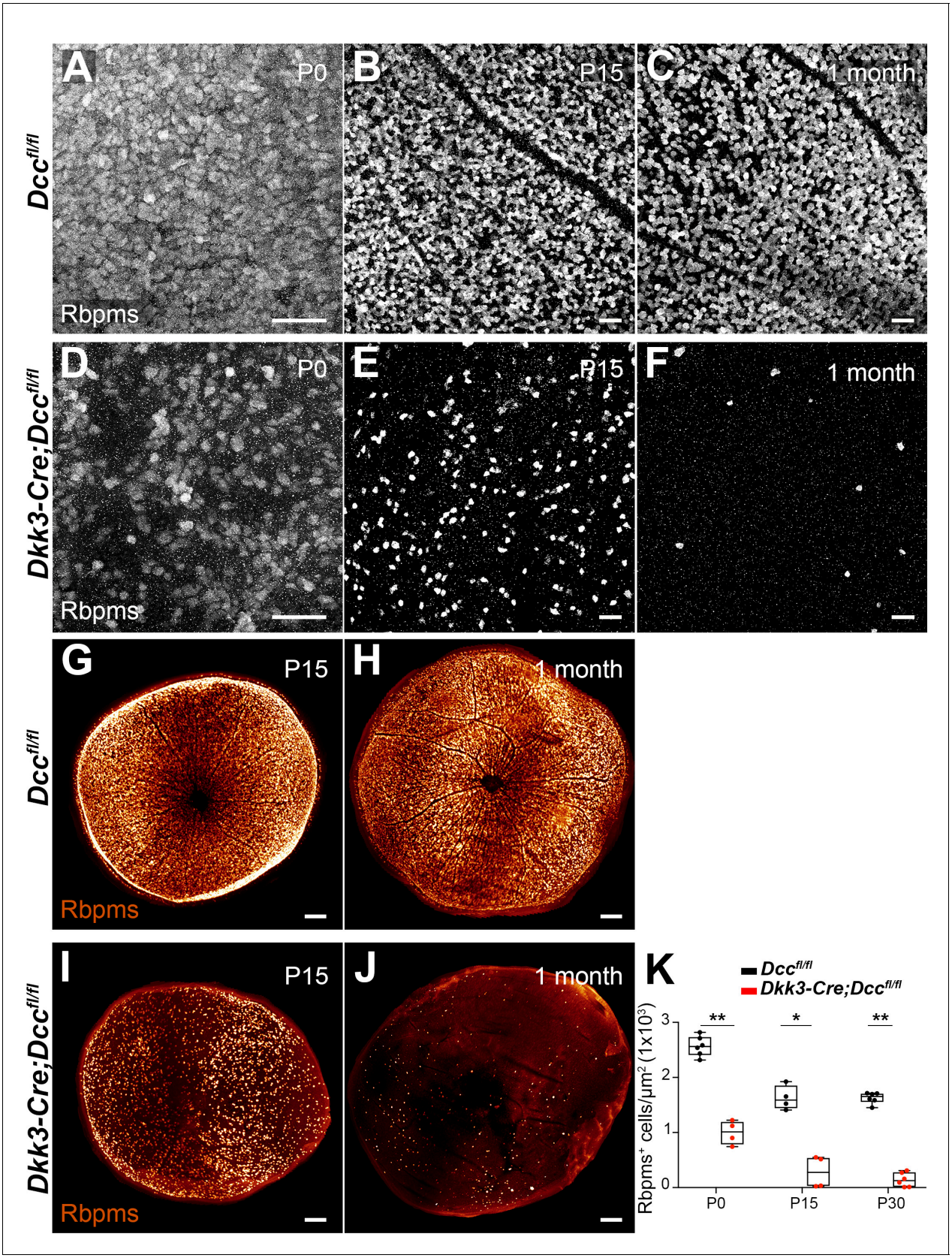

Figure 7—figure supplement 1. Eye-specific *Dcc* deletion leads to a dramatic reduction of RGC number. (**A–F**) Flat-mounted retinas of *Dcc*$^{fl/fl}$ and *Dkk3:cre;Dcc*$^{fl/fl}$ mice immunolabeled for the pan-RGC marker Rbpms. (**A,D**) P0 (**B,E**) P15 (**C,F**) 1 month flat-mounted retinas. (**G–J**) Whole-mount eyes

Figure 7—figure supplement 1 continued on next page

Figure 7—figure supplement 1 continued

of *Dcc*$^{fl/fl}$ and *Dkk3:cre;Dcc*$^{fl/fl}$ mice treated with EyeDISCO and immunolabeled for Rbpms, (**G,I**) at P15 and (**H,J**) 1 month. (**K**) Quantification of Rbpms positive cell per μm^2 represented as a box plot; whiskers display min to max values. A Mann-Whitney test was carried out. ****=$p < 0.0001$. Scale bars: (**A–F**) 50 µm, (**G–J**) 200 µm.

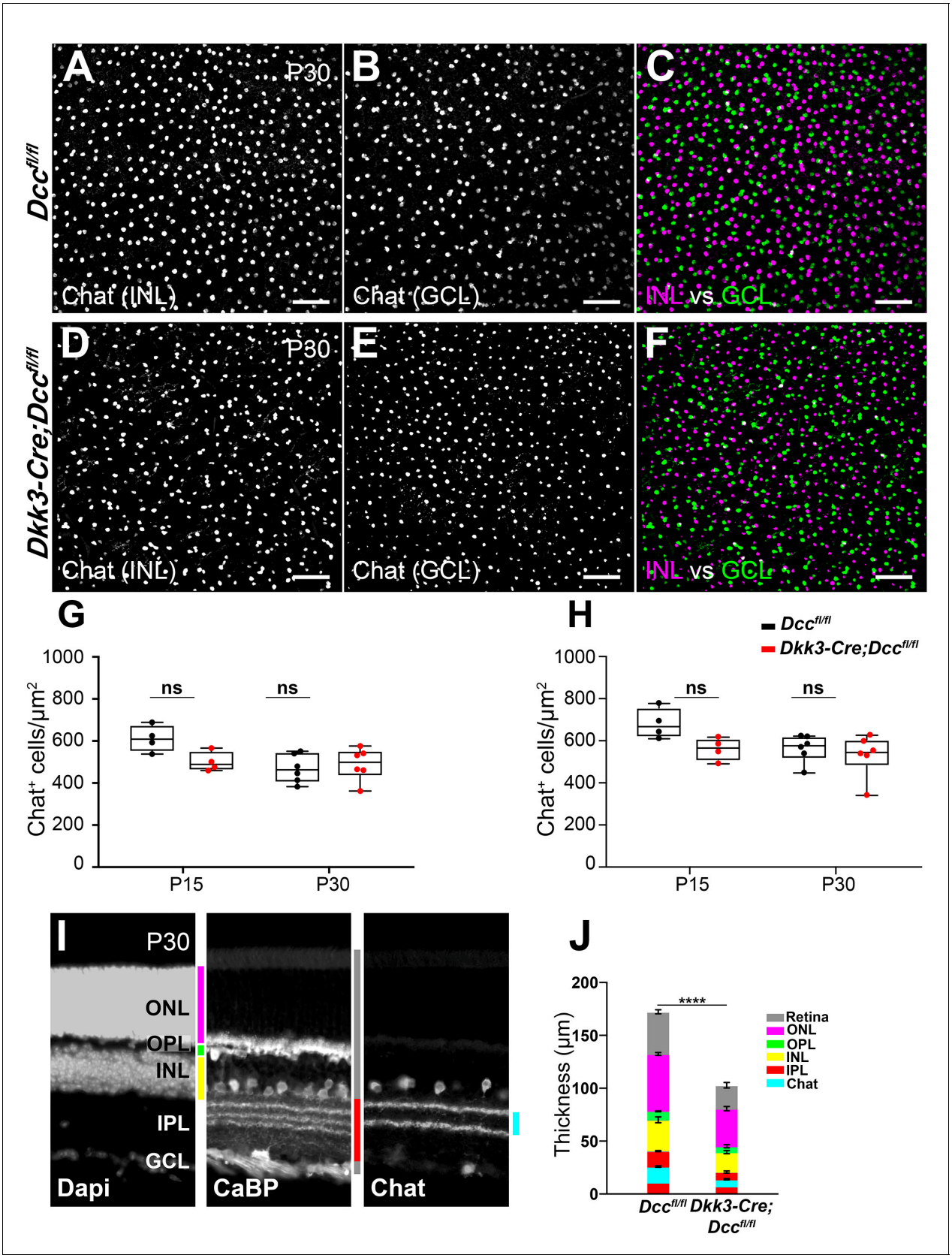

Figure 7—figure supplement 2. *Dcc* deletion does not affect Chat$^+$ cell number. (**A–F**) 1 month-old flat-mounted retinas of *Dcc*$^{fl/fl}$ and *Dkk3:cre;Dcc*$^{fl/fl}$ mice immunolabeled for choline O-acetyltransferase (Chat). (**A,D**) Chat$^+$ cells in the inner nuclear layer (INL). (**B,E**) Chat$^+$ cells in the ganglion cell layer

Figure 7—figure supplement 2 continued on next page

Figure 7—figure supplement 2 continued

(GCL). (**C,F**) Chat$^+$ cells in the INL (magenta) and GCL (green). (**G,H**) Quantification of Chat$^+$ cells per µm^2 in the GCL (**G**) and the INL (**H**) represented as a box plot; whiskers display min to max values. A Mann-Whitney test was carried out. Results were considered non-significant (ns) when p>0.05. (**I,J**) Retinal layer thickness. (**I**) Cryosection of 1month-old *Dcc*$^{fl/fl}$ retina immunolabeled for the amacrine and horizontal cell marker Calbindin (CaBP) as well as the Staburst amacrine cell marker Chat. Retinas were counterstained with the nuclear marker, Hoechst. ONL, outer nuclear layer (Magenta band); OPL, outer plexiform layer (green band); INL, inner nuclear layer (yellow band); IPL, inner plexiform layer (red band); GCL, retinal ganglion cell layer. The grey band corresponds to the whole retina, and the cyan band to distance between the two Chat$^+$ sublayers. (**J**) Quantification of retinal layers thickness (µm) as a bar graph. Results are presented as mean ± SEM. A Welch's t test was used. ****=p < 0.0001. Scale bars: (**A–F**) 80 µm.

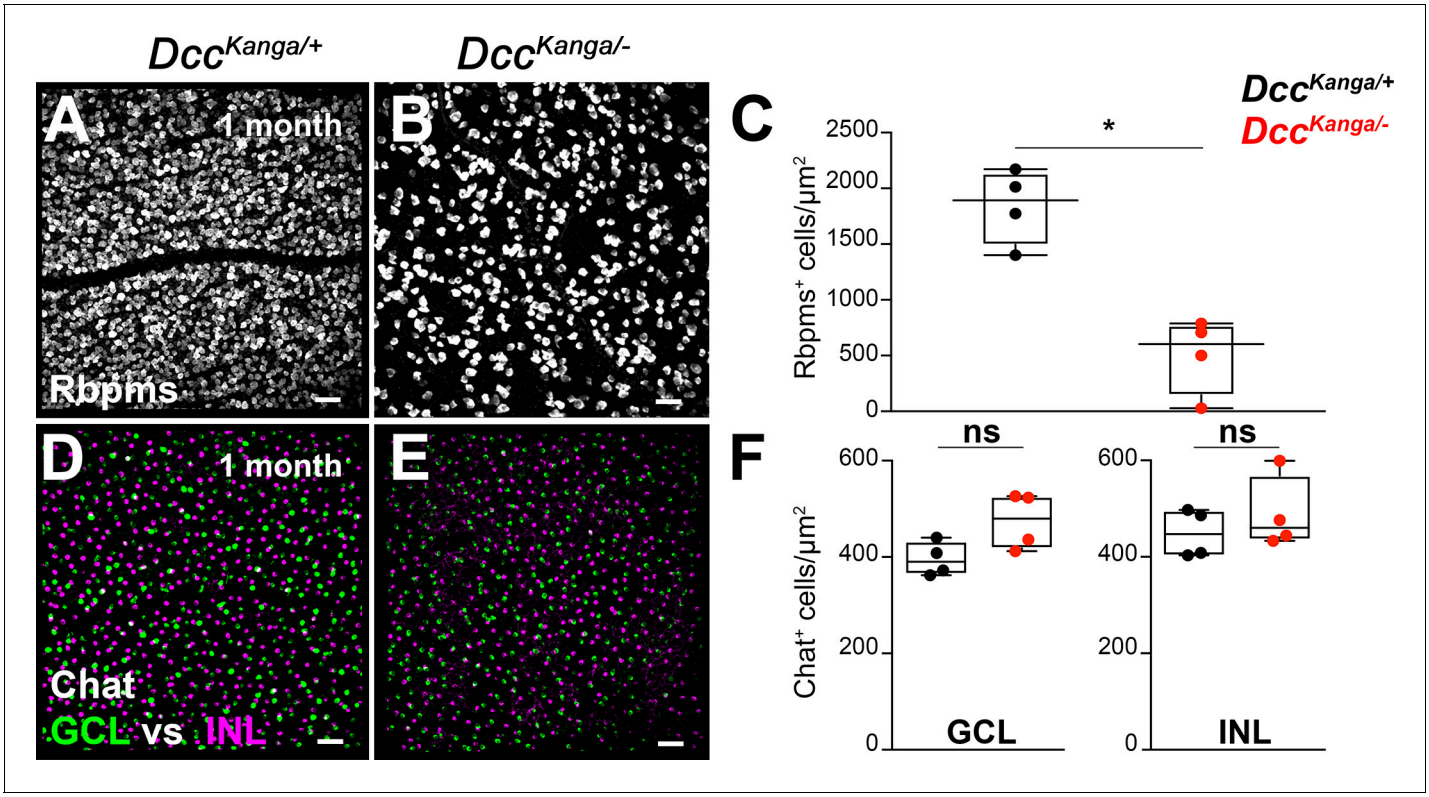

Figure 7—figure supplement 3. Dcc signaling is critical for RGC survival. (**A,B**) 1 month-old retinas of *Dcc*$^{kanga/-}$ and *Dcc*$^{kanga/+}$ control littermates were flat-mounted and immunolabeled for the pan-RGC marker, Rbpms (white). (**C**) Quantification of Rbpms-positive cells represented as a box plot; whiskers represent min to max values. A Mann-Whitney test was used. Results were considered non-significant (ns) if p>0.05. *=p < 0.05. (**D,E**) Flat-mounted retinas labeled for Chat in the ganglion cell layer (GCL, green) and the inner nuclear layer (INL, magenta). (**F**) Quantification of Chat^{+} cells represented as a box plot; whiskers represent min to max values. A Mann-Whitney test was used. Scale bars: (**A,B,D,E**) 300 µm.

Figure 8 continued

eyes are cleared and imaged using light sheet microscopy. (**B, B'**) Side view image of an adult eye (1 month) before and after EyeDISCO clearing. (**C,D**) Eye fundoscopy of a 1 month-old *Dcc*$^{fl/fl}$ and a *Dkk3:cre;Dcc*$^{fl/fl}$ eye. *Dkk3:cre;Dcc*$^{fl/fl}$ fundoscopy shows a severe dysplasia (yellow arrows). Eye coordinates are highlighted, D, dorsal, V, ventral,N, nasal, T, temporal. (**E,F**) Whole eye of *Dcc*$^{fl/fl}$ and *Dkk3:cre;Dcc*$^{fl/fl}$ mice after EyeDISCO treatment labeled with a nuclear marker (TO-PRO-3, white). Major dysplasia can still be observed in *Dkk3:cre;Dcc*$^{fl/fl}$ eyes (yellow arrows). (**G**) Represents a slice of the 3D stack from a *Dkk3:cre;Dcc*$^{fl/fl}$ eye. The dysplasia can be isolated by manual segmentation with Imaris (magenta, yellow arrow). (**H**) The affected area visualized in 3D (magenta) following manual segmentation. (**I–N**) 3D surfaces of rosette masks in 3 separate *Dkk3:cre;Dcc*$^{fl/fl}$ mice showing both the left and right eye. (**O, P**) Whole-mount IHC of eyes of *Dcc*$^{fl/fl}$ and *Dkk3:cre;Dcc*$^{fl/fl}$ 1 month-old eyes labeled for short-wavelength Opsin (Opn1sw, white). (**Q**) A merge of 3 separate masks using Imaris from *Dkk3:cre;Dcc*$^{fl/fl}$ mice showing rosette area coverage and retina circumference. (**R**) Quantification of rosette area coverage in retinas. No differences in rosette coverage were seen between *Dcc* cKO and control littermates at P15 (21.85 ± 2.48%; n = 5 eyes), 1 month (20.11 ± 1.67%; n = 5 eyes; p>0.999) and 6 months (17.68 ± 3.76%; n = 5 eyes; p=0.6176). A Kruskal-Wallis test was used to measure significance. Data are represented as a box plot; whiskers represent min to max values. Results were considered non-significant (ns) if p>0.05. Scale bars: (**E–H, I–N**) 300 μm, (**O, P**) 500 μm, (**O, P**) high magnification) 150 μm, (**Q**) 400 μm.

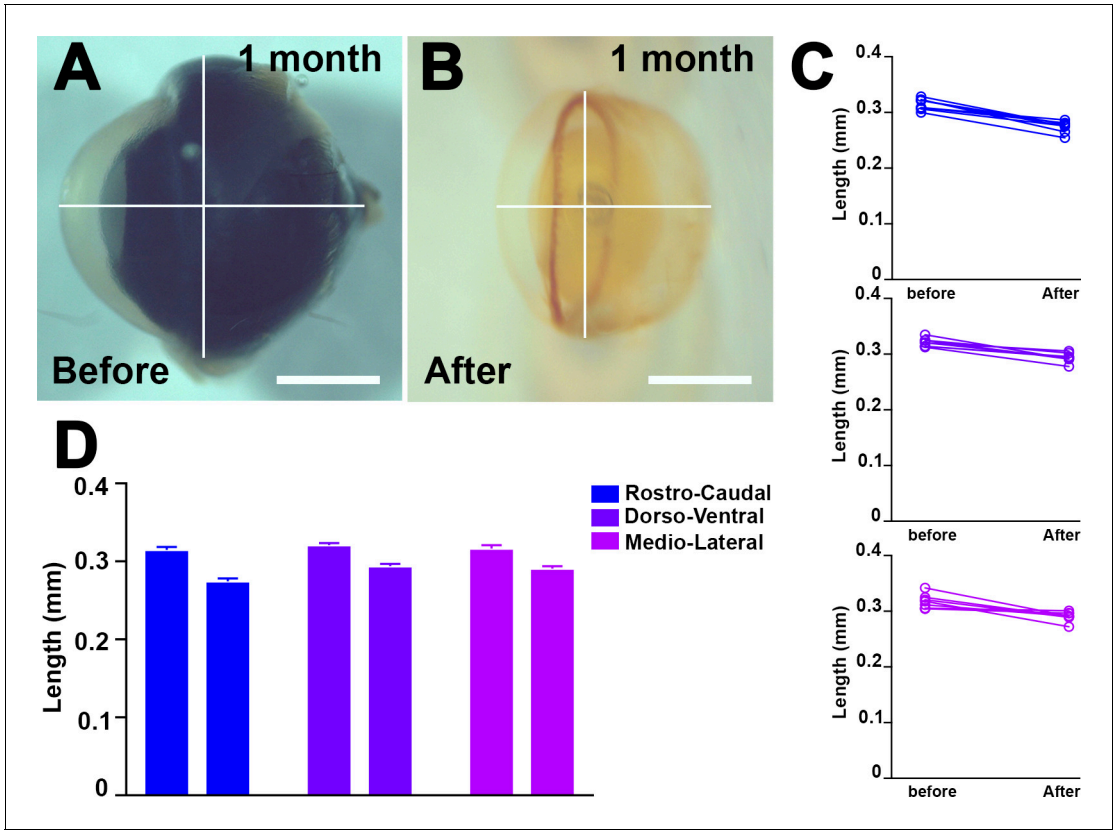

Figure 8—figure supplement 1. EyeDISCO leads to a mild and isotropic shrinkage of the adult eye. (**A–B**) A 1 month old mouse eye before and after EyeDISCO clearing. White bars indicate measurements in rostro-caudal, dorso-ventral, and medio-lateral. (**C**) Quantification of 1 month old mouse eyes in rostro-caudal (12.78 ± 1.31%; n = 8), dorso-ventral (8.387 ± 1.03%; n = 8), and medio-lateral (7.875 ± 1.89%; n = 8) following EyeDISCO clearing. Results are presented as mean ± SEM with individual values. (**D**) Bar graph representation of a 1-month-old mouse eye shrinkage following EyeDISCO.

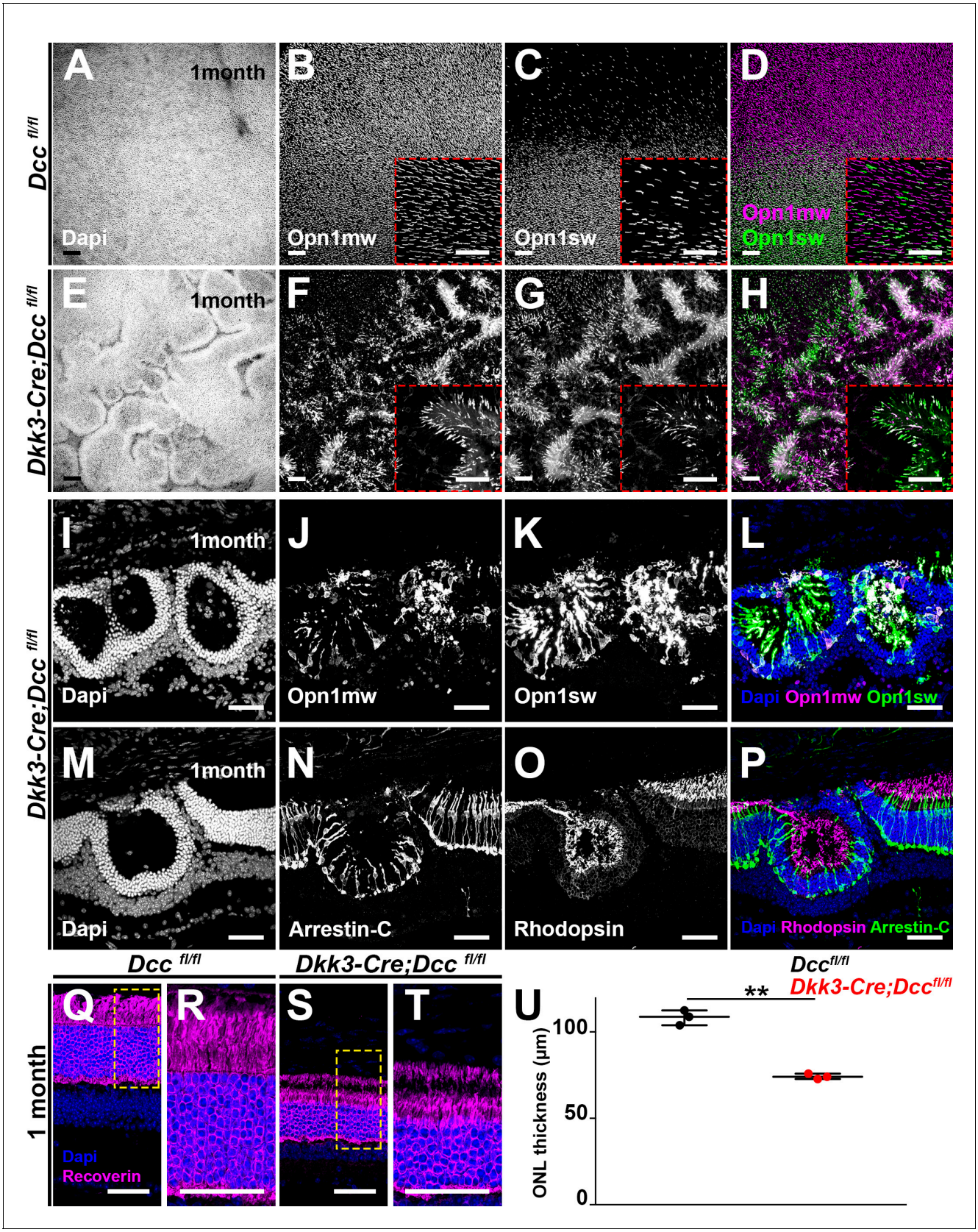

Figure 8—figure supplement 2. Photoreceptors are ubiquitously present within rosettes. (**A–H**) Whole-mount immunostaining of *Dcc*$^{fl/fl}$ and *Dcc* cKO retinas at 1 month labeled for short- (green; Opn1sw) and mid-wavelength (Opn1mw, magenta) opsins. (**I–L**) Cryosections of 1-month-old *Dkk3:cre;*

Figure 8—figure supplement 2 continued on next page

Figure 8—figure supplement 2 continued

Dcc$^{fl/fl}$ retinas labeled for short- (green) and mid-wavelength (magenta) opsins. (**M–P**) Cryosections from 1-month-old *Dcc* cKO retinas labeled for cones (Arrestin-C, magenta) and Rods (Rhodopsin, green). (**Q–T**) Cryosections from 1-month-old retinas immunolabeled for a pan photoreceptor marker (Recoverin, magenta). (**R,T**) show high magnification images. (**U**) Quantification of the photoreceptor layer using Recoverin as a marker. *Dcc* cKO retinas display a dramatic reduction in photoreceptor layer (74.22 ± 0.89 μm; n = 3 compared to 108.3 ± 2.482 μm in *Dcc*$^{fl/fl}$ control littermates; n = 3; p=0.0023. A Welch's t-test was performed. **=p < 0.01. Scale bars: (**A–T**) 50 μm.

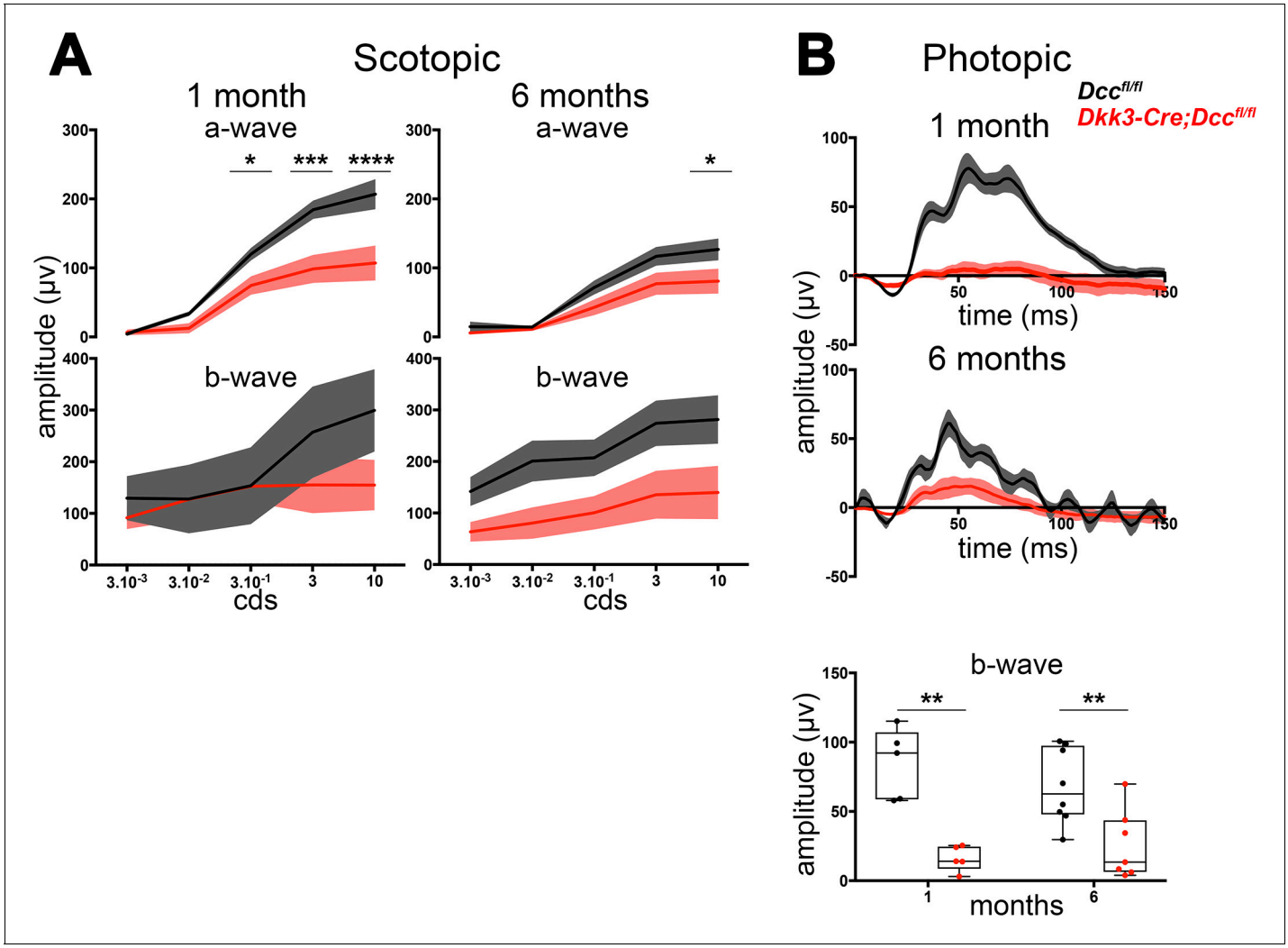

Figure 8—figure supplement 3. Eye-specific deletion of *Dcc* leads to functional visual deficits. (**A**) Scotopic response of *Dcc* cKO and control littermates are shown for 1 month and 6-month-old mice. A Bonferroni's test was used. (**B**) Shows the photopic response at 1 (84.743 ± 11.33; n = 5 compared to 16.1 ± 4.07; n = 5; p=0.0079) and 6 months (68.176 ± 9.56; n = 8 compared to 25.752 ± 9.33; n = 7; p=0.0093). A Mann-Whitney test was used. Results were considered non-significant (ns) if p>0.05. *=p < 0.05; **=p < 0.01; ***=p < 0.001; ****=p < 0.0001.

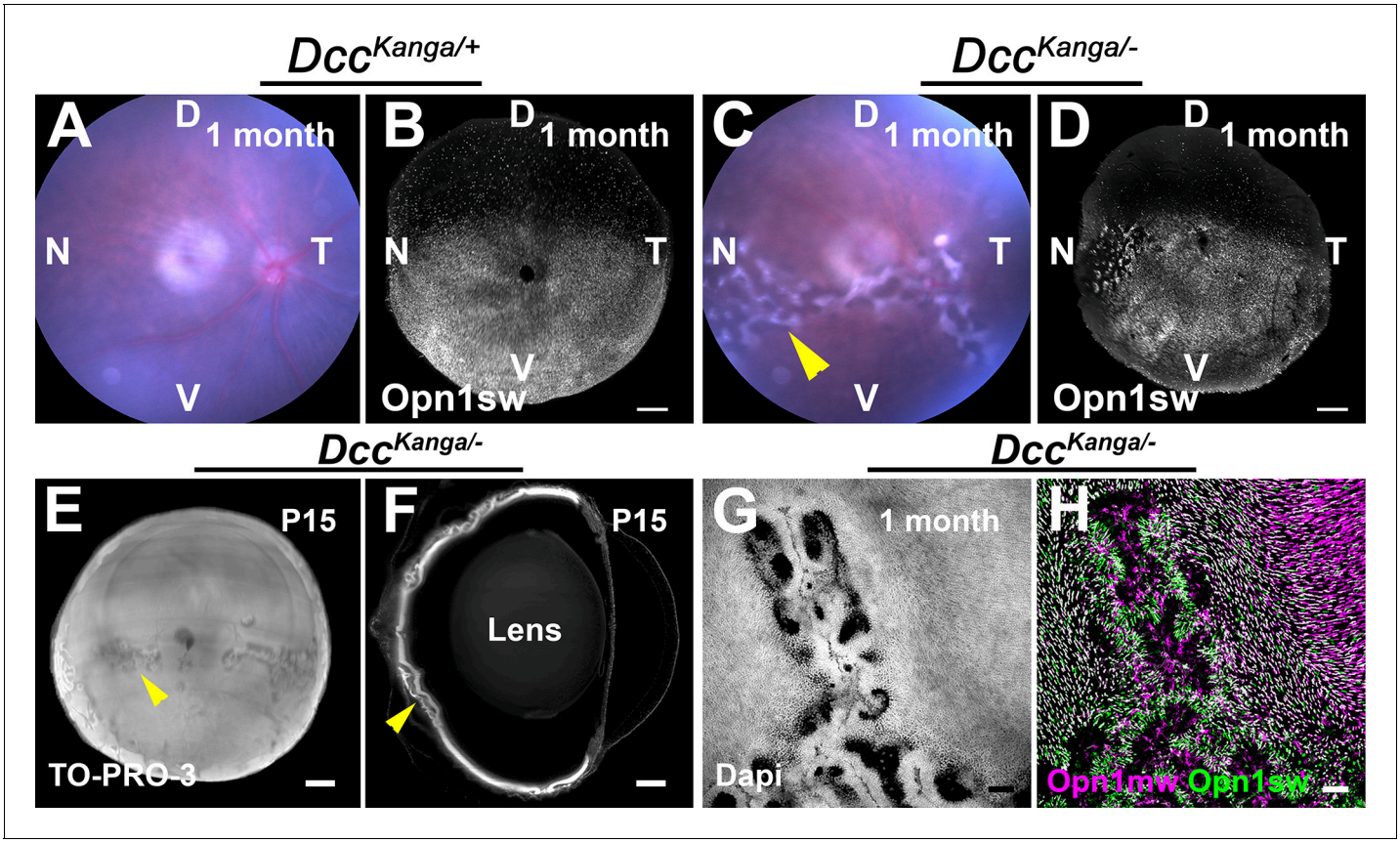

Figure 8—figure supplement 4. Dcc Kanga mutants display retinal dysplasia. (**A,C**) Eye fundoscopy showing an eye fundoscopy of *Dcc* $^{Kanga/-}$ mice and *Dcc*$^{kanga/+}$ mice, rosettes can be seen in mutant retinas (yellow arrowhead). (**B,D**) show whole-mount immunolabeling of the short-wavelength Opsin (Opn1sw, white) of 1 month-old *Dcc*$^{kanga/-}$ and *Dcc*$^{Kanga/+}$ mice following the EyeDISCO protocol. Rosettes can be seen. (**E**) Frontal view of a whole Dcc kanga eye immunolabeled for the nuclear marker TO-PRO-3 (white). (**F**) z-slice from a 3D-rendered Dcc kanga eye immunolabeled for TO-PRO-3 (white). Rosettes are observed in the naso-temporal retina (yellow arrowhead). (**G-H**) Flat-mounted retinas of adult *Dcc*$^{kanga/-}$ and *Dcc*$^{kanga/+}$ control littermates immunolabeled for mid-wavelength opsin (Opn1mw, magenta), and short-wavelength opsins (Opn1sw, green). Rosette structures can be seen. Scale bars: (**B,D**) 300 µm, (**E,F**) 200 µ m, (**G,H**) 50 µm.

Chapter 3 : Complementary results

Netrin-1 acts in short-range in the developing visual system

Robin J. Vigouroux, Manuela Argentini, Yvrick Zagar, Patrick Mehlen, Alain Chédotal and Kim Nguyen-Ba-Charvet

Contribution: R. J. Vigouroux, K. Nguyen-Ba-charvet, and A. Chédotal designed the experiments, the figures and wrote the manuscript. R. J. Vigouroux carried out the experiments that make up Figures 1 to 4 and Supplementary Figure 1. Y. Zagar and M. Argentini carried out the eye lysis and western blot analysis on Figure 2A and Supplementary Figure 1A.

Introduction

Following their differentiation, Retinal Ganglion Cells (RGCs) project a single axon along the permissive outer fiber layer of the retina towards the optic disc (Goldberg and Coulombre, 1972; Grant et al., 1980; Halfter et al., 1985). At the presumptive optic disc, RGCs exit the eye and fasciculate to form the optic nerve (Halfter et al., 1983; Holt, 1989; Prada et al., 1981). Seminal grafting experiments in chick showed that guidance of RGC axons at the optic disc is mediated by short-range cues (Halfter, 1996). The extracellular matrix protein Netrin-1 was initially identified in the floor plate of the spinal cord to guide growing commissural neurons (Kennedy et al., 1994; Serafini et al., 1994). Using a gene-trap strategy, a hypomorph *Ntn1* mutant (*Ntn1*$^{\beta geo}$) was generated that displayed optic nerve hypoplasia (Deiner et al., 1997; Serafini et al., 1996). Netrin-1 was subsequently shown to bind to a transmembrane receptor, Deleted in Colorectal Carcinoma (Dcc) (Keino-Masu et al., 1996). *In vitro* Netrin-1 promotes neurite outgrowth and growth cone turning of RGC axons which are inhibited by Dcc-blocking antibodies (de la Torre et al., 1997; Deiner et al., 1997; Wang et al., 1996). *Dcc* null mice display severe optic nerve hypoplasia and intra retinal axon defects (Fazeli et al., 1997). Recently, *Dcc* was shown to play a major role in RGC and photoreceptor survival. Moreover, subsets of RGCs projecting to the medial terminal nucleus (MTN) of the accessory optic system (AOS) were found to be perturbed in *Dcc* conditional mutants (Vigouroux et al., 2020). Our understanding of Netrin-1 signaling in the visual system still remains elusive as *Ntn1*$^{\beta geo}$ mutants die a few hours following birth. Recent developments of *Ntn1* floxed (*Ntn1*$^{fl/fl}$) mice have shifted our understanding of Netrin-1 function in the spinal cord and hindbrain from a long-range chemotactic model to a short-range haptotactic model (Dominici et al., 2017; Moreno-Bravo et al., 2019; Varadarajan et al., 2017; Wu et al., 2019; Yamauchi et al., 2017).

Here, we generated a viable retinal-specific *Ntn1* mutant which displays significant optic nerve hypoplasia as well as RGC projection defects in the AOS. We also generated a novel transgenic Netrin-1 mutant overexpressing human *NTN1* (*NTN1*$^{tg/+}$) that photocopies *Ntn1*$^{-/-}$ null and *cKO* mice. Our data are consistent with the current proposed model that Netrin-1 acts as a short-range cue during intra-retinal path finding.

Results

Netrin-1 at the optic disc is critical for RGC exit.

Netrin-1 expression was previously reported at the OD (Deiner et al., 1997). To elucidate whether Netrin-1 expression within the retina is critical for optic nerve development, we generated a conditional deletion of *netrin-1* by crossing *Ntn1* floxed mice with a retinal-specific Cre driver line, *Dickopf-3* (*Dkk3:Cre-Ntn1*$^{fl/fl}$) (Sato et al., 2007; Vigouroux et al., 2020). Whole-mount immunohistochemistry of an E10 embryo showed a complete cre-recombination in the eye, heart and notochord, as well as in craniofacial neural crest cells (Figure 1A, n=3). Moreover, Cre expression strongly co-localized with the pan-retinal progenitor cell marker, Ceh-10 homeodomain-containing homologue (Chx10, also referred to as visual system homeobox 2, Vsx2)(Figure 1B-D, n=3) (Liu et al., 1994). In *Dkk3:Cre-Ntn1*$^{fl/fl}$ mice, *Netrin-1* coding mRNA was not detected at the optic disc of E12 mice when compared to *Ntn1*$^{fl/fl}$ littermates (Figure 1E,H, n=3). However, while a noticeable decrease in *Netrin-1* mRNA levels was observed along the optic nerve of *Ntn1* cKO mice, a significant amount remained expressed when compared to control mice

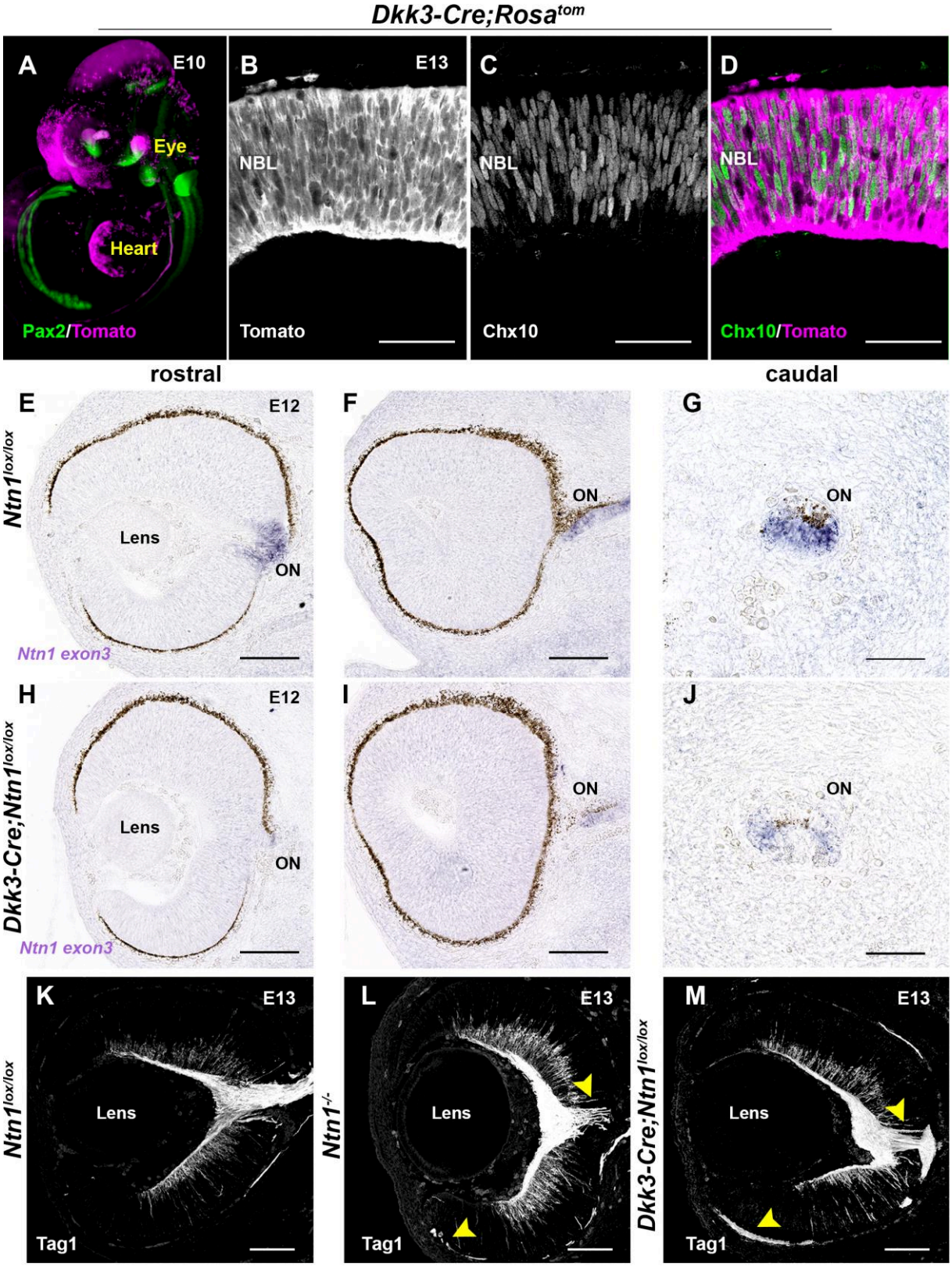
Dkk3-Cre;Rosa^tom
A
E10
Eye
Heart
Pax2/Tomato
B
E13
NBL
Tomato
C
NBL
Chx10
D
NBL
Chx10/Tomato
rostral
caudal
E
E12
Ntn1^lox/lox
Lens
ON
Ntn1 exon3
F
ON
G
ON
H
E12
Dkk3-Cre;Ntn1^lox/lox
Lens
ON
Ntn1 exon3
I
ON
J
ON
K
E13
Ntn1^lox/lox
Lens
Tag1
L
E13
Ntn1^-/-
Lens
Tag1
M
E13
Dkk3-Cre;Ntn1^lox/lox
Lens
Tag1

Figure 1. Netrin-1 functions as a short-range cue to guide RGC axons along the optic nerve. **A** Whole-mount immunohistochemistry of an E10 *Dkk3:Cre-Rosa*^{Tom} embryo labeled with Dsred (cyan) and Pax2 (magenta). **B-D** cryosections of E13 *Dkk3:Cre-Rosa*^{Tom} labelled with DsRed (green) and the RPC marker Chx10 (magenta). **E-J** *In situ* hybridization with an exon3 riboprobe for *netrin-1* on rostro-caudal coronal cryosections of E12 embryos. **E-G** shows cryosections from an E12 *Ntn1*$^{fl/fl}$ embryo. **H-J** shows cryosections from an E12 *Dkk3:Cre-Ntn1*$^{fl/fl}$ embryo. **K-M** immunohistochemistry of coronal cryosections on E13 embryos labeled with Tag1 (white). **K** cryosection from a *Ntn1*$^{fl/fl}$ embryo. **L** cryosection from a *Ntn1*$^{-/-}$ embryo, arrowheads indicate aberrantly projecting RGC axons. **M** cryosection from a *Dkk3:Cre-Ntn1*$^{fl/fl}$ embryo, arrowheads indicate aberrantly projecting RGC axons. **Scale bars**: **B-D** 50 μm, **E-M** 100 μm. ON = Optic Nerve, NBL = neuroblastic layer.

(Figure 1F,G,I,J, n=3). Despite this expression, *Dkk3:Cre-Ntn1*$^{fl/fl}$ mice displayed a severe optic nerve defect which phenocopies Ntn1 null mice (Figure 1K-M, n=3). These results support the idea that Netrin-1 functions as a short-range cue at the optic disc.

Relative Netrin-1 expression is critical for proper intra-retinal guidance

The observation that eye-specific deletion of *Netrin-1* led to significant intra-retinal defects prompted us to question whether Netrin-1 could function as a short-range cue. To test this, we generated a transgenic mouse line by inserting a floxed-stop cassette upstream to the human *NTN1* cDNA in the constitutively active Rosa26 locus (Srinivas et al., 2001) (see methods, Figure 2A). By crossing *NTN1*$^{tg/+}$ mice with the *Dkk3:Cre* driver line, we revealed a significant overexpression of Netrin-1 in whole protein lysates of E15 eyes (Figure 2A, n=5). At E13, Netrin-1 is expressed in the optic nerve (Figure 2B, n=3). In contrast, *Dkk3:Cre-NTN1*$^{tg/+}$ mice displayed ectopic expression of netrin-1 across the entire retina and developing lens (Figure 2C, n=3).

Previous *in vitro* studies showed that application of exogenous Netrin-1 to neuronal cultures led to the ubiquitination and proteasomal degradation of its receptor, Dcc (Kim et al., 2005). Interestingly, Dcc has been largely implicated in intra-retinal pathfinding (Deiner et al., 1997; Vigouroux et al., 2020). To assess whether overexpression of Netrin-1 affects Dcc levels, we carried out a western blot analysis on E15 eyes of *Dkk3:Cre-NTN1*$^{tg/+}$ cKO mice. Dcc levels were strongly decreased following Netrin-1 overexpression (Supplementary Figure 1A, n=5). We next carried out an immunostaining of Dcc. At E13, Dcc was specifically expressed in RGCs with a strong expression in the optic nerve (Supplementary Figure 1B, n=3). In contrast,

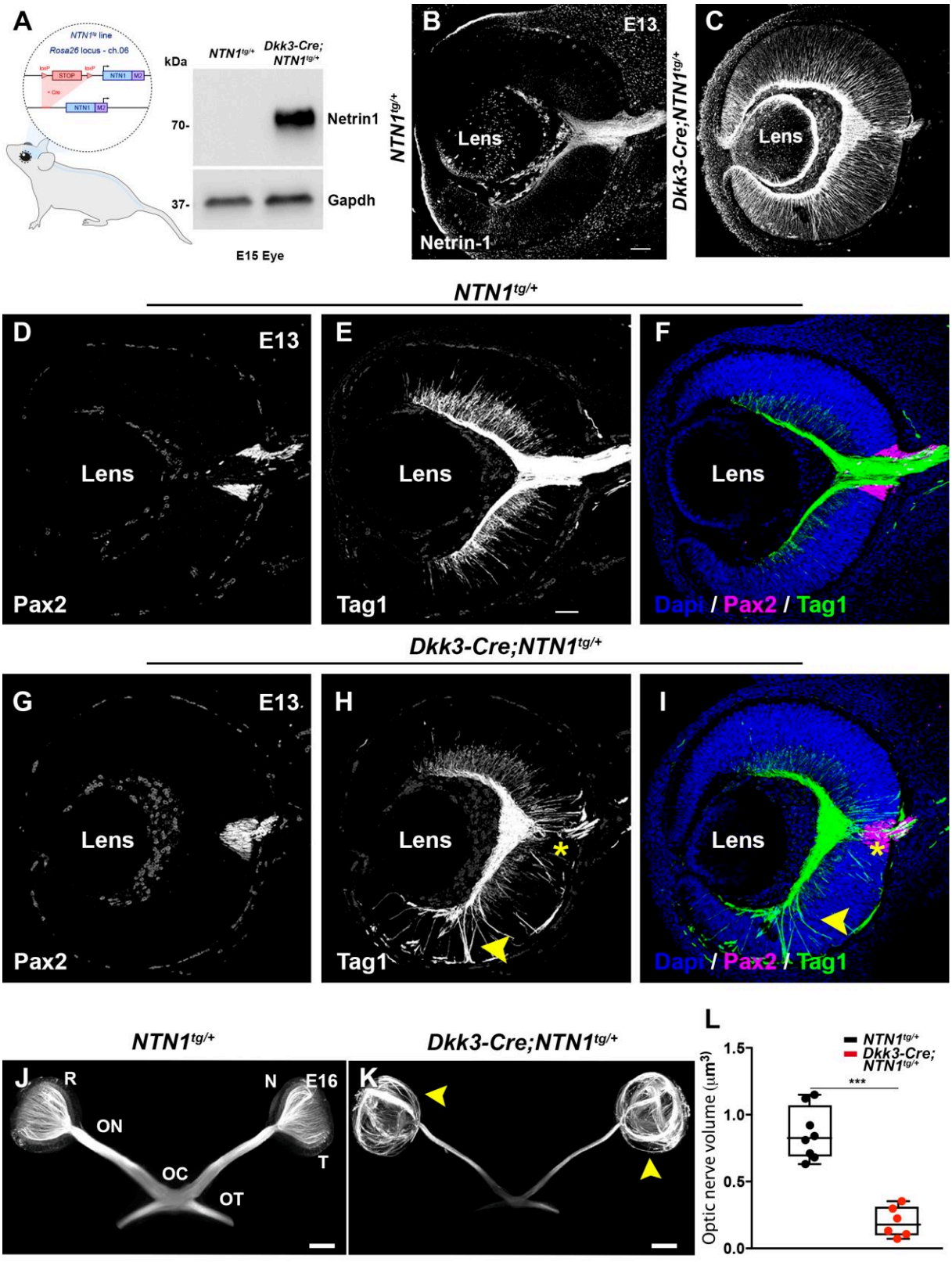
A
NTN1tg line
Rosa26 locus - ch.06
STOP
NTN1 M2
+ Cre
kDa
NTN1tg/+
Dkk3-Cre; NTN1tg/+
70-
Netrin1
37-
Gapdh
E15 Eye
B
E13
Lens
Netrin-1
NTN1tg/+
C
Lens
Dkk3-Cre;NTN1tg/+
NTN1tg/+
D
E13
Lens
Pax2
E
Lens
Tag1
F
Lens
Dapi / Pax2 / Tag1
Dkk3-Cre;NTN1tg/+
G
E13
Lens
Pax2
H
Lens
Tag1
I
Lens
Dapi / Pax2 / Tag1
NTN1tg/+
Dkk3-Cre;NTN1tg/+
J
R
N
E16
ON
OC
T
OT
K
L
NTN1tg/+
Dkk3-Cre; NTN1tg/+
***
Optic nerve volume (µm3)
1.5
1.0
0.5
0.0

Figure 2. Ectopic expression of netrin-1 leads to major intra-retinal pathfinding defects. **A** Schematic representation of the human *NTN1*$^{tg/+}$ mutant mouse line. Immunoblotting of E15 whole eye extracts against Netrin-1 (70kDa) on *NTN1*$^{tg/+}$ and *Dkk3:Cre-NTN1*$^{tg/+}$ mice with the loading control, Gapdh (37kDa). **B,C** Coronal cryosections of E13 on *NTN1*$^{tg/+}$ (**B**) and *Dkk3:Cre-NTN1*$^{tg/+}$ mice (**C**) labeled with netrin-1 (White). **D-I** Cryosections of E13 retinas labeled with the optic disc marker, Pax2 (magenta) and the RGC projection marker Tag1 (green). **D-F** represent E13 *NTN1*$^{tg/+}$ mice. **G-I** represent E13 *Dkk3:Cre-NTN1*$^{tg/+}$ mice, arrowheads indicate aberrantly projecting RGCs whereas the asterisk indicates the optic nerve hypoplasia. **J,K** show a whole-mount immunohistochemistry on E16 heads labeled with Tag1 (White) in *NTN1*$^{tg/+}$ mice (**J**) and *Dkk3:Cre-NTN1*$^{tg/+}$ mice (**K**). Arrowheads indicate aberrantly projecting RGCs invading the sub-retinal space. **L** Quantification of optic nerve volumes (μm^3) are represented as a box plot, whiskers represent min to max values. Mann-Whitney test was used to determine significance. Results were considered significant when $p<0.05$, ***=$p<0.001$. **Scale bars**: **B,C,D-I** 50 μm, **J,K** = 300 μm. R = retina, ON = optic nerve, OC = optic chiasm, OT = optic tract, N = nasal, T = temporal.

Dkk3:Cre-NTN1$^{tg/+}$ mice displayed a massive loss of Dcc immunostaining across the entire retina (Supplementary Figure 1C, n=3). These findings highlight the idea that Netrin-1 overexpression may not only reflect Netrin1 function but also the loss of function of Dcc.

Next, we asked whether overexpression of Netrin-1 impacted developing RGC axons. At E13, RGCs and their projections along the optic nerve expressed the Transient axonal glycoprotein 1 (Tag1, also known as Contactin 2)(Figure 2E,F,H,I) (Chatzopoulou et al., 2008). *Dkk3:Cre-NTN1*$^{tg/+}$ mice displayed severe RGC guidance defects with several axons aberrantly exiting the retina and invading the sub-retinal space (Figure 2H,I, arrowhead, n = 3). Moreover, *Dkk3:Cre-NTN1*$^{tg/+}$ mice also showed optic nerve hypoplasia (Figure 2H,I, asterisk, n = 3). Netrin-1 was reportedly expressed by Pax2-positive cells of the OD (Deiner et al., 1997). Also, perturbation in Pax2 induced improper choroid fissure closure and colobomas (Torres et al., 1996). Despite having a reduced OD size, *Dkk3:Cre-NTN1*$^{tg/+}$ mutant mice showed the correct localization of Pax2-positive cells within the retina when compared to control mice (Figure 2D,F,G,I, n = 3).

To further analyze RGC projections in *Dkk3:Cre-NTN1*$^{tg/+}$ mutant mice, we carried out a whole-mount immunostaining using Tag1. Strikingly, *Dkk3:Cre-NTN1*$^{tg/+}$ cKO mice displayed aberrant RGC projections within the subretinal space when compared to control littermates (Figure 2J,K, arrowheads, n = 3 and n = 4 respectively). We then measured the total optic nerve volume of control and cKO mice at E16. Control mice displayed a correct optic nerve fasciculation ($0.858\pm0.07\mu m^3$, n = 8 nerves) (Figure 2L). In contrast, *Dkk3:Cre-NTN1*$^{tg/+}$ showed a dramatic reduction of optic nerve volume ($0.198\pm0.07\mu m^3$, n = 6 nerves, p = 0.0007 using a Mann-Whitney test). Interestingly, the optic nerve volume of *Dkk3:Cre-NTN1*$^{tg/+}$ resembled that of *Ntn1*$^{-/-}$ null mice and

Dcc eye-specific cKO mice. Together, our results indicate that relative Netrin-1 levels are critical for proper RGC intra-retinal pathfinding. Moreover, loss of Dcc immunostaining in *Dkk3:Cre-NTN1$^{tg/+}$* mice could imply a molecular regulation between these molecules.

Loss and gain of function of Netrin-1 leads to specific retinal projection defects

In *Ntn1$^{-/-}$* mice, a significant subset of RGCs project correctly into the optic nerve. However, *Ntn1$^{-/-}$* mice die a few hours following birth due to vascular defects (Bin et al., 2015; Serafini et al., 1996). To assess the targeting of RGCs in the absence or exogenous presence of *Netrin-1*, we traced RGC projections in both *Dkk3:Cre-Ntn1$^{fl/fl}$* and *Dkk3:Cre-NTN1$^{tg/+}$* viable mice using an Alexa-coupled β-subunit of the cholera toxin (CTB), as previously described (Vigouroux et al., 2020). Injecting distinct Alexa-coupled CTB in each eye revealed normally segregated RGC projections in 1-month-old control mice (Figure3 A-E, n = 5). At 1 month, *Dkk3:Cre-Ntn1$^{fl/fl}$* mice displayed a decreased optic nerve size but proper targeting of major visual nuclei (Figure 3F-J, n = 5). However, targeting to the accessory optic nucleus, the olivary pretectal nucleus (OPN), appeared to be strongly perturbed (Figure 3F,G, n = 5). Moreover, while the overall size of the contra-lateral and ipsi-lateral lateral geniculate nucleus (LGN) seemed reduced, the gross segregation pattern was conserved in *Dkk3:Cre-Ntn1$^{fl/fl}$* mice (Figure 3I, J, n = 5). Therefore, loss of *Netrin-1* results in a specific RGC targeting defect of the OPN.

Next, we assessed the impact of ectopic Netrin-1 expression on RGC projections in the brain. At 1 month, a severe targeting defect of the OPN was observed in *Dkk3:Cre-NTN1$^{tg/+}$* mice (Figure 3 K, L, n = 5). Moreover, optic nerve size also appeared dramatically reduced in *Dkk3:Cre-NTN1$^{tg/+}$* (Figure 3M, n = 5). Segregation

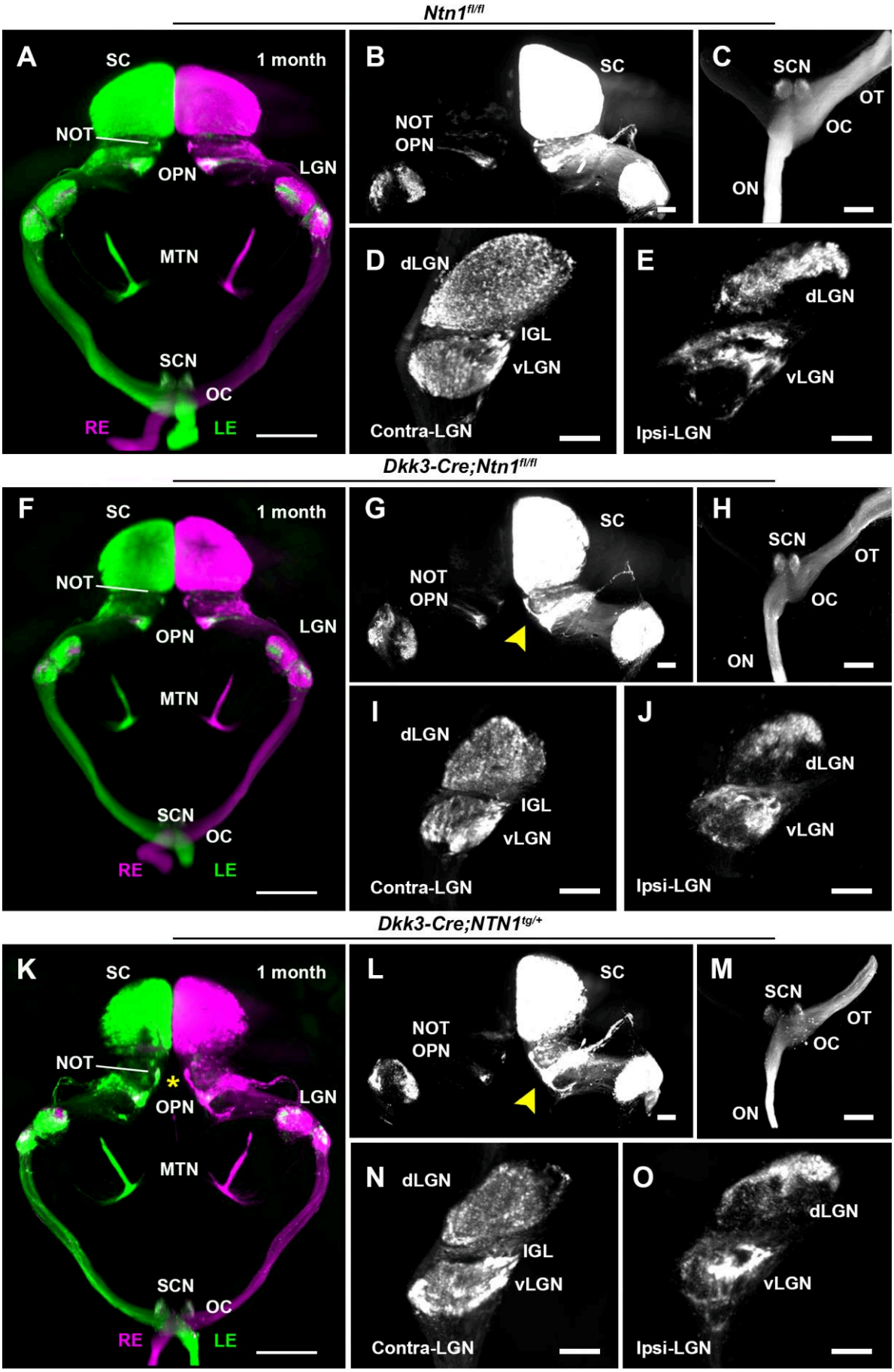
Ntn1fl/fl
A
SC
1 month
NOT
OPN
LGN
MTN
SCN
OC
RE
LE
B
SC
NOT
OPN
C
SCN
OT
OC
ON
D
dLGN
IGL
vLGN
Contra-LGN
E
dLGN
vLGN
Ipsi-LGN
Dkk3-Cre;Ntn1fl/fl
F
SC
1 month
NOT
OPN
LGN
MTN
SCN
OC
RE
LE
G
SC
NOT
OPN
H
SCN
OT
OC
ON
I
dLGN
IGL
vLGN
Contra-LGN
J
dLGN
vLGN
Ipsi-LGN
Dkk3-Cre;NTN1tg/+
K
SC
1 month
NOT
OPN
LGN
MTN
SCN
OC
RE
LE
L
SC
NOT
OPN
M
SCN
OT
OC
ON
N
dLGN
IGL
vLGN
Contra-LGN
O
dLGN
vLGN
Ipsi-LGN

Figure 3. RGC projections to the AOS are affected in netrin-1 mutants. 3D rendering of visual projections from both eyes using AlexaFluor-555 and AlexaFluor-647-conjugated Cholera toxin β subunit (CTB). **A-E** RGC tracing of a 1 month old control mouse. (**A**) Frontal view of the entire visual pathways. Top view of the SC, NOT and OPN (**B**) and the optic chiasm (**C**). Sagittal view of the contra-lateral LGN (**D**) and ipsi-lateral LGN (**E**). **F-J** RGC projections from *Dkk3:Cre-Ntn1*$^{fl/fl}$ cKO mice. Yellow arrowhead indicates aberrantly projecting RCCs. **K-O** RGC projections from *Dkk3:Cre-NTN1*$^{tg/+}$ mice. Yellow arrowhead indicates aberrantly projecting RGCs. LE = Left eye, RE = Right eye, SCN = suprachiasmatic nucleus, MTN = medial termainl nucleus, OPN = olivary pretectal nucleus, LGN = Lateral geniculate nucleus, dLGN = dorsal lateral geniculate nucleus, vLGN = ventral lateral geniculate nucleus, IGL = inner geniculate leaflet, NOT = nucleus of the optic tract, SC = superior colliculus. **Scale bars**: **A,F,K** 500μm, **B-E, G-J, L-O** 300μm.

of ipsi-lateral RGC projections in the superior colliculus as well as the LGN seemed preserved (Figure 3L, N,O, n=5).

RGC projections to the medial terminal nucleus are dependent on Netrin-1 expression.

RGCs project to as many as forty-six different brain nuclei that can be grossly divided into image-forming and non-image forming nuclei (Morin and Studholme, 2014). The non image forming nuclei belong to the AOS. The MTN of the AOS is responsible for vertical image stabilization. Recently, Sema6A expressed by direction-selective ganglion cells (DSGCs) was shown to bind PlexinA2/A4 expressing cells of the MTN of the AOS (Sun et al., 2015). Interestingly, eye-specific deletion of *Dcc* leads to significant targeting defects of the MTN, suggesting a role for Dcc/Netrin-1 signaling in MTN targeting (Vigouroux et al., 2020). Our previous analysis in *Dkk3:Cre-Ntn1*$^{fl/fl}$ mice showed that eye-specific deletion of Netrin-1 did not lead to MTN targeting defects, suggesting either a Netrin-1 independent or non-cell autonomous mechanism. The MTN is located at the basal plate and is mainly composed of migratory cells from prosomere 1 (P1) (Ferran et al., 2009). The first DSGCs to target the MTN arrive at E14.5 (Sun et al., 2015). By postnatal day 1, the ventral and dorsal nuclei of the MTN have both been innervated by DSGCs and appear mature (Sun et al., 2015). To delete *Netrin-1* expression specifically from the basal plate, we used the *Engrailed-1* (*En1:Cre*)(Kimmel et al., 2000) and the *Sonic Hedgehog* (*Shh:Cre*)(Harfe et al., 2004) Cre driver lines. Both *En1:Cre* and *Shh:Cre* mice were crossed with the *Ai9 Rosa*^{Tdtomato} reporter line (Jackson laboratories). At E11, *En1:Cre-Rosa*^{Tom} was strongly expressed in the midbrain and basal plate (Figure 4A, n=2). At E13, *En1:Cre-Rosa*^{Tom} was not expressed in the retina (Figure 4A,B, n = 2).

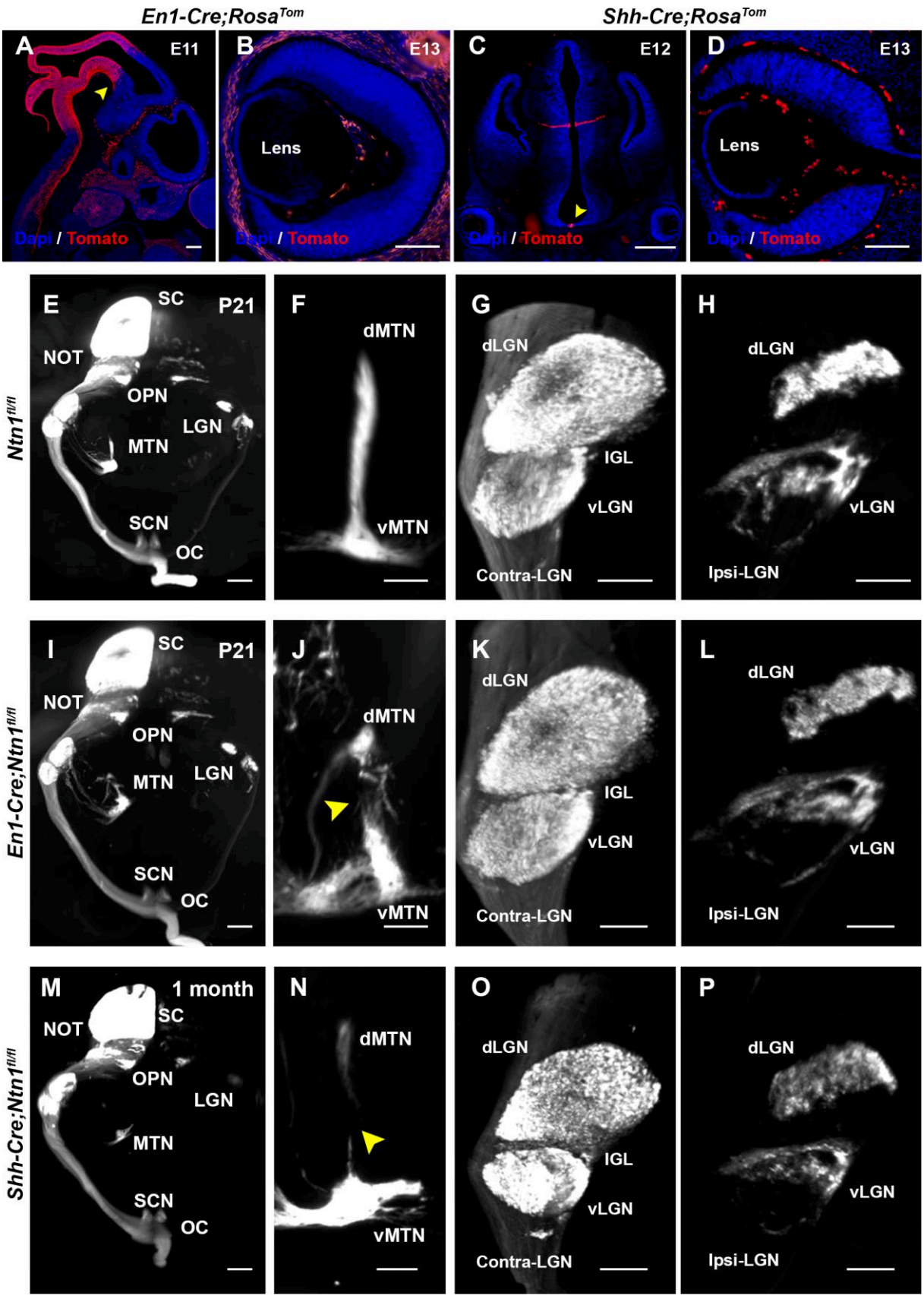
En1-Cre;Rosa^Tom
Shh-Cre;Rosa^Tom
A
E11
B
E13
C
E12
D
E13
Lens
Lens
Dapi / Tomato
Dapi / Tomato
Dapi / Tomato
Dapi / Tomato
Ntn1^fl/fl
E
P21
SC
NOT
OPN
LGN
MTN
SCN
OC
F
dMTN
vMTN
G
dLGN
IGL
vLGN
Contra-LGN
H
dLGN
vLGN
Ipsi-LGN
En1-Cre;Ntn1^fl/fl
I
P21
SC
NOT
OPN
MTN
LGN
SCN
OC
J
dMTN
vMTN
K
dLGN
IGL
vLGN
Contra-LGN
L
dLGN
vLGN
Ipsi-LGN
Shh-Cre;Ntn1^fl/fl
M
1 month
SC
NOT
OPN
LGN
MTN
SCN
OC
N
dMTN
vMTN
O
dLGN
IGL
vLGN
Contra-LGN
P
dLGN
vLGN
Ipsi-LGN

Figure 4. RGC targeting to the MTN requires netrin-1. **A** Sagittal cryosection of an E11 *En1:Cre-Rosa*^{Tom} embryo labeled with Dapi (Blue) and DsRed (red). **B** Sagittal retinal section of an E13 *En1:Cre-Rosa*^{Tom} embryo labeled with Dapi (blue) and DsRed (red). **C** Coronal section of an E12 *Shh:Cre-Rosa*^{Tom} embryo labeled for DsRed (red) and Dapi (blue), the basal plate is labeled (arrowhead). **D** A saggital section of an E13 retina from a *Shh:Cre-Rosa*^{Tom} embryo labeled with DsRed (red) and Dapi (blue). **E-P** 3D rendering of RGC projections traced with an AlexaFluor-555-conjugated Cholera toxin β subunit (CTB). **E-H** shows visual projections from a P21 control mouse. RGC projections are already segregated (**E**) and both the dMTN and vMTN are fully innervated (**F**)**.** Both Contra-lateral projections (**G**) as well as ipsi-lateral projections (**H**) are well segregated. **I-L** RGC projections in P21 *En1:Cre-Ntn1*$^{fl/fl}$ cKO mice. **I** Overall projections to image-forming nuclei project correctly and are well segregated. **J** Projections to the MTN are disorganized between the dMTN and vMTN (arrowhead). **K-L** contra-lateral and ipsi-lateral projections to the LGN segregate correctly. **M-P** visual projections from 1 month old *Shh:Cre-Ntn1*$^{fl/fl}$ cKO mice. **M** RGC projections correctly target and segregate in image-forming nuclei. **N** RGCs aberrantly project to the MTN, with a distinct lack of connection between the vMTN and dMTN. **O-P** RGC projections segregate correctly in the LGN. SCN = suprachiasmatic nucleus, dMTN = dorsal medial terminal nucleus, vMTN = ventral medial terminal nucleus, MTN = medial termainl nucleus, OPN = olivary pretectal nucleus, LGN = Lateral geniculate nucleus, dLGN = dorsal lateral geniculate nucleus, vLGN = ventral lateral geniculate nucleus, IGL = inner geniculate leaflet, NOT = nucleus of the optic tract, SC = superior colliculus. **Scale bars**: **A** 200μm**, B,D** 100μm, **C** 500μm, **E,I,M** 500μm, **F,J,N,** 200μm, **G,H,K,L,O,P**, 300μm.

Moreover, *Shh:Cre-Rosa*^{Tom} mice showed a strong recombination in the basal plate at E12 (Figure 4C, arrowhead, n = 2). At E13 *Shh:Cre-Rosa*^{Tom} was not observed in the retina (Figure 4C,D, n = 2). At P21, control mice injected with CTB displayed a mature visual system with complete RGC segregation in the superior colliculus and LGN (Figure 4E-H, n= 3). Likewise, P21 *En1:Cre-Ntn1*$^{fl/fl}$ mice showed correct RGC targeting and segregation within the superior colliculus and the LGN (Figure 4I,K,L, n = 3). However, a severe RGC projection defect was observed in the MTN of *En1:Cre-Ntn1*$^{fl/fl}$ mice when compared to control littermates (Figure 4J, arrowhead, n = 3). *En1:Cre* was broadly expressed in the midbrain and basal plate of the developing central nervous system. Therefore, MTN defects could be a result of gross anatomical abnormalities in these mutants. As a result, we generated *Shh:Cre-Ntn1*$^{fl/fl}$ cKO mice devoid of Netrin-1 expression at the floor plate and basal plate. 1 month-old *Shh:Cre-Ntn1*$^{fl/fl}$ mice displayed a severe perturbation of targeting to the MTN without any other RGC targeting or segregation defects (Figure 4M-P, arrowhead, n = 3). Together, our results point towards a novel role of Netrin-1 in the AOS.

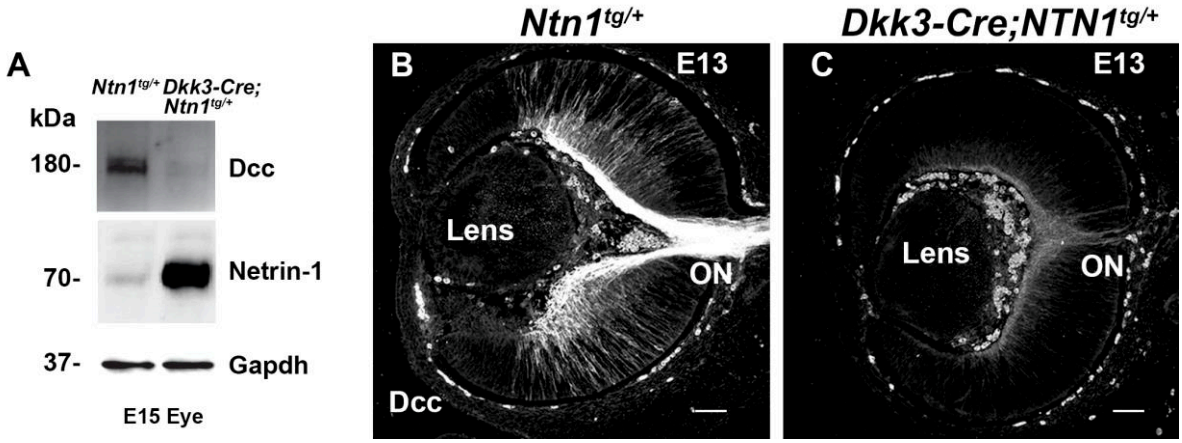

Supplementary Figure 1. Netrin-1 overexpression induces a decrease in Dcc levels. **A** Western blot analysis of E15 whole eye extracts against Dcc (180kDa) and Netrin-1 (70kDa) on *NTN1*$^{tg/+}$ and *Dkk3:Cre-NTN1*$^{tg/+}$ mice, with the loading control, Gapdh (37KDa). **B,C** Coronal cryosections of E13 on *NTN1*$^{tg/+}$ (**B**) and *Dkk3:Cre-NTN1*$^{tg/+}$ mice (**C**) labeled with Dcc (White). **Scale bars**: **B,C** 50 μm

Discussion

We generated a novel eye-specific *Ntn-1* cKO mutant mouse that removes *Netrin-1* specifically from the optic disc. This *Netrin-1* deletion is sufficient to induce severe intra-retinal RGC defects which lead to ON hypoplasia. We also generated a transgenic *NTN-1* cKO mouse that induces a broad Netrin-1 expression across the entire eye. This overexpression gives rise to severe RGC defects in the retina that lead to severe ON thinning. Therefore, both Netrin-1 loss and gain of function are associated with defects in the RGC targeting to the brain proper, including the OPN. Interestingly, we also show a novel role of Netrin-1 in RGC targeting to the MTN, as deletion of Netrin-1 in the floor plate and midbrain provokes significant MTN defects.

The observation that *Netrin-1* deletion at the optic disc is sufficient to induce RGC defects suggests a role for Netrin-1 as a short-range guidance cue. As a result, we speculate that RGCs could use Netrin-1 as a scaffold at the optic disc to enter the ON. This model is in line with recent studies outlining a haptotactic role for Netrin-1 (Dominici et al., 2017; Meijers et al., 2019; Varadarajan et al., 2017; Yamauchi et al., 2017). A previous report eluded to the short-range role of Netrin-1 in the visual system. In the absence of *Netrin-1*, *Drosophila melanogaster* R8 photoreceptor growth cones are able to project properly but are unable to adhere to their terminal zone (Akin and Zipursky, 2016).

It is essential to stress that we also show *in vivo* that Netrin-1 overexpression induces a redistribution of its trophic receptor Dcc. This finding confirms a previous *in vitro* study that revealed that exogenous Netrin-1 application leads to the proteasomal degradation of Dcc (Kim et al., 2005). Such a result raises strong concerns about the effect of *Netrin-1* loss and gain-of-function and the sole implication of *Netrin-1 in the observed* intra-retinal RGC defects. The *Netrin-1* cKO and gain-of-function mice do

nonetheless show specificities such as guidance defects to the AOS and to the OPN. Guidance of RGC axons to the accessory visual system remains elusive. However, cadherins have been implicated in the proper targeting of intrinsically photosensitive RGCs (ipRGCs) to the OPN (Osterhout et al., 2011). Indeed, cadherin-6 null mice display severe OPN targeting defects (Osterhout et al., 2011). Of interest, both cadherins -3 and -6 have been shown to be expressed in the OPN, further work should study whether a larger complex could be created with Netrin-1.

Finally, we reveal a novel role for Netrin-1 in the proper targeting of RGCs to the MTN. Interestingly, we previously showed that deletion of *Dcc* in RGCs led to aberrant RGC projections to the MTN (Vigouroux et al., 2020). We speculate that Dcc-positive direction-sensitive RGCs project to the Netrin-1-expressing MTN. However, the precise mechanism by which RGCs may require Dcc and Netrin-1 for proper targeting of the MTN is a topic of significant interest that is poorly understood. While Dcc appears broadly expressed in the developing RGCs (Vigouroux et al., 2020), whether Netrin-1 is expressed in the developing MTN remains unknown. In the developing spinal cord, Netrin-1 is expressed, transported and released in the pial surface by ventricular progenitors (Dominici et al., 2017; Varadarajan et al., 2017; Yamauchi et al., 2017). This transport of Netrin-1, from the ventricular surface to the pial surface was also shown in radial glia of the ventral midbrain (Brignani et al., 2020). We hypothesize that Netrin-1 could be transported in this manner at the ventral midbrain, where the MTN is localized (Ferran et al., 2009). Alternatively, Netrin-1 in midbrain dopaminergic neurons has been recently shown to be transported by axon projections from a distant source in the forebrain (Brignani et al., 2020). As a result, a source of Netrin-1 in the ventral midbrain could guide RGC axons towards the MTN.

Materials and Methods

Animals

Ntn1 conditional knockout (*Ntn1*^{fl}) (Srinivas et al., 2001), *Ntn1* hypomorphs (*Ntn1*$^{\beta geo}$) (Serafini et al., 1996), *Sonic hedgehog:Cre* (*Shh:Cre*) (Harfe et al., 2004), *Engrailed-1:Cre* (*En1:Cre*) (Kimmel et al., 2000), and *Dickopf-3:Cre* (*Dkk3:Cre*) (Sato et al., 2007) mice were previously described. Cre expression was monitored by crossing the Cre driver lines with the *Ai9 Rosa*^{tdTomato} reporter line (*RosaTom*; Jackson laboratories). Genotypes were determined by a polymerase chain reaction using genomic DNA from tail extracts. Embryonic day 0.5 was considered the day of the vaginal plug. Male and females were sued without distinction. Mice care and housing followed the institutional guidelines, approved by the Charles Darwin Ethics Committee of Sorbonne Université.

Generation of *NTN1*$^{tg/+}$ mouse line

The NTN1$^{tg/+}$ mouse line was generated by the SEAT (service d'experimentation animale de transgénèse et de recombinaison homologue) by inserting a floxed-STOP cassette (3x PolyA) followed by a human *NTN1* cDNA and an M2 flag sequence into the Rosa26 locus (Srinivas et al., 2001). The linearized construct was electroporated into 129Sv/Pas mouse embryonic stem (ES) cells. After selection, targeted clones were identified by polymerase chain reaction using external primers. The positive ES clones were injected into C57BL/6J blastocysts and gave rise to male chimeras. Breeding was established with C57BL/6J mice expressing the Flp-recombinase, to produce the heterozygous *NTN1*$^{tg/+}$ line devoid of the neomycin cassette.

In Situ Hybridization

Sections were hybridized with digoxinegin-labeled riboprobes as described in (Marillat et al., 2002). Briefly, sections were hybridized overnight at 72°C with a Netrin-1^{exon3}-specific riboprobe (1/200) (Dominici et al., 2017). The riboprobe was revealed using an anti-DIG antibody conjugated with the alkaline phosphatase (1/5000, Roche Diagnostics).

Western blotting

E15 eyes from control or *NTN1*$^{tg/+}$ mice were harvested and lysed in 10mM HEPES pH7.0, 100mM NaCl, 2mM EDTA, 0.5%NP-40 supplemented with protease and phosphatase inhibitors (Sigma). For immunoblotting, samples were separated on a 4-15% Mini-Protean TGX Tris-Glycine buffer SDS PAGE (Biorad) and transferred onto a 0.2µm Trasn-Blot Turbo nitrocellulose membrane (Biorad). Membranes were blocked for 1h at RT in blocking buffer (1X TBS(10mM Tris pH8.0, 150mM NaCl), 5% (w/v) dried skim milk powder. Primary antibodies were incubated o/n at 4°C (see supplementary file 1). Membranes were washed in TBST (2.5% Tween-20 in 1X TBS). Western blots were then incubated for 1h with HRP-conjugated secondary antibodies (see supplementary file 1) and were revealed using ECL prime (Amersham)

Immunohistochemistry

Cryosections

Samples were fixed by immersion in 4% paraformaldehyde (PFA) in 0.12 M phosphate buffer (VWR, 28028.298 and 28015.294), pH 7.4 (PBS) o/n at 4°C. Following three washes in 1XPBS, the samples were incubated in 10% sucrose (VWR, 27478.296) in 0.12 M phosphate buffer o/n at 4°C. The next day, samples were transferred to a 30% sucrose solution in 0.12 M phosphate buffer o/n at 4°C. Samples were then embedded in 0.12 M phosphate containing 7.5% gelatin (Sigma, 62500) and 10% sucrose, frozen in isopentane at -40°C and then cut at 16 µm with a cryostat (Leica, CM3050S). Sections were blocked in PBS containing 0.2% gelatin (VWR) and 0.25% Triton-X100 (PBS-GT) for 1 h at RT. Following the blocking, sections were incubated with primary antibodies (see supplementary file 1) diluted in a PBS-GT solution o/n at RT. Following three washes in PBST (0.05% Trinton-X100) secondary antibodies coupled to the appropriate fluorophore (see supplementary file 1) were diluted in PBS-GT and incubated for 2 h at RT. Sections were counterstained with Hoechst (Sigma, B2883, 1:1000). For Netrin-1 staining, an antigen retrieval step was performed by boiling sections in a 1X Sodium Citrate solution pH 6.0 for 5 mins using a microwave. Slides were scanned with a laser scanning confocal microscope (Olympus, FV1000).

Whole-Mount Immunostaining

E16 embryos were processed as previously described (Vigouroux et al., 2020). Briefly, embryos were de-pigmented in a solution of 11% H_2O_2 (VWR, 216763) at 70 rpm exposed to an 11W warm white Light-Emitting Diode (LED) (3000° Kelvin) for 1-3 days. Samples were then blocked and permeabilized before being incubated with the primary antibodies for 7 days at RT (see Table 1) in a solution containing: 0.5% Tirton-X100,

5% donkey normal serum, 20% Dimethyl Sulfoxide, 1XPBS, 0.1 g/L thimerosal. The samples were further labeled with secondary antibodies (see supplementary file 1) for 2 days at RT under agitation.

Tracing of visual projections

Adult mice were anesthetized with Isoflurane and injected with cholera toxin β subunit as described in (Vigouroux et al., 2020). Using a capillary, approximately 1µl of 2 µg/µl of AlexaFluor-conjugated cholera toxin β subunit (Thermo Fischer, AlexaFluor555-CTB C22843 and AlexaFluor647-CTB C34778) was injected intravitreally. 72 h following CTB injection, specimens were transcardially perfused with 4%PFA and the brains were dissected for tissue clearing.

Tissue clearing and imaging

E16 embryos and adult mouse brains were processed as described in (Vigouroux et al., 2020). Samples were gently de-hydrated in ascending baths of methanol (1h30). Samples were further treated with a solution containing 2/3 Dichloromethane (DCM, Sigma) 1/3 methanol o/n. The next day, samples were placed in DCM for 30 min prior to being immersed in Di-benzyl Ether (DBE, Sigma). Acquisitions were performed using an ultramicroscope I with the ImspectorPro software (LaVision BioTec, Miltenyi Biotec company, 5.1.328 version).

Supplementary File 1					
Primary antibodies					
Antigen	**Species**	**Catalog #**	**Company**	**Dilution**	**Immunohistochemistry**
Netrin-1	Rat	MAB1109	R&D systems	1:500	Cryosections/immunoblotting
GAPDH	Rabbit	CS2118	Cell Signaling	1:2000	immunoblotting
DCC(A20)	Goat	SC-6535	SantaCruz	1:500	Cryosections/immunoblotting
DsRed	Rabbit	632496	Clonetech	1:300	Cryosection/whole-mount
CHX10	Sheep	X1180-P	Exalpha	1:300	Cryosection
Pax2	Rabbit	71-6000	Life Technologies	1:500	Cryosection/whole-mount
Tag1	Goat	AF4439	R&D systems	1:500	Crosection/Whole-mount
Secondary antibodies					
Anti Rat HRP	Donkey	212-035-153	Jackson Immunoresearch	1:500	immunoblotting
Anti Goat HRP	Donkey	705-035-003	Jackson Immunoresearch	1:500	immunoblotting
Anti Rabbit HRP	Goat	111-035-003	Jackson Immunoresearch	1:500	immunoblotting
Anti Rabbit cy3 mcr	Donkey	711-165-152	Jackson Immunoresearch	1:500	cryosections/whole-mount
Anti Rabbit Alexa 647 mcr	Donkey	711-605-152	Jackson Immunoresearch	1:500	cryosections/whole-mount
Anti Goat Alexa 488	Donkey	A11055	Life Technologies	1:500	cryosections/whole-mount
Anti Goat Alexa 555	Donkey	A21432	Life Technologies	1:500	cryosections/whole-mount
Anti Goat cy3 mcr	Donkey	705-165-147	Jackson Immunoresearch	1:500	cryosections/whole-mount
Anti Sheep cy3 mcr	Donkey	713-165-1471:500	Jackson Immunoresearch	1:500	cryosections/whole-mount
Anti Sheep Alexa 647 mcr	Donkey	713-605-147	Jackson Immunoresearch	1:500	cryosections/whole-mount
Anti Sheep Alexa 488	Donkey	A11015	Life Technologies	1:500	cryosections/whole-mount
Anti mouse Alexa 488	Donkey	A21202	Life Technologies	1:500	cryosections/whole-mount
Anti mouse Alexa 647 mcr	Donkey	715-605-150	Jackson Immunoresearch	1:500	cryosections/whole-mount

Eye-specific deletion of Dcc induces persistent fetal vasculature

Robin J. Vigouroux, Patrick Mehlen, Alain Chédotal and Kim Nguyen-Ba-Charvet

Contribution: R. J. Vigouroux, K. Nguyen-Ba-charvet, and A. Chédotal designed the experiments, the figures and wrote the manuscript. R. J. Vigouroux carried out the experiments that make up Figures 1 to 3.

Introduction

During development, periocular mesenchymal (POM) cells invade the eye through the choroid fissure (Le Lievre and Le Douarin, 1975). POM cells subsequently differentiate into endothelial cells forming a transient vascular network composed of the hyaloid artery (HA) and the vasa hyaloidea propria (VHP) that nourish the embryonic lens and retina (Cairns, 1959). This development process shares many characteristics of axonal guidance mechanisms (Carmeliet, 2003). Hyaloid vessel regression begins at birth in mice and is concomitant with the onset of retinal vessels (Rao et al., 2013). During the first postnatal week, retinal vessels form the primary plexus that completely covers the retinal epithelium (Fruttiger, 2007). Persistent fetal vasculature is a common human disorder resulting from an improper regression of hyaloid vessels that accounts for 5% of blindness in the United States (Zigler et al., 2016).

The laminin-like protein Netrin-1 plays a significant role during angiogenesis (Bouvrée et al., 2008; Castets et al., 2009; Ding et al., 2014; Larrivée et al., 2007; Liu et al., 2014; Lu et al., 2004; Nguyen and Cai, 2006; Park et al., 2004; Shao et al., 2015; Wilson, 2006). However, its precise role is an active area of debate since reports suggest both a pro- and anti-angiogenic role of Netrin-1 (Lu et al., 2004; Wilson, 2006). Netrin-1 mediates its angiogenic action through the repulsive Uncoordinated 5B (UNC5B) receptor expressed on the surface of endothelial tip cells (Hong et al., 1999; Larrivée et al., 2007; Leonardo et al., 1997; Lu et al., 2004). Netrin-1 is also known to bind the transmembrane receptor Deleted in Colorectal Cancer (Dcc) to mediate permissive responses (Fazeli et al., 1997; Keino-Masu et al., 1996). However, the role of Dcc during angiogenesis remains unstudied.

Here, we studied the role of Dcc in angiogenesis by generating an eye-specific conditional mutant (Dcc cKO). We observed that adult Dcc cKO mice display severe retinal vascular defects. These defects occured embryonically, and hyaloid vessels persisted into the first postnatal month. Finally, we showed that retinal astrocyte migration is compromised in Dcc cKO mutant mice yielding dramatic vascular defects.

Results

Eye-specific deletion of Dcc dramatically impairs the retinal vascular network.

Angiogenesis is a highly stereotypical process that is replicated throughout the organism. The retina provides a unique system to study angiogenesis as it is easily amenable to imaging. Until now, retinal angiogenesis was studied using retinal flat mounts. However, several features of the retinal vasculature are fragile to dissection, making it challenging to visualize the entire network. Blood vessels are inherently complex, spanning many centimeters, analyzing vessel networks in 2D thus leads to a great loss of information.

To assess the role of Dcc during angiogenesis, we took advantage of *Dcc* conditional knock-out (cKO) mice under the Dickopf-3 promoter, expressed in all retinal progenitors (Sato et al., 2007; Vigouroux et al., 2020). Observation of the retinal vasculature using eye fundoscopy coupled to a systemic injection of a fluorescein dye revealed a complete vascular network in control mice (Figure 1A,B, n = 5). We next evaluated the retinal vasculature of 1-month old *Dkk3-Cre;Dcc*$^{lox/lox}$ mice. As previously reported, we observed a dramatic optic nerve (ON) hypoplasia in *Dkk3-Cre;Dcc*$^{lox/lox}$ mice using eye fundoscopy (Figure 1C, n = 5). Surprisingly, analysis of the retinal

vasculature of *Dkk3-Cre;Dcc*$^{lox/lox}$ using eye fundoscopy showed a dramatic reduction of the retinal vasculature (Figure 1D, n = 5).

In *Dkk3-Cre;Dcc*$^{lox/lox}$ mice, several vessels appeared in the vitreous, suggesting hyaloid vessel persistence. In mice, the transient hyaloid vessel network begins to regress at postnatal day 0 (P0) and is concomitant with the onset of retinal vessel angiogenesis at the optic nerve head (Rao et al., 2013). In order to bypass the retinal dissection required for retinal flat mounts, we adapted whole-mount immunohistochemistry and EyeDISCO clearing protocol coupled to light sheet fluorescence microscopy for the unbiased study of the retinal vasculature in 3D (see Methods). To visualize the entire vascular network, we immunolabelled vessels using collagen IV (Coll IV), which is a major component of the basement membrane lining all blood vessels. Following imaging, we manually segmented the retinal and hyaloid vessels using Imaris software (Bitplane). At P0, retinal vessels began to proliferate at the optic nerve head (Figure 1E, n = 3 eyes). The VHP began to detach from the lens and circumferentially span the retina (Figure 1E, n = 3 eyes). A major branch remained attached to the lens (Figure 1F, n = 3 eyes). At this stage, *Dkk3-Cre;Dcc*$^{lox/lox}$ mice showed close to no retinal vascular proliferation (Figure 1G, n = 7 eyes). VHPs revealed a reduced vascular complexity, with major gaps in the central retina (Figure 1G, n = 7 eyes). In addition, the length of the primary branch appeared much longer than in control mice (Figure 1G, n = 7 eyes). A major branch of hyaloid vessels remained attached to the lens (Figure 1H, n = 7 eyes).

In the first postnatal week, the VHP undergoes vast regression, only leaving the several hyaloid vessels attached to the lens (Ito and Yoshioka, 1999). At P7, no VHPs were observed in control mice (Figure 1I, n = 8 eyes). Furthermore, the primary retinal vascular plexus had fully invaded the retina at P7 (Figure 1I, n = 8 eyes).

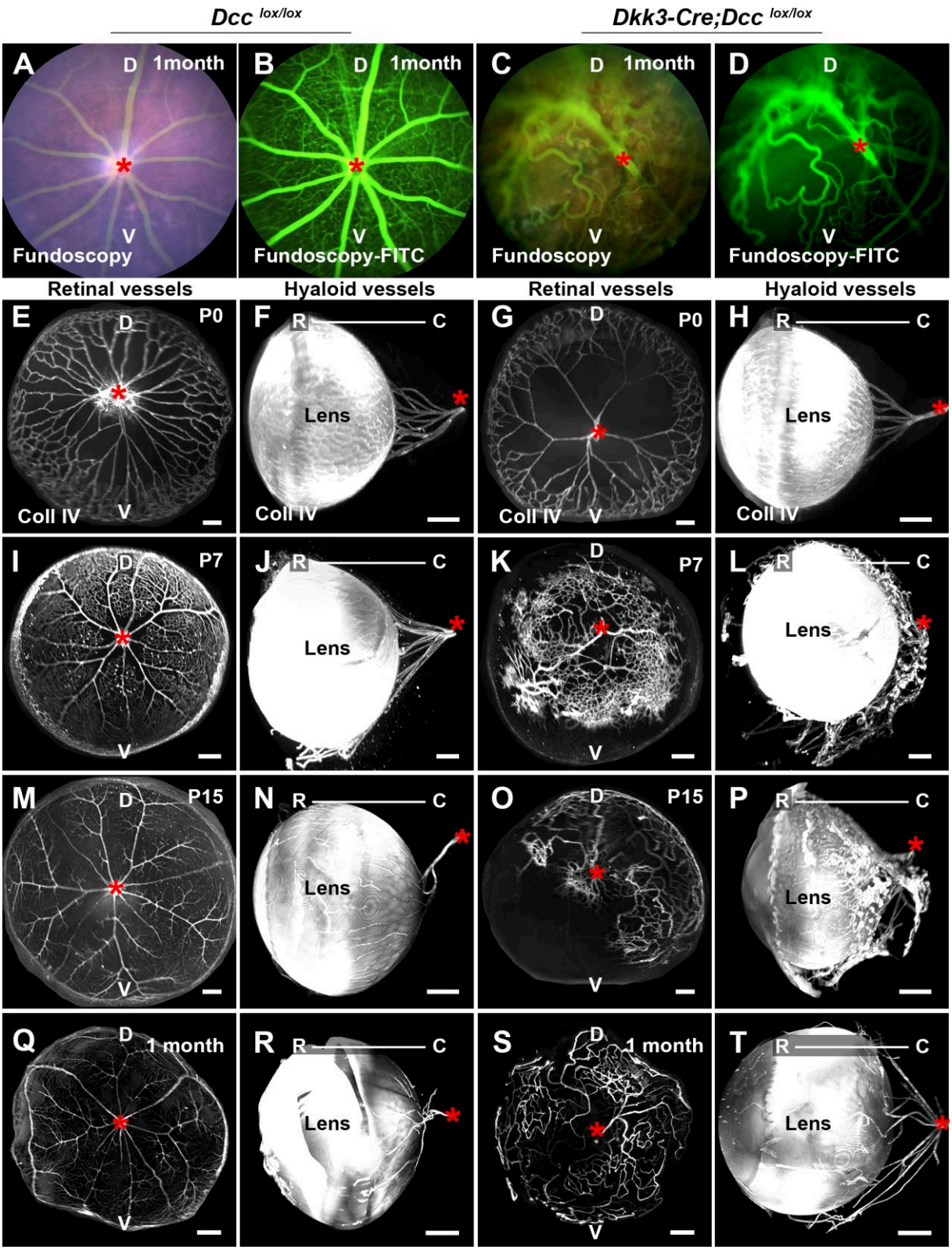
Dcc lox/lox
Dkk3-Cre;Dcc lox/lox
A
D 1month
V
Fundoscopy
B
D 1month
V
Fundoscopy-FITC
C
D 1month
V
Fundoscopy
D
D
V
Fundoscopy-FITC
Retinal vessels
Hyaloid vessels
Retinal vessels
Hyaloid vessels
E
D
P0
Coll IV
V
F
R
C
Lens
Coll IV
G
D
P0
Coll IV
V
H
R
C
Lens
Coll IV
I
D
P7
V
J
R
C
Lens
K
D
P7
V
L
R
C
Lens
M
D
P15
V
N
R
C
Lens
O
D
P15
V
P
R
C
Lens
Q
D
1 month
V
R
R
C
Lens
S
D
1 month
V
T
R
C
Lens

Figure 1. Dcc cKO mice display major retinal vascular defects. **A-D** Eye fundoscopy of 1-month old mice injected with a fluorescein dye. **A,B** show a control eye. **C,D** Show *Dkk3:Cre-Dcc*$^{lox/lox}$ eye. **E-T** 3D rendering of whole eyes labelled with the pan blood vessel marker Collagen IV (Coll IV, white). **E-H** represent P0 eyes. **I-L** P7 eyes. **M-P** P15 eyes. **Q-T** 1-month old eyes. **E,I,M,Q** show a frontal view of retinal vessels of control mice and **G,K,O,S** show retinal vessels of *Dkk3:Cre-Dcc*$^{lox/lox}$ mice manually segmented. **F,J,N,R** show hyaloid vessels attached to the lens of control mice and **H,L,P,T** of *Dkk3:Cre-Dcc*$^{lox/lox}$ eyes. Red asterisk shows the optic nerve head; D = Dorsal; V = Ventral; R = Rostral; C = Caudal. **Scale bars**: **E,G,I-T** = 200 μm; **F,H** = 150 μm.

Several hyaloid vessels were still observed attached to the postnatal lens (Figure 1J, n = 8). Strikingly, *Dkk3-Cre;Dcc*$^{lox/lox}$ mice only showed a partial vascular network that did not cover the entire retinal surface (Figure 1K, n = 8 eyes). Moreover, the vessel network appeared strongly disorganized (Figure 1K, n = 8 eyes).The hyaloid vessels in *Dkk3-Cre;Dcc*$^{lox/lox}$ mice looked more tortuous than in control mice (Figure 1L, n = 8 eyes).

The retinal vasculature undergoes vast remodeling and appears mature by the second postnatal week (Rao et al., 2013). P15 control mice displayed a mature vascular network with only few hyaloid vessel branches attached to the lens (Figure 1M,N, n = 4 eyes). In contrast, *Dkk3-Cre;Dcc*$^{lox/lox}$ mice still possessed a partial retinal vascular coverage with little to no organization (Figure 1O, n = 7 eyes). In addition, *Dcc* cKo mice displayed an abundant hyaloid vasculature that sometimes innervated the avascular retinal portions (Figure 1P, n = 7 eyes).

Several mouse mutants display hyaloid vessels persistence (Nayak et al., 2018; Nguyen et al., 2019; Rao et al., 2013; Salvucci et al., 2015; Zigler et al., 2016). These models induce a delay in the hyaloid regression with an almost completely regressed hyaloid vasculature by the second postnatal week. To assess the hyaloid vessel network in older mice, we carried out whole-mount immunostaining of 1-month old mice. Unlike control mice, *Dkk3-Cre;Dcc*$^{lox/lox}$ mice still possessed a strong hyaloid vasculature at 1 month (Figure 1Q-T, n = 3 eyes for both genotypes). Moreover, retinal vessels in *Dkk3-Cre;Dcc*$^{lox/lox}$ mice remained partial, leaving major avascular portions of the retina.

Retinal astrocytes do not properly migrate in *Dcc* conditional mutant mice.

Retinal vasculature development is closely linked to retinal astrocyte as well as retinal ganglion cell projections (Fruttiger et al., 1996; O'Sullivan et al., 2017). Retinal ganglion cell projections guide migrating astrocytes which themselves establish the adequate terrain for endothelial cells by secreting vascular endothelial cell growth factor (Vegf) (Dorrell et al., 2002; Fruttiger et al., 1996; Gerhardt et al., 2003; O'Sullivan et al., 2017). Retinal depletion of astrocytes leads to major retinal vascular defects (Tao and Zhan 2016). Throughout development, both retinal astrocytes and endothelial cells enter the retina through the optic nerve head (Selvam et al., 2018). Since *Dcc* cKO mice display severe ON defects (Deiner et al., 1997), we wondered whether retinal astrocytes could be perturbed in our *Dcc* cKO mice. During retinal vessel development, the arrival of endothelial cells induces retinal astrocyte maturation by downregulating Vegf while upregulating the glial fibrillary acidic protein (GFAP) (Gerhardt et al., 2003). To test whether *Dcc* ckO mice possessed retinal astrocyte migration defects, we carried out whole-mount immunostaining of eyes with the retinal astrocyte marker GFAP (O'Sullivan et al., 2017). At P0, we observed a circumferential migration of GFAP-positive astrocytes from the optic nerve head in both control and *Dkk3-Cre;Dcc*$^{lox/lox}$ mice (Figure 2A,B, n = 3 eyes and n = 7 eyes respectively). By P7, retinal astrocytes in *Dcc*$^{lox/lox}$ mice had fully covered the retinal surface (Figure 2C, n = 8 eyes). Moreover, retinal astrocytes were highly organized and followed the major blood vessels (Figure 2C, n = 8 eyes). In contrast, retinal astrocytes in *Dkk3-Cre;Dcc*$^{lox/lox}$ mice displayed a partial coverage of the retinal surface (Figure 2D, n = 8 eyes). In regions of astrocytic coverage, the retinal astrocytes were arranged into large polygons with major uncovered portions.

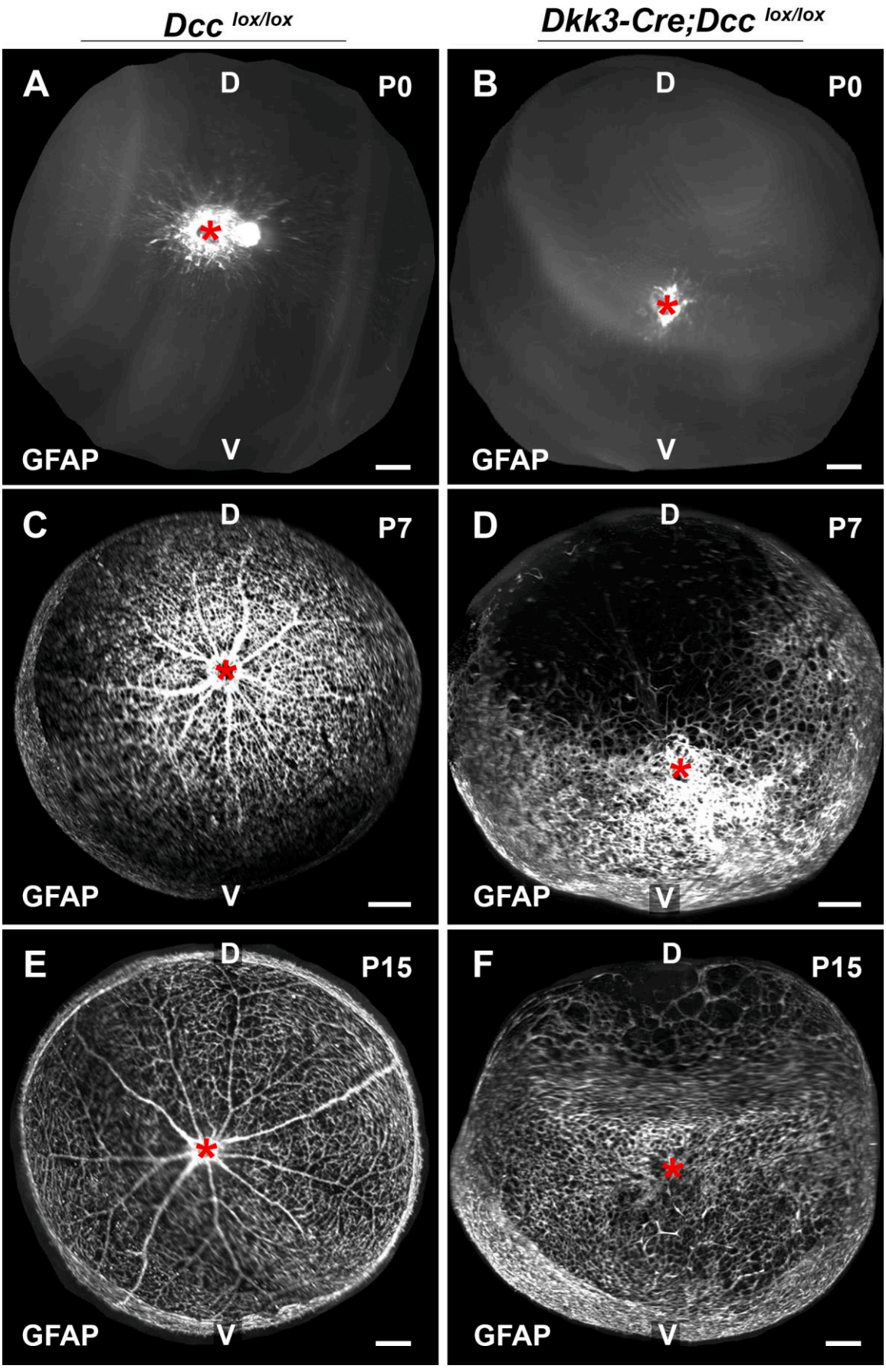
Dcc lox/lox
Dkk3-Cre;Dcc lox/lox
A
D
P0
GFAP
V
B
D
P0
GFAP
V
C
D
P7
GFAP
V
D
D
P7
GFAP
V
E
D
P15
GFAP
V
F
D
P15
GFAP
V

Figure 2. Dcc cKO mice possess retinal astrocyte migration defects. **A-F** show 3D rendering of whole eyes labelled with the astrocytic marker GFAP (white). **A** A frontal view of P0 control eyes. *De novo* retinal vessels begin to proliferate at the optic nerve head. **B** P0 eye of *Dkk3:Cre-Dcc*$^{lox/lox}$ mice. No retinal vessels can be seen at the optic nerve head. **C** show P7 eyes of control mice. Retinal astrocytes have fully migrated to the retinal periphery. **D** P7 *Dkk3:Cre-Dcc*$^{lox/lox}$ mice. Retinal astrocytes only partially cover the retina and lack proper organization. **E** Control mouse P15 eyes. Retinal astrocytes are fully mature and line the major blood vessels. **F** Retinal astrocytes labelled with GFAP in P15 *Dkk3:Cre-Dcc*$^{lox/lox}$ mice. Large portions of the retina remain uncovered. Retinal astrocytes in *Dkk3:Cre-Dcc*$^{lox/lox}$ mice form large polygon structures. Red asterisk represents the ON; D = Dorsal; V = ventral. **Scale bars**: **A-F** = 200 μm

Recent reports suggest that early postnatal manipulation in oxygen supply to the retina induces a delay in astrocyte migration (Perelli et al., 2019). To test whether astrocyte migration resumed in our *Dcc* cKO mice, we carried out whole-mount immunostaining of P15 eyes. Control eyes at P15 possessed a mature astrocyte coverage of the retina, with major blood vessel delineated by retinal astrocytes (Figure 2E, n = 4 eyes). Strikingly, *Dkk3-Cre;Dcc*$^{lox/lox}$ mice still displayed large portions of the retina devoid of astrocytic arbors (Figure 2F, n = 7 eyes). Furthermore, sites of astrocyte coverage still lacked proper organization (Figure 2F, n = 7 eyes). Considering that retinal vascularization normally follows the astrocyte template, the irregular organization of retinal astrocytes observed in *Dkk3-Cre;Dcc*$^{lox/lox}$ mice may be the cause of the major vessel defects.

The pro-apoptotic activity of Dcc is not required for hyaloid vessel regression.

Dcc was initially identified as a tumor suppressor gene which functions as a dependence receptor (DR) (Mehlen et al., 1998). In the absence of its trophic ligand (Netrin-1), Dcc induces a pro-apoptotic signal. This creates a dependency to Netrin-1 for the cell expressing Dcc. Interestingly, hyaloid regression is dependent on the apoptotic signal induced by retinal macrophages (Diez-Roux and Lang, 1997; Lang and Bishop, 1993; Lang et al., 1994). This raises the possibility that Dcc may be required by endothelial cells to induce a pro-apoptotic signal. The pro-apoptotic signal mediated by Dcc requires the cleavage of its intracellular domain (D1290) in a caspase-dependent manner (Castets et al., 2011; Forcet et al., 2001; Mehlen et al., 1998). To assess the role of Dcc in macrophage-induced endothelial-cell apoptosis, we used a transgenic mouse line carrying a point mutation at the Aspartic acid residue (D1290N, *Dcc*$^{mut/mut}$) on the intracellular domain of Dcc (Castets et al., 2011). Of note,

this point mutation significantly affected the pro-apoptotic signal induced by Dcc without altering its Netrin-1-mediated signal (Castets et al., 2011). At P15, mice heterozygous for the point mutation (*Dcc*$^{mut/+}$) displayed a large vascular tree that covered the entire retinal surface (Figure 3A, n = 5). Moreover, the hyaloid vascular network had regressed, leaving several branches attached to the lens (Figure 3B, n = 5 eyes). Similarly, P15 *Dcc*$^{mut/mut}$ mice showed a completely regressed hyaloid vasculature as well as a mature retinal vasculature covering the central-to-peripheral retina (Figure 3C,D, n = 3 eyes). To visualize the mature retinal vasculature, we analyzed 1-month old mice. Both control and *Dcc*$^{mut/mut}$ mice revealed a complete retinal vasculature with a fully regressed hyaloid vasculature at 1 month (Figure 3E-H, n = 3 eyes for both genotypes). To further probe the idea that retinal blood vessels depend on the correct migration of astrocytes, we next assessed the development of retinal astrocytes. In both P15 *Dcc*$^{mut/+}$ and *Dcc*$^{mut/mut}$ mice, GFAP-positive retinal astrocytes fully migrated along the entire retinal surface with a mature organization which co-localized to the major retinal blood vessels (Figure 3I-L, n = 5 eyes for control and n = 3 eyes for *Dcc*$^{mut/mut}$). Together these results show that the pro-apoptotic signal induced by Dcc is dispensable for proper hyaloid vessel regression.

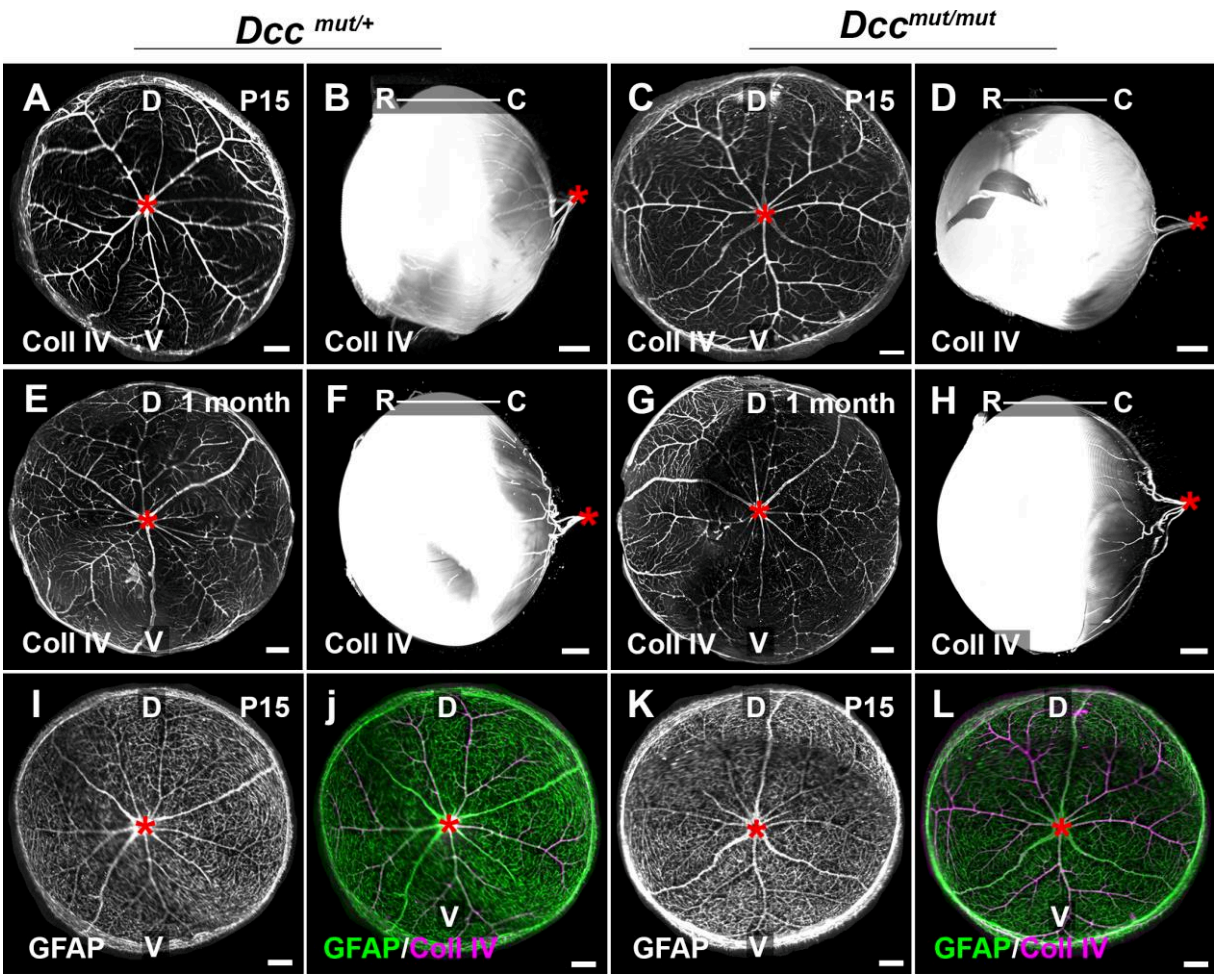

Figure 3. The pro-apoptotic activity of Dcc is dispensable for hyaloid vessel regression. **A-L** represent frontal views of whole eyes labelled with the blood vessel marker Collagen IV (Coll IV, white or magenta) or the astrocyte marker glial fibrillary acidic protein (GFAP, white or green). **A-D** show control or *Dcc*$^{mut/mut}$ P15 eyes. **A,C** show the retinal vessels **B,D** show the hyaloid vasculature. **E-H** represent 1-month old eyes of control and *Dcc*$^{mut/mut}$ mice. **E,G** show retinal vessels whereas **F**,**H** show hyaloid vessels. **I-L** show the retinal astrocytes and blood vessels of control and *Dcc*$^{mut/mut}$ mice. **I,K** show retinal astrocytes. **J,L** show retinal astrocytes and blood vessels. Red asterisk outlines the ON; D = dorsal; V = ventral; R = rostral: C = caudal. **Scale bars**: **A-L** = 200μm

Discussion

Using eye specific *Dcc* cKO mice, we show that hyaloid vasculature does not regress adequately in the absence of *Dcc*. In addition to the hyaloid vessel persistence, *Dcc* cKO mice display a dramatically reduced retinal vasculature coverage. Interestingly, the lack of retinal vessels in *Dcc* cKO mice is accompanied by a migration defect of retinal astrocytes.

To our knowledge, we provide the first evidence of the role of Dcc in hyaloid vessel regression. Hyaloid vessel regression is heavily reliant upon the adequate recruitment of retinal macrophages and removal of apoptotic endothelial cells (Diez-Roux and Lang, 1997; Lang and Bishop, 1993; Lang et al., 1994). It would therefore be of particular interest to investigate whether macrophage-induced apoptosis of endothelial cells is impacted in *Dcc* cKo mice.

Dcc deletion was induced using the Dkk3 promoter, which is expressed by all retinal progenitor cells but is absent from retinal blood vessels (Fukusumi et al., 2015; Muranishi and Furukawa, 2012; Sato et al., 2007). It is therefore important to mention that the vascular defects observed in our *Dcc* cKO mice are a secondary effect due to the retina specific loss of *Dcc*. Moreover, such vascular defects appear during early retinal development and must precede the retinal angiogenic wave. Retinal astrocytes invade the embryonic retina from the optic nerve head at E18 (O'Sullivan et al., 2017). Retinal astrocytes are critical for the correct proliferation of endothelial cells (Tao and Zhang, 2016). In line with these studies, our *Dcc* cKO mice display a large reduction in astrocyte coverage during early retinal development. Several hypotheses have been put forward to explain the precise mechanism responsible for this astrocyte migration defect. One hypothesis posits that the correct organization of RGCs is the building block to adequate astrocyte migration along the retinal lamina (Fruttiger et al., 1996).

RGC axons provide directional cues for astrocyte guidance (O'Sullivan et al., 2017). Disorganized RGC axons, such as in *Robo1/Robo2* KO mice, lead to aberrant astrocyte orientations (O'Sullivan et al., 2017). Moreover, complete ablation of RGCs using *Math5* KO gives rises to incomplete astrocyte migration to the peripheral retina (O'Sullivan et al., 2017). Of note, Dcc KO as well as Dcc cKO mice exhibit severe intra-retinal defects, an interesting topic for future research lies in understanding the role of Dcc in astrocyte migration during retinal development (Deiner et al., 1997; Vigouroux et al., 2020).

An alternative hypothesis postulates that the defect observed in astrocyte coverage may be a consequence of oxygen stress. A recent study in mice showed that neonatal exposure to hyperoxic conditions leads to a decreased astrocyte proliferation and retinal vessel defects (Perelli et al., 2019). It thus appears that retinal astrocytes respond to the retinal metabolic needs. In the peripheral retina with low oxygen conditions, there is an increase in astrocyte proliferation coupled to an augmented release of Vegf and pro-angiogenic response. In contrast, in the central retina, where blood vessels arrive sooner, hyperoxic conditions hinder astrocyte proliferation and inhibit Vegf release. As a result, hyperoxic conditions in the developing retina lead to a reduction in astrocyte number, a delay in retinal vessel development and hyaloid vessel persistence PERELI2020. Future research should investigate the switch in metabolic demand in *Dcc* cKO mice.

Lastly, it is also possible that astrocyte migration defects occur as a result of a physical hindrance and an improper entry into the optic nerve head. *Dcc* cKO mice display severe optic nerve hypoplasia (Vigouroux et al., 2020). Future work should focus on the ON defect observed in *Dcc* cKO mice and its impact on astrocyte migration along the ON and their entry into the retina.

Materials and Methods

Animals

Dcc floxed mice(Krimpenfort et al., 2012), *Dcc*^{D1290N} *(Dcc*$^{mut/mut}$*)* (Castets et al., 2011) and *Dickopf-3:Cre* (*Dkk3:Cre*) (Sato et al., 2007) mice were previously described. All mice were kept in C57BL/6J background. Genotypes were determined by a polymerase chain reaction using genomic DNA from tail extracts. Embryonic day 0.5 was considered the day of the vaginal plug. Male and females were used without distinction. Mice care and housing followed the institutional guidelines. Approved by the Charles Darwin Ethics Committee of Sorbonne Université.

Immunohistochemistry

Eyes were processed using the EyeDISCO protocol as previously described (Vigouroux et al., 2020). Following a de-pigmentation step in a solution of 11% H_2O_2 (VWR, 216763) at 70 rpm exposed to an 11W warm white Light-Emitting Diode (LED) (3000° Kelvin) for 1-3 days. Samples were then blocked and permeabilized before being incubated with the primary antibodies for 7 days at RT (see supplementary file 1) in a solution containing: 0.5% Tirton-X100, 5% donkey normal serum, 20% Dimethyl Sulfoxide, 1XPBS, 0.1 g/L thimerosal. The samples were further labelled with secondary antibodies (see supplementary file 1) for 2 days at RT under agitation.

Tissue clearing and imaging

Following immunohistochemistry, eyes were cleared as previously described (Vigouroux et al., 2020). Samples were gently de-hydrated in ascending baths of methanol (1h30). Samples were further treated with a solution containing 2/3 Dichloromethane (DCM, Sigma) 1/3 methanol o/n. The next day, samples were placed in DCM for 30 min prior to being immersed in Di-benzyl Ether (DBE, Sigma).

Acquisitions were performed using an ultramicroscope I, with the ImspectorPro software (LaVision BioTec, Miltenyi Biotec company, 5.1.328 version). All tiff images are generated in 16-bit.

Image processing and vessel segmentation

3D rendering of light sheet stacks were converted to an Imaris file (.ims) using ImarisFileConverter (Bitplane, 9.2.1 version) and then visualized using the Imaris x64 software (Bitplane, 9.2.1 version).

To isolate retinal astrocytes, eyes were labeled with GFAP (see supplementary file 1), and manually segmented using the “surface” tool. The masks were then extracted from the original image by adjusting outside pixels to 0 (black). For blood vessels, retinal vessels or hyaloid vessels were labeled using Collagen IV (see supplementary file) and manually segmented.

Supplementary File 1					
Primary antibodies					
Antigen	**Species**	**Catalog #**	**Company**	**Dilution**	**Immunohistochemistry**
Collagen IV	Goat			1:400	Whole-mount
GFAP	Rabbit			1:500	Whole-mount
Secondary antibodies					
Anti Rabbit cy3 mcr	Donkey	711-165-152	Jackson Immunoresearch	1:500	whole-mount
Anti Goat Alexa 647 mcr	Bovine	705-165-147	Jackson Immunoresearch	1:500	whole-mount

Discussion

The results of these studies cast light on the emergence of ipsi-lateral retinal projections (IRPs) across vertebrate evolution. Indeed, we uncovered that IRPs were present in the most basal Actinopterygians and Sarcopterygians, suggesting that IRPs most likely appeared in the common vertebrate ancestor. We further proposed that the molecular program responsible for IRP specification is more complex and diverse than previously thought. Indeed, the only known ipsi-lateral transcription factor Zic2 is absent from basal actinopterygians. We next showed that Dcc and Netrin-1 are critical for the proper targeting of RGCs during visual system development. In accordance with the extant literature, we found that *in vivo* Netrin-1 acts in short range at the optic disc for the proper exit of RGCs. We revealed for the first time that the early axon guidance defects observed in Dcc cKo mice lead to major retinal impairments including vascular defects and photoreceptor degeneration. Several pressing questions remain that open up new research avenues: What evolutionary pressures are at play for the maintenance or loss of IRPs? What mechanisms modulate the response of RGCs to Dcc/Netrin-1 mediated guidance at the optic disc? Below, we strive to provide some answers.

1.1 Defining the emergence of ipsilateral retinal projections

Early reports showed that IRPs arise at least as early as jawless vertebrates, more than 500mya (Vesselkin et al., 1980; Wicht and Northcutt, 1990). Despite this observation, our current understanding of ipsi-RGCs is restricted to a small number of species. In this next chapter, I argue that studying a greater diversity of species may shed new light on the diversity of molecular mechanisms responsible for the development of IRPs.

1.1.1 A unifying requirement for depth perception

Previous studies reported the presence of IRPs in the common vertebrate ancestor. In accordance with a previous study, our results showed that the common ancestor to tetrapods, the lungfish, also displays preserved IRPs (Glenn Northcutt, 1980). We further revealed that IRPs were independently lost in ray-finned fish following teleost genome duplication approximately 320 million years ago. What are the evolutionary selections that maintained or eliminated IRPs? The tree of life is composed of species

with a multitude of ecological niches. Accordingly, a single model for visual perception appears unlikely at best. Despite this heterogeneity, convergent evolution has replicated many anatomical aspects of an organism, such as the independent adaptation of the crystalline lens (Schwab, 2018). As a result, one can wonder whether one or multiple strategies evolved in different taxa for depth perception.

As eluded to in section 1.3 of the Introduction, early anatomists attempted to describe the emergence of binocular disparity (the Newton-Muller-Gudden law) (Walls, 1942). In mammals, a significant proportion of RGCs do not decussate at the OC, resulting in RGCs from both eyes to project to the same hemisphere. Subtle disparities of object perception between the left and right visual field were thus speculated to constitute the basis of depth perception or binocular disparity. It was further proposed that the proportion of IRPs was positively correlated with the degree of eye convergence of a given species. However, when conducting a thorough review of the literature it appears clear that eye laterality is not always proportional to the number of IRPs and may not even be associated with their presence. The latter is perfectly exemplified by the predatory leatherback turtle, *Trionyx cartilgineus*, that possesses frontal eyes but entirely lacks IRPs (Hergueta et al., 1992). In contrast, the closely related Chinese pond-turtle (*Chynemis reevesi*) possesses laterally-positioned eyes and an extensive number of IRPs (Hergueta et al., 1992).

If eye laterality cannot fully explain the occurrence of IRPs, can the specific ecological niche of a given organism do so? This question is at the core of both the “camouflage-breaking” hypothesis and the “visual predation” hypothesis (Heesy, 2009; Rill, 1995). Both hypotheses postulate that the predatory lifestyle of an organism selected the occurrence of IRPs throughout evolution. Depth of perception may have evolved as a result of an evolutionary arms race between a camouflaging prey and the predator. Indeed, discerning fine patterns in a complex ecological niche, such as the arboreal forest, may have selected predatory organisms with high visual acuity. Additionally, nocturnal animals might have strongly benefited from the increased contrast sensitivity provided by a higher binocular visual field. Basal primates possess each of these ecological constraints and indeed evolved a large component of IRPs (Heesy, 2009). However, such theories fail to account for the modest amount of IRPs (2-3%) found in organisms such as rodents that evolved in similar ecological niches (Rice et al., 1995). Strikingly, the European chameleon (*Chamaeleo chameleon*) also shares these

ecological constraints but completely lacks IRPs and achieves binocular disparity nonetheless using corneal accommodation (discussed later) (Bennis et al., 1994; Harkness, 1977; Ott, 2001).

IRPs arose at the most basal branch of the vertebrate subphylum (lampreys and hagfish) and appear to be independent of the terrestrial to land transition. Perhaps understanding the emergence of IRPs requires an even earlier analysis of an organisms' physiological constraints. Sensory perception and motor coordination are governing principles that have guided bilaterian evolution from protostomes to vertebrates. All sensory inputs: auditory, proprioceptive and visual, are perceived from the periphery and send afferent projections to the contralateral CNS nuclei. Once processed, motor signals are relayed via efferent projections to the contralateral limbs. Consequently, all sensory and motor processing occur locally in a single hemisphere, maximizing neuronal processing speed. This chief principle is at the basis of the Eye-forelimb hypothesis which suggests that in order to maximize motor coordination, an organism must maintain local processing (Larsson, 2011). This is the case for IRPs, which locally provide binocular neurons in the tectum/colliculus with information from both eye fields to generate motor coordination. A pressing question now remains as to why limbless common ancestors such as the jawless vertebrates (lampreys and hagfish) also possess IRPs. Indeed, alike basal fish that possess pectoral fins, limbless species must maintain a correct representation of their rostro-caudal body plan. Possessing IRPs in such species may be critical for proper representation of the body with respect to the environment (Larsson, 2015).

1.1.2 What are the molecular determinants of IRPs?

Ipsi-RGCs are currently defined molecularly by the presence of the transcription factor Zic2 (Herrera et al., 2003). Zic2-expressing RGCs upregulate the tyrosine kinase receptor EphB1 along their axonal projections (Lee et al., 2008). At the OC, EphB1 expressing RGCs turn ipsi-laterally in contact with the repulsive guidance cue, ephrinB2 (Lee et al., 2008; Nakagawa et al., 2000; Williams et al., 2003). This textbook model was described in mammals but was also observed in amphibians, suggesting that this mechanism could be evolutionarily conserved (Nakagawa et al., 2000). Moreover, species lacking IRPs, such as chick or zebrafish, completely lack the presence of an ipsilateral machinery (Herrera et al., 2003). My results attempted to extend these discoveries to the spotted gar (*Lepisosteus oculatus*), a fish species that

possesses a significant number of IRPs. Surprisingly, we found that in the spotted gar Zic2 was restricted to the proliferative CMZ region of the retina and was absent from RGCs at all developmental stages. Using *Slc6A4* mice that specifically expressed a tomato reporter in ipsi-RGCs, Lo Guidice and colleagues carried out single-cell RNA sequencing on E15 mice (Lo Giudice et al., 2019). In addition to known transcription factors, they identified two gene orthologs to Zic2, namely Zic1 and Zic5. Of particular interest, the Zic5 gene is flanking that of Zic2 suggesting they share similar regulatory elements. Notwithstanding the literature, we showed that neither Zic1 nor Zic5 were expressed in RGCs of the spotted gar. In addition, EphB1 wasn't expressed in RGCs and no expression of ephrinB2 was reported at the OC. The absence of ephrinB2 suggests that an alternative ligand may be present at the OC of the spotted gar.

Is there a single mechanism to generate IRPs? Our results showed that this may not be the case. Zebrafish do not express ephrinB2 at the OC. Moreover, zebrafish *Zic2* orthologs, Zic*2a* and *Zic2b*, are not expressed in RGCs. Intriguingly however, overexpressing *Zic2* in RGCs using the *Atoh7* Gal4 line, led to aberrant ipsilateral projections. This result highlights the novel idea that in a system completely devoid of Zic2, introducing this transcription factor can be sufficient to induce IRPs. While it remains to be understood which downstream targets Zic2 may upregulate, a promiscuity in the transcriptional machinery seems required to induce IRPs. In line with this hypothesis, while Neuropilin-1-expressing RGCs are attracted by Vegfa in mice, they are attracted by Sema3D/Sema3E in zebrafish (Dell et al., 2013; Erskine et al., 2017; Tillo et al., 2015). Moreover, a recent report in mice revealed that Zic2 induces the turning of ipsi-RGCs at the OC in a Wnt5a-dependent manner (Morenilla-Palao et al., 2019).

Overall, the multiple independent losses of IRPs during evolution, even sometimes within the same species (see section: 1.3.1 phylogeny of visual projection), point to the dynamic emergence of IRPs through evolution. Moreover, numerous molecular programs seem to have evolved to generate ipsi-RGCs. Future work is warranted to search for gene regulatory elements that may dynamically induce or repress transcription factors such as Zic2.

1.1.3 Is there a single strategy to obtain binocular disparity?

Importantly, some species are entirely devoid of ipsi-RGCs but may nonetheless be able to achieve depth perception. Tied to this idea is the speculation that multiple strategies exist to obtain binocularity.

In ray-finned fish, an important event took place 300mya which led to the duplication of the entire genome in teleost fish (Hughes et al., 2018). Teleosts are essentially devoid of IRPs and represent approximately 25 000 species with diverse lifestyles and ecological niches. My results showed that preceding this event, basal fish possessed a significant proportion of IRPs (see Results: Chapter 1). One of the most studied teleost fish, the zebrafish (*Danio rerio*), have been widely used due to their ease in genetic manipulation and transparency during development. Their visual system is well characterized and is entirely devoid of IRPs (Robles et al., 2014). In line with the Newton-Muller-Gudden law, zebrafish possess laterally-positioned eyes with a minor binocular field (Easter and Nicola, 1997). Zebrafish do nonetheless exhibit prey-capture behavior when feeding on paramecia (Bianco et al., 2011). When engaged in such behavior, zebrafish can triple their binocular overlap from 12% to 36% of their field of view (Bianco et al., 2011). Interestingly, single eye stimulation of zebrafish larvae induced activity in the ipsilateral tectal neuropil, hinting at the possibility of binocular disparity (Gebhardt et al., 2019). Closer analysis revealed a commissural population of interneurons connecting both tecta, which were coined intertectal neurons (ITNs) (Gebhardt et al., 2019). Strikingly, specific ablation of ITNs significantly impaired capture swim initiation in zebrafish larvae. The authors proposed a model whereby prey visualization is relayed to the contralateral OT as well as the contralateral ITNs. These cells are GABAergic neurons that relay the visual information to the ipsi-lateral OT and that induce a motor response through a disinhibition mechanism (Gebhardt et al., 2019).

Are ITNs a common mechanism for binocular disparity? Interestingly, the existence of tectal-tectal projections has been reported in amphibians, birds and reptiles (Auen, 1978; Gruberg and Udin, 1978; Voneida and Mello, 1975). In particular, amphibians (*Anurans*) possess neurons in the *nucleus isthmi* that connect to the anterior contralateral OT (Gruberg and Udin, 1978). In contrast to findings on zebrafish, ablation of these neurons does not lead to binocular deficits during prey-capture behavior (Collett et al., 1987; Glasser and Ingle, 1978). Worthy of note, anurans

possess IRPs following metamorphosis emphasizing the eventuality that ITNs and IRPs have complementary or even redundant functions (Currie and Cowan, 1974). Such a hypothesis could explain the significant prey-capture impairments observed in zebrafish, that lack IRPs, but not in amphibians, that possess IRPs. The combination of IRPs together with ITNs is evolutionarily conserved since collicular commissures have been reported in cats (Sprague, 1966). An evolutionary description of ITN emergence and whether it preceded IRPs would be critical to gain a better understanding of their joint function during binocular disparity.

Other strategies have been described to achieve binocular disparity. Chameleons provide a unique example of monocular depth perception (Ott, 2001). They possess a negative (concave) lens, that functions by enlarging the image onto the retina. In contrast, they possess a positive (convex) cornea that is able to accommodate each eye independently on a prey (Bennis et al., 1994; Harkness, 1977). Invertebrate species have also been reported to display binocular disparity. By placing prismatic lenses in front of the compound eyes of a Praying mantis, Rossel showed that the animal stroke short of its prey during capture, and that the error was proportional to the prism angle (Rossel, 1983). These data suggest that Praying mantis carry out prey-capture behavior using binocular cues. Cephalopods (cuttlefish) have also been shown to display binocular disparity (Feord et al., 2020) but the precise mechanism used to compute binocular disparity remains unknown.

The sheer diversity of strategies organisms may use to obtain binocular disparity is currently unknown. Multiple outstanding questions remain pertaining to the evolutionary advantage of IRP maintenance and to the existence of species-dependent molecular mechanisms. As a result, future work should attempt to better characterize binocular disparity using novel model organisms.

1.2 How do RGC projections specifically navigate to their retinorecipient target?

1.2.1 Reconciling the narrow set of guidance cues with the diversity of RGC types

We know from studies carried out in mice that thirty to forty different RGC types exist (Baden et al., 2016; Rheaume et al., 2018; Roska and Werblin, 2001; Sanes and Masland, 2015). Each of these RGC types respond to varying visual features and project to as many as forty six different brain nuclei with distinct physiological functions (Morin and Studholme, 2014). This RGC diversity begins during development as the neurogenic birthdate of the various types of RGCs differs in time (Osterhout et al., 2014). Interestingly, the projection pattern of RGCs also differs in time since early-born RGCs were shown to innervate a vast number of visual nuclei whereas late-born RGCs target specific nuclei (Osterhout et al., 2014).

Our results revealed that this heterogeneity could indeed be observed during the first guidance steps of RGC axons. In *Dcc* and *Netrin-1* cKO mice, while a significant proportion of RGCs project correctly towards the optic disc, a ventral population of RGCs aberrantly project into the sub-retinal space. Other reports in the literature highlight heterogeneous phenotypes during intra-retinal pathfinding. For instance, *EphB2*$^{-/-}$*/EphB3*$^{-/-}$ dKO mice display severe intra-retinal pathfinding defects in the dorsal retina, whereas *Bmpr1b*$^{-/-}$ null mice display defects in a ventral-specific manner (Birgbauer et al., 2001; Liu et al., 2003). In addition, both *Robo2*$^{-/-}$ and *Slit1*$^{-/-}$*/Slit2*$^{-/-}$ dKO mice display an asymmetric intra-retinal phenotype affecting the dorso-peripheral retina specifically (Thompson et al., 2006). While EphB and Bmpr1b receptors are expressed in a graded manner within the retina, the transmembrane Robo2 and Dcc receptors are homogeneously expressed in all RGCs (Deiner et al., 1997; Erskine et al., 2000). This suggests that not all RGC types respond similarly to the available guidance cues and that other guidance cues must be at play during intra-retinal pathfinding. Recent technological developments in single-cell RNA sequencing have begun to shed light on the transcriptional heterogeneity of RGCs (Lo Giudice et al., 2019). Retinal development follows a central-to-peripheral wave, Lo Guidice and colleagues thus separated “young” (peripheral) RGCs from “old” (central) RGCs and

identified several novel ligand/receptor pairs, including the ligand *Kitl* and its receptor *Kit* (Lo Giudice et al., 2019). Whether the pairs identified in this study are necessary for proper intra-retinal pathfinding remains to be validated.

One can now wonder whether this heterogeneity is restricted to the retina. Our results indicated that it is also maintained for RGC targeting to various brain nuclei. Our *Dcc* cKO mice displayed specific guidance defects in the MTN of the AOS as well as segregation defects in the SC. Moreover, eye-specific deletion or overexpression of *Netrin-1* led to specific defects in the olivary pretectal tract of the AOS. Overall, these observations point towards the multiplicity of RGC responses to distinct guidance cues. Interestingly, the heterogeneous guidance of RGCs within brain nuclei has been emphasized in several other reports. The adhesion molecules Cntn4 and Cdh6 specifically mediate the targeting of RGCs to the NOT and the OPN respectively (Osterhout et al., 2011; Osterhout et al., 2015). Moreover, DSGCs expressing Sema6A selectively target the MTN and DTN of the AOS via an adhesive interaction with PlexinA2/PlexinA4 (Sun et al., 2015). Of note, the described Sema6A/PlexinA2 interaction at the MTN has the opposite effect than the one described for the retina which results in a repulsive effect (Sun et al., 2013). 90% of RGCs project collaterals to the SC, meaning that the majority of RGCs project to multiple target nuclei (Linden and Perry, 1983). For example, DSGCs project to as many as four separate nuclei (Yonehara et al., 2008). It is therefore relevant to ask how a single RGC can mediate such complex targeting. This will be discussed in the next section.

1.2.2 Axon guidance is a dynamic process

Our results showed that specific populations of RGCs projected aberrantly in *Dcc* and *Netrin-1* cKO mice. This is rather unsurprising as RGCs project several collaterals to multiple brain nuclei that can reach from 3.5 mm in rats to 2 cm in humans (Curcio and Allen, 1990; Fukuda, 1977). As a result, a single RGC axon will come across countless cellular, axonal, and molecular interactors in its journey to its final target. How can a given growth cone make sense of which cues/cells to “listen” to and which to “ignore”? It has been known for more than a decade that guidance cues in the environment can elicit cytoskeletal protein synthesis in RGCs (Campbell and Holt, 2001; Leung et al., 2006). Furthermore, mRNAs could be transported and translated locally within axonal

compartments (Bassell et al., 1998; Shigeoka et al., 2016; Zivraj et al., 2010). Interestingly, Dcc associates with ribosomal machinery in order to elicit local protein synthesis (Tcherkezian et al., 2010). Upon Netrin-1 binding, these ribosomes dissociate from the Dcc P1 cytoplasmic domain and initiate local protein synthesis (Tcherkezian et al., 2010). It was recently shown that a 5 min stimulation of Netrin-1 on RGC growth cones led to the translation of more than 100 mRNAs (Cagnetta et al., 2018). Remarkably, co-stimulation of EphrinA1 together with Netrin-1 abrogates Dcc/ribosome uncoupling (Koppers et al., 2019). Receptor/ribosome coupling was recently demonstrated in several other guidance receptors such as Robo2, EphB2, and Neuropilin-1, arguing that this could be a widespread mechanism (Koppers et al., 2019; Piper et al., 2006). Interestingly, specific ligand/receptor binding associates with different RNA binding proteins and specific mRNAs, therefore mediating discrete functions (Cagnetta et al., 2018; Koppers et al., 2019). Receptor/ribosome uncoupling is incredibly dynamic and occurs in < 2 min to elicit local protein translation (Koppers et al., 2019). Of note, a large proportion of these mRNAs belonged to proteins of the metabolic pathway (Cagnetta et al., 2018). Growth cones may therefore function as a soma-independent compartment. Our current understanding of local protein translation only represents the tip of the iceberg and many open questions remain. For example, it would be important to understand how specific mRNAs are translated since a large number resides in sub-axonal compartments. Could inhibition or activation of microRNAs by extracellular cues be responsible for the proper targeting of RGC projections? Future work should aim at untangling these questions.

1.2.3 Other cues that modulate Dcc/Netrin-1 signaling

Our results showed that eye-specific deletion of *Dcc* or *Netrin-1* induce aberrantly projecting RGCs into the subretinal space. Classic studies found that the initial guidance of RGCs towards the OD may depend on the early fasciculation of RGCs (Brittis et al., 1995; Ott et al., 1998). This raises the possibility that intra-retinal pathfinding defects seen in *Dcc* and *Netrin-1* cKO mice is the result of a defasciculation phenotype. Recently, Dcc and Netrin-1 were proposed to mediate axon fasciculation via a third partner, the dorsal repulsive guidance molecule (Draxin) (Islam et al., 2009; Liu et al., 2018; Shinmyo et al., 2015). Crystal structure shows that Netrin-1 can associate to both Dcc and Draxin in trans (between two axons) by forming the following molecular bridge: Dcc-Draxin-Netrin-Dcc (Liu et al., 2018). In fact, *Draxin*$^{-/-}$ mice

display severe defasciculation defects (Islam et al., 2009). Alternatively, as Draxin is a secreted molecule it could be expressed in the ECM by binding sulfated glycosaminoglycans and act as an anchor point for the proper steering of growth cones. Support for this hypothesis comes from Draxin expression in the spinal cord where it overlaps with the protein expression of Netrin-1 at the pial surface (Dominici et al., 2017; Islam et al., 2009; Kociok et al., 2016; Varadarajan et al., 2017). Despite being studied in several systems, the role of Draxin in visual system development remains unstudied.

Critically, we shed light on a significant proportion of RGCs that projects correctly to the optic disc in *Dcc* and *Netrin-1* cKO mice. This raises the possibility that other guidance molecules may compensate for the loss of Dcc or Netrin-1. In that respect, Dcc was recently shown to bind to a member of the Cerebellin (Cbln) secreted proteins, Cbln4 (Haddick et al., 2014; Wei et al., 2012). Intriguingly, *Cbln4*$^{-/-}$ null mice do not phenocopy *Dcc* null mice and only display a moderate guidance defect in the dorsal bundle of the brachial plexus (Haddick et al., 2014). While this moderate phenotype could be explained by a redundancy of Cbln proteins, a recent analysis of *Cbln1*$^{-/-}$*/Cbln2*$^{-/-}$*/Cbln4*$^{-/-}$ tKO mice confirmed that they did not phenocopy *Dcc* null mice (Seigneur and Südhof, 2018).

Conclusion

In the early 90's the classic model posited that axon guidance molecules were conserved in all bilaterian species (Goodman, 1994). However, this model relied on specific sets of commissural neurons and receptor/ligand couples. In the past years, several studies have begun to put the theory into question by highlighting the molecular diversity of guidance molecules during evolution (Belle et al., 2014; Friocourt et al., 2017). Here, we showed that the emergence of ipsi-lateral retinal projections is conserved in the common vertebrate ancestor. However, we found that the molecular pathway responsible for specifying these projections is not conserved in fish. In mice diverse retinal projections seemed to respond to guidance cues in distinct ways. This heterogeneity in retinal projection responses to specific guidance cues may reveal the true complexity for retinal projections navigating the central nervous system. It thus seems clear that studying the development of the visual system in a restricted number of model systems significantly hinders our understanding of biological processes. We stress the importance of widenening research studies to a broader variety of species in order to draw evolutionary pertinent conclusions.

The present work was made possible with the recent technological advances in the field of tissue clearing and 3D light-sheet fluorescence microscopy. The advent of multiple tissue clearing protocols set the stage for the re-interpretation of complex anatomical structures. Despite these advances, the visual system remained obscured to tissue clearing technologies due to the dense pigmentation of the eye. Our research questions led to the development of a novel tissue clearing protocol (EyeDISCO) rendering the eye and the entire visual system amenable to tissue clearing. Thus far, we have used this protocol successfully for the study of retinal projections in a vast array of species, including human, mice and fish. However, this technique provides a large number of applications. For the field of ophthalmology, this technique could provide the unique opportunity to visualise the complex interaction between the retinal pigment epithelium with the photoreceptors. This interplay is critical during the early steps of retinal degeneration. For the broader application in the field of neuroscience, our technique is easily scalable and provides a unique tool for the unbiased analysis of forward genetic screens with the aim to uncover novel axon guidance genes.

Bibliography

Ackman, J. B., Burbridge, T. J. and Crair, M. C. (2012). Retinal waves coordinate patterned activity throughout the developing visual system. *Nature* **490**, 219–225.

Adelmann, H. B. (1929). Experimental studies on the development of the eye. I. The effect of the removal of median and lateral areas of the anterior end of the urodelan neural plate on the development of the eyes (Triton tenatus and Amblystoma punctatum). *J. Exp. Zool.*

Akin, O. and Zipursky, S. L. (2016). Frazzled promotes growth cone attachment at the source of a Netrin gradient in the Drosophila visual system. *Elife* **5**,.

Amini, R., Rocha-Martins, M. and Norden, C. (2018). Neuronal Migration and Lamination in the Vertebrate Retina. *Front. Neurosci.* **11**, 742.

Apkarian, P. and Bour, L. J. (2001). See-saw nystagmus and congenital nystagmus identified in the non-decussating retinal-fugal fiber syndrome. *Strabismus* **9**, 143–163.

Apkarian, P., Bour, L. and Barth, P. G. (1994). A Unique Achiasmatic Anomaly Detected in Non-albinos with Misrouted Retinal-fugal Projections. *Eur. J. Neurosci.* **6**, 501–507.

Auen, E. L. (1978). Axonal transport of HRP in descending tectal fibers of the pit viper. *Neurosci. Lett.* **9**, 137–140.

Avellaneda-Chevrier, V. K., Wang, X., Hooper, M. L. and Chauhan, B. C. (2015). The retino-retinal projection: Tracing retinal ganglion cells projecting to the contralateral retina. *Neurosci. Lett.* **591**, 105–109.

Baden, T., Berens, P., Franke, K., Román Rosón, M., Bethge, M. and Euler, T. (2016). The functional diversity of retinal ganglion cells in the mouse. *Nature* **529**, 345–350.

Bansal, A., Singer, J. H., Hwang, B. J., Xu, W., Beaudet, A. and Feller, M. B. (2000). Mice lacking specific nicotinic acetylcholine receptor subunits exhibit dramatically altered spontaneous activity patterns and reveal a limited role for retinal waves in forming ON and OFF circuits in the inner retina. *J. Neurosci.* **20**, 7672–81.

Bao, Z.-Z. (2008). Intraretinal projection of retinal ganglion cell axons as a model system for studying axon navigation. *Brain Res.* **1192**, 165–77.

Barbieri, A. M., Broccoli, V., Bovolenta, P., Alfano, G., Marchitiello, A., Mocchetti, C., Crippa, L., Bulfone, A., Marigo, V., Ballabio, A., et al. (2002). Vax2 inactivation in mouse determines alteration of the eye dorsal-ventral axis, misrouting of the optic fibres and eye coloboma. *Development* **129**, 805–813.

Barlow, H. B. and Hill, R. M. (1963). Selective Sensitivity to Direction of Movement in Ganglion Cells of the Rabbit Retina. *Science (80-.).* **139**, 412–412.

Barresi, M. J. F., Hutson, L. D., Chien, C.-B. and Karlstrom, R. O. (2005). Hedgehog regulated Slit expression determines commissure and glial cell position in the zebrafish forebrain. *Development* **132**, 3643–3656.

Bassell, G. J., Zhang, H., Byrd, A. L., Femino, A. M., Singer, R. H., Taneja, K. L., Lifshitz, L. M., Herman, I. M. and Kosik, K. S. (1998). Sorting of β-actin mRNA and protein to neurites and growth cones in culture. *J. Neurosci.* **18**, 251–265.

Bastmeyer, M., Ott, H., Leppert, C. A. and Stuermer, C. A. O. (1995). Fish E587 glycoprotein, a member of the L1 family of cell adhesion molecules, participates in axonal fasciculation and the age-related order of ganglion cell axons in the goldfish retina. *J. Cell Biol.* **130**, 969–976.

Belle, M., Godefroy, D., Dominici, C., Heitz-Marchaland, C., Zelina, P., Hellal, F., Bradke, F. and Chédotal, A. (2014). A

Simple Method for 3D Analysis of Immunolabeled Axonal Tracts in a Transparent Nervous System. *Cell Rep.* **9**, 1191–1201.

Belliveau, M. J. and Cepko, C. L. (1999). Extrinsic and intrinsic factors control the genesis of amacrine and cone cells in the rat retina. *Development* **126**, 555–66.

Benhayon, D., Magdaleno, S. and Curran, T. (2003). B inding of purified Reelin to ApoER2 and VLDLR mediates tyrosine phosphorylation of Disabled-1. *Mol. Brain Res.* **112**, 33–45.

Benjumeda, I., Escalante, A., Law, C., Morales, D., Chauvin, G., Muça, G., Coca, Y., Márquez, J., López-Bendito, G., Kania, A., et al. (2013). Uncoupling of EphA/ephrinA signaling and spontaneous activity in neural circuit wiring. *J. Neurosci.* **33**, 18208–18218.

Bennis, M., Repérant, J., Rio, J.-P. and Ward, R. (1994). An Experimental Re-Evaluation of the Primary Visual System of the European Chameleon, *Chamaeleo chameleon*. *Brain. Behav. Evol.* **43**, 173–188.

Berson, D. M., Dunn, F. A. and Takao, M. (2002). Phototransduction by retinal ganglion cells that set the circadian clock. *Science (80-.).* **295**, 1070–3.

Bertuzzi, S., Hindges, R., Mui, S. H., O'Leary, D. M. and Lemke, G. (1999). The homeodomain protein Vax1 is required for axon guidance and major tract formation in the developing forebrain. *Genes Dev.* **13**, 3092–3105.

Bhansali, P., Rayport, I., Rebsam, A. and Mason, C. (2014). Delayed neurogenesis leads to altered specification of ventrotemporal retinal ganglion cells in albino mice. *Neural Dev.* **9**, 11.

Bianco, I. H., Kampff, A. R. and Engert, F. (2011). Prey Capture Behavior Evoked by Simple Visual Stimuli in Larval Zebrafish. *Front. Syst. Neurosci.* **5**, 101.

Biega, T. J., Khademian, Z. P. and Vezina, G. (2007). Isolated absence of the optic chiasm: a rare cause of congenital nystagmus. *AJNR Am. J. Neuroradiol.* **28**, 392–393.

Bin, J. M., Han, D., Lai Wing Sun, K., Croteau, L.-P., Dumontier, E., Cloutier, J.-F., Kania, A. and Kennedy, T. E. (2015). Complete Loss of Netrin-1 Results in Embryonic Lethality and Severe Axon Guidance Defects without Increased Neural Cell Death. *Cell Rep.* **12**, 1099–1106.

Birgbauer, E., Cowan, C. A., Sretavan, D. W. and Henkemeyer, M. (2000). Kinase independent function of EphB receptors in retinal axon pathfinding to the optic disc from dorsal but not ventral retina. *Development* **127**, 1231–41.

Birgbauer, E., Oster, S. F., Severin, C. G. and Sretavan, D. W. (2001). Retinal axon growth cones respond to EphB extracellular domains as inhibitory axon guidance cues. *Development* **128**, 3041–8.

Blankenship, A. G. and Feller, M. B. (2010). Mechanisms underlying spontaneous patterned activity in developing neural circuits. *Nat. Rev. Neurosci.* **11**, 18–29.

Böcker-Meffert, S., Rosenstiel, P., Röhl, C., Warneke, N., Held-Feindt, J., Sievers, J. and Lucius, R. (2002). Erythropoietin and VEGF promote neural outgrowth from retinal explants in postnatal rats. *Investig. Ophthalmol. Vis. Sci.* **43**, 2021–2026.

Bouvrée, K., Larrivée, B., Lv, X., Yuan, L., DeLafarge, B., Freitas, C., Mathivet, T., Bréant, C., Tessier-Lavigne, M., Bikfalvi, A., et al. (2008). Netrin-1 inhibits sprouting angiogenesis in developing avian embryos. *Dev. Biol.* **318**, 172–183.

Bovolenta, P. and Mason, C. (1987). Growth cone morphology varies with position in the developing mouse visual pathway from retina to first targets. *J. Neurosci.* **7**, 1447–1460.

Braisted, J. E., McLaughlin, T., Wang, H. U.,

Friedman, G. C., Anderson, D. J. and O'leary, D. D. M. (1997). Graded and Lamina-Specific Distributions of Ligands of EphB Receptor Tyrosine Kinases in the Developing Retinotectal System. *Dev. Biol.* **191**, 14–28.

Brankatschk, M. and Dickson, B. J. (2006). Netrins guide Drosophila commissural axons at short range. *Nat. Neurosci.* **9**, 188–194.

Brenner, S. (1974). The Geneticas of Caenorhabditis elegans. *Genetics* **77**, 71–94.

Brignani, S., Raj, D. D. A., Schmidt, E. R. E., Düdükcü, Ö., Adolfs, Y., De Ruiter, A. A., Rybiczka-Tesulov, M., Verhagen, M. G., van der Meer, C., Broekhoven, M. H., et al. (2020). Remotely Produced and Axon-Derived Netrin-1 Instructs GABAergic Neuron Migration and Dopaminergic Substantia Nigra Development. *Neuron* **107**, 684-702.e9.

Brittis, P. A. and Silver, J. (1994). Exogenous glycosaminoglycans induce complete inversion of retinal ganglion cell bodies and their axons within the retinal neuroepithelium. *Proc. Natl. Acad. Sci.* **91**, 7539–7542.

Brittis, P. A., Canning, D. R. and Silver, J. (1992). Chondroitin sulfate as a regulator of neuronal patterning in the retina. *Science (80-.).* **255**, 733–736.

Brittis, P. A., Lemmon, V., Rutishauser, U. and Silver, J. (1995). Unique Changes of Ganglion Cell Growth Cone Behavior Following Cell Adhesion Molecule Perturbations: A Time-Lapse Study of the Living Retina. *Mol. Cell. Neurosci.* **6**, 433–449.

Brown, A., Yates, P. A., Burrola, P., Ortuno, D., Vaidya, A., Jessell, T. M., Pfaff, S. L., O'Leary, D. D. M., Lemke, G., Ortuo, D., et al. (2000). Topographic mapping from the retina to the midbrain is controlled by relative but not absolute levels of EphA receptor signaling. *Cell* **102**, 77–88.

Brunet, I., Weinl, C., Piper, M., Trembleau, A., Volovitch, M., Harris, W. A., Prochiantz, A. and Holt, C. E. (2005). The transcription factor Engrailed-2 guides retinal axons. *Nature* **438**, 94–8.

Bunt, S. M. and Lund, R. D. (1981). *Development of a transient retino-retinal pathway in hooded and albino rats*.

Burns, A. H. and Goodman, D. C. (1967). Retinofugal projections of Caiman sklerops. *Exp. Neurol.*

Burrill, J. D. and Easter, S. S. (1994). Development of the retinofugal projections in the embryonic and larval zebrafish (Brachydanio rerio). *J. Comp. Neurol.* **346**, 583–600.

Cagnetta, R., Frese, C. K., Shigeoka, T., Krijgsveld, J. and Holt, C. E. (2018). Rapid Cue-Specific Remodeling of the Nascent Axonal Proteome. *Neuron* **99**, 29-46.e4.

Cairns, J. E. (1959). NORMAL DEVELOPMENT OF THE HYALOID AND RETINAL VESSELS IN THE RAT. *Br. J. Ophthalmol.* **43**, 385–393.

Campbell, D. S. and Holt, C. E. (2001). Chemotropic Responses of Retinal Growth Cones Mediated by Rapid Local Protein Synthesis and Degradation. *Neuron* **32**, 1013–1026.

Cang, J., Wang, L., Stryker, M. P. and Feldheim, D. A. (2008). Roles of ephrin-as and structured activity in the development of functional maps in the superior colliculus. *J. Neurosci.* **28**, 11015–11023.

Carmeliet, P. (2003). Blood vessels and nerves: Common signals, pathways and diseases. *Nat. Rev. Genet.* **4**, 710–720.

Carreres, M. I., Escalante, A., Murillo, B., Chauvin, G., Gaspar, P., Vegar, C. and Herrera, E. (2011). Transcription Factor Foxd1 Is Required for the Specification of the Temporal Retina in Mammals. *J. Neurosci.* **31**, 5673–5681.

Castets, M., Coissieux, M.-M., Delloye-Bourgeois, C., Bernard, L., Delcros, J.-G., Bernet, A., Laudet, V. and Mehlen, P.

(2009). *Inhibition of Endothelial Cell Apoptosis by Netrin-1 during Angiogenesis*.

Castets, M., Broutier, L., Molin, Y., Brevet, M., Chazot, G., Gadot, N., Paquet, A., Mazelin, L., Jarrosson-Wuilleme, L., Scoazec, J.-Y., et al. (2011). DCC constrains tumour progression via its dependence receptor activity. *Nature* **482**, 534–537.

Cepko, C. (2014). Intrinsically different retinal progenitor cells produce specific types of progeny. *Nat. Rev. Neurosci.* **15**, 615–627.

Cepko, C. L. C., Austin, C. P., Yang, X., Alexiades, M. and Ezzeddine, D. (1996). Cell fate determination in the vertebrate retina. *Proc. Natl. Acad. Sci.* **93**, 589–595.

Chan, S. O. and Guillery, R. W. (1993). Developmental changes produced in the retinofugal pathways of rats and ferrets by early monocular enucleations: the effects of age and the differences between normal and albino animals. *J. Neurosci.* **13**, 5277–5293.

Chan, S. O. and Guillery, R. W. (1994). Changes in fiber order in the optic nerve and tract of rat embryos. *J. Comp. Neurol.* **344**, 20–32.

Chan, S. S. Y., Zheng, H., Su, M. W., Wilk, R., Killeen, M. T., Hedgecock, E. M. and Culotti, J. G. (1996). UNC-40, a C. elegans homolog of DCC (Deleted in Colorectal Cancer), is required in motile cells responding to UNC-6 netrin cues. *Cell* **87**, 187–195.

Chandrasekaran, A. R., Plas, D. T., Gonzalez, E. and Crair, M. C. (2005). Evidence for an instructive role of retinal activity in retinotopic map refinement in the superior colliculus of the mouse. *J. Neurosci.* **25**, 6929–38.

Chang, K.-C. C., Hertz, J., Zhang, X., Jin, X.-L. L., Shaw, P., Derosa, B. A., Li, J. Y., Venugopalan, P., Valenzuela, D. A., Patel, R. D., et al. (2017). Novel Regulatory Mechanisms for the SoxC Transcriptional Network Required for Visual Pathway Development. *J. Neurosci.* **37**, 4967–4981.

Chase, J. (1982). The Evolution of Retinal Vascularization in Mammals: A Comparison of Vascular and Avascular Retinae. *Ophthalmology* **89**, 1518–1525.

Chatzopoulou, E., Miguez, A., Savvaki, M., Levasseur, G., Muzerelle, A., Muriel, M.-P., Goureau, O., Watanabe, K., Goutebroze, L., Gaspar, P., et al. (2008). Structural Requirement of TAG-1 for Retinal Ganglion Cell Axons and Myelin in the Mouse Optic Nerve. *J. Neurosci.* **28**, 7624–7636.

Chen, S.-K., Badea, T. C. and Hattar, S. (2011). Photoentrainment and pupillary light reflex are mediated by distinct populations of ipRGCs. *Nature* **476**, 92–5.

Chen, Q., Sun, X., Zhou, X. hong, Liu, J. huan, Wu, J., Zhang, Y. and Wang, J. huai (2013). N-terminal horseshoe conformation of DCC is functionally required for axon guidance and might be shared by other neural receptors. *J. Cell Sci.* **126**, 186–195.

Cheng, H.-J. and Flanagan, J. G. (1994). *Identification and Cloning of ELF-I, a Developmentally Expressed Ligand for the Mek4 and Sek Receptor Tyrosine Kinases*.

Cheng, H. J., Nakamoto, M., Bergemann, A. D. and Flanagan, J. G. (1995). Complementary gradients in expression and binding of ELF-1 and Mek4 in development of the topographic retinotectal projection map. *Cell* **82**, 371–381.

Chiang, C., Litingtung, Y., Lee, E., Young, K. E., Corden, J. L., Westphal, H. and Beachy, P. A. (1996). Cyclopia and defective axial patterning in mice lacking Sonic hedgehog gene function. *Nature* **383**, 407–413.

Cima, C. and Grant, P. (1982). Development of the optic nerve in Xenopus laevis I. Early development ancl organization. *J*

Embryol exp Morph **72**, 225–249.

Cline, H. T. and Constantine-Paton, M. (1989). *NMDA Receptor Antagonists Retinotectal Topographic Map Disrupt the*.

Colavita, A. and Culotti, J. G. (1998). Suppressors of ectopic UNC-5 growth cone steering identify eight genes involved in axon guidance in Caenorhabditis elegans. *Dev. Biol.* **194**, 72–85.

Colello, R. J. and Guillery, R. W. (1990). The early development of retinal ganglion cells with uncrossed axons in the mouse: retinal position and axonal course. *Development* **108**, 515–23.

Collett, T. S., Udin, S. B. and Finch, D. J. (1987). A possible mechanism for binocular depth judgements in anurans. *Exp. Brain Res.* **66**, 35–40.

Connor, R. J., Menzel, P. and Pasquale, E. B. (1998). Expression and Tyrosine Phosphorylation of Eph Receptors Suggest Multiple Mechanisms in Patterning of the Visual System. *Dev. Biol.* **193**, 21–35.

Conte, W. L., Kamishina, H. and Reep, R. L. (2009a). Multiple neuroanatomical tract-tracing using fluorescent Alexa Fluor conjugates of cholera toxin subunit B in rats. *Nat. Protoc.* **4**, 1157–1166.

Conte, W. L., Kamishina, H. and Reep, R. L. (2009b). The efficacy of the fluorescent conjugates of cholera toxin subunit B for multiple retrograde tract tracing in the central nervous system. *Brain Struct. Funct.* **213**, 367–373.

Cowan, W. M., Gottlieb, D. I., Hendrickson, A. E., Price, J. L. and Woolsey, T. A. (1972). The autoradiographic demonstration of axonal connections in the central nervous system. *Brain Res.* **37**, 21–51.

Creel, D., Hendrickson, A. and Leventhal, A. (1982). Retinal projections in tyrosinase-negative albino cats. *J. Neurosci.* **2**, 907–911.

Cronin, C. A., Ryan, A. B., Talley, E. M. and Scrable, H. (2003). Tyrosinase expression during neuroblast divisions affects later pathfinding by retinal ganglion cells. *J. Neurosci.* **23**, 11692–11697.

Cruz-Martín, A., El-Danaf, R. N., Osakada, F., Sriram, B., Dhande, O. S., Nguyen, P. L., Callaway, E. M., Ghosh, A. and Huberman, A. D. (2014). A dedicated circuit links direction-selective retinal ganglion cells to the primary visual cortex. *Nature* **507**, 358–361.

Cunningham, T. J. and Freeman, J. A. (1977). Bilateral ganglion cell branches in the normal rat: A demonstration with electrophysiological collision and cobalt tracing methods. *J. Comp. Neurol.* **172**, 165–175.

Curcio, C. A. and Allen, K. A. (1990). Topography of ganglion cells in human retina. *J. Comp. Neurol.* **300**, 5–25.

Currie, J. and Cowan, W. M. (1974). Evidence for the late development of the uncrossed retinothalamic projections in the frog, Rana pipiens. *Brain Res.* **71**, 133–139.

Dakubo, G. D., Wang, Y. P., Mazerolle, C., Campsall, K., McMahon, A. P. and Wallace, V. A. (2003). Retinal ganglion cell-derived sonic hedgehog signaling is required for optic disc and stalk neuroepithelial cell development. *Development* **130**, 2967–80.

de la Torre, J. R., Höpker, V. H., Ming, G. L., Poo, M. M., Tessier-Lavigne, M., Hemmati-Brivanlou, A. and Holt, C. E. (1997). Turning of retinal growth cones in a netrin-1 gradient mediated by the netrin receptor DCC. *Neuron* **19**, 1211–1224.

Deiner, M. S., Kennedy, T. E., Fazeli, A., Serafini, T., Tessier-Lavigne, M. and Sretavan, D. W. (1997). Netrin-1 and DCC mediate axon guidance locally at the optic disc: loss of function leads to optic nerve hypoplasia. *Neuron* **19**, 575–89.

Dell, A. L., Fried-Cassorla, E., Xu, H. and Raper, J. A. (2013). cAMP-induced

expression of Neuropilin1 promotes retinal axon crossing in the zebrafish optic chiasm. *J. Neurosci.* **33**, 11076–11088.

Delogu, A., Sellers, K., Zagoraiou, L., Bocianowska-Zbrog, A., Mandal, S., Guimera, J., Rubenstein, J. L. R., Sugden, D., Jessell, T. and Lumsden, A. (2012). Subcortical Visual Shell Nuclei Targeted by ipRGCs Develop from a Sox14+-GABAergic Progenitor and Require Sox14 to Regulate Daily Activity Rhythms. *Neuron* **75**, 648–662.

Denis, D., Aziz-alessi, A., Defoort-dhellemmes, S., Gastaud, P., Meur, G. Le, Lebranchu, P., Levy-gabriel, C., Meunier, I., Milazzo, S., Orssaud, C., et al. (2017). *Ophtalmologie pédiatrique*.

Dhande, O. S. and Huberman, A. D. (2014). Retinal ganglion cell maps in the brain: implications for visual processing. *Curr. Opin. Neurobiol.* **24**, 133–142.

Dhande, O. S., Hua, E. W., Guh, E., Yeh, J., Bhatt, S., Zhang, Y., Ruthazer, E. S., Feller, M. B. and Crair, M. C. (2011). Development of single retinofugal axon arbors in normal and β2 knock-out mice. *J. Neurosci.* **31**, 3384–3399.

Dhande, O. S., Estevez, M. E., Quattrochi, L. E., El-Danaf, R. N., Nguyen, P. L., Berson, D. M. and Huberman, A. D. (2013). Genetic dissection of retinal inputs to brainstem nuclei controlling image stabilization. *J. Neurosci.* **33**, 17797–813.

Dhande, O. S., Stafford, B. K., Lim, J.-H. A. and Huberman, A. D. (2015). Contributions of Retinal Ganglion Cells to Subcortical Visual Processing and Behaviors. *Annu. Rev. Vis. Sci.* **1**, 291–328.

Dharmaratne, N., Glendining, K. A., Young, T. R., Tran, H., Sawatari, A. and Leamey, C. A. (2012). Ten-m3 Is Required for the Development of Topography in the Ipsilateral Retinocollicular Pathway. *PLoS One* **7**, e43083.

Di Donato, V., De Santis, F., Albadri, S., Auer, T. O., Duroure, K., Charpentier, M., Concordet, J. P., Gebhardt, C. and Del Bene, F. (2018). An Attractive Reelin Gradient Establishes Synaptic Lamination in the Vertebrate Visual System. *Neuron* **97**, 1049-1062.e6.

Diez-Roux, G. and Lang, R. A. (1997). Macrophages induce apoptosis in normal cells in vivo. *Development* **124**, 3633–3638.

Ding, Q., Liao, S.-J. and Yu, J. (2014). Axon guidance factor netrin-1 and its receptors regulate angiogenesis after cerebral ischemia. *Neurosci. Bull.* **30**, 683–691.

Dodt, H.-U., Leischner, U., Schierloh, A., Jährling, N., Mauch, C. P., Deininger, K., Deussing, J. M., Eder, M., Zieglgänsberger, W. and Becker, K. (2007). Ultramicroscopy: three-dimensional visualization of neuronal networks in the whole mouse brain. *Nat. Methods* **4**, 331–336.

Dominici, C., Moreno-Bravo, J. A., Puiggros, S. R., Rappeneau, Q., Rama, N., Vieugue, P., Bernet, A., Mehlen, P. and Chédotal, A. (2017). Floor-plate-derived netrin-1 is dispensable for commissural axon guidance. *Nature* **545**, 350–354.

Dorrell, M. I., Aguilar, E. and Friedlander, M. (2002). Retinal vascular development is mediated by endothelial filopodia, a preexisting astrocytic template and specific R-cadherin adhesion. *Invest. Ophthalmol. Vis. Sci.* **43**, 3500–10.

Drager, U. C. (1985). Birth Dates of Retinal Ganglion Cells Giving Rise to the Crossed and Uncrossed Optic Projections in the Mouse. *Proc. R. Soc. B Biol. Sci.* **224**, 57–77.

Drager, U. C. and Hubel, D. H. (1975). Responses to visual stimulation and relationship between visual, auditory, and somatosensory inputs in mouse superior colliculus. *J. Neurophysiol.* **38**, 690–713.

Drager, U. C. and Hubel, D. H. (1976). Topography of visual and somatosensory

projections to mouse superior colliculus. *J. Neurophysiol.* **39**, 91–101.

Dräger, U. C. and Olsen, J. F. (1980). Origins of crossed and uncrossed retinal projections in pigmented and albino mice. *J. Comp. Neurol.* **191**, 383–412.

Drazba, J. and Lemmon, V. (1994). The role of cell adhesion molecules in neurite outgrowth on Müller cells. *Dev. Biol.* **15**, 251–255.

Drescher, U., Kremoser, C., Handwerker, C., Löschinger, J., Noda, M. and Bonhoeffer, F. (1995). In vitro guidance of retinal ganglion cell axons by RAGS, a 25 kDa tectal protein related to ligands for Eph receptor tyrosine kinases. *Cell* **82**, 359–70.

Droz, B. and Leblond, C. P. (1962). Migration of proteins along the axons of the sciatic nerve. *Science (80-.).* **137**, 1047–1048.

Droz, B. and Leblond, C. P. (1963). Axonal migration of proteins in the central nervous system and peripheral nerves as shown by radioautography. *J. Comp. Neurol.* **121**, 325–346.

Easter, S. S. and Nicola, G. N. (1997). The development of eye movements in the zebrafish (Danio rerio). *Dev. Psychobiol.* **31**, 267–276.

Easter, S. S., Rusoff, A. C. and Kish, P. E. (1981). The growth and organization of the optic nerve and tract in juvenile and adult goldfish. *J. Neurosci.* **1**, 793–811.

Ebbesson, S. E., Ito, H. and Projections, B. R. (1980). Bilateral Retinal Projections in the Black Piranah (Serrasalmus niger). *Cell Tissue Res.* **213**, 483–495.

Ecker, J. L., Dumitrescu, O. N., Wong, K. Y., Alam, N. M., Chen, S.-K. K., LeGates, T., Renna, J. M., Prusky, G. T., Berson, D. M. and Hattar, S. (2010). Melanopsin-expressing retinal ganglion-cell photoreceptors: cellular diversity and role in pattern vision. *Neuron* **67**, 49–60.

Ekström, P. (1982). Retinofugal projections in the eel, Anguilla anguilla L. (Teleostei), visualized by the cobalt-filling technique. *Cell Tissue Res.* **225**, 507–524.

Ellis, E. M., Gauvain, G., Sivyer, B. and Murphy, G. J. (2016). Shared and distinct retinal input to the mouse superior colliculus and dorsal lateral geniculate nucleus. *J. Neurophysiol.* **116**, 602–610.

Erskine, L., Williams, S. E., Brose, K., Kidd, T., Rachel, R. A., Goodman, C. S., Tessier-Lavigne, M. and Mason, C. A. (2000). Retinal ganglion cell axon guidance in the mouse optic chiasm: expression and function of robos and slits. *J. Neurosci.* **20**, 4975–4982.

Erskine, L., Reijntjes, S., Pratt, T., Denti, L., Schwarz, Q., Vieira, J. M., Alakakone, B., Shewan, D. and Ruhrberg, C. (2011). VEGF Signaling through Neuropilin 1 Guides Commissural Axon Crossing at the Optic Chiasm. *Neuron* **70**, 951–965.

Erskine, L., François, U., Denti, L., Joyce, A., Tillo, M., Bruce, F., Vargesson, N. and Ruhrberg, C. (2017). VEGF-A and neuropilin 1 (NRP1) shape axon projections in the developing CNS via dual roles in neurons and blood vessels. *Development*.

Ertürk, A., Becker, K., Jährling, N., Mauch, C. P., Hojer, C. D., Egen, J. G., Hellal, F., Bradke, F., Sheng, M. and Dodt, H.-U. U. (2012). Three-dimensional imaging of solvent-cleared organs using 3DISCO. *Nat. Protoc.* **7**, 1983–1995.

Fabre, P. J., Shimogori, T. and Charron, F. (2010). Segregation of Ipsilateral Retinal Ganglion Cell Axons at the Optic Chiasm Requires the Shh Receptor Boc. *J. Neurosci.* **30**, 266–275.

Fawcett, J. W., O'Leary, D. D. M. and Cowan, W. M. (1984). Activity and the control of ganglion cell death in the rat retina. *Proc. Natl. Acad. Sci. U. S. A.* **81**, 5589–5593.

Fazeli, A., Dickinson, S. L., Hermiston, M. L., Tighe, R. V, Steen, R. G., Small, C. G., Stoeckli, E. T., Keino-Masu, K., Masu, M., Rayburn, H., et al. (1997). Phenotype of mice lacking functional Deleted in

colorectal cancer (Dcc) gene. *Nature* **386**, 796–804.

Fearon, E. R., Cho, K. R., Nigro, J. M., Kern, S. E., Simons, J. W., Ruppert, J. M., Hamilton, S. R., Preisinger, A. C., Thomas, G. and Kinzler, K. W. (1990). Identification of a chromosome 18q gene that is altered in colorectal cancers. *Science (80-.).* **247**, 49–56.

Feldheim, D. A., Kim, Y. I., Bergemann, A. D., Frisén, J., Barbacid, M. and Flanagan, J. G. (2000). Genetic analysis of ephrin-A2 and ephrin-A5 shows their requirement in multiple aspects of retinocollicular mapping. *Neuron* **25**, 563–574.

Feldheim, D. A., Nakamoto, M., Osterfield, M., Gale, N. W., DeChiara, T. M., Rohatgi, R., Yancopoulos, G. D. and Flanagan, J. G. (2004). Loss-of-function analysis of EphA receptors in retinotectal mapping. *J. Neurosci.* **24**, 2542–2550.

Feng, K., Zhou, X. H., Oohashi, T., Mörgelin, M., Lustig, A., Hirakawa, S., Ninomiya, Y., Engel, J., Rauch, U. and Fässler, R. (2002). All four members of the Ten-m/Odz family of transmembrane proteins form dimers. *J. Biol. Chem.* **277**, 26128–26135.

Feord, R. C., Sumner, M. E., Pusdekar, S., Kalra, L., Gonzalez-Bellido, P. T. and Wardill, T. J. (2020). Cuttlefish use stereopsis to strike at prey. *Sci. Adv.* **6**, eaay6036.

Ferran, J. L., de Oliveira, E. D., Merchán, P., Sandoval, J. E., Sánchez-Arrones, L., Martínez-de-la-Torre, M. and Puelles, L. (2009). Genoarchitectonic profile of developing nuclear groups in the chicken pretectum. *J. Comp. Neurol.* **517**, 405–451.

Finci, L. I., Krüger, N., Sun, X., Zhang, J., Chegkazi, M., Wu, Y., Schenk, G., Mertens, H. D. T., Svergun, D. I., Zhang, Y., et al. (2014). The Crystal Structure of Netrin-1 in Complex with DCC Reveals the Bifunctionality of Netrin-1 As a Guidance Cue. *Neuron* **83**, 1–11.

Fink, R. P. and Heimer, L. (1967). Two methods for selective silver impregnation of degenerating axons and their synaptic endings in the central nervous system. *Brain Res.* **4**, 369–374.

Forcet, C., Ye, X., Granger, L., Corset, V., Shin, H., Bredesen, D. E. and Mehlen, P. (2001). The dependence receptor DCC (deleted in colorectal cancer) defines an alternative mechanism for caspase activation. *Proc. Natl. Acad. Sci. U. S. A.* **98**, 3416–21.

Fricke, C., Lee, J., Geiger-Rudolph, S., Bonhoeffer, F. and Chien, C.-B. (2001). astray, a zebrafish roundabout homolog required for retinal axon guidance. *Science (80-.).* **292**, 507–510.

Friocourt, F., Lafont, A.-G., Kress, C., Pain, B., Manceau, M., Dufour, S., Chédotal, A., Laffont, A.-G., Kress, C., Pain, B., et al. (2017). Recurrent DCC gene losses during bird evolution. *Sci. Rep.* **7**, 37569.

Frisén, J., Yates, P. A., McLaughlin, T., Friedman, G. C., O'Leary, D. D. M. and Barbacid, M. (1998). Ephrin-A5 (AL-1/RAGS) Is Essential for Proper Retinal Axon Guidance and Topographic Mapping in the Mammalian Visual System. *Neuron* **20**, 235–243.

Fruttiger, M. (2007). Development of the retinal vasculature. *Angiogenesis* **10**, 77–88.

Fruttiger, M., Calver, A. R., Krüger, W. H., Mudhar, H. S., Michalovich, D., Takakura, N., Nishikawa, S. I. and Richardson, W. D. (1996). PDGF Mediates a Neuron–Astrocyte Interaction in the Developing Retina. *Neuron* **17**, 1117–1131.

Fuhrmann, S. (2010). Eye Morphogenesis and Patterning of the Optic Vesicle. In *Current Topics in Developmental Biology*, pp. 61–84.

Fukuda, Y. (1977). A three-group classification of rat retinal ganglion cells: histological and physiological studies. *Brain Res.* **119**, 327–344.

Fukusumi, Y., Meier, F., Gotz, S., Matheus, F., Irmler, M., Beckervordersandforth, R., Faus-Kessler, T., Minina, E., Rauser, B., Zhang, J., et al. (2015). Dickkopf 3 Promotes the Differentiation of a Rostrolateral Midbrain Dopaminergic Neuronal Subset In Vivo and from Pluripotent Stem Cells In Vitro in the Mouse. *J. Neurosci.* **35**, 13385–13401.

Fuller, P. M. and Prior, D. J. (1975). Cobalt iontophoresis techniques for tracing afferent and efferent connections in the vertebrate CNS. *Brain Res.* **88**, 211–220.

Furukawa, T., Kozak, C. A. and Cepko, C. L. (1997). rax, a novel paired-type homeobox gene, shows expression in the anterior neural fold and developing retina. *Proc. Natl. Acad. Sci. U. S. A.* **94**, 3088–3093.

Gage, P. J., Rhoades, W., Prucka, S. K. and Hjalt, T. (2005). Fate Maps of Neural Crest and Mesoderm in the Mammalian Eye. *Investig. Opthalmology Vis. Sci.* **46**, 4200.

Gale, N. W., Holland, S. J., Valenzuela, D. M., Flenniken, A., Pan, L., Ryan, T. E., Henkemeyer, M., Strebhardt, K., Hirai, H., Wilkinson, D. G., et al. (1996). Eph receptors and ligands comprise two major specificity subclasses and are reciprocally compartmentalized during embryogenesis. *Neuron* **17**, 9–19.

Galli, L. and Maffei, L. (1988). Spontaneous impulse activity of rat retinal ganglion cells in prenatal life. *Science (80-.).* **242**, 90–91.

García-Frigola, C. and Herrera, E. (2010). Zic2 regulates the expression of Sert to modulate eye-specific refinement at the visual targets. *EMBO J.* **29**, 3170–3183.

García-Frigola, C., Carreres, M. I., Vegar, C., Mason, C. A. and Herrera, E. (2008). Zic2 promotes axonal divergence at the optic chiasm midline by EphB1-dependent and -independent mechanisms. *Development* **135**, 1833–1841.

Gariano, R. F. and Gardner, T. W. (2005). Retinal angiogenesis in development and disease. *Nature* **438**, 960–966.

Gaspar, P., Cases, O. and Maroteaux, L. (2003). The developmental role of serotonin: news from mouse molecular genetics. *Nat. Rev. Neurosci.* **4**, 1002–1012.

Gebhardt, C., Auer, T. O., Henriques, P. M., Rajan, G., Duroure, K., Bianco, I. H. and Del Bene, F. (2019). An interhemispheric neural circuit allowing binocular integration in the optic tectum. *Nat. Commun.* **10**, 5471.

Geisbrecht, B. V, Dowd, K. A., Barfield, R. W., Longo, P. A. and Leahy, D. J. (2003). Netrin binds discrete subdomains of DCC and UNC5 and mediates interactions between DCC and heparin. *J. Biol. Chem.* **278**, 32561–32568.

Gerhardt, H., Golding, M., Fruttiger, M., Ruhrberg, C., Lundkvist, A., Abramsson, A., Jeltsch, M., Mitchell, C., Alitalo, K., Shima, D., et al. (2003). VEGF guides angiogenic sprouting utilizing endothelial tip cell filopodia. *J. Cell Biol.* **161**, 1163–77.

Glaser, T., Jepeal, L., Edwards, J. G., Young, S. R., Favor, J. and Maas, R. L. (1994). Erratum: PAX6 gene dosage effect in a family with congential cataracts, aniridia, anophthalmia and central nervous system defects. *Nat. Genet.* **8**, 203–203.

Glasser, S. and Ingle, D. (1978). The nucleus isthmus as a relay station in the ipsilateral visual projection to the frog's optic tectum. *Brain Res.* **159**, 214–218.

Glees, P. (1946). Terminal Degeneration within the Central Nervous System as Studied by a New Silver Method. *J. Neuropathol. Exp. Neurol.* **5**, 54–59.

Glendining, K. A., Liu, S. C., Nguyen, M., Dharmaratne, N., Nagarajah, R., Iglesias, M. A., Sawatari, A. and Leamey, C. A. (2017). Downstream mediators of Ten-m3 signalling in the developing visual pathway. *BMC Neurosci.* **18**, 78.

Glenn Northcutt, R. (1980). Retinal projections in the australian lungfish. *Brain Res.* **185**, 85–90.

Glover, J. C., Petursdottir, G. and Jansen, J. K. S. (1986). *Fluorescent dextran-amines used as axonal tracers in the nervous system of the chicken embryo*.

Glucksmann, A. (1940). DEVELOPMENT AND DIFFERENTIATION OF THE TADPOLE EYE. *Br. J. Ophthalmol.* **24**, 153–178.

Godement, P. and Mason, C. A. (1993). Guidance of retinal fibers in the optic chiasm. *Perspect. Dev. Neurobiol.* **1**, 217–225.

Godement, P., Vanselow, J., Thanos, S. and Bonhoeffer, F. (1987). A study in developing visual systems with a new method of staining neurones and their processes in fixed tissue. *Development* **101**, 697–713.

Godement, P., Salaün, J. and Mason, C. A. (1990). Retinal axon pathfinding in the optic chiasm: divergence of crossed and uncrossed fibers. *Neuron* **5**, 173–186.

Godement, P., Wang, L. C. and Mason, C. A. (1994). Retinal axon divergence in the optic chiasm: dynamics of growth cone behavior at the midline. *J. Neurosci.* **14**, 7024–7039.

Goldberg, S. and Coulombre, A. J. (1972). Topographical development of the ganglion cell fiber layer in the chick retina. A whole mount study. *J. Comp. Neurol.* **146**, 507–18.

Golgi, C. (1873). Sulla struttura della sostanza grigia del cervello (Comunicazione preventiva). *Gazz. Medica Ital. Lomb.* 244–246.

Gonatas, N. K., Harper, C., Mizutani, T. and Gonatas, J. O. (1979). Superior sensitivity of conjugates of horseradish peroxidase with wheat germ agglutinin for studies of retrograde axonal transport. *J. Histochem. Cytochem.* **27**, 728–734.

Goñi, G. M., Epifano, C., Boskovic, J., Camacho-Artacho, M., Zhou, J., Bronowska, A., Martín, M. T., Eck, M. J., Kremer, L., Gräter, F., et al. (2014). Phosphatidylinositol 4,5-bisphosphate triggers activation of focal adhesion kinase by inducing clustering and conformational changes. *Proc. Natl. Acad. Sci. U. S. A.* **111**,.

Goodman, C. S. (1994). The likeness of being: Phylogenetically conserved molecular mechanisms of growth cone guidance. *Cell* **78**, 353–356.

Gooley, J. J., Lu, J., Chou, T. C., Scammell, T. E. and Saper, C. B. (2001). Melanopsin in cells of origin of the retinohypothalamic tract. *Nat. Neurosci.* **4**, 1165.

Grant, P., Rubin, E. and Cima, C. (1980). Ontogeny of the retina and optic nerve in Xenopus laevis. I. Stages in the early development of the retina. *J. Comp. Neurol.* **189**, 593–613.

Gruberg, E. R. and Udin, S. B. (1978). Topographic projections between the nucleus isthmi and the tectum of the frog rana pipiens. *J. Comp. Neurol.* **179**, 487–500.

Guillery, R. W. W. (1969). An abnormal retinogeniculate projection in Siamese cats. *Brain Res.* **14**, 739–741.

Guillery, R. W. (1971). An abnormal retinogeniculate projection in the albino ferret (Mustela furo). *Brain Res.* **33**, 482–485.

Guillery, R. W. (1989). Early monocular enucleations in fetal ferrets produce a decrease of uncrossed and an increase of crossed retinofugal components: a possible model for the albino abnormality. *J. Anat.* **164**, 73–84.

Guillery, R. W. and Kaas, J. H. (1973). Genetic abnormality of the visual pathways in a “white” tiger. *Science (80-.).* **180**, 1287–1289.

Guillery, R. W. and Updyke, B. V. (1976). Retinofugal pathways in normal and albino axolotls. *Brain Res.* **109**, 235–244.

Guillery, R. W., Casagrande, V. A. and

Oberdorfer, M. D. (1974). Congenitally abnormal vision in Siamese cats. *Nature* **252**, 195–199.

Guillery, R. W., Okoro, A. N. and Witkop, C. J. (1975). Abnormal visual pathways in the brain of a human albino. *Brain Res.* **96**, 373–377.

Guillery, R. W., Mason, C. A. and Taylor, J. S. H. (1995). Developmental determinants at the mammalian optic chiasm. *J. Neurosci.* **15**, 4727–4737.

Haddick, P. C. G., Tom, I., Luis, E., Quiñones, G., Wranik, B. J., Ramani, S. R., Stephan, J.-P. P., Tessier-Lavigne, M. and Gonzalez, L. C. (2014). Defining the ligand specificity of the Deleted in Colorectal Cancer (DCC) receptor. *PLoS One* **9**, 1–12.

Halfter, W. (1996). Intraretinal grafting reveals growth requirements and guidance cues for optic axons in the developing avian retina. *Dev. Biol.* **177**, 160–177.

Halfter, W. (1998). Disruption of the retinal basal lamina during early embryonic development leads to a retraction of vitreal end feet, an increased number of ganglion cells, and aberrant axonal outgrowth. *J. Comp. Neurol.* **397**, 89–104.

Halfter, W., Newgreen, D. F., Sauter, J. and Schwarz, U. (1983). Oriented axon outgrowth from avian embryonic retinae in culture. *Dev. Biol.* **95**, 56–64.

Halfter, W., Deiss, S. and Schwarz, U. (1985). The formation of the axonal pattern in the embryonic avian retina. *J. Comp. Neurol.* **232**, 466–480.

Halfter, W., Dong, S., Balasubramani, M. and Bier, M. E. (2001). Temporary disruption of the retinal basal lamina and its effect on retinal histogenesis. *Dev. Biol.* **238**, 79–96.

Hallonet, M., Hollemann, T., Wehr, R., Jenkins, N. A., Copeland, N. G., Pieler, T. and Gruss, P. (1998). Vax1 is a novel homeobox-containing gene expressed in the developing anterior ventral forebrain. *Development* **125**, 2599–610.

Hallonet, M., Hollemann, T., Pieler, T. and Gruss, P. (1999). Vax1, a novel homeobox-containing gene, directs development of the basal forebrain and visual system. *Genes Dev.* **13**, 3106–14.

Hamelin, M., Zhou, Y., Su, M. W., Scott, I. M. and Culotti, J. G. (1993). Expression of the UNC-5 guidance receptor in the touch neurons of C. elegans steers their axons dorsally. *Nature* **364**, 327–330.

Harada, H., Farhani, N., Wang, X. F., Sugita, S., Charish, J., Attisano, L., Moran, M., Cloutier, J. F., Reber, M., Bremner, R., et al. (2019). Extracellular phosphorylation drives the formation of neuronal circuitry. *Nat. Chem. Biol.* **15**, 1035–1042.

Hardy, H., Prendergast, J. G., Patel, A., Dutta, S., Trejo-Reveles, V., Kroeger, H., Yung, A. R., Goodrich, L. V, Brooks, B., Sowden, J. C., et al. (2019). Detailed analysis of chick optic fissure closure reveals Netrin-1 as an essential mediator of epithelial fusion. *Elife* **8**,.

Harfe, B. D., Scherz, P. J., Nissim, S., Tian, H., McMahon, A. P. and Tabin, C. J. (2004). Evidence for an Expansion-Based Temporal Shh Gradient in Specifying Vertebrate Digit Identities. *Cell* **118**, 517–528.

Harkness, L. (1977). Chameleons use accommodation cues to judge distance. *Nature* **267**, 346–349.

Harris, W. A. (1989). Local positional cues in the neuroepithelium guide retinal axons in embryonic Xenopus brain. *Nature* **339**, 218–221.

Harris, W. A. (1997). Cellular diversification in the vertebrate retina. *Curr. Opin. Genet. Dev.* **7**, 651–658.

Harris, R., Sabatelli, L. M. and Seeger, M. A. (1996). Guidance cues at the Drosophila CNS midline: identification and characterization of two Drosophila

Netrin/UNC-6 homologs. *Neuron* **17**, 217–228.

Hatini, V., Huh, S. O., Herzlinger, D., Soares, V. C. and Lai, E. (1996). Essential role of stromal mesenchyme in kidney morphogenesis revealed by targeted disruption of Winged Helix transcription factor BF-2. *Genes Dev.* **10**, 1467–1478.

Hattar, S., Liao, H. W., Takao, M., Berson, D. M. and Yau, K. W. (2002). Melanopsin-Containing Retinal Ganglion Cells: Architecture, Projections, and Intrinsic Photosensitivity. *Science (80-.).* **295**, 1065–1070.

Hattar, S., Kumar, M., Park, A., Tong, P., Tung, J., Yau, K.-W. and Berson, D. M. (2006). Central projections of melanopsin-expressing retinal ganglion cells in the mouse. *J. Comp. Neurol.* **497**, 326–349.

He, J., Zhang, G., Almeida, A. D., Cayouette, M., Simons, B. D. D. and Harris, W. A. (2012). How Variable Clones Build an Invariant Retina. *Neuron* **75**, 786–798.

Heavner, W. and Pevny, L. (2012). Eye Development and Retinogenesis. *Cold Spring Harb. Perspect. Biol.* **4**, a008391–a008391.

Hedgecock, E. M., Culotti, J. G. and Hall, D. H. (1990). The unc-5, unc-6, and unc-40 genes guide circumferential migrations of pioneer axons and mesodermal cells on the epidermis in C. elegans. *Neuron* **4**, 61–85.

Heesy, C. P. (2009). Seeing in stereo: The ecology and evolution of primate binocular vision and stereopsis. *Evol. Anthropol.* **18**, 21–35.

Hegde, S. and Srivastava, O. (2016). Different gene knockout/transgenic mouse models manifesting persistent fetal vasculature: Are integrins to blame for this pathological condition? *Life Sci.* **171**, 30–38.

Helmstaedter, M., Briggman, K. L., Turaga, S. C., Jain, V., Seung, H. S. and Denk, W. (2013). Connectomic reconstruction of the inner plexiform layer in the mouse retina. *Nature* **500**, 168–174.

Henkemeyer, M., Orioli, D., Henderson, J. T., Saxton, T. M., Roder, J., Pawson, T. and Klein, R. (1996). Nuk Controls Pathfinding of Commissural Axons in the Mammalian Central Nervous System. *Cell* **86**, 35–46.

Hergueta, S., Ward, R., Lemire, M., Rio, J. P., Repérant, J. and Weidner, C. (1992). Overlapping visual fields and ipsilateral retinal projections in turtles. *Brain Res. Bull.* **29**, 427–433.

Hero, I. (1989). The optic fissure in the normal and microphthalmic mouse. *Exp. Eye Res.* **49**, 229–239.

Hero, I. (1990). Optic fissure closure in the normal cinnamon mouse: An ultrastructural study. *Investig. Ophthalmol. Vis. Sci.* **31**, 197–216.

Hero, I., Farjah, M. and Scholtz, C. L. (1991). The prenatal development of the optic fissure in colobomatous microphthalmia. *Investig. Ophthalmol. Vis. Sci.* **32**, 2622–2635.

Herrera, E., Brown, L., Aruga, J., Rachel, R. A., Dolen, G., Mikoshiba, K., Brown, S. and Mason, C. A. (2003). Zic2 Patterns Binocular Vision by Specifying the Uncrossed Retinal Projection. *Cell* **114**, 545–557.

Herrera, E., Marcus, R., Li, S., Williams, S. E., Erskine, L., Lai, E. and Mason, C. (2004). Foxd1 is required for proper formation of the optic chiasm. *Development* **131**, 5727–5739.

Hill, R. E., Favor, J., Hogan, B. L. M., Ton, C. C. T., Saunders, G. F., Hanson, I. M., Prosser, J., Jordan, T., Hastie, N. D. and Van Heyningen, V. (1991). Mouse Small eye results from mutations in a paired-like homeobox-containing gene. *Nature* **354**, 522–525.

Hindges, R., McLaughlin, T., Genoud, N., Henkemeyer, M. and O'Leary, D. D. M.

(2002). EphB forward signaling controls directional branch extension and arborization required for dorsal-ventral retinotopic mapping. *Neuron* **35**, 475–87.

Hinds, J. W. and Hinds, P. L. (1974). Early ganglion cell differentiation in the mouse retina: An electron microscopic analysis utilizing serial sections. *Dev. Biol.* **37**, 381–416.

Hirai, H., Maru, Y., Hagiwara, K., Nishida, J. and Takaku, F. (1987). A novel putative tyrosine kinase receptor encoded by the eph gene. *Science (80-.).* **238**, 1717–1720.

Hoff, E. . (1932). Central nerve terminals in the mamalian spinal cord and their examination by experimental degeneration. *Proc. R. Soc. London. Ser. B, Contain. Pap. a Biol. Character* **111**, 175–188.

Holash, J. A. and Pasquale, E. B. (1995). Polarized Expression of the Receptor Protein Tyrosine Kinase Cek5 in the Developing Avian Visual System. *Dev. Biol.* **172**, 683–693.

Holland, S. J., Gale, N. W., Mbamalu, G., Yancopoulos, G. D., Henkemeyer, M. and Pawson, T. (1996). Bidirectional signalling through the EPH-family receptor Nuk and its transmembrane ligands. *Nature* **383**, 722–725.

Holmes, G. P., Negus, K., Burridge, L., Raman, S., Algar, E., Yamada, T. and Little, M. H. (1998). Distinct but overlapping expression patterns of two vertebrate slit homologs implies functional roles in CNS development and organogenesis. *Mech. Dev.* **79**, 57–72.

Holt, C. E. (1984). Does timing of axon outgrowth influence initial retinotectal topography in Xenopus? *J. Neurosci.* **4**, 1130–1152.

Holt, C. E. (1989). A single-cell analysis of early retinal ganglion cell differentiation in Xenopus: from soma to axon tip. *J. Neurosci.* **9**, 3123–45.

Holt, C. E. and Harris, W. A. (1983). Order in the initial retinotectal map in Xenopus: a new technique for labelling growing nerve fibres. *Nature* **301**, 150–152.

Hong, K., Hinck, L., Nishiyama, M., Poo, M. M., Tessier-Lavigne, M. and Stein, E. (1999). A Ligand-Gated Association between Cytoplasmic Domains of UNC5 and DCC Family Receptors Converts Netrin-Induced Growth Cone Attraction to Repulsion. *Cell* **97**, 927–941.

Honig, M. G. and Hume, R. I. (1986). Fluorescent carbocyanine dyes allow living neurons of identified origin to be studied in long-term cultures. *J. Cell Biol.* **103**, 171–187.

Höpker, V. H., Shewan, D., Tessier-Lavigne, M., Poo, M. M. and Holt, C. (1999). Growth-cone attraction to netrin-1 is converted to repulsion by laminin-1. *Nature* **401**, 69–73.

Huberman, A. D., Wei, W., Elstrott, J., Stafford, B. K., Feller, M. B. and Barres, B. A. (2009). Genetic identification of an On-Off direction-selective retinal ganglion cell subtype reveals a layer-specific subcortical map of posterior motion. *Neuron* **62**, 327–34.

Hughes, L. C., Ortí, G., Huang, Y., Sun, Y., Baldwin, C. C., Thompson, A. W., Arcila, D., Betancur, R., Li, C., Becker, L., et al. (2018). Comprehensive phylogeny of ray-finned fishes (Actinopterygii) based on transcriptomic and genomic data. *Proc. Natl. Acad. Sci. U. S. A.* **115**, 6249–6254.

Hutson, L. D. and Chien, C. Bin (2002). Pathfinding and error correction by retinal axons: the role of astray/robo2. *Neuron* **33**, 205–17.

Hutson, L. D., Jurynec, M. J., Yeo, S.-Y. Y., Okamoto, H. and Chien, C.-B. Bin (2003). Two Divergent slit1 Genes in Zebrafish. *Dev. Dyn.* **228**, 358–369.

Ishii, N., Wadsworth, W. G., Stern, B. D., Culotti, J. G. and Hedgecock, E. M. (1992). UNC-6, a laminin-related protein, guides cell and pioneer axon migrations

in C. elegans. *Neuron* **9**, 873–881.

Islam, S. M., Shinmyo, Y., Okafuji, T., Su, Y., Naser, I. Bin, Ahmed, G., Zhang, S., Chen, S., Ohta, K., Kiyonari, H., et al. (2009). Draxin, a Repulsive Guidance Protein for Spinal Cord and Forebrain Commissures. *Science (80-.).* **323**, 388–393.

Ito, M. and Yoshioka, M. (1999). Regression of the hyaloid vessels and pupillary membrane of the mouse. *Anat. Embryol. (Berl).* **200**, 403–411.

Itoh, a, Miyabayashi, T., Ohno, M. and Sakano, S. (1998). Cloning and expressions of three mammalian homologues of Drosophila slit suggest possible roles for Slit in the formation and maintenance of the nervous system. *Mol. brain Res.* **62**, 175–86.

Iwai-Takekoshi, L., Balasubramanian, R., Sitko, A., Khan, R., Weinreb, S., Robinson, K. and Mason, C. (2018). Activation of Wnt signaling reduces ipsilaterally projecting retinal ganglion cells in pigmented retina. *Development* **145**, dev163212.

Jeon, C. J., Strettoi, E. and Masland, R. H. (1998). The major cell populations of the mouse retina. *J. Neurosci.* **18**, 8936–46.

Jimmy Zhou, Z. (1998). Direct participation of starburst amacrine cells in spontaneous rhythmic activities in the developing mammalian retina. *J. Neurosci.* **18**, 4155–4165.

Jin, Z., Zhang, J., Klar, A., Chédotal, A., Rao, Y., Cepko, C. L. and Bao, Z.-Z. Z. (2003). Irx4-mediated regulation of Slit1 expression contributes to the definition of early axonal paths inside the retina. *Development* **130**, 1037–48.

Jongbloets, B. C. and Pasterkamp, R. J. (2014). Semaphorin signalling during development. *Development* **141**, 3292–3297.

Karlstrom, R. O., Trowe, T., Klostermann, S., Baier, H., Brand, M., Crawford, a D., Grunewald, B., Haffter, P., Hoffmann, H., Meyer, S. U., et al. (1996). Zebrafish mutations affecting retinotectal axon pathfinding. *Development* **123**, 427–38.

Karlstrom, R. O., Talbot, W. S. and Schier, A. F. (1999). Comparative synteny cloning of zebrafish you-too: mutations in the Hedgehog target gli2 affect ventral forebrain patterning. *Genes Dev.* **13**, 388–393.

Karlstrom, R. O., Tyurina, O. V., Kawakami, A., Nishioka, N., Talbot, W. S., Sasaki, H. and Schier, A. F. (2003). Genetic analysis of zebrafish gli1 and gli2 reveals divergent requirements for gli genes in vertebrate development. *Development* **130**, 1549–1564.

Karten, H. J., Hodos, W., Nauta, W. J. H. and Revzin, A. M. (1973). Neural connections of the “visual wulst” of the avian telencephalon. Experimental studies in the pigeon (Columba livia) and owl (Speotyto cunicularia). *J. Comp. Neurol.* **150**, 253–277.

Keino-Masu, K., Masu, M., Hinck, L., Leonardo, E. D., Chan, S. S.-Y., Culotti, J. G. and Tessier-Lavigne, M. (1996). Deleted in Colorectal Cancer (DCC) Encodes a Netrin Receptor. *Cell* **87**, 175–185.

Kennedy, T. E., Serafini, T., de la Torre, J. and Tessier-Lavigne, M. (1994). Netrins are diffusible chemotropic factors for commissural axons in the embryonic spinal cord. *Cell* **78**, 425–435.

Kennedy, T. E., Wang, H., Marshall, W. and Tessier-Lavigne, M. (2006). Axon guidance by diffusible chemoattractants: a gradient of netrin protein in the developing spinal cord. *J. Neurosci.* **26**, 8866–8874.

Kidd, T., Bland, K. S. and Goodman, C. S. (1999). Slit is the midline repellent for the robo receptor in Drosophila. *Cell* **96**, 785–794.

Kim, T.-H., Lee, H. K., Seo, I. A., Bae, H. R., Suh, D. J., Wu, J., Rao, Y., Hwang, K.-G.

and Park, H. T. (2005). Netrin induces down-regulation of its receptor, Deleted in Colorectal Cancer, through the ubiquitin-proteasome pathway in the embryonic cortical neuron. *J. Neurochem.* **95**, 1–8.

Kim, N., Min, K. W. oo., Kang, K. H. w., Lee, E. J. un., Kim, H. T., Moon, K., Choi, J., Le, D., Lee, S. H. and Kim, J. W. o. (2014). Regulation of retinal axon growth by secreted Vax1 homeodomain protein. *Elife* **3**, e02671.

Kim, K.-Y. Y., Rios, L. C., Le, H., Perez, A. J., Phan, S., Bushong, E. A., Deerinck, T. J., Liu, Y. H., Ellisman, M. H. M. A. M. H., Lev-Ram, V., et al. (2019). Synaptic Specializations of Melanopsin-Retinal Ganglion Cells in Multiple Brain Regions Revealed by Genetic Label for Light and Electron Microscopy. *Cell Rep.* **29**, 628-644.e6.

Kimmel, R. A., Turnbull, D. H., Blanquet, V., Wurst, W., Loomis, C. a. and Joyner, A. L. (2000). Two lineage boundaries coordinate vertebrate apical ectodermal ridge formation. *Genes Dev.* **14**, 1377–1389.

Köbbert, C., Apps, R., Bechmann, I., Lanciego, J. L., Mey, J. and Thanos, S. (2000). Current concepts in neuroanatomical tracing. *Prog. Neurobiol.* **62**, 327–351.

Kociok, N., Crespo-Garcia, S., Liang, Y., Klein, S. V., Nürnberg, C., Reichhart, N., Skosyrski, S., Moritz, E., Maier, A.-K., Brunken, W. J., et al. (2016). Lack of netrin-4 modulates pathologic neovascularization in the eye. *Sci. Rep.* **6**, 18828.

Kolodziej, P. A., Timpe, L. C., Mitchell, K. J., Fried, S. R., Goodman, C. S., Jan, L. Y. and Jan, Y. N. (1996). frazzled Encodes a Drosophila Member of the DCC Immunoglobulin Subfamily and Is Required for CNS and Motor Axon Guidance. *Cell* **87**, 197–204.

Kolpak, A., Zhang, J. and Bao, Z.-Z. (2005). Sonic hedgehog has a dual effect on the growth of retinal ganglion axons depending on its concentration. *J. Neurosci.* **25**, 3432–41.

Koppers, M., Cagnetta, R., Shigeoka, T., Wunderlich, L. C., Vallejo-Ramirez, P., Qiaojin Lin, J., Zhao, S., Jakobs, M. A., Dwivedy, A., Minett, M. S., et al. (2019). Receptor-specific interactome as a hub for rapid cue-induced selective translation in axons. *Elife* **8**, 1–27.

Krimpenfort, P., Song, J.-Y., Proost, N., Zevenhoven, J., Jonkers, J. and Berns, A. (2012). Deleted in colorectal carcinoma suppresses metastasis in p53-deficient mammary tumours. *Nature* **482**, 538–541.

Kristensson, K. and Olsson, Y. (1971a). Uptake and retrograde axonal transport of peroxidase in hypoglossal neurones. *Acta Neuropathol.* **19**, 1–9.

Kristensson, K. and Olsson, Y. (1971b). Retrograde axonal transport of protein. *Brain Res.* **29**, 363–5.

Kruger, K., Tam, A. S., Lu, C. and Sretavan, D. W. (1998). Retinal ganglion cell axon progression from the optic Chiasm to initiate optic tract development requires cell autonomous function of GAP- 43. *J. Neurosci.* **18**, 5692–5705.

Kruger, R. P., Lee, J., Li, W. and Guan, K.-L. (2004). Mapping netrin receptor binding reveals domains of Unc5 regulating its tyrosine phosphorylation. *J. Neurosci.* **24**, 10826–34.

Kuwajima, T., Yoshida, Y., Takegahara, N., Petros, T. J., Kumanogoh, A., Jessell, T. M., Sakurai, T. and Mason, C. (2012). Optic Chiasm Presentation of Semaphorin6D in the Context of Plexin-A1 and Nr-CAM Promotes Retinal Axon Midline Crossing. *Neuron* **74**, 676–690.

Kuwajima, T., Sitko, A. A., Bhansali, P., Jurgens, C., Guido, W. and Mason, C. (2013). ClearT: a detergent- and solvent-free clearing method for neuronal and non-neuronal tissue. *Development* **140**, 1364–1368.

Kuwajima, T., Soares, C. A., Sitko, A. A., Lefebvre, V. and Mason, C. (2017). SoxC Transcription Factors Promote Contralateral Retinal Ganglion Cell Differentiation and Axon Guidance in the Mouse Visual System. *Neuron* **93**, 1110-1125.e5.

Laessing, U. and Stuermer, C. A. O. (1996). Spatiotemporal pattern of retinal ganglion cell differentiation revealed by the expression of neurolin in embryonic zebrafish. *J. Neurobiol.* **29**, 65–74.

Lamb, T. D., Collin, S. P. and Pugh, E. N. (2007). Evolution of the vertebrate eye: opsins, photoreceptors, retina and eye cup. *Nat. Rev. Neurosci.* **8**, 960–976.

Lambot, M. A., Depasse, F., Noel, J. C. and Vanderhaeghen, P. (2005). Mapping labels in the human developing visual system and the evolution of binocular vision. *J. Neurosci.* **25**, 7232–7237.

Lanciego, J. L. and Wouterlood, F. G. (2011). A half century of experimental neuroanatomical tracing. *J. Chem. Neuroanat.* **42**, 157–183.

Lang, R. A. and Bishop, J. M. (1993). Macrophages are required for cell death and tissue remodeling in the developing mouse eye. *Cell* **74**, 453–462.

Lang, R., Lustig, M., Francois, F., Sellinger, M. and Plesken, H. (1994). Apoptosis during macrophage-dependent ocular tissue remodelling. *Development* **120**, 3395–3403.

Larrivée, B., Freitas, C., Trombe, M., Lv, X., Delafarge, B., Yuan, L., Bouvrée, K., Bréant, C., Del Toro, R., Bréchot, N., et al. (2007). Activation of the UNC5B receptor by Netrin-1 inhibits sprouting angiogenesis. *Genes Dev.* **21**, 2433–47.

Larsson, M. (2011). Binocular vision and ipsilateral retinal projections in relation to eye and forelimb coordination. *Brain. Behav. Evol.* **77**, 219–30.

Larsson, M. L. (2015). Binocular vision, the optic chiasm, and their associations with vertebrate motor behavior. *Front. Ecol. Evol.* **3**, 89.

Lavail, J. H. and Lavail, M. M. (1972). Retrograde Axonal Transport in the Central Nervous System. *Science (80-.).* **176**, 1416–1417.

Lavail, J. H., Nixon, R. A. and Sidman, R. L. (1978). Genetic control of retinal ganglion cell projections. *J. Comp. Neurol.* **182**, 399–421.

Lázár, G. (1978). Application of cobalt-filling technique to show retinal projections in the frog. *Neuroscience* **3**, 725–736.

Le Lievre, C. S. and Le Douarin, N. M. (1975). *Mesenchymal derivatives of the neural crest: analysis of chimaeric quail and chick embryos*.

Leamey, C. A. and Sawatari, A. (2019). Teneurins: Mediators of Complex Neural Circuit Assembly in Mammals. *Front. Neurosci.* **13**, 580.

Leamey, C. A., Merlin, S., Lattouf, P., Sawatari, A., Zhou, X., Demel, N., Glendining, K. A., Oohashi, T., Sur, M. and Fässler, R. (2007). Ten_m3 regulates eye-specific patterning in the mammalian visual pathway and is required for binocular vision. *PLoS Biol.* **5**, 2077–2092.

Lee, C.-H., Herman, T., Clandinin, T. R., Lee, R. and Zipursky, S. L. (2001). N-Cadherin Regulates Target Specificity in the Drosophila Visual System. *Neuron* **30**, 437–450.

Lee, R., Petros, T. J. and Mason, C. A. (2008). Zic2 Regulates Retinal Ganglion Cell Axon Avoidance of ephrinB2 through Inducing Expression of the Guidance Receptor EphB1. *J. Neurosci.* **28**, 5910–5919.

Leonardo, E. D., Hinck, L., Masu, M., Keino-Masu, K., Ackerman, S. L. and Tessier-Lavigne, M. (1997). Vertebrate homologues of C. elegans UNC-5 are candidate netrin receptors. *Nature* **386**, 833–838.

Leung-Hagesteijn, C., Spence, A. M., Stern, B.

D., Zhou, Y., Su, M. W., Hedgecock, E. M. and Culotti, J. G. (1992). UNC-5, a transmembrane protein with immunoglobulin and thrombospondin type 1 domains, guides cell and pioneer axon migrations in C. elegans. *Cell* **71**, 289–299.

Leung, K.-M., van Horck, F. P. G., Lin, A. C., Allison, R., Standart, N. and Holt, C. E. (2006). Asymmetrical beta-actin mRNA translation in growth cones mediates attractive turning to netrin-1. *Nat. Neurosci.* **9**, 1247–56.

Leung, V., Iliescu, A., Jolicoeur, C., Gravel, M., Apuzzo, S., Torban, E., Cayouette, M. and Gros, P. (2015). The planar cell polarity protein Vangl2 is required for retinal axon guidance. *Dev. Neurobiol.* **in press**,.

Levine, R. L. (1980). An autoradiographic study of the retinal projection in Xenopus laevis with comparisons to Rana. *J. Comp. Neurol.* **189**, 1–29.

Li, Q., Shirabe, K., Thisse, C., Thisse, B., Okamoto, H., Masai, I. and Kuwada, J. Y. (2005). Chemokine signaling guides axons within the retina in zebrafish. *J. Neurosci.* **25**, 1711–7.

Li, X., Gao, X., Liu, G., Xiong, W., Wu, J. and Rao, Y. (2008). Netrin signal transduction and the guanine nucleotide exchange factor DOCK180 in attractive signaling. *Nat. Neurosci.* **11**, 28–35.

Linden, R. and Perry, V. H. (1983). Massive retinotectal projection in rats. *Brain Res.* **272**, 145–149.

Liu, I. S. C., Chen, J., Ploder, L., Vidgen, D., van der Kooy, D., Kalnins, V. I. and McInnes, R. R. (1994). Developmental expression of a novel murine homeobox gene (Chx10): Evidence for roles in determination of the neuroretina and inner nuclear layer. *Neuron* **13**, 377–393.

Liu, J., Wilson, S. and Reh, T. (2003). BMP receptor 1b is required for axon guidance and cell survival in the developing retina. *Dev. Biol.* **256**, 34–48.

Liu, G., Beggs, H., Jürgensen, C., Park, H.-T., Tang, H., Gorski, J., Jones, K. R., Reichardt, L. F., Wu, J. and Rao, Y. (2004). Netrin requires focal adhesion kinase and Src family kinases for axon outgrowth and attraction. *Nat. Neurosci.* **7**, 1222–1232.

Liu, D., Xiong, S.-Q., Shang, L., Tian, X.-F., Yang, J. and Xia, X.-B. (2014). Expression of netrin-1 receptors in retina of oxygen-induced retinopathy in mice. *BMC Ophthalmol.* **14**, 102.

Liu, Y. Y., Bhowmick, T., Liu, Y. Y., Gao, X., Mertens, H. D. T., Svergun, D. I., Xiao, J., Zhang, Y., Wang, J. and Meijers, R. (2018). Structural Basis for Draxin-Modulated Axon Guidance and Fasciculation by Netrin-1 through DCC. *Neuron* **97**, 1261-1267.e4.

Lo Giudice, Q., Leleu, M., La Manno, G., Fabre, P. J., Giudice, Q. Lo, Leleu, M., Manno, G. La, Fabre, P. J., Lo Giudice, Q., Leleu, M., et al. (2019). Single-cell transcriptional logic of cell-fate specification and axon guidance in early-born retinal neurons. *Development* **146**, dev178103.

Lobov, I. B., Brooks, P. C. and Lang, R. A. (2002). Angiopoietin-2 displays VEGF-dependent modulation of capillary structure and endothelial cell survival in vivo. *Proc. Natl. Acad. Sci.* **99**, 11205–11210.

Lobov, I. B., Rao, S., Carroll, T. J., Vallance, J. E., Ito, M., Ondr, J. K., Kurup, S., Glass, D. A., Patel, M. S., Shu, W., et al. (2005). WNT7b mediates macrophage-induced programmed cell death in patterning of the vasculature. *Nature* **437**, 417–421.

Long, J. A., Choo, B. and Clement, A. (2019). The Evolution of Fishes through Geological Time. In *Evolution and Development of Fishes*, .

Lu, X., le Noble, F., Yuan, L., Jiang, Q., de Lafarge, B., Sugiyama, D., Bréant, C., Claes, F., De Smet, F., Thomas, J.-L., et al. (2004). The netrin receptor UNC5B

mediates guidance events controlling morphogenesis of the vascular system. *Nature* **432**, 179–186.

Lund, R. D. (1965). Uncrossed Visual Pathways of Hooded and Albino Rats. *Science (80-.).* **149**, 1506–1507.

Luppi, P.-H., Fort, P. and Jouvet, M. (1990). *Iontophoretic application of unconjugated cholera toxin B subunit (CTb) combined with immunohistochemistry of neurochemical substances: a method for transmitter identification of retrogradely labeled neurons*.

Lustig, M., Erskine, L., Mason, C. A., Grumet, M. and Sakurai, T. (2001). Nr-CAM expression in the developing mouse nervous system: ventral midline structures, specific fiber tracts, and neuropilar regions. *J. Comp. Neurol.* **434**, 13–28.

Lyckman, A. W., Fan, G., Rios, M., Jaenisch, R. and Sur, M. (2005). Normal eye-specific patterning of retinal inputs to murine subcortical visual nuclei in the absence of brain-derived neurotrophic factor. *Vis. Neurosci.* **22**, 27–36.

M Hogan, D. L., A Hirst, E. M., Horsburgh, G. and Hetherington, C. M. (1988). small eye (Sey): a mouse model for the genetic analysis of craniofacial abnormalities. *Development* **103 Suppl**, 115–119.

Marcos, S., Nieto-Lopez, F., Sandonis, A., Cardozo, M. J., Di Marco, F., Esteve, P. and Bovolenta, P. (2015). Secreted Frizzled Related Proteins Modulate Pathfinding and Fasciculation of Mouse Retina Ganglion Cell Axons by Direct and Indirect Mechanisms. *J. Neurosci.* **35**, 4729–4740.

Marcucci, F., Murcia-Belmonte, V., Wang, Q., Coca, Y., Ferreiro-Galve, S., Kuwajima, T., Khalid, S., Ross, M. E., Mason, C. and Herrera, E. (2016). The Ciliary Margin Zone of the Mammalian Retina Generates Retinal Ganglion Cells. *Cell Rep.* **17**, 3153–3164.

Marcucci, F., Soares, C. A. and Mason, C. (2019). Distinct timing of neurogenesis of ipsilateral and contralateral retinal ganglion cells. *J. Comp. Neurol.* **527**, 212–224.

Marcus, R. C. and Mason, C. A. (1995). The first retinal axon growth in the mouse optic chiasm: Axon patterning and the cellular environment. *J. Neurosci.* **15**, 6389–6402.

Marcus, R. C., Blazeski, R., Godement, P. and Mason, C. A. (1995). Retinal axon divergence in the optic chiasm: uncrossed axons diverge from crossed axons within a midline glial specialization. *J. Neurosci.* **15**, 3716–3729.

Marcus, R. C., Wang, L. C. and Mason, C. a (1996). Retinal axon divergence in the optic chiasm: midline cells are unaffected by the albino mutation. *Development* **122**, 859–68.

Marcus, R. C., Shimamura, K., Sretavan, D., Lai, E., Rubenstein, J. L. R. R. and Mason, C. A. (1999). Domains of regulatory gene expression and the developing optic chiasm: Correspondence with retinal axon paths and candidate signaling cells. *J. Comp. Neurol.* **403**, 346–358.

Marg, E. (2006). THE ACCESSORY OPTIC SYSTEM *. *Ann. N. Y. Acad. Sci.* **117**, 35–51.

Marillat, V., Cases, O., Nguyen-Ba-Charvet, K. T., Tessier-Lavigne, M., Sotelo, C. and Chédotal, A. (2002). Spatiotemporal expression patterns of slit and robo genes in the rat brain. *J. Comp. Neurol.* **442**, 130–155.

Martersteck, E. M., Hirokawa, K. E., Evarts, M., Bernard, A., Duan, X., Li, Y., Ng, L., Oh, S. W., Ouellette, B., Royall, J. J., et al. (2017). Diverse Central Projection Patterns of Retinal Ganglion Cells. *Cell Rep.* **18**, 2058–2072.

Martin, P. R. (1986). The projection of different retinal ganglion cell classes to the dorsal lateral geniculate nucleus in

the hooded rat. *Exp. Brain Res.* **62**, 77–88.

Mason, C. and Guillery, R. (2019). Conversations with Ray Guillery on albinism: linking Siamese cat visual pathway connectivity to mouse retinal development. *Eur. J. Neurosci.* **49**, 913–927.

Masseck, O. A. and Hoffmann, K.-P. P. (2009). Comparative neurobiology of the optokinetic reflex. *Ann. N. Y. Acad. Sci.* **1164**, 430–439.

Mathers, P. H., Grinberg, A., Mahon, K. A. and Jamrich, M. (1997). The Rx homeobox gene is essential for vertebrate eye development. *Nature* **387**, 603–607.

Matsunaga, E. (2006). Repulsive Guidance Molecule Plays Multiple Roles in Neuronal Differentiation and Axon Guidance. *J. Neurosci.* **26**, 6082–6088.

McFarlane, S., McNeill, L. and Holt, C. E. (1995). FGF signaling and target recognition in the developing xenopus visual system. *Neuron* **15**, 1017–1028.

McFarlane, S., Cornel, E., Amaya, E. and Holt, C. E. (1996). Inhibition of FGF receptor activity in retinal ganglion cell axons causes errors in target recognition. *Neuron* **17**, 245–254.

McLaughlin, T., Torborg, C. L., Feller, M. B. and O'Leary, D. D. M. (2003). Retinotopic Map Refinement Requires Spontaneous Retinal Waves during a Brief Critical Period of Development. *Neuron* **40**, 1147–1160.

Mcloon, S. C. and Lund, R. D. (1982). *Experimental Br'&in Research Transient Retinofugal Pathways in the Developing Chick:**.

Mehlen, P. and Thibert, C. (2004). Dependence receptors: between life and death. *Cell. Mol. Life Sci.* **61**, 1854–1866.

Mehlen, P., Rabizadeh, S., Snipas, S. J., Assa-Munt, N., Salvesen, G. S. and Bredesen, D. E. (1998). The DCC gene product induces apoptosis by a mechanism requiring receptor proteolysis. *Nature* **395**, 801–804.

Mehlen, P., Delloye-Bourgeois, C. and Chédotal, A. (2011). Novel roles for Slits and netrins: axon guidance cues as anticancer targets? *Nat. Rev. Cancer* **11**, 188–197.

Meijers, R., Smock, R. G., Zhang, Y. and Wang, J.-H. H. (2019). Netrin Synergizes Signaling and Adhesion through DCC. *Trends Biochem. Sci.* **45**, 6–12.

Miller, E. D., Tran, M. N., Wong, G. K., Oakley, D. M. and Wong, R. O. L. (1999). Morphological differentiation of bipolar cells in the ferret retina. *Vis. Neurosci.* **16**, 1133–1144.

Ming, G. L., Song, H., Berninger, B., Holt, C. E., Tessier-Lavigne, M. and Poo, M. M. (1997). cAMP-dependent growth cone guidance by netrin-1. *Neuron* **19**, 1225–1235.

Mitchell, K. J., Doyle, J. L., Serafini, T., Kennedy, T. E., Tessier-Lavigne, M., Goodman, C. S. and Dickson, B. J. (1996). Genetic analysis of Netrin genes in Drosophila: Netrins guide CNS commissural axons and peripheral motor axons. *Neuron* **17**, 203–215.

Monnier, P. P., Sierra, A., Macchi, P., Deitinghoff, L., Andersen, J. S., Mann, M., Flad, M., Hornberger, M. R., Stahl, B., Bonhoeffer, F., et al. (2002). RGM is a repulsive guidance molecule for retinal axons. *Nature* **419**, 392–395.

Moore, S. W., Biais, N. and Sheetz, M. P. (2009). Traction on Immobilized Netrin-1 Is Sufficient to Reorient Axons. *Science (80-.).* **325**, 166–166.

Morcillo, J., Martinez-Morales, J.-R., Trousse, F., Fermin, Y., Sowden, J. C. and Bovolenta, P. (2006). Proper patterning of the optic fissure requires the sequential activity of BMP7 and SHH. *Development* **133**, 3179–3190.

Morenilla-Palao, C., Teresa López-Cascales,

M., López-Atalaya, J. P., Baeza, D., Calvo-Diaz, L., Giner De Gracia, A., Barco, A. and Herrera, E. (2019). Zic2 abrogates an alternative Wnt signaling pathway to convert axon attraction into repulsion. *bioRxiv* 759407.

Moreno-Bravo, J. A., Roig Puiggros, S., Mehlen, P. and Chédotal, A. (2019). Synergistic Activity of Floor-Plate- and Ventricular-Zone-Derived Netrin-1 in Spinal Cord Commissural Axon Guidance. *Neuron* **101**, 625-634.e3.

Morin, L. P. and Studholme, K. M. (2014). Retinofugal projections in the mouse. *J. Comp. Neurol.* **522**, 3733–3753.

Mühleisen, T. W., Agoston, Z. and Schulte, D. (2006). Retroviral misexpression of cVax disturbs retinal ganglion cell axon fasciculation and intraretinal pathfinding in vivo and guidance of nasal ganglion cell axons in vitro. *Dev. Biol.* **297**, 59–73.

Müller, B. K., Jay, D. G. and Bonhoeffer, F. (1996). Chromophore-assisted laser inactivation of a repulsive axonal guidance molecule. *Curr. Biol.* **6**, 1497–1502.

Muranishi, Y. and Furukawa, T. (2012). BAC-Dkk3-EGFP transgenic mouse: an in vivo analytical tool for Dkk3 expression. *J. Biomed. Biotechnol.* **2012**, 973140.

Murcia-Belmonte, V., Coca, Y., Vegar, C., Negueruela, S., de Juan Romero, C., Valiño, A. J., Sala, S., DaSilva, R., Kania, A., Borrell, V., et al. (2019). A Retino-retinal Projection Guided by Unc5c Emerged in Species with Retinal Waves. *Curr. Biol.* **29**, 1149-1160.e4.

Nakagawa, S., Brennan, C., Johnson, K. G., Shewan, D., Harris, W. a and Holt, C. E. (2000). Ephrin-B regulates the Ipsilateral routing of retinal axons at the optic chiasm. *Neuron* **25**, 599–610.

Nakamoto, M., Cheng, H. J., Friedman, G. C., Mclaughlin, T., Hansen, M. J., Yoon, C. H., Oleary, D. D. M. and Flanagan, J. G. (1996). Topographically specific effects of ELF-1 on retinal axon guidance in vitro and retinal axon mapping in vivo. *Cell* **86**, 755–766.

Nakamoto, C., Durward, E., Horie, M. and Nakamoto, M. (2019). Nell2 regulates the contralateral-versus-ipsilateral visual projection as a domain-specific positional cue. *Development* **146**, dev170704.

Nakayama, M., Nakajima, D., Nagase, T., Nomura, N., Seki, N. and Ohara, O. (1998). Identification of high-molecular-weight proteins with multiple EGF-like motifs by motif-trap screening. *Genomics* **51**, 27–34.

Nassi, J. J., Cepko, C. L., Born, R. T. and Beier, K. T. (2015). Neuroanatomy goes viral! *Front. Neuroanat.* **9**, 80.

Nauta, W. J. H. and Ryan, L. F. (1952). Selective silver impregnation of degenerating axons in the central nervous system. *Biotech. Histochem.*

Navankasattusas, S., Whitehead, K. J., Suli, A., Sorensen, L. K., Lim, A. H., Zhao, J., Park, K. W., Wythe, J. D., Thomas, K. R., Chien, C.-B., et al. (2008). The netrin receptor UNC5B promotes angiogenesis in specific vascular beds. *Development* **135**, 659–667.

Nayak, G., Odaka, Y., Prasad, V., Solano, A. F., Yeo, E.-J., Vemaraju, S., Molkentin, J. D., Trumpp, A., Williams, B., Rao, S., et al. (2018). Developmental vascular regression is regulated by a Wnt/β-catenin, MYC and CDKN1A pathway that controls cell proliferation and cell death. *Development* **145**, dev154898.

Negulescu, A.-M. and Mehlen, P. (2018). Dependence receptors - the dark side awakens. *FEBS J.* **285**, 3909–3924.

Nguyen, A. and Cai, H. (2006). Netrin-1 induces angiogenesis via a DCC-dependent ERK1/2-eNOS feed-forward mechanism. *Proc. Natl. Acad. Sci. U. S. A.* **103**, 6530–5.

Nguyen, M.-T. T., Vemaraju, S., Nayak, G., Odaka, Y., Buhr, E. D., Alonzo, N., Tran,

U., Batie, M., Upton, B. A., Darvas, M., et al. (2019). An opsin 5–dopamine pathway mediates light-dependent vascular development in the eye. *Nat. Cell Biol.* **21**, 420–429.

Niclou, S. P., Jia, L. and Raper, J. A. (2000). Slit2 is a repellent for retinal ganglion cell axons. *J. Neurosci.* **20**, 4962–74.

Niederkofler, V., Salie, R., Sigrist, M. and Arber, S. (2004). Repulsive Guidance Molecule (RGM) Gene Function Is Required for Neural Tube Closure but Not Retinal Topography in the Mouse Visual System. *J. Neurosci.* **24**, 808–818.

Northcutt, R. G. (1977). Retinofugal projections in the lepidosirenid lungfishes. *J. Comp. Neurol.* **174**, 553–573.

Northcutt, R. G. and Butler, A. B. (1976). Retinofugal pathways in the longnose gar Lepisosteus osseus (linnaeus). *J. Comp. Neurol.* **166**, 1–15.

O'Sullivan, M. L., Puñal, V. M., Kerstein, P. C., Brzezinski, J. A., Glaser, T., Wright, K. M., Kay, J. N., Sullivan, M. L. O., Pu, V. M., Brzezinski, J. A., et al. (2017). Astrocytes follow ganglion cell axons to establish an angiogenic template during retinal development. *Glia* **65**, 1697–1716.

Ohta, K., Tannahill, D., Yoshida, K., Johnson, A. R., Cook, G. M. W. and Keynes, R. J. (1999). Embryonic Lens Repels Retinal Ganglion Cell Axons. *Dev. Biol.* **211**, 124–132.

Oster, S. F. (2003). Invariant Sema5A inhibition serves an ensheathing function during optic nerve development. *Development* **130**, 775–784.

Osterfield, M., Egelund, R., Young, L. M. and Flanagan, J. G. (2008). Interaction of amyloid precursor protein with contactins and NgCAM in the retinotectal system. *Development* **135**, 1189–1199.

Osterhout, J. A., Josten, N., Yamada, J., Pan, F., Wu, S., Nguyen, P. L., Panagiotakos, G., Inoue, Y. U., Egusa, S. F., Volgyi, B., et al. (2011). Cadherin-6 Mediates Axon-Target Matching in a Non-Image-Forming Visual Circuit. *Neuron* **71**, 632–639.

Osterhout, J. A., El-Danaf, R. N., Nguyen, P. L. and Huberman, A. D. (2014). Birthdate and Outgrowth Timing Predict Cellular Mechanisms of Axon Target Matching in the Developing Visual Pathway. *Cell Rep.* **8**, 1006–1017.

Osterhout, J. A., Stafford, B. K., Nguyen, P. L., Yoshihara, Y. and Huberman, A. D. (2015). Contactin-4 Mediates Axon-Target Specificity and Functional Development of the Accessory Optic System. *Neuron* **86**, 985–999.

Ott, M. (2001). Chameleons have independent eye movements but synchronise both eyes during saccadic prey tracking. *Exp. Brain Res.* **139**, 173–179.

Ott, H., Bastmeyer, M. and Stuermer, C. A. O. (1998). Neurolin, the goldfish homolog of DM-GRASP, is involved in retinal axon pathfinding to the optic disk. *J. Neurosci.* **18**, 3363–3372.

Pak, W., Hindges, R., Lim, Y.-S. S., Pfaff, S. L. and O'leary, D. D. M. M. (2004). Magnitude of Binocular Vision Controlled by Islet-2 Repression of a Genetic Program that Specifies Laterality of Retinal Axon Pathfinding. *Cell* **119**, 567–578.

Panza, P., Sitko, A. A., Maischein, H.-M., Koch, I., Flötenmeyer, M., Wright, G. J., Mandai, K., Mason, C. A. and Söllner, C. (2015). The LRR receptor Islr2 is required for retinal axon routing at the vertebrate optic chiasm. *Neural Dev.* **10**, 23.

Park, K. W., Crouse, D., Lee, M., Karnik, S. K., Sorensen, L. K., Murphy, K. J., Kuo, C. J. and Li, D. Y. (2004). The axonal attractant Netrin-1 is an angiogenic factor. *Proc. Natl. Acad. Sci.* **101**, 16210–16215.

Patel, A. and Sowden, J. C. (2017). Genes and pathways in optic fissure closure. *Semin. Cell Dev. Biol.* **91**, 55–65.

Peng, J., Fabre, P. J., Dolique, T., Swikert, S. M., Kermasson, L., Shimogori, T. and Charron, F. (2018). Sonic Hedgehog Is a Remotely Produced Cue that Controls Axon Guidance Trans-axonally at a Midline Choice Point. *Neuron* **97**, 326-340.e4.

Perelli, R. M., O'Sullivan, M. L., Zarnick, S. and Kay, J. N. (2019). Environmental Oxygen Regulates Astrocyte Proliferation to Guide Angiogenesis during Retinal Development. *bioRxiv* 861948.

Pettigrew, J. (1986). The Evolution of Binocular Vision. *Cambridge Cambridge Univ. Press* 208–222.

Pettigrew, J. and Konishi, M. (1976). Neurons selective for orientation and binocular disparity in the visual Wulst of the barn owl (Tyto alba). *Science (80-.).* **193**, 675–678.

Pfeiffenberger, C., Cutforth, T., Woods, G., Yamada, J., Rentería, R. C., Copenhagen, D. R., Flanagan, J. G. and Feldheim, D. A. (2005). Ephrin-As and neural activity are required for eye-specific patterning during retinogeniculate mapping. *Nat. Neurosci.* **8**, 1022–1027.

Pfeiffenberger, C., Yamada, J. and Feldheim, D. A. (2006). Ephrin-As and patterned retinal activity act together in the development of topographic maps in the primary visual system. *J. Neurosci.* **26**, 12873–12884.

Pinter, R. and Hindges, R. (2010). Perturbations of MicroRNA Function in Mouse Dicer Mutants Produce Retinal Defects and Lead to Aberrant Axon Pathfinding at the Optic Chiasm. *PLoS One* **5**, e10021.

Piper, M., Anderson, R., Dwivedy, A., Weinl, C., van Horck, F., Leung, K.-M. M., Cogill, E. and Holt, C. E. (2006). Signaling mechanisms underlying Slit2-induced collapse of Xenopus retinal growth cones. *Neuron* **49**, 215–228.

Pitman, R. M., Tweedle, C. D. and Cohen, M. J. (1972). Branching of Central Neurons: Intracellular Cobalt Injection for Light and Electron Microscopy. *Science (80-.).* **176**, 412–414.

Plachez, C., Andrews, W., Liapi, A., Knoell, B., Drescher, U., Mankoo, B., Zhe, L., Mambetisaeva, E., Annan, A., Bannister, L., et al. (2008). Robos are required for the correct targeting of retinal ganglion cell axons in the visual pathway of the brain. *Mol. Cell. Neurosci.* **37**, 719–730.

Plas, D. T., Lopez, J. E. and Crair, M. C. (2005). Pretarget sorting of retinocollicular axons in the mouse. *J. Comp. Neurol.* **491**, 305–319.

Plump, A. S., Erskine, L., Sabatier, C., Brose, K., Epstein, C. J., Goodman, C. S., Mason, C. A. and Tessier-Lavigne, M. (2002). Slit1 and Slit2 cooperate to prevent premature midline crossing of retinal axons in the mouse visual system. *Neuron* **33**, 219–32.

Polyak, S. (1957). The Vertebrate Visual System. *Univ. chicago Press* **277**,.

Porter, F. D., Drago, J., Xu, Y., Cheema, S. S., Wassif, C., Huang, S. P., Lee, E., Grinberg, A., Massalas, J. S., Bodine, D., et al. (1997). Lhx2, a LIM homeobox gene, is required for eye, forebrain, and definitive erythrocyte development. *Development* **124**, 2935–2944.

Prada, C., Puelles, L. and Génis-Gálvez, J. M. (1981). A golgi study on the early sequence of differentiation of ganglion cells in the chick embryo retina. *Anat. Embryol. (Berl).* **161**, 305–17.

Prakash, S., Caldwell, J. C., Eberl, D. F. and Clandinin, T. R. (2005). Drosophila N-cadherin mediates an attractive interaction between photoreceptor axons and their targets. *Nat. Neurosci.* **8**, 443–450.

Pratt, T., Tian, N. M. M. L., Simpson, T. I., Mason, J. O. and Price, D. J. (2004). The winged helix transcription factor Foxg1 facilitates retinal ganglion cell axon crossing of the ventral midline in the mouse. *Development* **131**, 3773–3784.

Preising, M. N., Forster, H., Gonser, M. and Lorenz, B. (2011). Screening of TYR, OCA2, GPR143, and MC1R in patients with congenital nystagmus, macular hypoplasia, and fundus hypopigmentation indicating albinism. *Mol. Vis.* **17**, 939–948.

Puelles, L. and Rubenstein, J. L. R. (1993). Expression patterns of homeobox and other putative regulatory genes in the embryonic mouse forebrain suggest a neuromeric organization. *Trends Neurosci.* **16**, 472–479.

Quina, L. A., Pak, W., Lanier, J., Banwait, P., Gratwick, K., Liu, Y., Velasquez, T., O'Leary, D. D. M. M., Goulding, M. and Turner, E. E. (2005). Brn3a-expressing retinal ganglion cells project specifically to thalamocortical and collicular visual pathways. *J. Neurosci.* **25**, 11595–604.

Rachel, R. A., Dölen, G., Hayes, N. L., Lu, A., Erskine, L., Nowakowski, R. S., Mason, C. A., Dolen, G., Hayes, N. L., Lu, A., et al. (2002). Spatiotemporal features of early neuronogenesis differ in wild-type and albino mouse retina. *J. Neurosci.* **22**, 4249–4263.

Rajagopalan, S., Deitinghoff, L., Davis, D., Conrad, S., Skutella, T., Chédotal, A., Mueller, B. K. and Strittmatter, S. M. (2004). Neogenin mediates the action of repulsive guidance molecule. *Nat. Cell Biol.* **6**, 756–762.

Ramón y Cajal, S. (1892). La rétine des vertébrés. *Cellule* **1**, 119–257.

Ramón y Cajal, S. (1894). *Les nouvelles idées sur la structure du système nerveux chez l'homme et chez les vertébrés*. (ed. C. reinwald & Cie) Paris.

Ramón y Cajal, S. (1909). *Histologie du système nerveux de l'homme & des vertébrés*.

Rao, S., Lobov, I. B., Vallance, J. E., Tsujikawa, K., Shiojima, I., Akunuru, S., Walsh, K., Benjamin, L. E. and Lang, R. A. (2007). Obligatory participation of macrophages in an angiopoietin 2-mediated cell death switch. *Development* **134**, 4449–4458.

Rao, S., Chun, C., Fan, J., Kofron, J. M., Yang, M. B., Hegde, R. S., Ferrara, N., Copenhagen, D. R. and Lang, R. A. (2013). A direct and melanopsin-dependent fetal light response regulates mouse eye development. *Nature* **494**, 243–246.

Raper, H. S. (1927). The Tyrosinase-tyrosine Reaction. *Biochem. J.* **21**, 89–96.

Rebsam, A., Petros, T. J. and Mason, C. A. (2009). Switching retinogeniculate axon laterality leads to normal targeting but abnormal eye-specific segregation that is activity dependent. *J. Neurosci.* **29**, 14855–63.

Renier, N., Wu, Z., Simon, D. J., Yang, J., Ariel, P. and Tessier-Lavigne, M. (2014). iDISCO: A Simple, Rapid Method to Immunolabel Large Tissue Samples for Volume Imaging. *Cell* **159**, 896–910.

Repérant, J., Lemire, M., Miceli, D. and Peyrichoux, J. (1976). A radioautographic study of the visual system in fresh water teleosts following intraocular injection of tritiated fucose and proline. *Brain Res.* **118**, 123–131.

Repérant, J., Rio, J. P., Miceli, D., Amouzou, M. and Peyrichoux, J. (1981). The retinofugal pathways in the primitive African bony fish Polypterus senegalus (Cuvier, 1829). *Brain Res.* **217**, 225–43.

Repérant, J., Vesselkin, N. P., Ermakova, T. V, Rustamov, E. K., Rio, J. P., Palatnikov, G. K., Peyrichoux, J. and Kasimov, R. V (1982). The Retinofugal Pathways in a primitive actinopterygian, the chondrostean Acipenser güldenstädti. An experimental study using degeneration, radioautographic and HRP methods. *Brain Res.* **251**, 1–23.

Retaux, S. and Harris, W. A. (1996). Engrailed and retinotectal topography. *Trends Neurosci.* **19**, 542–546.

Rheaume, B. A., Jereen, A., Bolisetty, M., Sajid, M. S., Yang, Y., Renna, K., Sun, L.,

Robson, P. and Trakhtenberg, E. F. (2018). Single cell transcriptome profiling of retinal ganglion cells identifies cellular subtypes. *Nat. Commun.* **9**,.

Rice, D. S., Williams, R. W. and Goldowitz, D. (1995). Genetic control of retinal projections in inbred strains of albino mice. *J. Comp. Neurol.* **354**, 459–469.

Rill, M. H. (1995). Dialogues on perception, by bela julesz, MIT press, Cambridge, Massachusetts, 1995. 276 pp., $49.95. *Color Res. Appl.* **20**, 404–406.

Ringstedt, T., Braisted, J. E., Brose, K., Kidd, T., Goodman, C. S., Tessier-Lavigne, M. and O'Leary, D. D. (2000). Slit inhibition of retinal axon growth and its role in retinal axon pathfinding and innervation patterns in the diencephalon. *J. Neurosci.* **20**, 4983–91.

Robles, E., Laurell, E. and Baier, H. (2014). The Retinal Projectome Reveals Brain-Area-Specific Visual Representations Generated by Ganglion Cell Diversity. *Curr. Biol.* **24**, 2085–2096.

Roffler-Tarlov, S., Liu, J. H., Naumova, E. N., Bernal-Ayala, M. M. and Mason, C. A. (2013). L-Dopa and the Albino Riddle: Content of L-Dopa in the Developing Retina of Pigmented and Albino Mice. *PLoS One* **8**, e57184.

Rogers, S., Letourneau, P. ~, Palm, S. L., Mccarthy, J. and Furcht, -~andleo T (1983). *Neurite Extension by Peripheral and Central Nervous System Neurons in Response to Substratum-Bound Fibronectin and Laminin'*.

Rompani, S. B., Müllner, F. E., Wanner, A., Zhang, C., Roth, C. N., Yonehara, K. and Roska, B. (2017). Different Modes of Visual Integration in the Lateral Geniculate Nucleus Revealed by Single-Cell-Initiated Transsynaptic Tracing. *Neuron* **93**, 767-776.e6.

Roska, B. and Werblin, F. (2001). Vertical interactions across ten parallel, stacked representations in the mammalian retina. *Nature* **410**, 583–587.

Rossel, S. (1983). Binocular stereopsis in an insect. *Nature* **302**, 821–822.

Rothberg, J. M., Jacobs, J. R., Goodman, C. S. and Artavanis-Tsakonas, S. (1990). slit: an extracellular protein necessary for development of midline glia and commissural axon pathways contains both EGF and LRR domains. *Genes Dev.* **4**, 2169–2187.

Saint-Geniez, M. and D'Amore, P. A. (2004). Development and pathology of the hyaloid, choroidal and retinal vasculature. *Int. J. Dev. Biol.* **48**, 1045–1058.

Sakai, J. A. and Halloran, M. C. (2006). Semaphorin 3d guides laterality of retinal ganglion cell projections in zebrafish. *Development* **133**, 1035–44.

Saleeba, C., Dempsey, B., Le, S., Goodchild, A. and McMullan, S. (2019). A Student's Guide to Neural Circuit Tracing. *Front. Neurosci.* **13**, 897.

Salichon, N., Gaspar, P., Upton, A. L., Picaud, S., Hanoun, N. N., Hamon, M., De Maeyer, E., Murphy, D. L., Mössner, R., Lesch, K. P., et al. (2001). Excessive Activation of Serotonin (5-HT) 1B Receptors Disrupts the Formation of Sensory Maps in Monoamine Oxidase A and 5-HT Transporter Knock-Out Mice. *J. Neurosci.* **21**, 884–896.

Salvucci, O., Ohnuki, H., Maric, D., Hou, X., Li, X., Yoon, S. O., Segarra, M., Eberhart, C. G., Acker-Palmer, A. and Tosato, G. (2015). EphrinB2 controls vessel pruning through STAT1-JNK3 signalling. *Nat. Commun.* **6**, 6576.

Sanchez-Arrones, L., Nieto-Lopez, F., Sanchez-Camacho, C., Carreres, M. I., Herrera, E., Okada, A. and Bovolenta, P. (2013). Shh/Boc Signaling Is Required for Sustained Generation of Ipsilateral Projecting Ganglion Cells in the Mouse Retina. *J. Neurosci.* **33**, 8596–8607.

Sánchez-Camacho, C. and Bovolenta, P. (2008). Autonomous and non-autonomous Shh signalling mediate the

in vivo growth and guidance of mouse retinal ganglion cell axons. *Development* **135**, 3531–41.

Sanderson, K. J. (1975). Retinogeniculate projections in the rabbits of the albino allelomorphic series. *J. Comp. Neurol.* **159**, 15–27.

Sanes, J. R. and Masland, R. H. (2015). The Types of Retinal Ganglion Cells: Current Status and Implications for Neuronal Classification. *Annu. Rev. Neurosci.* **38**, 221–246.

Sanes, J. R. and Zipursky, S. L. (2020). Synaptic Specificity, Recognition Molecules, and Assembly of Neural Circuits. *Cell* **181**, 536–556.

Sato, S., Inoue, T., Terada, K., Matsuo, I., Aizawa, S., Tano, Y., Fujikado, T. and Furukawa, T. (2007). Dkk3-Cre BAC Transgenic Mouse Line : A Tool for Highly Efficient Gene Deletion in Retinal Progenitor Cells. *Genesis* **45**, 502–507.

Schmitt, E. A. and Dowling, J. E. (1996). Comparison of topographical patterns of ganglion and photoreceptor cell differentiation in the retina of the zebrafish, Danio rerio. *J. Comp. Neurol.* **371**, 222–234.

Schmitt, A. M., Shi, J., Wolf, A. M., Lu, C. C., King, L. A. and Zou, Y. (2006). Wnt-Ryk signalling mediates medial-lateral retinotectal topographic mapping. *Nature* **439**, 31–37.

Scholes, J. H. (1979). Nerve fibre topography in the retinal projection to the tectum. *Nature* **278**, 620–624.

Schwab, I. R. (2018). The evolution of eyes: major steps. The Keeler lecture 2017: centenary of Keeler Ltd. *Eye* **32**, 302–313.

Schwarz, M., Cecconi, F., Bernier, G., Andrejewski, N., Kammandel, B., Wagner, M. and Gruss, P. (2000). Spatial specification of mammalian eye territories by reciprocal transcriptional repression of Pax2 and Pax6. *Development* **127**, 4325–4334.

Seabrook, T. A., Burbridge, T. J., Crair, M. C. and Huberman, A. D. (2017). Architecture, Function, and Assembly of the Mouse Visual System. *Annu. Rev. Neurosci.* **40**, 499–538.

Seigneur, E. and Südhof, T. C. (2018). Genetic ablation of all cerebellins reveals synapse organizer functions in multiple regions throughout the brain. *J. Neurosci.* **38**, 4774–4790.

Selvam, S., Kumar, T. and Fruttiger, M. (2018). Retinal vasculature development in health and disease. *Prog. Retin. Eye Res.* **63**, 1–19.

Serafini, T., Kennedy, T. E., Galko, M. J., Mirzayan, C., Jessell, T. M., Tessler-Lavigne, M., Gaiko, M. J., Mirzayan, C., Jessell, T. M. and Tessier-Lavigne, M. (1994). The netrins define a family of axon outgrowth-promoting proteins homologous to C. elegans UNC-6. *Cell* **78**, 409–424.

Serafini, T., Colamarino, S. A., Leonardo, E. D., Wang, H., Beddington, R., Skarnes, W. C. and Tessier-Lavigne, M. (1996). Netrin-1 is required for commissural axon guidance in the developing vertebrate nervous system. *Cell* **87**, 1001–14.

Shao, Y., Yu, Y., Zou, J., Quyang, L., Hu, P.-H., Tu, P., Han, Y. and He, H. (2015). Effects of intravitreal injection of netrin-1 in retinal neovascularization of streptozotocin-induced diabetic rats. *Drug Des. Devel. Ther.* **9**, 6363.

Shatz, C. J. and Stryker, M. P. (1988). Prenatal tetrodotoxin infusion blocks segregation of retinogeniculate afferents. *Science (80-.).* **242**, 87–89.

Shekhar, K., Lapan, S. W., Whitney, I. E., Tran, N. M., Macosko, E. Z., Kowalczyk, M., Adiconis, X., Levin, J. Z., Nemesh, J., Goldman, M., et al. (2016). Comprehensive Classification of Retinal Bipolar Neurons by Single-Cell Transcriptomics. *Cell* **166**, 1308-

1323.e30.

Sheldon, M., Rice, D. S., D'Arcangelo, G., Yoneshima, H., Nakajima, K., Mikoshiba, K., Howell, B. W., Cooper, J. a, Goldowitz, D. and Curran, T. (1997). Scrambler and yotari disrupt the disabled gene and produce a reeler -like phenotype in mice. *Nature* **389**, 730–733.

Shigeoka, T., Jung, H., Jung, J., Turner-Bridger, B., Ohk, J., Lin, J. Q., Amieux, P. S. and Holt, C. E. (2016). Dynamic Axonal Translation in Developing and Mature Visual Circuits. *Cell* **166**, 181–192.

Shinmyo, Y., Asrafuzzaman Riyadh, M., Ahmed, G., Bin Naser, I., Hossain, M., Takebayashi, H., Kawasaki, H., Ohta, K. and Tanaka, H. (2015). Draxin from neocortical neurons controls the guidance of thalamocortical projections into the neocortex. *Nat. Commun.* **6**, 10232.

Silver, J. (1984). Studies on the factors that govern directionality of axonal growth in the embryonic optic nerve and at the chiasm of mice. *J. Comp. Neurol.* **223**, 238–251.

Silver, J. and Sapiro, J. (1981). Axonal guidance during development of the optic nerve: The role of pigmented epithelia and other extrinsic factors. *J. Comp. Neurol.* **202**, 521–538.

Silver, J. and Sidman, R. L. (1980). A mechanism for the guidance and topographic patterning of retinal ganglion cell axons. *J. Comp. Neurol.* **189**, 101–111.

Simon, D. K. and O'Leary, D. D. M. (1990). Limited topographic specificity in the targeting and branching of mammalian retinal axons. *Dev. Biol.* **137**, 125–134.

Simon, D. K. and O'Leary, D. D. M. (1991). Relationship of retinotopic ordering of axons in the optic pathway to the formation of visual maps in central targets. *J. Comp. Neurol.* **307**, 393–404.

Simon, D. K. D. K. and O'Leary, D. D. M. D. (1992). Development of topographic order in the mammalian retinocollicular projection. *J. Neurosci.* **12**, 1212–1232.

Simpson, J. I. (1984). The Accessory Optic System. *Annu. Rev. Neurosci.* **7**, 13–41.

Singman, E. L. and Scalia, F. (1991). Quantitative study of the tectally projecting retinal ganglion cells in the adult frog. II. Cell survival and functional recovery after optic nerve transection. *J. Comp. Neurol.* **307**, 351–369.

Sitko, A. A., Kuwajima, T. and Mason, C. A. (2018). Eye-specific segregation and differential fasciculation of developing retinal ganglion cell axons in the mouse visual pathway. *J. Comp. Neurol.* **526**, 1077–1096.

Skarnes, W. C., Moss, J. E., Hurtley, S. M. and Beddington, R. S. (1995). Capturing genes encoding membrane and secreted proteins important for mouse development. *Proc. Natl. Acad. Sci. U. S. A.* **92**, 6592–6.

Slavotinek, A. M., Chao, R., Vacik, T., Yahyavi, M., Abouzeid, H., Bardakjian, T., Schneider, A., Shaw, G., Sherr, E. H., Lemke, G., et al. (2012). VAX1 mutation associated with microphthalmia, corpus callosum agenesis, and orofacial clefting: The first description of a VAX1 phenotype in humans. *Hum. Mutat.* **33**, 364–368.

Snow, D. M., Watanabe, M., Letourneau, P. C. and Silver, J. (1991). A chondroitin sulfate proteoglycan may influence the direction of retinal ganglion cell outgrowth. *Development* **113**, 1473–1485.

Soares, C. A. and Mason, C. A. (2015). Transient ipsilateral retinal ganglion cell projections to the brain: Extent, targeting, and disappearance. *Dev. Neurobiol.* **75**, 1385–1401.

Soker, S., Takashima, S., Miao, H. Q., Neufeld, G. and Klagsbrun, M. (1998). Neuropilin-1 Is Expressed by Endothelial and Tumor

Cells as an Isoform-Specific Receptor for Vascular Endothelial Growth Factor. *Cell* **92**, 735–745.

Spalteholz, W. (1914). Über das Durchsichtigmachen von menschlichen und tierischen Präparaten und seine theoretischen Bedingungen, nebst Anhang: Über Knochenfärbung. *S. Hirzel, Leipzig*.

Sperry, R. W. (1943). Visuomotor coordination in the newt (triturus viridescens) after regeneration of the optic nerve. *J. Comp. Neurol.* **79**, 33–55.

Sperry, R. W. W. (1963). CHEMOAFFINITY IN THE ORDERLY GROWTH OF NERVE FIBER PATTERNS AND CONNECTIONS. *Proc. Natl. Acad. Sci.* **50**, 703–710.

Sprague, J. M. (1966). Interaction of cortex and superior colliculus in mediation of visually guided behavior in the cat. *Science (80-.).* **153**, 1544–1547.

Sretavan, D. (1990). Specific routing of retinal ganglion cell axons at the mammalian optic chiasm during embryonic development. *J. Neurosci.* **10**, 1995–2007.

Sretavan, D. W. and Reichardt, L. F. (1993). Time-lapse video analysis of retinal ganglion cell axon pathfinding at the mammalian optic chiasm: growth cone guidance using intrinsic chiasm cues. *Neuron* **10**, 761–777.

Sretavan, D. W., Shatz, C. J. and Stryker, M. P. (1988). Modification of retinal ganglion cell axon morphology by prenatal infusion of tetrodotoxin. *Nature* **336**, 468–471.

Sretavan, D. W., Feng, L., Puré, E. and Reichardt, L. F. (1994). Embryonic neurons of the developing optic chiasm express L1 and CD44, cell surface molecules with opposing effects on retinal axon growth. *Neuron* **12**, 957–975.

Sretavan, D., Pure, E., Siegel, M. and Reichardt, L. (1995). Disruption of retinal axon ingrowth by ablation of embryonic mouse optic chiasm neurons. *Science (80-.).* **269**, 98–101.

Srinivas, S., Watanabe, T., Lin, C. S., William, C. M., Tanabe, Y., Jessell, T. M. and Costantini, F. (2001). Cre reporter strains produced by targeted insertion of EYFP and ECFP into the ROSA26 locus. *BMC Dev Biol* **1**, 4.

Stafford, B. K., Sher, A., Litke, A. M. and Feldheim, D. A. (2009). Spatial-Temporal Patterns of Retinal Waves Underlying Activity-Dependent Refinement of Retinofugal Projections. *Neuron* **64**, 200–212.

Stahl, B., Miiller, B., Von Boxberg, Y., Cox, E. C. and Bonhoeffer, F. (1990). *Biochemical Characterization of a Putative Axonal Guidance Molecule of the Chick Visual System*.

Stein, E., Zou, Y., Poo, M. and Tessier-Lavigne, M. (2001). Binding of DCC by netrin-1 to mediate axon guidance independent of adenosine A2B receptor activation. *Science (80-.).* **291**, 1976–1982.

Stellwagen, D. and Shatz, C. J. (2002). An instructive role for retinal waves in the development of retinogeniculate connectivity. *Neuron* **33**, 357–367.

Stier, H. and Schlosshauer, B. (1995). Axonal guidance in the chicken retina. *Development* **121**, 1443–54.

Stoeckel, K., Schwab, M. and Thoenen, H. (1977). Role of gangliosides in the uptake and retrograde axonal transport of cholera and tetanus toxin as compared to nerve growth factor and wheat germ agglutinin. *Brain Res.* **132**, 273–285.

Stone, J., Campion, J. E. and Leicester, J. (1978). The nasotemporal division of retina in the Siamese cat. *J. Comp. Neurol.* **180**, 783–798.

Strittmatter, S. M., Fankhauser, C., Huang, P. L., Mashimo, H. and Fishman, M. C. (1995). Neuronal pathfinding is abnormal in mice lacking the neuronal growth cone

protein GAP-43. *Cell* **80**, 445–452.

Stuermer, C. A. O. and Bastmeyer, M. (2000). The retinal axon's pathfinding to the optic disk. *Prog. Neurobiol.* **62**, 197–214.

Su, J., Haner, C. V, Imbery, T. E., Brooks, J. M., Morhardt, D. R., Gorse, K., Guido, W. and Fox, M. A. (2011). Reelin is required for class-specific retinogeniculate targeting. *J. Neurosci.* **31**, 575–86.

Su, J., Klemm, M. A., Josephson, A. M. and Fox, M. A. (2013). Contributions of VLDLR and LRP8 in the establishment of retinogeniculate projections. *Neural Dev.* **8**, 11.

Sun, L. O. L. O., Jiang, Z., Rivlin-Etzion, M., Hand, R., Brady, C. M., Matsuoka, R. L., Yau, K.-W. K. W., Feller, M. B. and Kolodkin, A. L. (2013). On and Off Retinal Circuit Assembly by Divergent Molecular Mechanisms. *Science (80-.).* **342**, 1241974–1241974.

Sun, L. O., Brady, C. M., Cahill, H., Al-Khindi, T., Sakuta, H., Dhande, O. S., Noda, M., Huberman, A. D., Nathans, J. and Kolodkin, A. L. (2015). Functional Assembly of Accessory Optic System Circuitry Critical for Compensatory Eye Movements. *Neuron* **86**, 971–984.

Sweeney, N. T., Tierney, H. and Feldheim, D. A. (2014). Tbr2 Is Required to Generate a Neural Circuit Mediating the Pupillary Light Reflex. *J. Neurosci.* **34**, 5447–5453.

Syed, M. M., Lee, S., Zheng, J. and Zhou, Z. J. (2004). Stage-dependent dynamics and modulation of spontaneous waves in the developing rabbit retina. *J. Physiol.* **560**, 533–549.

Takeichi, M. (2007). The cadherin superfamily in neuronal connections and interactions. *Nat. Rev. Neurosci.* **8**, 11–20.

Tao, C. and Zhang, X. (2016). Retinal Proteoglycans Act as Cellular Receptors for Basement Membrane Assembly to Control Astrocyte Migration and Angiogenesis. *Cell Rep.* **17**, 1832–1844.

Tassew, N. G., Chestopolava, L., Beecroft, R., Matsunaga, E., Teng, H., Chedotal, A. and Monnier, P. P. (2008). Intraretinal RGMa is involved in retino-tectal mapping. *Mol. Cell. Neurosci.* **37**, 761–769.

Tcherkezian, J., Brittis, P. A., Thomas, F., Roux, P. P. and Flanagan, J. G. (2010). Transmembrane Receptor DCC Associates with Protein Synthesis Machinery and Regulates Translation. *Cell* **141**, 1–13.

Tessier-Lavigne, M. and Goodman, C. S. (1996). The molecular biology of axon guidance. *Science (80-.).* **274**, 1123–33.

Tessier-Lavigne, M., Placzek, M., Lumsden, A. G., Dodd, J. and Jessell, T. M. (1988). Chemotropic guidance of developing axons in the mammalian central nervous system. *Nature* **336**, 775–778.

Thanos, S. and Bonhoeffer, F. (1983). Investigations on the development and topographic order of retinotectal axons: Anterograde and retrograde staining of axons and perikarya with rhodamine in vivo. *J. Comp. Neurol.* **219**, 420–430.

Thanos, S. and Bonhoeffer, F. (1984). Development of the transient ipsilateral retinotectal projection in the chick embryo: A numerical flourescence-microscopic analysis. *J. Comp. Neurol.* **224**, 407–414.

Thanos, S. and Bonhoeffer, F. (1987). Axonal arborization in the developing chick retinotectal system. *J. Comp. Neurol.* **261**, 155–164.

Thompson, H., Camand, O., Barker, D. and Erskine, L. (2006). Slit proteins regulate distinct aspects of retinal ganglion cell axon guidance within dorsal and ventral retina. *J. Neurosci.* **26**, 8082–91.

Thompson, H., Andrews, W., Parnavelas, J. G. and Erskine, L. (2009). Robo2 is required for Slit-mediated intraretinal axon guidance. *Dev. Biol.* **335**, 418–426.

Tillo, M., Erskine, L., Cariboni, A., Fantin, A.,

Joyce, A., Denti, L. and Ruhrberg, C. (2015). VEGF189 binds NRP1 and is sufficient for VEGF/NRP1-dependent neuronal patterning in the developing brain. *Development* **142**, 314–319.

Tong, J., Killeen, M., Steven, R., Binns, K. L., Culotti, J. and Pawson, T. (2001). Netrin stimulates tyrosine phosphorylation of the UNC-5 family of netrin receptors and induces Shp2 binding to the RCM cytodomain. *J. Biol. Chem.* **276**, 40917–25.

Torres, M., Gómez-Pardo, E., Gruss, P., Zellbiologie, A. M., Chemie, M. B., Gomez-Pardo, E. and Gruss, P. (1996). Pax2 contributes to inner ear patterning and optic nerve trajectory. *Development* **122**, 3381–91.

Traiffort, E., Moya, K. L., Faure, H., Hässig, R. and Ruat, M. (2001). High expression and anterograde axonal transport of aminoterminal sonic hedgehog in the adult hamster brain. *Eur. J. Neurosci.* **14**, 839–850.

Tran, N. M., Shekhar, K., Whitney, I. E., Jacobi, A., Benhar, I., Hong, G., Yan, W., Adiconis, X., Arnold, M. E., Lee, J. M., et al. (2019). Single-Cell Profiles of Retinal Ganglion Cells Differing in Resilience to Injury Reveal Neuroprotective Genes. *Neuron* **104**, 1039-1055.e12.

Trejo, L. J. and Cicerone, C. M. (1984). *Cells in the Pretectal Olivary Nucleus are in the Pathway for the Direct Light Reflex of the Pupil in the Rat*.

Triplett, J. W. and Feldheim, D. a (2012). Eph and ephrin signaling in the formation of topographic maps. *Semin. Cell Dev. Biol.* **23**, 7–15.

Triplett, J. W., Wei, W., Gonzalez, C., Sweeney, N. T., Huberman, A. D., Feller, M. B. and Feldheim, D. A. (2014). Dendritic and axonal targeting patterns of a genetically-specified class of retinal ganglion cells that participate in image-forming circuits. *Neural Dev.* **9**, 2.

Trojanowski, J. Q., Gonatas, J. O. and Gonatas, N. K. (1981). *Conjugates of horseradish peroxidase (HRP) with cholera toxin and wheat germ agglutinin are superior to free HRP as orthogradely transported markers*.

Trousse, F., Martí, E., Gruss, P., Torres, M. and Bovolenta, P. (2001). Control of retinal ganglion cell axon growth: a new role for Sonic hedgehog. *Development* **128**, 3927–36.

Tucker, P., Laemle, L., Munson, A., Kanekar, S., Oliver, E. R., Brown, N., Schlecht, H., Vetter, M. and Glaser, T. (2001). The eyeless mouse mutation(ey1) removes an alternative start codon from the Rx/rax homeobox gene. *genesis* **31**, 43–53.

Turner, D. L., Snyder, E. Y. and Cepko, C. L. (1990). Lineage-independent determination of cell type in the embryonic mouse retina. *Neuron* **4**, 833–45.

Tuttle, R., Braisted, J. E., Richards, L. J. and O'Leary, D. D. (1998). Retinal axon guidance by region-specific cues in diencephalon. *Development* **125**, 791–801.

Tzavlaki, K. and Moustakas, A. (2020). TGF-β Signaling. *Biomolecules* **10**, 487.

Upton, A. L., Salichon, N., Lebrand, C., Ravary, A., Blakely, R., Seif, I. and Gaspar, P. (1999). Excess of serotonin (5-HT) alters the segregation of ispilateral and contralateral retinal projections in monoamine oxidase A knock-out mice: possible role of 5-HT uptake in retinal ganglion cells during development. *J. Neurosci.* **19**, 7007–24.

Varadarajan, S. G. and Huberman, A. D. (2018). Assembly and repair of eye-to-brain connections. *Curr. Opin. Neurobiol.* **53**, 198–209.

Varadarajan, S. G., Kong, J. H., Phan, K. D., Kao, T.-J., Panaitof, S. C., Cardin, J., Eltzschig, H., Kania, A., Novitch, B. G. and Butler, S. J. (2017). Netrin1 Produced by Neural Progenitors, Not

Floor Plate Cells, Is Required for Axon Guidance in the Spinal Cord. *Neuron* **94**, 790-799.e3.

Vesselkin, N. P., Ermakova, T. V, Repérant, J., Kosareva, A. A. and Kenigfest, N. B. (1980). The retinofugal and retinopetal systems inLampetra fluviatilis an experimental study using radioautographic and HRP methods. *Brain Res.* **195**, 453–460.

Vigouroux, R. J., Belle, M. and Chédotal, A. (2017). Neuroscience in the third dimension: shedding new light on the brain with tissue clearing. *Mol. Brain* **10**, 33.

Vigouroux, R. J., Cesar, Q., Chédotal, A. and Nguyen-Ba-Charvet, K. T. (2020). Revisiting the role of Dcc in visual system development with a novel eye clearing method. *Elife* **9**, e51275.

Voneida, T. J. and Mello, N. K. (1975). Interhemispheric Projections of the Optic Tectum in Pigeon. *Brain. Behav. Evol.* **11**, 91–108.

Voneida, T. J. and Sligar, C. M. (1976). A comparative neuroanatomic study of retinal projections in two fishes: Astyanax hubbsi (the blind cave fish), and Astyanax mexicanus. *J. Comp. Neurol.* **165**, 89–105.

Voronina, V. A., Kozhemyakina, E. A., O'Kernick, C. M., Kahn, N. D., Wenger, S. L., Linberg, J. V, Schneider, A. S. and Mathers, P. H. (2004). Mutations in the human RAX homeobox gene in a patient with anophthalmia and sclerocornea. *Hum. Mol. Genet.* **13**, 315–322.

Waller, A. (1850). *Experiments on the Section of the Glossopharyngeal and Hypoglossal Nerves of the Frog, and Observations of the Alterations Produced Thereby in the Structure of Their Primitive*.

Walls, G. L. (1942). *The vertebrate eye and its adaptive radiation*. Bloomfield. Bloomfield Hills, Mich., Cranbrook Institute of Science.

Walter, J., Kern-Veits, B., Huf, J., Stolze, B. and Bonhoeffer, F. (1987a). *Recognition of position-specific properties of tectai cell membranes by retinal axons in vitro*.

Walter, J., Henke-Fahle, S. and Bonhoeffer, F. (1987b). *Avoidance of posterior tectal membranes by temporal retinal axons*.

Wan, X. S. T., Trojanowski, J. Q., Gonatas, J. O. and Liu, C. N. (1982). Cytoarchitecture of the extranuclear and commissural dendrites of hypoglossal nucleus neurons as revealed by conjugates of horseradish peroxidase with cholera toxin. *Exp. Neurol.* **78**, 167–175.

Wang, L. C., Dani, J., Godement, P., Marcus, R. C. and Mason, C. a (1995). Crossed and uncrossed retinal axons respond differently to cells of the optic chiasm midline in vitro. *Neuron* **15**, 1349–64.

Wang, L. C., Rachel, R. a, Marcus, R. C. and Mason, C. a (1996). Chemosuppression of retinal axon growth by the mouse optic chiasm. *Neuron* **17**, 849–62.

Wang, R., Wei, Z., Jin, H., Wu, H., Yu, C., Wen, W., Chan, L.-N., Wen, Z. and Zhang, M. (2009). Autoinhibition of UNC5b revealed by the cytoplasmic domain structure of the receptor. *Mol. Cell* **33**, 692–703.

Wang, L., Sarnaik, R., Rangarajan, K., Liu, X. and Cang, J. (2010). Visual receptive field properties of neurons in the superficial superior colliculus of the mouse. *J. Neurosci.* **30**, 16573–16584.

Wang, Q., Marcucci, F., Cerullo, I. and Mason, C. (2016). Ipsilateral and Contralateral Retinal Ganglion Cells Express Distinct Genes during Decussation at the Optic Chiasm. *eNeuro* **3**, ENEURO.0169-16.2016.

Ward, R., Repérant, J., Hergueta, S., Miceli, D. and Lemire, M. (1995). Ipsilateral visual projections in non-eutherian species: random variation in the central nervous system? *Brain Res. Rev.* **20**, 155–170.

Wei, P., Pattarini, R., Rong, Y., Guo, H.,

Bansal, P. K., Kusnoor, S. V, Deutch, A. Y., Parris, J. and Morgan, J. I. (2012). The Cbln family of proteins interact with multiple signaling pathways. *J. Neurochem.* **121**, 717–729.

Weidner, C., Repérant, J., Miceli, D., Haby, M. and Rio, J. P. P. (1985). An anatomical study of ipsilateral retinal projections in the quail using radioautographic, horseradish peroxidase, fluorescence and degeneration techniques. *Brain Res.* **340**, 99–108.

Weiner, J. A., Koo, S. J., Nicolas, S., Fraboulet, S., Pfaff, S. L., Pourquié, O., Sanes, J. R., Pourquie, O. and Sanes, J. R. (2004). Axon fasciculation defects and retinal dysplasias in mice lacking the immunoglobulin superfamily adhesion molecule BEN/ALCAM/SC1. *Mol. Cell. Neurosci.* **27**, 59–69.

Weiss, P. and Hiscoe, H. B. (1948). Experiments on the mechanism of nerve growth. *J. Exp. Zool.* **107**, 315–395.

Wicht, H. and Northcutt, R. G. (1990). Retinofugal and retinopetal projections in the pacific hagfish, eptatretus stouti (myxinoidea). *Brain. Behav. Evol.* **36**, 315–328.

Williams, R. W. and Rakic, P. (1985). Dispersion of growing axons within the optic nerve of the embryonic monkey. *Proc. Natl. Acad. Sci.* **82**, 3906–3910.

Williams, R. W., Hogan, D. and Garraghty, P. E. (1994). Target recognition and visual maps in the thalamus of achiasmatic dogs. *Nature* **367**, 637–639.

Williams, S. E., Mann, F., Erskine, L., Sakurai, T., Wei, S., Rossi, D. J., Gale, N. W., Holt, C. E., Mason, C. A. and Henkemeyer, M. (2003). Ephrin-B2 and EphB1 Mediate Retinal Axon Divergence at the Optic Chiasm. *Neuron* **39**, 919–935.

Wilson, B. D. (2006). Netrins Promote Developmental and Therapeutic Angiogenesis. *Science (80-.).* **313**, 640–644.

Witkop, C. J., Nance, W. E., Rawls, R. F. and White, J. G. (1970). Autosomal recessive oculocutaneous albinism in man. Evidence for genetic heterogeneity. *Am. J. Hum. Genet.* **22**, 55–74.

Wizenmann, A., Thanos, S., Boxberg, Y. V. and Bonhoeffer, F. (1993). Differential reaction of crossing and non-crossing rat retinal axons on cell membrane preparations from the chiasm midline: An in vitro study. *Development* **117**, 725–735.

Wizenmann, A., Brunet, I., Lam, J., Sonnier, L., Beurdeley, M., Zarbalis, K., Weisenhorn-Vogt, D., Weinl, C., Dwivedy, A., Joliot, A., et al. (2009). Extracellular Engrailed participates in the topographic guidance of retinal axons in vivo Europe PMC Funders Group. *Neuron* **64**, 355–366.

Wong, R. O. L. (1999). RETINAL WAVES AND VISUAL SYSTEM DEVELOPMENT. *Annu. Rev. Neurosci.* **22**, 29–47.

Wong, R. O. L., Chernjavsky, A., Smith, S. J. and Shatz, C. J. (1995). Early functional neural networks in the developing retina. *Nature* **374**, 716–718.

Wright, S. (1925). The Factors of the Albino Series of Guinea-Pigs and Their Effects on Black and Yellow Pigmentation. *Genetics* **10**, 223–22360.

Wu, Z., Makihara, S., Yam, P. T., Teo, S., Renier, N., Balekoglu, N., Moreno-Bravo, J. A., Olsen, O., Chédotal, A., Charron, F., et al. (2019). Long-Range Guidance of Spinal Commissural Axons by Netrin1 and Sonic Hedgehog from Midline Floor Plate Cells. *Neuron* **101**, 635-647.e4.

Xu, K., Wu, Z., Renier, N., Antipenko, A., Tzvetkova-Robev, D., Xu, Y., Minchenko, M., Nardi-Dei, V., Rajashankar, K. R., Himanen, J., et al. (2014). Structures of netrin-1 bound to two receptors provide insight into its axon guidance mechanism. *Science (80-.).* **344**, 1275–1279.

Xu, S., Liu, Y., Li, X., Liu, Y., Meijers, R., Zhang, Y. and Wang, J. (2018). The binding of DCC-P3 motif and FAK-FAT domain mediates the initial step of netrin-1/DCC signaling for axon attraction. *Cell Discov.* **4**, 8.

Yaginuma, H. and Oppenheim, R. W. (1991). An experimental analysis of in vivo guidance cues used by axons of spinal interneurons in the chick embryo: evidence for chemotropism and related guidance mechanisms. *J. Neurosci.* **11**, 2598–2613.

Yamauchi, K., Yamazaki, M., Abe, M., Sakimura, K., Lickert, H., Kawasaki, T., Murakami, F. and Hirata, T. (2017). Netrin-1 Derived from the Ventricular Zone, but not the Floor Plate, Directs Hindbrain Commissural Axons to the Ventral Midline. *Sci. Rep.* **7**, 11992.

Yan, W., Laboulaye, M. A., Tran, N. M., Whitney, I. E., Benhar, I. and Sanes, J. R. (2020). MOLECULAR IDENTIFICATION OF SIXTY-THREE AMACRINE CELL TYPES COMPLETES A MOUSE RETINAL CELL ATLAS. *bioRxiv* 2020.03.10.985770.

Yates, P. A., Roskies, A. L., McLaughlin, T. and O'Leary, D. D. M. (2001). Topographic-specific axon branching controlled by ephrin-As is the critical event in retinotectal map development. *J. Neurosci.* **21**, 8548–63.

Yoda, H., Hirose, Y., Yasuoka, A., Sasado, T., Morinaga, C., Deguchi, T., Henrich, T., Iwanami, N., Watanabe, T., Osakada, M., et al. (2004). Mutations affecting retinotectal axonal pathfinding in Medaka, Oryzias latipes. *Mech. Dev.* **121**, 715–728.

Yonehara, K., Shintani, T., Suzuki, R., Sakuta, H., Takeuchi, Y., Nakamura-Yonehara, K. and Noda, M. (2008). Expression of SPIG1 Reveals Development of a Retinal Ganglion Cell Subtype Projecting to the Medial Terminal Nucleus in the Mouse. *PLoS One* **3**, e1533.

Yonehara, K., Ishikane, H., Sakuta, H., Shintani, T., Nakamura-Yonehara, K., Kamiji, N. L., Usui, S. and Noda, M. (2009). Identification of retinal ganglion cells and their projections involved in central transmission of information about upward and downward image motion. *PLoS One* **4**, e4320.

Young, M. J. and Lund, R. D. (1994). The anatomical substrates subserving the pupillary light reflex in rats: Origin of the consensual pupillary response. *Neuroscience* **62**, 481–496.

Young, T. R., Bourke, M., Zhou, X., Oohashi, T., Sawatari, A., Fassler, R. and Leamey, C. A. (2013). Ten-m2 Is Required for the Generation of Binocular Visual Circuits. *J. Neurosci.* **33**, 12490–12509.

Yuan, W., Zhou, L., Chen, J. H., Wu, J. Y., Rao, Y. and Ornitz, D. M. (1999). The mouse SLIT family: secreted ligands for ROBO expressed in patterns that suggest a role in morphogenesis and axon guidance. *Dev. Biol.* **212**, 290–306.

Yun, S., Saijoh, Y., Hirokawa, K. E., Kopinke, D., Murtaugh, L. C., Monuki, E. S. and Levine, E. M. (2009). Lhx2 links the intrinsic and extrinsic factors that control optic cup formation. *Development* **136**, 3895–3906.

Yung, A. R., Nishitani, A. M. and Goodrich, L. V. (2015). Phenotypic analysis of mice completely lacking netrin 1. *Development* **142**, 3686–3691.

Zelina, P., Avci, H. X., Thelen, K. and Pollerberg, G. E. (2005). The cell adhesion molecule NrCAM is crucial for growth cone behaviour and pathfinding of retinal ganglion cell axons. *Development* **132**, 3609–18.

Zhang, F., Lu, C., Severin, C. and Sretavan, D. W. (2000). GAP-43 mediates retinal axon interaction with lateral diencephalon cells during optic tract formation. *Development* **127**, 969–980.

Zhang, J., Jin, Z. and Bao, Z. Z. (2004). Disruption of gradient expression of Zic3 resulted in abnormal intra-retinal axon

projection. *Development* **131**, 1553–1562.

Zhou, Z. J. (2001). The function of the cholinergic system in the developing mammalian retina. *Prog. Brain Res.* **131**, 599–613.

Zhu, M., Madigan, M. C., Van Driel, D., Maslim, J., Billson, F. A., Provis, J. M. and Penfold, P. L. (2000). The Human Hyaloid System: Cell Death and Vascular Regression. *Exp. Eye Res.* **70**, 767–776.

Zigler, J. S., Valapala, M., Shang, P., Hose, S., Goldberg, M. F. and Sinha, D. (2016). βA3/A1-crystallin and persistent fetal vasculature (PFV) disease of the eye. *Biochim. Biophys. Acta - Gen. Subj.* **1860**, 287–298.

Zivraj, K. H., Tung, Y. C. L., Piper, M., Gumy, L., Fawcett, J. W., Yeo, G. S. H. and Holt, C. E. (2010). Subcellular profiling reveals distinct and developmentally regulated repertoire of growth cone mRNAs. *J. Neurosci.* **30**, 15464–15478.

Zolessi, F. R., Poggi, L., Wilkinson, C. J., Chien, C.-B. and Harris, W. A. (2006). Polarization and orientation of retinal ganglion cells in vivo. *Neural Dev.* **1**, 2.

Zuber, M. E. (2003). Specification of the vertebrate eye by a network of eye field transcription factors. *Development* **130**, 5155–5167.

Annexes

Article: Glycogen Synthase Kinase 3 regulates the determination of the rare displaced ganglion cell retinal subtype

Elena Braginskaja, **Robin J Vigouroux**, Catherine Hottin, Leah Thomas, Parth Shah, Alain Chédotal, Muriel Perron, Anand Swaroop and Jerome E Roger

Contribution: R. J. Vigouroux, designed and carried out the visual projection tracing experiments and analysis of whole brain rendering outlined in Figure 5. Moreover R. J. Vigouroux carried out the cryosections on RGC subtype analysis as well as the flat-mount immunostaining and qualifications that make up Figure 4D and E; Supplementary Figure 4; Supplementary Figure 6.

Glycogen Synthase Kinase 3 regulates the determination of the rare displaced ganglion cell retinal subtype

Elena Braginskaja[1,2], Robin J Vigouroux[4], Catherine Hottin[1,2], Leah Thomas[1,2], Parth Shah[3], Alain Chédotal[4], Muriel Perron[1,2,3]*, Anand Swaroop[3]* and Jerome E Roger[1,2,3]*

[1] Centre d'Etude et de Recherches Thérapeutiques en Ophthalmologie, Retina France, Orsay, France
[2] Université Paris-Saclay, CNRS, Institut des Neurosciences Paris-Saclay, 91405 Orsay, France
[3] Neurobiology-Neurodegeneration and Repair Laboratory, National Eye Institute, National Institutes of Health, Bethesda, MD, USA
[4] Sorbonne Universités, UPMC Université Paris 06, INSERM, CNRS, Institut de la Vision, 75012 Paris, France

Running Title: **GSK3 negatively regulates displaced ganglion cell genesis**

*Corresponding authors:

- Jerome E Roger. jerome.roger@ universite-paris-saclay.fr
- Anand Swaroop. swaroopa@nei.nih.gov
- Muriel Perron. muriel.perron@universite-paris-saclay.fr

ABSTRACT

Glycogen Synthase Kinase 3 (GSK) proteins (GSK3α and GSK3β) are key mediators of signaling pathways, with crucial roles in coordinating fundamental biological processes during neural development. Here we show that the complete loss of GSK3 signaling in mouse retinal progenitors leads to microphtalmia with broad morphological defects. Both proliferation of retinal progenitors and neuronal differentiation are impacted and associated with enhanced cell death. A single wild type allele of either *Gsk3α* or *Gsk3β* was able to rescue these phenotypes. In this genetic context, all retinal cell types were present and the retina was functional. However, we unexpectedly detected a large number of cells in the inner nuclear layer expressing retinal ganglion cell (RGC)-specific markers (displaced RGCs, dRGCs). Excess dRGCs observed when at least one allele of *Gsk3α* is expressed resulted in an increased number of RGC axonal projections into the ipsilateral medial terminal nucleus, an area of the brain poorly targeted by RGCs in wild type belonging to the non-image-forming visual circuit. Whole transcriptome analysis revealed deregulated genes and pathways which could correspond to dRGC molecular signature related to their differentiation and function. Our study thus uncovers an unsuspected role of GSK3 in controlling the genesis of dRGCs, a rare retinal cell type with unknown function, and provides a novel repertoire of genes potentially representing the molecular identity of dRGCs.

Key words: Retinal development, Glycogen Synthase Kinase 3, Posttranslational modifications, Displaced ganglion cells, Cell death, Proliferation

INTRODUCTION

Glycogen Synthase Kinase 3 alpha (GSK3α) and beta (GSK3β) are serine/threonine kinases encoded by two different genes, sharing 95 % of identity in their kinase domain and of well-known functional redundancy (Doble et al., 2007). Among the signaling pathways regulated by GSK3 kinases, Wnt canonical pathway is the most well described, with GSK3β inhibition triggering an increase of β-catenin protein levels and its nuclear translocation to activate target gene expression (Doble and Woodgett, 2003). GSK3 exists at the crossroads of multiple pathways and acts as a key molecular switch to mediate their output and guide distinct cellular processes (Cole, 2012; Doble and Woodgett, 2003; Espinosa et al., 2003; Jin et al., 2009; Shimizu et al., 2008; Wang and Li, 2006).

GSK3 is a key regulator of neural stem/precursor cell proliferation during development and in the adult brain (Eom and Jope, 2009; Hur and Zhou, 2010; Kim et al., 2009; Pachenari et al., 2017). Conditional deletion or gain of function experiments indicate that GSK3 inactivation promotes neural progenitor proliferation, whereas GSK3 activation promotes neuronal differentiation (Hur and Zhou, 2010; Kim et al., 2009). GSK3 exerts its effects through the phosphorylation of keys proteins involved in neural development, including proneural factors like Neurogenin 2 or NeuroD (Li et al., 2012; Moore et al., 2002). Besides, GSK3 also fine-tunes the balance between cell death and survival, and alteration of its function has been associated with neurodegenerative pathologies including Alzheimer's disease, bipolar disorders, and Parkinson's disease (Golpich et al., 2015; Jacobs et al., 2012; Kremer, 2011; Li et al., 2014; Maurer et al., 2014; Medina et al., 2011).

GSK3 kinases are also expressed widely in the developing retina (Pérezleón et al., 2013). GSK3-dependent phosphorylation was shown to control the timing of proneural factor activity and thereby regulate retinal cell fate determination. For

instance, inhibition of GSK3 signaling in the developing *Xenopus* retina causes enhanced early-born cell type at the expense of late-born cells (Marcus et al., 1998; Moore et al., 2002).

To investigate GSK3 function in mammalian retinal development, we generated conditional loss-of-function alleles of *Gsk3α* and *Gsk3β* in retinal progenitors (MacAulay et al., 2007; Marquardt et al., 2001; Patel et al., 2008). We showed that the complete loss of both GSK3 kinases severely impacts retinal morphology with microphthalmia phenotype, which could be completely rescued by just one *Gsk3α* or *Gsk3β* wild type allele. Interestingly, in the absence of *Gsk3β*, a large number of retinal ganglion cells (RGCs) were located in the inner nuclear layer. Anterograde labeling of the axonal ganglion cell projections into the brain and whole transcriptome analysis allowed further characterization of these displaced RGCs (dRGCs). Our study thus identifies GSK3 as a possible fate determinant of dRGCs and shades more light on the molecular signature of this poorly investigated cell subtype in the retina.

RESULTS

Retinal progenitor-specific deletion of *Gsk3α* and *Gsk3β* results in microphtalmia

To investigate the role of GSK3 during early retinal development, we crossed the floxed *Gsk3α*$^{f/f}$*β*$^{f/f}$ with the *α-Cre* mouse lines to generate *Gsk3α*$^{f/f}$*β*$^{f/f}$*;α-Cre* line in which *Gsk*3 deletion occurs only in retinal progenitors as early as E10.5 (Marquardt et al., 2001). We first validated our model by assessing the efficacy of *Gsk3α* and *Gsk3β* deletion as early as E12.5 (Fig. 1A). Immunohistochemistry (IHC) using an antibody recognizing both GSK3 proteins showed ubiquitous expression in control retinas (Fig. 1A). In the peripheral retina of *Gsk3α*$^{f/f}$*β*$^{f/f}$*;α-Cre* mice, both *Gsk3* genes were efficiently

deleted, but expression in the central retina remained preserved consistently with the α-Cre expression pattern previously described (Marquardt et al., 2001).

H&E staining revealed major morphological defects with profound retinal disorganization in *Gsk3α*$^{f/f}$*β*$^{f/f}$*;α-Cre* retina as early as E12.5 such as the loss of radial arrangement as well as folds and aggregates of RPCs (Fig. 1B). In addition, blood was detected inside the retinal neuroblastic layer. The structure of the retina worsened rapidly during development although the central part was unperturbed, consistent with the maintenance of *Gsk3* expression in this region. After E14.5, the retina was largely reduced whereas the eye size itself was comparable to littermate controls (Fig. 1B). A large quantity of blood was accumulated inside the eyeball at P2. Finally, after P2, the growth of the eyeball was severely reduced leading to microphtalmia in adult (data not shown).

Because of the severe phenotype in the adult, we focused our histological analyses to early retinal development. We first investigated the subcellular localization of β-catenin, an established GSK3 target mediating the activation of the canonical Wnt pathway (Doble and Woodgett, 2003). In control retinas, β-catenin expression was mostly cytoplasmic (Fig. 1C). Upon *Gsk3α* and *Gsk3β* deletion, β-catenin was still expressed in the cytoplasm but it was also translocated to the nucleus in some cells as early as E12.5. *Gsk3α*$^{f/f}$*β*$^{f/f}$*;α-Cre* retina at E14.5 revealed a clearly-defined boundary between the Cre-positive region (GSK3-negative cells) at the periphery with nuclear translocation and large accumulation of β-catenin in the nucleus and the Cre-negative region (GSK3-positive cells) in the center (Fig. 1C). Such an expression pattern supports the expected strong activation of canonical Wnt pathway in the absence of both *Gsk3α* and *Gsk3β*. Altogether, our findings demonstrate that GSK3 in RPCs regulates Wnt signaling and is essential for proper retinal development.

Lack of *Gsk3α* and *Gsk3β* in RPCs leads to cell cycle aberrations and retinal progenitor gene deregulation

We next sought to investigate cellular defects in the retina of *Gsk3α$^{f/f}$β$^{f/f}$;α-Cre* mice. We focused our analysis on early developmental stages (E12.5 and E14.5) to better elucidate the cause of the microphtalmia phenotype and investigated whether proliferation was altered in *Gsk3α$^{f/f}$β$^{f/f}$;α-Cre* mouse retina. A single dose of EdU (to label RPCs in the S-phase) was injected 16 hours before harvesting embryos at E12.5 and E14.5. The number of EdU-positive cells increased significantly from E12.5 to E14.5 in control retinas (Fig. 2A, B). In contrast, this number remained unchanged between the two stages in *Gsk3α$^{f/f}$β$^{f/f}$;α-Cre* retinas, with a reduced number of RPCs in S-phase at E14.5 compared to controls, suggesting proliferation defects. We further examined cell proliferation by labeling late-G2/M-phase retinal progenitors using phospho-histone 3 (pH3) antibody. In control retinas, strongly labeled pH3-positive cells were positioned in the apical surface of the retina where mitosis occurs (M-phase cells). Cells with less intense labeling, presumably late-G2 cells, were present in the outer part of the retinal neuroblastic layer. At both stages, pH3-positive cells located at the periphery of *Gsk3α$^{f/f}$β$^{f/f}$;α-Cre* retina were positioned distant from the apical side (located at the opposite side of the lens) (Fig. 2A). Moreover, their number at the periphery was abnormal compared to control retinas, being increased at E12.5 and decreased at E14.5 (Fig. 2B). The number of double pH3- and EdU-positive cells were increased in *Gsk3α$^{f/f}$β$^{f/f}$;α-Cre* retinas compared to controls, at both stages (Fig. 2B). To investigate the effects of such aberrant cell cycle kinetics on the pool of RPC in the absence of GSK3, we used an anti-HES1 antibody (Nadal-Nicolás et al., 2014). At E12.5 and E14.5, HES1 labeled all RPCs throughout control retinas with the exception of the basal side where differentiating ganglion cells are located. In *Gsk3α$^{f/f}$β$^{f/f}$;α-Cre*

retinas, HES1 expression was similar to controls at E12.5 indicating the maintenance of RPC pools (S.D. 1A). However, by E14.5, HES1 positive cells were sparser at the periphery where *Gsk3* expression was absent (S.D. 1B) correlating with less EdU- and pH3-positive cells than observed previously at the same stage (Fig. 2B). In the same area lacking *Gsk3* expression, other progenitor markers, such as Pax6 and Sox2, were similarly decreased in *Gsk3α$^{f/f}$β$^{f/f}$;α-Cre* retina compared to controls (data not shown). Thus, our results show that GSK3 kinases are required for cell cycle progression and maintenance of the pool of RPCs.

Loss of *Gsk3α* and *Gsk3β* impairs retinal progenitor differentiation and leads to cell death

To examine whether neuronal differentiation is impacted by the absence of GSK3, we performed IHC using two neuronal markers, Doublecortin (Dcx) and Brn3a, to label neuronal precursor cells and RGCs, respectively (Fig. 3). At E12.5 and E14.5, Dcx- and Brn3a-positive cells were localized in the inner part of the neuroblastic layer of the control retina where retinal differentiation occurs first. In contrast, neuronal differentiation was completely abolished at both stages in *Gsk3α$^{f/f}$β$^{f/f}$;α-Cre* retina (Dcx- and Brn3a-negative cells), except in the most central part corresponding to the non-expressing Cre area. Lack of neuronal differentiation in the absence of both *Gsk3* genes was confirmed at later stages using Calbindin, an amacrine cell marker (data not shown). The absence of retinal differentiation at early stages together with the decreased expression of proliferation markers, prompted us to investigate whether the loss of *Gsk3* in RPCs could trigger cell death. We indeed detected a significant increase in the number of TUNEL-positive cells in *Gsk3α$^{f/f}$β$^{f/f}$;α-Cre* retina at both embryonic stages (S.D.2). Thus, microphtalmia observed in the absence of both *Gsk3α and Gsk3β* is likely due to a succession of catastrophic events ranging from impaired

proliferation and differentiation of RPCs to increased cell death.

The expression of only one allele of either *Gsk3α* or *Gsk3β* does not prevent the development of a functional retina

The severe deleterious effect of the lack of both *Gsk3α and Gsk3β* in RPCs during early development precludes the analysis of late retinal histogenesis. To circumvent this, we generated animals with different degrees of *Gsk3* deletion (loss of only one *Gsk3* gene: *Gsk3α$^{f/f}$β$^{+/+}$;α-Cre* or *Gsk3α$^{+/+}$β$^{f/f}$;α-Cre* or ¾ deletion: *Gsk3α$^{f/f}$β$^{f/+}$;α-Cre* or *Gsk3α$^{f/+}$β$^{f/f}$;α-Cre*). Immunoblot analysis using anti-GSK3 antibody (recognizing both proteins) in 2-month-old animals with different combination of *Gsk3α* and *Gsk3β* floxed alleles (*Gsk3α$^{f/f}$β$^{+/+}$, Gsk3α$^{+/+}$β$^{f/f}$*, *Gsk3α$^{f/+}$β$^{f/f}$* or *Gsk3α$^{f/f}$β$^{f/+}$*) demonstrated the efficacy of *Gsk3α* and *Gsk3β* deletion (S.D. 3A). In addition, IHC analysis using anti-GSK3β showed ubiquitous expression of *Gsk3β* in adult control retinas and its complete loss in *Gsk3α$^{f/+}$β$^{f/f}$;α-Cre* retinas (S.D. 3B). Histological analysis in 2-month old animals revealed the formation of a normal retina in the presence of only one allele of *Gsk3α* or *Gsk3β* with normal photoreceptors and interneurons (S.D 3C,D). Photopic (S.D. 3E) and scotopic (S.D. 3F) electroretinogram (ERG) recordings did not show any difference between *Gsk3α$^{f/+}$β$^{f/f}$;α-Cre* and control retinas. These results were similar in mice carrying the other combination of *Gsk3* deletion (data not shown). Altogether these results demonstrate that a single wild type allele of *Gsk3α* or *Gsk3β* is sufficient to compensate the effects observed by the absence of the 4 alleles, at both cellular and functional levels. Therefore, they clearly highlight the functional redundancy of these two kinases in the retina.

Loss of either *Gsk3α* or *Gsk3β* in RPCs leads to an increased number of displaced retinal ganglion cells

Although the expression of a single allele of either *Gsk3α* or *Gsk3β* allows RPCs to

produce a functional retina with nuclear cell layers correctly organized (S.D. 3), we observed a striking increase in the number of Brn3a-positive cells (RGCs) located in the INL of *Gsk3α$^{f/+}$β$^{f/f}$;α-Cre* retina compared to the controls (Fig. 4A). Brn3a-positive cells in the INL are described as displaced retinal ganglion cells (dRGCs), a rare cell type in the mammalian retina (Galli-Resta and Ensini, 1996; Young, 1984). All Brn3a-positive cells in the INL of *Gsk3α$^{f/+}$β$^{f/f}$;α-Cre* retina also expressed NF68 that labels cell bodies and axons of RGCs (Fig. 4A). The increased number of such dRGCs was observed in retinas with different combinations of *Gsk3* deletions (*Gsk3α$^{f/f}$β$^{+/+}$*, *Gsk3α$^{+/+}$β$^{f/f}$*, *Gsk3α$^{f/+}$β$^{f/f}$* or *Gsk3α$^{f/f}$β$^{f/+}$*), with the highest number observed in *Gsk3α$^{f/+}$β$^{f/f}$;α-Cre* mice compared to controls (10-fold increase) (Fig. 4B). Interestingly, the increase in dRGCs number is not associated with a decreased number of RGCs located in the GCL, referred to as orthotopic RGCs (oRGCs) (Fig. 4B). To validate that these Brn3a-positive cells in the INL were indeed RGCs with axonal projection encompassed in the optic nerve, we performed retrograde labeling with Rhodamine-Dextran applied onto the optic nerve of *Gsk3α$^{f/+}$β$^{f/f}$;α-Cre* mice. Subsequent 3D reconstructions on flat mount retinas revealed the presence of numerous fluorescent cell bodies located in the INL compared to controls demonstrating that axons of dRGCs indeed reached the optic nerve (Fig. 4C). This result confirms the RGC identity of the Brn3a-positive cells located in the INL of *Gsk3α$^{f/+}$β$^{f/f}$;α-Cre* retinas.

Due to their low number in WT retinas (around 2%), dRGCs have been poorly characterized with very few markers identified, such as Brn3a (Nadal-Nicolás et al., 2012; Nadal-Nicolás et al., 2014). In this context, further immunostaining with additional RGC markers revealed that dRGCs in *Gsk3α$^{f/+}$β$^{f/f}$;α-Cre* retina were also positive for Rbpms (Rodriguez et al., 2014), (Fig.4D) (Rodriguez et al., 2014) and counting on flat mount retinas clearly confirmed their increased number in the INL compared to controls (Fig. 4E). A similar result was observed with Islet1 labeling (S.D.

4)(Bejarano-Escobar et al., 2015). Finally, Brn3a-positive dRGCs did not express markers of other INL neurons such as Choline-Acetyltransferase (CHAT, amacrine cells), Calretinin (amacrine cells), or Calbindin (horizontal cells) confirming the RGC identity (data not shown).

To test whether the dRGCs in *Gsk3* mutant mice were produced during the same developmental window than oRGCs, we performed EdU pulse chase experiments. EdU was injected at E12.5, at the peak of RGC birth, and retinal sections from one-month-old animals were immunolabelled using anti-Brn3a antibody (Fig. 5A). In control and *Gsk3α$^{f/+}$β$^{f/f}$;α-Cre* retina, we identified 40-50% of RGCs that were Brn3a/EdU-positive in all layers examined (GCL and INL), indicating that both dRGCs and oRGCs were born at similar timing (Fig. 5B). We next examined whether dRGCs are usually overproduced during normal retinal development and eliminated later on. In this context, increased number of dRGCs in *Gsk3α$^{f/+}$β$^{f/f}$;α-Cre* retinas could result from a defect in dRGC riddance occurring usually during the first two postnatal weeks, a period of developmental cell death in the retina (Cook and Podugolnikova, 2001). At P0, the number of Brn3a-positive oRGCs was similar between littermate control and *Gsk3α$^{f/+}$β$^{f/f}$;α-Cre* retinas (Fig. 5C and D). In contrast, the proportion of Brn3a-positive cells located in the inner part of the neuroblastic layer corresponding presumably to dRGCs was much lower in control retinas (6±0.1%) compared to *Gsk3α$^{f/+}$β$^{f/f}$;α-Cre* retinas (30±1.4%). On one hand such results confirms our previous data (Fig. 5A,B) about dRGCs being overproduced in mutant retina early during development and on the other hand demonstrates that during normal retinal development dRGCs are not overproduced and eliminated postnatally. Altogether, our results demonstrates that dRGCs are produced during early waves of retinogenesis in *Gsk3α$^{f/+}$β$^{f/f}$;α-Cre* retinas and strongly suggest that GSK3 play a role in restricting the number of dRGCs produced in the retina during normal development.

dRGCs play a critical role in accessory visual system circuitry

Previous studies in birds and reptiles have reported that dRGCs could be responsible for optokinetic nystagmus, as they mostly project to the accessory optic nuclei (AOS) (Cook and Podugolnikova, 2001). To test whether the increased dRGCs in *Gsk3* mutants project into specific visual nuclei in the brain, we traced the total pool of RGCs, including dRGCs, with the Cholera Toxin beta subunit (CTB). Bi-lateral injection of CTB coupled to either an alexa-555 or -647 followed by 3D imaging, allowed us to trace both ipsi- and contra-lateral projecting axons. We first confirmed that CTB injections indeed marked the dRGCs based on flat mounts retinas after Brn3a immunolabelling (data not shown). To visualize the entire visual projection network, we carried whole-brain clearing using iDISCO+ followed by light-sheet fluorescent imaging and 3D reconstruction (Fig 6A). Interestingly, mutants lacking completely *GSk3β* displayed a specific increase in ipsilateral projecting RGCs specifically in the AOS, the Medial Terminal Nucleus (MTN). Calculation of the signal intensity ratio between the ipsilateral and contralateral MTN demonstrated a significant increase of RGC projections into the ipsilateral MTN in retinas with *Gsk3β* deletion (Fig. 6B).

Whole transcriptome analysis to reveal potential molecular signature of dRGCs.

We next performed whole transcriptome sequencing in adult retina in order to better characterize the molecular changes occurring in *Gsk3α*$^{f/+}$*β*$^{f/f}$;*α-Cre* retina and used *Gsk3α*$^{f/+}$*β*$^{f/f}$ as controls. Gene level analysis revealed 111 differentially expressed genes (DEGs) using the filtering criteria Fold Change (FC) 1.5 with a False Discovery rate (FDR) cutoff of $\leq$ 0.05 and a minimum mean expression value of one FPKM (fragments per kilobase of exon per million reads mapped) in at least one of the two experimental group. Clustering of these genes by their z-score highlighted 56 DEGs upregulated whereas 55 were downregulated (Fig. 7A). Volcano plot representation

highlighted among the most upregulated and significant DEGs, *Col4a3* a gene coding for collagen Type IV, alpha 3 protein. Mutations in this gene are associated with the autosomal recessive form of Alport Syndrome characterized by a severe form of maculopathy leading to vision loss (Fig. 7B) (Savige et al., 2015). Along this line, *Prss56* code for a serine protease expressed in Müller cells and with known mutations associated with microphtalmia due to its role during eye development (Gal et al., 2011; Paylakhi et al., 2018). In addition, three highly upregulated genes are poorly described (*Gm10857, Gje1* and *6430562015Rik*). *Nefh* increased expression is in line with increased expression of NF68 (*Nefl*) observed by IHC in *Gsk3α$^{f/+}$β$^{f/f}$;α-Cre* retina (Fig. 4A) and several genes appeared to be related to synapses and neurotransmission such as *Cplx1* coding for Complexin 1, a protein involved in synaptic vesicle exocytosis (Brose, 2008) or *Chrna5 and Chrna2*, coding for cholinergic receptor, nicotinic, alpha polypeptides. To go further on the identification of the potential molecular signature of the dRGCs and gain insight into their potential function, we performed pathway analysis using the 111 identified DEGs. Thus, multiple pathways were significantly overrepresented such as cholinergic synaptic transmission, adult behavior, catecholamine biosynthetic process, regulation of kinase activity and eye development among the biological processes (S.D. 5A). For molecular function, two interesting pathways were overrepresentated such as extracellular matrix structural constituent and postsynaptic nicotinic acetylcholine receptors. Circular visualization of genes in the eight selected biological processes and the two molecular functions indicated that overall gene expression was increased within these pathway as indicated by the z-score (S.D. 5B) at the exception of extracellular matrix structural constituent. The selected biological processes and molecular function related pathways were represented by 48 DEGs among the 111 originally identified. Several of these genes belonged to multiple pathways as shown by Chord plot representation (Fig 7C). Among

these 48 DEGs, 69% were expressed in RGCs based on published whole transcriptome data from purified RGCs (Sajgo et al., 2017). (Kim et al., 2016)(Corbo et al., 2010; Hao et al., 2012)(Sajgo et al., 2017)(Sajgo et al., 2017)It includes nuclear factors with upregulated expression in *Gsk3α$^{f/+}$β$^{f/f}$;α-Cre* retina (*MafA*, *Nr4a2*) and two downregulated (*Zic1*, *Mdfic*). (Ochi et al., 2004)(Templeton et al., 2013)(Han et al., 2007; Rocques et al., 2007)(Rheaume et al., 2018)Among other potential relevant deregulated genes, we identified *Grik3,* which encodes a protein of the kainate family of glutamate receptors functioning as ligand-activated ion channels, as well as *Chrna2*, *Chrna5, Chrna7,* and *Chrnb4* encoding for postsynaptic subunits of the nicotinic cholinergic receptor. At the exception of *Chrna2*, they were all upregulated in *Gsk3α$^{f/+}$β$^{f/f}$;α-Cre* retina. Interestingly, Acetylcholine (ACh) is released by the cholinergic/GABAergic starburst amacrine cells and most ganglion cells express nicotinic receptors (Baldridge, 1996; Lee et al., 2010). In direction-selective ganglion cells (DSGCs), glutamate is proposed to be the main source of excitation (Park et al., 2014; Sethuramanujam et al., 2018). Along this line, we identified *Cartpt* significantly upregulated in *Gsk3α$^{f/+}$β$^{f/f}$;α-Cre* retina. This gene encoding for the preprotein CART is expressed in ON-OFF direction-selective RGCs (DS-RGCs) (Kay et al., 2011). We confirmed by qRT-PCR the upregulation of *Chrna5, and Cartpt* as well as the downregulation of *Chrnab4* (Fig. 7D). Our transcriptomic data prompted us to hypothesize that dRGCs in *Gsk3α$^{f/+}$β$^{f/f}$;α-Cre* retina might be direction-selective ganglion cells. Such hypothesis is also supported also by the high amount of projections to the ipsilateral MTN, one of the nuclei forming the AOS and therefore belonging to the non-image-forming visual circuit. To test this hypothesis, we performed IHC with anti-CART antibody but unfortunately only the IPL of the retina was labelled making impossible to visualize a specific increased expression in dRGCs (data not shown). Anti-Chrna2 antibody labeled only the axons in the GCL whereas anti-

Chrna5 did not work making impossible to assess the expression of this markers in dRGCs. However, we could find a limited number of dRGCs in *Gsk3α$^{f/+}$β$^{f/f}$;α-Cre* and littermate control retinas positive for the transcription factor Tbr2, described as essential for RGC specification participating in non-image-forming visual circuits (arrows in S.D. 6). A small subset of dRGCs also expressed Foxp2, a transcription factor involved in direction-selective RGC differentiation in mice (Rousso et al., 2016; Sato et al., 2017). These two factors were expressed in a mutually exclusive way in Rpbms-positive dRGCs suggesting that dRGCs in *Gsk3α$^{f/+}$β$^{f/f}$;α-Cre* might encompass several subtypes. These results with our transcriptomic data strongly suggests that at least a proportion of dRGCs in mice expressing only one allele of *Gsk3α* might be direction-selective ganglion cells.

DISCUSSION

Our study reports the function *of Gsk3α* and *Gsk3β* during early retinal development. Complete loss of GSK3 activity in retinal progenitors results in severe morphological defects with progressive death of the pool of proliferative retinal progenitors and lack of neuronal differentiation, leading to microphtalmic eyes in adult mice. Such phenotype was completely rescued by the expression of only one *Gsk3α* or *Gsk3β* allele confirming the functional redundancy of these two kinases (Kim et al., 2009). However, further analysis of mouse retinas with only one allele of *Gsk3* revealed the presence of an excessive number of dRGCs, a specific RGC subtype located in the INL with a concomitant large increase of the axonal projection to the ipsilateral MTN. Our data thus identified GSK3 as the first dRGCs determinant during retinal histogenesis and suggests that dRGCs could be direction-sensitive ganglion cells.

The lack of neuronal differentiation that we observed in the retina in double *Gsk3* knockout mice, was similar to the phenotype described in the developing brain of *Gsk3*

mutant mice (Kim et al., 2009). Therefore, in the whole central nervous system, GSK3 signaling appears essential for progenitors to differentiate into neurons. Surprisingly however, we demonstrate that the absence of GSK3 impairs the maintenance of the pool of retinal progenitors, their differentiation and their survival leading subsequently to microphtalmia in adults. Our results are in striking contrast with the "big head phenotype" due to a large expansion of the pool of neural progenitors by hyperproliferation and the absence of cell death at early stages observed in *Gsk3α*$^{-/-}$;*Gsk3β*$^{f/f}$; nestin-cre embryos (Doble and Woodgett, 2003). Thus, we suggest that the retinal progenitors are more prompt to cell death when GSK3 activity is missing compared to the neural progenitors in the brain. GSK3 kinases are established regulators of the Wnt canonical pathway and inhibit Wnt ligand binding to Frizzled receptors, leading to stabilization and nuclear translocation of *β*-catenin (Liu and Nathans, 2008; Liu et al., 2012). Alteration of Wnt signaling during early retinal development due to the absence of Frizzled 5 receptors (*Fz5*) and/or Frizzled 8 (*Fz8*) leads to microphtalmia and incomplete closure of the optic fissure causing coloboma (Liu et al., 2016). In humans, an autosomal dominant mutation in *FZD5* that antagonizes both canonical (involving GSK3 regulation) and non-canonical pathways leads to coloboma (Fu et al., 2006; Ouchi et al., 2011). Interestingly, in the absence of Wnt signaling, β-catenin remains cytoplasmic unlike in our model where lack of GSK3 largely increases its amount and its nuclear translocation. Based on these results, it is likely that the severe phenotype of *Gsk3* knockout mice results from more than just Wnt/*β*-catenin pathway activation. In contrast, the effect of *Gsk3* loss of function in the retina mimics the effect of *β*-catenin gain of function. Indeed, constitutive retinal activation of *β*-catenin does not elicit an hyperproliferation of retinal cells. Instead, it decreases cell proliferation and leads to a loss of neural differentiation, resulting in a small eye phenotype (Fu et al., 2006). Besides, *β*-catenin has been recognized as a

key regulator of cell adhesion (Ouchi et al., 2011). The lamination defects observed in *Gsk3* knockout mice may thus also result from altered cell adhesion due to *β*-catenin activation. However, unlike *Gsk3* knockout, *β*-catenin gain of function does not lead to increased retinal cell death (Goold et al., 1999; Ka et al., 2014; Sang et al., 2001; Xu et al., 2009; Zumbrunn et al., 2001).

In pigmented wild-type mice, dRGCs in the INL are a very rare and poorly-described type of cells representing only 2 % of RGCs (Balkema and Dräger, 1990; Doi et al., 1994; Dräger and Olsen, 1980; Nadal-Nicolás et al., 2014). The observation that when a single copy of *Gsk3α* is present in retinal progenitors leads to a 15% increase in dRGCs is a remarkable phenotype. To our knowledge, such high increased number of dRGCs has never been reported in a transgenic animal (Buhl and Dann, 1988; Doi et al., 1994). A previous study hypothesized that dRGCs are misplaced in the INL due to an ontogenic aberration rather than representing an independent class of RGCs (Fu et al., 2006). Indeed, differential cell adhesion plays a key role in sorting and migration of retinal cells in their appropriate layers, especially of RGCs (Fu et al., 2006). One can therefore hypothesize that enhanced dRGCs in mice lacking at least *Gsk3β* are the consequence of increased aberration events. Although our RNA-Seq data led to the identification of upregulated genes coding for collagen subunits (*Col18a1*, *Col4a3*, *Col9a1*, *Col9a2*) and extracellular matrix proteins in *Gsk3α*$^{f/+}$*β*$^{f/f}$;*α-Cre* retina, a conundrum in our study is that the oRGC number in GCL is unaltered in mutant mice strongly suggesting that dRGCs represent a specific subset of RGCs which might be regulated by GSK3.

Topographic and quantitative analysis of RGCs in albinos and pigmented rats support this hypothesis that Brn3-positive dRGCs are not misplaced by ontogenic mistakes but indeed represent a subset of RGCs (Li et al., 2012; Moore et al., 2002). Along this line, GSK3β is involved in neural cell fate decision by controlling the timing

of the activity of bHLH transcription factors, such as NeuroD or Neurog2 (Linden and Perry, 1983; Nadal-Nicolás et al., 2014; Salinas-Navarro et al., 2009c, 2009a, 2009b). If dRGCs are not produced following ontogenic aberrations but are instead determined by a proper genetic program, it would be interesting to identify the transcription factors involved and seek for any regulation by GSK3 kinases. Our RNA-Seq data identified *MafA* as an upregulated transcription factor in *Gsk3α$^{f/+}$β$^{f/f}$;α-Cre*. Its expression and function in RGCs is poorly described although previous studies showed that Maf family member are expressed in RGCs and control specific gene regulatory network (Ochi et al., 2004; Templeton et al., 2013). Interestingly, it is well described that GSK3-dependent phosphorylation of MAFA regulates its activity and stability through degradation by the proteasome (Han et al., 2007; Rocques et al., 2007). In this context, one can hypothesize that *MafA* could contribute to dRGC differentiation and their limited number in WT retina is due to GSK3-dependent degradation of MAFA during early development. Such tight control of transcription factor activity by posttranslational modifications has already been described as a crucial mechanism controlling ganglion cell differentiation (Moore et al., 2002), as well as other retinal cell types such as photoreceptors (Onishi et al., 2009, 2010; Roger et al., 2010).

In reptiles, amphibians and birds, only dRGCs project into the MTN, whereas in mammals RGC projecting into the MTN appear to be scattered in all quadrants of the retina (Fite et al., 1981; Krause et al., 2014). Despite the fact that dRGCs in mammals have not been reported to project into the MTN, our results obtained from anterograde labeling clearly demonstrated a large increase of signal in the ipsilateral MTN in absence of *Gsk3β*, whereas it was absent or very dim in control animals. So far, it is unclear if the increased signal observed in absence of *Gsk3β* originates solely from dRGCs projections or if oRGCs also participate to the ipsilateral MTN projections, although the contralateral projection did not seem to be affected. We can speculate

that the weak signal observed in the control ipsilateral MTN is linked to the low number of dRGC present in the WT retina and therefore it may explain that such observation could not be done so far. Altogether, our results strongly suggest that these displaced cells may primarily project into the ipsilateral MTN since the intensity of the signal followed the increased number of dRGCs (Fig. 8B). In mice, it has been shown by retrograde labeling from the superior colliculus (SC), which receive large amount of RGC projections, that dRGCs/oRGCs project to one or both SCs (Karten et al., 1977). Although challenging, same experiments by injecting fluorescent dye into the ipsilateral MTN may allow to discriminate whether the increased signal in absence of *Gsk3β* originates from dRGCs and whether these cells also project into this area in WT retina.

Given the very low percentage of dRGCs in the control retina, their function is poorly studied in mammals. In contrast, dRGCs function, brain projections and topography have been extensively investigated in bird and reptile retina (Mouritsen et al., 2004). In birds, cryptochrome-expressing dRGCs are used as a magnetic compass for orientation (Nießner et al., 2016). In European Robin birds, *Erithacus rubecula,* a low number of dRGCs have been identified but specifically express Cryptochrome 1b only during nocturnal migration period (Nießner et al., 2016). In rodents, different dRGCs are proposed to exist with independent function based on their projection to the brain and their topography in the retina (Badea and Nathans, 2004; Pang and Wu, 2011; Pang et al., 2010; Völgyi et al., 2009). Retrograde labeling from the optic nerve led to the identification of 16 classes of dRGCs based on their ramification levels of their dendrites as wells as the dendritic field size (Pang and Wu, 2011). Combined with IHC labelling, these dRGCs were negative for glycine, GAD (glutamate decarboxylase) as well as ChAT as observed in *Gsk3α*$^{f/+}$*β*$^{f/f}$;*α-Cre* retina. Based on the dRGC dendrites projection into the IPL, it has been proposed that most dRGCs in WT retina are

functionally more involved in retinal OFF light pathways (Pang and Wu, 2011). The same tedious method applied on *Gsk3α*$^{f/+}$*β*$^{f/f}$;*α-Cre* retina may definitively shade more light on dRGC function and establish if all the different classes are present.

As part of the AOS, the MTN receives afferent signal from the eye and sends efferent signal to the motor neurons controlling the position of the eye. As such, optokinetic reflex relies on direction specific retinal projections to the AOS. The neurons of the dorsal terminal nucleus (DTN) codes for horizontal stimulus whereas the neurons of the MTN codes for vertical stimulus (Giolli et al., 2006; Yonehara et al., 2009). As such, the direction of image motion relies on direction-selective (DS) ganglion cells in the retina. Testing *Gsk3α*$^{f/+}$*β*$^{f/f}$;*α-Cre* OKR response might allow to test if an ipsilateral MTN projection influences motion detection. Interestingly, we could find a small subset of dRGCs in *Gsk3α*$^{f/+}$*β*$^{f/f}$;*α-Cre* and littermate control retina positive for the transcription factors Tbr2 and Foxp2, markers for non-image-forming RGCs and DS-RGCs respectively (Rousso et al., 2016; Sato et al., 2017). Altogether with our transcriptomic data, these results strongly suggest that the large number of dRGCs in *Gsk3α*$^{f/+}$*β*$^{f/f}$;*α-Cre* retina might be DS-RGCs projecting into the MTN to detect motion. Along this line, it has been proposed that dRGC function to increase the delay of visual information coming from above their head due to their apical position in the retina, thereby allowing a quick detection of predators (Nadal-Nicolás et al., 2014). Such hypothesis could be tested in our mouse models using suitable behavior tests.

Overall, *Gsk3* mutant mice displaying enhanced dRGCs offer a powerful system to further study the embryonic origin, synaptic connections and visual function of dRGCs in the mammal retina.

MATERIALS AND METHODS

Animals and tissue collection

All animal experiments have been carried out in accordance with the European Communities Council Directive of 22 September 2010 (2010/63/EEC), European Union guidelines effective and with the Association for Research in Vision and Ophthalmology statement for the Use of animals in ophthalmic and visual Research. All animal care and experimentation were also conducted in accordance with guidelines, under the license APAFIS#1018-2016072611404304 by the Institutional animal care committee n°059 in France and by Animal Care and Use Committee at the National Institutes of Health (ASP#650). *Gsk3α* and *Gsk3β* floxed mice were generously provided by Dr. Jim Woodgett (University of Toronto, Canada) (MacAulay et al., 2007; Patel et al., 2008). Floxed *Gsk3* mice were mated with those carrying the retina-specific regulatory element of murine *Pax6* driving the expression of the Cre recombinase (*α-Cre*) in retinal progenitors as early as E10.5 (Marquardt et al., 2001). Mice from either sex were used for experimental procedures. All mouse genotyping was performed as described (Roger et al., 2014). Animals were killed by CO_2 inhalation followed by cervical dislocation, and all efforts were made to minimize suffering.

Hematoxylin & eosin (H&E) staining, and immunostaining

Methacrylate sections were used for H&E staining as described (Roger et al., 2010). For IHC on frozen sections, enucleated eyeballs were fixed at the required stage in 4% PFA for 60 min on ice and incubated in an increasing concentration of sucrose (10%, 20% and 30%), then embedded in OCT. Embedded eyeballs were serially cut to 12 µm sections using a cryostat. For embryonic stages, pregnant females were euthanized and whole heads of pups were harvested in paraffin. IHC was performed as described (Cabochette et al., 2015).

Primary and secondary antibodies are listed in Supplementary Table 1. Sections were counterstained with 1:1000 4′,6-diamidino-2-phenylindole (DAPI) (1 mg/mL (Thermo Scientific).

EdU labeling and TUNEL assay

For EdU labelling, females were injected intraperitoneally with 10 mM of 5-ethynyl-20-deoxyuridine (EdU) (Life Technology). EdU incorporation was detected on paraffin sections or frozen sections using the Click-iT EdU Imaging Kit following manufacturer's recommendations (Life Technology) (Roger et al., 2010). Apoptosis was detected by terminal deoxynucleotidyl transferase-mediated biotinylated UTP nick end labeling (TUNEL) assays using in situ cell death detection kit (Promega). All images were acquired using a Zeiss LSM710 confocal microscope and Zen software (Zeiss).

Immunoblotting

Frozen retinas were lysed by sonication in lysis buffer (20 mM Na_2HPO4, 250 mM NaCl, 30 mM NaPPi, 0.1% NP40, 5mM EDTA, 5mM DTT) supplemented with protease inhibitor cocktail (Sigma-Aldrich). Lysates concentration was determined using a Lowry protein assay kit (Bio-Rad) following sonication and centrifugation. The supernatant proteins were separated under denaturing condition by SDS-PAGE, transferred onto nitrocellulose membrane and probed with various antibodies, as described (Liebmann et al., 2016; Renier et al., 2014). Proteins were visualized using enhanced chemiluminescence kit (Bio-Rad). α-tubulin was used as the loading control. Quantification was performed using ImageJ software (http://imagej.nih.gov/ij/; provided in the public domain at NIH).

Retinal flat mount

Fixed retinas were permeabilized and blocked in a solution containing 0.5% Triton-X100, 5% donkey normal serum, 1XPBS, 0.1 g/L thimerosal for 1 day at RT under agitation. Primary antibodies were diluted in a solution containing 0.5% Triton-X100,

5% donkey normal serum, 10% Dimethyl Sulfoxide, 1XPBS, 0.1 g/L thimerosal for 3 days at RT under agitation. The retinas were then washed for 1 day in PBST (1XPBS, 0.5% Triton-X100). The secondary antibodies were diluted in the same solution as primary antibodies and left for 2 days. After washing retinas for 1 day, they were mounted on slides and imaged using a scanning confocal microscope (Olympus, FV1000). For quantifications of Rbpms^{+} cells, manual segmentation was carried out followed by quantification using the Imaris X 64 “Spots” tool (Bitplane, version 9.1.2).

Electroretinography

Electroretinogram (ERG) recordings were performed using a focal ERG module attached to Micron IV (Phoenix Research Laboratory). Briefly, mice were dark-adapted overnight and prepared for the experiment under dim-red light. The mice were anesthetized with ketamine (100 mg/kg) and xylazine (10mg/kg) and received topical proparacaine hydrochloride (0.5%, Alcon) via eye drops. Pupils were dilated with tropicamide (1%, Alcon) and phenylephrine (2.5%, Alcon) and lightly coated with GONAK hypromellose ophthalmic demulcent solution (2.5%, Akorn). Lens of the Micron IV was placed directly on the cornea, and a reference electrode was placed on the mouse head. Scotopic responses were elicited with a series of flashes of increasing light intensities from -1.7 to 2.2 cd.s/m2. Photopic responses were elicited under rod-desensitizing background light with a series of flashes of increasing light intensities from -0.5 to 2.8 cd.s/m2. Values of a- and b-wave were extracted and plotted for comparisons between groups of interest.

Retrograde labeling of retinal ganglion cells

For retrograde labeling eyes were enucleated with a piece of the optic nerve and fixed in PFA for 30 min. Rhodamine B isothiocyanate–Dextran (Sigma-Aldrich) was applied on the top of the optic nerve and incubated for 60 min. Eyes were flat mounted after the remaining dye was washed out for 48 hours in PBS at 4 °C. Z series images were

584 acquired using SP5 confocal microscope (Leica Biosystems), and 3D reconstruction
585 was performed using Volocity (Perkin Elmer).

586 **Anterograde labeling of retinal ganglion cell projections**

587 *Anterograde labeling*

588 For anterograde tracing of retinal projections, a Cholera Toxin beta subunit (CTB) was
589 used. Animal were anesthetized using a cocktail of ketamine (60 mg/kg) and xylazine
590 (10 mg/kg) and a subsequent bilateral injection of 1.2 ul CTB at 1mg/ml coupled to
591 either an Alexa-555 or -647 (Lifesciences) were performed intravitreally. Three days
592 following the injection, mice were perfused with 4% PFA.

593 *Tissue Clearing and 3D imaging*

594 For 3D imaging of CTB-labelled brains, a methanol clearing protocol was carried out
595 using modification from the iDISCO+ protocol (Belle et al., 2014, 2017). Briefly, brains
596 were de-hydrated by immersion in progressive baths of methanol/1X PBS (20%, 40%,
597 60%, 80%, 100%, 100%) for 2 hours each at room temperature on a tube rotator (SB3,
598 Stuart) at 14rpm, using a 15 ml centrifuge tube (TPP, Dutcher) protected from light.
599 Following these baths, samples were immersed overnight in 2/3 Dichloromethane
600 (DCM; Sigma-Aldrich) and then a 30-min bath in 100 % DCM before being transferred
601 in Di-Benzyl Ether (DBE; Sigma-Aldrich) overnight prior imaging.
602 3D imaging / Image acquisition for all samples was performed as previously described
603 (Belle et al., 2014, 2017). Acquisitions were done using an ultramicroscope I (LaVison
604 Biotec) with the ImspectorPro software (LaVision Biotech). The step size between each
605 image was fixed at 2 µm with a numerical aperture of 0.120 and 150ms acquistion
606 using a PCO Edge SCMOS CCD camera (2,560 x 2,160 pixel size, LaVison BioTec).

607 *Image analysis*

608 Imaris x64 software (Version9.1.2, Bitplane) was used for all image analysis. Stack
609 images were first converted from .tiff to .ims files using the Imaris file converter v9.1.2.

3D reconstruction was visualised with the “volume rendering” function. To isolate ipsi- and contralateral MTN volumes, manual segementation was carried out using the “surface” tool and the isoline selection (density, 10%). Each ipsi- and contra-lateral projection of the MTN was segmented to generate a volume (μm^3). Movie reconstruction with .tiff series were done with ImageJ (1.50e, Java 1.8.0_60, 64-bit) and iMovie (version 10.1.1).

Statistical analysis

Results are reported as mean ± SEM. Nonparametric Mann-Whitney U test was used to analyze cell counting. *P* value ≤ 0.05 was considered significant.

Whole transcriptome sequencing and data analysis

Whole transcriptome analysis was performed on three independent biological replicates from *Gsk3α$^{f/f}$β$^{f/f}$;α-Cre* and *Gsk3α$^{f/f}$β$^{f/f}$* retina at P60. After harvesting, both retinas for each animal were immediately frozen. RNA was extracted using Nucleospin RNA Plus kit (Macherey-Nagel). RNA quality and quantity were evaluated using a BioAnalyzer 2100 with RNA 6000 Nano Kit (Agilent Tech- nologies). Stranded RNA-Seq libraries were constructed from 100 ng high-quality total RNA (RIN > 8) using the TruSeq Stranded mRNA Library Preparation Kit (Illumina). Paired-end sequencing of 40 bases length was performed on a NextSeq 500 system (Illumina). Pass-filtered reads were mapped using STAR and aligned to mouse reference genome GRCm38.94 (Dobin et al., 2013). Count table of the gene features was obtained using FeatureCounts (Liao et al., 2014). Normalization, differential expression analysis and FPKM (fragments per kilobase of exon per million fragments mapped) values were computed using EdgeR (Chen et al., 2015). An FPKM filtering cutoff of 1 in at least one of the 6 samples was applied. A False Discovery Rate (FDR) of less than or equal to 0.05 was considered significant and a fold change cutoff of 1.5 was applied to identify differentially expressed genes. Comprehensive gene list analysis, enriched biological

pathways, gene annotation, were based on Gene Ontology classification system using Metascape (Zhou et al., 2019). Data visualization was done using GOplot R package (Walter et al., 2015). To evaluate the expression of the DEGs in RGCs, we used published whole transcriptome analysis from purified RGCs available on Gene Expression Omnibus database (GSE87647) (Sajgo et al., 2017)

Gene expression analysis by Real-Time PCR (RT-qPCR)

After RNA extraction using Nucleospin RNA Plus kit (Macherey-Nagel), 500 ng of total RNA was reverse transcribed using the iScript cDNA Synthesis Kit according to manufacturer instructions (BioRad). For each qRT-PCR, 2 µL of a ten-fold dilution of synthetized cDNA was used, and the reactions were performed in technical triplicates on a C1000 thermal cycler (CFX96 real-time system, BioRad) using SsoFast EvaGreen Supermix (BioRad) as previously described (Hamon et al., 2017). RT-qPCR experiments were performed on three to four independent biological replicates. Differential expression was determined using the ΔΔCt method with the geometric average of Rps26 and Srp72 as endogenous controls (Livak and Schmittgen, 2001).

ACKNOWLEDGEMENT

We are grateful to Elodie-Kim Grellier, Sophie Lourdel, Yide Mi, and Jessica Gumerson for their help with mouse colonies and technical support. This research was supported by the CNRS, Retina France and by the Intramural Research Program of the National Eye Institute (EY000450 and EY000546). Elena Braginskaja is supported by the Ernst Ludwig Ehrlich Studienwerk.

REFERENCES

Badea, T.C., and Nathans, J. (2004). Quantitative analysis of neuronal morphologies in the mouse retina visualized by using a genetically directed reporter. Journal of Comparative Neurology *480*, 331–351.

Baldridge, W.H. (1996). Optical recordings of the effects of cholinergic ligands on neurons in the ganglion cell layer of mammalian retina. Journal of Neuroscience *16*, 5060–5072.

Balkema, G.W., and Dräger, U.C. (1990). Origins of uncrossed retinofugal projections in normal and hypopigmented mice. Visual Neuroscience *4*, 595–604.

Bejarano-Escobar, R., Álvarez-Hernán, G., Morona, R., González, A., Martín-Partido, G., and Francisco-Morcillo, J. (2015). Expression and function of the LIM-homeodomain transcription factor Islet-1 in the developing and mature vertebrate retina. Experimental Eye Research *138*, 22–31.

Belle, M., Godefroy, D., Dominici, C., Heitz-Marchaland, C., Zelina, P., Hellal, F., Bradke, F., and Chédotal, A. (2014). A simple method for 3D analysis of immunolabeled axonal tracts in a transparent nervous system. Cell Reports *9*, 1191–1201.

Belle, M., Godefroy, D., Couly, G., Malone, S.A., Collier, F., Giacobini, P., and Chédotal, A. (2017). Tridimensional Visualization and Analysis of Early Human Development. Cell *169*, 161-173.e12.

Brose, N. (2008). For better or for worse: Complexins regulate SNARE function and vesicle fusion. Traffic *9*, 1403–1413.

Buhl, E.H., and Dann, J.F. (1988). Morphological diversity of displaced retinal ganglion cells in the rat: A lucifer yellow study. Journal of Comparative Neurology *269*, 210–218.

Cabochette, P., Vega-Lopez, G., Bitard, J., Parain, K., Chemouny, R., Masson, C., Borday, C., Hedderich, M., Henningfeld, K.A., Locker, M., et al. (2015). YAP controls retinal stem cell DNA replication timing and genomic stability. ELife *4*, e08488.

Chen, Y., Mccarthy, D., Robinson, M., and Smyth, G.K. (2015). edgeR : differential expression analysis of digital gene expression data User ' s Guide.

Cole, A.R. (2012). GSK3 as a Sensor Determining Cell Fate in the Brain. Frontiers in Molecular Neuroscience *5*, 1–10.

Cook, J.E., and Podugolnikova, T.A. (2001). Evidence for spatial regularity among retinal ganglion cells that project to the accessory optic system in a frog, a reptile, a bird, and a mammal. Visual Neuroscience *18*, 289–297.

Dobin, A., Davis, C.A., Schlesinger, F., Drenkow, J., Zaleski, C., Jha, S., Batut, P., Chaisson, M., and Gingeras, T.R. (2013). STAR: Ultrafast universal RNA-seq aligner. Bioinformatics *29*, 15–21.

Doble, B.W., and Woodgett, J.R. (2003). GSK-3: Tricks of the trade for a multi-tasking kinase. Journal of Cell Science *116*, 1175–1186.

Doble, B.W., Patel, S., Wood, G.A., Kockeritz, L.K., and Woodgett, J.R. (2007). Functional redundancy of GSK-3alpha and GSK-3beta in Wnt/beta-catenin signaling shown by using an allelic series of embryonic stem cell lines. Developmental Cell *12*, 957–971.

Doi, M., Imatani, H., Sasoh, M., Uji, Y., and Yamamura, H. (1994). Displaced retinal ganglion cells in the Chinese hamster. Japanese Journal of Ophthalmology *38*, 139–143.

703 Dräger, U.C., and Olsen, J.F. (1980). Origins of crossed and uncrossed retinal projections in
704 pigmented and albino mice. Journal of Comparative Neurology *191*, 383–412.

705 Eom, T.Y., and Jope, R.S. (2009). Blocked Inhibitory Serine-Phosphorylation of Glycogen
706 Synthase Kinase-3α/β Impairs In Vivo Neural Precursor Cell Proliferation. Biological
707 Psychiatry *66*, 494–502.

708 Espinosa, L., Inglés-Esteve, J., Aguilera, C., and Bigas, A. (2003). Phosphorylation by glycogen
709 synthase kinase-3β down-regulates Notch activity, a link for Notch and Wnt pathways. Journal
710 of Biological Chemistry *278*, 32227–32235.

711 Fite, K. v, Brecha, N., Karten, H.J., and Hunt, S.P. (1981). Displaced ganglion cells and the
712 accessory optic system of pigeon. The Journal of Comparative Neurology *195*, 279–288.

713 Fu, X., Sun, H., Klein, W.H., and Mu, X. (2006). B-Catenin Is Essential for Lamination But
714 Not Neurogenesis in Mouse Retinal Development. Developmental Biology *299*, 424–437.

715 Gal, A., Rau, I., el Matri, L., Kreienkamp, H.J., Fehr, S., Baklouti, K., Chouchane, I., Li, Y.,
716 Rehbein, M., Fuchs, J., et al. (2011). Autosomal-recessive posterior microphthalmos is caused
717 by mutations in PRSS56, a gene encoding a trypsin-like serine protease. American Journal of
718 Human Genetics *88*, 382–390.

719 Galli-Resta, L., and Ensini, M. (1996). An intrinsic time limit between genesis and death of
720 individual neurons in the developing retinal ganglion cell layer. Journal of Neuroscience *16*,
721 2318–2324.

722 Giolli, R.A., Blanks, R.H.I., and Lui, F. (2006). The accessory optic system: basic organization
723 with an update on connectivity, neurochemistry, and function. Progress in Brain Research *151*,
724 407–440.

725 Golpich, M., Amini, E., Hemmati, F., Ibrahim, N.M., Rahmani, B., Mohamed, Z., Raymond,
726 A.A., Dargahi, L., Ghasemi, R., and Ahmadiani, A. (2015). Glycogen synthase kinase-3 beta
727 (GSK-3β) signaling: Implications for Parkinson's disease. Pharmacological Research *97*, 16–
728 26.

729 Goold, R.G., Owen, R., and Gordon-Weeks, P.R. (1999). Glycogen synthase kinase 3β
730 phosphorylation of microtubule-associated protein 1B regulates the stability of microtubules in
731 growth cones. Journal of Cell Science *112*, 3373–3384.

732 Hamon, A., Masson, C., Bitard, J., Gieser, L., Roger, J.E., and Perron, M. (2017). Retinal
733 degeneration triggers the activation of YAP/TEAD in reactive Müller cells. Investigative
734 Ophthalmology and Visual Science *58*.

735 Han, S.-I., Aramata, S., Yasuda, K., and Kataoka, K. (2007). MafA stability in pancreatic beta
736 cells is regulated by glucose and is dependent on its constitutive phosphorylation at multiple
737 sites by glycogen synthase kinase 3. Molecular and Cellular Biology *27*, 6593–6605.

738 Hur, E.-M., and Zhou, F.-Q. (2010). GSK3 signalling in neural development. Nature Reviews.
739 Neuroscience *11*, 539–551.

740 Jacobs, K.M., Bhave, S.R., Ferraro, D.J., Jaboin, J.J., Hallahan, D.E., and Thotala, D. (2012).
741 GSK-3β: A Bifunctional Role in Cell Death Pathways. International Journal of Cell Biology
742 *2012*, 930710.

743 Jin, Y.H., Kim, H., Oh, M., Ki, H., and Kim, K. (2009). Regulation of Notch1/NICD and Hes1
744 expressions by GSK-3α/β. Molecules and Cells *27*, 15–19.

Ka, M., Jung, E.M., Mueller, U., and Kim, W.Y. (2014). MACF1 regulates the migration of pyramidal neurons via microtubule dynamics and GSK-3 signaling. Developmental Biology *395*, 4–18.

Karten, H.J., Fite, K. v., and Brecha, N. (1977). Specific projection of displaced retinal ganglion cells upon the accessory optic system in the pigeon (Columbia livia). Proceedings of the National Academy of Sciences of the United States of America *74*, 1753–1756.

Kay, J.N., de la Huerta, I., Kim, I.J., Zhang, Y., Yamagata, M., Chu, M.W., Meister, M., and Sanes, J.R. (2011). Retinal ganglion cells with distinct directional preferences differ in molecular identity, structure, and central projections. Journal of Neuroscience *31*, 7753–7762.

Kim, W.-Y., Wang, X., Wu, Y., Doble, B.W., Patel, S., Woodgett, J.R., and Snider, W.D. (2009). GSK-3 is a master regulator of neural progenitor homeostasis. Nature Neuroscience *12*, 1390–1397.

Krause, M., Distler, C., and Hoffmann, K.P. (2014). Retinal ganglion cells projecting to the accessory optic system in optokinetic blind albinotic rats are direction-selective. European Journal of Neuroscience *40*, 2274–2282.

Kremer, A. (2011). GSK3 and Alzheimer's disease: facts and fiction…. Frontiers in Molecular Neuroscience *4*, 1–10.

Lee, S., Kim, K., and Zhou, Z.J. (2010). Role of ACh-GABA Cotransmission in Detecting Image Motion and Motion Direction. Neuron *68*, 1159–1172.

Li, D.W., Liu, Z.Q., Chen, W., Yao, M., and Li, G.R. (2014). Association of glycogen synthase kinase-3β with Parkinson's disease (Review). Molecular Medicine Reports *9*, 2043–2050.

Li, S., Mattar, P., Zinyk, D., Singh, K., Chaturvedi, C.-P., Kovach, C., Dixit, R., Kurrasch, D.M., Ma, Y.-C., Chan, J.A., et al. (2012). GSK3 temporally regulates neurogenin 2 proneural activity in the neocortex. The Journal of Neuroscience : The Official Journal of the Society for Neuroscience *32*, 7791–7805.

Liao, Y., Smyth, G.K., and Shi, W. (2014). FeatureCounts: An efficient general purpose program for assigning sequence reads to genomic features. Bioinformatics *30*, 923–930.

Liebmann, T., Renier, N., Bettayeb, K., Greengard, P., Tessier-Lavigne, M., and Flajolet, M. (2016). Three-Dimensional Study of Alzheimer's Disease Hallmarks Using the iDISCO Clearing Method. Cell Reports *16*, 1138–1152.

Linden, R., and Perry, V.H. (1983). Massive retinotectal projection in rats. Brain Research *272*, 145–149.

Liu, C., and Nathans, J. (2008). An essential role for frizzled 5 in mammalian ocular development. Development *135*, 3567–3576.

Liu, C., Bakeri, H., Li, T., and Swaroop, A. (2012). Regulation of retinal progenitor expansion by Frizzled receptors: implications for microphthalmia and retinal coloboma. Human Molecular Genetics *21*, 1848–1860.

Liu, C., Widen, S.A., Williamson, K.A., Ratnapriya, R., Gerth-Kahlert, C., Rainger, J., Alur, R.P., Strachan, E., Manjunath, S.H., Balakrishnan, A., et al. (2016). A secreted WNT-ligand-binding domain of FZD5 generated by a frameshift mutation causes autosomal dominant coloboma. Human Molecular Genetics *25*, 1382–1391.

Livak, K.J., and Schmittgen, T.D. (2001). Analysis of relative gene expression data using real-time quantitative PCR and the 2-ΔΔCT method. Methods *25*, 402–408.

MacAulay, K., Doble, B.W., Patel, S., Hansotia, T., Sinclair, E.M., Drucker, D.J., Nagy, A., and Woodgett, J.R. (2007). Glycogen synthase kinase 3alpha-specific regulation of murine hepatic glycogen metabolism. Cell Metabolism *6*, 329–337.

Marcus, E.A., Kintner, C., and Harris, W. (1998). The role of GSK3β in regulating neuronal differentiation in Xenopus laevis. Molecular and Cellular Neurosciences *12*, 269–280.

Marquardt, T., Ashery-Padan, R., Andrejewski, N., Scardigli, R., Guillemot, F., and Gruss, P. (2001). Pax6 is required for the multipotent state of retinal progenitor cells. Cell *105*, 43–55.

Maurer, U., Preiss, F., Brauns-Schubert, P., Schlicher, L., and Charvet, C. (2014). GSK-3 - at the crossroads of cell death and survival. Journal of Cell Science *127*, 1369–1378.

Medina, M., Garrido, J.J., and Wandosell, F.G. (2011). Modulation of GSK-3 as a Therapeutic Strategy on Tau Pathologies. Frontiers in Molecular Neuroscience *4*, 1–10.

Moore, K.B., Schneider, M.L., and Vetter, M.L. (2002). Posttranslational mechanisms control the timing of bHLH function and regulate retinal cell fate. Neuron *34*, 183–195.

Mouritsen, H., Janssen-Bienhold, U., Liedvogel, M., Feenders, G., Stalleicken, J., Dirks, P., and Weiler, R. (2004). Cryptochromes and neuronal-activity markers colocalize in the retina of migratory birds during magnetic orientation. Proceedings of the National Academy of Sciences of the United States of America *101*, 14294–14299.

Nadal-Nicolás, F.M., Jiménez-López, M., Salinas-Navarro, M., Sobrado-Calvo, P., Alburquerque-Béjar, J.J., Vidal-Sanz, M., and Agudo-Barriuso, M. (2012). Whole Number, Distribution and Co-Expression of Brn3 Transcription Factors in Retinal Ganglion Cells of Adult Albino and Pigmented Rats. PLoS ONE *7*, e49830.

Nadal-Nicolás, F.M., Salinas-Navarro, M., Jiménez-López, M., Sobrado-Calvo, P., Villegas-Pérez, M.P., Vidal-Sanz, M., and Agudo-Barriuso, M. (2014). Displaced retinal ganglion cells in albino and pigmented rats. Frontiers in Neuroanatomy *8*, 1–21.

Nießner, C., Gross, J.C., Denzau, S., Peichl, L., Fleissner, G., Wiltschko, W., and Wiltschko, R. (2016). Seasonally changing cryptochrome 1b expression in the retinal ganglion cells of a migrating passerine bird. PLoS ONE *11*, e0150377.

Ochi, H., Sakagami, K., Ishii, A., Morita, N., Nishiuchi, M., Ogino, H., and Yasuda, K. (2004). Temporal expression of L-Maf and RaxL in developing chicken retina are arranged into mosaic pattern. Gene Expression Patterns *4*, 489–494.

Onishi, A., Peng, G.H., Hsu, C., Alexis, U., Chen, S., and Blackshaw, S. (2009). Pias3-Dependent SUMOylation Directs Rod Photoreceptor Development. Neuron *61*, 234–246.

Onishi, A., Peng, G.-H., Chen, S., and Blackshaw, S. (2010). Pias3-dependent SUMOylation controls mammalian cone photoreceptor differentiation. Nature Neuroscience *13*, 1059–1065.

Ouchi, Y., Baba, Y., Koso, H., Taketo, M.M., Iwamoto, T., Aburatani, H., and Watanabe, S. (2011). β-Catenin signaling regulates the timing of cell differentiation in mouse retinal progenitor cells. Molecular and Cellular Neuroscience *46*, 770–780.

Pachenari, N., Kiani, S., and Javan, M. (2017). Inhibition of glycogen synthase kinase 3 increased subventricular zone stem cells proliferation. Biomedicine & Pharmacotherapy = Biomedecine & Pharmacotherapie *93*, 1074–1082.

Pang, J.-J., and Wu, S.M. (2011). Morphology and immunoreactivity of retrogradely double-labeled ganglion cells in the mouse retina. Investigative Ophthalmology & Visual Science *52*, 4886–4896.

831 Pang, J.J., Gao, F., and Wu, S.M. (2010). Light responses and morphology of
832 bNOSimmunoreactive neurons in the mouse retina. Journal of Comparative Neurology *518*,
833 2456–2474.

834 Park, S.J.H., Kim, I.J., Looger, L.L., Demb, J.B., and Borghuis, B.G. (2014). Excitatory
835 synaptic inputs to mouse on-off direction- selective retinal ganglion cells lack direction tuning.
836 Journal of Neuroscience *34*, 3976–3981.

837 Patel, S., Doble, B.W., MacAulay, K., Sinclair, E.M., Drucker, D.J., and Woodgett, J.R. (2008).
838 Tissue-specific role of glycogen synthase kinase 3beta in glucose homeostasis and insulin
839 action. Molecular and Cellular Biology *28*, 6314–6328.

840 Paylakhi, S., Labelle-Dumais, C., Tolman, N.G., Sellarole, M.A., Seymens, Y., Saunders, J.,
841 Lakosha, H., deVries, W.N., Orr, A.C., Topilko, P., et al. (2018). Müller glia-derived PRSS56
842 is required to sustain ocular axial growth and prevent refractive error. PLoS Genetics *14*,
843 e1007244.

844 Pérezleón, J.A., Osorio-Paz, I., Francois, L., and Salceda, R. (2013). Immunohistochemical
845 localization of glycogen synthase and GSK3β: Control of glycogen content in retina.
846 Neurochemical Research *38*, 1063–1069.

847 Renier, N., Wu, Z., Simon, D.J., Yang, J., Ariel, P., and Tessier-Lavigne, M. (2014). IDISCO:
848 A simple, rapid method to immunolabel large tissue samples for volume imaging. Cell *159*,
849 896–910.

850 Rocques, N., Abou Zeid, N., Sii-Felice, K., Lecoin, L., Felder-Schmittbuhl, M.P., Eychène, A.,
851 and Pouponnot, C. (2007). GSK-3-Mediated Phosphorylation Enhances Maf-Transforming
852 Activity. Molecular Cell *28*, 584–597.

853 Rodriguez, A.R., de Sevilla Müller, L.P., and Brecha, N.C. (2014). The RNA binding protein
854 RBPMS is a selective marker of ganglion cells in the mammalian retina. Journal of Comparative
855 Neurology *522*, 1411–1443.

856 Roger, J.E., Hiriyanna, A., Gotoh, N., Hao, H., Cheng, D.F., Ratnapriya, R., Kautzmann, M.-
857 A.I., Chang, B., and Swaroop, A. (2014). OTX2 loss causes rod differentiation defect in CRX-
858 associated congenital blindness. The Journal of Clinical Investigation *124*, 631–643.

859 Roger, J.E.J.E., Nellissery, J., Kim, D.S.D.S.D.S., and Swaroop, A. (2010). Sumoylation of
860 bZIP transcription factor NRL modulates target gene expression during photoreceptor
861 differentiation. Journal of Biological Chemistry *285*, 25637–25644.

862 Rousso, D.L., Qiao, M., Kagan, R.D., Yamagata, M., Palmiter, R.D., and Sanes, J.R. (2016).
863 Two Pairs of ON and OFF Retinal Ganglion Cells Are Defined by Intersectional Patterns of
864 Transcription Factor Expression. Cell Reports *15*, 1930–1944.

865 Sajgo, S., Ghinia, M.G., Brooks, M., Kretschmer, F., Chuang, K., Hiriyanna, S., Wu, Z.,
866 Popescu, O., and Badea, T.C. (2017). Molecular codes for cell type specification in Brn3 retinal
867 ganglion cells. Proceedings of the National Academy of Sciences of the United States of
868 America *114*, E3974–E3983.

869 Salinas-Navarro, M., Alarcón-Martínez, L., Valiente-Soriano, F.J., Ortín-Martínez, A.,
870 Jiménez-López, M., Avilés-Trigueros, M., Villegas-Pérez, M.P., de la Villa, P., and Vidal-Sanz,
871 M. (2009a). Functional and morphological effects of laser-induced ocular hypertension in
872 retinas of adult albino Swiss mice. Molecular Vision *15*, 2578–2598.

873 Salinas-Navarro, M., Jiménez-López, M., Valiente-Soriano, F.J., Alarcón-Martínez, L., Avilés-
874 Trigueros, M., Mayor, S., Holmes, T., Lund, R.D., Villegas-Pérez, M.P., and Vidal-Sanz, M.

(2009b). Retinal ganglion cell population in adult albino and pigmented mice: A computerized analysis of the entire population and its spatial distribution. Vision Research *49*, 637–647.

Salinas-Navarro, M., Mayor-Torroglosa, S., Jiménez-López, M., Avilés-Trigueros, M., Holmes, T.M., Lund, R.D., Villegas-Pérez, M.P., and Vidal-Sanz, M. (2009c). A computerized analysis of the entire retinal ganglion cell population and its spatial distribution in adult rats. Vision Research *49*, 115–126.

Sang, H., Lu, Z., Li, Y., Ru, B., Wang, W., and Chen, J. (2001). Phosphorylation of tau by glycogen synthase kinase 3beta in intact mammalian cells influences the stability of microtubules. Neuroscience Letters *312*, 141–144.

Sato, C., Iwai-Takekoshi, L., Ichikawa, Y., and Kawasaki, H. (2017). Cell type-specific expression of FoxP2 in the ferret and mouse retina. Neuroscience Research *117*, 1–13.

Savige, J., Sheth, S., Leys, A., Nicholson, A., Mack, H.G., and Colville, D. (2015). Ocular features in Alport syndrome: Pathogenesis and clinical significance. Clinical Journal of the American Society of Nephrology *10*, 703–709.

Sethuramanujam, S., Awatramani, G.B., and Slaughter, M.M. (2018). Cholinergic excitation complements glutamate in coding visual information in retinal ganglion cells. Journal of Physiology *596*, 3709–3724.

Shimizu, T., Kagawa, T., Inoue, T., Nonaka, A., Takada, S., Aburatani, H., and Taga, T. (2008). Stabilized beta-catenin functions through TCF/LEF proteins and the Notch/RBP-Jkappa complex to promote proliferation and suppress differentiation of neural precursor cells. Molecular and Cellular Biology *28*, 7427–7441.

Templeton, J.P., Wang, X. di, Freeman, N.E., Ma, Z., Lu, A., Hejtmancik, F., and Geisert, E.E. (2013). A crystallin gene network in the mouse retina. Experimental Eye Research *116*, 129–140.

Völgyi, B., Chheda, S., and Bloomfield, S.A. (2009). Tracer coupling patterns of the ganglion cell subtypes in the mouse retina. The Journal of Comparative Neurology *512*, 664–687.

Walter, W., Sánchez-Cabo, F., and Ricote, M. (2015). GOplot: an R package for visually combining expression data with functional analysis. Bioinformatics (Oxford, England) *31*, 2912–2914.

Wang, B., and Li, Y. (2006). Evidence for the direct involvement of βTrCP in Gli3 protein processing. Proceedings of the National Academy of Sciences of the United States of America *103*, 33–38.

Xu, C., Kim, N.G., and Gumbiner, B.M. (2009). Regulation of protein stability by GSK3 mediated phosphorylation. Cell Cycle *8*, 4032–4039.

Yonehara, K., Ishikane, H., Sakuta, H., Shintani, T., Nakamura-Yonehara, K., Kamiji, N.L., Usui, S., and Noda, M. (2009). Identification of retinal ganglion cells and their projections involved in central transmission of information about upward and downward image motion. PLoS ONE *4*, e4320.

Young, R.W. (1984). Cell death during differentiation of the retina in the mouse. Journal of Comparative Neurology *229*, 362–373.

Zhou, Y., Zhou, B., Pache, L., Chang, M., Khodabakhshi, A.H., Tanaseichuk, O., Benner, C., and Chanda, S.K. (2019). Metascape provides a biologist-oriented resource for the analysis of systems-level datasets. Nature Communications *10*, 1523.

Zumbrunn, J., Kinoshita, K., Hyman, A.A., and Näthke, I.S. (2001). Binding of the adenomatous polyposis coli protein to microtubules increases microtubule stability and is regulated by GSK3β phosphorylation. Current Biology *11*, 44–49.

FIGURE LEGENDS

Figure 1. Developmental defects and microphtalmia in *Gsk3*-deficient retina with aberrant nuclear translocation of β-catenin, a key effector of the Wnt canonical pathways. (A) Immunohistochemistry (IHC) of E12.5 retina from *Gsk3α$^{f/f}$β$^{f/f}$* mice expressing or not α-Cre using a pan-Gsk3 antibody (*green*) shows efficient deletion at the periphery where the Cre expression has been previously reported (delimited by dashed-line) Scale bar: 100 μm. (B) Hematoxylin and eosin (H&E) staining on methacrylate sections at E12.5, E14.5 and P2 reveals large retinal morphogenesis defects in *Gsk3α$^{f/f}$β$^{f/f}$;α-Cre* with blood invasion into the eyeball (showed by white arrow). L, Lens; NR, neural retina. Scale bar: 100 μm at E12.5 and E14.5. 500 μm at P2. For the magnification of P14.5, scale bar: 50 μm. (C) β-catenin accumulation (*red*) at E12.5 and E14.5 in the Cre-expressing area of *Gsk3α$^{f/f}$β$^{f/f}$;α-Cre* animals especially at E14.5. Magnification on the right panel shows the squared delimited area. L, Lens; NR, neural retina; + Cre, Cre-expressing area; - Cre, area without Cre expression Scale bar: 100 μm, magnification area scale bar: 40 μm.

Figure 2. Lack of GSK3 signaling alters cell cycle progression of retinal progenitor cells. (A) Mislocalisation of pH3-positive cells in the neuroblastic layer of *Gsk3α$^{f/f}$β$^{f/f}$;α-Cre* retina. E12.5 and E14.5 retina stained for pH3 (late-G2/M-phase, green) and EdU (marker of S-phase, *red*) following a 16H chase. EdU-positive cells are observed in the absence of GSK3 at both stages. Magnification on the right panel shows the squared delimited area. *Arrowheads*, pH3-positive and Edu-negative cells ; *Arrows*, pH3- and Edu-positive cells. Scale bar: 100 μm, magnification area scale bar: 100 μm. (B) Lack of GSK3 signaling alters cell cycle progression of retinal progenitors. Quantification at E12.5 and E14.5 of the number of EdU-positive cells (*left panel*), pH3-positive cells (*middle panel*) and double positive cells for EdU and pH3 among pH3-

positive cells (*right panel*) in *Gsk3α$^{f/f}$β$^{f/f}$;α-Cre* animals and controls. Mean ± SEM values are presented from 4 to 6 independent retinas for each genotype, * indicates *P* ≤ 0.05.

Figure 3. Lack of *Gsk3α* and *Gsk3β* expression in retinal progenitors blocks retinal progenitor differentiation. IHC using Doublecortin (Dcx) (*green*) and Brn3a (*red*) antibodies shows the localization of neuronal precursor cells and RGCs, respectively, at the central and basal part of the neuroblastic layer of E12.5 control retina. In contrast, neural differentiation is not observed in *Gsk3α$^{f/f}$β$^{f/f}$;α-Cre* retina, with the exception of a small central area where Cre is not expressed. At E14.5, Dcx- and Brn3a-positive cells are distributed across the whole retina in controls, whereas they are absent in periphery in *Gsk3α$^{f/f}$β$^{f/f}$;α-Cre* mice. Magnification on the right-hand side shows the squared delimited area and depicts the boundary between a Cre-positive and a Cre-negative area. Scale bar: 100 μm, magnification 40 μm.

Figure 4. Gradual loss of *Gsk3α* and/or *Gsk3β* leads to an increased number of Brn3a-positive retinal ganglion cells displaced in the inner nuclear layer (INL) of adult retina. (A) Brn3a (*red*) and NF68 (*green*) IHC on 2-month-old *Gsk3α$^{f/+}$β$^{f/f}$; α-Cre* mouse retina reveals the presence of supernumerary displaced retinal ganglion cells (dRGCs, *white arrows*) in the INL of *Gsk3α$^{f/+}$β$^{f/f}$; α-Cre* compared to littermate controls. Top panel represents control retinas, middle panel a peripheral retinal area, and bottom panel a more central area*. Scale bar: 20 μm*. (B) Gradual loss of *Gsk3α* and *Gsk3β* alleles (*Gsk3α$^{f/f}$β$^{+/+}$, Gsk3α$^{+/+}$β$^{f/f}$*, *Gsk3α$^{f/+}$β$^{f/f}$* or *Gsk3α$^{f/f}$β$^{f/+}$*) leads to a gradual increase of Brn3a-positive RGC located to the INL, with the highest number observed in *Gsk3α$^{f/+}$β$^{f/f}$*; *α-Cre animals.* Left stacked histogram represents counting of the total number of Brn3a-positive cells per section located in the GCL (*white bars*) and in the INL (*black bars*). Right histogram represents the percentage of the dRGCs among the

total number of Brn3a-positive cells per section for each combination. Mean ± SEM values are presented from 5-6 biological replicates, * indicates $P \leq 0.05$. (C) dRGCs send their axons into the optic nerve. Visualization of dRGCs after 3D reconstruction of 2-month-old flat mounted retina of control and *Gsk3α$^{f/+}$β$^{f/f}$*; *α-Cre* animals following retrograde labelling with Rhodamin-Dextran applied onto the optic nerve. inl: inner nuclear layer, gcl: ganglion cell layer. (D) Brn3a (*red*) and Rbpms (*green*) IHC on 2-month-old mouse retina reveal the co-expression of these two RGC markers in the dRGCs of both *Gsk3α$^{f/+}$β$^{f/f}$; α-Cre* dRGCs and in littermate controls. * indicates $P \leq 0.05$. Scale bar: 20 μm. (E) Flat mounted retina from *Gsk3α$^{f/+}$β$^{f/f}$; α-Cre* and littermate controls labelled with anti-Rbpms antibody demonstrated the large number of Rbpms-positive dRGCs in the INL of *Gsk3α$^{f/+}$β$^{f/f}$; α-Cre* mice. Quantification of the number of Rbpms-positive dRGCs in the INL of *Gsk3α$^{f/+}$β$^{f/f}$; α-Cre* and littermate control retinas per μm^2. Mean ± SEM values are presented from 3 biological replicates, **** indicates $P \leq 0.0001$. *Scale bar: 50 μm*.

Figure 5. dRGCs are produced in the same differentiation wave as oRGC located in the GCL. (A) EdU- (*green*) and Brn3a-positive cells (*red*) were found both in the GCL and in the INL of 30-days old *Gsk3α$^{f/+}$β$^{f/f}$*; *α-Cre* animals after a single injection of EdU at E12.5. (B) Percentage of EdU- and Brn3a-positive cells located either in the GCL or in the INL among total number of Brn3a-positive cells. Mean ± SEM values are presented from 4 biological replicates, ns: not significant (C) Brn3a (*red*) and NF68 (*green*) immunostaining on P0 mouse retina revealed that a large number of dRGCs were already present in *Gsk3α$^{f/+}$β$^{f/f}$; α-Cre* but they were fewer in littermate controls *(white arrows)*. (D) Left stacked histogram represents counting of the total number of Brn3a-positive cells per section located in the GCL (*white bars*) and in the INL (*black bars*) of *Gsk3α$^{f/+}$β$^{f/f}$; α-Cre* retina. Right histogram represents the percentage of the dRGCs among the total number of Brn3a-positive cells per section. Mean ± SEM

values are presented from 4 biological replicates, * indicates $P \leq 0.05$. *inl*, inner nuclear layer; *gcl*, ganglion cell layer. *Scale bar: 20μm.*

Figure 6. Lack of Gsk3β results in RGC projections into the ipsilateral Medial Terminal Nucleus. (A) All panels are light sheet fluorescence microscopy of solvent-cleared adult brain from control, *Gsk3α$^{f/f}$β$^{+/+}$; α-Cre*, *Gsk3α$^{+/+}$β$^{f/f}$; α-Cre* and *Gsk3α$^{f/+}$β$^{f/f}$; α-Cre* animals after intravitreal injection of CTB coupled to either an Alexa-555 or -647. Ipsilateral projections of RGCs into the MTN was observed in the absence of *Gsk3β* expression. SC, superior colliculus; NOT, nucleus of optic tract; dLGN, dorsal lateral geniculate nucleus; vLGN, ventral lateral geniculate nucleus; IGL, intergeniculate leaflet; OPT, Olivary Pretectal Nucleus; dMTN, dorsal medial terminal nucleus; MTN, medial terminal nucleus; vMTN, ventral medial terminal nucleus; OT, Optic tract; SCN, suprachiasmatic nucleus; ON, optic nerve. *Scale bar: 1mm*; * indicates the ipsilateral MTN. (B) Quantification of the signal intensity ratio between ipsilateral and contralateral MTN in controls and *Gsk3* mutants (including *Gsk3α$^{f/f}$β$^{+/+}$; α-Cre*, *Gsk3α$^{+/+}$β$^{f/f}$; α-Cre*, and *Gsk3α$^{f/+}$β$^{f/f}$; α-Cre*). ns: non significant, ** $P \leq 0.01$.

Figure 7. Whole transcriptome analysis of P60 *Gsk3α$^{f/+}$β$^{f/f}$; α-Cre* retina. (A) Heatmap representing the 111 differentially expressed genes (DEGs) (abs(FC)≥1.5; FDR≤0.05; FPKM>1) between 2-month-old *Gsk3α$^{f/+}$β$^{f/f}$; α-Cre* retina and littermate control were clustered by their Z-score. (B) Volcano plot representation of differentially expressed genes between Gsk3αf/+βf/f; α-Cre and control retina plotted on the x-axis (log2 scale). FDR adjusted significance is plotted on the y-axis. Orange and blue dots: significantly up-regulated and down-regulated genes in *Gsk3α$^{f/+}$β$^{f/f}$; α-Cre* retina, respectively. Vertical dashed lines represent FC=1.5. horizontal dashed line represents FDR=0.05. (C) Chord plot representation of DEGs related to GO annotations belonging to either molecular functions (MF) or biological process (BP).

Overlaps in GO annotation amongst genes within each category are visualized. * correspond to genes expressed in previously published purified RGCs (*blue,* slightly expressed genes in RGCs between 1 and 5 FPKM; *red*, highly expressed genes in RGCs more than 5 FPKM). (D) RT-qPCR validation of selected DEGs identified by RNA-seq analysis. Differential expression analysis by RT-qPCR of *Cartpt, Th, Epha2, Cplx1, Chrna5, Chrna2, Chrna7, Chrnb4* in *Gsk3α$^{f/+}$β$^{f/f}$; α-Cre* retina at 2-months of age, relative to littermate control retina levels. All values are expressed as the Mean ± SEM from three biological replicates. The data were normalized against the geometric average of two housekeeping genes: *Srp72*, and *Rps26*.

Supplementary data 1. Lack of *Gsk3α* and *Gsk3β* expression impairs the maintenance of the pool of retinal progenitors. IHC on E12.5 and E14.5 *Gsk3α$^{f/f}$β$^{f/f}$* and *Gsk3α$^{f/f}$β$^{f/f}$;α-Cre* retina using HES1 (*red*) and GSK3 (*green*) indicates a loss of retinal progenitors at E14.5. Magnification on the right panel shows the squared delimited area. *Dashed lines* delimit the central *Gsk3*-expressing area and the *Gsk3*-deleted area at the periphery Scale bar: 100 μm, magnification area scale bar 40 μm.

Supplementary data 2. Lack of *Gsk3α* and *Gsk3β* expression in retinal progenitors leads to increased cell death. (A) TUNEL assay on E12.5 and E14.5 *Gsk3α$^{f/f}$β$^{f/f}$;α-Cre* and control animals reveals an increase of cell death (TUNEL-positive cells, *green*) in *Gsk3α$^{f/f}$β$^{f/f}$;α-Cre* animals compared to littermate controls. (B) Quantification of the number of TUNEL-positive cells per retinal section. Mean ± SEM values are presented from 5 to 6 biological replicates for E12.5, 4 biological replicates for E14.5, * indicates $P \leq 0.05$.

Supplementary data 3. One allele of either *Gsk3α* or *Gsk3β* is sufficient for the development of a functional retina. (A) Immunoblot analysis of protein extracts from 2-month-old animals with different combination of *Gsk3α* and *Gsk3β* floxed alleles

(*Gsk3α*$^{f/f}$*β*$^{+/+}$, *Gsk3α*$^{+/+}$*β*$^{f/f}$, *Gsk3α*$^{f/+}$*β*$^{f/f}$ or *Gsk3α*$^{f/f}$*β*$^{f/+}$) with or without *Cre* recombinase using anti-panGSK3 antibody (recognizing both isoforms) reveals decreased expression of *Gsk3α* or *Gsk3β* (*arrowheads*). *α*-Tubulin is used as loading control. (B) IHC on 2-month-old retinal sections from control and *Gsk3α*$^{f/+}$*β*$^{f/f}$; *α-Cre* retinas with or without Cre recombinase using anti-GSK3β antibody (*red*) showing ubiquitous *Gsk3* expression in all retinal layers, whereas its expression is lost in the Cre-expressing retina. (C) Expression of only one *Gsk3* allele (*Gsk3α*) is sufficient for proper photoreceptor development. IHC using anti-Rhodopsin (Rho, *red*) and anti-Cone arrestin (Arr3, *red*) antibodies to label rod and cone photoreceptors, respectively. (D) Expression of only one Gsk3 allele (*Gsk3α*) is sufficient for proper interneuron development. IHC using anti-Calretinin (Calr, *green*) and anti-Calbindin (Calb, *red*) antibodies to label horizontal and amacrine cells, respectively. (B-D) *onl*, outer nuclear layer; *inl*, inner nuclear layer; *gcl*, ganglion cell layer. *Scale bar: 20μm*. (E, F) Electroretinogram (ERG) recording in 2-month-old *Gsk3α*$^{f/+}$*β*$^{f/f}$*;α-Cre* animals and littermate controls. Photopic (cone) (E) and scotopic (rods) (F) response in *Gsk3α*$^{f/+}$*β*$^{f/f}$*;α-Cre* animals are similar to controls. Mean ± SEM intensity response curves of a- and b-wave responses averaged from 8 biological replicates of each genotype.

Supplementary data 4. dRGCs express the nuclear factor Islet-1. IHC on 2-month-old mouse retina reveals that most dRGCs (Brn3a-positive dRGCs, white arrows, *red*) in the INL of *Gsk3α*$^{f/+}$*β*$^{f/f}$*; α-Cre* and littermate controls were positive for Islet-1 (*green*), a marker expressed in the nuclei of ganglion cells, and of cholinergic amacrine cells, ON-bipolar cells, and subpopulations of horizontal cells. *Scale bar: 50 μm*.

Supplementary data 5. Identification of enriched pathways from DEGs identified in 2-month-old *Gsk3α*$^{f/+}$*β*$^{f/f}$*; α-Cre* retina. (A) Gene ontology (GO) annotations of DEGs in *Gsk3α*$^{f/+}$*β*$^{f/f}$*; α-Cre* retina compared to littermate controls. Top over-

represented pathways for Biological process (BP), Molecular Function (MF), KEGG (Kyoto Encyclopedia of Genes and Genomes) and TRRUST (Transcriptional Regulatory Relationships Unrevealed by Sentence-based Text mining) were identified by enrichment analysis using Metascape. (B) Circular visualization for BP and MF of GO enrichment analysis. Down-regulated genes (blue dots) and up-regulated genes (red dots) within each GO pathway are plotted based on logFC. Z-score bars indicate if an entire GO category is more likely to be increased or decreased based on the genes within it.

Supplementary data 6. Lack of *Gsk3β* might lead to the production of different subtype of dRGCs. IHC on 2-month-old mouse retina reveals the presence of a subset of dRGCs (Rbpms-positive dRGCs, *red*) in *Gsk3α$^{f/+}$β$^{f/f}$; α-Cre* expressing either the transcription factor Tbr2 (*green*) or Foxp2 (*grey*). Arrows indicate Tbr2 and Rbpms-positive dRGCs; arrowheads represent Foxp2 and Rbpms-positive dRGCs. *Scale bar: 50 μm*.

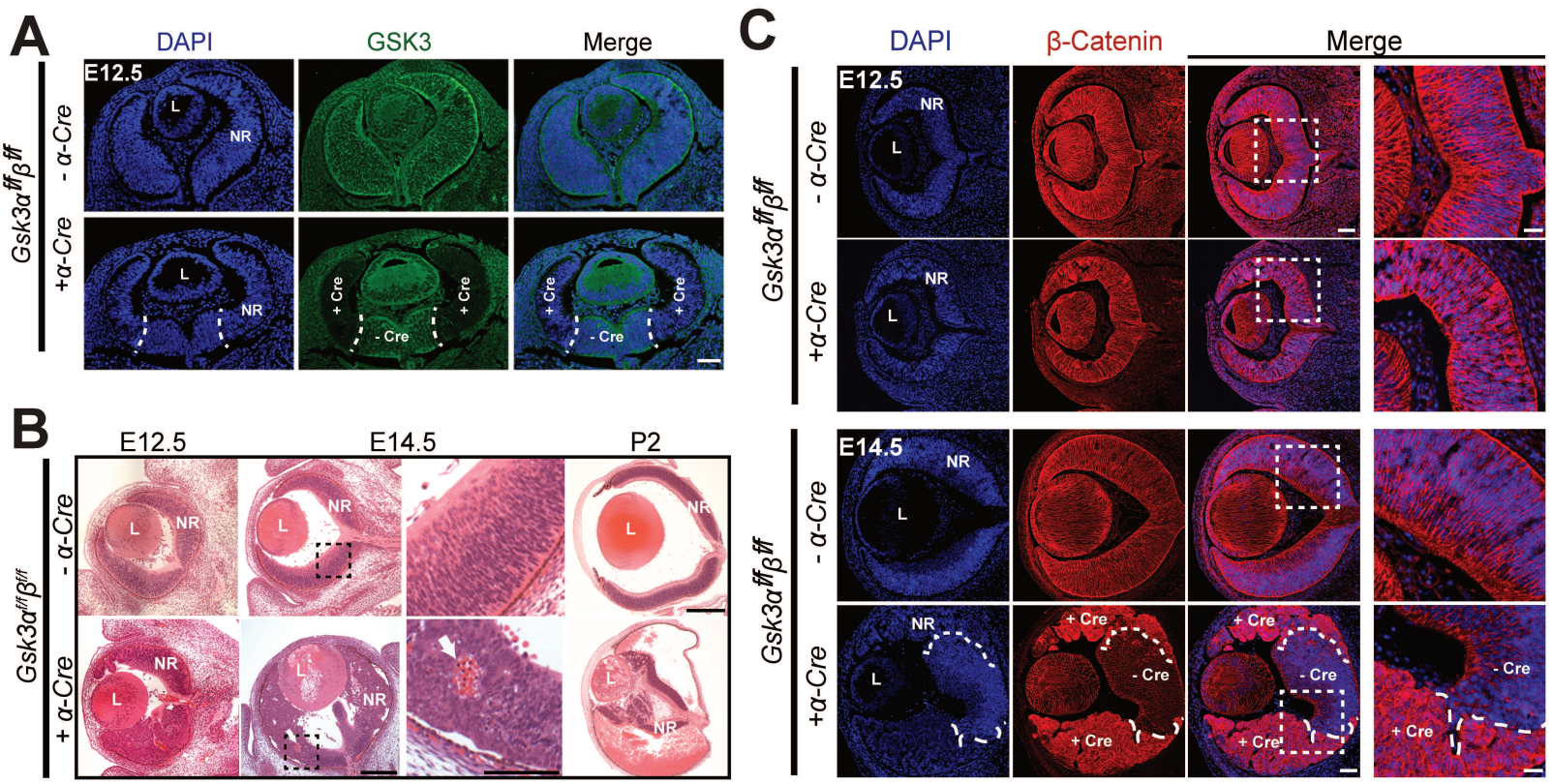
A
DAPI
GSK3
Merge
E12.5
Gsk3α^fffβ^fff
- α-Cre
+α-Cre
L
NR
+ Cre
- Cre
B
E12.5
E14.5
P2
Gsk3α^fffβ^fff
- α-Cre
+ α-Cre
C
DAPI
β-Catenin
Merge
E12.5
E14.5
Gsk3α^fffβ^fff
- α-Cre
+α-Cre
+ Cre
- Cre

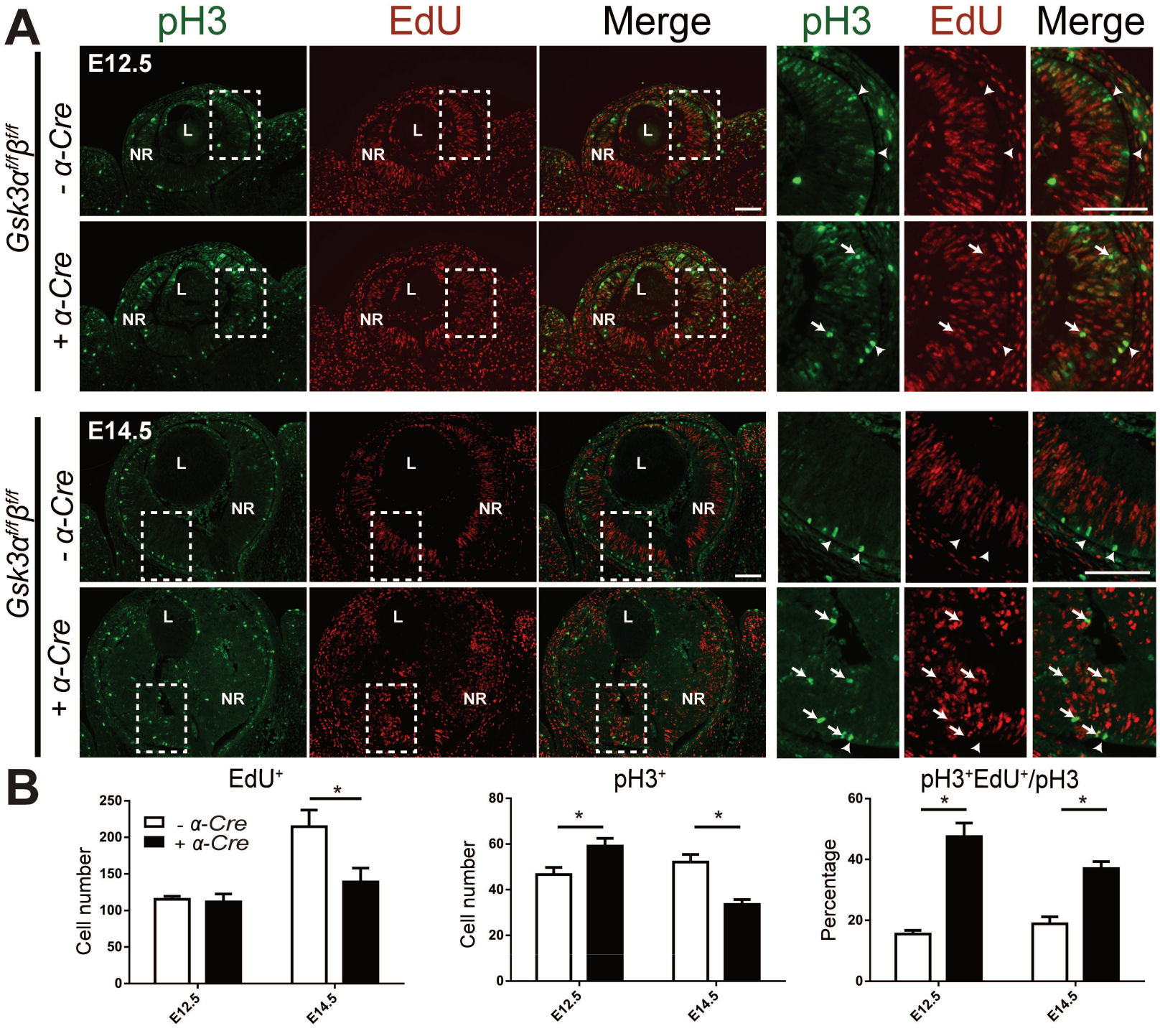
A
pH3
EdU
Merge
pH3
EdU
Merge
E12.5
E14.5
Gsk3α^f/fβ^f/f
- α-Cre
+ α-Cre
L
NR
B
EdU⁺
pH3⁺
pH3⁺EdU⁺/pH3
Cell number
Percentage
- α-Cre
+ α-Cre
E12.5
E14.5
*

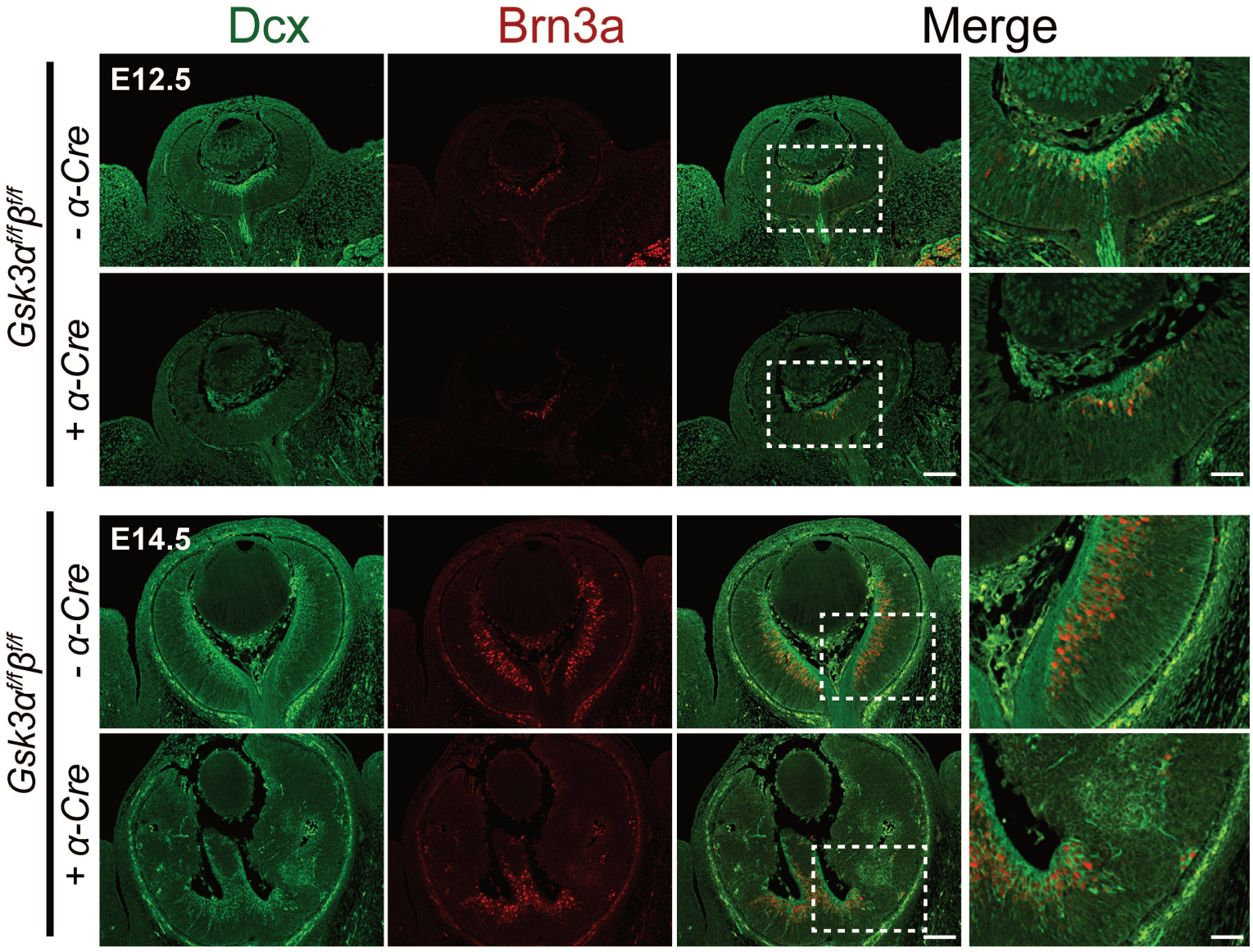
Dcx
Brn3a
Merge
E12.5
E14.5
Gsk3α^f/fβ^f/f
- α-Cre
+ α-Cre

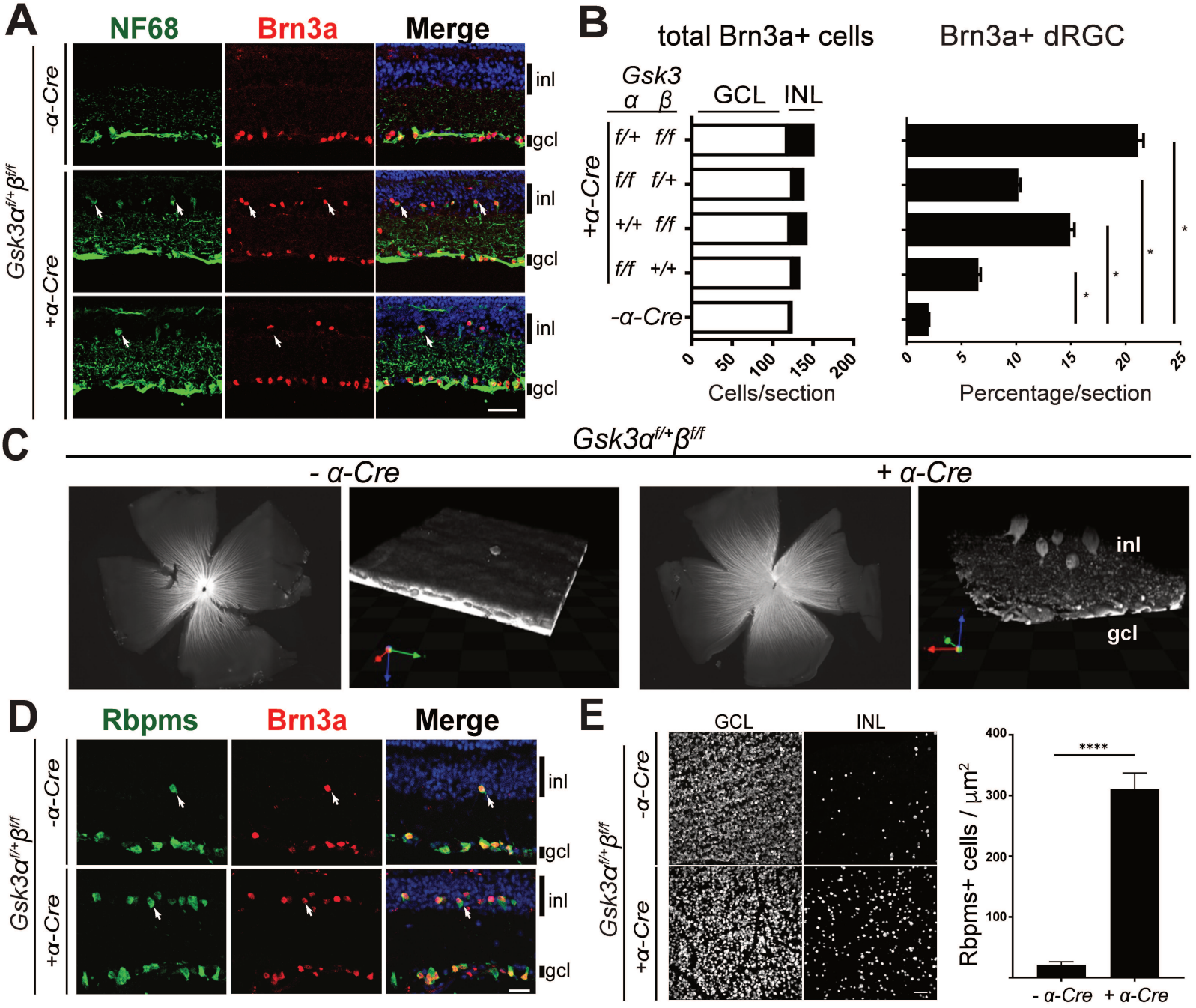
A
NF68
Brn3a
Merge
Gsk3α^f/+β^f/f
-α-Cre
+α-Cre
inl
gcl
B
total Brn3a+ cells
Brn3a+ dRGC
Gsk3
α β
GCL INL
f/+ f/f
f/f f/+
+/+ f/f
f/f +/+
-α-Cre
+α-Cre
0 50 100 150 200
Cells/section
0 5 10 15 20 25
Percentage/section
C
Gsk3α^f/+β^f/f
- α-Cre
+ α-Cre
inl
gcl
D
Rbpms
Brn3a
Merge
E
GCL
INL
Rbpms+ cells / μm²
400
300
200
100
****
- α-Cre
+ α-Cre

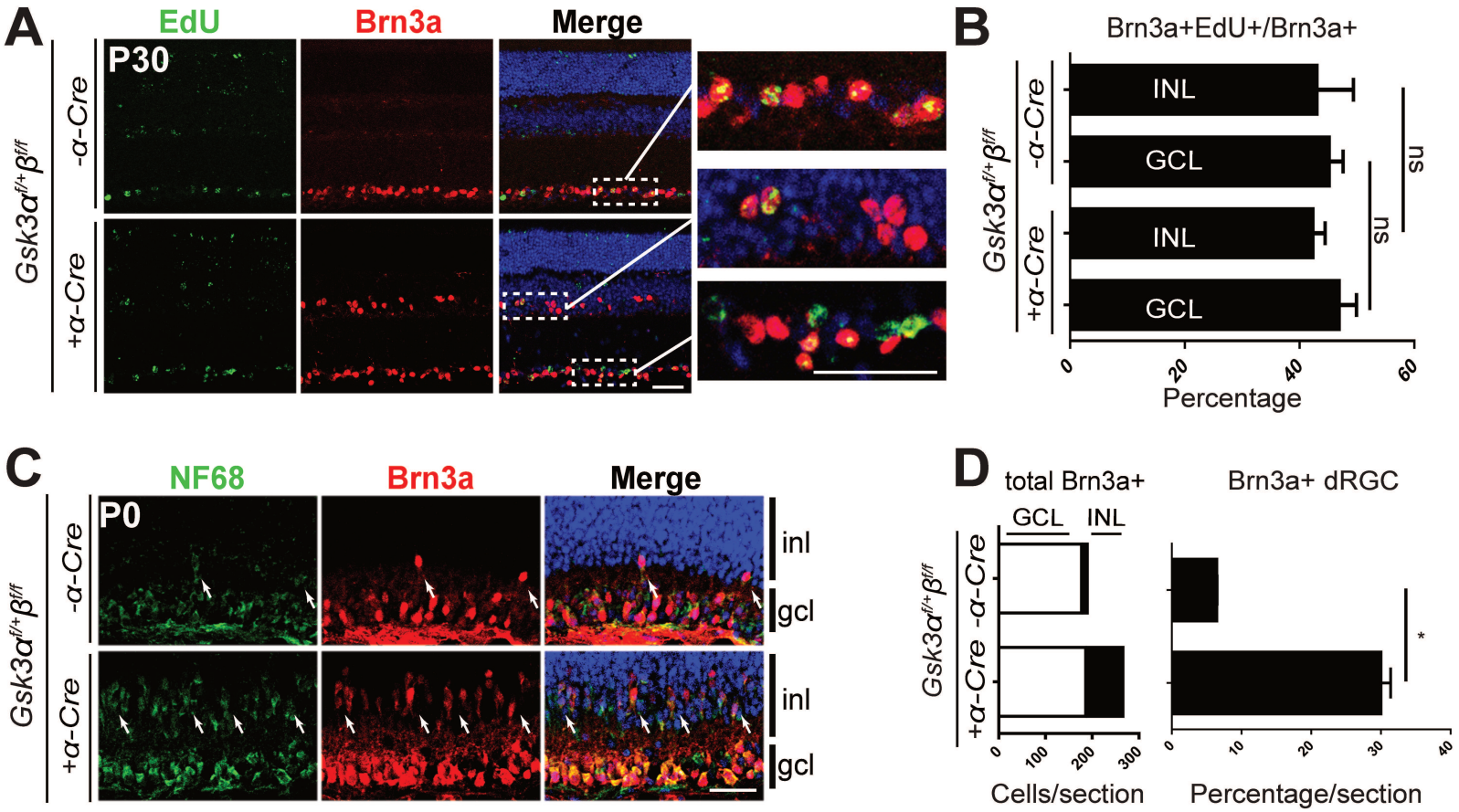
A
EdU
Brn3a
Merge
P30
-α-Cre
+α-Cre
Gsk3α^f/+β^f/f
B
Brn3a+EdU+/Brn3a+
INL
GCL
INL
GCL
ns
ns
0
20
40
60
Percentage
C
NF68
Brn3a
Merge
P0
-α-Cre
+α-Cre
Gsk3α^f/+β^f/f
inl
gcl
inl
gcl
D
total Brn3a+
Brn3a+ dRGC
GCL
INL
-α-Cre
+α-Cre
Gsk3α^f/+β^f/f
0
100
200
300
Cells/section
0
10
20
30
40
Percentage/section
*

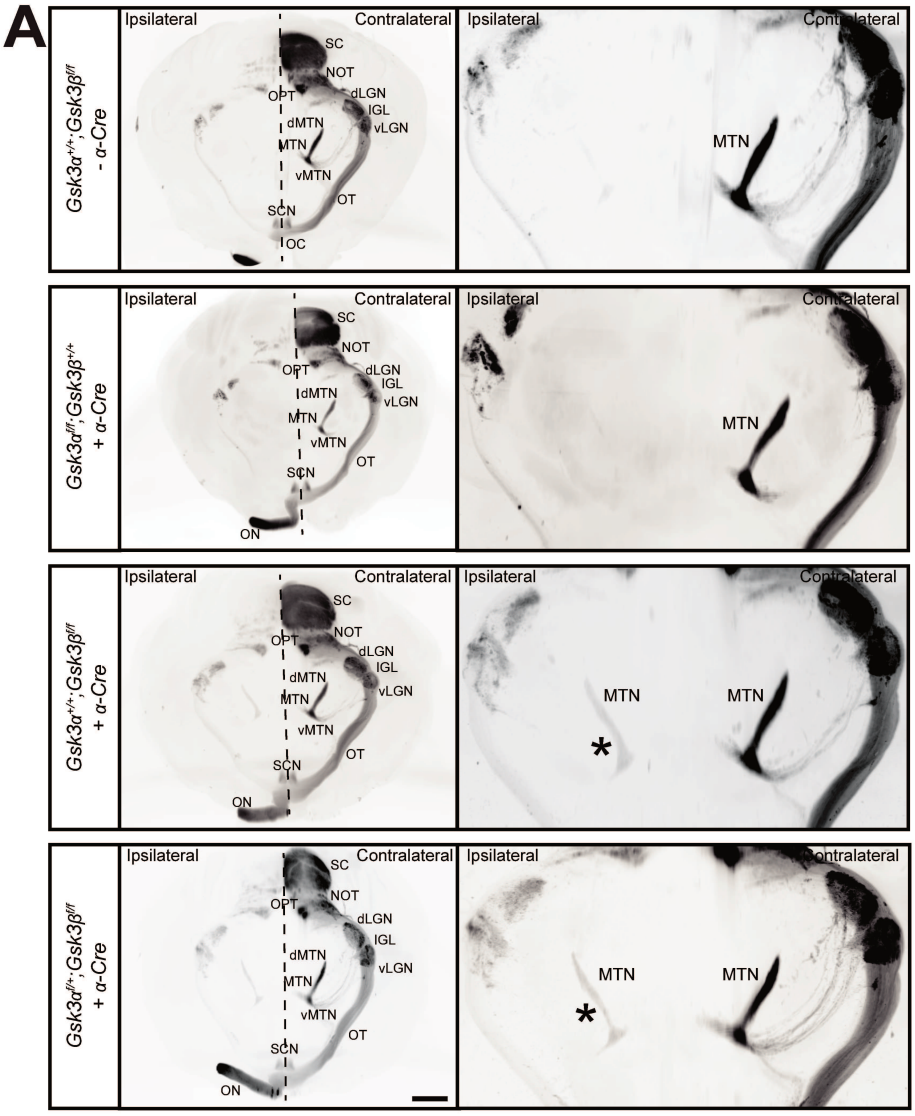
A
Gsk3α+/+;Gsk3βf/f - α-Cre
Gsk3αf/f;Gsk3β+/+ + α-Cre
Gsk3α+/+;Gsk3βf/f + α-Cre
Gsk3αf/+;Gsk3βf/f + α-Cre
Ipsilateral
Contralateral
SC
NOT
OPT
dLGN
IGL
vLGN
dMTN
MTN
vMTN
OT
SCN
OC
ON
*

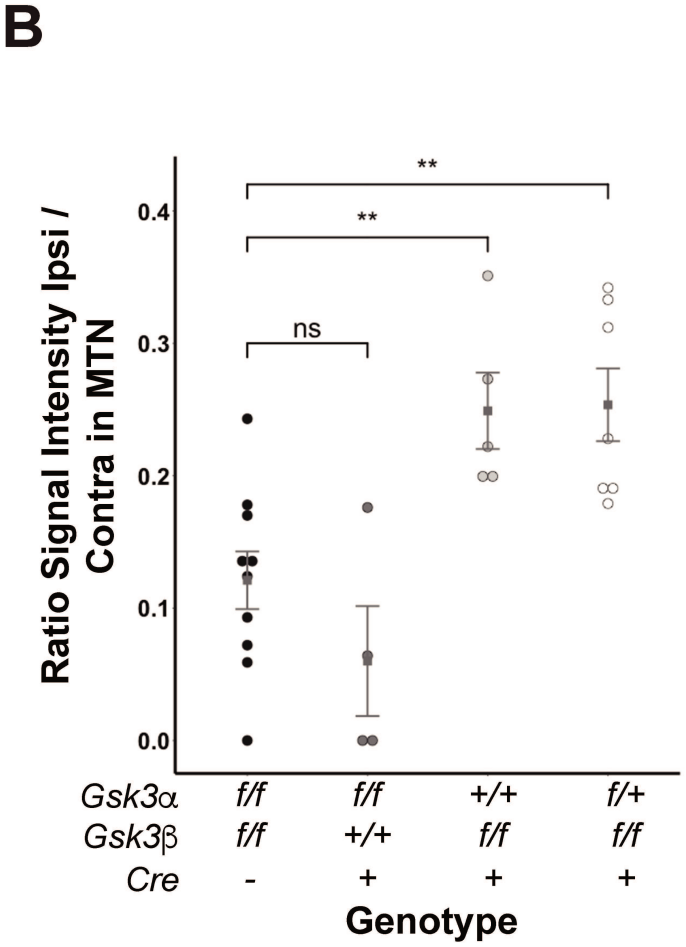
B
Ratio Signal Intensity Ipsi / Contra in MTN
0.0
0.1
0.2
0.3
0.4
ns
**
**
Gsk3α f/f f/f +/+ f/+
Gsk3β f/f +/+ f/f f/f
Cre - + + +
Genotype

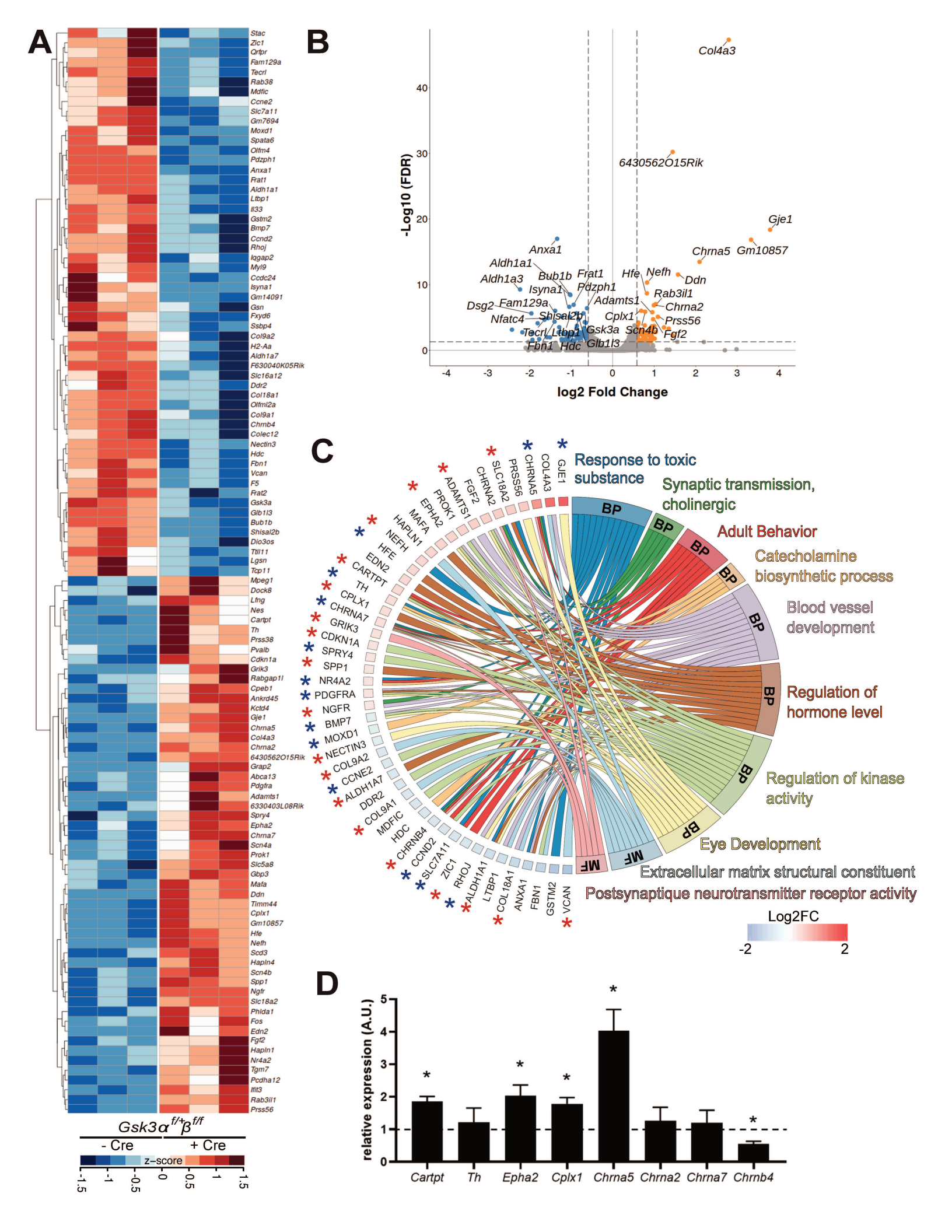
A
Stac
Zic1
Qrfpr
Fam129a
Tecrl
Rab38
Mdfic
Ccne2
Slc7a11
Gm7694
Moxd1
Spata6
Olfm4
Pdzph1
Anxa1
Frat1
Aldh1a1
Ltbp1
Il33
Gstm2
Bmp7
Ccnd2
Rhoj
Iqgap2
Myl9
Ccdc24
Isyna1
Gm14091
Gsn
Fxyd6
Ssbp4
Col9a2
H2-Aa
Aldh1a7
F630040K05Rik
Slc16a12
Ddr2
Col18a1
Olfml2a
Col9a1
Chrnb4
Colec12
Nectin3
Hdc
Fbn1
Vcan
F5
Frat2
Gsk3a
Glb1l3
Bub1b
Shisal2b
Dio3os
Ttll11
Lgsn
Tcp11
Mpeg1
Dock8
Lfng
Nes
Cartpt
Th
Prss38
Pvalb
Cdkn1a
Grik3
Rabgap1l
Cpeb1
Ankrd45
Kctd4
Gje1
Chrna5
Col4a3
Chrna2
6430562O15Rik
Grap2
Abca13
Pdgfra
Adamts1
6330403L08Rik
Spry4
Epha2
Chrna7
Scn4a
Prok1
Slc5a8
Gbp3
Mafa
Ddn
Timm44
Cplx1
Gm10857
Hfe
Nefh
Scd3
Hapln4
Scn4b
Spp1
Ngfr
Slc18a2
Phlda1
Fos
Edn2
Fgf2
Hapln1
Nr4a2
Tgm7
Pcdha12
Ifit3
Rab3il1
Prss56
Gsk3α f/+β f/f
- Cre
+ Cre
z-score
-1.5
-1
-0.5
0
0.5
1
1.5
B
Col4a3
6430562O15Rik
Gje1
Chrna5
Gm10857
Anxa1
Aldh1a1
Aldh1a3
Bub1b
Frat1
Hfe
Nefh
Ddn
Isyna1
Pdzph1
Rab3il1
Dsg2
Fam129a
Adamts1
Chrna2
Nfatc4
Shisal2b
Cplx1
Prss56
Tecrl
Ltbp1
Gsk3a
Scn4b
Fgf2
Fbn1
Hdc
Glb1l3
-Log10 (FDR)
log2 Fold Change
C
Response to toxic substance
Synaptic transmission, cholinergic
Adult Behavior
Catecholamine biosynthetic process
Blood vessel development
Regulation of hormone level
Regulation of kinase activity
Eye Development
Extracellular matrix structural constituent
Postsynaptique neurotransmitter receptor activity
BP
MF
Log2FC
-2
2
D
relative expression (A.U.)
Cartpt
Th
Epha2
Cplx1
Chrna5
Chrna2
Chrna7
Chrnb4

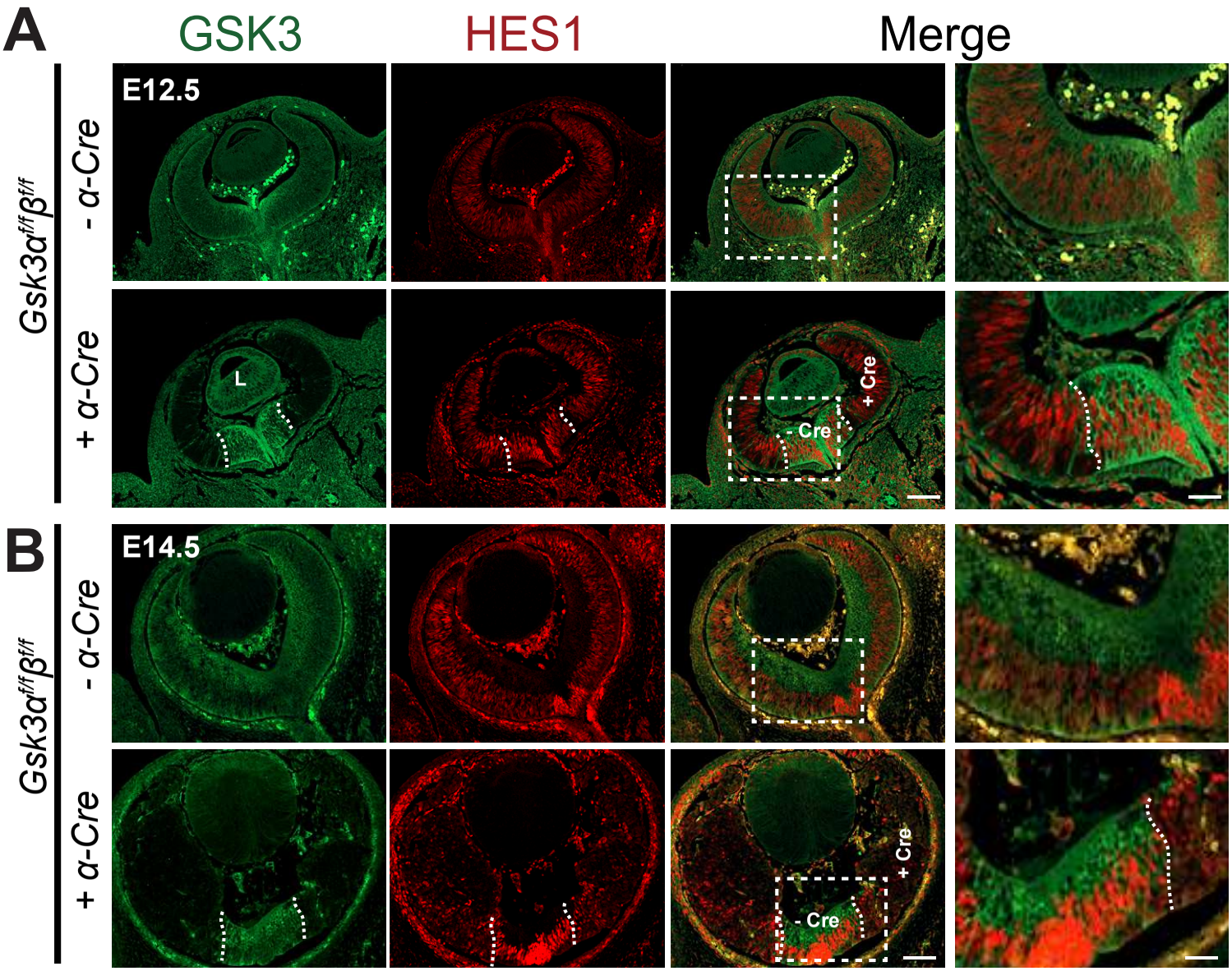
A
GSK3
HES1
Merge
E12.5
Gsk3α^f/fβ^f/f
- α-Cre
+ α-Cre
L
+ Cre
- Cre
B
E14.5
Gsk3α^f/fβ^f/f
- α-Cre
+ α-Cre
+ Cre
- Cre

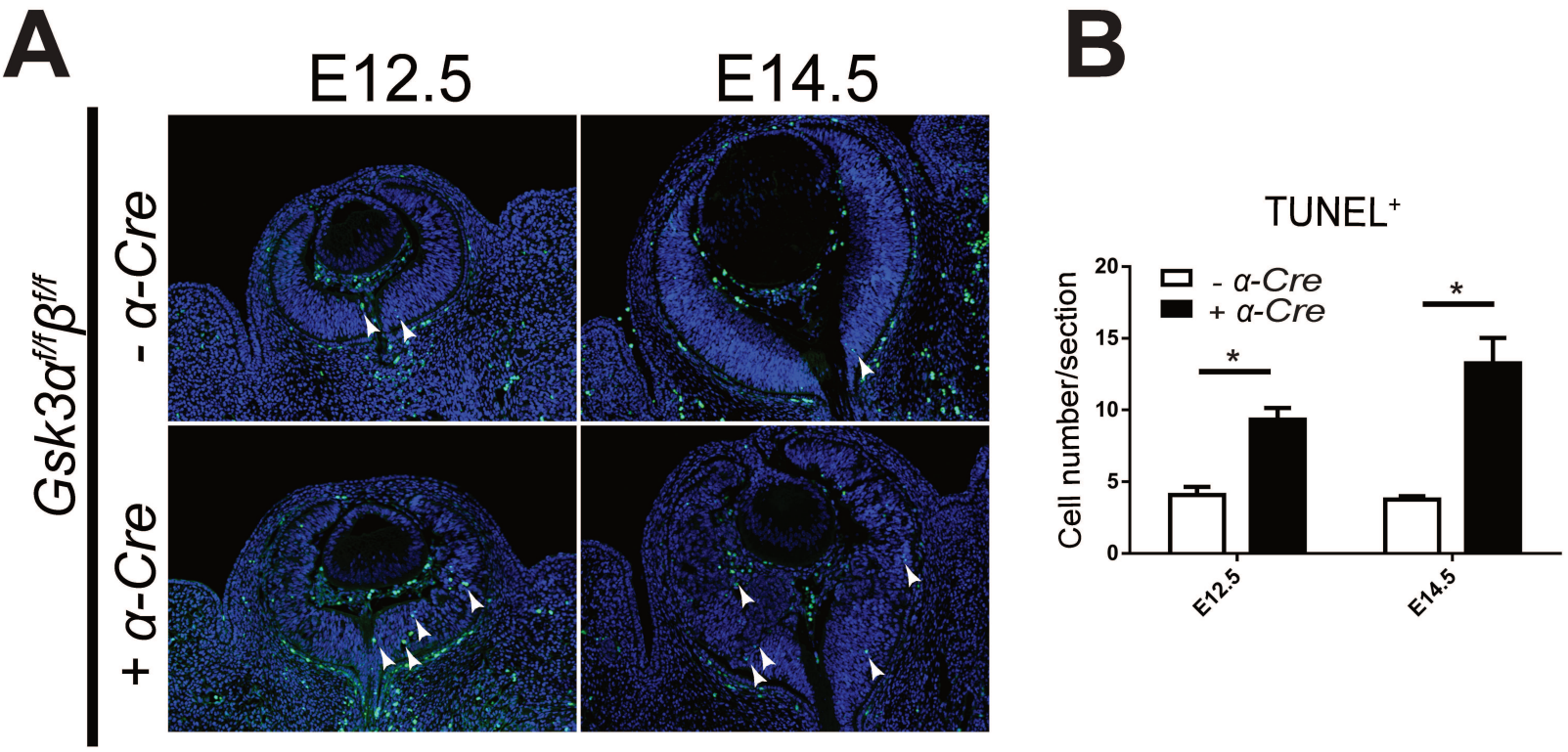
A
E12.5
E14.5
Gsk3α^f/fβ^f/f
- α-Cre
+ α-Cre
B
TUNEL+
- α-Cre
+ α-Cre
Cell number/section
20
15
10
5
0
*
*
E12.5
E14.5

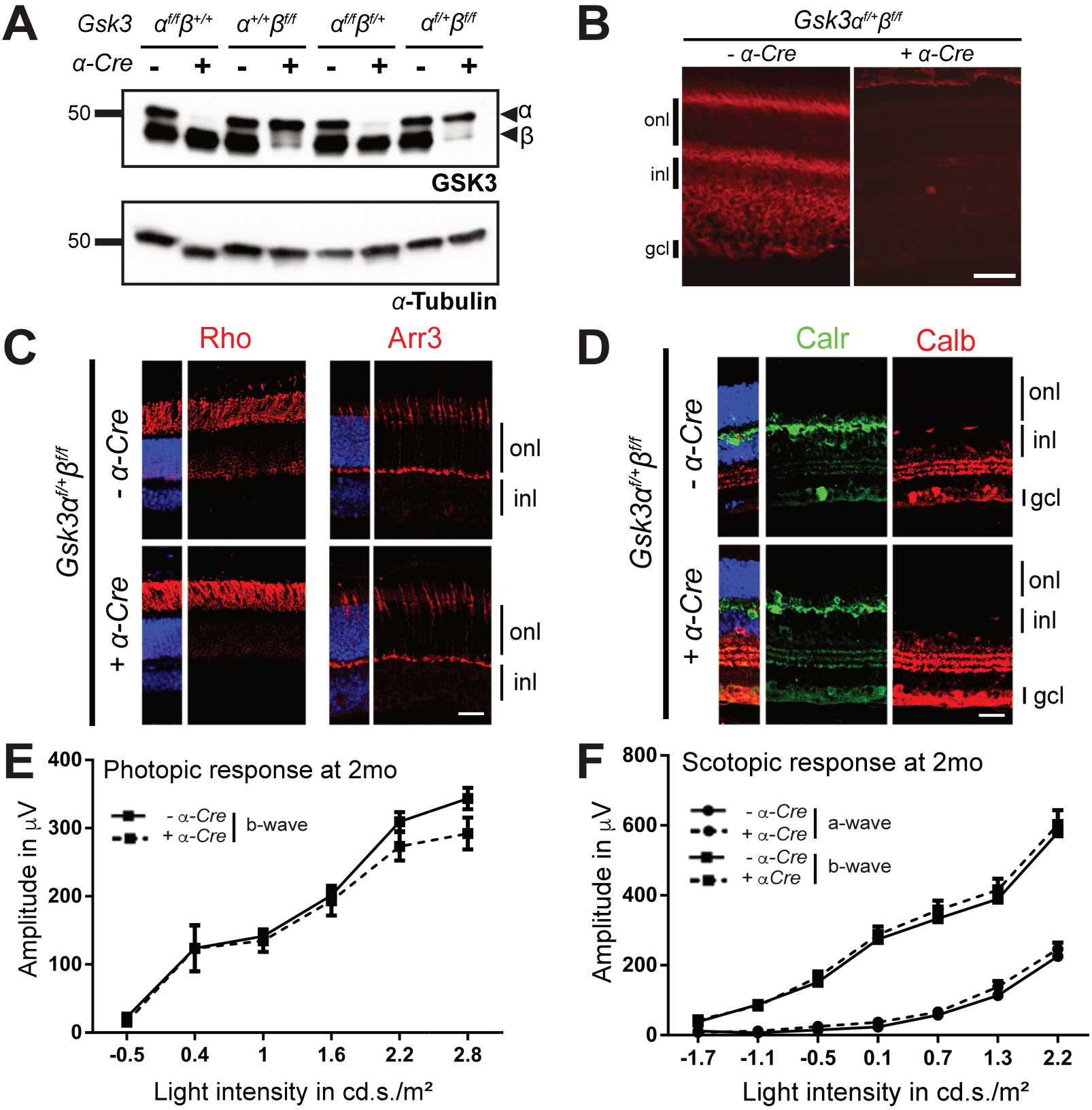
A
Gsk3
α-Cre
50
GSK3
α-Tubulin
B
Gsk3α+/+β+/+
- α-Cre
+ α-Cre
onl
inl
gcl
C
Rho
Arr3
Gsk3α+/+β+/+
onl
inl
D
Calr
Calb
E
Photopic response at 2mo
- α-Cre
+ α-Cre
b-wave
Amplitude in µV
Light intensity in cd.s./m²
F
Scotopic response at 2mo
a-wave
b-wave

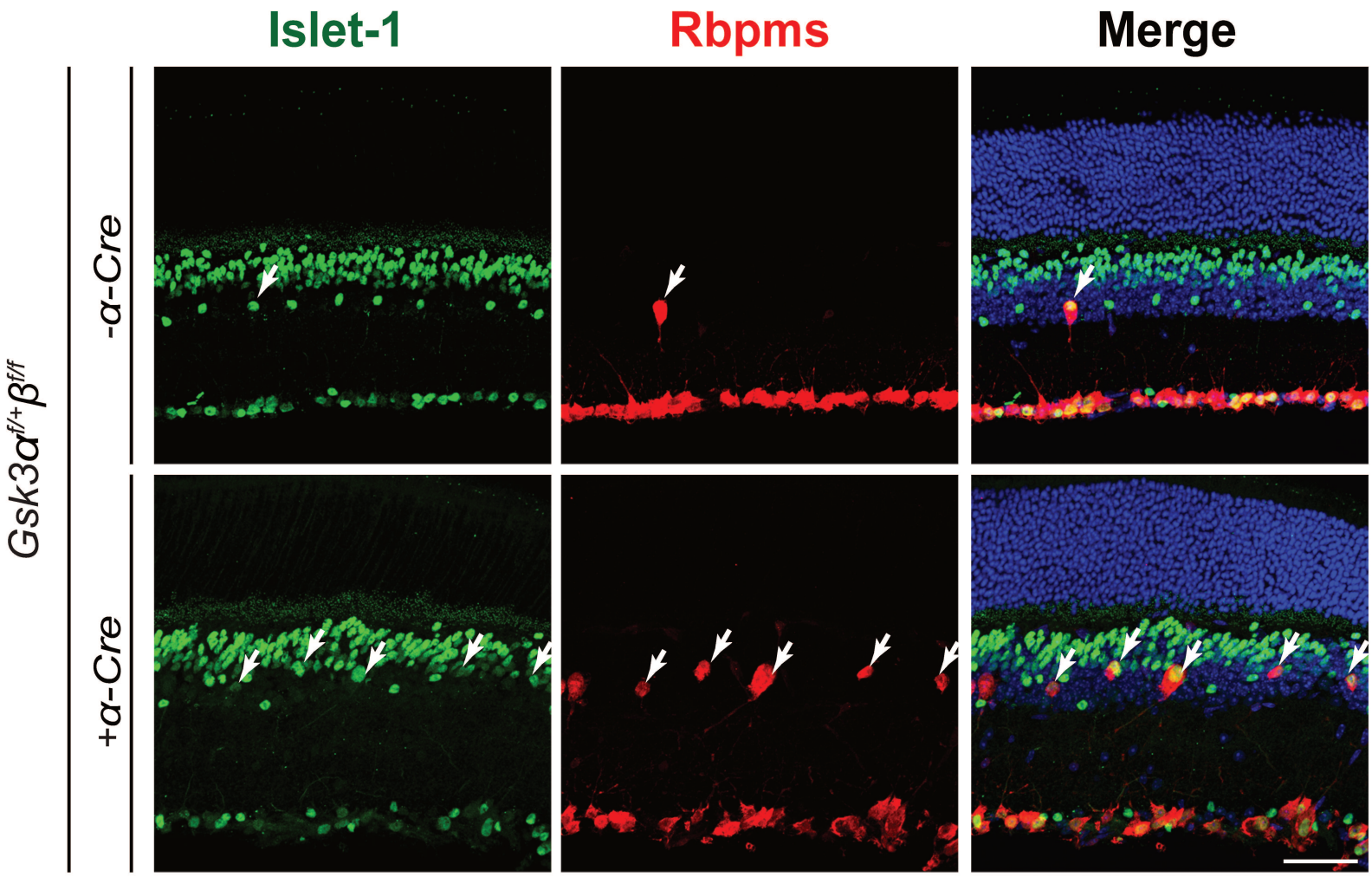
Islet-1
Rbpms
Merge
-α-Cre
+α-Cre
Gsk3α^f/+β^f/f

A

Category	ID	Term	Count	List Total	Genes	FDR
BP	GO:0009636	response to toxic substance	12	354	Chrna7, Aldh1a1, Gstm2, Anxa1, Nr4a2, Th, Slc7a11, Chrnb4, Chrna5, Chrna2, Slc18a2, Nefh	1.72E-03
BP	GO:0007271	synaptic transmission, cholinergic	5	34	Chrna7, Ngfr, Chrnb4, Chrna5, Chrna2	2.38E-03
BP	GO:0030534	adult behavior	8	193	Chrna7, Ccnd2, Nr4a2, Zic1, Slc7a11, Cartpt, Chrnb4, Chrna5	9.01E-03
BP	GO:0042423	catecholamine biosynthetic process	4	26	Hdc, Nr4a2, Th, Moxd1	1.03E-02
BP	GO:0010817	regulation of hormone levels	12	574	Chrna7, Aldh1a1, Cplx1, Edn2, Hfe, Anxa1, Pdgfra, Spp1, Aldh1a7, Cartpt, Slc18a2, Mafa	2.18E-02
BP	GO:0043549	regulation of kinase activity	14	774	Chrna7, Bmp7, Ccnd2, Ccne2, Cdkn1a, Epha2, Fbn1, Fgf2, Mdfic, Ddr2, Pdgfra, Spry4, Cartpt, Prok1	2.18E-02
BP	GO:0001654	eye development	10	402	Aldh1a1, Bmp7, Epha2, Fgf2, Pdgfra, Th, Nectin3, Prss56, Gje1, Rhoj	2.26E-02
BP	GO:0001568	blood vessel development	13	731	Chrna7, Adamts1, Bmp7, Col18a1, Col4a3, Epha2, Fgf2, Anxa1, Ngfr, Pdgfra, Rhoj, Prok1, Ltbp1	3.46E-02
KEGG	mmu04151	PI3K-Akt signaling pathway	11	346	Ccnd2, Ccne2, Cdkn1a, Col4a3, Col9a1, Col9a2, Epha2, Fgf2, Ngfr, Pdgfra, Spp1	2.69E-03
MF	GO:0005201	extracellular matrix structural constituent	8	143	Col18a1, Col4a3, Col9a1, Col9a2, Hapln1, Vcan, Fbn1, Ltbp1	2.38E-03
MF	GO:0098960	postsynaptic neurotransmitter receptor activity	5	58	Chrna7, Grik3, Chrnb4, Chrna5, Chrna2	1.03E-02
RGS	R-MMU-622327	Postsynaptic nicotinic acetylcholine receptors	4	13	Chrna7, Chrnb4, Chrna5, Chrna2	2.08E-03
RGS	R-MMU-1474244	Extracellular matrix organization	10	266	Bmp7, Col18a1, Col4a3, Col9a1, Hapln1, Fbn1, Fgf2, Ddr2, Spp1, Ltbp1	2.38E-03
TRRUST	TRR00919	Regulated by: Egr1	5	71	Chrna7, Ccnd2, Fgf2, Ngfr, Th	2.18E-02
TRRUST	TRR00820	Regulated by: Atf4	3	13	Cdkn1a, Fgf2, Ddr2	2.26E-02
TRRUST	TRR01387	Regulated by: Rbpj	3	18	Cdkn1a, Fos, Lfng	4.45E-02

B

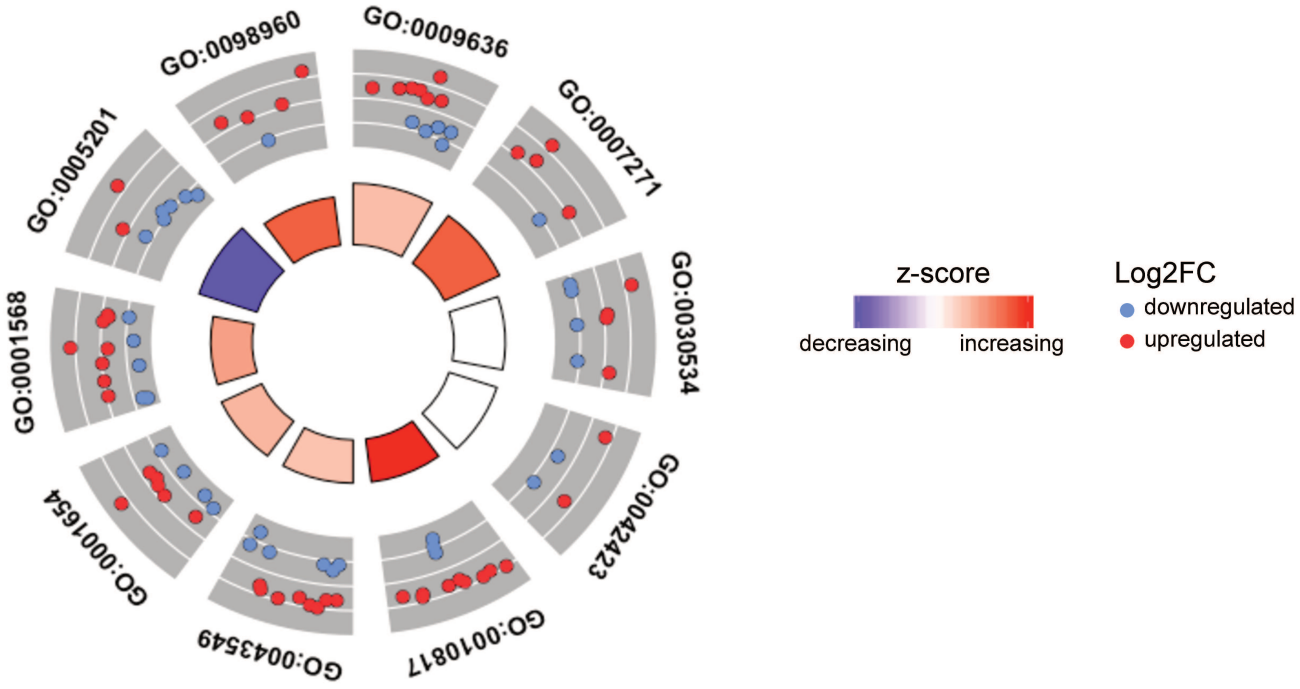

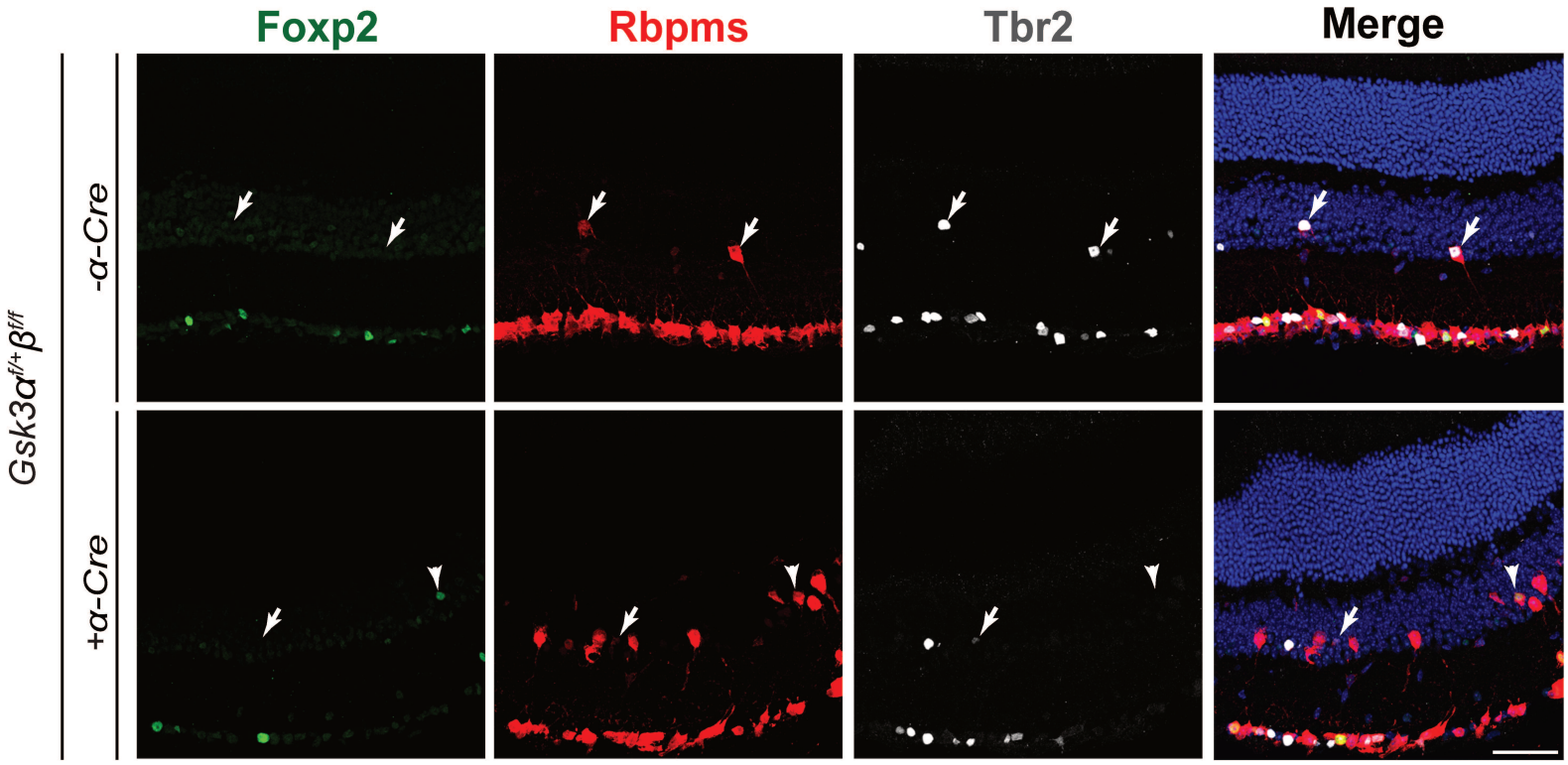
Foxp2
Rbpms
Tbr2
Merge
-α-Cre
+α-Cre
Gsk3α^f/+β^f/f

Review article: Neuroscience in the third dimension: shedding new light on the brain with tissue clearing

Robin J. Vigouroux, Morgane Belle and Alain Chédotal

Vigouroux et al. Molecular Brain (2017) 10:33
DOI 10.1186/s13041-017-0314-y

Molecular Brain

REVIEW Open Access

Neuroscience in the third dimension: shedding new light on the brain with tissue clearing

Robin J. Vigouroux, Morgane Belle and Alain Chédotal*

Abstract: For centuries analyses of tissues have depended on sectioning methods. Recent developments of tissue clearing techniques have now opened a segway from studying tissues in 2 dimensions to 3 dimensions. This particular advantage echoes heavily in the field of neuroscience, where in the last several years there has been an active shift towards understanding the complex orchestration of neural circuits. In the past five years, many tissue-clearing protocols have spawned. This is due to varying strength of each clearing protocol to specific applications. However, two main protocols have shown their applicability to a vast number of applications and thus are exponentially being used by a growing number of laboratories. In this review, we focus specifically on two major tissue-clearing method families, derived from the 3DISCO and the CLARITY clearing protocols. Moreover, we provide a "hands-on" description of each tissue clearing protocol and the steps to look out for when deciding to choose a specific tissue clearing protocol. Lastly, we provide perspectives for the development of tissue clearing protocols into the research community in the fields of embryology and cancer.

Keywords: 3DISCO, iDISCO, Clarity, Tissue-clearing, Neuroscience

Introduction

Over the past century, biological sciences have evolved from a physiological to a cellular and then a molecular understanding. In the forefront of biological sciences, novel imaging techniques have increased our ability to image biological samples to molecular resolutions through the development of two-photon microscopy, stimulated emission depletion microscopy (STED) and stochastic optical reconstruction microscopy (STORM) amongst others. Although these techniques allow high resolution, the depth at which they can image tissues is limited and as a result constrains our analysis to small volume samples or histological sections.

In recent years there has been an active shift from imaging thin samples to whole-organ, and more recently whole mammalian animals thanks to novel tissue clearing protocols. The notion of tissue clearing took birth over 100 years ago through the work of Spalteholz [1, 2]. It stemmed from an anatomical perspective to fully understand how an organ worked in its "natural" 3 dimensional (3D) form rather than in two-dimensions. Researchers quickly understood that to observe an organ in 3D they had to: i) minimize light artifacts (scattering and absorption) from the tissue, and ii) optimize microscopy techniques to achieve high resolution.

Light absorption is an inherent property of tissues due to their different chemical composition (water, proteins and lipids), which result in a heterogeneous refractive index. The key to reduce light absorption is to homogenize the refractive index of the sample by removing lipids and subsequently immersing it into a medium with a refractive index matching that of the fixed proteins in the sample. This achieves an equilibration of both intra- and extra-cellular refractive indices thereby rendering the tissue "transparent".

The quest for the ideal agent capable of homogenizing the refractive indices of tissues took a burst in early 2000's. Tissue clearing protocols have since diversified into over 10 different clearing agents. The diversity of clearing protocols is beyond the scope of this article, for a comprehensive discussion on this topic you can refer to the following recent reviews [3–6]. What has become apparent in the past five years is that the field has split

* Correspondence: alain.chedotal@inserm.fr
Sorbonne Universités, UPMC Univ Paris 06, INSERM, CNRS, Institut de la Vision, 17 Rue Moreau, 75012 Paris, France

BioMed Central

© The Author(s). 2017 **Open Access** This article is distributed under the terms of the Creative Commons Attribution 4.0 International License (http://creativecommons.org/licenses/by/4.0/), which permits unrestricted use, distribution, and reproduction in any medium, provided you give appropriate credit to the original author(s) and the source, provide a link to the Creative Commons license, and indicate if changes were made. The Creative Commons Public Domain Dedication waiver (http://creativecommons.org/publicdomain/zero/1.0/) applies to the data made available in this article, unless otherwise stated.

into two main approaches: i) solvent-based clearing, and ii) aqueous-based clearing techniques.

In this review, we aim to focus on 3D imaging of solvent-cleared organs (3DISCO) and the Clear Lipid-exchanged Acrylamide-hybridized Rigid Imaging/immunostaining/in situ hybridization-compatible Tissue hYdrogel (CLARITY)-based clearing protocols. We investigate the recent optimizations of each technique and propose a guideline for choosing the appropriate protocol for your specific scientific question.

Clearing strategies

The organic approach

Since Spalteholz's clearing procedure, using a mixture of methyl salicylate/benzyl benzoate and wintergreen oil [1, 2], three main limitations have persisted in solvent-based clearing protocols: i) tissue transparency, ii) immuno-labeling, and iii) endogenous fluorescence stability. The search for the ideal combination of solvents took a turn in the early 2000's, Dodt et al. proposed a novel combination of ethanol and hexane dehydration followed by an immersion in Benzyl Alcohol/Benzyl Benzoate (BABB) for clearing tissues [7]. This method was efficient for clearing tissues and for the first time could be coupled to Light Sheet Fluorescence Microscopy (LSFM), to image centimeter-sized samples. Whilst this method allowed the visualization of endogenous fluorescence and was amenable to immuno-labelling, the authors noted that this procedure could not fully clear adult tissues and that fluorescence was rapidly quenched (within a few hours).

To overcome these limitations, in 2012 Ertürk et al. developed a clearing protocol named 3DISCO. Instead of alcohol, the authors proposed tetrahydrofuran (THF). Whilst being a strong de-hydrating agent, THF is also a very potent de-lipidating agent. Thus, enhancing the homogeneity of the samples' refractive index. This is coupled with a supplementary de-lipidation treatment in dichloromethane (DCM) and an immersion in dibenzyl ether (DBE) as the imaging medium. The authors show that unlike the BABB protocol, they could efficiently clear entire adult tissues while maintaining the analysis of proteins using either endogenous fluorescence or immunolabelling [8–10]. In addition, they showed that 3DISCO increased the signal to noise ratio while prolonging the integrity of the fluorescence. Furthermore, this protocol could be applied to a vast array of tissues ranging from lipid-rich structures such as the brain, but also extracellular matrix-rich structures such as gingiva [6]. Overall, 3DISCO offered a standardized protocol for clearing multiple tissues in a simple, efficient and cost-effective manner that was widely applicable.

A hallmark of 3DISCO-clearing is the resulting tissue-shrinkage (Table 1). In an attempt to prevent this, Renier and colleagues developed a novel clearing protocol solely based on methanol de-hydration, the immunolabeling-enabled three-dimensional imaging of solvent-cleared organs (iDISCO+) [11]. The steadily increasing methanol concentrations result in modest tissue-shrinkage (about 10%). In addition, the "transparency" of an adult mouse brain is highly increased. Making use of this mild tissue shrinkage, Renier et al. have developed a computational pipeline for iDISCO + −cleared brains to precisely analyze axonal tracts and nuclei in respect to their anatomical location, called Clearmap.

Nonetheless, there remained the issue of endogenous fluorescence stability. To this end, Pan et al. designed a novel clearing protocol, ultimate-3DISCO (uDISCO) [12]. Firstly, using *tert*-butanol as a more stable dehydrating agent, the tissue is then treated with DCM as in prior protocols. Finally, the authors immerse the sample in an imaging medium composed of di-phenyl ether (DPE)/BABB and the anti-oxidant alpha-tocopherol (vitamin E). This imaging medium, renamed BABB-DA, was identified following a screen of organic compounds to promote both the stability of proteins and maintain high tissue transparency. Endogenous fluorescence and tissue transparency are at two ends of the spectrum. Pan et al. show that the uDISCO protocol can fluctuate between higher transparency and better endogenous fluorescence integrity depending on the ratio of DPE to BABB. Indeed, this is applied by either carrying whole-body clearing (using a high DPE ratio) or brain clearing (using a low DPE ratio). However, tuning the appropriate ratio of DPE to BABB for individual tissues to balance between endogenous fluorescence and tissue transparency is an important drawback with this protocol. Furthermore, to achieve whole-body clearing, the authors carry out a tedious protocol that requires perfusing mice for several days to weeks using BABB-DA. Together, the applicability of using uDISCO on a large scale will be quite challenging until further optimizations to the protocol are made.

The detergent approach

In 2011, Hama et al. proposed for the first time the possibility to clear tissues using an aqueous-based approach, Scale [13]. The authors showed that by using concentrated urea in an aqueous solution they could efficiently render tissue transparent. However, the harsh conditions of clearing led to significant protein loss (~41%), which brought severe limitations to studying the tissue following clearing [14].

To limit damage while maintaining high tissue transparency, Chung et al. developed in 2013 an aqueous-based clearing technique, termed CLARITY [14–16]. In principle, CLARITY consists of infusing the sample with hydrogel monomers together with temperature-sensitive

Table 1 A hands-on comparison of tissue clearing protocols

	Mouse Stages			Immuno-staining		Clearing	Endogenous Fluorescence	Tissue shrinkage	Clearing Performance	Cost	Toxicity	
	<E15	E15-P0	Adult	Before Clearing	After Clearing						Clearing Solutions	Imaging Medium
Solvents												
3DISCO	Entire embryo	Isolated organs	Isolated organs	1–3 wks	–	1 d	–	+++ (up to 50%)	+++	+	+++	+
iDISCO+	Entire embryo	Entire embryo	Isolated organs	2 wks	–	2 d	–	+ (up to 10%)	+++	+	+++	+
uDISCO	–	–	Entire animal	2 wks	–	3 d - 1 wk	Yes (up to 4 wks)	+++ (up to 40%)	+++	+	+++	+++
Reagents												
CLARITY	Entire embryo	Entire embryo	Isolated organs	–	1–3 wks	5 d - 2 m	Yes	*	++	+++	+++	–
PACT	–	–	3 mm slice	–	1–2 wks	2 wks	Yes (up to 2 m)	*	++	++	+++	–
PARS	–	–	Entire animal	–	10 d	4 d - 2 wks	Yes (up to 3 m)	*	++	++	+++	–

A comparison of most used clearing protocols. – = no information/ not applicable; + = short/low; +++ = long/high; * = varies between mounting media

polymerization initiators. Upon heating, the hydrogel polymerizes creating covalent bonds to proteins as well as taking the shape of the tissue. To clear the tissues rapidly, the authors remove lipids by bathing the sample in an ionic detergent solution coupled to an electrophoretic machine. Finally, the sample is immersed in an imaging medium. Recently, a lot of work has been done to expand the repertoire of imaging media compatible for CLARITY-cleared samples (FocusClear, RIMS, RapidClear, Diatrizoate-derived), these all contain variations of resonant rings and iodine complexes. Of note, depending on the immersion medium, the sample can either expand, shrink or maintain its initial size [17]. Alterations to this protocol are constantly updated; you can refer to the online platform: forum.claritytechniques.org. However, many aspects of CLARITY hinder its usage. Firstly, the expense of the materials from the electrophoretic tissue clearing machines to the FocusClear immersion agent (Table 1). In addition, Electrophoretic tissue clearing (active CLARITY) is relatively efficient (~5 days for an adult mouse brain) but can result in tissue degradation/distortion due to heat production by the electrophoretic machine. Finally, whilst the passive CLARITY protocol avoids this tissue perturbation, the protocol is incredibly long (~2 months for an adult mouse brain) [14, 16].

The limiting factor in the process of tissue clearing is the de-lipidation step. To address this, Yang et al. proposed an optimized passive CLARITY protocol, named passive CLARITY technique (PACT) [18]. By altering the hydrogel matrix, the authors were able to increase (passively) the rate of de-lipidation of the sample in a bath of ionic detergent, from months to 12 days for a 3 mm adult mouse brain block. PACT was shown to be suitable with immunohistochemistry and for the first time could be amenable to small-molecule fluorescent in situ hybridization (smFISH), to visualize mRNA transcripts [18]. Whilst increasing the rate of tissue clearing, Yang et al. only carry out the PACT protocol on 1-3 mm tissue blocks and not on entire organs. Indeed, the smFISH immuno-labelling was only carried out on 100 μm-thick brain slices. Furthermore, by reducing the acrylamide content of the hydrogel matrix the cleared samples are extremely fragile, which can significantly hinder the imaging potential of the tissue.

To increase the rate of de-lipidation further, the authors described an alternate protocol named perfusion assisted agent release in situ (PARS) [18]. In contrast to bathing the sample in the ionic detergent, PARS consists in continuous perfusion of clearing agents either by intra-cardiac or intra-cerebrospinal administration. Here, the authors attain a modest clearing by 4 days for an adult mouse brain to 2 weeks for an adult mouse spinal cord (Table 1). However, reproducibility of tissue clearing between animals using this method is a significant issue. Indeed, obstruction of major vessels could dramatically hinder the clearing of the tissues. In addition, the complexity of the perfusion procedure limits ones ability to screen a large number of animals at once.

Recently, an enhanced CLARITY protocol was developed. This protocol made use of both PACT and PARS protocols by reducing the acrylamide percentage and by circulating an SDS-rich solution to increase the de-lipidation rate. The authors report clearing an adult mouse brain in 12 days [19]. This is a great improvement of passive techniques, however, owing to the low acrylamide mesh, the fragility of the samples remains a major issue.

Visualizing your sample

The vast catalogue of tissue-clearing protocols published attest to the diversity of requirements from the scientific community. The purpose of clearing any tissue is to analyze a specific cell type and its distribution within a tissue of interest. This goal can be achieved by using a transgenic reporter, a viral infection, or by antibody labeling. In this section, we will describe the limitations and advantages of solvent-based or aqueous-based clearing methods in answering each of these three questions.

Immuno-fluorescence

Basic histological staining and immuno-histochemistry remain a central part of all research areas. However, immuno-stained tissues have for decades relied on thin sections and therefore a 2-dimensional observation, which inevitably provided only partial information in regards to the organization of a tissue. One striking example of this is portrayed by mouse retinal ganglion cells of the retina that extend in various directions to reach several brain targets which can span several millimeters apart [20]. To date, research groups have adapted immuno-labelling using IgG, Fab, and nanobodies ranging from 14KDa to 150KDa respectively [21, 22]. However, since most assays commonly use IgG antibodies, our discussion will focus on these.

Initially, aqueous-based protocols, such as CLARITY, provided a strong platform for immuno-labelling compatibility. Indeed, Chung et al. showed that total protein loss following 0.1% TritonX-100 treatment of paraformaldehyde fixed tissues was comparable to protein loss following CLARITY tissue clearing (24 and 8%, respectively) [14]. Whilst the authors showed CLARITY was amenable to immuno-labelling, the majority of their molecular phenotyping rested on 1 mm-thick brain blocks and only a single antibody, Tyrosine Hydroxylase, was validated for whole-brain immuno-labeling. Another strength of the CLARITY protocol was the possibility for multiple rounds of immuno-labelling by eluting previously cross-linked

antibodies. To our knowledge, until this day, only the developers of the Clarity protocol have shown multiple-round immuno-labelling on 1 mm-thick brain blocks using five antibodies (tyrosine hydroxylase, parvalbumin, glial fribrillary acidic protein (GFAP), choline acetyltransferase (ChAT), and DAPI) [14, 16]. Of note, the impact of several rounds of elution on tissues remains to be investigated, particularly whether certain epitopes could be affected in a heterogeneous manner and thus result in tissue labeling variability.

Nonetheless, one major limitation associated with CLARITY remains the diffusion of antibodies through the hydrogel matrix which depends on simple diffusion of antibodies and is a notoriously lengthy process (up to 6 weeks for an adult mouse brain) [15]. Since, derivatives of CLARITY have provided altered immuno-staining protocols by altering the hydrogel matrix which only provided a modest increase in the rate of labeling but consisted of constant antibody replenishing (every 3 days) and large volumes resulting in incredibly costly procedures [18, 21].

To optimize immuno-staining of whole-tissue, several groups have since developed a variety of protocols. The overall procedures of whole-mount immuno-labelling protocols closely resemble classical histological immuno-staining. However, one major limiting factor for in toto immuno-staining is the penetration of antibodies, which needs to be reconciled with the molecular integrity of the tissue. Espinoza et al. proposed an initial protocol which consisted in methanol de-hydration coupled to multiple freeze-thawing steps for tissue permeabilisation [23]. This protocol reduced whole-mount immuno-labeling to under a week, but was strictly applied to small mouse embryos (E10.5).

To further optimize the quality as well as the diversity of tissue types for immuno-labelling, Renier et al. proposed the immunolabeling-enabled 3DISCO protocol (iDISCO). To increase tissue permeabilisation as well as to minimize laser absorption from heme-rich tissues (hematomas), Renier et al. carry out a "bleaching" pre-treatment consisting of hydrogen peroxide in methanol (to avoid tissue damage). To further permeabilise the tissues, the authors subject them to an overnight incubation in dimethyl sulfoxide (DMSO). To increase the signal-to-noise ratio the samples are then treated with heparin and glycine. Initially coupled to 3DISCO clearing, Renier et al. have since coupled the iDISCO protocol to the iDISCO+ clearing protocol to prevent morphological damages to the tissue during clearing. The combined use of methanol and dichloromethane is aimed at permeabilizing lipid-rich adult tissues, containing complex lipids that are not soluble in the low concentrations of detergents used in classical immuno-histochemistry protocols. However, this comes with a catch 22 situation. Indeed, the iDISCO+ clearing protocol enables a greater diffusion of the IgGs in adult tissues (especially brains), but the use of methanol restricts the repertoire of antibodies compatible for immuno-labelling.

Belle et al. have since proposed an alternate immuno-labeling protocol amenable to diverse tissue types that circumvent the tedious pre-treatment steps of the iDISCO protocol [24, 25]. We propose a simple/easy-to-implement protocol that only consists of blocking buffer in combination with a detergent, saponin. The strength of using saponin is that it is a mild non-ionic surfactant with reversible permeabilising effect. Whilst currently only used in the antibody solutions, saponin could be supplemented in all incubation steps to further increase the quality of immuno-labeling. This protocol provides several advantages to the iDISCO protocol. Firstly, by removing methanol treatments, the adaptability of this immuno-labeling protocol can be applied to a wider array of antibodies. Furthermore, by removing treatments with reagents such as heparin and DMSO, the endogenous epitopes are more stable. To date, we, and others, have combined this immuno-labeling protocol to a vast diversity of tissue types and species (mouse, primate, human, xenopus, zebrafish, other mammals and birds) [24–29]. We have currently tested 102 antibodies, 64 of which have been validated and 38 that have not worked (unpublished). Currently, the specificity in epitope labeling is very diverse, ranging from trans-membrane proteins to transcription factors. Thus, we cannot yet discuss on epitope-specific limitations of our immuno-labelling protocol to clearing protocols. That being said, out of the 38 antibodies that did not work, several may be incompatible to our immuno-labeling protocol. For instance, we see that while some antibodies did not work, incubations at 24–25 °C instead of 37 °C could successfully label the samples.

All immuno-labeling protocols listed above are amenable to every solvent-based tissue clearing (Table 1). However, we suggest that when dealing with the Belle et al. immuno-labeling protocol, one should carry out the iDISCO+ clearing protocol only on large samples (such as an adult mouse brain). When working with small samples (such as mouse embryos) we suggest using the 3DISCO clearing protocol, by-passing the lengthy iDISCO+ pre-treatments that are unnecessary in small sample sizes and could potentially disrupt endogenous epitopes.

Although an incredible push has been made to apply immuno-labelling to tissue clearing, the duration of incubation remains relatively slow (Table 1). Furthermore, there is a lack of studies attempting to answer questions relating to antibody penetration patterns in 3D. To this end, Li et al. proposed to apply a linear current (<30 V) to aid in antibody penetration [21]. Indeed, the authors

report a 800-fold increase in penetration when compared to simply diffusing antibodies (staining a 4 mm-thick brain section within 30 min). Whilst this approach brings a wave of excitement, it needs to be taken with caution. Indeed, the authors reported that a net temperature increase was observed in the tissue by applying the current, which could alter epitope conformation. In addition, the tissue itself possesses a net charge and thus will also be altered by the electric current thereby altering its morphology. Further studies must focus on specific conditions required to increase antibody labeling without perturbing the tissue morphology. Recently, Kim et al. suggested that by exposing the tissue to a circular electric field rather than linear one, they could increase antibody penetration without perturbing the tissue [30]. This protocol rests on the idea that the freely moving charged antibodies would be subject to a greater displacement than the cross-linked charged proteins of the tissue. The strength in this model is that it could be coupled to other models of circular forces other than electrical. For instance, several groups have already proposed other models of forces for molecular targeting. The ACT-PRESTO protocol makes use of hydrodynamic pressure generated from a centrifugal rotation to immuno-label tissues [31]. Furthermore, one could potentially propose a magnetic force for molecular targeting.

An interesting perspective for immuno-labeling efficiency might come from the development of conjugated nanobodies, which possess lower molecular sizes (14KDa) and will bypass secondary antibody labeling. Although theoretically possible, it remains to be fully tested whether this would be compatible with clearing protocols, such as 3DISCO or CLARITY.

Endogenous fluorescence

Advances in molecular biology brought with it the era of transgenic mouse lines. This powerful tool allowed researchers for the first time to explore in vivo a diverse range of previously validate in vitro results. One of these specific tools was the use of reporters (GFP, YFP, mCherry) to observe and locate in vivo the distribution of a specific protein. With this approach, researchers could by-pass immuno-cytochemistry to label specifically a protein. A huge advantage of tissue clearing brought the potential to visualize the expression of reporter lines in 3 dimensions. With this came the question of its compatibility with clearing protocols. Indeed, this would dramatically increase the rate at which we could visualize a specific protein without the need for time-consuming sectioning techniques.

However, this task became more complicated than anticipated. Indeed, upon the first test of tissue clearing using the BABB protocol, Dodt et al. quickly realized that the endogenous fluorescence in *Thy1-eYFP* mice, although initially present, rapidly quenched (within a few hours) [7]. Presumably, the stability of the endogenous fluorescent proteins may be altered following clearing as a result of multiple factors, such as de-hydration and pH alterations. Indeed, residual water must be present for the fluorescence to persist, although this remains to be fully studied and shown.

The first protocol that offered a more stable visualization of endogenous fluorescence came with the 3DISCO protocol. Ertürk et al. could visualize: dendritic cells, macrophages, B cells, microglia, neurons, and astrocytes in the spinal cord, spleens, and lymph nodes of transgenic mice expressing *MHCII-eGFP*, *CD11c-Venus*, *CX3CR1-eGFP*, *Thy1-eYFP*, and *hGFAP-eCFP* respectively [8, 9]. Though more stable than the BABB clearing protocol, endogenous fluorescence dissipates within 2 days [9] or in cases of lower GFP expression up to 16 h (unpublished data). More recently, Pan et al. showed that the solvent-based uDISCO tissue clearing protocol maintained endogenous fluorescence for up to 4 weeks in *Thy1-eYFP*, *CX3CR1–eGFP*, and *β-actin-eGFP* mice [12] (Table 1). In addition to analyzing GFP expression in the brain, the authors demonstrate they maintain endogenous fluorescence in multiple tissue types, including bones.

The development of CLARITY-based clearing protocols led to other protocols for the study of endogenous fluorescence. Indeed, using *Thy1-eYFP* mice, Chung et al. successfully observed GFP-expressing axons in adult mouse brains following clearing [15, 16]. More recently, *Ye* et al. have successfully maintained endogenous fluorescence of brains from the *Arc-TdTomato* mouse trap line [19]. However, It remains relatively unclear the length of time CLARITY-cleared samples can maintain endogenous fluorescence. Furthermore, although CLARITY-based protocols maintain GFP/RFP expression they have only been tested using the *Arc-TdTomato* or the *Thy1-eYFP* mouse lines, both of which are notoriously known for expressing high levels of fluorescence.

Recently, a novel solvent-based clearing protocol using ethyl cinnamate (Eci) was proposed by Klingberg et al. [32]. The authors are able to clear various tissues types and maintain endogenous fluorescence in *Cd11c-eYFP* mice for up to 14 days. The de-hydration steps are done in ethanol and can be combined to all solvent-based imaging media, such as BABB and DBE. In regards to its toxicity, similarly to DBE, Eci is also a Food and Drug Administration-approved compound. However, since the de-hydration steps are carried out in ethanol, the transparency attained by this protocol remains to be fully evaluated.

Currently, the most successful clearing protocols for maintaining endogenous fluorescence remain the SeeDB 2 (See Deep Brain) and CUBIC protocols, which rely on

fructose and sucrose/triethanol amine solutions respectively [33, 34]. The main limitation with this procedure is the size of samples processed. Indeed, as of now, only small specimens or tissue slices have been successfully cleared using SeeDB or SeeDB 2. Moreover, samples are incompatible to macromolecule labeling and hence cannot be coupled to immuno-histochemistry [35].

An alternative for visualizing proteins of interest following tissue clearing is to package a reporter construct into a high-titer adeno-associated virus (AAV). In recent years, both aqueous and solvent-based clearing protocols have adapted the use of viral reporter protein expression to their protocols. *Pan* et al. have successfully traced motor neuron projections using a viral infection of AAV2-Synapsin-GFP/RFP construct [12]. On the other hand, the compatibility of AAV and rabies-virus tracing to the CLARITY protocol have also been successful to label distinct neuronal populations or to distinguish neuronal activity [19, 36, 37].

Collectively, the study of endogenous fluorescence with CLARITY and 3DISCO-related protocols remain largely to be studied. Of note, whilst several protocols have successfully maintained endogenous fluorescence none have compared the fluorescent signal levels to traditional 2D Immuno-histochemistry preparations. As a result, these studies may be underestimating the endogenous fluorescence expression patterns within the sample. Effort needs to be invested in testing supplemental transgenic reporter lines with varying expression levels in order to attest the full potential of clearing protocols in maintaining endogenous fluorescence. Importantly, an alternative strategy to by-pass endogenous fluorescence stability is by using antibodies targeted against the endogenous fluorescent proteins (GFP, YFP, mCherry) [24, 38].

The world of RNA

Until recently, clearing protocols have focused on targeting proteins, either using macromolecules such as antibodies or using transgenic mice expressing reporters. However, it has been known for some time that whole-mount in situ hybridization works relatively well. Still, most clearing protocol have not yet adapted to this approach. Yet, a wealth of information is waiting to be seized with acquiring molecular information of cells using in situ probes such as smFISH techniques.

Early reports of in situ hybridization compatible to the PACT clearing protocol were initially reported on the abundantly expressed RNA, b-actin [18]. Whilst promising, this study focused on 100 μm-thick tissue sections. Recently, the group of Deisseroth provided an optimized CLARITY protocol, compatible with smFISH labeling following clearing [39]. Sylwestrak et al. propose an improved protocol for in situ hybridization increasing cross-linking of hydrogel amine-containing monomers to nucleic acid arms, using 1-Ethyl- 3-3-dimethyl-aminopropyl carbodimide (EDC). They could efficiently label miRNAs and visualize their expression in 3-dimension. This study expands the sample size of study to 3 mm-thick brain blocks.

Thus far, no studies have proved the adaptability of solvent-based clearing protocols to mRNA analysis. However, methanol is sometimes used for whole-mount in situ hybridization and thus the iDISCO+ protocol could likely be compatible to RNA analysis. Other solvent-based protocols, such as 3DISCO and uDISCO, are yet to be studied.

Handling cleared tissues: From physical to software limitations

The "physicality" of cleared samples

Before choosing a specific clearing protocol, one should assess the "physical" components of their specific tissue. Indeed, tissues are very heterogeneous and therefore will respond differently to each clearing protocol. As listed in Table 1, the transparency reached by each clearing protocol will depend on the tissue studied. For these reasons, the following section will focus on the effect of size, handling, and further processing of tissues following solvent-based and aqueous-based clearing.

One of the critical differences between clearing protocols is the size alteration of the samples (Table 1). Whilst some aqueous-based clearing protocols have reported little-to-no size alterations, the solvent-based clearing protocols differ in that respect. CLARITY and its derivatives have shown a dynamic alteration in size, with an initial swelling of the sample, which can reduce to non-significant differences depending on the imaging medium used [17]. On the other hand, tissues cleared with 3DISCO lead to tissue shrinkage between 30 and 50% depending on tissues (with a higher shrinkage in water-rich tissues). Following methanol clearing, using the iDISCO+ protocol, tissue-shrinkage reduces modestly (About 10% in Methanol/H_2O, higher in Methanol/PBS). In addition to maintaining size, methanol-cleared tissues remain "softer". The advantage of this allows further tissue processing. However, the disadvantage is that the tissue remains more fragile than with 3DISCO-cleared samples.

Following clearing, tissues must be observed either by light-sheet, confocal, or multi-photon microscopy. However, the issue of size really comes into play when acquiring images using a light-sheet microscope. Indeed, the strength of this tool is to image large samples with little acquisition time. Whilst initially limited by the commercially available platforms, the size of samples that can be placed into the imaging reservoir has increased owing to the development of homemade platforms. However, one is restricted in regards to the size of the sample by the

working distance of the lens used. As a result, 3DISCO and uDISCO-cleared samples have an advantage over other methods such as the iDISCO+ and CLARITY. For instance, using the 3DISCO protocol, our group and others have reported successful clearing and imaging of entire human embryos and fetuses without the need for dissection [25, 40]. 3DISCO-cleared samples result in anisotropic shrinkage and therefore are incompatible with template-based registration algorithms, such as ClearMap. It remains to be studied whether uDISCO-cleared samples could be registered [11].

What the future holds

With the field only being in its infancy, one can only predict a bright future for the field of tissue clearing. Over the past decade, tissue clearing strategies have become more attuned to the ever-expending demands of cellular and molecular biology research, allowing laboratories to no longer choose between breadth and depth when analyzing a said sample.

One major potential of tissue clearing strategies is their adaptability to multiple species. Whilst several groups have successfully applied tissue clearing protocols to post-mortem human tissue sections, the full extent of human tissue applicability to clearing has not yet been studied. Undeniably, the study of human development has been a key topic of interest for many scientists and has for a century relied on 2D tissue sections of paraffin embedded embryos. Until recently, modern embryology textbooks still portrayed many of these representations. To address this, using 3DISCO and iDISCO+ clearing, we were able to successfully validate over 40 different antibodies and image entire human embryos and fetuses in 3D at cellular resolution [25]. Our findings provide insights into the specificities of human peripheral nervous system, vascular, cardiopulmonary, urogenital, and muscular development. We have elaborated a repository to harbor around 1000 acquisitions of 36 human embryos and fetuses which can be visited here: https://transparent-human-embryo.com/. Our vision is a collaborative effort of several laboratories to expand this repository into a 3D atlas for the study of human development. Tissue clearing for the study of human development is only beginning, Casoni et al. have already shed light on the advantages of using tissue clearing to study the development of gonadotropin-releasing hormone neurons in the hypothalamus of human embryos [40]. These novel studies allow for the first time an in-depth molecular analysis of human development and thus will certainly shed new light on pathological developments of human embryos and fetuses.

A further application of tissue clearing has become critical in the field of oncology. Until recently, little was known about the three-dimensional complexity of tumors in many cancers. Clinically, diagnoses have for centuries relied on 2-dimensional analysis of sections from biopsied tumors. Such techniques limit pathologists to a snapshot of the tumor. Furthermore, artifacts linked to tissue processing such as sectioning may impede the evaluation of the biopsied specimen. Since, developments of imaging tools such as X-ray computed tomography or optical coherence tomography have provided better 3D characterization of tumor but still provided poor resolution. To address these limitations, Torres et al. used BABB clearing on kidney, breast, prostate and liver biopsies followed by multi-photon microscopy [41]. The authors reported advantages such as the analysis of low-grade abnormalities in cellular growth, neoplasia, as well as a stronger detection of tumor invasion within the tissue. In addition, Van Royen et al. using BABB clearing could further apply immunohistochemistry to cleared prostate biopsies followed by confocal microscopy. Of interest, the authors note that the cleared specimens retained a high DNA yield and could further be subjected to a polymerase chain reaction [42]. The extent of tissue clearing techniques application towards the field of cancer is not limited to its clinical applications. More particularly in the field of breast cancer, several laboratories have recently begun to apply these techniques for the cellular and molecular analysis of mammary gland development as well as mammary glands dysplasia. Davis et al. recently described using CUBIC and SeeDB clearing the clonal analysis of mammary glands [43]. Furthermore, Lloyd-Lewis et al. further described the use of multiple clearing protocols on mammary gland clearing [44]. Finally, one exciting avenue for tissue clearing strategies will be the unbiased observation of entire tissues following drug administration. Such applications have already been shown on whole-brains of mice treated with antipsychotic drugs, haloperidol [11].

However, acquisition of such large raw data comes with a cost. For instance, acquiring an entire adult mouse brain can go up to 2 terabytes of data, depending on the machine used, objectives, resolution, and magnification. This number increases exponentially if this acquisition is tiled or if multiple channels of emission are acquired. As a result, the bottleneck in the field of tissue clearing is fast-becoming how to handle this complex data set. Many of the existing compression software available poorly answer the need of light-sheet acquisitions of cleared tissues; this is mostly due to the size and complexity of the data set. Though several laboratories are beginning to make ground, research will need to expand in to develop novel compression formats [45].

Taken together, whilst tissue clearing protocols have already began to shatter many of our common understandings of how tissues are organized in 3D, it is without

a doubt that its applications in new fields of research further change our understanding of function in health and disease and will become a key component of cellular and molecular biology techniques in laboratories across the globe.

Abbreviations

3DISCO: 3D imaging of solvent-cleared organs; AAV: Adeno-Associated Virus; BABB: Benzyl Alcohol/Benzyl Benzoate; CLARITY: Clear Lipid-exchanged Acrylamide-hybridized Rigid Imaging / immunostaining / in situ hybridization-compatible Tissue hYdrogel; DBE: Dibenzyl ether; DCM: Dichloromethane; DPE: Di-phenyl ether; Eci: Ethyl cinnamate; EDC: 1-Ethyl- 3-3-dimethyl-aminopropyl carbodimide; iDISCO: Immunolabeling-enabled 3DISCO protocol; iDISCO$_+$: Immunolabeling-enabled three-dimensional imaging of solvent-cleared organs; LSFM: Light sheet fluorescence microscopy; PACT: Passive CLARITY technique; PARS: Perfusion assisted agent release in situ; SeeDB: See deep brain; smFISH: small-molecule fluorescent in situ hybridization; THF: Tetrahydrofuran; uDISCO: ultimate-3DISCO

Acknowledgements:

This work was supported by grants from the Agence Nationale de la Recherche (ANR-14-CE13-0004-01) (AC). It was performed in the frame of the LABEX LIFESENSES (reference ANR-10-LABX-65) supported by French state funds managed by the ANR within the Investissements d'Avenir programme under reference ANR-11-IDEX-0004-02 (AC).

Funding

Not applicable.

Availability of data and materials

Not applicable.

Authors' contributions

RV, MB and AC contributed equally to the writing of the manuscript. All authors read and approved the final manuscript.

Ethics approval and consent to participate

Not applicable.

Consent for publication

Not applicable.

Competing interests

The authors declare that they have no competing interests.

Received: 27 April 2017 Accepted: 12 July 2017
Published online: 20 July 2017

References

1. Spalteholz W. Über das Durchsichtigmachen von menschlichen und tierischen Präparaten und seine theoretischen Bedingungen, nebst Anhang. 1914.
2. Spalteholz W. Uber das durchsichtigmachen von menchlichen und Tierichen Praparaten und Seine Theoretischen Bedingungen. Leipzig: S Hirzel; 1911.
3. Richardson D, Lichtman J. Clarifying tissue clearing. Cell. 2015;162:246–57. doi:10.1016/j.cell.2015.06.067.
4. Susaki EA, Ueda HR. Whole-body and whole-organ clearing and imaging techniques with single-cell resolution: toward organism-level systems biology in mammals. Cell Chem Biol. 2016;23:137–57. doi:10.1016/j.chembiol.2015.11.009.
5. Seo J, Choe M, Kim S-Y. Clearing and Labeling Techniques for Large-Scale Biological Tissues. Mol Cells. 2016;39:439–46. doi:10.14348/molcells.2016.0088.
6. Azaripour A, Lagerweij T, Scharfbillig C, Jadczak AE, Willershausen B, Van Noorden CJF. A survey of clearing techniques for 3D imaging of tissues with special reference to connective tissue. Prog Histochem Cytochem. 2016;51:9–23. doi:10.1016/j.proghi.2016.04.001.
7. Dodt H, Leischner U, Schierloh A, Jährling N, Mauch CP, Deininger K, et al. Ultramicroscopy: three-dimensional visualization of neuronal networks in the whole mouse brain. Nat Methods. 2007;4:331–6. doi:10.1038/nmeth1036.
8. Ertürk A, Mauch CP, Hellal F, Förstner F, Keck T, Becker K, et al. Three-dimensional imaging of the unsectioned adult spinal cord to assess axon regeneration and glial responses after injury. Nat Med. 2012;18:166–71. doi:10.1038/nm.2600.
9. Ertürk A, Becker K, Jährling N, Mauch CP, Hojer CD, Egen JG, et al. Three-dimensional imaging of solvent-cleared organs using 3DISCO. Nat Protoc. 2012;7:1983–95. doi:10.1038/nprot.2012.119.
10. Becker K, Jährling N, Saghafi S, Weiler R, Dodt H-U Chemical Clearing and Dehydration of GFP Expressing Mouse Brains PLoS One 2012;7:e33916. doi:10.1371/journal.pone.0033916.
11. Renier N, Adams EL, Kirst C, Wu Z, Azevedo R, Kohl J, et al. Mapping of brain activity by automated volume analysis of immediate early genes. Cell. 2016;165:1789–802. doi:10.1016/j.cell.2016.05.007.
12. Pan C, Cai R, Quacquarelli FP, Ghasemigharagoz A, Lourbopoulos A, Matryba P, et al. Shrinkage-mediated imaging of entire organs and organisms using uDISCO. Nat Methods. 2016;13:859–67. doi:10.1038/nmeth.3964.
13. Hama H, Kurokawa H, Kawano H, Ando R, Shimogori T, Noda H, et al. Scale: a chemical approach for fluorescence imaging and reconstruction of transparent mouse brain. Nat Neurosci. 2011;14:1481–8. doi:10.1038/nn.2928.
14. Chung K, Wallace J, Kim S-Y, Kalyanasundaram S, Andalman AS, Davidson TJ, et al. Structural and molecular interrogation of intact biological systems. Nature. 2013;497:332–7. doi:10.1038/nature12107.
15. Chung K, Deisseroth K. CLARITY for mapping the nervous system. Nat Methods. 2013;10:508–13. doi:10.1038/nmeth.2481.
16. Tomer R, Ye L, Hsueh B, Deisseroth K. Advanced CLARITY for rapid and high-resolution imaging of intact tissues. Nat Protoc. 2014;9:1682–97. doi:10.1038/nprot.2014.123.
17. Costantini I, Ghobril J-P, Di Giovanna AP, Mascaro ALA, Silvestri L, Müllenbroich MC, et al. A versatile clearing agent for multi-modal brain imaging. Sci Rep. 2015;5:9808. doi:10.1038/srep09808.
18. Yang B, Treweek J, Kulkarni R, Deverman B, Chen C-K, Lubeck E, et al. Single-cell phenotyping within transparent intact tissue through whole-body clearing. Cell. 2014;158:945–58. doi:10.1016/j.cell.2014.07.017.
19. Ye L, Allen W, Thompson K, Tian Q, Hsueh B, Ramakrishnan C, et al. Wiring and molecular features of prefrontal ensembles representing distinct experiences. Cell. 2016;165:1776–88. doi:10.1016/j.cell.2016.05.010.
20. Martersteck EM, Hirokawa KE, Evarts M, Bernard A, Duan X, Li Y, et al. Diverse central projection patterns of retinal ganglion cells. Cell Rep. 2017;18:2058–72.
21. Li J, Czajkowsky DM, Li X, Shao Z. Fast immuno-labeling by electrophoretically driven infiltration for intact tissue imaging. Sci Rep. 2015;5:10640. doi:10.1038/srep10640.
22. Lehermayr C, Mahler H-C, Mäder K, Fischer S. Assessment of net charge and protein–protein interactions of different monoclonal antibodies. J Pharm Sci. 2011;100:2551–62. doi:10.1002/jps.22506.
23. Espinosa-Medina I, Outin E, Picard CA, Chettouh Z, Dymecki S, Consalez GG, et al. Parasympathetic ganglia derive from Schwann cell precursors. Science (80-). 2014;345:87–90. doi:10.1126/science.1253286.
24. Belle M, Godefroy D, Dominici C, Heitz-Marchaland C, Zelina P, Hellal F, et al. A simple method for 3D analysis of immunolabeled axonal tracts in a transparent nervous system. Cell Rep. 2014;9:1191–201. doi:10.1016/j.celrep.2014.10.037.
25. Belle M, Godefroy D, Couly G, Malone SA, Collier F, Giacobini P, et al. Tridimensional Visualization and Analysis of Early Human Development. Cell. 2017;169:161–173.e12. doi:10.1016/j.cell.2017.03.008.
26. Reichman S, Slembrouck A, Gagliardi G, Chaffiol A, Terray A, Nanteau C, et al. Generation of storable retinal organoids and retinal pigmented epithelium from adherent human iPS cells in Xeno-free and feeder-free conditions. Stem Cells. 2017;35:1176–88. doi:10.1002/stem.2586.
27. Friocourt F, Lafont A-G, Kress C, Pain B, Manceau M, Dufour S, et al. Recurrent DCC gene losses during bird evolution. Sci Rep. 2017;7 February: 37569. doi:10.1038/srep37569.
28. Casoni F, Malone SA, Belle M, Luzzati F, Collier F, Allet C, et al. Development of the neurons controlling fertility in humans: new insights from 3D imaging and transparent fetal brains. Development. 2016;143:3969–81. doi:10.1242/dev.139444.
29. Welniarz Q, Morel M-P, Pourchet O, Gallea C, Lamy J-C, Cincotta M, et al. Non cell-autonomous role of DCC in the guidance of the corticospinal tract at the midline. Sci Rep. 2017;7:410. doi:10.1038/s41598-017-00514-z.

30. Kim S-Y, Cho JH, Murray E, Bakh N, Choi H, Ohn K, et al. Stochastic electrotransport selectively enhances the transport of highly electromobile molecules. Proc Natl Acad Sci. 2015;112:E6274–83. doi:10.1073/pnas.1510133112.
31. Lee E, Choi J, Jo Y, Kim JY, Jang YJ, Lee HM, et al. ACT-PRESTO: rapid and consistent tissue clearing and labeling method for 3-dimensional (3D) imaging. Sci Rep. 2016;6:18631. doi:10.1038/srep18631.
32. Klingberg A, Hasenberg A, Ludwig-Portugall I, Medyukhina A, Männ L, Brenzel A, et al. Fully Automated Evaluation of Total Glomerular Number and Capillary Tuft Size in Nephritic Kidneys Using Lightsheet Microscopy. J Am Soc Nephrol. 2017;28:452–9. doi:10.1681/ASN.2016020232.
33. Susaki E, Tainaka K, Perrin D, Kishino F, Tawara T, Watanabe T, et al. Whole-brain imaging with single-cell resolution using chemical cocktails and computational analysis. Cell. 2014;157:726–39. doi:10.1016/j.cell.2014.03.042.
34. Ke M-T, Fujimoto S, Imai T. SeeDB: a simple and morphology-preserving optical clearing agent for neuronal circuit reconstruction. Nat Neurosci. 2013;16:1154–61. doi:10.1038/nn.3447.
35. Poguzhelskaya E, Artamonov D, Bolshakova A, Vlasova O, Bezprozvanny I. Simplified method to perform CLARITY imaging. Mol Neurodegener. 2014;9:19. doi:10.1186/1750-1326-9-19.
36. Menegas W, Bergan JF, Ogawa SK, Isogai Y, Umadevi Venkataraju K, Osten P, et al. Dopamine neurons projecting to the posterior striatum form an anatomically distinct subclass. elife. 2015;4:1–30. doi:10.7554/eLife.10032.
37. Lerner TN, Shilyansky C, Davidson TJ, Evans KE, Beier KT, Zalocusky KA, et al. Intact-brain analyses reveal distinct information carried by SNc dopamine subcircuits. Cell. 2015;162:635–47. doi:10.1016/j.cell.2015.07.014.
38. Renier N, Wu Z, Simon D, Yang J, Ariel P, Tessier-Lavigne M. iDISCO: a simple, rapid method to Immunolabel large tissue samples for volume imaging. Cell. 2014;159:896–910. doi:10.1016/j.cell.2014.10.010.
39. Sylwestrak E, Rajasethupathy P, Wright M, Jaffe A, Deisseroth K. Multiplexed intact-tissue transcriptional analysis at cellular resolution. Cell. 2016;164:792–804. doi:10.1016/j.cell.2016.01.038.
40. Casoni F, Malone SA, Belle M, Luzzati F, Collier F, Allet C, et al. Development of the neurons controlling fertility in humans: new insights from 3D imaging and transparent fetal brains. Development. 2016;143:3969–81.
41. Torres R, Vesuna S, Levene MJ. High-resolution, 2- and 3-dimensional imaging of uncut, unembedded tissue biopsy samples. Arch Pathol Lab Med. 2014;138:395–402. doi:10.5858/arpa.2013-0094-OA.
42. van Royen ME, Verhoef EI, Kweldam CF, van Cappellen WA, Kremers G-J, Houtsmuller AB, et al. Three-dimensional microscopic analysis of clinical prostate specimens. Histopathology. 2016;69:985–92. doi:10.1111/his.13022.
43. Davis FM, Lloyd-Lewis B, Harris OB, Kozar S, Winton DJ, Muresan L, et al. Single-cell lineage tracing in the mammary gland reveals stochastic clonal dispersion of stem/progenitor cell progeny. Nat Commun. 2016;7:13053. doi:10.1038/ncomms13053.
44. Lloyd-Lewis B, Davis FM, Harris OB, Hitchcock JR, Lourenco FC, Pasche M, et al. Imaging the mammary gland and mammary tumours in 3D: optical tissue clearing and immunofluorescence methods. Breast Cancer Res. 2016;18:127. doi:10.1186/s13058-016-0754-9.
45. Amat F, Höckendorf B, Wan Y, Lemon WC, McDole K, Keller PJ. Efficient processing and analysis of large-scale light-sheet microscopy data. Nat Protoc. 2015;10:1679–96. doi:10.1038/nprot.2015.111.

Submit your next manuscript to BioMed Central and we will help you at every step:

- We accept pre-submission inquiries
- Our selector tool helps you to find the most relevant journal
- We provide round the clock customer support
- Convenient online submission
- Thorough peer review
- Inclusion in PubMed and all major indexing services
- Maximum visibility for your research

Submit your manuscript at
www.biomedcentral.com/submit


BioMed Central

Review article: Tissue clearing and light sheet microscopy – the perfect match for 3D imaging

Robin J. Vigouroux and Alain Chédotal

Tissue clearing and light sheet microscopy – the perfect match for 3D imaging

Robin Vigouroux and Alain Chédotal
Institut de la vision, INSERM UMRS 968, Paris, France

Recent developments for visualizing biological samples in three dimensions (3D) has led the biological community to re-interpret complex biological systems. This has been made possible due to converging advances in light sheet fluorescence microscopy (LSFM), tissue clearing, and molecular targeting. Here, we describe the recent advances, current limitations, and outlooks in the field.

Light sheet microscopy – a not so old principle

Since the discovery of the light sheet microscope (LSM) by Siedentopf and Zsigmondy in 1903, using illumination of colloidal solutions, LSM has become an incredibly attractive choice for biologists across the globe[1]. Indeed, it was elected method of the year by Nature Methods in 2014 [2]. Since, many developments in LSM have been made, and we will attempt to summarize these advances.

Instead of illuminating the entire sample (resulting in photobleaching), a light sheet microscope shines an orthogonal sheet of light on the sample, eliminating the optical aberrations of the classical wide-field microscopes[1]. The detection arm is placed perpendicular to the illumination laser. This simple and elegant principle provided for the first time the ability to image large biological samples without depth of scattering. Several groups applied this principle to view the surface of the *Drosophila melanogaster* compound eye or rhodamine-labeled pig cochlea[3,4]. Strikingly, it was not until a century later that the LSM was used to its full potential. In 2004, the compatibility of LSM with fluorescence signals drew much attention. However, this remained restricted to optically clear samples such as zebra fish larvae[5]. In 2007, Dodt and colleagues developed the ultramicroscope, which combined tissue clearing (BABB, see next chapter) and light sheet fluorescence microscopy (LSFM) to visualize GFP-positive neurons in large biological tissues such as the brain[6].

Although standard LSM provided an incredible step forward for biological sample imaging, several issues remained. Due to the Gaussian nature of the light sheet, the light distribution on the sample implies that only a specific area could reach maximum optical resolution (Rayleigh range). However, in LSM this range is notoriously short. Some commercial microscopes have addressed this by acquiring the area of highest resolution and tiling, a feature called dynamic focusing (LaVision Biotec, a Miltenyi Biotec company). However, this results in longer imaging times and larger datasets. Other strategies have been developed in parallel. Saghafi *et al.* proposed an ingenious setup by combining two to three aspheric lenses, which transformed the Gaussian beam into an elliptical beam, with a cylindrical lens. That way they could create an ultra-thin light sheet[7]. Recent developments of non-Gaussian beams, such as Bessel beams[8] or lattice light sheet[9], have helped reach nanometer resolution.

Multiview light sheet microscopy has been used as another strategy to reach nanometer axial and lateral resolution. In any imaging system, axial resolution remains the poorest. To circumvent this drawback, several groups have developed a method of imaging the sample in multiple orthogonal views and merging the datasets to enhance the low axial resolution by the much improved lateral resolution, resulting in an isotropic image[10–13]. Recently, the Keller group has made great improvements to these microscopes by creating adaptive optics combined with multiview light sheet microscope, SiMView, to image the developing mouse embryo from gastrulation to early embryogenesis with single-cell resolution [11,14]. McDole *et al.* were able to image the entire developing mouse embryo for up to 48 hours, a tissue whose size increases by 250-fold during this time period, without losing the tissue from the field of view.

Altogether, recent technological advances in light sheet microscopy have allowed us to gain a better understanding of developmental biology by providing i) rapid illumination – resulting in extremely low phototoxicity and photobleaching and ii) thin light sheets coupled to multiview scanning – resulting in highly resolved axial and lateral resolution.

Tissue clearing – a 3D revolution

The notion of tissue clearing began over a century ago with the work of the German anatomist Werner Spalteholz. He achieved clearing of tissues by testing different organic solvents, such as combinations of benzyl alcohol and methyl salicylate[15]. Due to the heterogeneous refractive index (RI) in a given biological sample, light is both absorbed and diffracted, resulting in an opaque appearance. However, if one harmonizes the RI of a biological tissue, by removing water and lipids, then immersion of the tissue in a medium with the same RI would render it "transparent" (fig. 1). For a long time, this practice was restricted to medical diagnostics with preparations such as Murrays clear (benzyl alcohol and benzyl benzoate, BABB) being used by embryologists. It was not until the early 2000's that the group of Hans Ulrich Dodt made this technique widely attractive to the scientific community. By combining ethanol dehydration and RI matching in BABB, Dodt *et al.* applied tissue clearing to light sheet fluorescence microscopy to visualize axons expressing a green fluorescent protein (GFP) in the whole brain of transgenic mice and to show blood vessels by making use of autofluorescent signals[6]. The sheer number of tissue clearing protocols can be reduced to two main approaches, organic solvents and aqueous solutions. We will not attempt to give a complete picture of tissue clearing protocols, but rather focus on recent advances in the most frequently used protocols. For a more thorough overview on protocols refer to these reviews [16–18].

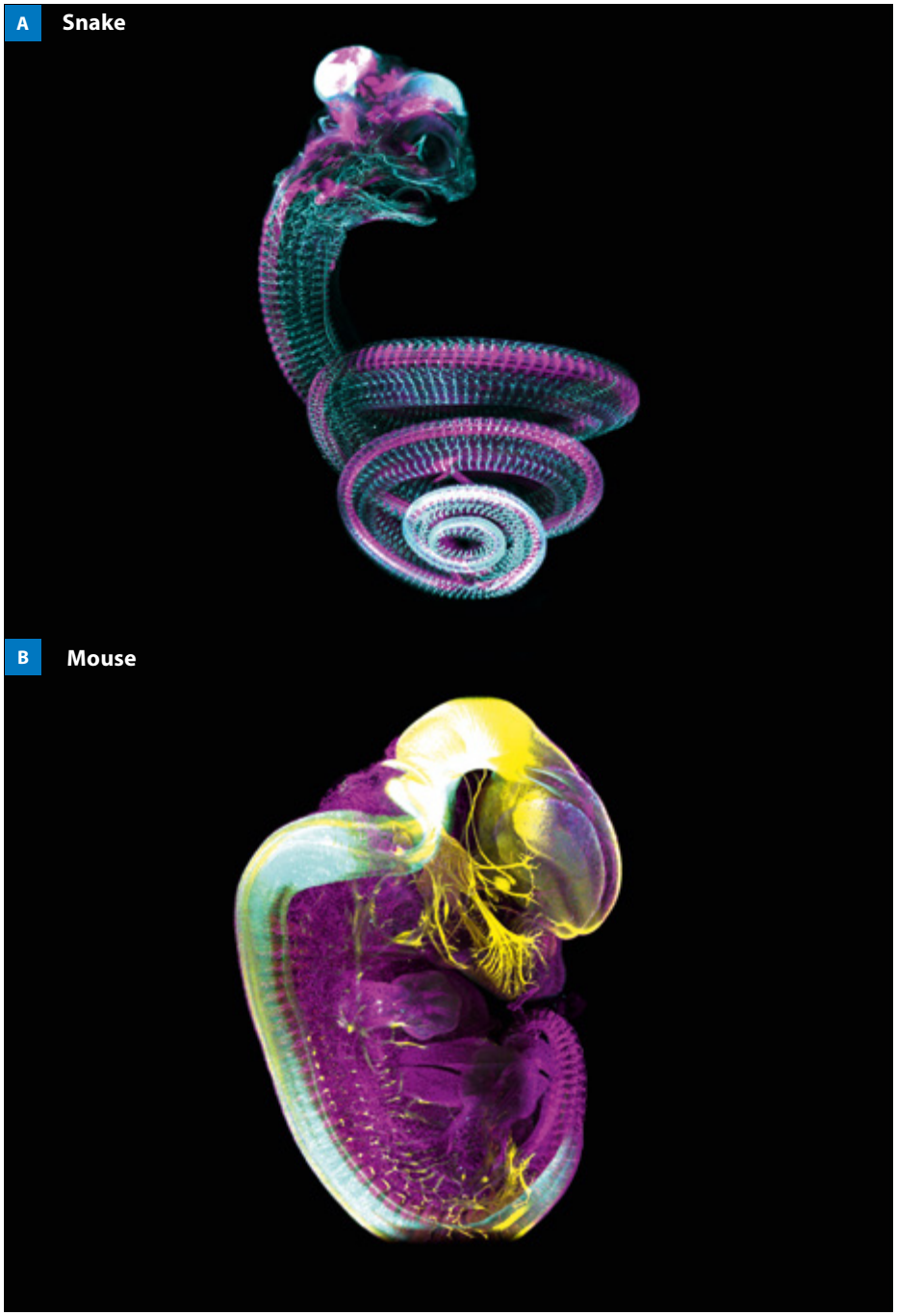

Figure 1: Tissue clearing techniques are amenable to a diversity of species. Panel A, shows a snake embryo stained for β-III tubulin (axonal marker, cyan), and FoxP2 (neuronal marker, magenta). Panel B, shows a mouse embryo stained for Robo3 (commissural neuron marker, cyan), β-III tubulin (axonal marker, yellow), and plasmalemma vesicle-associated protein (blood vessel marker, magenta).

Organic solvents have remained an attractive choice for laboratories due to the efficiency and robustness in tissue clearing. Clearing based on organic solvents consists of dehydration steps followed by delipidation and RI matching in the range of 1.56. Improvements on the initial BABB protocol led to the development of the three-dimensional imaging of solvent-cleared organs (3DISCO) protocol[19]. By replacing ethanol with tetrahydrofuran (THF) and using dibenzyl ether (DBE) instead of BABB, this protocol increased the transparency of the tissue (especially complex tissue such as the central nervous system) and reduced fluorescence quenching. This allowed the study of larger, more complex organs such as adult mouse brains. Several issues remained though. For instance, reports of anisotropic tissue shrinkage caused by the 3DISCO protocol hindered the ability to reconstruct or map areas of interest in 3D. To address this, Renier and colleagues developed the iDISCO+ protocol, which consisted of gradual dehydration of the sample in methanol followed by delipidation and RI matching in DBE[20]. This protocol significantly reduced the extent of tissue shrinkage. Altogether, Renier and colleagues could develop a mapping

system to track newly activated neurons in intact brains, ClearMap.

The loss of endogenous fluorescence remained a major hurdle for clearing protocols based on organic solvents. To this end, Pan *et al.* proposed the ultimate DISCO (uDISCO) protocol combining tert-butanol dehydration and RI matching in a cocktail of BABB, diphenyl ether, and vitamin E. The authors reported endogenous fluorescence pre- servation for up to 4 weeks [21]. However, this protocol remained challenging due to i) thetoxicity of the reagents, ii) the need to carry out the reactions at 35–40 °C, and iii) the need to fully perfuse the mice for several days. Although the effects of both temperature and pH on fluorescent proteins had previously been reported in the literature [22], none of the publications connected these effects with organic-solvent clearing protocols. To address this, the group of Matthias Gunzer developed an ethanol-based clearing protocol followed by RI matching in ethyl cinnamate (ECi) [23]. ECi is a compound approved by the US Food and Drug Administration, and therefore biosafety is an interesting feature of this protocol. In addition, by adjusting the pH of ethanol, Klingberg *et al.* maintained endogenous fluorescence for up to 14 days. However, ethanol-based dehydration provides only a moderate dehydration method. Therefore, ECi-based clearing should be chosen for samples that can be cleared easily.

Since then, Masselink *et al.* have generated a second-generation ECi protocol based on pH-adjusted propanol [24]. It should be noted that the RI of ECi closely matches that of DBE or BABB (ECi: 1.558; BABB: 1.559; DBE: 1.562). We have observed that following 3DISCO/iDISCO+ clearing, the samples can be imaged successfully in ECi for up to 3 hours (data not shown). Recently, Qi *et al.* proposed an alternative protocol for the preservation of endogenous fluorescence by altering pH and temperature of THF, the DISCO with superior fluorescence-preserving capability (FDISCO) [25]. The authors reported eGFP maintenance for up to 7 months. However, a major drawback exists when modulating the temperature of organic-based clearing: Storage of samples at 4 °C will lead to condensation in the vials and thus result in the presence of water which can re-opacify the sample.

To bypass the necessity of endogenous fluorescence preservation, several groups, including ours, developed immunolabeling protocols compatible with tissue clearing. These protocols closely resemble classical histological immunostaining with the main difference being antibody penetration. Espinosa *et al.* carried out multiple freeze-thaw cycles in methanol prior to immunolabeling [26]. Renier *et al.* developed a bleaching step (removal of hematomas) together with the use of heparin and glycine and reported an increase in the signal to-noise ratio [27]. Belle *et al.* increased antibody penetration by i) combining permeabilization reagents (Triton X-100® and saponin) and ii) increasing antibody mechanics (incubation at 37 °C) [28]. More recently, the group of Ali Ertürk has developed a perfusion-assisted protocol, the so-called nanobody (VHH)-boosted 3D imaging of solvent-cleared organs (vDISCO) [29]. This protocol comprises intracardial perfusion of Atto/Alexa Fluor®–coupled nanobodies to enhance endogenous fluorescent epitopes by a factor of 1–2. Nanobody-driven immunostaining will be discussed later.

Although, initially, organic-based clearing has been implemented in laboratories more easily than aqueous-based clearing, recent development in aqueous-based protocols has quickly leveled the two techniques in regard to their feasibility, reproducibility, and efficiency. In addition, aqueous-based processes have the advantage of biosafety and endogenous fluorescent protein maintenance. Two main principles exist in aqueous-based clearing, hydrogel-based clearing and RI matching using low RI media. Initial drawbacks of aqueous tissue clearing were either i) high transparency only after long incubation times, ii) costly procedures, or iii) high transparency only with small sample size (1 cm^3 slices). To address these main issues, the group of Ueda deconstructed the clearing process into four main steps: decalcification, decolorization, delipidation, and RI matching. They then developed a screening strategy to identify major functional groups required in hydrophilic compounds to achieve each critical step. Over 1,600 chemical compounds were screened. Amino alcohols resulted in most efficient delipidation and decolorization, whereas aromatic amides provided best RI matching. Taken together, Tainaka and colleagues provided four novel clear unobstructed brain imaging cocktails and computational analysis (CUBIC) protocols for: i) mouse organs, ii) whole mouse or bones, iii) human tissues, and iv) complex tissues [30]. To date, recent CUBIC protocols have been used on multiple organs as well as whole mouse [30–33].

In addition to hydrophilic aqueous solutions, hydrogel-based clearing protocols have provided another platform for robust tissue clearing. The first hydrogel-based clearing method, named CLARITY, depended on the perfusion of the organ with hydrogel monomers and subsequent heating for polymerization. This resulted in a scaffold that covalently cross-linked to protein in the tissue. The remaining "undesired" tissue was then removed using electrophoresis or a passive SDS bath. The major issue with this protocol was the implementation of the technique in non-expert laboratories. Although this technique became commercialized, the cost to carry out the protocol was incredibly high. To address these issues, several protocols were developed by the Gradinaru group at Caltech. The passive clarity technique (PACT) protocol decreased the hydrogel matrix concentration, which noticeably reduced the duration of the clearing procedure (~3 days for an adult mouse brain) [34]. However, reducing the hydrogel matrix concentration turned out to be a double-edged sword as it resulted in incredibly fragile tissues that became very difficult to image or handle. In addition, Yang *et al.* proposed the perfusion-assisted agent release *in situ* (PARS) protocol [34]. In contrast to passive clearing, this protocol took advantage of the vasculature to perfuse the clearing agents, for time efficiency as well increased delivery. Here, the problem became the difficult implementation of large-scale clearing.

By making use of hydrogel technologies, the Boyden group devised a protocol for polymer scaffolding that could swell when subjected to hyper-hydrating solutions[35]. This neat technique allowed for the first time the visualization of nanometer resolution and propelled the field forward towards superresolution imaging. Recently, the Ueda group has developed a CUBIC protocol compatible with expansion microscopy to expand the volume of the whole mouse brain by 10-fold and thus reach single-cell resolution[33].

Decolorization of a sample is critical since it helps to harmonize the color of the tissue. In addition, certain tissues possess concentrated coloration which blocks the laser path even following clearing, for example the retinal pigment epithelium or the melanin present in the skin. The group of Hans Ulrich Dodt has recently published a decolorization protocol for *Drosophila melanogaster* clearing, termed Flyclear[10]. This procotol stems from the first-generation CUBIC protocols, except for a change from Quadrol to 2,2',2'',2'''-ethylenedinitrilo-tetraethanol (THEED). The group of Ueda has also proposed an efficient decolorization protocol using N-alkylimidazole. However, this protocol was specifically designed to decolor heme-rich tissues[30]. Until now no protocol has been able to completely decolor the heavily pigmented mouse retinal pigment epithelium. To address this major void in the literature, we have developed a protocol which allows the clearing of the entire pigmented eye (manuscript in preparation). This protocol is compatible with multiple organic-based solvents, iDISCO+, 3DISCO, and ECi clearing. We have also attempted to adapt our protocol to aqueous-based clearing. However, the eye is composed of heterogeneous tissues which vary in composition, from the very dense sclera to the much softer retina. Clearing with aqueous solutions results in expansion of the tissue and strong deformation, and therefore, such techniques are not appropriate for clearing the entire intact eye. Our protocol provides the opportunity to remove highly concentrated melanophores from tissues and therefore provides a protocol that could clear difficult tissues such as highly vascularized samples or highly pigmented tissues such as skin.

Within the immensity of tissue clearing protocols available, new users are often left with the dilemma of which one to choose. Here the key is always the precise biological question one is attempting to answer. There is no universal best choice, because each protocol has its own advantages or disadvantages.

Detection of endogenous proteins – the last limiting step

The combination of advanced LSFM coupled to efficient and robust tissue clearing techniques now pave the way for solving complex biological questions. Although several protocols help to preserve endogenous fluorescence, we are currently restricted to only few fluorescent reporters. In addition, the expression of fluorescent reporters is restricted to transgenic models, and thus limits the molecular analysis of other species. Therefore, the development of new strategies for molecular targeting are required. Here, we will describe novel protocols and future possibilities.

A major approach for molecular targeting is antibody labeling. However, the main hurdle for whole-mount immunolabeling remains the passive diffusion of large antibody complexes across biological samples. In addition, antibody penetration across the entire sample is not always achieved, depending on tissue properties and size. To increase the rate of antibody labeling, several approaches are conceivable: exposing the sample to an electrical current or subjecting the sample to hydrodynamic pressure, thus driving convective flows across the sample. However, both approaches would damage soft and fragile tissues. In this effort, Kim *et al.* proposed a stochastic electrotransport protocol to increase the rate of antibody diffusion[36]. The authors theorized that by applying a rotational electric field around a biological sample, only freely available charged molecules would be displaced, whereas cross-linked molecules would be unaltered. Their protocol enabled labeling of an 8 mm × 7 mm polymer using BSA-FITC in under 3 hours. In addition to immunolabeling, the authors also reported increasing rates of tissue clearing.

More recently, the group of Erturk proposed the vDISCO protocol to amplify the signal of endogenous fluorescent proteins by perfusing fluorescently coupled nanobodies (V_HH)[29]. To this day, the use of V_HH in whole-mount immunostaining is poorly studied. In comparison to traditional primary and secondary antibody complexes (>300 kDa), coupled nanobodies are more than 20-fold smaller (12–15 kDa). This provides a major step towards effective antibody diffusion and penetration across complex biological samples. Moreover, fluorochrome-conjugated nanobodies bypass the need for labeling with secondary antibodies and thus provide an invaluable gain of time. However, to date the usage of passive whole-mount immunostaining with nanobodies has not been tested. Another area of advancement will be the generation of more robust and photostable fluorescent dyes. Currently available dyes, i.e., Atto and Abberior® STAR dyes, possess high fluorescence quantum yields and decay times. They have been heavily used in superresolution microscopy, which demands robust and bright dyes. Their use in whole-mount immunostaining coupled to tissue clearing however has been very little studied.

One major hurdle when it comes to tissue processing, be it sectioning or tissue clearing, is the finality of the process. Whilst several groups have focused on optimizing the antibody labeling or imaging quality, little efforts have been made towards maximizing the usage of a given biological sample. To that end, we have developed a protocol, multiple round DISCO (MR-DISCO) (manuscript in preparation), that allows: i) sectioning and imaging of cleared tissues at high resolution, ii) sectioning and targeting of mRNA, and iii) multiple rounds of immunolabeling of 3D tissue. This provides for the first time the possibility to reuse a sample and potentially describe highly complex structures in a single specimen (fig. 2). Whilst these developments provide a huge step forward in the field, there are certain limitations to this process. Consecutive rounds of clearing lead to a progressive shrinkage of the sample. Therefore, the development of software that enables adaptive measurement of tissue shrinkage must be developed to fully merge consecutive rounds of imaging into a single individual atlas.

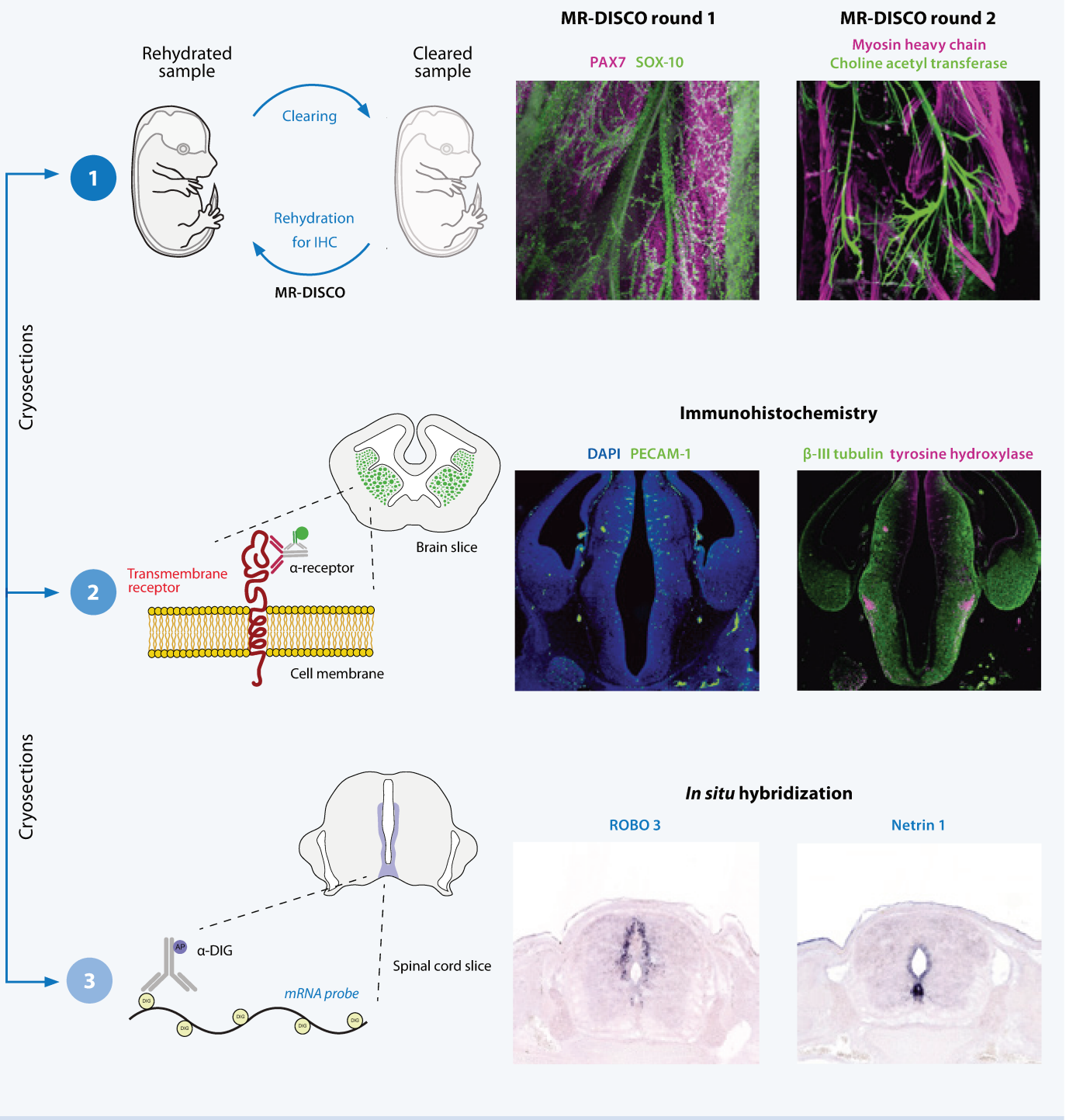

Figure 2: Multiple-Round DISCO, a novel tissue processing workflow. MR-DISCO provides the ability to carry out a classical whole-mount immunostaining followed by tissue clearing, which can then be reversed by re-hydrating the sample and immunostaining again. This process can be coupled to tissue clearing, as shown in panel 1, or be coupled to cryosectioning for either immunohistochemistry (panel 2) or *in situ* hybridization (panel 3). Panel 1 shows an embryonic limb labeled for PAX7 (muscle precursors, magenta), and SOX-10 (Schwann cell precursors, green). Following re-hydration (MR-DISCO round 2), the same sample was immunostained for myosin heavy chain (muscle fibers, magenta), and choline acetyl transferase (motor axons, green). Panels 2 and 3 show sections from embryos first processed with MR-DISCO and then cryosectioned. For panel 2, brain sections were then immunostained for DAPI (nuclear marker, blue), PECAM-1 (blood vessel marker, green), tyrosine hydroxylase (dopaminergic and noradrenergic neurons, magenta), and β-III tubulin (axonal marker, green). For panel 3, spinal cord sections were hybridized with probes for ROBO3 mRNA (commissural neurons) and netrin 1 mRNA (floor plate and ventricular zone).

Outlook

Tissue clearing rose to fame in the past few years thanks to a century of optimizations in: i) optical devices such as LSFM, ii) robust, bright, and stable dyes, and iii) tissue clearing reagents. This interdisciplinary field is fast moving and has indisputably become central to biological research.

Protein targeting has been made possible thanks to multiple protocols adapting immunolabeling towards tissue clearing techniques. In recent years, novel technologies have allowed us to visualize multiple RNAs using small molecule fluorescent *in situ* hybridization (smFISH)[37,38]. Furthermore, the development of multiplexed *in situ* hybridization (MERFISH) and seqFISH provide an unlimited targeting of RNA in tissue sections[39,40]. Coupling this with tissue clearing techniques could give us access to data on single-cell RNA expression and localization in entire organs. Towards this goal, the group of Deisseroth developed a spatially-resolved transcript amplicon readout mapping (STARmap). The authors could amplify over 1,000 genes in cortical slices. Combinations of molecular analysis (MERFISH), cellular lineage labeling (brainbow), and tissue clearing could deliver data on molecular identity through to cellular morphology. Therefore, the development of tissue clearing techniques combined with molecular targeting approaches is at the forefront of the field.

In regard to public health, it is without a doubt that tissue clearing technologies will lead to breakthroughs in the fields of embryology[41] or cancer biology[31,32]. For instance, the development of 3D tissue clearing protocol applicable to cancer biopsy samples will provide an immensely more comprehensive picture to pathologist than current techniques.

References

1. Siedentopf, H. and Zsigmondy, R. (1903) Ann. Phys. 10: 1–39.
2. Method of the Year 2014. (2015) Nat. Methods 12: 1.
3. McLachlan, D. (1964) Appl. Opt. 3: 1009–1013.
4. Voie, A. H.*et al.* (1993) J. Microsc. 170: 229–236.
5. Huisken, J. *et al.* (2004) Science 305: 1007–1009.
6. Dodt, H. U. *et al.* (2007) Nat. Methods 4: 331–336.
7. Saghafi, S. *et al.* (2018) Microsc. Res. Tech. 81: 929–935.
8. Planchon, T. A. *et al.* (2011) Nat. Methods 8: 417–423.
9. Chen, B. C. *et al.* (2014) Science 346: 1257998.
10. Pende, M. *et al.* (2018) Nat. Commun. 9: 4731.
11. McDole, K. *et al.* (2018) Cell 175: 859–876
12. Royer, L. A. *et al.*, (2016) Nat. Biotechnol. 34: 1267–1278.
13. Tomer, R. *et al.* (2012) Nat. Methods 9: 755–763.
14. Royer, L. A. *et al.* (2018) Nat. Protoc. 13: 2462–2500.
15. Spalteholz, W. (1914) S. Hirzel, Leipzig.
16. Jensen, J. H. (2015) Annu. Rev. Biophys. 47: 355–376.
17. Richardson, D. S., and Lichtman, J. W. (2015) Cell 162: 246–257.
18. Vigouroux, R. J. *et al.* (2017) Mol. Brain 10: 33.
19. Ertürk, A. *et al.* (2012) Nat. Protoc. 7: 1983–1995.
20. Renier, N. *et al.* (2016) Cell 165: 1789–1802.
21. Pan, C. *et al.* (2016) Nat. Methods 13: 859–867.
22. Alkaabi, K. M. *et al.* (2005) 126: 149–156.
23. Klingberg, A. *et al.* (2017) J. Am. Soc. Nephrol. 28: 452–459.
24. Masselink, W. *et al.* (2019) Development 146: dev166884.
25. Qi, Y. *et al.* (2019) Sci. Adv. 5: eaau8355.
26. Espinosa-Medina, I. *et al.* (2014) Science 345: 87–90.
27. Renier, N. *et al.* (2014) Cell 159: 896–910.
28. Belle, M. *et al.* (2014) Cell Rep. 9: 1191–1201.
29. Cai, R. *et al.* (2019) Nat. Neurosci. 22: 317–327.
30. Tainaka, K. *et al.* (2018) Cell Rep. 24: 2196–2210.
31. Nojima, S. *et al.* (2017) Sci. Rep. 7: 1–14.
32. Kubota, S. I. *et al.* (2017) Cell Rep. 20: 236–250.
33. Murakami, T. C. *et al.* (2018) Nat. Neurosci. 21: 625–637.
34. Yang, B. *et al.* (2014) Cell 158: 945–958.
35. Chen, F. *et al.* (2015) Science 347: 543–548.
36. Kim, S. Y. *et al.* (2015) Proc. Natl. Acad. Sci. USA 112: E6274–E6283.
37. Raj, A. *et al.* (2006) PLoS Biol. 4: e309.
38. Thummel, C. *et al.* (1992) Science 255: 39–40.
39. Chen, K. H. *et al.* (2015) Science 348: aaa6090-aaa6090.
40. Lubeck, E. *et al.* (2014) Nat. Methods. 11: 360–361.
41. Belle, M. *et al.* (2017) Cell 169: 161–173.

Review article: Construction and reconstruction of brain circuits: normal and pathological axon guidance

Robin J. Vigouroux*; Sergi Roig-Puiggros*, Danielle Beckman, Nadia I Bocai, Brian Chiou, Joshua Davimes, Gimena Gomez, Sara Grassi, Ashfaqul Hoque, Thomas K Karikari, Frederico Kiffer, Mary Lopez, Giulia Lunghi, Pedzisai Mazengenya, Sonja Meier, Mauricio Olguín-Albuerne, Mauricio M Oliveira, Juan Paraíso-Luna, Jonu Pradhan, Andressa Radiske, Ana Belén Ramos-Hryb, Mayara C Ribeiro, Roberta Schellino, Maria Clara Selles, Shripriya Singh, Paschalis Theotokis, Alain Chédotal

Contribution: R. J. Vigouroux, S. R. Puiggros, and A Chédotal led and coordinated the overall review. R. J. Vigouroux wrote the sections on forebrain development and spinal cord regeneration.

Journal of Neurochemistry

JNC

JOURNAL OF NEUROCHEMISTRY | 2020 | 153 | 10–32

doi: 10.1111/jnc.14900

REVIEW

Construction and reconstruction of brain circuits: normal and pathological axon guidance

Sergi Roig-Puiggros[1,*], Robin J. Vigouroux[1,*], Danielle Beckman[2], Nadia I. Bocai[3,4], Brian Chiou[5], Joshua Davimes[6], Gimena Gomez[7], Sara Grassi[8], Ashfaqul Hoque[9], Thomas K. Karikari[10,11,12], Frederico Kiffer[13,14,15], Mary Lopez[16], Giulia Lunghi[17], Pedzisai Mazengenya[18], Sonja Meier[19], Mauricio Olguín-Albuerne[20], Mauricio M. Oliveira[21], Juan Paraíso-Luna[22,23], Jonu Pradhan[24], Andressa Radiske[25], Ana Belén Ramos-Hryb[26,27], Mayara C. Ribeiro[28], Roberta Schellino[29], Maria Clara Selles[30], Shripriya Singh[31], Paschalis Theotokis[32] and Alain Chédotal[1]

[1]*Sorbonne Université, INSERM, CNRS, Institut de la Vision, Paris, France*

[2]*California National Primate Research Center, UC Davis, Davis, California, USA*

[3]*Laboratory of Amyloidosis and Neurodegeneration, Fundación Instituto Leloir, Buenos Aires, Argentina*

[4]*Instituto de Investigaciones Bioquímicas de Buenos Aires, Consejo Nacional de Investigaciones Científicas y Técnicas (CONICET), Buenos Aires, Argentina*

[5]*Department of Pediatrics, University of California - San Francisco, San Francisco, California, USA*

[6]*Faculty of Health Sciences School of Anatomical Sciences, University of the Witwatersrand, Parktown Johannesburg, South Africa*

[7]*Laboratorio de Parkinson Experimental, Instituto de Investigaciones Farmacológicas (ININFA-CONICET-UBA), Ciudad Autónoma de Buenos Aires, Argentina*

[8]*Department of Medical Biotechnology and Translational Medicine, University of Milan, Milan, Italy*

[9]*Metabolic Signalling Laboratory, St Vincent's Institute of Medical Research, Fitzroy, Victoria, Australia*

[10]*Department of Psychiatry and Neurochemistry, Institute of Neuroscience and Physiology, The Sahlgrenska Academy at the University of Gothenburg, Gothenburg, Sweden*

[11]*School of Life Sciences, University of Warwick, Coventry, UK*

[12]*Midlands Integrative Biosciences Training Partnership, University of Warwick, Coventry, UK*

[13]*Division of Radiation Health, College of Pharmacy, University of Arkansas for Medical Sciences, Little Rock, Arkansas, USA*

[14]*Department of Pharmaceutical Sciences, College of Pharmacy, University of Arkansas for Medical Sciences, Little Rock, Arkansas, USA*

[15]*Department of Anesthesiology and Critical Care Medicine, Children's Hospital of Philadelphia, Philadelphia, Pennsylvania, USA*

[16]*Institute for Stroke and Dementia Research, LMU Munich, Munich, Germany*

[17]*Department of Medical Biotechnology and Translational Medicin, University of Milano, Segrate, Italy*

Received August 16, 2019; revised manuscript received October 14, 2019; accepted October 17, 2019.

Address correspondence and reprint requests to Alain Chédotal, Sorbonne Université, INSERM, CNRS, Institut de la Vision, 17 rue Moreau, F-75012 Paris, France. E-mail: alain.chedotal@inserm.fr

*Equal contribution.

Abbreviations: CC, corpus callosum; Dcc, deleted in colorectal cancer; Sema3C, semaphorin3C; Nrp1, neuropilin 1; RGCs, retinal ganglion cells; OC, optic chiasm; Zic2, Zic family member 2.

© 2019 International Society for Neurochemistry,

[18]*School of Anatomical Sciences, Faculty of Health Sciences, University of the Witwatersrand, Johannesburg, South Africa*
[19]*Queensland Brain Institute, The University of Queensland, St Lucia, Queensland, Australia*
[20]*División de Neurociencias, Instituto de Fisiología Celular, Universidad Nacional Autónoma de México, Ciudad de México, México*
[21]*Institute of Biophysics Carlos Chagas Filho, Federal University of Rio de Janeiro, Rio de Janeiro, Brazil*
[22]*Ramó*n y Cajal Institute of Health Research (IRYCIS), Department of Biochemistry and Molecular Biology and University Research Institute in Neurochemistry (IUIN), Complutense University, Madrid, Spain
[23]*Network Center for Biomedical Research in Neurodegenerative Diseases (CIBERNED), Madrid, Spain*
[24]*Faculty of Medicine, School of Biomedical Sciences, The University of Queensland, Brisbane, Queensland, Australia*
[25]*Memory Research Laboratory, Brain Institute, Federal University of Rio Grande do Norte, Natal, Brazil*
[26]*Instituto de Biología* y Medicina Experimental (IBYME)-CONICET, Buenos Aires, Argentina
[27]*Grupo de Neurociencia de Sistemas, Instituto de Fisiología* y Biofísica (IFIBIO) Bernardo Houssay, Universidad de Buenos Aires, CONICET, Buenos Aires, Argentina
[28]*Department of Biology, Program in Neuroscience, Syracuse University, Syracuse, New York, USA*
[29]*Neuroscience Department "Rita Levi-Montalcini" and Neuroscience Institute Cavalieri Ottolenghi, University of Torino, Torino, Italy*
[30]*Institute of Medical Biochemistry Leopoldo de Meis, Federal University of Rio de Janeiro, Rio de Janeiro, Brazil*
[31]*System Toxicology and Health Risk Assessment Group, CSIR*-Indian Institute of Toxicology Research, Lucknow, India
[32]*Department of Neurology, Laboratory of Experimental Neurology and Neuroimmunology, AHEPA University Hospital, Thessaloniki, Macedonia, Greece*

Abstract
Perception of our environment entirely depends on the close interaction between the central and peripheral nervous system. In order to communicate each other, both systems must develop in parallel and in coordination. During development, axonal projections from the CNS as well as the PNS must extend over large distances to reach their appropriate target cells. To do so, they read and follow a series of axon guidance molecules. Interestingly, while these molecules play critical roles in guiding developing axons, they have also been shown to be critical in other major neurodevelopmental processes, such as the migration of cortical progenitors. Currently, a major hurdle for brain repair after injury or neurodegeneration is the absence of axonal regeneration in the mammalian CNS. By contrasts, PNS axons can regenerate. Many hypotheses have been put forward to explain this paradox but recent studies suggest that hacking neurodevelopmental mechanisms may be the key to promote CNS regeneration. Here we provide a seminar report written by trainees attending the second Flagship school held in Alpbach, Austria in September 2018 organized by the International Society for Neurochemistry (ISN) together with the *Journal of Neurochemistry* (JCN). This advanced school has brought together leaders in the fields of neurodevelopment and regeneration in order to discuss major keystones and future challenges in these respective fields.
Keywords: JNC-ISN Flagship School, review, cell therapy, spinal cord, axon guidance, regeneration.
J. Neurochem. (2020) **153**, 10–32.

The first anatomical reference of the brain dates back to the ancient Egyptian mummifications. However, the tremendous complexity of this organ was revealed by the work of the world-renowned neuroscientist Santiago Ramón y Cajal. Nevertheless, his anatomical descriptions could not fully explain the cellular and molecular events at the origin of behavioral, motor or sensitive responses. Today, it is clear that the CNS is the processing center for these events. Moreover fine sensory perception and intricate motor control are orchestrated by a discrete and permanent communication

between the CNS and the PNS. In the last century, neuroscientists have investigated the mechanisms involved in the development and plasticity of this structure. To address these fundamental questions, researchers made use of simple and accessible animal models. *Drosophila melanogaster* was one of the first organisms used because of several technical advantages: amenability to genetic manipulation, short lifespan and large number of offsprings. Studies emanating from this model system paved the path toward our understanding of major neurodevelopmental mechanisms involved in vertebrate behavior, neuronal migration and differentiation among many others (Bellen *et al.* 2010). *Danio rerio* (zebrafish), quickly emerged as an attractive more complex animal model. Like the *Drosophila melanogaster*, the zebrafish model also possessed a short lifespan and a large number of offsprings. However, it provided the advantage of studying neurodevelopmental mechanisms in vertebrates (d'Amora and Giordani 2018). While findings in these two models have led to major findings in the field of neuroscience, there are still significant gaps in our understanding of human development. Over the last 50 years, *Mus musculus* and *Rattus norvegicus* are classic models in neuroscience research because of their closer phylogenetic proximity to humans (Ellenbroek and Youn 2016).

In parallel to these findings, a large number of pathologies related to the CNS have emerged over the last century. This is mainly related to the aging population, encountering previously unknown neuro-degenerative diseases. The rising prevalence of these neurodegenerative diseases has urged the need for novel and more effective therapies (Gitler *et al.* 2017). Quickly, the idea emerged that developmental processes could be reinitiated to induce regeneration and brain repair. In an effort to target these fundamental questions, the Journal of Neurochemistry organized in September 2018 a workshop in Alpbach, Austria, gathering some of the most prominent researchers in the field of developmental neurobiology and regeneration in order to discuss the most significant findings and current challenges in these fields. Trainees attending this workshop have drafted a seminar report of this workshop listing the major advances and putting forward major questions in the field.

The developing nervous system

Metazoans all possess an axis of symmetry. In contrast to *radiata* (radial symmetry), *Bilateria* possess a two-fold symmetry. Thus, *bilateria* have a front and rear as well as left and right sides. To connect its two lateral halves, the CNS of *bilateria* possesses commissural neurons. These neurons, which are born embryonically, project their axons contralaterally to connect the left and right side of the organism. Together, these commissural networks not only allow for integration and coordination of left-right neuronal activities, but are essential for the correct processing and interpretation of various sensory information, the coordination of motor responses and other brain functions (Stoeckli 2018; Gaudet and Fonken 2018; Ducuing *et al.* 2019). Many commissural tracts exist in the CNS (Chédotal 2014). Here, we will discuss the three major systems: the corpus callosum, the ventral commissure of the spinal cord, and the optic chiasm.

Forebrain

The forebrain possesses two main cortical projection neurons: cortico-cortical, that form the corpus callossum, and cortico-fugal, further subdivided into corticothalamic and coroticospinal tracts (Leyva-Díaz and López-Bendito 2013).

The corpus callosum (CC) is the largest brain commissure and develops alongside neocortex expansion. Interestingly, this structure is unique to eutherian mammals and relays information between left and right hemispheres via the midline (Gazzaniga 2000; Suárez *et al.* 2014). Corpus Callosum dysgenesis affects ~ 1 : 4000 live births that result in either partial or complete absence (agenesis) of the CC (Edwards *et al.* 2014). Initially the two hemispheres are separated, at the midline, by the interhemispheric fissure (Rakic and Yakovlev 1968). This region is lined by specialized astroglial and neuronal cells that are required for proper CC tract formation (Silver *et al.* 1982; Niquille *et al.* 2009; Gobius *et al.* 2016; Gobius *et al.* 2017). In addition to providing a permissive substrate for callosal growth cones to grow across the midline, midline cells also secrete guidance cues. Pre-crossing CC axons are sensitive to Slit2, expressed by these astroglia, which acts as a repulsive cue to constrain callosal axons expressing the Roundabout (Robo) receptors 1/2 (Unni *et al.* 2012). In contrast, netrin-1, expressed by the cingulate cortex, counteracts the Slit2 repulsive signal by attracting callosal axons expressing the transmembrane receptor deleted in colorectal cancer (Dcc) (Fothergill *et al.* 2014). Indeed, loss of Dcc or netrin-1 leads to CC agenesis (Serafini *et al.* 1996; Fothergill *et al.* 2014). In addition to netrin-1, semaphorin (Sema3C) is secreted at the midline and attracts callosal axons expressing the receptor neuropilin 1 (Nrp1, Fig. 1a) (Niquille *et al.* 2009). Once CC axons have reached and crossed the midline, this attractive signal is switched off (Mire *et al.* 2018). This coincides with an up-regulation of the transmembrane protein ephrin-B1 in post-crossing CC axons. Interestingly, ephrin-B1 possesses a unique Asparagine residue (N-139), not shared by other ephrins, which once glycosylated can allow ephrin-B1 interaction with Nrp1 and silence Sema3C/Nrp1 attraction (Mire *et al.* 2018) (Fig. 1b). These findings identify a novel mechanism involving interaction between Sema3c/Nrp1 and Ephrinb1 during midline crossing in the corpus callosum (Fig. 1).

Optic chiasm

Another critical component of the CNS is visual perception. The functional unit of the eye is the retina (Fig. 2a), which is

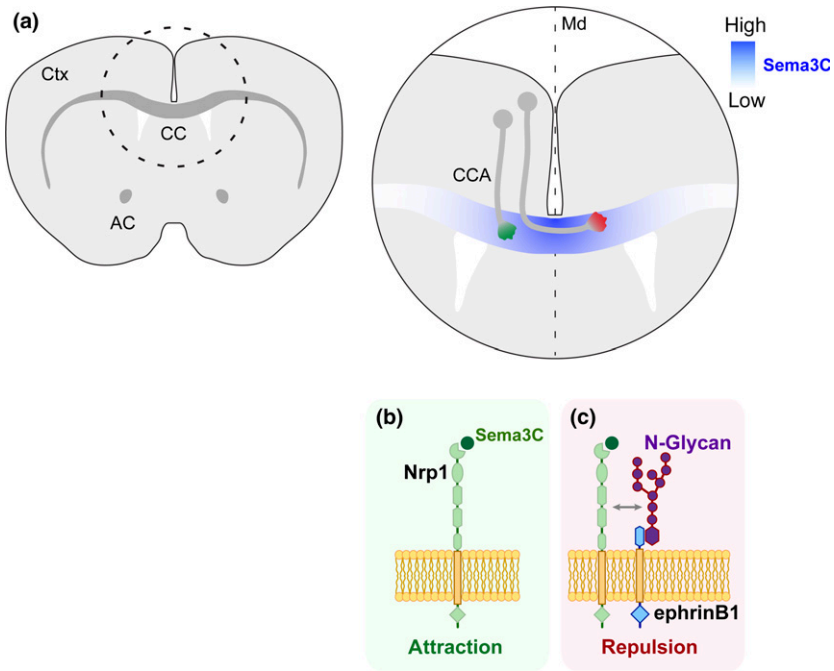

Fig. 1 Sema3C controls midline crossing in the developing *corpus callosum*. (a) The role of semaphorin in midline crossing in the *corpus callosum* has been recently elucidated. Sema3C is expressed in a gradient across the callosal midline. It binds the Nrp1 receptor on callosal axon growth cones (b) acting as an attractive cue. (c) The Sema3C/Nrp1 complex is silenced by the presence of trans-membrane protein ephrinB1. This requires an N-Glycan post-traductional modification of ephrinB1. Ctx, cortex; CC, *corpus callosum*; AC, anterior commissure; CCA, *corpus callosum* axon.

a highly organized structure. Photoreceptor cells are photosensitive cells that transform photons of light into an electrical impulse that is transmitted to bipolar cells and subsequently to Retinal ganglion cells (RGCs). RGCs relay this electrical signal to the brain along their axons that form the optic nerve. Importantly, whilst other retinal cell types can modulate the electrical signal mediated by photoreceptor cells, such as amacrine and horizontal cells, RGCs are the only output neuron from the retina and connecting it to the brain. During visual system development, retinal ganglion cells (RGCs) extend axons toward a specialized structure at the midline, named the optic chiasm (OC). At this point, RGCs will either project to the same hemisphere (ipsi-lateral) or cross the midline to project to the opposite hemisphere (contra-lateral). Therefore, two types of RGCs, ipsilateral RGCs (iRGCs) and contralateral RGCs (cRGCs) can be defined by the laterality of their projections (Williams *et al.* 2004).

This process is critical for depth perception, stereopsis. Indeed, since both eyes will obtain a "picture" of our environment, by combining these pictures we will generate a three-dimensional (3D) representation of the picture. Interestingly, the amount of overlap between each eye is directly proportional to the amount of ipsi-lateral projections. For instance, species with laterally positioned eyes, such as mice, possess only 3–5% of ipsi-laterally projecting RGCs. However, humans and primates, with more frontally positioned eyes, possess approximately 50% of ipsi-laterally projecting RGCs (Guillery *et al.* 1995; Jeffery and Erskine 2005; Herrera *et al.* 2019). Mouse iRGCs and cRGCs are characterized by specific transcriptional patterns and, in part, spatial localization, with iRGCs residing in the ventro-temporal retina, and cRGCs being dispersed across the retina (Herrera *et al.* 2003; Pak *et al.* 2004; Williams *et al.* 2006; García-Frigola *et al.* 2008; Kuwajima *et al.* 2017) (Fig. 2b and c).

In order to control the crossing of RGC axons at the OC, two processes take place: repulsion of axons with an ipsi-lateral fate, and the crossing of contralateral axons across the midline (Fig. 2d). EphB1/ephrin-B2 signaling pathway is a key component of ipsi-lateral axon repulsion. Expression of the EphB1 tyrosine kinase receptor is restricted to axons of iRGCs, while its ligand, the repulsive axon guidance molecule ephrin-B2, is expressed at the OC (Williams *et al.* 2003). When the axons reach the proximity of the OC, a chemo-repulsive gradient of ephrin-B2 leads to growth cone collapse and pausing of axonal outgrowth, eventually causing changes of trajectory and driving the axon toward ipsi-lateral visual nuclei (Petros *et al.* 2010). It was further shown that RGC axon laterality is transcriptionally regulated. The transcription factor Zic family member 2 (Zic2) was identified as a key regulator of iRGCs identity (Herrera *et al.* 2003; Wang *et al.* 2016). Furthermore, Zic2 is sufficient to induce the expression of EphB1 receptor in iRGCs (Lee *et al.* 2008; García-Frigola *et al.* 2008) (Fig. 2c). In addition, the transcription factor Forkhead box D1 was shown to be critical in maintaining iRGCs fate by promoting the expression of Zic2 (Herrera 2004). In addition to the EphB1/ephrin-B2 repulsion pathway, another pathway also controls ipsilateral RGC repulsion: Shh is expressed by contralateral RGCs and transported axonally and anterogradely to the optic chiasm (Peng *et al.* 2018). At the optic chiasm, ipsilateral

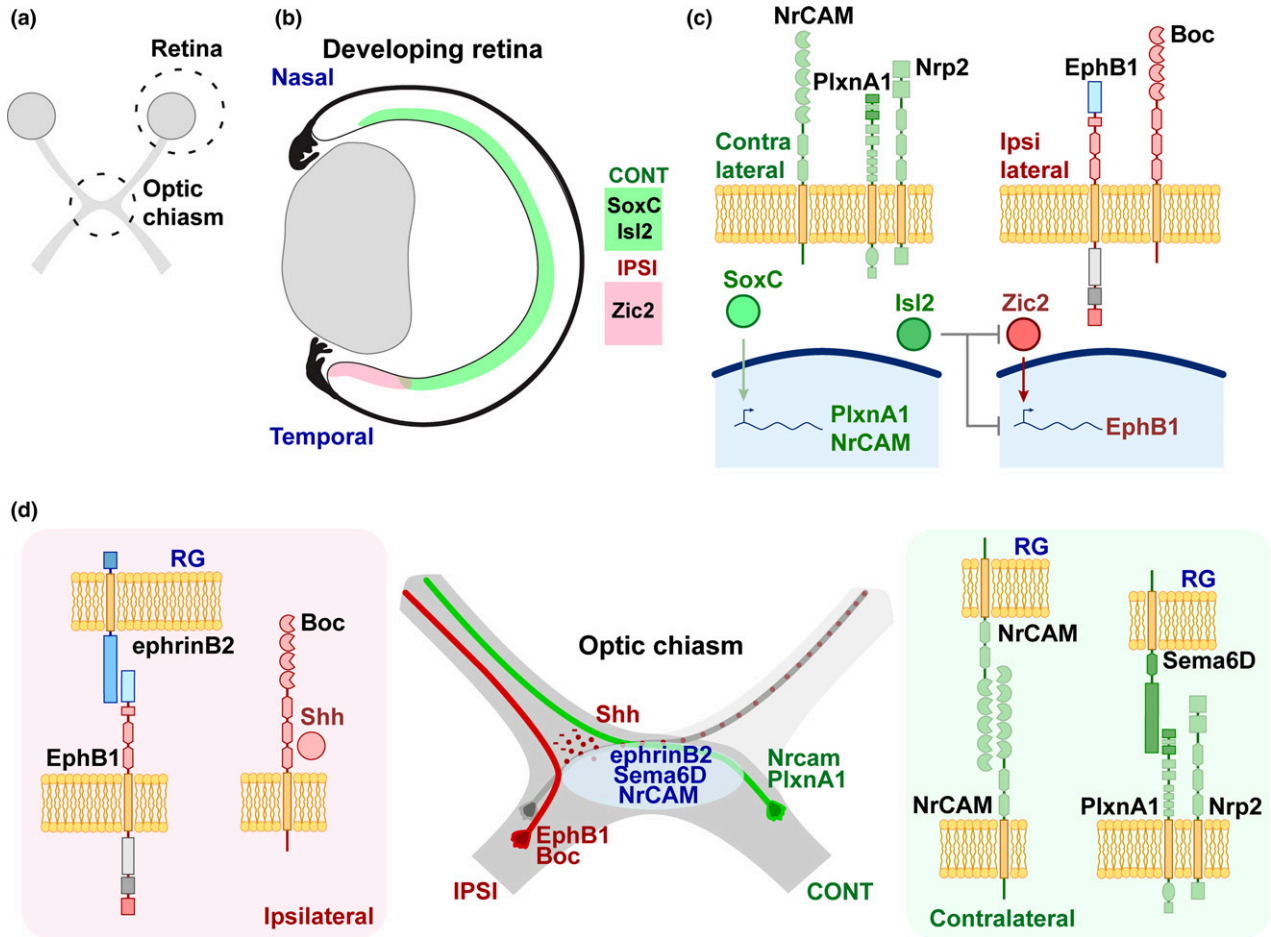

Fig. 2 Retinal ganglion cells development and their pathfinding at the optic chiasm. (a) In the developing visual system, retinal ganglion cells (RGCs) project from the retina to the brain nuclei. During this process, some RGC axons cross the midline at the optic chiasm. (b) RGCs projecting towards the contra or ipsilateral side are already specified in the retina by two sets of transcription factors: *SoxC* and *Islet2* in contralateral RGCs and *Zic2* in ipsilateral RGCs. The Sonic hedgehog (Shh) receptor Boc, is also expressed by ipsilateral RGCs. (c) These two different combinations allow the expression of guidance effectors, regulating the pathfinding choices at the optic chiasm. Moreover *Islet2* is also blocking the expression of *Zic2* and *Boc* expression in contralateral RGCs. (d) The optic chiasm is the intermediate target where contralateral RGCs (green) project towards the contralateral side of the CNS whereas ipsilateral RGCs (red) follow the visual tract on their original side. Shh, transported by the contra-lateral RGCs (gray), is released at the optic chiasm. Ipsi-lateral RGCs expressing the transmembrane receptors Boc as well as EphB1 are repelled by Shh and ephrinB2 at the optic chiasm. An attraction of contralateral RGCs to the midline is mediated by the cell adhesion molecule NrCAM and transmembrane semaphorin Sema6D, through their interaction with NrCAM and the complex PlexinA1-Neuropilin2. RG, radial glia.

RGCs, which express the Shh receptor Boc, are repelled by Shh and therefore do not cross the optic chiasm, remaining ipsilateral (Fabre *et al.* 2010; Peng *et al.* 2018) (Fig. 2d).

In contrast, cRGC axons express the L1 cell adhesion molecule, the neuronal cell adhesion molecule (NrCAM), and the semaphorin receptor Plexin-A1. Together, these molecules provide a permissive substrate for cRGCs to invade and cross the OC (Williams *et al.* 2006; Kuwajima *et al.* 2012). Transcriptionally, the Sox C family of transcription factors (Sox4, Sox11, Sox12) was identified as key regulators for cRGC fate by regulating NrCAM and PlexinA1 expression (Kuwajima *et al.* 2017) (Fig. 2c and d). In addition, the transcription factor Islet2 is expressed by ~ 30% of cRGCs, mainly expressed by late-born cRGCs (Pak *et al.* 2004; Kuwajima *et al.* 2017). Furthermore, the leucine-rich repeat receptor Islr2 has been shown to be expressed on cRGCs and its deletion leads to aberrant ipsi-lateral projections in *Danio Rerio* (Panza *et al.* 2015).

Interestingly, binocular vision is impaired in patients with albinism (an absence of melanin production of the retinal pigmented epithelium). This led researchers to study the role of pigmentation on iRGCs. It was found that albino mice have less iRGCs, but a normal number of cRGCs (Rebsam *et al.* 2012). This appears to be linked to the timing of RGC

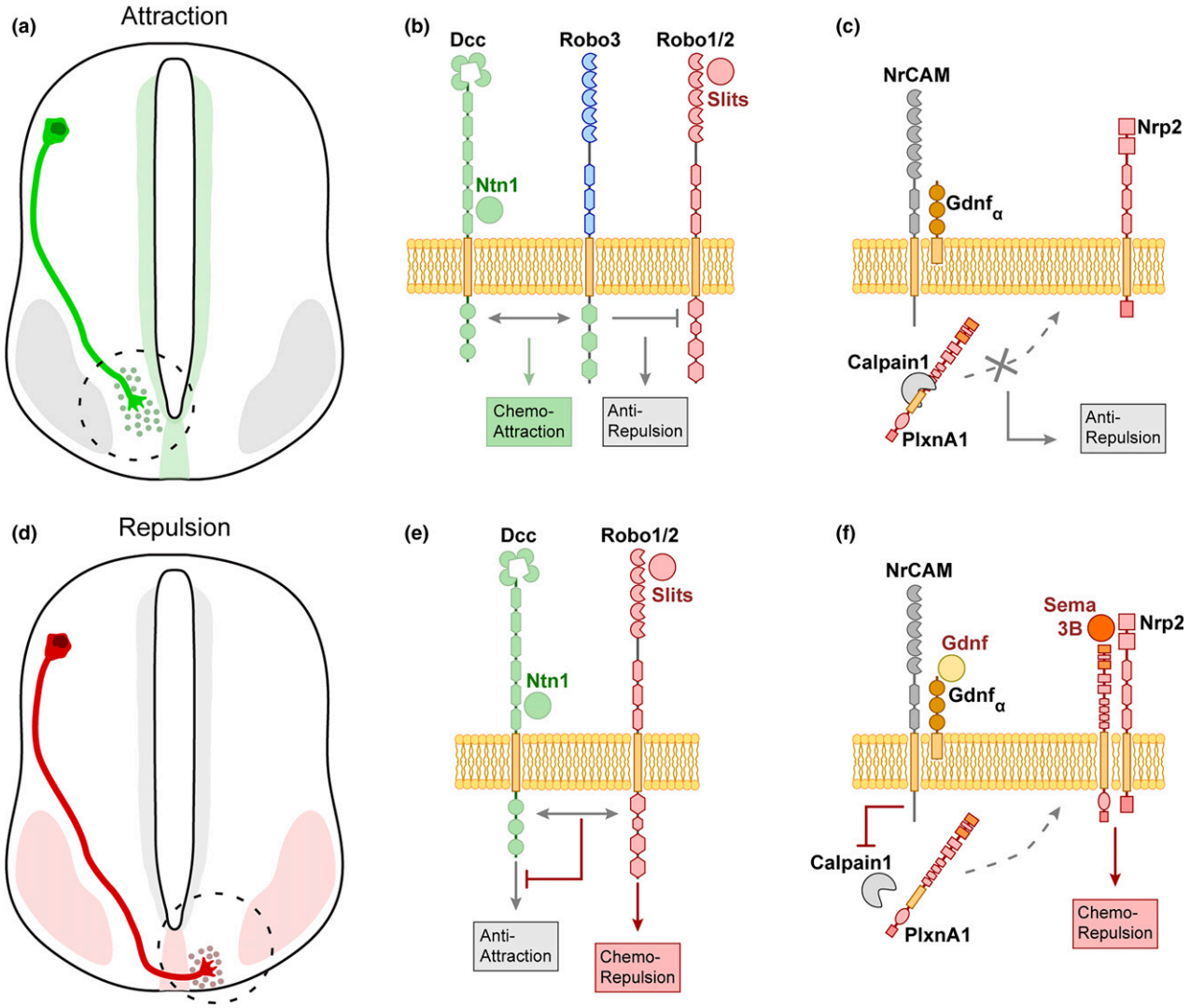

Fig. 3 Spinal cord commissural axons development: pre and post-crossing guidance mechanisms. (a) Commissural axons arise from the dorsal portion of the spinal cord. To cross the midline, they first have to be guided to the floor plate. This first process involves several guidance receptors that trigger the axon outgrowth toward the ventral midline. (b) Pre-crossing axons express the Roundabout 3 (Robo3) receptor. Robo3 interacts with deleted in colorectal cancer (Dcc) receptor and both promote axon extension to the floor plate in response to Netrin-1. Netrin-1 was first thought to act as long-range cue but recent studies suggest that it acts as short-range cue. Robo3 might also prevent Slit repulsion by interacting with the Robo1/2 receptors. (c) Moreover in pre-crossing commissural axons, the presence of calpain induces a cleavage of the PlexinA1 receptor, inactivating this repulsive signalling pathway. (d) After midline crossing, commissural axons switch from midline attraction to repulsion. They become sensitive to repulsive cues secreted by floor plate cells which prevent midline re-crossing. Axon then start to extend rostrally toward their final targets. (e) At the floor plate, Robo3 is down-regulated, and Robo1/2 interaction with Slits blocks the Dcc-Netrin-1 attractive signalling. (f) In addition, the expression of Gdnf by floor plate cells inhibits calpain activity on crossing fibres, allowing PlexinA1 to reach the membrane where it interacts with Neuropilin2, where this receptor complex triggers midline repulsion upon binding Sema3B.

differentiation: albino animals have a shorter time window during which iRGCs are born which is compensated by an increased number of cRGCs (Bhansali *et al.* 2014). Furthermore, the functional comparison of gene expression in albino and pigmented retinas, showed that the Wnt-pathway, which controls iRGC differentiation and cell proliferation, is dysregulated in albino animals (Iwai-Takekoshi *et al.* 2018). Rescue of ipsi-lateral deficit via blockage of Nr-CAM may improve visual capability in albino animals, thereby providing a paradigm for functionally investigating the consequences of natural ipsi-lateral depletion (Williams *et al.* 2006).

Interestingly, the existence of another population of RGCs has been described to project between the two retinas (retino-

retinal projection) in various vertebrate species (Müller and Holländer 1988; Tóth and Strznicky 1989; Nadal-Nicolás *et al.* 2015). More recently, it was described that this population resides in the ventro-nasal retina and is transient (E16.5 to postnatal day 4) (Murcia-Belmonte *et al.* 2019). These late-born RGCs were shown to express Unc5c, a netrin-1 receptor. Upon reaching the optic chiasm, Unc5c-positive RGCs are repelled by netrin-1 and project into the contralateral optic nerve. Indeed, Unc5c is both sufficient and necessary for retino-retinal projections (Murcia-Belmonte *et al.* 2019). However, the precise connection and function of this projection remains to be characterized. Moreover the implication of this projection in co-ordinating spontaneous activity remains to be studied.

Spinal cord

In the developing spinal cord, midline crossing takes place ventrally through a structure named the floor plate (FP). The FP is a crucial patterning center composed of specialized cells that contribute to the specification of the neuronal lineages of the neural tube and adjacent territories.

Moreover the FP is a source of both growth-promoting and growth-repulsive cues for commissural axons, such as netrin-1 and Slits (Chédotal 2019). In vertebrates, spinal commissural axons navigate first ventrally toward the floor plate (Fig. 3a), cross the midline and then turn rostrally or caudally (Fig. 3d). According to the current model, the sensitivity to midline repellents is silenced in pre-crossing commissural growth cones as they navigate toward the FP. However, during FP crossing, commissural growth cones gain responsiveness to FP repulsive cues. The post-crossing commissural neurons are thus expelled from the midline, and also prevented from re-crossing the FP. At later stages, they follow rostro-caudal gradients of guidance cues, turning rostrally or caudally in the ventral or lateral funiculi (Gaudet and Fonken 2018; Ducuing *et al.* 2019; Chédotal 2019).

Commissural axon guidance before midline crossing

The earliest born spinal commissural neurons will extend their axons toward the pial surface of the spinal cord and ventrally toward the FP (Fig. 3a). For many years it was thought that a long-range gradient of the secreted protein netrin-1 is generated by the FP and attracts commissural neurons ventrally upon binding the receptor Dcc (Hiramoto *et al.* 2000; Finci *et al.* 2015). However, recent studies have challenged this model and rather support a local and haptotactic function of netrin-1. Indeed, netrin-1 is not only expressed by FP cells but also by the neural progenitors of the ventricular zone of the spinal cord and brainstem. In support to this model, specific deletion of netrin-1 at the FP, does not perturb commissural axon crossing in the hindbrain (Dominici *et al.* 2017; Yamauchi *et al.* 2017). Interestingly, in the spinal cord, midline crossing appears slightly delayed (Moreno-Bravo *et al.* 2019) and some axons are misguided before crossing (Varadarajan *et al.* 2017; Moreno-Bravo *et al.* 2019; Wu *et al.* 2019). These results suggest that floor plate-derived netrin-1 is dispensable for commissural axon crossing, but also highlight a different mechanism of action of netrin-1 between the hindbrain and the spinal cord. Importantly, ablating netrin-1 expression in ventricular zone progenitors severely perturbs midline crossing in the brainstem (Dominici *et al.* 2017; Yamauchi *et al.* 2017) but only mildly in the spinal cord (Moreno-Bravo *et al.* 2019). However, the simultaneous deletion of ventricular and FP derived netrin-1 prevents midline crossing (Moreno-Bravo *et al.* 2019). Therefore, in the spinal cord, both sources of netrin-1 cooperate to guide commissural neuron at the midline. Other secreted proteins such as VEGF (Ruiz de Almodovar *et al.* 2011) and Shh (Charron *et al.* 2003; Bovolenta and Sanchez-Arrones 2012; Sloan *et al.* 2015; Wu *et al.* 2019) are expressed at the floor plate and act redundantly with netrin-1 to attract axons as they get close to the FP.

Robo3, a member of the Roundabout (Robo) family, plays a key role in midline guidance. This receptor is expressed transiently by commissural axons in mouse spinal cord, midbrain and hindbrain and then is rapidly down-regulated after the axons have crossed the FP (Belle *et al.* 2014; Zelina *et al.* 2014). It is expressed in human pontine neurons (Jen *et al.* 2004) and in hindbrain and spinal cord commissural axons of birds (Philipp *et al.* 2012; Escalante *et al.* 2013; Friocourt and Chédotal 2017) and other vertebrate species (Friocourt *et al.* 2019). The absence of Robo3 leads to a complete loss of several commissures in mice and in humans (Jen *et al.* 2004; Marillat *et al.* 2004; Sabatier *et al.* 2004; Renier *et al.* 2010; Michalski *et al.* 2013). The mechanism through which Robo3 controls commissure development is not completely understood. However, it was proposed that Robo3 expression in pre-crossing commissural neurons repress Slit/Robo repulsion (Fig. 3b), thus allowing commissural axons to reach, enter, and cross the ventral midline in response to netrin-1 attraction (Sabatier *et al.* 2004; Jaworski *et al.* 2010; Chédotal 2011). This mechanism has been validated in the spinal cord and lateral reticular nucleus. Interestingly, the inferior olivary nucleus does not seem to follow the same mechanism (Di Meglio *et al.* 2008). However, it was initially proposed that Robo3 may facilitate attraction of commissural neurons to the floor plate, independently of Slit/Robo signaling (Sabatier *et al.* 2004; Di Meglio *et al.* 2008; Jaworski *et al.* 2010). More recent studies support this notion. Indeed, whilst non-mammalian Robo3 retained its ability to bind Slits, the mammalian orthologue of Robo3 has lost key residues in the Slit/Robo binding domain (Zelina *et al.* 2014). Instead, it possesses the ability to bind to netrin-1, by creating a receptor complex between Dcc and Robo3 via Src kinases, on a conserved tyrosine residue and contributes to the attractive actions of netrin-1 (Zelina *et al.* 2014). Therefore, Robo3 might

promote attraction to the ventral midline rather than counteract repulsion.

To date, several transcription factors have been associated with the most dorsal commissural population, dI1, which arises from the *Atoh1*$^{+}$ domain (Chédotal 2014). These interneurons are divided in two different subtypes depending on the location of their targets: ipsilateral (dI1i) or contralateral (dI1c) (Wilson *et al.* 2008). Interestingly, their projection pattern relies on the balance between the expression of two transcription factors *Lhx2* and *Lhx9* (Lim homeobox) and their upstream activation by the transcription factor *Barhl2* (Ding *et al.* 2012). Lhx2 is able to directly bind to the regulatory region of *Robo3* and modulate its expression in a dose-dependent manner. Moreover in *Lhx2/9* knockouts, most of dI1 interneurons fail to cross the midline and project ipsilaterally (Wilson *et al.* 2008; Marcos-Mondejar *et al.* 2012).

Furthermore, the transcription factor Zic2 triggers an ipsilateral transcriptional program but also inactivates a contralateral one (Escalante *et al.* 2013). Indeed, down-regulation of *Zic2* by *in utero* electroporation of siRNA induces an abnormal up-regulation of Robo3 and a contralateral projection of dorsal horn neurons. A *Zic2* gain of function has the reverse effect, reducing *Robo3* expression and an increase of ipsilateral projections. In addition to modulating Robo3 expression, Zic2 is necessary and sufficient to induce EphA4 expression and commissural neuron repulsion in response to midline ephrinB's.

Commissural axon guidance after midline crossing

Upon FP crossing, commissural axons become sensitive to a myriad of repulsive guidance molecules expressed at the FP. However, prior to midline crossing, commissural axons do not express the receptors (at the surface) required to sense this repulsive environment. One such example is the repulsive receptor, PlexinA1, which is down-regulated at the surface of commissural neurons prior to midline crossing (Fig. 3c). PlexinA1 down-regulation at the growth cone involves the protease, Calpain-1 (Nawabi *et al.* 2010; Charoy *et al.* 2012). However upon FP entry, commissural neurons become exposed to the NrCAM that inhibits calpain-1 activity (Fig. 3f). As a result, PlexinA1 can accumulate at the growth cone which becomes sensitive to the repulsive cue Sema3B (expressed at the FP) (Nawabi *et al.* 2010; Charoy *et al.* 2012). In addition to PlexinA1, the semaphorin receptor Neuropilin 2 (Nrp2) is also expressed at the growth cone following FP entry. Indeed, Sema3B and Nrp2 double mutants display FP stalling as well as post-crossing misrouting (Nawabi *et al.* 2010; Parra and Zou 2010).

Slits are other repulsive cues expressed at the FP (Brose *et al.* 1999). As with PlexinA1 and Nrp2, commissural axon growth cones start expressing the Robo 1 and Robo2 receptors only after midline crossing, and become sensitive to Slit repulsion (Fig. 3e). Indeed, deletion of Robo receptors results in commissural axons stalling at the FP (Long *et al.* 2004; Garbe and Bashaw 2007; Blockus and Chédotal 2016). However, Silts can also function independently of Robo receptors. In vertebrates, Slits can be cleaved into two separate fragments (Brose *et al.* 1999; Wang *et al.* 1999). The shorter fragment (Slit-C) is able to bind to PlexinA1 in commissural neurons to induce growth cone collapse (Delloye-Bourgeois *et al.* 2015).

Once commissural axons have exited the FP, they are then guided by other cues to continue either rostrally or caudally. Little is known about the cues guiding postcrossing axons along the midline. However, Wnt signaling has been shown to be critical in this process (Onishi *et al.* 2014). An expression gradient of several Wnt family proteins controls the rostral turning of post-crossing commissural axons through an attractive mechanism involving the Frizzled3 (Fzd3) receptor (Lyuksyutova *et al.* 2003; Yoshikawa *et al.* 2003). The disruption of the Wnt gradient, results in a randomization of the growth of post-crossing commissural axons, which randomly turn toward the anterior or posterior part (Yoshikawa *et al.* 2003; Zou 2004). Recently, a mechanism orchestrating Wnt activation has been proposed. During FP crossing, commissural neurons expressing Smoothened (Smo) are exposed to the morphogen sonic hedgehog (Shh). This interaction leads to the reduction in mRNA translation of Shisa2, a well-known Wnt signaling inhibitor. Shisa2 inhibits the Wnt receptor Frizzled (Fzd3) trafficking to the cell surface by interfering with its glycosylation, inactivating Wnt signaling (Onishi and Zou 2017). Moreover it has been shown that components of the planar cell polarity signaling pathway mediate Wnt attraction and the anterior turning of commissural axons (Lyuksyutova *et al.* 2003; Zou 2012; Onishi *et al.* 2014). In addition to the planar cell polarity pathway, the canonical Wnt signaling pathway is critical in mediating post-crossing commissural neuron turning. Indeed, down-regulation of both Lrp5 and Lrp6 (Low density lipoprotein receptor-related protein, co-receptors for Frizzled), which are required in the β-catenin-mediated canonical Wnt pathway, lead to major defects in post-crossing commissural neurons (Avilés *et al.* 2016).

Shh also guides post-crossing commissural axons (Bourikas *et al.* 2005; Yam *et al.* 2012). After crossing, commissural axons become repelled by Shh and project anteriorly along a posterior-high Shh and anterior-high Wnt4 gradients. However, instead of mediating its action through Patched or smoothened, Shh acts through the Hedgehog interacting protein. Further experiments showed that this switch in Shh responsiveness depended on the levels of 14-3-3 proteins, which are low in pre-crossing and high in post-crossing commissural neurons, and modulate Protein Kinase A activity (Yam *et al.* 2012).

Peripheral nervous system development

The bilaterian nervous system is subdivided in two main components: the central and the peripheral nervous systems

(CNS and PNS). Permanent cross-talk between the CNS and PNS is critical for integration of sensory inputs. In the 4th century BC, *Alcmaeon of Croton* (Goddard *et al.* 1996) (Zolog 1994) proposed the first theory about channels ("poroi" in ancient greek) that would connect the senses and the brain, this last one being the center of human perception. Later, it became clear that all sensory perception being mechanical, auditory, gustatory, and olfactory were relayed to the CNS through the "nerves" (Mazengenya and Bhikha 2017). Indeed, the precise interplay between these two networks develop in parallel during embryonic development (Ben-Arie *et al.* 2000). Additionally, it has been demonstrated that both axon guidance and neuronal activity can strongly modulate connections between the PNS and the CNS (Bonanomi and Pfaff 2010; Wang and Bergles 2015). Nevertheless, the PNS is itself formed by different components, each specialized in the transmission of a specific signal to the CNS. These signals are transmitted by mechanosensory, chemical or thermal receptors projecting to the mammalian spinal cord via nociceptive afferents.

Drosophila bristles are sensory organs that are tightly distributed and contain one single mechanosensory neuron that specifically projects to the CNS. These axons can be guided by cell adhesion molecules, such as Neuroglian or Flamingo (Martin *et al.* 2008; Steinel and Whitington 2009), but also by other guidance molecules, such as Plexins or semaphorins (Wu *et al.* 2011). Down syndrome cell adhesion molecule (DSCAM) is a transmembrane receptor of the immunoglobulin-superfamily (Chen *et al.* 2006). DSCAM has since been described to regulate cell targeting, axon branch specification, and dendrite patterning (Schmucker *et al.* 2000; Wang *et al.* 2002a; Dascenco *et al.* 2015). The repulsive molecule, Slit, has been shown to bind and signal through DSCAM1 independently of Robo receptors (Chen *et al.* 2006). Indeed, local binding to Slit drives spatial specificity of axon collateral formation. Furthermore, Chen *et al.* (2006) report that many DSCAM isoforms exist and particular DSCAM isoform mosaicism in a specific growth cone appears to dictate local guidance decisions, such as the formation of axon collateral projections.

The inner ear is essential for the transmission of sounds and their integration by the CNS. This complex sensory organ is composed of bipolar spiral ganglion neurons (SGN) that connect the ipsilateral cochlear nucleus and the mechanosensory inner and outer hair cells located in the organ of Corti (Nayagam *et al.* 2011). SGNs project to both the inner (IHC) and the outer hair cells (OHC). During the course of development, both type I and II project to the OHC but type I SGNs appear to refine in later stages and only project to the IHC (Huang *et al.* 2012; Safieddine *et al.* 2012; Druckenbrod and Goodrich 2015). The use of molecular markers to target single spiral ganglia has revealed key morphological differences between type I and type II SGNs as well as their specific projection patterns to the IHC or outer hair cells OHC (Druckenbrod and Goodrich 2015; Coate *et al.* 2015). Indeed, type I and II SGNs were shown to be molecularly different. Type I SGNs express the semaphorin receptor Nrp2 and its co-receptor PlexinA3 (Coate *et al.* 2015). Upon binding Sema3F, secreted by the OHC, type I SGNs are repulsed and restrict their projections to the IHC (Coate *et al.* 2015). More recently, the use of single sequencing has allowed a more in depth characterization of SGNs. In this study, Shrestha *et al.* (2018) identified that type I SGNs can be further classified into three different subtypes. These data suggest a growing complexity of the auditory system formation and integration of external signals.

These examples underline the complexity of PNS development. With the aim of understanding the surrounding environment, each of these systems seems to have its own guidance mechanisms, which through a tight and orchestrated regulation, establish an essential pathway between sensory neurons and superior brain areas. Novel genetic and technical approaches also highlight the cellular heterogeneity in these systems, most of them considered quite homogeneous until recently. The understanding of the molecular differences between cell types in a determined structure is a key element in establishing therapeutic approaches such as stem cell therapy. Moreover these molecular differences can also help to understand the possible effects of different known guidance mechanisms. Lastly, several groups have tried to understand the role of spontaneous activity in these structures. Neural activity has been observed to happen randomly in most structures, since early development (Shrestha *et al.* 2018). This neuronal activity could be essential to pattern and reinforce synapses, as was shown in the visual system (Ackman and Crair 2014).

Non-traditional roles of axon guidance molecules

Axon guidance molecules have been extensively studied during axonal development but have also been shown to be critical in many diverse biological processes such as angiogenesis and cell migration (Castets and Mehlen 2010; Aberle 2019). Undeniably, cortical development is dependent on cellular migration. A fundamental question for the past decades has been the emergence of the neocortex, a specific feature of the mammalian brain (Finlay and Darlington 1995; Northcutt 2006). Cortical development begins with the division of radial glial progenitor cells (RGPCs), which gives rise to all cortical neurons and glia. RGPCs are aligned at the cortical ventricular zone and undergo mitosis to either self-renew (symmetric division = indirect neurogenesis), or differentiate into cortical neurons (asymmetric division = direct neurogenesis). However, in mammals RGPCs can also divide symmetrically to give rise to an intermediate progenitor cell (IPCs) (Haubensak *et al.* 2004; Noctor *et al.* 2004; Miyata *et al.* 2004). IPCs can either self renew or differentiate into cortical neurons.

Thus, IPCs have been proposed to serve as the main determinant for cortex expansion in mammals (Malatesta *et al.* 2000; Noctor *et al.* 2001; Smart 2002; Noctor *et al.* 2004; Kriegstein *et al.* 2006; Hansen *et al.* 2010). Recently, Cárdenas *et al.* (2018) have identified a novel role for Robo 1/2 in regulating radial glia cortical migration. By comparing the mouse olfactory bulb (OB) (reminiscent of the reptilian paleocortex) to the cortex (Cx), Cárdenas *et al.* (2018) observed that the OB solely developed by direct neurogenesis whereas the Cx was developed mostly by indirect neurogenesis. Interestingly, Robo1/2 were expressed in a gradient, with a high-low expression in the OB compared to the Cx. Furthermore, it was shown that Robo1/2 can regulate the notch canonical signaling pathway via Delta-like 1 as well as the ligands *jagged* 1 (*Jag1*) and *Jag2*. The mechanism put forward is that high Robo1/2 expression in the OB reduces Delta-like 1 expression and increases *Jag1* and *Jag2* expression, resulting in asymmetric division and direct neurogenesis. Indeed, gain of function experiments showed that high Robo1/2 expression is sufficient to induce direct neurogenesis in the mouse Cx (Cárdenas *et al.* 2018). Interestingly, amniotes deprived of a neocortex, such as birds and reptiles, show high Robo1/2 expression in the cortex (Cárdenas *et al.* 2018). Thus, the authors propose silencing of Robo1/2 as an evolutionary switch giving rise to indirect neurogenesis in mammals.

The Fibronectin Leucine Rich-repeat Transmembrane (FLRTs) proteins have also been identified as axon guidance molecules. For instance, thalamocortical axons expressing Dcc are not sensitive to the netrin-1 gradient present in the thalamus because of Robo1 silencing (Leyva-Díaz *et al.* 2014). However, FLRT3 can sequester Robo1 to allow for Dcc expression at the surface of thalamocortical neurons, thereby activating netrin-1 responsiveness (Leyva-Díaz *et al.* 2014). More recently, FLRTs have also been implicated with cortical progenitor migration (del Toro *et al.* 2017). In mammals the cortex initially forms as a laminar sheet. Whilst some mammals (mice and rats) will retain this smooth cortical development (lissencephaly, Fig. 4a), other mammals (primates and ferrets) develop cortical folds (gyrencephaly, Fig. 4b). FLRT1/3 have recently been shown to be critical players in this process (del Toro *et al.* 2017). Interestingly, genetic ablation in mice of FLRT1/3 promotes cortical folding (del Toro *et al.* 2017). Whilst the proliferation rate of radial glia cells was unchanged, their migratory patterns were significantly perturbed. Indeed, loss of FLRT1/3 increased neuronal clustering and radial migration rate. This creates columns of migrating progenitors, inducing an asymmetric proliferation across the surface of the cortex and as a result creating sulci. Of note, FLRT1/3 expression is reduced in gyrencephalic species, suggesting that the abundance of FLRT1/3 during evolution promoted cortical smoothing (lissencephaly).

Whilst typical axon guidance proteins such as Slits and ephrins have been largely discussed, a growing body of literature has shown that some lipids could be atypical guidance molecules. Phospholipids are considered the major components of cell membranes and they have the ability to form amphipathic lipid bilayers. Their role in axon guidance was first proposed by some in vitro experiments in which Lysophosphatidic acid, an intermediate substance of lipid synthesis, was shown to be able to induce growth cone collapse, neurite retraction and cell rounding in neuroblastoma-derived neuronal cell cultures (Jalink *et al.* 1993). Later on, further evidence highlighted their role on primary cultured chick embryo neurons and on isolated retinal growth cones (Saito 1997; Campbell and Holt 2001). Additional *in vivo* evidence of the axon guidance role of lysophospholypids were obtained in the *Xenopus* visual system. In absence of sphingosine 1-phosphate, retinal projections were misguided and invaded abnormal areas (Strochlic *et al.* 2007). Recently, a novel role for phospholipids on axon guidance was brought to light: Phosphatidyl-B-D-Glucoside (PtdGlc) is localized in radial glia and nascent astrocytes *in vivo* (Nagatsuka *et al.* 2006; Kinoshita *et al.* 2009). PtdGlc can be hydrolysed in *lyso*PtdGlc and released into the extracellular environment (Guy *et al.* 2015). In the embryonic chick and mouse spinal cord, TrkA and TrkC dorsal root ganglion axons enter the CNS through the dorsal root entry zone. Only TrkC axons get into the primordial dorsal funiculus where *Lyso*PtdGlc is found (Guy *et al.* 2015), suggesting a possible repulsive role for nociceptive afferences (TrkA). TrkA enriched dorsal root ganglia (DRG) explants showed chemorepulsion *in vitro* in presence of a *lyso*PtdGlc gradient. Furthermore, blocking antibodies for *lyso*PtdGlc used *in ovo*, showed a misprojection of TrkA axons in the primordial dorsal funiculus. Finally, a receptor screening proposed GPR55 as putative receptor for this extracellular cue. GPR55 *knockout* mice phenocopy the DRG axon misprojections induced by *lyso*PtdGlc blocking antibodies, confirming the role of this receptor-sensing glia released *lyso*PtdGlc in this system (Guy *et al.* 2015).

Axonal regeneration

In the early 20th century, pioneering studies from Ramón y Cajal showed that the mammalian CNS is unable to regenerate following a lesion (Ramón y Cajal 1914). Neuroscientists have since delved on the idea that understanding CNS development could be the key to hi-jack regenerative mechanisms following CNS injury. Interestingly, similar lesion experiments carried out on dorsal root ganglia axons (which belong to the PNS) resulted in robust regeneration of their peripheral branch and functional recovery following the lesion, whereas their central branch projecting into the CNS did not regenerate. Therefore, something either intrinsic or extrinsic to CNS neurons is responsible for their lack of regeneration (Fig. 5a). This fundamental question has sparked years of intensive research

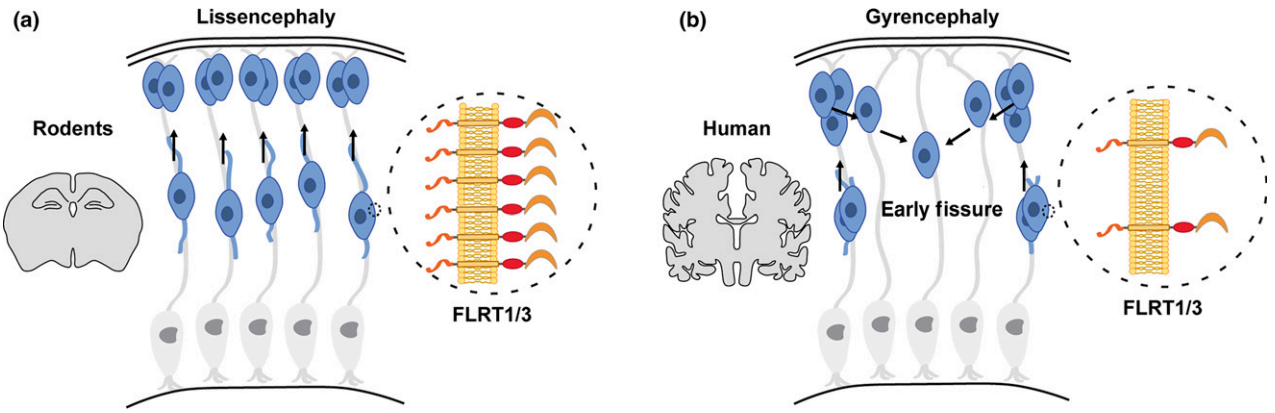

Fig. 4 Cortical folding relies on Fibronectin Leucine Rich-repeat Transmembranes (FLRTs) expression. Cortical folding appears to be dependent on the presence of the cell adhesion proteins FLRT1 and FLRT3 during cortical expansion, where (a) higher expression in migrating cortical progenitors is associated with parallel migration, resulting in a lissencephalic cortex. Conversely, (b) lower FLRT1 and 3 expression favors lower migration rates, and promotes lateral adhesion resulting in a gyrencephalic cortex.

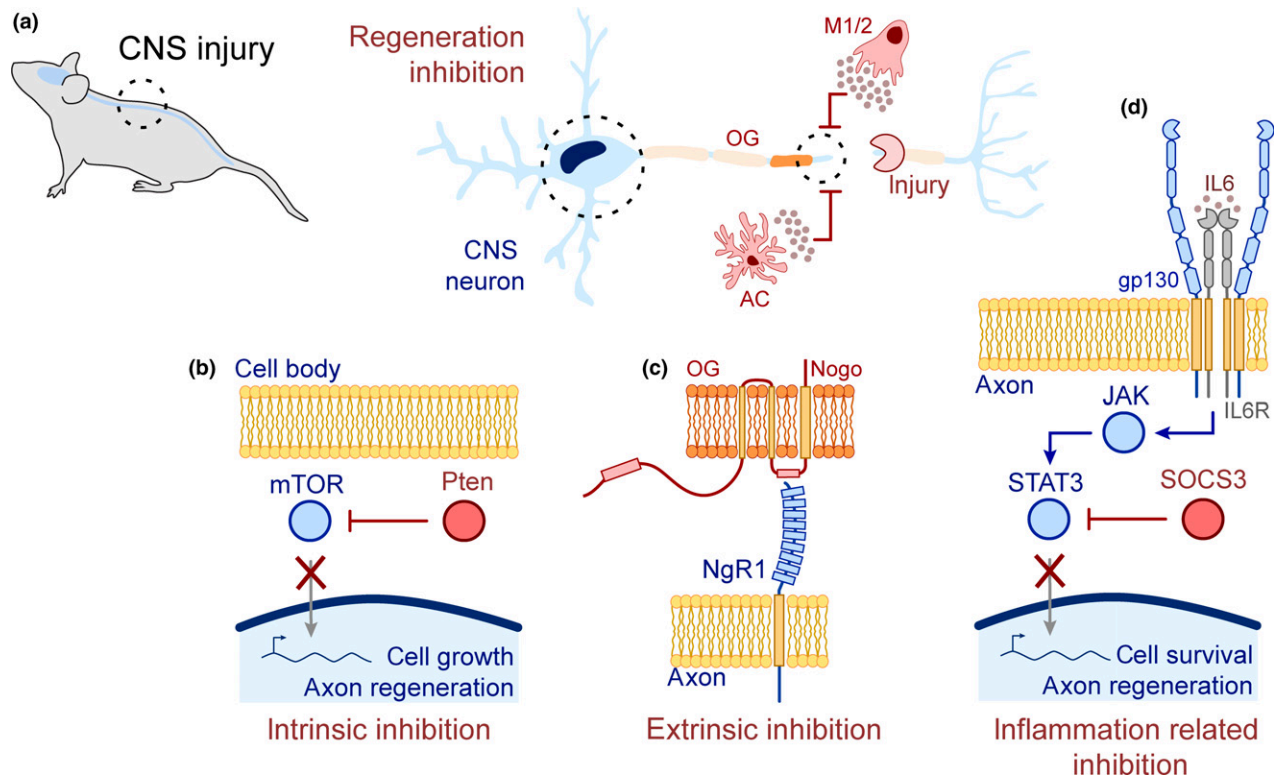

Fig. 5 Molecular mechanisms for CNS regeneration. (a) After CNS injury, extrinsic and intrinsic mechanisms impair axonal regeneration. These events occur both in the cell soma and the injure site and they are the main targets of strategies aiming at promoting regeneration. Most of the extrinsic inhibition comes from the recruitment of astrocytes and macrophages to the injury area and the "activation" of local oligodendrocytes. (b) In injured neurons, Pten blocks the mammalian target of rapamycin (mTOR) pathway that induces axon regeneration. The complete or conditional depletion of Pten in RGCs or corticospinal tract neurons, promotes the regeneration of their axons after injury. (c) Moreover oligodendrocytes at the lesion site, start to express inhibitory signalling molecules such as Nogo and myelin associated glycoproteins that will block axonal regeneration. The simultaneous depletion of Pten and Nogo, significantly promotes axonal regeneration. (d) Finally, The expression of cytokines by macrophages also promote axon outgrowth. Suppressor of cytokine signaling 3 (SOCS3) expression in lesioned axons blocks signal transducer and activator of transcription 3 (STAT3), a downstream effector of this cascade. Together with Pten, the depletion of SOCS3 also increases the regeneration rate of RGC axons.

to understand the molecular mechanisms activated after axotomy and to develop strategies for inducing axonal regeneration. Here, we will discuss some of the current approaches and challenges in regeneration of CNS and PNS axons.

Central nervous system regeneration

Visual system regeneration

Optic nerve (ON) transection or crush, have become a predominant models for studying CNS regeneration. The ON only contains axons which originate from RGC neurons in the retina. Directly following ON lesions, multiple inhibitory pathways are triggered. The activator protein 1 and the transcription factor subunit c-Jun (Fos-binding protein p39) both act in synergy to trigger cell death in RGCs following an experimental axotomy (Hüll and Bähr 1994). In addition, interplay between c-Jun and the activating transcription factor 2 dictates cell fate following ON crush. When both are up-regulated, they promote cell survival. However, reduction in activating transcription factor 2 expression induces apoptosis (Martin-Villalba *et al.* 1998). The activation of c-Jun is driven by calcium influx, since specific inhibition of calcium channels leads to reduction of c-Jun activity in ON crush models. Remarkably, the inhibition of calcium channels not only reduces acute axon neurodegeneration, but also improves axonal regeneration (Ribas *et al.* 2017). The RhoA/ROCK/LIMK pathway, which can be activated by a variety of cytokines and inflammatory mediators, is another critical inhibitory mechanism that mediates repulsive signals in the injured CNS. The knockdown of either Rho associated coiled-coil containing protein kinase 2 (ROCK2) or its downstream substrate LIM domain kinase 1 promotes neuronal regeneration following ON crush. However, only ROCK2 knockdown was found to be neuroprotective in RGCs following ON axotomy (Koch *et al.* 2014). ROCK2 down-regulation leads to reduced calpain and caspase3 activity and a concurrent increase in protein kinase B (Akt) activity (Koch *et al.* 2014). Pharmacological inhibition of RhoA/ROCK pathway through Y-27632 or Fasudil administration promotes neuronal regeneration in a dose-dependent manner, probably because of enhanced MAPK and Akt phosphorylation (Lingor *et al.* 2007; Lingor *et al.* 2008). Pharmacological modulation of this pathway, thus, could represent a therapeutic approach for CNS cell restoration.

Another inhibitory pathway exists in the surrounding environment of the lesion (Fig. 5b-d). The myelin inhibitory proteins: Nogo, myelin-associated glycoprotein (MAG), and oligodendrocyte-myelin glycoprotein suppress axonal growth in the optic nerve by acting through Nogo receptors where they act in an orchestrated manner with other co-receptors, such as p75 neurotrophin receptor and epidermal growth factor receptor (Domeniconi *et al.* 2002; Wang *et al.* 2002b; Wang *et al.* 2002c; Koprivica 2005). Notably, deletion of its downstream signaling pathway, through protein kinase C appears to restore axonal growth by blocking Rho activation (Sivasankaran *et al.* 2004). Furthermore, the over-expression of dominant negative Nogo receptors in RGCs promoted axonal regeneration (Fischer 2004).

Alternatively to extrinsic factors inhibiting axon regeneration, many groups have shown that the intrinsic mechanisms prevent CNS axon regeneration (He and Jin 2016). One critical pathway, put forward by the group of Zhigang He, was the phosphoinositide 3-kinase/mammalian target of rapamycin (mTOR) signaling pathway. Following ON crush, a dramatic decrease in phosphoinositide 3-kinase/mTOR activity is observed (Park *et al.* 2008). Indeed, following ON crush, mTOR activity is suppressed by the phosphatase and tensin homolog (PTEN) (Fig. 5b). Genetically deleting PTEN in RGCs, using an adeno-associated virus, induces robust and long-distance axon regeneration following ON crush (Park *et al.* 2008). Interestingly, PTEN deletion following ON crush only stimulates the regeneration of a subset of RGCs (Park *et al.* 2008). A large number of RGC types exists with distinct physiology and projection patterns (Sanes and Masland 2015; Martersteck *et al.* 2017). Therefore, it is not surprising that distinct RGCs types respond heterogeneously to injury. Further studies have shown that a specific subtype of RGCs, the α-RGCs, are able to survive following ON crush and express insulin-like growth factor receptor (IGF1) as well as osteopontin (OPN) (Duan *et al.* 2015). Reprogramming of RGCs after injury is accompanied by changes in mRNA expression profiles. The transcription factors that are expressed after injury appear to determine whether a specific sub-type of RGC will regrow. The Kruppel-like factors 4 and 9 (KLF4 and KLF9), for example, play a major role suppressing axon development (Qin *et al.* 2013; Apara *et al.* 2017). KLF4 interacts with Tyr705-phosphorylated signal transducer and activator of transcription 3 (STAT3) suppressing its activity and function as an intrinsic barrier for regeneration of damaged adult RGC axons (Qin *et al.* 2013). KLF9 functions as another intrinsic inhibitor for axon regeneration as shRNA mediated knockdown of KLF9 promote RGC survival and axon regeneration following optic nerve injury *in vivo* (Apara *et al.* 2017). This KLF9-mediated inhibition is via interaction of the upstream kinase c-Jun N-terminal kinase 3 (JNK3) (Apara *et al.* 2017). Recent findings indicate that micro RNAs 135a and 135b (miRNA135s) could regulate KLF4 expression during axon development. Intravitreal administration of miRNA135 induced axon regeneration following ON injury, in part by suppressing KLF4 expression in RGCs (van Battum *et al.* 2018). SOX11, on the other hand, plays a dual role. When overexpressed, it can stimulate axon growth of non-α-RGCs while it induces cell death of α-RGCs following ON crush (Norsworthy *et al.* 2017). In addition to intrinsic growth metabolism, neuroinflammation has been shown to be critical

for RGCs axonal regeneration (Smith *et al.* 2009). The simple intraocular injection of Zymosan (protein-carbohydrate complexes derived from yeast cell wall), which enhances macrophage infiltration in the injured ON, greatly stimulates the expression of GAP-43 in RGC axons, resulting in accelerated axonal regeneration (Leon *et al.* 2000).

During the past decades, major effort has been made toward the development of combinatorial therapeutic approaches, targeting two or more neuronal pathways. Over stimulating cell growth programs by deleting PTEN and suppressor of cytokine signaling 3 (SOCS3) promotes a well-sustained axon regeneration (Fig. 5d), by brake-releasing two independent pathways that converge into axon growth-related gene expression (Sun *et al.* 2011). In an alternative approach, the use of the pro-inflammatory Zymosan, in combination to PTEN inhibition and cAMP analogue administration promotes axonal regeneration, and allows the recovery of long distance axonal degeneration (Kurimoto *et al.* 2010). The critical step following regeneration and functional synapses formation is the restoration of the conductance and visual function following injury. Treatment with the voltage-gated potassium channel blocker 4-aminopyridine (4-AP) or its methyl derivative 4-AP-3-Me restores conduction and visual acuity following PTEN/SOCS3 co-deletion. Similar phenomena were observed when mice were treated with 4-AP following OPN overexpression in the presence of IGF1 and ciliary neurotrophic factor. This highlights the importance of combination therapy for axon regeneration and improving visual conduction (Bei *et al.* 2016).

Spinal cord regeneration

Another attractive model for studying CNS regeneration is that of spinal cord injury (SCI). In addition to its scientific interest, SCI has a dramatic clinical impact, with the world health organization approximating between 250 000 to 500 000 people suffer from SCI each year (Courtine and Sofroniew 2019). The Cortico spinal neurons (CSNs) located in the mammalian neocortex are the major output from the brain to the spinal cord (making up to 90% of projections), which mediate both motor and sensory functions (Wang *et al.* 2017). Indeed, corticospinal tract (CST) lesions, such as a bilateral pyramidotomy, lead to the complete loss of voluntary movement. Following a spinal cord lesion, extrinsic mechanisms such as growth inhibitors or glial scars, inhibit axonal regeneration (Gaudet and Fonken 2018). Several inhibitory signaling molecules have since been identified such as Nogo or myelin-associated glycoproteins (Caroni and Schwab 1988; McKeon *et al.* 1991; Afshari *et al.* 2009; Lang *et al.* 2015). Indeed silencing these inhibitory cues in mouse or rat models of spinal cord injury has shown some success (Schmandke *et al.* 2014). Another approach, led by Zhigang He's group, questioned whether the inability of CNS neurons to regenerate involved intrinsic factors. They identified that mTOR (mammalian target of rapamycin) activity and *de novo* protein synthesis are suppressed after CNS lesions (Park *et al.* 2008). Reactivation of the mTOR pathway by silencing of PTEN (phosphatase and tensin homolog) and TSC1 (tuberous sclerosis complex 1), leads to extensive CST axon regeneration (Park *et al.* 2008). Together, these findings proved that both intrinsic and extrinsic mechanisms were responsible for inhibiting CST axon regeneration after spinal cord injury. Accordingly, the combined genetic deletion of Nogo receptors and PTEN, led to a major increase in the regeneration and sprouting of lesioned CSNs (Geoffroy *et al.* 2015). However, there was little to no functional amelioration in lesioned animals.

The lack of functional rescue observed in double mutants of Nogo and PTEN led to the idea that a better understanding of the locomotor system was required. Indeed, very little was known about the localization, development, and function of the CSNs responsible for voluntary movement. Using retrograde viral tracing strategies, it was found that CSNs were localized in both the motor and somatosensory cortex. Two major nuclei were identified, the rostral forelimb area (RFA) and the caudal forelimb area (CFA) (Wang *et al.* 2017). To better understand the precise function of RFA and CFA CSNs in voluntary task, a food pellet retrieval task was used to tease apart which CSNs were responsible for specific motor movements. Using AAV:Cre-driven GCamp6 expression in CSNs, it was shown that RFA CSNs fired prior to grasping the food-pellet, whereas CFA CSNs fired prior to reaching as well as post-grasping the food pellet (Wang *et al.* 2017). These data provide evidence supporting a parallel organization of motor tasks responsible for specific behavior organized in a topographic manner.

While much work has focused on spinal cord lesions, the majority of patients suffer from partial lesions. However, partial spinal cord injuries still result in complete loss of motor function below the site of injury. This hints toward the idea that unlesioned axons are unable to properly function despite being spared from injury. By carrying out a staggered hemisection of the thoracic spinal cord on opposing sides, Chen *et al.* (2018) took advantage of a partial spinal cord injury model to carry out a small compound screening approach. They identified that an agonist of the potassium/chloride transporter (KCC2) resulted in increased weight bearing strength in mice following lesion (Chen *et al.* 2018). Because of the complexity of spinal circuits, they questioned whether KCC2 activity was required by multiple or distinct neuronal subsets (excitatory, inhibitory, motor). Interestingly, only overexpression of KCC2 in inhibitory neurons (Vgat:Cre) resulted in an improved weight-bearing strength in injured mice. Moreover inhibitory neurons below the staggered lesion were dispensable for this rescue, since overexpressing KCC2 only in inhibitory neurons between the lesions was sufficient to rescue the weight bearing strength. Overall, this identifies a crucial role for inhibitory interneurons in a closed-circuit to be critical in associating the

excitation to inhibition ratio required to regulate functional recovery following a lesion (Chen *et al.* 2018).

The translation of these findings to the treatment of spinal cord injury, won't be simple as the genetic manipulation of tumor suppressor genes may not be suitable for the clinic. Attractive treatment alternatives could consist of applying growth factors (which occur endogenously in the CNS). However, adult CNS neurons lose their sensitivity to growth factors such as brain-derived neurotrophic factor (Liu *et al.* 2017). Moreover adult CSNs treated with OPN can be sensitized to the IGF1 by reactivating the mTOR pathway (Liu *et al.* 2017).

Furthermore, the identification that spared axons following partial spinal cord injury could be re-synchronized to induce functional recovery opens many questions, one of which, is the importance of inhibitory synapses conserved amongst other species. Indeed, the complexity in human spinal cord circuitry may pose a major challenge toward this clinical implication.

For instance, how does our current understanding on excitatory/inhibitory ratios in the rodent spinal cord translate to the human spinal cord? This is a daunting question since inhibitory feedback loops in human spinal cord may be more complex and thus more challenging to re-stimulate. Furthermore, more research should focus on understanding the coordinated action between neurons and glial cells. Synaptic activity, axonal and dendritic growth and regeneration are fine-tuned by glial cells (Liu *et al.* 2017). There are a few studies investigating how glial scar-induced disruption may be overcome by improving the communication between neurons and glial cells. Of note, exosomes released by glial cells in the PNS have shown to promote robust axonal regeneration and survival (Lopez-Leal and Court 2016). A similar result was obtained from mesenchymal stem cells releasing exosomes following spinal cord injury (Li *et al.* 2018; Liu *et al.* 2019).

Peripheral nerve regeneration

Insults such as physical trauma, chemotherapy or metabolic disorders can lead to peripheral nerve damage (Scholz *et al.* 2009). As previously mentioned, PNS axons have retained considerable capacity to regenerate following injury and to form functional connections with their original targets (Bremer *et al.* 2017). This seems in part because of a cell-intrinsic growth-promoting response of PNS neurons and to a favorable environment for axonal regeneration (Bremer *et al.* 2017). However, many aspects of this process, including how regenerating axons navigate across the lesion site and select their original trajectory at branch choice points, are not well understood *in vivo*. Whilst many animal models have been used to study PNS regeneration, the zebrafish has been heavily studied because of its transparency (allowing for *in vivo* live imaging) as well as the ability for genetic manipulation. Adult and larval fish both have well-defined PNS circuits and stereotyped behaviors, facilitating cell biology studies underlying PNS axon regrowth and synapse re-establishment (He and Jin 2016; Rasmussen and Sagasti 2017).

In vertebrates, spinal motor nerve degeneration after transection occurs through morphological hallmarks characteristic of Wallerian degeneration (Fig. 6a), a stereotyped form of degeneration (Waller 1851). Live imaging on zebrafish showed that following nerve transection, degradation of the distal axon happens within 120–240 min (Rosenberg *et al.* 2012). Moreover it highlighted that individual axons within the transected nerves initiate fragmentation at different times independent of myelination and thickness of the axons. Once initiated, fragmentation occurs along the entire length of the axon within minutes. Recruitment of macrophages to the injury site starts between 60–120 min before nerve fragmentation, and with the onset of axonal fragmentation, macrophages enter the nerve and begin to phagocytose nerve debris. Experimental elimination of Schwann cells through genetic ablation does not change the recruitment and behavior of macrophages to the injury site suggesting that this process is independent on Schwann cells (Dutton *et al.* 2001; Rosenberg *et al.* 2012).

In zebrafish, 80% of regenerating axons retain the ability to select their original branch-specific trajectory in both ventral and dorsal nerve branches following complete nerve transection (Isaacman-Beck *et al.* 2015). After complete nerve transection, usually a single axon emerges from the proximal nerve stump to pioneer a regenerative path across the injury site. At later stages, multiple emerging axons join the pioneering axon and extend with about twice the speed of the pioneering axon across the injury gap. The synaptic low-density lipoprotein receptor-related protein 4 is critical for the regrowth of follower axons across the injury gap and toward their original targets (Gribble *et al.* 2018) (Fig. 6c). Live-cell imaging shows that Schwann cells provide directionality to axons, by crossing the injury site and navigating to their original trajectory. An interaction between Schwann cells and motor axons is triggered following motor nerve transection leading to highly coordinated changes in axonal and Schwann cell morphology during both degeneration and regeneration (Fig. 6b). For instance, once axons start to fragment, Schwann cell membranes, localized distal to the lesion site, undergo dramatic morphological changes returning to a more immature state (Rosenberg *et al.* 2014). Lrp4 promotes the morphological changes associated with Schwann cells re-differentiation after injury-induced de-differentiation. *In vivo* evidence suggests that low-density lipoprotein receptor-related protein 4 promotes peripheral nerve regeneration through a non-canonical, Agrin/MuSK independent signalling pathway that is critical for neuromuscular synapse development in mammals and zebrafish (Gribble *et al.* 2018). The importance of this process in promoting vertebrate nerve regeneration is also confirmed by

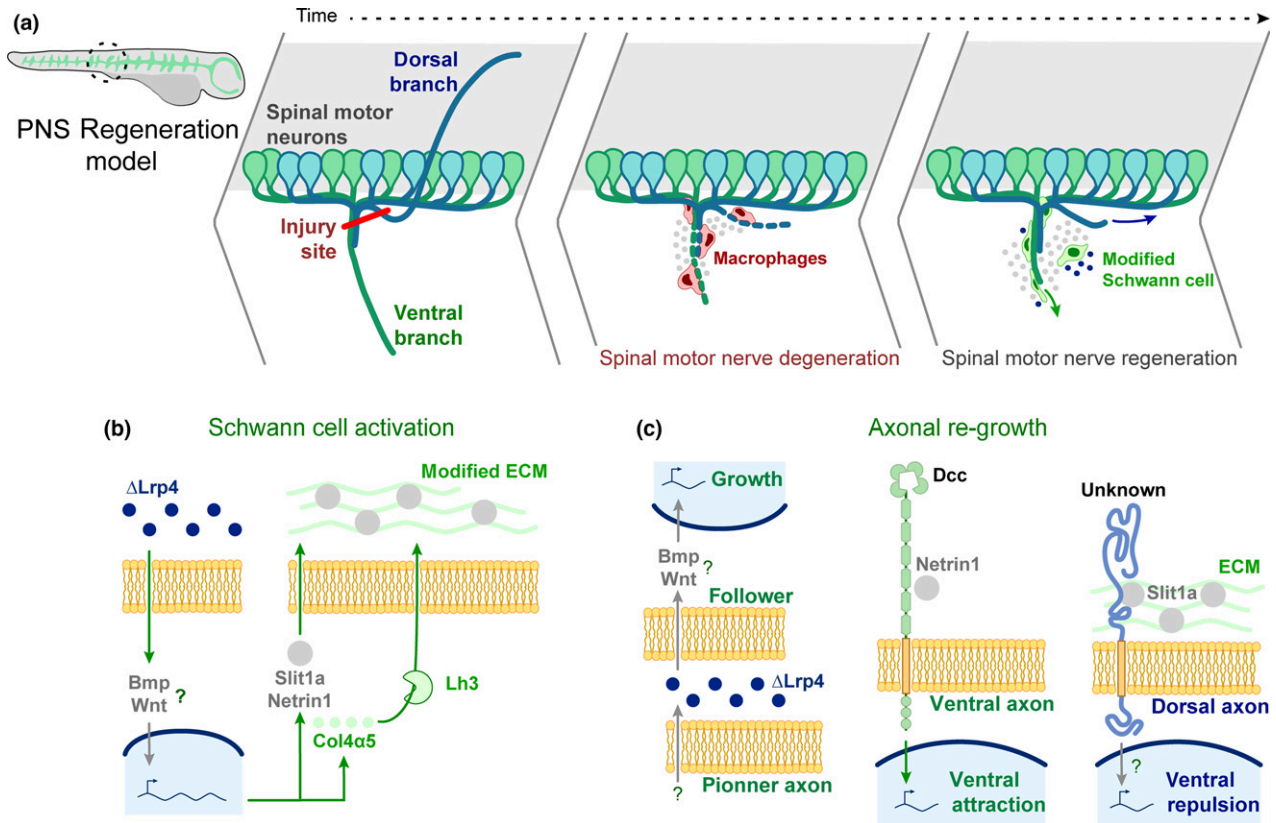

Fig. 6 PNS axon regeneration in zebrafish spinal motor nerves. (a) Zebrafish has extensively been used as PNS regeneration model. Its transparency allows live-imaging of axons and genetic manipulations remain simpler than in mammals. In this model, a transection of both, dorso-ventral spinal cord motor branches is performed. First, a Wallerian degeneration of the sectioned nerves occurs, dependent on macrophages activity. Then, spontaneous regeneration occurs, promoted by intrinsic and extrinsic signals. (b) After injury, 80% of the lesioned axons retain the ability to regenerate. This relies on Schwann cell activation that will ensure the proper pathfinding of the regenerating axons through different mechanisms. This activation occurs by exposure to ΔLrp4 and triggers the expression of axon guidance molecules (Netrin-1 and Slit1a) and the remodelling of the extracellular matrix (ECM). (c) There is evidence that nerve regrowth relies on the extension of a single pioneer axon that will be used as migration scaffold by follower axons. This process seems dependent on ΔLrp4 but no receptors have been identified yet. Axon guidance of dorsal or ventral projections differs. Netrin-1 and Dcc promotes the growth of ventral axons while Slit1a prevent dorsal axon from growing dorsally, through a yet unknown receptor.

the impairment of peripheral nerve regeneration by Topoisomerase I inhibitor, identified through a fin removal assay performed by Bremer and colleagues, which hypothesizes that Topoisomerase I promotes peripheral nerve regeneration by regulating gene transcription specifically in de-differentiated Schwann cells (Bremer *et al.* 2017).

In zebrafish mutants lacking Schwann cells, 50–80% of transected nerves show a failure in regenerating axons along their original trajectory through the ventral myotome compared with 20% in wild-type (Rosenberg *et al.* 2014). Netrin1 and its receptor DCC have been implicated in promoting the extent of axon regeneration (Fig. 6c): *in vivo Netrin1b* mRNA is expressed in Schwann cells before and after motor nerve transection, and *dcc* mRNA is detectable in motor neurons during initial axonal regrowth. In $dcc^{zm130198}$ mutants, characterized by a 90% reduction of *dcc* mRNA, 40% of regenerating motor axons extended not only along their original path but also along ectopic lateral trajectories. This suggests that DCC is required to guide regenerating ventral motor axons across the injury gap toward their original trajectory *in vivo* (Rosenberg *et al.* 2014).

Early after transection (7–11 h post transection), dorsal axons sprout growth cones that explore the environment with multi-directional extensions and retractions. In the following 2–4 h, only the growth cones extending along the correct dorsal path are stabilized and quickly extend, supporting the existence of extrinsic cues that drive the growth cones through the branch point (Isaacman-Beck *et al.* 2015). Among these cues, the collagen-modifying glycosyltransferase lysyl hydroxylase 3 (*lh3*), expressed by Schwann cells, has a crucial role in promoting target selectivity of regenerating dorsal, but not ventral nerve axons (Fig. 6b). For this

process, equally fundamental is Collagen4a5 (col4a5), the *lh3* substrate, which is over expressed in a small group of Schwann cells located ventral and ventrolaterally to the transection gap. Col4a5 destabilizes mistargeted axons, directing regenerating axons toward their original targets. Following the nerve transection there is an up-regulation of the canonical axon guidance repellent *slit1a* in cells expressing col4a5. Hypothetically, in response to injury, Schwann cells ventral to the transection site, secrete col4a5, which binds and accumulates Slit, thereby forming a repulsive barrier to direct dorsal axons onto their original dorsal path (Isaacman-Beck *et al.* 2015) (Fig. 6c).

Real-time imaging on live zebrafish has allowed deciphering some of the intrinsic and extrinsic mechanisms responsible for peripheral nerve regeneration, but the molecular mechanisms and the specific cellular interactions which are vital for axon regeneration are not completely understood. Furthermore, the identification of other regeneration-promoting molecules could allow the development of new neuronal repair strategies. Based on that premise a fin removal assay was developed that enabled to perform the first whole organism small molecule screen to identify pathways that promote vertebrate nerve regeneration (Bremer *et al.* 2017). The approach utilized the regeneration of the ring-like nerve of zebrafish larvae pectoral fin after removal as readout of axonal regrowth. 480 bioactive compounds with known biological targets were screened to identify molecular pathways promoting nerve regrowth. After excluding 134 compounds which affected larvae health, the remaining compounds were combined in 69 distinct pools and added each of these pool to larvae immediately following fin amputation to evaluate the re-formation of regenerating axons of a ring-like nerve network at the fin base that normally occurs in 24 hours. In larvae exposed to 15 pools regenerating axons failed to form the characteristic ring-like network. Next, each of the compounds was tested within a given pool individually. This failed to identify a singly effective compound in 20% of pools which reduced nerve regrowth in the first pass of the screen. Despite the fin removal assay is a powerful screening method to study nerve regeneration, the high false positive rate indicates the importance of a second method to confirm the results (Fig. 7).

Other strategies for CNS/PNS repair

Many strategies have shown incredible potential for regeneration of the CNS following an injury, but a major concern remains the significant death of neurons (Ling *et al.* 2015; Mckee and Daneshvar 2015). Moreover complex diseases such as stroke, amyloid-β plaque accumulation and inflammatory-mediated neurodegeneration lead to broad defects such as defective communication, glial scar formation and ultimately neuronal loss, which make it challenging to repair (Chauhan 2014; Albrecht *et al.* 2015). In such cases, the development of cell therapy has shown some promising results (Gates *et al.* 2000). Stem cell manipulation is a powerful tool to understand neurodevelopment and its integration into developing tissue can recapitulate neurogenesis. In vivo strategies based on stem cell replacement such as human and mice-derived embryonic stem cells (ESCs) for brain repair in models of neurological diseases, have made significant progress in pre-clinical trials (Barker *et al.* 2015; Péron *et al.* 2017). It is known that the lack of endogenous repair in the brain leads to a condition of life-long disease and disability after a neuronal damage. Thus, understanding how well the transplanted neurons are able to mature and integrate into damaged circuits is a challenging task (Fig. 7a).

Because of the complexity of the organization of the cerebral cortex in terms of highly specific topography and connectivity (Guillemot *et al.* 2006; Tiberi *et al.* 2012), the replacement of lost neurons is a daunting challenge. A notable initial attempt at regenerative cortical cell therapy showed that transplanting embryonic cortical tissue from transgenic mice to lesioned cortex in an adult brain could regenerate neurons and establish neuronal projections and synaptic connections (Wernig 2004; Gaillard *et al.* 2007). These findings have been corroborated by data from other studies which have shown that not only ESCs have intrinsic mechanisms of corticogenesis (Gaspard *et al.* 2008) but induced pluripotent stem cell-derived neurons also can regenerate functional cortical neurons (Falkner *et al.* 2016; Espuny-Camacho *et al.* 2018).

There are certain prerequisites for the ESCs to successfully integrate the malfunctioning adult cortex (Fig. 7b). Re-establishment of neuronal connectivity and function requires identity match between the damaged brain area and the transplanted material (Michelsen *et al.* 2015). Human embryonic stem cell-derived visual cortical neurons, once grafted into the lesioned adult murine cortex, are able to mature and integrate into the corresponding cortical layers, acquiring a visual-like identity and rewiring the circuit with appropriate inputs and outputs (Espuny-Camacho *et al.* 2018). Interestingly, Human embryonic stem-derived cells transplanted into motor cortical areas showed a reduced maturation and a lower capacity to send long-range projections, suggesting that the areal identity match represents an important factor for successful cortical transplantation.

Another key factor accompanying identify match (Fig. 7c), is the adaptation to the extrinsic *in vivo* environment to establish polarity, such as microenvironment generated by blood vessels (Javaherian and Kriegstein 2009) or composition of extracellular matrix (Fietz *et al.* 2012). Context-wise, junctional complexes block the incorporation of grafted cells at the apical surface (Espuny-Camacho *et al.* 2013). For this reason, a new grafting method called TETCaD (transplantation to epithelial tissue with calcium depletion) has been developed, using moderate concentrations of EGTA (ethylene glycol tetra-acetic acid) to chelate calcium,

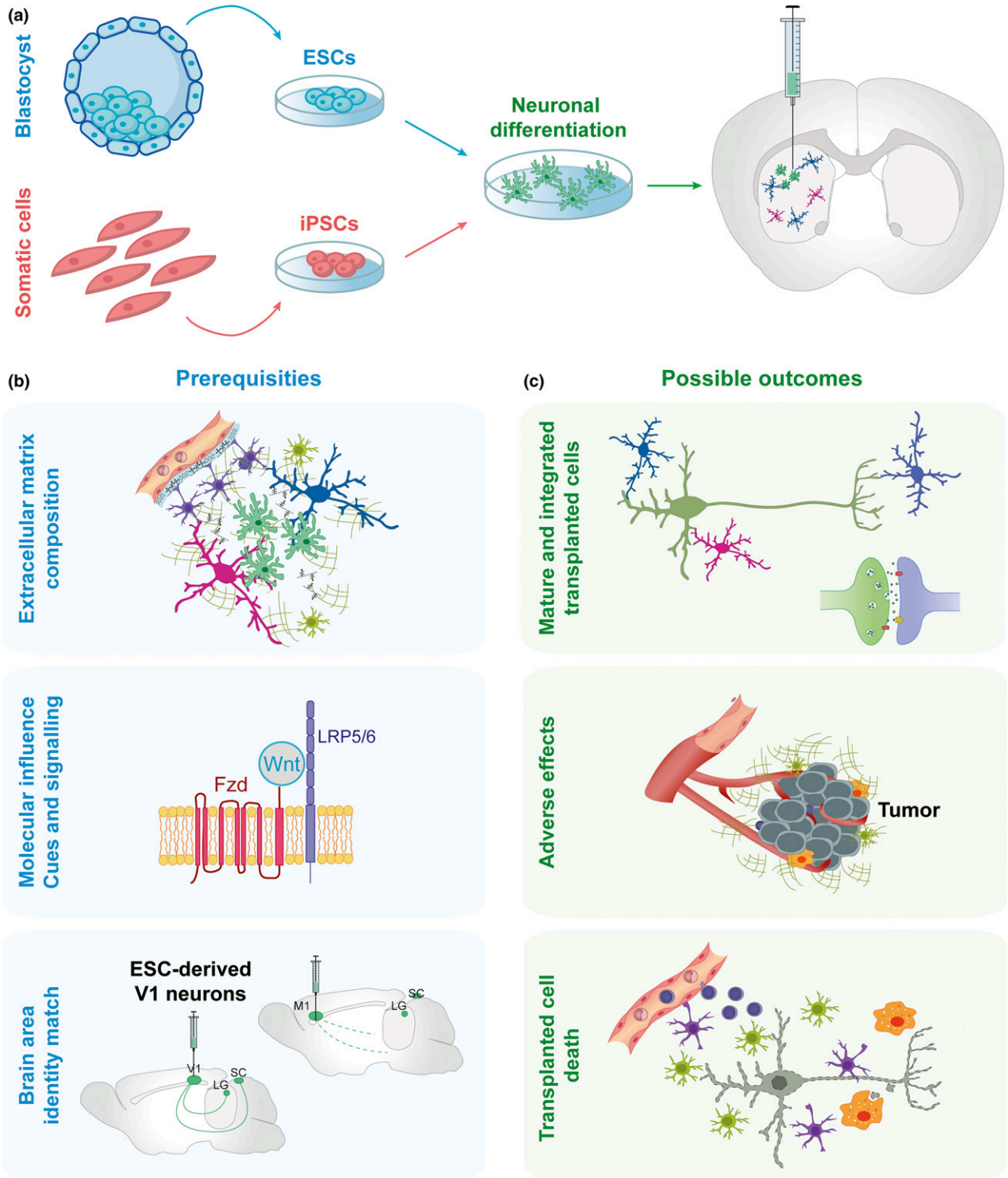

Fig. 7 Cell therapy. (a) Strategies based on stem cell replacement such as human- and mouse-derived embryonic stem cells (ESCs) and induced pluripotent stem cell (iPSC)-derived neurons. Grafting iPSC-derived neurons in brain circuits requires (b) adaptation to the extrinsic in vivo microenvironment or composition of extracellular matrix, lesion site-specific cues and signalling pathways, and identity match between the damaged brain area and the transplanted material. (c) Transplanted neurons could mature and integrate into damaged circuits; however, potential adverse effects as tumors or neuron death should be addressed before these strategies are transferred to the clinic.

increasing efficiency of transplantation and dissociating adherents junctions in the epithelial tissue (Nagashima *et al.* 2014). Lastly in the molecular level, lesion site-specific cues and signalling pathways such as the WNT signalling and NOTCH2NL genes have been implicated in human corticogenesis (Raitano *et al.* 2015; Fiddes *et al.* 2018; Suzuki *et al.* 2018). *In vitro* and *in vivo* use of induced pluripotent stem cells in animal models simulating human diseases such as stroke (Tornero *et al.* 2013), Alzheimer's disease (AD) (Espuny-Camacho *et al.* 2017) and multiple sclerosis (Theotokis *et al.* 2015), highlight the hallmarks of synaptic activity, connectivity and cortical neuronal maturation (Suzuki and Vanderhaeghen 2015). Specifically for AD, the significant expression of non- coding RNA sequences in grafted human neurons further opens up an entirely new avenue for investigating the involvement of non-coding RNAs in AD-induced neurodegeneration.

Altogether, establishing the molecular mechanisms regulating fate acquisition and plasticity after cell transplantation is of great importance in the light of preclinical studies. Determining which cues are involved in fate maintenance, area specificity and functional integration in the adult brain will be pivotal for successful outcomes in stem cell-based therapies. These signaling events may also play major roles in neurodegeneration so targeting pathways such as the Wnt pathway, may result in the establishment of novel therapeutic approaches. Nonetheless, potential adverse effects and host-transplant compatibility should be addressed before these approaches can be considered for clinical applications.

Acknowledgements and conflict of interest disclosure

This Review was invited following the 2nd JNC-ISN Flagship School held in 2018 in Alpbach, Austria. Alain Chédotal was the Scientific Head of that Flagship School. The co-authors are students participating in the Flagship School.

References

Aberle H. (2019) Axon guidance and collective cell migration by substrate-derived attractants. *Front. Mol. Neurosci.* **12**, 148.

Ackman J. B. and Crair M. C. (2014) Role of emergent neural activity in visual map development. *Curr. Opin. Neurobiol.* **24**, 166–175.

Afshari F. T., Kappagantula S. and Fawcett J. W. (2009) Extrinsic and intrinsic factors controlling axonal regeneration after spinal cord injury. *Expert Rev. Mol. Med.* **11**, e37.

Albrecht J. S., Liu X., Smith G. S., Baumgarten M., Rattinger G. B., Gambert S. R., Langenberg P. and Zuckerman I. H. (2015) Stroke incidence following traumatic brain injury in older adults. *J. Head Trauma Rehabil.* **30**, E62–E67.

Apara A., Galvao J., Wang Y. *et al.* (2017) KLF9 and JNK3 interact to suppress axon regeneration in the adult CNS. *J. Neurosci.* **37**, 9632–9644.

Avilés E. C., Stoeckli E. T., Avil E. C. and Stoeckli E. T. (2016) Canonical wnt signaling is required for commissural axon guidance. *Dev. Neurobiol.* **76**, 190–208.

Barker R. A., Drouin-Ouellet J. and Parmar M. (2015) Cell-based therapies for Parkinson disease—past insights and future potential. *Nat. Rev. Neurol.* **11**, 492–503.

van Battum E. Y., Verhagen M. G., Vangoor V. R. *et al.* (2018) An image-based miRNA screen identifies miRNA-135s as regulators of CNS axon growth and regeneration by targeting Krüppel-like factor 4. *J. Neurosci.* **38**, 613–630.

Bei F., Lee H. H. C., Liu X. *et al.* (2016) Restoration of visual function by enhancing conduction in regenerated axons. *Cell* **164**, 219–232.

Belle M., Godefroy D., Dominici C., Heitz-Marchaland C., Zelina P., Hellal F., Bradke F. and Chédotal A. (2014) A simple method for 3D analysis of immunolabeled axonal tracts in a transparent nervous system. *Cell Rep.* **9**, 1191–1201.

Bellen H. J., Tong C. and Tsuda H. (2010) 100 years of Drosophila research and its impact on vertebrate neuroscience: a history lesson for the future. *Nat. Rev. Neurosci.* **11**, 514–522.

Ben-Arie N., Hassan B. A., Bermingham N. A., Malicki D. M., Armstrong D., Matzuk M., Bellen H. J. and Zoghbi H. Y. (2000) Functional conservation of atonal and Math1 in the CNS and PNS. *Development* **127**, 1039–48.

Bhansali P., Rayport I., Rebsam A. and Mason C. (2014) Delayed neurogenesis leads to altered specification of ventrotemporal retinal ganglion cells in albino mice. *Neural Dev.* **9**, 11.

Blockus H. and Chédotal A. (2016) Slit-Robo signaling. *Development* **143**, 3037–3044.

Bonanomi D. and Pfaff S. L. (2010) Motor axon pathfinding. *Cold Spring Harb. Perspect. Biol.* **2**, a001735.

Bourikas D., Pekarik V., Baeriswyl T., Grunditz Å., Sadhu R., Nardó M. and Stoeckli E. T. (2005) Sonic hedgehod guides commissural axons along the longitudinal axis of the spinal cord. *Nat. Neurosci.* **8**, 297–304.

Bovolenta P. and Sanchez-Arrones L. (2012) Shh goes multidirectional in axon guidance. *Cell Res.* **22**, 611–613.

Bremer J., Skinner J. and Granato M. (2017) A small molecule screen identifies in vivo modulators of peripheral nerve regeneration in zebrafish. *PLoS ONE.*

Brose K., Bland K. S., Wang K. H., Arnott D., Henzel W., Goodman C. S., Tessier-Lavigne M. and Kidd T. (1999) Slit proteins bind robo receptors and have an evolutionarily conserved role in repulsive axon guidance. *Cell* **96**, 795–806.

Campbell D. S. and Holt C. E. (2001) Chemotropic responses of retinal growth cones mediated by rapid local protein synthesis and degradation. *Neuron* **32**, 1013–1026.

Cárdenas A., Villalba A., Juan Romero C. *et al.* (2018) Evolution of cortical neurogenesis in amniotes controlled by robo signaling levels. *Cell* **174**, 590–606.e21.

Caroni P. and Schwab M. E. (1988) Antibody against myelin associated inhibitor of neurite growth neutralizes nonpermissive substrate properties of CNS white matter. *Neuron* **1**, 85–96.

Castets M. and Mehlen P. (2010) Netrin-1 role in angiogenesis: to be or not to be a pro-angiogenic factor? *Cell Cycle* **9**, 1466–71.

Charoy C., Nawabi H., Reynaud F., Derrington E., Bozon M., Wright K., Falk J., Helmbacher F., Kindbeiter K. and Castellani V. (2012) gdnf Activates midline repulsion by Semaphorin3b via NCAM during commissural axon guidance. *Neuron* **75**, 1051–1066.

Charron F., Stein E., Jeong J., McMahon A. P. and Tessier-Lavigne M. (2003) The morphogen sonic hedgehog is an axonal chemoattractant that collaborates with netrin-1 in midline axon guidance. *Cell* **113**, 11–23.

Chauhan N. B. (2014) Chronic neurodegenerative consequences of traumatic brain injury. *Restor. Neurol. Neurosci.* **32**, 337–65.

Chédotal A. (2011) Further tales of the midline. *Curr. Opin. Neurobiol.* **21**, 68–75.

Chédotal A. (2014) Development and plasticity of commissural circuits: from locomotion to brain repair. *Trends Neurosci.* **37**, 551–562.

Chédotal A. (2019) Roles of axon guidance molecules in neuronal wiring in the developing spinal cord. *Nat. Rev. Neurosci.* **20**, 380–396.

Chen B. E., Kondo M., Garnier A., Watson F. L., Püettmann-Holgado R., Lamar D. R. and Schmucker D. (2006) The molecular diversity of dscam is functionally required for neuronal wiring specificity in Drosophila. *Cell* **125**, 607–620.

Chen B., Li Y., Yu B. *et al*. (2018) Reactivation of dormant relay pathways in injured spinal cord by KCC2 manipulations. *Cell*.

Coate T. M., Spita N. A., Zhang K. D., Isgrig K. T. and Kelley M. W. (2015) Neuropilin-2/Semaphorin-3F-mediated repulsion promotes inner hair cell innervation by spiral ganglion neurons. *Elife* **4**, e07830.

Courtine G. and Sofroniew M. V. (2019) Spinal cord repair: advances in biology and technology. *Nat. Med.* **25**, 898–908.

d'Amora M. and Giordani S. (2018) The utility of Zebrafish as a model for screening developmental neurotoxicity. *Front. Neurosci.* **12**, 976.

Dascenco D., Erfurth M.-L., Izadifar A. *et al*. (2015) Slit and receptor tyrosine phosphatase 69D confer spatial specificity to axon branching via Dscam1. *Cell* **162**, 1140–1154.

Delloye-Bourgeois C., Jacquier A., Charoy C. *et al*. (2015) PlexinA1 is a new Slit receptor and mediates axon guidance function of Slit C-terminal fragments. *Nat. Neurosci.* **18**, 36–45.

Di Meglio T., Nguyen-Ba-Charvet K. T., Tessier-Lavigne M., Sotelo C., Di Meglio T. and Chédotal A. (2008) Molecular mechanisms controlling midline crossing by precerebellar neurons. *J. Neurosci.* **28**, 6285–94.

Ding Q., Joshi P., Xie Z., Xiang M. and Gan L. (2012) BARHL2 transcription factor regulates the ipsilateral/contralateral subtype divergence in postmitotic dl1 neurons of the developing spinal cord. *Proc. Natl Acad. Sci. USA* **109**, 1566–1571.

Domeniconi M., Cao Z., Spencer T. *et al*. (2002) Myelin-associated glycoprotein interacts with the Nogo66 receptor to inhibit neurite outgrowth. *Neuron* **35**, 283–290.

Dominici C., Moreno-Bravo J. A., Puiggros S. R., Rappeneau Q., Rama N., Vieugue P., Bernet A., Mehlen P. and Chédotal A. (2017) Floor-plate-derived netrin-1 is dispensable for commissural axon guidance. *Nature* **545**, 350–354.

Druckenbrod N. R., and Goodrich L.V. (2015) Sequential retraction segregates SGN processes during target selection in the cochlea. *J. Neurosci.* **35**, 16221–16235.

Duan X., Qiao M., Bei F., Kim I. J., He Z. and Sanes J. R. (2015) Subtype-specific regeneration of retinal ganglion cells following axotomy: effects of osteopontin and mtor signaling. *Neuron* **85**, 1244–1256.

Ducuing H., Gardette T., Pignata A., Tauszig-Delamasure S. and Castellani V. (2019) Commissural axon navigation in the spinal cord: a repertoire of repulsive forces is in command. *Semin. Cell Dev. Biol.* **85**, 3–12.

Dutton K. A., Pauliny A., Lopes S. S., Elworthy S., Carney T. J., Rauch J., Geisler R., Haffter P. and Kelsh R. N. (2001) Zebrafish colourless encodes sox10 and specifies non-ectomesenchymal neural crest fates. *Development* **128**, 4113–25.

Edwards T. J., Sherr E. H., Barkovich A. J. and Richards Linda J. (2014) Clinical, genetic and imaging findings identify new causes for corpus callosum development syndromes. *Brain* **137**, 1579–613.

Ellenbroek B. and Youn J. (2016) Rodent models in neuroscience research: is it a rat race? *Dis. Model. Mech.* **9**, 1079–1087.

Escalante A., Murillo B., Morenilla-Palao C., Klar A. and Herrera E. (2013) Zic2-dependent axon midline avoidance controls the formation of major ipsilateral tracts in the CNS. *Neuron* **80**, 1392–1406.

Espuny-Camacho I., Michelsen K. A., Gall D. *et al*. (2013) Pyramidal neurons derived from human pluripotent stem cells integrate efficiently into mouse brain circuits in vivo. *Neuron* **77**, 440–456.

Espuny-Camacho I., Arranz A. M., Fiers M. *et al*. (2017) Hallmarks of Alzheimer's disease in stem-cell-derived human neurons transplanted into mouse brain. *Neuron* **93**, 1066–1081.e8.

Espuny-Camacho I., Michelsen K. A., Linaro D., Bilheu A., Acosta-Verdugo S., Herpoel A., Giugliano M., Gaillard A. and Vanderhaeghen P. (2018) Human pluripotent stem-cell-derived cortical neurons integrate functionally into the lesioned adult murine visual cortex in an area-specific way. *Cell Rep.* **23**, 2732–2743.

Fabre P. J., Shimogori T. and Charron F. (2010) Segregation of ipsilateral retinal ganglion cell axons at the optic chiasm requires the Shh receptor Boc. *J. Neurosci.* **30**, 266–75.

Falkner S., Grade S., Dimou L., Conzelmann K.-K., Bonhoeffer T., Götz M. and Hübener M. (2016) Transplanted embryonic neurons integrate into adult neocortical circuits. *Nature* **539**, 248–253.

Fiddes I. T., Lodewijk G. A., Mooring M., Salama S. R., Jacobs F. M. J. and Haussler D. (2018) Human-specific NOTCH2NL genes affect notch signaling and cortical neurogenesis. *Cell* **173**.

Fietz S. A., Lachmann R., Brandl H. *et al*. (2012) Transcriptomes of germinal zones of human and mouse fetal neocortex suggest a role of extracellular matrix in progenitor self-renewal. *Proc. Natl Acad. Sci. USA* **109**, 11836–11841.

Finci L., Zhang Y., Meijers R. and Wang J.-H. (2015) Signaling mechanism of the netrin-1 receptor DCC in axon guidance. *Prog. Biophys. Mol. Biol.* **118**, 153–160.

Finlay B. and Darlington R. (1995) Linked regularities in the development and evolution of mammalian brains. *Science* **268**, 1578–1584.

Fischer D. (2004) Counteracting the Nogo receptor enhances optic nerve regeneration if retinal ganglion cells are in an active growth state. *State. J. Neurosci.* **24**, 1646–1651.

Fothergill T., Donahoo A.-L. S., Douglass A., Zalucki O., Yuan J., Shu T., Goodhill G. J. and Richards L. J. (2014) Netrin-DCC signaling regulates corpus callosum formation through attraction of pioneering axons and by modulating Slit2-mediated repulsion. *Cereb. Cortex* **24**, 1138–1151.

Friocourt F. and Chédotal A. (2017) The Robo3 receptor, a key player in the development, evolution, and function of commissural systems. *Dev. Neurobiol.* **77**, 876–890.

Friocourt F., Kozulin P., Belle M., Suárez R., Di-Poï N., Richards L. J., Giacobini P. and Chédotal A. (2019) Shared and differential features of Robo3 expression pattern in amniotes. *J. Comp. Neurol.* **527**, 2009–2029.

Gaillard A., Prestoz L., Dumartin B., Cantereau A., Morel F., Roger M. and Jaber M. (2007) Reestablishment of damaged adult motor pathways by grafted embryonic cortical neurons. *Nat. Neurosci.* **10**, 1294–1299.

Garbe D. S. and Bashaw G. J. (2007) Independent functions of Slit-Robo repulsion and Netrin-Frazzled attraction regulate axon crossing at the midline in Drosophila. *J. Neurosci.* **27**, 3584–92.

García-Frigola C., Carreres M. I., Vegar C., Mason C. A. and Herrera E. (2008) Zic2 promotes axonal divergence at the optic chiasm midline by EphB1-dependent and -independent mechanisms. *Development* **135**, 1833–1841.

Gaspard N., Bouschet T., Hourez R. *et al*. (2008) An intrinsic mechanism of corticogenesis from embryonic stem cells. *Nature* **455**, 351–357.

Gates M. A., Fricker-Gates R. A. and Macklis J. D. (2000) Reconstruction of cortical circuitry. *Prog. Brain Res.* **127**, 115–156.

Gaudet A. D. and Fonken L. K. (2018) Glial cells shape pathology and repair after spinal cord injury. *Neurotherapeutics* **15**, 554–577.

Gazzaniga M. S. (2000) Cerebral specialization and interhemispheric communication: does the corpus callosum enable the human condition? *Brain* **123**, 1293–1326.

Geoffroy C. G., Lorenzana A. O., Kwan J. P. *et al*. (2015) Effects of PTEN and Nogo codeletion on corticospinal axon sprouting and regeneration in mice. *J. Neurosci.* **35**, 6413–6428.

Gitler A. D., Dhillon P. and Shorter J. (2017) Neurodegenerative disease: models, mechanisms, and a new hope. *Dis. Model. Mech.* **10**, 499–502.

Gobius I., Morcom L., Suárez R. *et al*. (2016) Astroglial-mediated remodeling of the interhemispheric midline is required for the formation of the corpus callosum. *Cell Rep.* **17**, 735–747.

Gobius I., Suárez R., Morcom L., Paolino A., Edwards T. J., Kozulin P. and Richards L. J. (2017) Astroglial-mediated remodeling of the interhemispheric midline during telencephalic development is exclusive to eutherian mammals. *Neural Dev.* **12**, 9.

Goddard J. M., Rossel M., Manley N. R. and Capecchi M. R. (1996) Mice with targeted disruption of Hoxb-1 fail to form the motor nucleus of the VIIth nerve. *Development* **122**, 3217–28.

Gribble K. D., Walker L. J., Saint-Amant L., Kuwada J. Y. and Granato M. (2018) The synaptic receptor Lrp4 promotes peripheral nerve regeneration. *Nat. Commun.* **9**, 2389.

Guillemot F., Molnár Z., Tarabykin V. and Stoykova A. (2006) Molecular mechanisms of cortical differentiation. *Eur. J. Neurosci.* **23**, 857–868.

Guillery R. W., Mason C. A. and Taylor J. S. H. (1995) Developmental determinants at the mammalian optic chiasm. *J. Neurosci.* **15**, 4727–4737.

Guy A. T., Nagatsuka Y., Ooashi N. *et al*. (2015) Glycerophospholipid regulation of modality-specific sensory axon guidance in the spinal cord. *Science* **349**, 974–977.

Hansen D. V., Lui J. H., Parker P. R. L. and Kriegstein A. R. (2010) Neurogenic radial glia in the outer subventricular zone of human neocortex. *Nature* **464**, 554–561.

Haubensak W., Attardo A., Denk W. and Huttner W. B. (2004) Neurons arise in the basal neuroepithelium of the early mammalian telencephalon: a major site of neurogenesis. *Proc. Natl Acad. Sci. USA* **101**, 3196–201.

He Z. and Jin Y. (2016) Intrinsic control of axon regeneration. *Neuron* **90**, 437–451.

Herrera E. (2004) Foxd1 is required for proper formation of the optic chiasm. *Development* **131**, 5727–5739.

Herrera E., Brown L., Aruga J., Rachel R. A., Dolen G., Mikoshiba K., Brown S. and Mason C. A. (2003) Zic2 patterns binocular vision by specifying the uncrossed retinal projection. *Cell* **114**, 545–557.

Herrera E., Erskine L. and Morenilla-Palao C. (2019) Guidance of retinal axons in mammals. *Semin. Cell Dev. Biol.* **85**, 48–59.

Hiramoto M., Hiromi Y., Giniger E. and Hotta Y. (2000) The Drosophila netrin receptor frazzled guides axons by controlling netrin distribution. *Nature* **406**, 886–889.

Huang L. C., Barclay M., Lee K., Peter S., Housley G. D., Thorne P. R. and Montgomery J. M. (2012) Synaptic profiles during neurite extension, refinement and retraction in the developing cochlea. *Neural Dev.* **7**, 38.

Hüll M. and Bähr M. (1994) Differential regulation of c-JUN expression in rat retinal ganglion cells after proximal and distal optic nerve transection. *Neurosci. Lett.* **178**, 39–42.

Isaacman-Beck J., Schneider V., Franzini-Armstrong C. and Granato M. (2015) The lh3 glycosyltransferase directs target-selective peripheral nerve regeneration. *Neuron* **88**, 691–703.

Iwai-Takekoshi L., Balasubramanian R., Sitko A., Khan R., Weinreb S., Robinson K. and Mason C. (2018) Activation of Wnt signaling reduces ipsilaterally projecting retinal ganglion cells in pigmented retina. *Development* **145**, dev163212.

Jalink K., Eichholtz T., Postma F. R., van Corven E. J. and Moolenaar W. H. (1993) Lysophosphatidic acid induces neuronal shape changes via a novel, receptor-mediated signaling pathway: similarity to thrombin action. *Cell Growth Differ* **4**, 247–255.

Javaherian A. and Kriegstein A. (2009) A stem cell niche for intermediate progenitor cells of the embryonic cortex. *Cereb. Cortex* **19**, i70–i77.

Jaworski A., Long H. and Tessier-Lavigne M. (2010) Collaborative and specialized functions of Robo1 and Robo2 in spinal commissural axon guidance. *J. Neurosci.* **30**, 9445–9453.

Jeffery G. and Erskine L. (2005) Variations in the architecture and development of the vertebrate optic chiasm. *Prog. Retin. Eye Res.* **24**, 721–753.

Jen J. C., Chan W.-M. M., Bosley T. M., *et al*. (2004) Mutations in a human ROBO gene disrupt hindbrain axon pathway crossing and morphogenesis. *Science* **304**, 1509–1513.

Kinoshita M. O., Furuya S., Ito S. *et al*. (2009) Lipid rafts enriched in phosphatidylglucoside direct astroglial differentiation by regulating tyrosine kinase activity of epidermal growth factor receptors. *Biochem. J.* **419**, 565–575.

Koch J. C., Tönges L., Barski E., Michel U., Bähr M. and Lingor P. (2014) ROCK2 is a major regulator of axonal degeneration, neuronal death and axonal regeneration in the CNS. *Cell Death Dis.* **5**, e1225–e1225.

Koprivica V. (2005) EGFR activation mediates inhibition of axon regeneration by myelin and chondroitin sulfate proteoglycans. *Science* **310**, 106–110.

Kriegstein A., Noctor S. and Martínez-Cerdeño V. (2006) Patterns of neural stem and progenitor cell division may underlie evolutionary cortical expansion. *Nat. Rev. Neurosci.* **7**, 883–890.

Kurimoto T., Yin Y., Omura K., Gilbert H.-Y., Kim D., Cen L.-P., Moko L., Kugler S. and Benowitz L. I. (2010) Long-distance axon regeneration in the mature optic nerve: contributions of oncomodulin, cAMP, and pten gene deletion. *J. Neurosci.* **30**, 15654–15663.

Kuwajima T., Yoshida Y., Takegahara N., Petros T. J., Kumanogoh A., Jessell T. M., Sakurai T. and Mason C. (2012) Optic chiasm presentation of Semaphorin6D in the context of plexin-A1 and Nr-CAM promotes retinal axon midline crossing. *Neuron* **74**, 676–690.

Kuwajima T., Soares C. A., Sitko A. A., Lefebvre V. and Mason C. (2017) SoxC transcription factors promote contralateral retinal ganglion cell differentiation and axon guidance in the mouse visual system. *Neuron* **93**, 1110–1125.e5.

Lang B. T., Cregg J. M., DePaul M. A. *et al*. (2015) Modulation of the proteoglycan receptor PTPσ promotes recovery after spinal cord injury. *Nature* **518**, 404–408.

Lee R., Petros T. J. and Mason C. A. (2008) Zic2 Regulates retinal ganglion cell axon avoidance of ephrinB2 through inducing expression of the guidance receptor EphB1. *J. Neurosci.* **28**, 5910–5919.

Leon S., Yin Y., Nguyen J., Irwin N. and Benowitz L. I. (2000) Lens injury stimulates axon regeneration in the mature rat optic nerve. *J. Neurosci.* **20**, 4615–26.

Leyva-Díaz E. and López-Bendito G. (2013) In and out from the cortex: development of major forebrain connections. *Neuroscience* **254**, 26–44.

Leyva-Díaz E., del Toro D., Menal M. J., Cambray S., Susín R., Tessier-Lavigne M., Klein R., Egea J. and López-Bendito G. (2014) FLRT3 is a Robo1-interacting protein that determines Netrin-1 attraction in developing axons. *Curr. Biol.* **24**, 494–508.

Li D., Zhang P., Yao X., Li H., Shen H., Li X., Wu J. and Lu X. (2018) Exosomes derived from miR-133b-modified mesenchymal stem cells promote recovery after spinal cord injury. *Front. Neurosci.* **12**, 845.

Ling H., Hardy J. and Zetterberg H. (2015) Neurological consequences of traumatic brain injuries in sports. *Mol. Cell. Neurosci.* **66**, 114–122.

Lingor P., Teusch N., Schwarz K., Mueller R., Mack H., Bähr M. and Mueller B. K. (2007) Inhibition of Rho kinase (ROCK) increases neurite outgrowth on chondroitin sulphate proteoglycan in vitro and axonal regeneration in the adult optic nerve in vivo. *J. Neurochem.* **103**, 181–9.

Lingor P., Tönges L., Pieper N., Bermel C., Barski E., Planchamp V. and Bähr M. (2008) ROCK inhibition and CNTF interact on intrinsic signalling pathways and differentially regulate survival and regeneration in retinal ganglion cells. *Brain* **131**, 250–263.

Liu Y., Wang X., Li W. *et al*. (2017) A sensitized IGF1 treatment restores corticospinal axon-dependent functions. *Neuron* **95**, 817–833.e4.

Liu W., Wang Y., Gong F. *et al*. (2019) Exosomes derived from bone mesenchymal stem cells repair traumatic spinal cord injury by suppressing the activation of A1 neurotoxic reactive astrocytes. *J. Neurotrauma* **36**, 469–484.

Long H., Sabatier C., Ma L., Plump A., Yuan W., Ornitz D. M., Tamada A., Murakami F., Goodman C. S. and Tessier-Lavigne M. (2004) Conserved roles for Slit and Robo proteins in midline commissural axon guidance. *Neuron* **42**, 213–223.

Lopez-Leal R. and Court F. A. (2016) Schwann cell exosomes mediate neuron–glia communication and enhance axonal regeneration. *Cell. Mol. Neurobiol.* **36**, 429–436.

Lyuksyutova A. I., Lu C.-C., Milanesio N., King L. A., Guo N., Wang Y., Nathans J., Tessier-Lavigne M. and Zou Y. (2003) Anterior-posterior guidance of commissural axons by Wnt-frizzled signaling. *Science* **302**, 1984–8.

Malatesta P., Hartfuss E. and Götz M. (2000) Isolation of radial glial cells by fluorescent-activated cell sorting reveals a neuronal lineage. *Development* **127**, 5253–63.

Marcos-Mondejar P., Peregrin S., Li J. Y., Carlsson L., Tole S. and Lopez-Bendito G. (2012) The Lhx2 transcription factor controls thalamocortical axonal guidance by specific regulation of Robo1 and Robo2 receptors. *J. Neurosci.* **32**, 4372–4385.

Marillat V., Sabatier C., Failli V., Matsunaga E., Sotelo C., Tessier-Lavigne M. and Chédotal A. (2004) The slit receptor Rig-1/Robo3 controls midline crossing by hindbrain precerebellar neurons and axons. *Neuron* **43**, 69–79.

Martersteck E. M., Hirokawa K. E., Evarts M. *et al*. (2017) Diverse central projection patterns of retinal ganglion cells. *Cell Rep.* **18**, 2058–2072.

Martin V., Mrkusich E., Steinel M. C., Rice J., Merritt D. J. and Whitington P. M. (2008) The L1-type cell adhesion molecule Neuroglian is necessary for maintenance of sensory axon advance in the Drosophila embryo. *Neural Dev.* **3**, 10.

Martin-Villalba A., Winter C., Brecht S., Buschmann T., Zimmermann M. and Herdegen T. (1998) Rapid and long-lasting suppression of the ATF-2 transcription factor is a common response to neuronal injury. *Mol. Brain Res.* **62**, 158–166.

Mazengenya P. and Bhikha R. (2017) The structure and function of the central nervous system and sense organs in the canon of medicine by avicenna. *Arch. Iran. Med.* **20**, 67–70.

Mckee A. C. and Daneshvar D. H. (2015) The neuropathology of traumatic brain injury. *Handb. Clin. Neurol.* 45–66.

McKeon R. J., Schreiber R. C., Rudge J. S. and Silver J. (1991) Reduction of neurite outgrowth in a model of glial scarring following CNS injury is correlated with the expression of inhibitory molecules on reactive astrocytes. *J. Neurosci.* **11**, 3398–411.

Michalski N., Babai N., Renier N., Perkel D. J., Chédotal A. and Schneggenburger R. (2013) Robo3-driven axon midline crossing conditions functional maturation of a large commissural synapse. *Neuron* **78**, 855–68.

Michelsen K. A., Acosta-Verdugo S., Benoit-Marand M., Espuny-Camacho I., Gaspard N., Saha B., Gaillard A. and Vanderhaeghen P. (2015) Area-specific reestablishment of damaged circuits in the adult cerebral cortex by cortical neurons derived from mouse embryonic stem cells. *Neuron* **85**, 982–997.

Mire E., Hocine M., Bazellières E., Jungas T., Davy A., Chauvet S. and Mann F. (2018) Developmental upregulation of Ephrin-B1 silences Sema3C/Neuropilin-1 signaling during post-crossing navigation of corpus callosum axons. *Curr. Biol.* **28**, 1768–1782.e4.

Miyata T., Kawaguchi A., Saito K., Kawano M., Muto T. and Ogawa M. (2004) Asymmetric production of surface-dividing and non-surface-dividing cortical progenitor cells. *Development* **131**, 3133–45.

Moreno-Bravo J. A., Roig Puiggros S., Mehlen P. and Chédotal A. (2019) Synergistic activity of floor-plate- and ventricular-zone-derived netrin-1 in spinal cord commissural axon guidance. *Neuron* **101**, 625–634.e3.

Müller M. and Holländer H. (1988) A small population of retinal ganglion cells projecting to the retina of the other eye - an experimental study in the rat and the rabbit. *Exp. Brain Res.* **71**, 611–617.

Murcia-Belmonte V., Coca Y., Vegar C. *et al*. (2019) A retino-retinal projection guided by Unc5c emerged in species with retinal waves. *Curr. Biol.* **29**, 1149–1160.e4.

Nadal-Nicolás F. M., Valiente-Soriano F. J., Salinas-Navarro M., Jiménez-López M., Vidal-Sanz M. and Agudo-Barriuso M. (2015) Retino-retinal projection in juvenile and young adult rats and mice. *Exp. Eye Res.* **134**, 47–52.

Nagashima F., Suzuki I. K., Shitamukai A., Sakaguchi H., Iwashita M., Kobayashi T., Tone S., Toida K., Vanderhaeghen P. and Kosodo Y. (2014) Novel and robust transplantation reveals the acquisition of polarized processes by cortical cells derived from mouse and human pluripotent stem cells. *Stem Cells Dev.* **23**, 2129–2142.

Nagatsuka Y., Horibata Y., Yamazaki Y., Kinoshita M., Shinoda Y., Hashikawa T., Koshino H., Nakamura T. and Hirabayashi Y. (2006) Phosphatidylglucoside exists as a single molecular species with saturated fatty acyl chains in developing astroglial membranes. *Biochemistry* **45**, 8742–8750.

Nawabi H., Briancon-Marjollet A., Clark C. *et al*. (2010) A midline switch of receptor processing regulates commissural axon guidance in vertebrates. *Genes Dev.* **24**, 396–410.

Nayagam B. A., Muniak M. A. and Ryugo D. K. (2011) The spiral ganglion: connecting the peripheral and central auditory systems. *Hear. Res.* **278**, 2–20.

Niquille M., Garel S., Mann F. *et al*. (2009) Transient neuronal populations are required to guide callosal axons: a role for semaphorin 3C. *PLoS Biol.* **7**, e1000230.

Noctor S. C., Flint A. C., Weissman T. A., Dammerman R. S. and Kriegstein A. R. (2001) Neurons derived from radial glial cells establish radial units in neocortex. *Nature* **409**, 714–720.

Noctor S. C., Martínez-Cerdeño V., Ivic L. and Kriegstein A. R. (2004) Cortical neurons arise in symmetric and asymmetric division zones and migrate through specific phases. *Nat. Neurosci.* **7**, 136–44.

Norsworthy M. W., Bei F., Kawaguchi R. *et al*. (2017) Sox11 expression promotes regeneration of some retinal ganglion cell types but kills others. *Neuron* **94**, 1112–1120.e4.

Northcutt R. G. (2006) Understanding vertebrate brain evolution. *Integr. Comp. Biol.* **42**, 743–756.

Onishi K. and Zou Y. (2017) Sonic hedgehog switches on Wnt/planar cell polarity signaling in commissural axon growth cones by reducing levels of Shisa2. *Elife* **6**, 1–20.

Onishi K., Hollis E. and Zou Y. (2014) Axon guidance and injury-lessons from Wnts and Wnt signaling. *Curr. Opin. Neurobiol.* **27**, 232–40.

Pak W., Hindges R., Lim Y.-S., Pfaff S. L. and O'Leary D. D. M. (2004) Magnitude of binocular vision controlled by Islet-2 repression of a

genetic program that specifies laterality of retinal axon pathfinding. *Cell* **119**, 567–578.

Panza P., Sitko A. A., Maischein H.-M., Koch I., Flötenmeyer M., Wright G. J., Mandai K., Mason C. A. and Söllner C. (2015) The LRR receptor Islr2 is required for retinal axon routing at the vertebrate optic chiasm. *Neural Dev.* **10**, 23.

Park K. K., Liu K., Hu Y., *et al*. (2008) Promoting axon regeneration in the adult CNS by modulation of the PTEN/mTOR pathway. *Science* **322**, 963–966.

Parra L. M. and Zou Y. (2010) Sonic hedgehog induces response of commissural axons to Semaphorin repulsion during midline crossing. *Nat. Neurosci.* **13**, 29–35.

Peng J., Fabre P. J., Dolique T. and Swikert S. M. (2018) Sonic hedgehog is a remotely produced cue that controls axon guidance trans-axonally at a midline choice point. *Neuron* **97**, 326–340.

Péron S., Droguerre M., Debarbieux F., Ballout N., Benoit-Marand M., Francheteau M., Brot S., Rougon G., Jaber M. and Gaillard A. (2017) A delay between motor cortex lesions and neuronal transplantation enhances graft integration and improves repair and recovery. *J. Neurosci.* **37**, 1820–1834.

Petros T. J., Bryson J. B. and Mason C. (2010) Ephrin-B2 elicits differential growth cone collapse and axon retraction in retinal ganglion cells from distinct retinal regions. *Dev. Neurobiol.* **70**, 781–794.

Philipp M., Niederkofler V., Debrunner M., Alther T., Kunz B. and Stoeckli E. T. (2012) RabGDI controls axonal midline crossing by regulating Robo1 surface expression. *Neural Dev.* **7**, 36.

Qin S., Zou Y. and Zhang C.-L. (2013) Cross-talk between KLF4 and STAT3 regulates axon regeneration. *Nat. Commun.* **4**, 2633.

Raitano S., Ordovàs L., Muynck L. *et al*. (2015) Restoration of progranulin expression rescues cortical neuron generation in an induced pluripotent stem cell model of frontotemporal dementia. *Stem Cell Rep.* **4**, 16–24.

Rakic P. and Yakovlev P. I. (1968) Development of the corpus callosum and cavum septi in man. *J. Comp. Neurol.* **132**, 45–72.

Ramón y Cajal S. (1914) *Estudios sobre la degeneración y regeneración del sistema nerviosa*, Vol. **2**. Hijos de Nicolás Moza, Madrid.

Rasmussen J. P. and Sagasti A. (2017) *Learning to Swim, Again: Axon Regeneration in Fish*. Academic Press, Cambridge, MA.

Rebsam A., Bhansali P. and Mason C. A. (2012) Eye-specific projections of retinogeniculate axons are altered in albino mice. *J. Neurosci.* **32**, 4821–4826.

Renier N., Schonewille M., Giraudet F., Badura A., Tessier-Lavigne M., Avan P., Zeeuw C. I. and De Chédotal A. (2010) Genetic dissection of the function of hindbrain axonal commissures. *PLoS Biol.* **8**, e1000325.

Ribas V. T., Koch J. C., Michel U., Bähr M. and Lingor P. (2017) Attenuation of axonal degeneration by calcium channel inhibitors improves retinal ganglion cell survival and regeneration after optic nerve crush. *Mol. Neurobiol.* **54**, 72–86.

Rosenberg A. F., Wolman M. A., Franzini-Armstrong C. and Granato M. (2012) In vivo nerve-macrophage interactions following peripheral nerve injury. *J. Neurosci.* **32**, 3898–3909.

Rosenberg A. F., Isaacman-Beck J., Franzini-Armstrong C. and Granato M. (2014) Schwann cells and deleted in colorectal carcinoma direct regenerating motor axons towards their original path. *J. Neurosci.* **34**, 14668–81.

Ruiz de Almodovar C., Fabre P. J., Knevels E. *et al*. (2011) VEGF mediates commissural axon chemoattraction through its receptor Flk1. *Neuron* **70**, 966–978.

Sabatier C., Plump A. S., Le Ma, Brose K., Tamada A., Murakami F., Lee E. Y.-H. and Tessier-Lavigne M. (2004) The divergent robo family protein Rig-1/Robo3 is a negative regulator of slit responsiveness required for midline crossing by commissural axons. *Cell* **117**, 157–169.

Safieddine S., El-Amraoui A. and Petit C. (2012) The auditory hair cell ribbon synapse: from assembly to function. *Annu. Rev. Neurosci.* **35**, 509–528.

Saito S. (1997) Effects of lysophosphatidic acid on primary cultured chick neurons. *Neurosci. Lett.* **229**, 73–76.

Sanes J. R. and Masland R. H. (2015) The types of retinal ganglion cells: current status and implications for neuronal classification. *Annu. Rev. Neurosci.* **38**, 221–246.

Schmandke A., Schmandke A. and Schwab M. E. (2014) Nogo-A: multiple roles in CNS development, maintenance, and disease. *Neuroscientist* **20**, 372–386.

Schmucker D., Clemens J. C., Shu H., Worby C. A., Xiao J., Muda M., Dixon J. E. and Zipursky S. L. (2000) Drosophila Dscam is an axon guidance receptor exhibiting extraordinary molecular diversity. *Cell* **101**, 671–84.

Scholz T., Krichevsky A., Sumarto A., Jaffurs D., Wirth G., Paydar K. and Evans G. (2009) Peripheral nerve injuries: an international survey of current treatments and future perspectives. *J. Reconstr. Microsurg.* **25**, 339–344.

Serafini T., Colamarino S. A., Leonardo E. D., Wang H., Beddington R., Skarnes W. C. and Tessier-Lavigne M. (1996) Netrin-1 is required for commissural axon guidance in the developing vertebrate nervous system. *Cell* **87**, 1001–14.

Shrestha B. R., Chia C., Wu L., Kujawa S. G., Liberman M. C. and Goodrich L. V. (2018) Sensory neuron diversity in the inner ear is shaped by activity. *Cell* **174**, 1229–1246.e17.

Silver J., Lorenz S. E., Wahlsten D. and Coughlin J. (1982) Axonal guidance during development of the great cerebral commissures: descriptive and experimental studies, in vivo, on the role of preformed glial pathways. *J. Comp. Neurol.* **210**, 10–29.

Sivasankaran R., Pei J., Wang K. C., Zhang Y. P., Shields C. B., Xu X.-M. and He Z. (2004) PKC mediates inhibitory effects of myelin and chondroitin sulfate proteoglycans on axonal regeneration. *Nat. Neurosci.* **7**, 261–268.

Sloan T. F. W. W., Qasaimeh M. A., Juncker D., Yam P. T. and Charron F. (2015) Integration of shallow gradients of Shh and netrin-1 guides commissural axons. *PLOS Biol.* **13**, e1002119.

Smart I. H. M. (2002) Unique morphological features of the proliferative zones and postmitotic compartments of the neural epithelium giving rise to striate and extrastriate cortex in the monkey. *Cereb. Cortex* **12**, 37–53.

Smith P. D., Sun F., Park K. K., Cai B., Wang C., Kuwako K., Martinez-Carrasco I., Connolly L. and He Z. (2009) SOCS3 deletion promotes optic nerve regeneration in vivo. *Neuron* **64**, 617–623.

Steinel M. C. and Whitington P. M. (2009) The atypical cadherin Flamingo is required for sensory axon advance beyond intermediate target cells. *Dev. Biol.* **327**, 447–457.

Stoeckli E. T. (2018) Understanding axon guidance: are we nearly there yet? *Development* **145**, dev151415.

Strochlic L., Dwivedy A., van Horck F. P. G., Falk J.and Holt C. E. (2007) A role for S1P signalling in axon guidance in the Xenopus visual system. *Development* **135**, 333–342.

Suárez R., Gobius I. and Richards L. J. (2014) Evolution and development of interhemispheric connections in the vertebrate forebrain. *Front. Hum. Neurosci.* **8**, 497.

Sun F., Park K. K., Belin S. *et al*. (2011) Sustained axon regeneration induced by co-deletion of PTEN and SOCS3. *Nature* **480**, 372–375.

Suzuki I. K. and Vanderhaeghen P. (2015) Is this a brain which I see before me? Modeling human neural development with pluripotent stem cells. *Development* **142**, 3138–3150.

Suzuki I. K., Gacquer D., Heurck R. *et al*. (2018) Human-specific NOTCH2NL genes expand cortical neurogenesis through Delta/Notch regulation. *Cell* **173**, 1370–1384.e16.

Theotokis P., Kleopa K. A., Touloumi O. *et al*. (2015) Connexin43 and connexin47 alterations after neural precursor cells transplantation in experimental autoimmune encephalomyelitis. *Glia* **63**, 1772–1783.

Tiberi L., Vanderhaeghen P. and van den Ameele J. (2012) Cortical neurogenesis and morphogens: diversity of cues, sources and functions. *Curr. Opin. Cell Biol.* **24**, 269–276.

Tornero D., Wattananit S., Grønning Madsen M. *et al*. (2013) Human induced pluripotent stem cell-derived cortical neurons integrate in stroke-injured cortex and improve functional recovery. *Brain* **136**, 3561–3577.

del Toro D., Ruff T., Cederfjäll E., Villalba A., Seyit-Bremer G., Borrell V. and Klein R. (2017) Regulation of cerebral cortex folding by controlling neuronal migration via FLRT adhesion molecules. *Cell* **169**, 621–635.e16.

Tóth P. and Strznicky C. (1989) Retino-retinal projections in three anuran species. *Neurosci. Lett.* **104**, 43–47.

Unni D. K., Piper M., Moldrich R. X., Gobius I., Liu S., Fothergill T., Donahoo A.-L. S., Baisden J. M., Cooper H. M. and Richards L. J. (2012) Multiple Slits regulate the development of midline glial populations and the corpus callosum. *Dev. Biol.* **365**, 36–49.

Varadarajan S. G., Kong J. H., Phan K. D., Kao T.-J., Panaitof S. C., Cardin J., Eltzschig H., Kania A., Novitch B. G. and Butler S. J. (2017) Netrin1 produced by neural progenitors, not floor plate cells, is required for axon guidance in the spinal cord. *Neuron* **94**, 790–799.e3.

Waller A. (1851) Experiments on the section of the glosso-pharyngeal and hypoglossal nerves of the frog, and observations of the alterations produced thereby in the structure of their primitive fibres. *Edinburgh Med. Surg. J.* **76**, 369–376.

Wang H. C. and Bergles D. E. (2015) Spontaneous activity in the developing auditory system. *Cell Tissue Res.* **361**, 65–75.

Wang K. H., Brose K., Arnott D., Kidd T., Goodman C. S., Henzel W. and Tessier-Lavigne M. (1999) Biochemical purification of a mammalian Slit protein as a positive regulator of sensory axon elongation and branching. *Cell* **96**, 771–784.

Wang J., Zugates C. T., Liang I. H., Lee C.-H. J. and Lee T. (2002a) Drosophila Dscam is required for divergent segregation of sister branches and suppresses ectopic bifurcation of axons. *Neuron* **33**, 559–71.

Wang K. C., Kim J. A., Sivasankaran R., Segal R. and He Z. (2002b) p75 interacts with the Nogo receptor as a co-receptor for Nogo, MAG and OMgp. *Nature* **420**, 74–78.

Wang K. C., Koprivica V., Kim J. A., Sivasankaran R., Guo Y., Neve R. L. and He Z. (2002c) Oligodendrocyte-myelin glycoprotein is a Nogo receptor ligand that inhibits neurite outgrowth. *Nature* **417**, 941–944.

Wang Q., Marcucci F., Cerullo I. and Mason C. (2016) Ipsilateral and contralateral retinal ganglion cells express distinct genes during decussation at the optic chiasm. *eNeuro* **3**, ENEURO.0169-16.2016.

Wang X., Liu Y., Li X. *et al*. (2017) Deconstruction of corticospinal circuits for goal-directed motor skills. *Cell* **171**, 440–455.e14.

Wernig M. (2004) Functional integration of embryonic stem cell-derived neurons in vivo. *J. Neurosci.* **24**, 5258–5268.

Williams S. E., Mann F., Erskine L., Sakurai T., Wei S., Rossi D. J., Gale N. W., Holt C. E., Mason C. A. and Henkemeyer M. (2003) Ephrin-B2 and EphB1 mediate retinal axon divergence at the optic chiasm. *Neuron* **39**, 919–35.

Williams S. E., Mason C. A. and Herrera E. (2004) The optic chiasm as a midline choice point. *Curr. Opin. Neurobiol.* **14**, 51–60.

Williams S. E., Grumet M., Colman D. R., Henkemeyer M., Mason C. A. and Sakurai T. (2006) A role for Nr-CAM in the patterning of binocular visual pathways. *Neuron* **50**, 535–547.

Wilson S. I., Shafer B., Lee K. J. and Dodd J. (2008) A molecular program for contralateral trajectory: Rig-1 control by LIM homeodomain transcription factors. *Neuron* **59**, 413–424.

Wu Z., Sweeney L. B., Ayoob J. C., Chak K., Andreone B. J., Ohyama T., Kerr R., Luo L., Zlatic M. and Kolodkin A. L. (2011) A Combinatorial semaphorin code instructs the initial steps of sensory circuit assembly in the Drosophila CNS. *Neuron* **70**, 281–298.

Wu Z., Makihara S., Yam P. T. *et al*. (2019) Long-range guidance of spinal commissural axons by Netrin1 and sonic hedgehog from midline floor plate cells. *Neuron* **101**, 635–647.e4.

Yam P. T., Kent C. B., Morin S., Farmer W. T., Alchini R., Lepelletier L., Colman D. R., Tessier-Lavigne M., Fournier A. E. and Charron F. (2012) 14-3-3 Proteins regulate a cell-intrinsic switch from sonic hedgehog-mediated commissural axon attraction to repulsion after midline crossing. *Neuron* **76**, 735–749.

Yamauchi K., Yamazaki M., Abe M., Sakimura K., Lickert H., Kawasaki T., Murakami F. and Hirata T. (2017) Netrin-1 derived from the ventricular zone, but not the floor plate, directs hindbrain commissural axons to the ventral midline. *Sci. Rep.* **7**, 11992.

Yoshikawa S., McKinnon R. D., Kokel M. and Thomas J. B. (2003) Wnt-mediated axon guidance via the Drosophila derailed receptor. *Nature* **422**, 583–588.

Zelina P., Blockus H., Zagar Y. *et al*. (2014) Signaling switch of the axon guidance receptor Robo3 during vertebrate evolution. *Neuron* **84**, 1258–1272.

Zolog A. (1994) Somatic motor nerve and function as conceived by Alcmaeon of Croton. *J. Hist. Neurosci.* **3**, 261–262.

Zou Y. (2004) Wnt signaling in axon guidance. *Trends Neurosci.* **27**, 528–532.

Zou Y. (2012) Does planar cell polarity signaling steer growth cones? *Curr. Top. Dev. Biol.* **101**, 141–160.

Abstract

The sole output of the eye are the retinal ganglion cells (RGCs) that project into multiple brain nuclei via the optic nerve (ON). A key choice point for RGC axons is to decussate at the midline to project either ipsi-laterally or contra-laterally. The first aim of this thesis is to evaluate whether the narrow set of molecules regulating RGC decussation is evolutionarily conserved. Secondly, we strive for a finer understanding of specific axon guidance molecules by using conditional mutant mice. To this end, we design a novel clearing tool (EyeDISCO) to access the entire visual system in three dimensions, from the eyes to the brain proper. First, we uncover that ipsi-lateral retinal projections (IRPs) are present in the first ray-finned fish as well as lobe-finned fish. These results suggest that IRPs most likely emerged in the common vertebrate ancestor. We further show that the molecular program orchestrating IRPs is not evolutionarily conserved in a ray-finned species. This hints at the fundamental idea that other cues may be responsible for the guidance of IRPs. Second, we shed light on the role of Dcc/Netrin-1 in RGC projections of mice. Remarkably, while a significant subset of RGC axons are unable to project into the ON, we reveal that a large population of RGCs still manages to project correctly in the absence of *Dcc* and *Netrin-1*. This heterogeneity underlines the probable interplay of multiple other, still undiscovered, guidance cues. Together, our work proposes a more complex model for RGC targeting across species and warrants future studies to take on an evolutionary perspective to better understand the fundamental mechanism at play during axon guidance.

Keywords

Axon guidance ; Visual system ; Tissue clearing